# Forward

I met Professor William Tifft in 1980 when I was a graduate student working for my doctorate in mathematics at the University of Arizona while teaching physics and mathematics courses at Pima Community College. One afternoon I was invited to join Bill for lunch with one of my mathematics professors, Dr. Carl DeVito. Carl and Bill had been meeting occasionally to discuss Bill's cosmological redshift research. It was quite an interesting discussion and I was introduced to Bill's observation of the existence of periodic redshift jumps of, or related to, 72 km/s in various types of galaxies. At the time, my graduate studies and eventually my research interests, would focus on gravity, quantum gravity in particular. I found this "quantum" jump to be quite fascinating, thinking there might be some aspect useful to my own research.

After completing my degree I continued my teaching at Pima Community College, moving on to assume the position of Chair of Physics at West Campus, Pima Community College in 1986. During this interval I continued my research with Professor Hanno Rund in the area of symplectic geometry and contact vector fields at the University of Arizona. During this time I read an interesting article on 'Quantum Dissidents' in *Scientific American* wherein Bill's work on redshift quantization was highlighted. I was immediately attracted to the idea that Bill's observations and conclusions might have a mathematical basis yet to be developed. I thought this to be the perfect opportunity to explore a new direction with possible applications to my research.

Upon contacting Bill, I discovered that he and Carl DeVito, together with astrophysicist John Cocke also from the University of Arizona Steward Observatory, had created a small discussion group specifically concerning quantized redshifts. In addition, Bill's work had expanded to include a more detailed study of the physical foundations of time, and their discussions broadened to consider such foundations. I knew that among the astronomical and scientific community, Professor Tifft's reputation as an exceptional observational astronomer was well known and, as such, I had little doubt that what he observed actually did exist. However, as with every outlier scientific idea, it generated quite a bit of criticism, which understandably resulted in much controversy, mostly negative and at times quite hostile. As such Bill did warn me that even referencing his work might result in my scientific demise. This did nothing but further excite me to investigate this most fascinating idea of quantum redshifts in galaxies.

I immediately asked to become a part of the group and became a member in 1996. By this time the entire subject had been raising further controversies since a few other observers came to similar observational conclusions. In addition several scientists from around the globe were questioning both the physical and mathematical basis of time. Because of this our group decided it was time to hold an international conference in order to bring together concerned scientists, pro and con, to discuss the current state of research in these areas.

Subsequently, we were able to obtain the necessary funding to establish the first International Conference on Modern Mathematical Models of Time and their Applications to Physics and Cosmology, held in April 1996 at the University of Arizona. The Proceedings of the

conference were published by Kluwer Academic Publishers in *Astrophysics and Space Science* in 1996, and book form the following year. To the best of my knowledge this was the first conference to consider seven fundamental areas we thought significant to bring together for the scientific community: (1) The Redshift; (2) Critical Properties of the Universe; (3) Statistical Methods; (4) New Approaches to Cosmology; (5) Gravitation and Time in General Relativity; (6) Nuclear and Particle Physics; and (7) Mathematical Models and Methods.

As a result of the works submitted during this conference our group of initial researchers, William Tifft, Anthony Pitucco, John Cocke, and Carl DeVito, established the Scientific Association for the Study of Time in Physics and Cosmology (SASTPC) in an effort to continue research in this area. In addition my colleague and friend Dr. Stewart Barr joined our group for contributions from the philosophical foundations of physics, mathematics and cosmology. Since that time Bill, myself and Stewart continued our research in the areas of alternative cosmologies, mathematical physics, and the philosophy of science. To date we have developed the SASTPC into an active blog site (http://sastpc.com) to encourage all interested to participate in active discussion and contemporary research in these areas.

The most important result though is this, Bill Tifft's most remarkable and extraordinary work "Redshift, Key to Cosmology". In this book Bill has introduced a truly innovative approach into understanding the foundations of cosmology and modern physics. Bill has been able to support his observational findings over the past 45 years with this comprehensive summary. With very little mathematical background one can begin with his observational findings and sift through a rather extensive and innovative treatment of the foundations of time and cosmology. His attention to detail is extensive and unwavering, which makes this an even more interesting and significant work.

As with any really new and creative approach, to understand this work a word of caution is in order. One must be able to suspend momentarily the standard approach to time and how it has been used since the 16th century in creating the physical model of the world we live in. As revolutionary as were the new ideas that emerged during the Enlightenment, so it is today with any emerging scientific ideas, the most common reaction is simply rejection. I do hope we have learned, after these many years, to distinguish between the outlandish and the outlier, and although Bill's work may be considered the former, closer inspection may yield, more likely, the latter.

Anthony Pitucco
Retired Chair of Physics, West Campus Pima Community College, Tucson, Arizona
September 23, 2014

# Preface

In year 2000 I developed a series of seminars to summarize my work on the nature of the cosmic redshift, which began in 1970. As I initiated work on a biography in 2010 it became apparent that an updated and supplemented form of the seminar series provided a good summary and extension of my work, which has come to be called Quantum Temporal Cosmology (QTC). As such the series provides a key part of my biography, a cohesive presentation of my life's work based upon my studies of the redshift. A more personal biographical work entitled "An Astronomer's Timeline" is in preparation which includes other aspects of my scientific work. Although most of my work with the redshift has been published professionally it has been controversial and widely ignored, but appears to give a much better picture of reality than conventional cosmology widely accepted today. This book presents and extends the data and analysis which led to QTC.

When I began the study of galaxies and the redshift not much was known but much was assumed. Conventional motion governed by gravitation was assumed to apply and virtually never seriously questioned (although various alternate theories have been suggested). As my early studies proceeded, however, it quickly became apparent that certain classical concepts did not stand up to new investigations, and two key questions, 'what really *is* the redshift' and 'what exactly *are* galaxies' took center stage. When really unexpected results to such questions continued to emerge I felt they must be pursued. The central challenge of my life in many respects has always been to go where no one has gone before. That led to deeper 'what is' questions, what really is gravity?, what really is the structure of matter and energy?, and finally what is space and time?, which has led to QTC. The pursuit of such findings, no matter how they threaten cherished older beliefs is the essence of science. In my mind many problems in classical cosmology appear to be there because too many 'what is' questions were not pursued or were ignored. QTC is very different from classical cosmology because it pursued such tests, and believe it or not, many classical cosmological problems seem to go away.

I have left the writing in seminar form with figures and tables presented as though they were a slide or transparency presented while lecturing. References in text direct attention to figures and external references as they occur and figures with captions are printed as close as possible to their first reference. Figure numbers in text are given as S#.Fig# to facilitate back reference in text and between seminars, for example 3.6 for the sixth figure in the third seminar. Section references are given as (S#.Sec#.subsec#) where S=Seminar, Sec= section, subsec = subsection, again for back reference. Publication references are given in brackets, for example [88] or [XY] where numbers refer to items by or about my work, and letters refer to external publications. The final appendix provides the conversion to actual publication locations. This process allows additions or commentary associated with references, for example listing a paper presented at a meeting as well as the related publication and including publications not specifically referenced in the text. A fairly comprehensive list of my publications is included in the listing which covers work extending beyond this book in a biographical sense.

I have been investigating the redshift for more than 40 years; this book provides an opportunity to bring together many of the ideas in one cohesive picture. The story of my original redshift work has three broad facets, 1) the early phase where the redshift was found to correlate with intrinsic properties of galaxies in violation with classical expectations, 2) the empirical study phase where the redshift was found to be a discreet globally 'quantized' quantity, and 3) detailed studies of the redshift after learning to predict the quantized values involved. The diagram at the end of this preface provides a broad historical timeline of my redshift investigations with publication references through about 1997. The reference numbers in the illustration use an older numbering system, however the references are listed directly within the diagram. As noted above, the reference listing for the book itself is provided in the fourth appendix.

This book, begun seriously in 2013, integrates original content with new analysis and understanding as I assembled the material. References in the historical outline at the end of this preface mark key stages in the development of Quantum Temporal Cosmology concepts. The first three seminars develop aspects of each major stage of my original research relating to the redshift. The fourth seminar applies concepts developed in particle physics, including major aspects added quite recently. The fifth seminar extends the concepts to high redshift, essentially as an outgrowth of my invited presentation at the Hoyle Memorial Conference in Cardiff, England in 2002 at the time of my retirement from the University of Arizona Steward Observatory. Seminars six through eight then bring the material together to develop the concepts and applications of Quantum Temporal Cosmology. Supplements provide supporting information including important unpublished writings utilized in the text along with important unpublished data and references.

Many direct and indirect personal contacts played a role in determining the nature of the type of scientist I became, and played roles at various stages as my scientific work evolved and ultimately led to Quantum Temporal Cosmology. I knew in grade school that my path lay in science and by high school in astronomy. My early fascination with galaxies, cemented with associations and encouragement by both Professors Shapley and Bok at Harvard clearly directed my path into the galactic and extragalactic field. Harvard opened the door to observationally driven research and especially the new opportunities in photoelectric photometry. With the startup help in association with then graduate students like Harlan Smith I developed programs of my own which led to early publications and active observational programs at Mount Wilson as I entered my graduate years at Caltech. With the encouragement of men like Professor Osterbrock and Code (my dissertation director) I carried out original eight color studies of galaxy nuclear and radial color patterns which revealed early information relating to the role of nuclei in defining galaxies. Perhaps the man I hold in highest regard as a role model to emulate is Dr. Walter Baade. I got to know him in part while working as a postdoctoral fellow at the Australian National University while at Mount Stromlo Observatory. During that time I carried photometry down to 20th magnitude to calibrate RR Lyrae stars in the Small Magellanic Cloud as a step in the extragalactic distance scale. To these men especially, I give my thanks for guiding me to become the scientist I am. Although I never actually met Professor Carl Seyfert, who offered me my first professional position at Vanderbilt University, Dyer Observatory, I hold him in especially high esteem as a pioneer in recognizing the key role of galactic nuclei. His tragic death (a few hours before I was to meet him for the first time) accelerated my move to Lowell Observatory in 1961. My galaxy photometry at Lowell, then under the fine

directorship of Dr John Hall, marks the real beginning of the road to QTC. I think it is interesting that the photometry was done using the same cold box I utilized in Australia. The box was constructed to my design by Edison Pettit who was the scientist who did most of the earliest photometry of galaxies at Mount Wilson. I plan to contribute that cold box to the archival collection at Lowell Observatory. It is with full appreciation that I also acknowledge educational support as a Westinghouse Science Talent Search winner in 1950, four years of Harvard scholarship support, Four years of NSF Graduate and two years of NSF Postdoctoral Fellowships.

After devoting several years to an association with Professor Meinel relating to the developing field of space astronomy at the University of Arizona I returned actively to extragalactic research in the early 1970s. The early work built upon follow-up from my IAU Symposium 44 presentation, as noted in the opening of this book, suggested anomalous behavior of redshifts and nuclear properties of galaxies. During early (and in several cases more recent and current) development of both redshift and large scale structure studies, I would like to acknowledge the involvement of graduate students including Steven Gregory, Leo Connolly and Daniel Christlein in particular who completed their doctorates during my tenure, and undergraduate Nowell Jobson. Massimo Tarenghi, at Steward Observatory as an ESO Fellow, also joined with me in several studies, especially involving active galaxies. My very highest level of appreciation goes to John Cocke who joined me directly in the redshift research in 1983, bringing his superb theoretical insight into the studies. The incredible contributions to understanding the quantized nature of redshifts by Ari Lehto and confirming quantization by William Napier and colleagues, stand by themselves as fundamental independent contributions to the redshift story and beyond to fundamental physics in the early 90s. Finally it is my pleasure to acknowledge the support, encouragement and assistance that developed between my work and Anthony Pitucco from Physics at Pima Community College, Carl DeVito in mathematics at the University of Arizona and Stuart Barr in Philosophy at Pima Community College in the 1990s that continues to flourish. Longer term archival links between my work and Lowell Observatory are also involved as the birthplace of the detailed data that basically opened the door that led to QTC. My beloved wife Janet, who added a world of art and culture to my life and consistently defended my work with anyone who questioned it, and two of my children Amy Lyons and Jennifer Tifft who specifically helped me put parts of this book together deserve my heartfelt appreciation.

William G. Tifft
Professor Emeritus, University of Arizona, Tucson, Arizona
September, 2014

## Historical Timelines

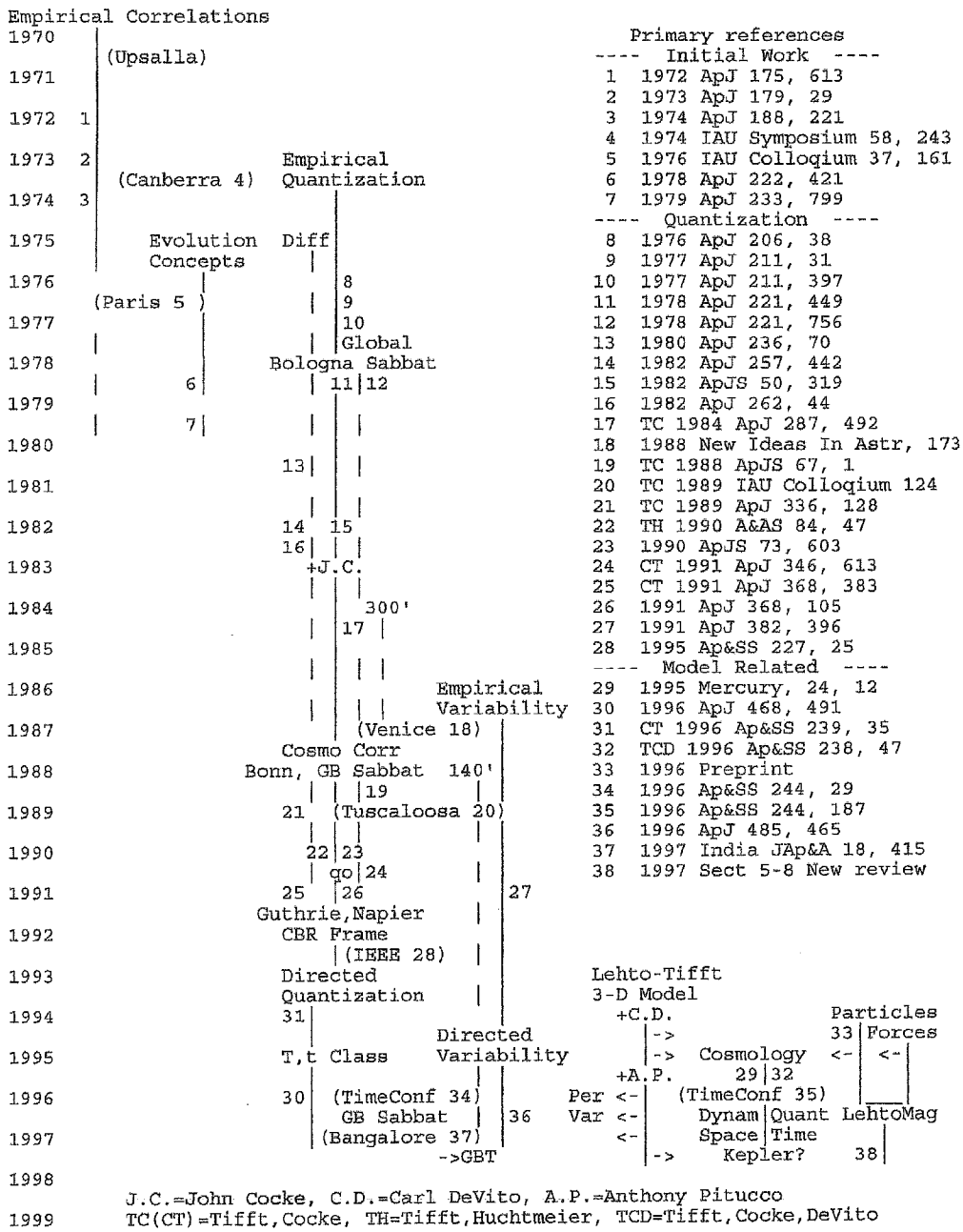


Primary references

---- Initial Work ----

1 1972 ApJ 175, 613
2 1973 ApJ 179, 29
3 1974 ApJ 188, 221
4 1974 IAU Symposium 58, 243
5 1976 IAU Colloqium 37, 161
6 1978 ApJ 222, 421
7 1979 ApJ 233, 799

---- Quantization ----

8 1976 ApJ 206, 38
9 1977 ApJ 211, 31
10 1977 ApJ 211, 397
11 1978 ApJ 221, 449
12 1978 ApJ 221, 756
13 1980 ApJ 236, 70
14 1982 ApJ 257, 442
15 1982 ApJS 50, 319
16 1982 ApJ 262, 44
17 TC 1984 ApJ 287, 492
18 1988 New Ideas In Astr, 173
19 TC 1988 ApJS 67, 1
20 TC 1989 IAU Colloqium 124
21 TC 1989 ApJ 336, 128
22 TH 1990 A&AS 84, 47
23 1990 ApJS 73, 603
24 CT 1991 ApJ 346, 613
25 CT 1991 ApJ 368, 383
26 1991 ApJ 368, 105
27 1991 ApJ 382, 396
28 1995 Ap&SS 227, 25

---- Model Related ----

29 1995 Mercury, 24, 12
30 1996 ApJ 468, 491
31 CT 1996 Ap&SS 239, 35
32 TCD 1996 Ap&SS 238, 47
33 1996 Preprint
34 1996 Ap&SS 244, 29
35 1996 Ap&SS 244, 187
36 1996 ApJ 485, 465
37 1997 India JAp&A 18, 415
38 1997 Sect 5-8 New review

*I dedicate this book to four wonderful women*
*My mother Marguerite*
*Who gave me life so I could see this incredible universe*
*My beloved wife and artist Janet Ann*
*Who greatly expanded my appreciation and understanding of what life is*
*And my daughters Jennifer Gail and Amy Kathleen*
*Who demonstrate and helped me tell the story of time*

A story of QTC by Jennifer

*What are stars*
*But Light*
*Leaking out of*
*Time*

*Do We Fly?*
*Fall?*
*Spin Within the Void*
*Of Nothingness*
*Unknowingness?*

*And Yet*
*We*
*Are*

# Table of Contents

**Chapter 1:** What is the Cosmic Redshift? Correlations and Implications 1970-1978

1.1 Introduction 1
1.1 Modern 'Classical' Cosmology 2
1.2 Problems and Questions 3

1.2 Testing the Nature of the Redshift 4

1.3 Correlations, How It All Began 5
3.1 Redshift-Magnitude Bands, Effects in the Coma Cluster 6
3.2 Verification, Evaluation, and Extensions to Other Clusters 10

1.4 Extending Work to Total Magnitudes, Outer Coma 13
4.1 Comparing Clusters, A1367 15
4.2 Redshift-Magnitude Bands in a High Redshift Cluster 17
4.3 What About Quasars? 18

1.5 Structure Within Redshift-Magnitude Bands 20
5.1 Structure and Morphology, Galaxy Evolution? 22

1.6 Introducing Active Galaxies 28
6.1 Radio Sources 28
6.2 Emission Line Galaxies 30

1.7 Cross-Bands and Vertical-Structures 32
7.1 Cross-Band Structure Development 34
7.2 Associating Vertical-Sequences with Cross-Bands 35

1.8 Summarizing Structures, and Changing Direction 38

1.9 Redshift Quantization 39

**Chapter 2:** Is the Redshift Quantized, Variable? The Empirical Period, 1973 to 1992, Learning About z

2.1 Introduction 41

2.2 The Discovery of Redshift Quantization 41
2.1 Introducing the Concepts to Astrophysics 42

2.3 Evaluating Quantization 44
3.1 What Is A Galaxy? 44
3.2 Binary Galaxies, The Perfect Test of Quantization 49
3.3 Karachentsev Pairs and the Peterson Sample 50
3.4 The Karachentsev Study Findings, Evaluating I/O Ratios 52
3.5 Later Precision Work 54
3.6 The Exclusion Principle 58
3.7 A Glance Ahead 59

2.4 Large Scale Structure, Clouds of Galaxies 61
4.1 The Orientation of Pairs 62

2.5 Global Quantization, Turning to 21 cm Data 65
5.1 The Galactocentric Rest Frame, The Solar Motion 67

2.6 Introducing Redshift Variability 71
6.1 Redshift Precision at 21 cm 71
6.2 Comparing With Older Observations, Deviations! 72
6.3 Using Phase-Deviation Diagrams, Transition Cascades 73
6.4 Redshift Accuracy, Consistency and Asymmetry 79

2.7 The Cosmological Correction 79

2.8 The Cosmic Background Rest Frame 82

2.9 Independent Confirmation! 86

**Chapter 3:** Redshifts and the Dimensions of Time, Defining the Properties of a New Cosmology, 1993 to Date

3.1 Introduction 89

3.2 The United Kingdom Stirs the Pot 89

3.3 Lehto's Concept 90
3.1 Virgo Opens the Door, Expanding Lehto's Concept 91
3.2 Statistical Methods 93
3.3 Rest Frames, The Cosmic Background Dipole Association 94

3.4 Exploring the Cosmic Rest Frame 98
4.1 Sorting Through Lehto-Tifft Redshift Periodicity Structure 98
4.2 Morphology and T, Intermediate Spirals, T=0 99
4.3 Spirals with Wide Profiles, T=6 100
4.4 Extreme Dwarfs with Narrow Profiles, T=7 102
4.5 The Consistency of Cosmic Vertex Transformations 104
4.6 Phase Relationships 106
4.7 What Could Cause the W=N00 Phase Breaks? 107

3.5 A Little Cosmology, $q_o$ and the Cosmic Correction 108
5.1 Verification of $q_o = 0.5$ 110

3.6 Uniqueness of the Set of QTC Redshift Periods 111
6.1 Binomial Testing 112

3.7 Applications of QTC, Phase-Deviation Waves 114

3.8 Metallicity and T in Local Dwarfs 116

3.9 A Close Look at W = 200, Phase Cascades 117
9.1 Enter Asymmetry 120
9.2 Transition Step Patterns Within Deviations 122
9.3 Separating Signal from Noise 124
9.4 The Dwarf Side of W = 200, T = 1 125

9.5 The Extreme Dwarfs 127

3.10 Exclusion and T Levels in Pairs 129

**Chapter 4:** Particle Physics and the Dimensions of Time, New Viewpoints on Matter and Energy

4.1 Introduction 133

4.2 Begin at the Beginning 133
2.1 The Planck Units and the Doubling Decay Process 134
2.2 Two Spaces, Tau and Sigma 135
2.3 Early Studies, Representing Particle Forms 136
2.4 Assigning Vector Modes, Magnetic Moments 140
2.5 Summarizing the Gamma and Pi Energy Levels 141

4.3 Baryons 141

4.4 Mesons, the Common Bosons 144

4.5 Summary and Discussion Concerning Transitions 145

4.6 Energy Levels, Moving up to Level 56 150
6.1 An Overview of Two Spaces 151

4.7 Quarks and Lepton Limits 152

4.8 The Structure of Fundamental Particles 155
8.1 Making Mesons, With A Lepton Limit 158
8.2 The Lambda Anomaly and Other Baryons 158
8.3 A Glimpse Of Where Particles Begin 159
8.4 It Seems that Quarks Are Made of Triads 160
8.5 And What About the Higgs? 162

4.9 The Fundamental Forces 163

4.10 Particle Generation and Decay 167

4.11 Introducing Cosmology 169

**Chapter 5:** Turning to High Redshift, Connecting Galaxies With Quasars

5.1 Introduction 173
1.1 When Did I Say That? 174

5.2 Preparation for High Redshift and Quasars 175
2.1 The Lehto-Tifft Equations 175

5.3 Progressing In Time, Characteristic Redshift Peaks 177

5.4 Connecting Galaxies to Quasars 181
4.1 Redshift Patterns 183
4.2 Planes of Time 184
4.3 Spatial Correlations Between Harmonic Levels 185
4.4 Discordant Redshifts 186

5.5 The Southern Deep Field 189

5.6 Extensions To Lower Redshift 191

5.7 Summary 195

**Chapter 6:** Introducing Quantum Temporal Cosmology

6.1 Introduction 199

6.2 What Is Space and Time? 200
2.1 Matter, Energy and Time 201
2.2 Now Define Spaces and Timelines 202
2.3 Transforming Between Tau and Sigma 203
2.4 Mass in Sigma-Space 203
2.5 Why Choose 3-d for Time? 204

6.3 Now Construct a Cosmology 205
3.1 The Origin of Time and Birth of QTC 206
3.2 Introducing the Redshift 208
3.3 The Cosmological Correction 209
3.4 Classical Lookback Structure 210
3.5 Defining the Task of QTC 211
3.6 Structures and Processes Within QTC 211
3.7 Photons and Redshifting 212
3.8 Communication Through Lookback Time 214
3.9 Derivation and Properties of a Lookback Line 218

6.4 Some Basic Tests and Illustrations Using QTC 220
4.1 Angular Size as a Function of z 222
4.2 Dealing with Dark Energy 222

**Chapter 7:** Quantum Temporal Cosmology, Langolier Effects

7.1 Introduction 227

7.2 Just What is Quantum Temporal Cosmology - QTC 227

7.3 Where QTC Is and Where It Is Going 229
3.1 The Cosmic Background Dipole Form 233

7.4 The Origin of Matter, Pair Formation 235
4.1 Temporal Commonality 236
4.2 The Higgs Resonance 238

7.5 Singularities, Supermassive Black Holes and Outflow 239
5.1 Dark Matter 240
5.2 Flowing Through Time 241
5.3 Lateral Evolution, Galaxy Aging 242
5.4 Radial Redshifting 245
5.5 The Asymmetry Parameter 247
5.6 Redshift Dipoles and Asymmetry in QTC 248
5.7 Asymmetry Trends in QTC 250

7.6 Introducing Origin and Evolution of the Cosmos
Early Physical Findings and Premises 253
A. The Redshift; 254
B. Time and Space; 255
C. Matter as Fundamental Particles; 256
D. Matter In the Form of Structures; 257
E. Energy; 257
F. Forces; 257
6.1 Moving to Higher z, Quasars 258
6.2 Constructing Superclusters 262
6.3 Double Galaxies, and Large Scale Structure 265
6.4 Timeline Development, Lets go Fissioning 269
6.5 Alignment 270

7.7 Sigma-Sources and Cycles 274
7.1 Timeline Growth, Fissioning, Sources and Flows 277
7.2 Dispersion Bands and Vertical Input 279
7.3 Lets Talk About $t_o$ 284

**Chapter 8:** Summarizing QTC, The Early Universe and Cycles in Time

8.1 Introduction 287

8.2 Some Starting Premises, and Objectives 288
2.1 $t_o$, The Early Universe, with Temporal Dipoles 288
2.2 Lets Talk About Dipoles 289
2.3 Dipole Bonding, Generating Photons 291
2.4 Triads, Quads and Photons 292
2.5 Photons and Timelines 294
2.6 Some Premises, and Moving On with Cosmic Time 295
2.7 Matter - Anti-Matter 299
2.8 Excitation and Mixing 300
2.9 Just What Is the Nature of Our Universe? 303

8.3 From Two Pi to Now 304
3.1 The Evolution of Sigma Sources 305
3.2 T Families, D Doubling and Harmonic Decay Within D 306
3.3 Quasar Decay into High Redshift Galaxies 307
3.4 Superclusters, Pairs and Clusters of Galaxies 311
3.5 Redshift-Magnitude Bands and Early Correlations 314

8.4 The Life Cycles of Galaxies 316
4.1 Vertical Sequences 317
4.2 Where Do We Fit Into QTC? Cross Band Evolution 319
4.3 Period Tripling 320
4.4 Morphological Evolution 321

**Epilogue** 324

**Index of Appendices** 325

# Chapter 1

## What is the Cosmic Redshift? Correlations and Implications 1970-1978

Seminar 1 Version 8

## 1.1 Introduction

This book asks the question 'what is the cosmic redshift' and begins by addressing some background of cosmology and early findings of what I call the 'correlation' phase of the study. That question is essentially where I started about 1970 and have been studying the problem long enough to be convinced that if we really understand the redshift we will have made a fundamental step in understanding cosmology. The redshift is the key that opens the door. It is remotely possible, but very unlikely, that the redshift is simply the result of expansion of space, moving things apart and stretching photons. That expansion, referred to as the Hubble flow, when combined with large scale dynamics in space and in dynamical systems, supposedly describes our universe. However, that 'key to cosmology', the redshift, seems to have a mind of its own. What really is the redshift?

The question is easy to test, and you would have thought such tests would have been routinely carried out. Hubble had doubts about how to interpret redshifts. However, the classical dynamical expanding universe model emerged before effective tests could be made. It was not possible with the technology existing then to make serious tests of the nature of the redshift. Classical cosmology was frozen in place before effective tests were possible. Now, if you do not believe the classical model you need to be very careful. You are supposed to believe the pundits and follow your leaders. Perhaps you have seen a book by Hoyle, Burbidge, and Narlikar [A] which includes a picture which portrays modern cosmologists as a flock of geese blindly following their leaders. It is extremely difficult to be heard if you raise questions concerning established ideas. Nevertheless, I have asked and pursued such questions, and it has led to quite a different cosmology, Quantum Temporal Cosmology or QTC for short. This book is the story of that quest, nearly all of which exists in the professional literature. Since conventional cosmology is beset by many problems it is time to tie all those pieces together and tell the redshift story.

For readers who do not know much about cosmology I will briefly review some history. In the early 1900s very little was known. Astronomers knew there were two things out there in the universe, stars and fuzzy things called nebulae or nebulous stars. The stars were things like the sun, but what were the nebulae? The answer was unknown. In the early 1900s two basic problems were being considered. One was 'what is this structure we are living within'? What is our 'galaxy', this 'Milky Way' structure? And, secondly, are these fuzzy nebulae a part of it, or are they something outside of it? The question was debated in the famous Curtis-Shapley debate in 1920. The debate did not resolve the question, but perhaps did help to clarify it.

### 1.1.1 Modern 'Classical' Cosmology

Modern cosmology began in 1924 when Edwin Hubble established that the nebulae were independent external systems, now known as galaxies. He found variable stars in the Andromeda Nebulae which placed it well outside local structure and concluded that other prominent galaxies must also be distant. In 1912, Vesto Slipher at Lowell Observatory obtained some of the initial spectra of galaxies and was the first person to observe large displacements, the redshifts, in their spectral lines. The fact that there were very few corresponding shifts toward the blue immediately posed a problem relating the shifts to local dynamics. By 1925 enough redshift information existed, about 20 values, for Hubble to recognize the relationship between redshift and distance, providing the second key element of modern cosmology, the Hubble Law. The third element required linking observations with gravitational theory. Einstein formulated General Relativity in 1912, but originally applied the theory only to static models of the universe. By 1922, Friedman and Lemaitre had developed dynamic solutions to Einstein's equations. Finally, about 1930, Eddington played a major role by bringing observations and Friedman models together, quickly leading to the concept of an expanding universe. 1930 was the launching point of current cosmology.

That was a good start, but to really develop and work with cosmology you have to wait until the 1950s before a satisfactory distance scale began to fall into place. The corresponding improvement of stellar properties meant the 1950s also marked the beginning of understanding stellar evolution, essential to working out a time scale for evolution of stars and the evolutionary history of the universe. It was the 1950s before modern photoelectric photometry was developed permitting precision measurements. This was also when radio astronomy began, greatly expanding the spectrum with which we viewed the universe. Even with these advances we have to wait until the 1970s before imaging techniques were advanced enough to permit modern redshift surveys to begin. Prior to about 1970 astronomers needed exposures of many hours using photographic techniques to obtain spectra of what we now consider to be relatively bright galaxies. Redshifts are now taken routinely, but it was the 1970s before we could begin to map and try to understand the distribution of galaxies on the large scale. It was consequently the 1970s before modern tests on the nature of the redshift became possible. We still needed to wait until the 1980s before radio astronomy reached the level where precision tests could be made. Achieving precision on the order of one kilometer per second in redshifts became possible about 40 years ago. Only in the last 40 years have we been in the position to really test the nature of the redshift. Cosmology was developed and essentially conceptually frozen in 1930. Scientists became so accustomed to the classical ideas it is hardly surprising that most presume they have the right answer. It is relevant to note that the ability to really test the role of the redshift in classical cosmology corresponds quite closely with my timeline as I entered astronomy and became the scientist I am. We are still learning critical new details. One critical element was the recognition of the cosmic background radiation field. Our knowledge of the CBR dates from the 1990s. New issues continue to appear observationally, dark energy and supermassive black holes to name two, and present theory may be rather hard pressed to explain it all. Perhaps it is time to look at an alternate cosmological model.

Cosmology is built upon a combination of theory and observation. Most modern theory is founded on General Relativity, a theory of gravity almost universally accepted, combined with the Standard Model of quantum physics used to describe properties of matter. Obser-

vations include energy distributions of objects which yield magnitudes, colors and spectra, therefore redshifts. Fritz Zwicky correctly described redshifts as 'symbolic velocities'. We really should not call them velocities because we do not know for sure what they are. I use the term 'redshift' and often use velocity units, (km/s), or the symbol V, for convenience, not to imply interpretation. The symbol z (= v/c, c is the velocity of light), widely used to denote redshift, is an awkward small decimal number at low redshifts where most of my work was concentrated; V = cz is much easier to visualize in the low redshift range. Using redshifts we are finally in a position to study both far and near structure in distance and angle.

### 1.1.2 Problems and Questions

At this point I need to focus on some problems and questions that arise from theories that underlie cosmology. Always bear in mind that theory does not tell you what reality is. It models the way things behave, it describes relationships, it is not an explanation. Gravitation for example, in General Relativity, or just Newtonian gravity, are we sure that gravitation theory is correct? Over what range can we actually test it? It has been tested down to a fraction of an inch; we have verified the inverse square law only down to that scale. We can measure gravitational effects up to the scale of star clusters, and it yields consistent results at that scale. If you go to the scale of galaxies, however, 'dark matter' must be invoked to explain unexpected behavior. Is that because there really is dark matter or does it mean that there is something happening to, or competing with, gravitation? Realistically we have not been able to test the theory of gravity beyond certain limits and yet we assume it applies all the way down to zero and out to infinity. And now dark energy is needed to fit the redshifts of distant supernovae which seem to be flying away too fast. A new approach through QTC offers solutions to both 'dark' problems.

General Relativity faces an even more serious challenge, it is a mathematically continuous theory. We know, however, if we look back to the origin of the universe or down to the singularity at the core of black holes we enter the quantum domain. Somehow quantum physics and General Relativity must merge. General Relativity must transition into a quantum theory. We do not have such a theory or much success in finding one. QTC provides evidence, and reasons why, gravity operates at neither zero or extragalactic scales.

Then there is the Standard Model of particle physics. It is a beautiful theory for describing how things behave, but major parameters in the Standard Model are determined by observation. It does not explain why the particle masses have particular values, but it will tell you how they behave under various conditions. It does not tell you what a photon is, but describes its behavior. It offers a hypothetical method for how force is transmitted but again the issue of scale enters. Exactly how does information such as gravity pass between such widely spaced things as galaxies? What exactly does a photon know about space or time, it cannot actually perceive either, and what kind of information can it transmit? What about entanglement and the possibility of neutrinos moving faster than the speed of light? QTC can address these problems.

There in another fundamental parameter, time. Most theorists treat time as just a sequencing parameter and fold it into relativity theory as a 1-dimensional fourth spatial parameter by multiplying by c. Inverse time is frequency which is proportional to energy, $E = h\nu$, but

modern physics does not use that link to explore the nature of time. We almost universally assume time is one-dimensional. We certainly do not know that as a fact, and later in this book I will indicate that time appears to have more dimensions. Another basic unanswered question is what is space and what is the detailed relationship between space and time? Modern physics utilizes 4-dimensional space-time, and string theory allows space to gain dimensions, but physics rarely expands on our concept of time. Why do we treat empty space as more fundamental than time? The issue of the nature of time, the role it plays in cosmology and the structure and behavior of matter is central to QTC. These issues will be discussed as the basis of QTC is developed.

Certain other cosmological problems are worthy of mention before beginning to develop the basis of QTC. I have already raised the issues of dark energy and dark matter but there are also problems relating to the age of the universe. Is the expansion age of the universe consistent with the time it takes to build the immense structures we find in the universe? Do galaxies actually form by gravitational clumping as widely assumed, and what about the origin of rotation and counter rotation or the interrelation of detailed morphologies? Precisely what are superclusters and voids? Can gravitational theory solve these problems? I believe the nature of time, as implied by the nature of the redshift can point to new ways of solving such problems within QTC.

What are galaxy nuclei where strange nuclear engines reside? Are they produced by inflow, an infall picture, producing massive 'nearly black holes'? I use the terminology 'nearly', because just about everyone agrees that you cannot collapse things to a point-like singularity. Something must happen before you reach a true singularity. There are some interesting relationships being found between nuclear masses and other properties of the parent galaxies. Perhaps galaxy nuclei are not the result of inflow. There are a few astronomers, including me, who suspect that nuclei of galaxies are the source, the origin point of galaxies. We certainly do see signs that galaxies 'seem' to interact with one another. Most astronomers think interaction involves dynamics and merging of galaxies, bringing them together. An alternative model suggests that such galaxies are in a process of fissioning. Could nuclei be source functions for galaxies? I will raise such questions and examine these possibilities because real observations say it may be so. Such questions are rarely addressed in present astrophysics, but they do arise within QTC. QTC is built upon *direct* observational evidence, and is highly verifiable! Much of the evidence is derived from my own studies, but many external sources contribute considerably and consistently to the QTC story.

## 1.2 Testing the Nature of the Redshift

I will now turn to discussing the role and properties of the redshift that have emerged from investigations using modern observations. We start by assuming the redshift is indeed a Doppler-like phenomena due to systematic expansion of the universe plus random motion related to the dynamics of objects in space. Technically there could be relativistic gravitational distortions, but such effects must be very small. The question then becomes, 'are there effects present that cannot be explained by Doppler-like effects?'

Three kinds of tests have been carried out beginning in the 1970s. The initial process involved correlation studies between the integrated redshift of galaxies and properties of galaxies. If the redshift is a purely dynamical quantity, if galaxies are just masses moving in

space, then the motions of objects, measured by the redshift, should have little or nothing to do with intrinsic properties of individual galaxies. It should not matter whether a galaxy is a spiral, an elliptical or a radio galaxy. In other words there should be no detailed correlations between extrinsic and intrinsic properties of galaxies. Such correlations are what we will be looking at in most of the remainder of this seminar.

The second type of test, which grew out of correlation studies, involves redshift continuity. If redshift in a related group of galaxies is indicative of random motion, there should be a smooth continuous distribution of redshift between dynamical limits. We should find no particular preferred values for redshifts. The redshift should not assume discreet 'quantized' values. The third type of test involves change, variability. Galaxies are very large hence photons must take a long time to move across one. You should not be able to detect changes in the redshift of an entire galaxy over short periods of time. Certain types of orientation and physical association effects are also involved in evaluating the nature of the redshift.

Now suppose that these tests are failed, as I shall demonstrate. They suggest the presence of distinct 'intrinsic' effects unrelated to dynamics. How does one proceed? We must carefully test any findings but recognize that they may involve new and unknown aspects of physics. At the same time we must preserve and smoothly interface with as much locally 'known' physics as possible. Here we must face the question of what is really known and what is assumed - which is why I began this seminar with a review of the classical model and the physics underlying it. I will present results which have led to an alternative cosmological model, and encourage all readers to look carefully at the findings and form your own conclusions. A specific finding may not seem decisive but the comprehensive interlinked picture is remarkably cohesive, and is the reason this book has been written, to bring all the evidence together.

Before proceeding to the discussion of the early discoveries I should explain the structure of this seminar/review. For continuity I have carried the discussion using nuclear region magnitudes, where the first correlations were found, to completion with a discussion of the Perseus cluster of galaxies. Total magnitude work and studies using quasars and radio sources, which are related but largely stand alone, are described later as are aspects of morphological relationships. In fact many of these studies were simultaneous or overlapping. Published references written at specific times therefore often include mixed discussions where several subject areas were in process simultaneously and incomplete. For example reference [43] from 1974 contains extensive discussion of statistical significance combining early nuclear and total magnitude studies of galaxies along with quasars. Review discussions from IAU activities [44] and [57] likewise cover a wide range of evidence with work still in progress. I have placed references as appropriate, but in many cases they refer to only specific portions or subjects within the references, and represent only the level of understanding of the subject at the time they were written. The integrated development of QTC, especially the beginning, is far easier to follow in this review than it is in the literature. Further detail relating to specific studies will then be found in published papers.

## 1.3 Correlations, How It All Began

My work with redshift correlations began in 1970 when I was invited to give a talk at an IAU (International Astronomical Union) symposium in Uppsala Sweden [25]. I had done early

photoelectric work on galaxies, including some of the earliest photometry of nuclear regions [8, 20]. My background and work prior to 1970 is documented in the first book of this biographical series. I thought it would be interesting to broaden the Uppsala presentation by seeing if there was anything else the photometry might relate to. I consequently collected information including redshifts. When I examined nuclear properties such as colors and light concentration and plotted nuclear region magnitudes against redshift in the Virgo cluster of galaxies I was struck by the suggestion of a possible subtle relationship, nuclear properties did not seem to be randomly related to redshift and magnitude. I was well aware of the missing mass problem and it appeared that there could be some unexpected phenomenon involved that we did not understand. At Uppsala I made the suggestion that the redshift might be an intrinsic aspect of galaxies. I had not been informed that such non-classical ideas are not discussed at such meetings. Pundits in the front row were shaking their heads. After learning that lesson I resolved that if no one else would look into the redshift question then I would. I returned to Tucson and began follow-up studies. That has been the story of my life ever since. The effects present in that original study are extremely subtle but I have no regrets that I presented that paper. My subsequent studies have convinced me that the underlying basis of the redshift is indeed intrinsic to galaxies. So begins the story.

### 1.3.1 Redshift-Magnitude Bands, Effects in the Coma Cluster

Classical dynamics indicates that if you examine redshifts in a cluster of galaxies you should find a dispersion or scatter caused by random motion within the gravitational potential field of the cluster. This motion should ideally produce a smooth velocity dispersion pattern shown in figure 1.1. In 1970 I was not convinced I was seeing that in Virgo cluster data.

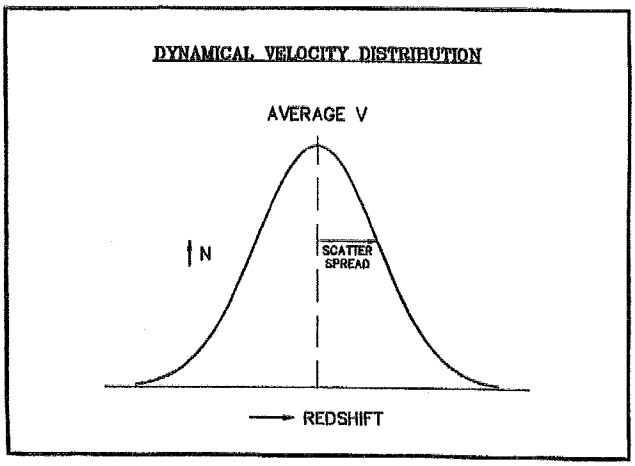


Figure 1.1: Classically expected redshift scatter in a cluster.

In the 1970s, very little high quality photometry or redshifts were available on galaxies in clusters. In order to do something similar to what I had done with my own photometry, mostly in the Virgo cluster, I turned to work that was available on the only other cluster

for which good photometry existed. Rood and Baum [B] had done detailed photometry of galaxies in the Coma cluster. The 90-inch telescope had also become operational at Steward and the development of the image tube made it possible to obtain many new redshifts of fainter galaxies. Using photometry derived from Rood and Baum, and many new redshifts, I constructed a redshift-nuclear magnitude diagram for the Coma cluster. Figure 1.2 shows the result [28]. The sample is complete to nearly magnitude 17 out to 20 arc minutes radius. Except for a few of the older redshifts for the brightest galaxies, which were soon replaced, redshift uncertainty is less than 50 km/s and magnitudes have uncertainties of less than 0.1 magnitude. Some magnitude scatter will be present simply due to the depth of the cluster.

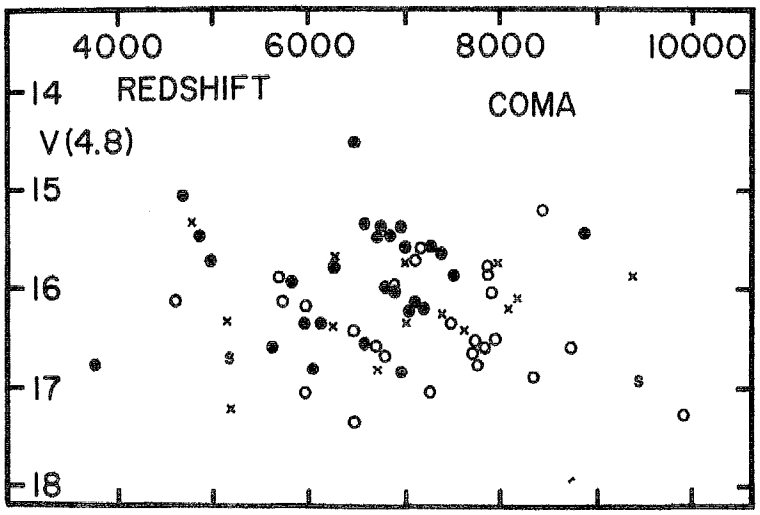


Figure 1.2: The original redshift-magnitude correlation for the central part of the Coma cluster of galaxies [28]. Magnitudes in the V band refer to the central 4.8 arc second nuclear regions. Filled circles denote elliptical galaxies, open circles So type, X symbols SBo, and S indicates spirals.

In place of a random pattern I found a 'band' correlation, where galaxies align in sloping bands within the redshift-nuclear magnitude diagram. If you project the redshift-magnitude diagram in the direction of the bands you get a highly nonrandom pattern of distinct clumps shown in figure 1.3. A power spectrum in Figure 1.4 demonstrates that the distribution is highly nonrandom, the probability of finding such a spectrum in a random distribution is on the order of 0.0005.

A second important correlation is readily apparent within the bands in figure 1.2. When the mean redshift of elliptical galaxies, shown with filled circles, is compared with the mean redshift of non-ellipticals (open circles), they are found to be very different. The ellipticals and later types differ in redshift, there is a morphological separation present. In fact morphology and the direction of the bands are correlated. The maximum redshift difference by morphology and magnitude for the cluster as a whole is closely aligned with the band direction and is clearly seen in each individual band in figure 1.2. Such a separation is unexpected dynamically, and is statistically non random. This correlation is confirmed

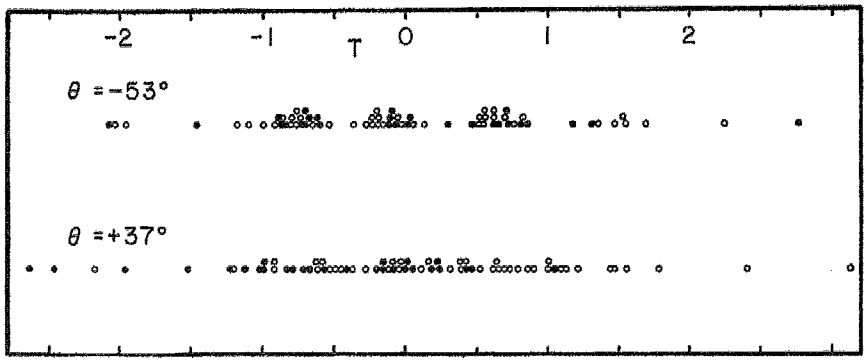


Figure 1.3: The Coma cluster redshift-magnitude correlation projected parallel and perpendicular to the band direction after each coordinate was normalized to a Gaussian fit [28]. Filled symbols denote ellipticals and open symbols refer to later morphological types.

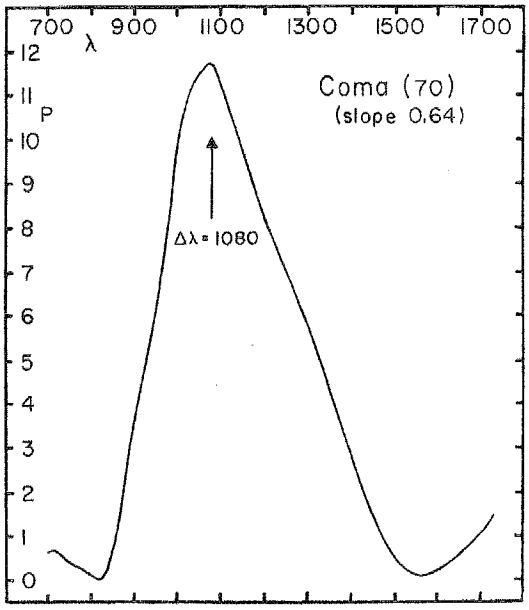


Figure 1.4: The power spectrum of the redshift distribution in the original Coma cluster redshift-magnitude correlation after projection to a uniform magnitude [43]. The abscissa indicates band spacing in km/s.

simply by using galaxy shape [34], ellipticity indicative of rotation increases systematically along each band

As a biographical note, it is useful to interject a comment at this point that very early in the history of my correlation studies I attempted to announce the findings. I prepared a paper, preserved now as Steward Preprint 37, in March of 1971 [27] which developed and extended work presented at Uppsala including early comparisons with the Coma cluster. The paper was rejected, and certainly was premature, but in retrospect the paper includes many of the concepts now central to QTC. The upper band in the Coma cluster was clearly visible and the first fragments of lower bands can now be recognized, although very few redshifts yet existed for fainter galaxies. Some morphological relationships can be recognized and evolutionary concepts were discussed. It was a very primitive paper, far too early for profound suggestions, but quite a remarkable indicator of what was to come. A "News and Views" note in *Nature* in 1971 [29] also makes a brief mention of my work on non-velocity redshifts.

Later, after the Coma cluster sample was further extended, a third correlation emerged [34], as shown in figure 1.5. Once the bands were defined to fairly faint limits the best fit through the points was shown to converge toward zero redshift.

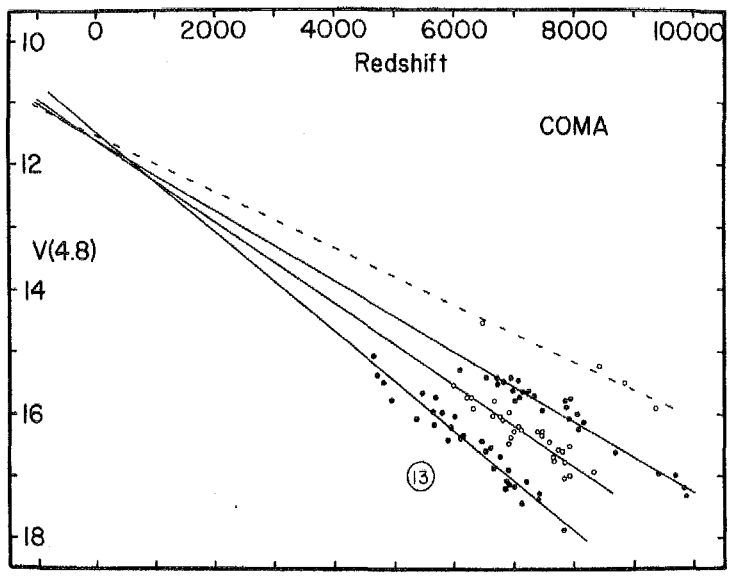


Figure 1.5: Convergence of the Coma redshift-magnitude bands toward zero redshift [34]. Scattered points below the main bands may represent another band but are two few or uncertain for fitting. Separate symbols are used to distinguish bands.

Convergence implies that the bands are scaled versions of one another. Since they appear to scale about zero, that suggests that the entire redshift could be an intrinsic property of galaxies. It is very hard to imagine dynamically how such banding with detailed morphological properties and convergence could be produced.

What do the correlations seen in the Coma cluster imply concerning the nature of the redshift? If the redshift is not due to motion or spatial expansion, what are the alternatives? One possibility is that you are seeing some evolutionary phenomenon displayed in lookback time. If redshift is an intrinsic property of galaxies, the redshift-magnitude diagram becomes an analog of a Hertzsprung-Russell diagram; galaxies, or the redshift effect, may evolve through or within the diagram as a function of time. That is a rather radical but perfectly good alternative way of explaining the Hubble law and redshift correlations.

### 1.3.2 Verification, Evaluation, and Extensions to Other Clusters

When the Coma cluster redshift-magnitude analysis was published in the *Astrophysical Journal* (ApJ) in 1972 [28], there was quite a reaction. The first thing to do was to verify the data. Dan Weedman [C] redid the photometry photoelectrically, and essentially confirmed it. There were a few discordant redshifts, but it was very quickly shown that the redshifts being produced at Kitt Peak were very good [66], there were no reliability problems. Susan Simpkin [D] attempted to show that interference from night sky emission might cause redshift errors. Such effects are important at some of the west coast sites near major cities, but were quickly shown [66] to be negligible for the 90-inch telescope at Kitt peak. The data involved was quickly confirmed. Much discussion then revolved around the significance of the correlations.

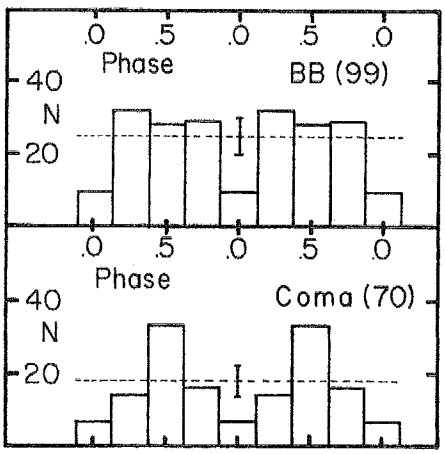


Figure 1.6: Band cross sections after projection and superimposition as a periodic pattern to show the distribution of points in and between bands [43]. The periodic cycle is repeated twice to show the deviations from the mean density (dashed line). A 1-sigma error bar is shown. BB (99) refers to a 99 point test sample; Coma (70) refers to the original 70 point Coma sample.

When you see a picture of stars on the sky it is easy to pick out lines and voids in the data. The first objection was that banding must be such an accidental alignment, the distribution is really random. I published a paper in the ApJ in 1974 [43] which addressed this question. It is true that when you look at a random pattern of points you can pick out

lines and voids. Most people may notice a few parallel voids or parallel excesses; between these features the distribution is normal and random. Properties of one example presented to me were discussed in the ApJ [43]; the results of the analysis are summarized in figure 1.6 where the periodic pattern in the distribution of points is shown after projection in the band direction.

The test example contained some roughly parallel voids within a random set. The pattern was not apparent to most observers whereas the Coma bands are visually striking. The projection pattern of the Coma bands in figure 1.6 explains the difference. The Coma bands consist of a combination of voids and excesses with no random intervals between them. The Coma bands consist of voids *aligned* with excesses. The Coma bands are not equivalent to seeing structure in random distributions of points.

The probability of seeing a random distribution with occasional gaps or excesses alone, as shown by the test sample, is about 20 percent, not significant. But now ask what is required to produce a pattern of voids aligned with a pattern of excesses. The probability of producing either voids or excesses is about 0.2, but the probability of lining up the two types of patterns precisely in the same direction is only about 0.02. The probability of getting a pattern like the Coma cluster is therefore about 0.2 times 0.02 or 0.004. Finally, if the morphological direction is taken to specify direction, if morphology independently determines the orientation, or because bands converge to a unique zero value so orientation is not a random variable, then the probability of seeing a Coma class pattern by accident is only about 0.02 times 0.02 or about 0.0004, consistent with the power spectrum in figure 1.4. The general conclusion is that the likelihood of accidentally finding the redshift-magnitude pattern seen in the Coma cluster is in the neighborhood of 0.0005. Most people do not argue much about the significance now, although few astronomers admit to the consequences of such a relationship.

When I presented the original paper showing the Coma diagram at the AAS (American Astronomical Society) meeting in 1972 [28a] it drew quite a crowd. One very prominent astronomer, who I will not name, strongly attacked the presentation in the post-presentation discussion, and I strongly defended it. The presentation drew applause after both the presentation and discussion, quite unusual. After the discussion the man who did not like the talk did say that if I could produce a second example he might take it seriously. I never heard back from him although as you will see equivalent sets of bands have now been demonstrated consistently in multiple clusters.

The next step did involve finding another major cluster, and bear in mind that in the 1970s it was hard to get good redshifts and magnitudes. By 1974 I was able to construct a redshift-magnitude diagram for another cluster, the A2199 cluster which is a little higher in redshift [43], and work on the Perseus Cluster at lower redshift was proceeding. The A2199 sample is nearly complete within 15 arc minutes of the cluster center above about magnitude 15.5. Most redshifts were mine, comparable with Coma cluster values in quality. Older values used, when compared with new values, rarely showed differences in excess of 150 km/s. Using the Coma analysis slope and spacing of bands in the A2199 cluster were predicted [43]. The cluster clearly shows the predicted pattern, as shown in figure 1.7, including a morphological gradient ($\Omega$ symbol). Banding was verified at the 99.9 confidence level.

The cluster was studied using nuclear photographic photometry obtained at the 90-inch Steward telescope. The effective aperture size was adjusted in inverse proportion to the

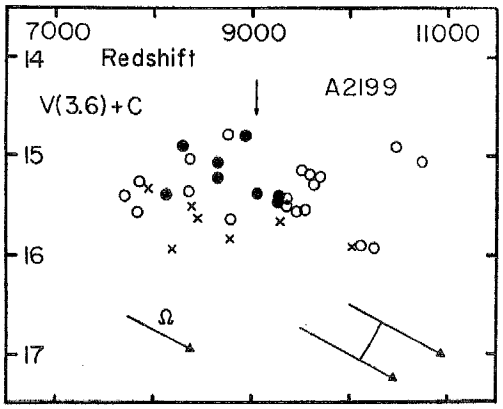


Figure 1.7: Redshift-magnitude diagram for the A2199 cluster [43]. Nuclear region magnitudes refer to a 3.6 arc second central region. The A2199 mean redshift, predicted band slope and spacing are extrapolated from the Coma pattern as shown. Filled symbols denote ellipticals, open symbols later types and x denotes unclassified objects. The magnitude scale is uncertain within a constant.

cluster mean redshift to compensate for different distances. Since I believe that important new discoveries should be promptly announced, and since I now had good evidence confirming the Coma cluster findings I attempted to publish a brief paper summarizing the preliminary findings in A2199. I was still learning how incredibly difficult it is to publish work strongly at variance with classical cosmology. The paper was rejected but exists as Steward Peprint 45 dated May, 1972 [32]. The paper included several tests I developed to show properties of the Coma bands.

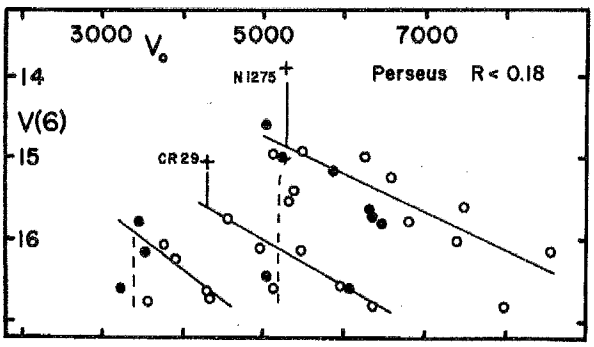


Figure 1.8: Redshift-magnitude diagram for the Perseus cluster [57]. Nuclear region magnitudes refer to a 6 arc second central region. Band lines are drawn convergent to zero redshift. Radio sources are marked by + symbols. Open circles indicate galaxies within 9 arc minutes of NGC1275.

A study of the Perseus cluster was completed and published in the proceedings of IAU

Colloquium 37 [57], held in Paris after the IAU General Assembly in Grenoble in 1976. This was one of the few IAU sponsored meetings which included controversial studies, which is perhaps why it was considered a colloquium rather than a symposium. The proceedings were published in paperback only. A clear three band diagram was found in the central core of the cluster (within 0.18 degree) as shown in figure 1.8. Band lines are shown converging to zero redshift. Redshifts include external data but many are from my work at the Steward 90-inch telescope at Kitt Peak. Magnitudes are photoelectric from Weedman [C]. Different aperture scales are, as for A2199, to compensate for different distances relative to Coma. Two radio sources are shown potentially associated with band heads, NGC1275 being one with an unusual morphological duplicity, elliptical/spiral. Band structure certainly is no statistical accident.

In anticipation of things to come, there are certain important changes in patterns with radius in clusters. The Perseus band structure may be traced out to to 0.3 degrees but seems to brighten or shift slightly in redshift. Related effects are present in outer Coma and elsewhere [57]. Beyond 0.3 degrees the Perseus diagram changes markedly and contains strong vertical structures related to dashed lines shown in figure 1.8 descending from band heads. There is good reason in QTC for such radial changes which will be discussed in later seminars. One of the most obvious radial changes is a change in the average redshift. The cluster core out to 0.3 degree is 700 km/s less than the outer body of the cluster, and in neither zone is the difference dependent on magnitude. The probability by t-test (which compares whether samples are derived from the same distribution) indicates that the probability the two portions arise from the same parent distribution is only 0.001. As I will show, this effect is present in all clusters studied and the QTC model of clusters predicts such an excess, although Perseus is remarkably extreme. However, to discuss such factors I need to extend correlation studies using total magnitudes. There was a lot to learn before it was possible to explain redshift-magnitude bands and related effects.

## 1.4 Extending Work to Total Magnitudes, Outer Coma

Early studies were done using nuclear magnitudes, which refer to the luminosity within a well defined circular region centered on the nucleus. They might better be called nuclear region magnitudes. Such magnitudes can be much more precisely determined than total magnitudes. Total magnitude correlations will often look less convincing than nuclear region correlations. Outer parts of galaxies contain structure and other complications which affect total magnitudes and increase scatter, but that in no way invalidates nuclear correlations. The increased sample furthermore allows important studies of such factors as morphological and larger scale structural effects to expand the interpretation of banding. Various forms of total magnitudes were all that existed for many galaxies, and it was necessary to show that galaxies for which only total magnitudes were available were consistent with band correlations.

The first step was to demonstrate the presence of band related effects in the outer portions of the Coma cluster [43]. The cluster extends radially at least three degrees whereas the original study covered only the central zone 20 arc minutes in radius where Rood-Baum photometry was available. For all galaxies in the region brighter than magnitude 15.7 moderately good integrated magnitudes are available from older sky surveys. There is more scatter in such

data however, which makes bands more difficult to see. As referred to in the previous section I will develop several good reasons within QTC to expect certain radial differences. There is no assurance that the cluster core and periphery will be identical since the regions differ significantly in galaxy and structural properties, etc. However, using integrated magnitudes for galaxies in the core, for which nuclear magnitudes determined band association, it is possible to determine where bands should extend in an outlying total magnitude diagram. Such locations for the Coma cluster are shown in figure 1.9 with solid lines. To minimize effects of scatter in outlying data morphological correlations were utilized to track band extensions.

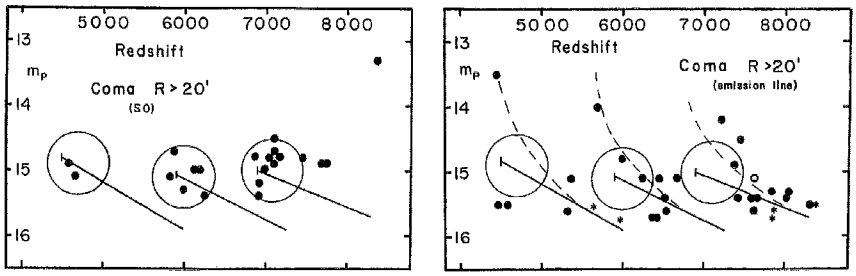


Figure 1.9: The association of outlying galaxies in the Coma cluster with expected band locations defined for total magnitudes [43]. The early type So galaxies, shown at the left, concentrate near band heads. Later emission type galaxies, shown at the right, are displaced down along bands toward higher redshift. Dashed extensions near band heads may associate with more luminous often active objects. Such associations are present at band heads involving active objects with emission and/or radio activity (see figure 1.8 as an example).

I initially used the earliest morphology, which in outer Coma consists of So galaxies. From morphological gradients seen within nuclear region bands such galaxies would be expected to concentrate in upper parts of bands, near band heads. Indeed, the So galaxies in outer Coma, in the magnitude 14.5 to 15.7 range, define three clumps which associate with the band head locations shown circled in the left part of figure 1.9. Later morphological types, which in accord with morphological correlations should be displaced to higher redshifts, were selected next. Since good later type structural morphology was lacking, emission line galaxies were used since weak emission is characteristic of ordinary later morphologies. Stronger, usually higher excitation emission is also present in active galaxies, but in this early study was not distinguished. Three groups are seen in the right portion of figure 1.9 shifted as expected, however, the brighter objects shown above band heads should probably be associated with activity at those locations and be distinguished (dashed lines) from ordinary weaker emission galaxies. The fainter ordinary population of later type galaxies are clearly displaced along bands to higher redshift and fainter magnitudes with respect to the So circled regions as expected. The distinction of active and ordinary emission classes is discussed further later in sections concerned with active objects.

Spacing between the Coma bands is a little more than 1000 km/s. A power spectrum periodicity analysis confirms that the same spacing is present in both samples even with the

mixed emission classes included. The expected correlations of morphology and magnitude are present to demonstrate banding in the outer parts of the cluster. Much of the early work is summarized in a review given at IAU symposium 58 in 1973 [44]. A paper was also presented at the Seattle AAS meeting in April 1972 discussing early total magnitude investigations [31].

### 1.4.1 Comparing Clusters, A1367

Total magnitudes were used for several redshift-magnitude studies. If bands are scaled versions of one another they will be parallel in a logarithmic diagram. Figure 1.10 (upper) shows this using the upper and lower Coma bands which are long enough to clearly illustrate the effect. Total magnitude bands are straight and parallel confirming convergence near zero redshift. The lower frame repeats the nuclear region diagram from figure 1.2 to show decrease in scatter when using nuclear magnitudes, although internal structure within bands, which I will shortly discuss, is also beginning to become apparent. The width of bands is not entirely due to data uncertainty.

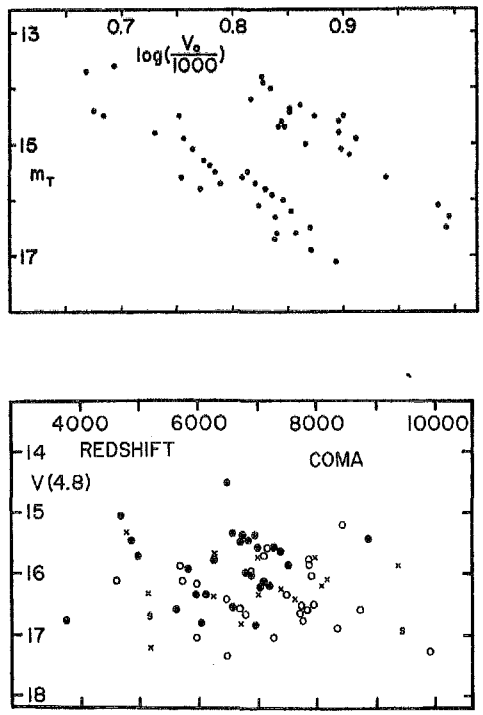


Figure 1.10: UPPER: The upper and lower Coma redshift-magnitude bands in total visual ($m_T$) magnitudes [34] available from the Rood and Baum [B] study illustrates that bands are scaled versions of one another and parallel in a log redshift diagram. An increased sample of faint galaxies in the total sample smoothly extends the bands. LOWER: The original nuclear region diagram from figure 1.2 is repeated to compare the samples.

The band slope is close to 4.3 magnitudes per factor of 2 in redshift. Once the slope and locations of Coma total magnitude bands were defined I could look for matching effects in other clusters. Figure 1.11 contains total magnitude-log redshift diagrams for the A1367 cluster [63]. Note that magnitude scales are equivalent only if the symbol identifying the scale is the same. For example m with a subscript p refers to photographic blue magnitudes used extensively from one source. V refers to visual yellow magnitudes. Refer to published papers for details concerning the limited sources available when the work was done.

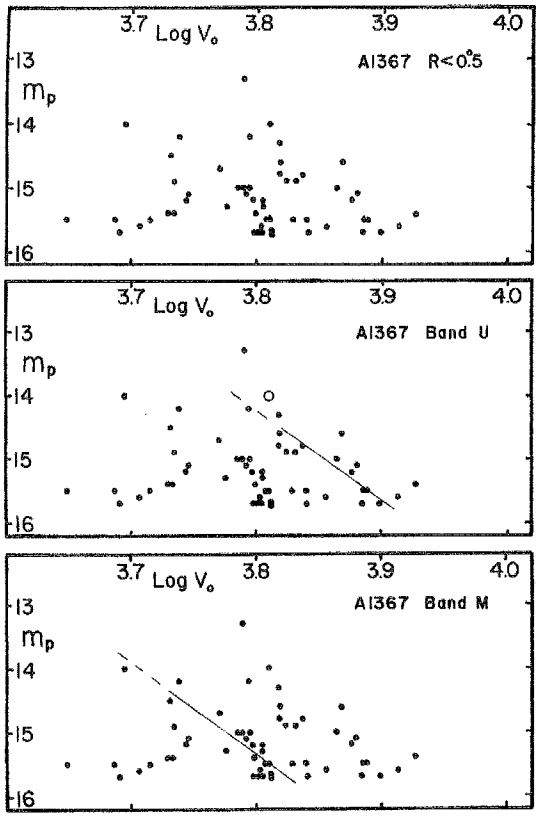


Figure 1.11: Band patterns in total blue magnitudes for the central portions of the A1367 cluster [63]. Lines mark predicted locations and slopes of bands defined in the Coma cluster to show bands correspond between clusters. A dominant radio galaxy, shown with an open circle, associates with the upper band head.

The upper frame suggests possible banding, but when a line is superimposed corresponding to the upper Coma band, in the middle frame, it matches the upper structure in A1367 perfectly. The middle Coma band likewise fits precisely through fainter points in the A1367 diagram. The clusters have identical redshift-magnitude band locations. Not only do clusters show redshift-magnitude bands, but the bands appear to superimpose from one cluster to another in some form of globally consistent pattern.

### 1.4.2 Redshift-Magnitude Bands in a High Redshift Cluster

Two later ApJ papers [E,F] contained data for the cluster 1358+62 at moderately high redshift, about z = 0.3. Figure 1.12 contains the Coma cluster redshift-nuclear V magnitude diagram [43] for reference; figure 1.13 is the actual discovery plot (using total red magnitudes) used to test the distant cluster for banding. It is a diagram of the first page (the southern end) of the ApJ data [E]. Both diagrams show three well defined bands (tip the diagrams and view them from lower right to show bands clearly) with scattered objects above and below. The total magnitude bands have the expected steeper slope. The banding appears to have extensions toward lower redshift (which will be discussed later concerning band structure).

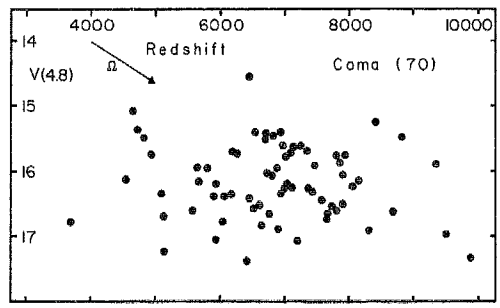


Figure 1.12: The original nuclear region 70-point Coma cluster redshift-magnitude diagram [43]. There is a scatter of high and low redshift objects above and below three main bands, possibly additional poorly defined bands. An arrow marks the morphological gradient within the bands.

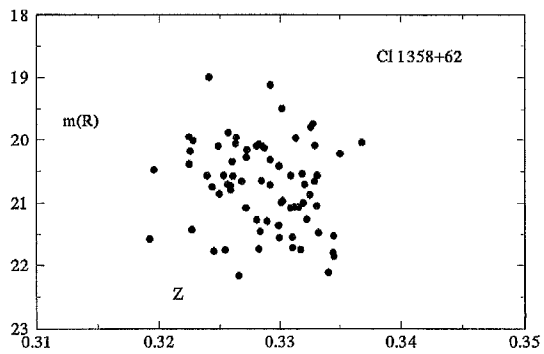


Figure 1.13: Redshift-magnitude diagram for the first page of data from the ApJ [E] covering the southern part of the region around the z = .3 cluster 1358+62. A three band pattern as seen in the Coma cluster is visible.

Figure 1.14, which defines the band pattern extremely well with five bands, contains data for the entire sample of galaxies more than 150 arc seconds from the cluster center. I placed

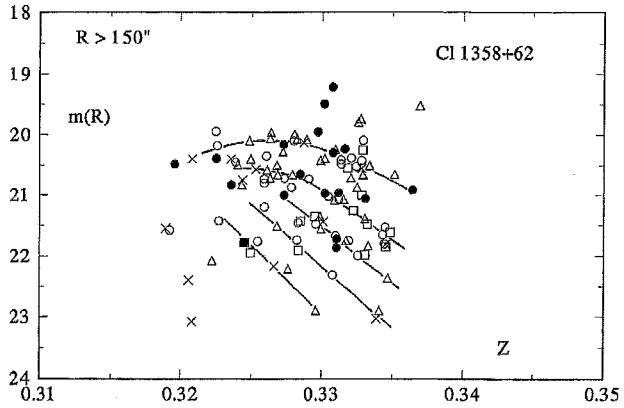


Figure 1.14: Redshift-magnitude diagram for all galaxies in the cluster 1358+62 more than 150 arc seconds from the cluster center. Bands are very well defined and the outlying objects define two additional bands. Solid dots are elliptical galaxies, other symbols mark different types.

this diagram here to make the demonstration of banding quite clear, and will discuss radial sampling distinction and low end redshift structure in Section 5 as further properties and potential interpretations of band structure are introduced. Figures 1.13 and 1.14 superimpose perfectly and have many objects not in common. Note that none of the data from the 1358+62 cluster came from my work. If the five clusters I have so far discussed do not convince you that there may be something wrong with a classical dynamical interpretation of the redshift consider that my story has just begun. Data was improving and one early study using quasars remains to be introduced. The authors of the paper on the 1358+62 cluster make no mention of banding and were apparently unaware of its presence.

### 1.4.3 What About Quasars?

Early work with total magnitude bands and their global similarity suggested one might expect to see effects using quasars. Quasar magnitudes are total magnitudes since quasars are star like, and it was quite possible that quasars were in some way related to galaxies. Figure 1.15 shows what I found when I took redshifts and magnitudes available in the 70s for emission line quasars, and plotted them in a log redshift-magnitude diagram [36]. When I drew lines at the total magnitude slope of 4.3 mag per factor of 2, derived from galaxies, and projected the data in that direction, I obtained clumps characteristic of a band system as shown in figure 1.16 [63]. A power spectrum analysis showed that optimum periodicity or clumping, with extremely high power [36], occurred for a slope of 4.28, directly consistent with galaxy total magnitude banding.

The quasar study suggested that bands formed regular systems of bands, with a characteristic slope which agreed with the total magnitude slope for galaxy bands and formed an apparent convergent sequence. Both galaxy and quasars are characterized by identical band slopes and a convergence factor Q (unrelated to the band numbering notation in figure 1.16).

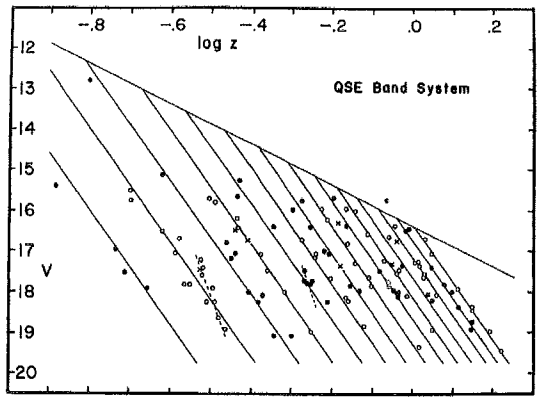


Figure 1.15: Redshift-magnitude banding for normal emission line quasars [36]. Lines are drawn at the slope predicted from total magnitude bands in galaxies as shown in figures 1.9 and 1.11.

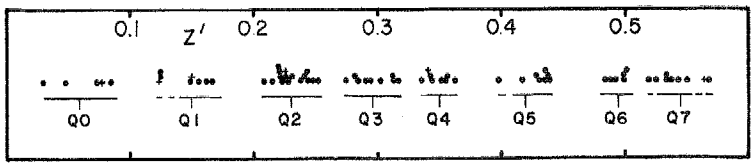


Figure 1.16: Periodic clumping characteristic of redshift-magnitude banding is apparent when quasar data is projected to a uniform magnitude at the slope of total magnitude bands seen for galaxies [63]. The Q notation identifies specific bands used in other overlap comparisons.

Since periodicity analysis using power spectra involve uniformly spaced data the analysis was done by projecting along the band direction to a uniform magnitude, then scaling projected redshifts (z') in a quadratic transformation (z' plus Q times z' squared) to generate z" for periodic analysis. Similar procedures were used originally to predict the spacing and location of bands in the A2199 cluster and outer Coma cluster shown in figures 1.7 and 1.9. The quasar and galaxy studies involved detailed searches over ranges of slope and convergence, which for total magnitudes consistently shows high power centered on 4.3 magnitudes per factor of two in redshift originally derived from the Coma cluster investigations. Add to that the completely independent analysis of the z = 0.3 cluster Cl 1358+62 and it was inconceivable to me that redshift-magnitude banding is just a statistical quirk, yet it has been completely ignored. The work and findings related to quasars was duly reported at the AAS meeting in Las Cruces in September 1973 [36a]. In Steward Preprint 48 quasar banding at still higher redshift was discussed [37] but not accepted for publication.

A fairly comprehensive review of the first years of redshift-magnitude bands work, the first glimpses of redshift quantization, and early thoughts about what it might mean are contained in the paper I presented at IAU Symposium 58 in Canberra in August 1973 [44].

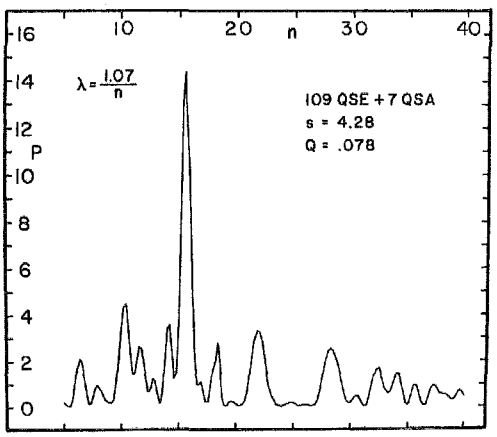


Figure 1.17: A power spectrum demonstrating strong periodic clumping in quasar redshifts when projected at the total magnitude band slope seen for galaxies [36]. A quadratic coefficient Q was used to compensate for decreased spacing with redshift. Power is optimized when the slope matches the slope found for galaxies.

## 1.5 Structure Within Redshift-Magnitude Bands

My story was just beginning. People who think that redshift-magnitude bands are just some curiosity limited to the Coma cluster should reconsider. The band phenomenon is something that cannot be casually dismissed. Banding characterized only the beginning of what would become a recognition of finer and finer structure in the redshift inconsistent with its classical velocity interpretation. As the quantity and precision of redshift data continued to increase, a finer substructure became apparent as shown in figure 1.18. The substructure was noted in 1973 [34,44] and discussed in detail in the ApJ in 1979 [75].

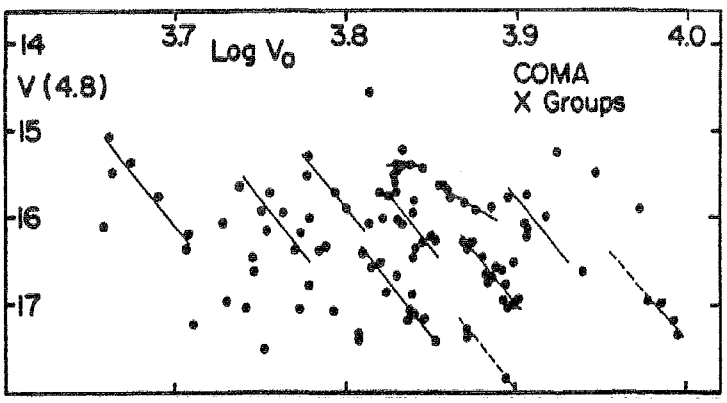


Figure 1.18: Substructure in Coma cluster nuclear redshift-magnitude bands [75].

The 1979 paper, entitled "Structure Within Redshift-Magnitude Bands, Morphological Evolution" was refereed by a very well known astronomer who developed a new statistical technique, two dimensional power spectra, to try to show that the effects were not significant. He was unable to disprove the structure and the paper was published, along with an editorial disclaimer. The disclaimer indicates how difficult it can be to publish controversial information. It states:

> After an extensive independent statistical analysis, the referee could not demonstrate that the bands discussed in this and previous papers do not exist, but he was also not convinced by the author's analyses that the bands and cross-bands do exist. In this stalemate on a question of possible considerable importance, we will permit the author to present his evidence in hopes that an open forum will encourage research and a resolution of this disagreement.

I know of no later external investigations that considered banding or its substructure.

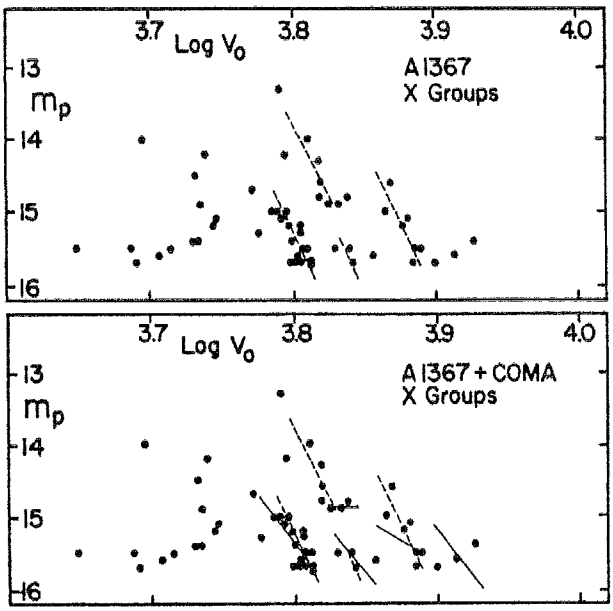


X-Group Band Crossing Points

| Group | log $V_x$ |
|---|---|
| CU55..... | 3.742 |
| CU65..... | 3.816 |
| CU76..... | 3.879 |
| CU86..... | 3.933 |
| CM50..... | 3.703 |
| CM57..... | 3.756 |
| CM63..... | 3.802 |
| CM70..... | 3.845 |
| CM77..... | 3.884 |
| CL47..... | 3.675 |
| CL54..... | 3.735 |

Figure 1.19: The upper frame shows substructure within the A1367 total magnitude redshift-magnitude bands [75]. The lower frame shows that the locations of the nuclear magnitude Coma substructure correspond in redshift [75]. The Coma features, now called cross-bands, are less steep since they omit increasing amounts of light from outer parts of more luminous galaxies or are less developed. A table gives notation and locations for substructures.

Figure 1.19 shows that substructure corresponds between clusters [75]. The figure compares the substructure in the Coma cluster with A1367. There is a one-to-one correspondence, the substructures align with one another in these and other systems. Not only do the large scale bands match between groups, the substructure within the bands also correspond.

Substructures were demonstrated to superimpose within up to five independent groups under study at the time [75]. A table to the right of figure 1.19 gives notations for the substructure, now called cross-bands. They are designated by C (Coma) U, M or L for upper, middle or lower band association and a numerical code for the first two digits of the redshift where the structure crosses its parent band. The uppermost structures on the brightest band are CU65 and CU76. The leading marked structure on the middle band is CM63. I will use angled marks to indicate the features within redshift-magnitude diagrams.

### 1.5.1 Structure and Morphology, Galaxy Evolution?

We next need to look at morphological correlations; there appears to be a consistent interrelationship between morphology and band structures [75]. This work began with investigations in the Coma cluster since it was one of the few places with quality data.

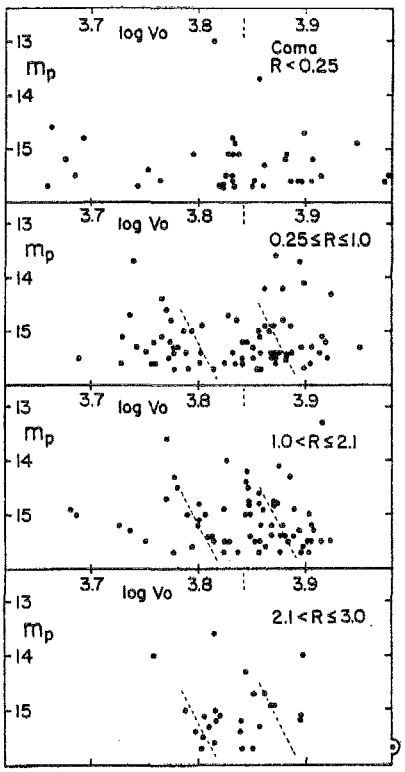


Figure 1.20: The redshift distribution in the Coma cluster as a function of radial distance (in degrees) from the cluster center [75] for all galaxies with total magnitudes brighter than 15.7. The sloping lines mark the location of specific cross-bands in the cluster core. The short vertical line indicates the mean redshift of the cluster.

I had or obtained data as a function of radius within the cluster, eventually complete to

magnitude 15.7 out to 3 degrees where the cluster fades into an associated supercluster substratum. Only the brightest core galaxies involved in the band studies could be included in this study because of the total magnitude limit. As you move out from the central core an interesting pattern develops in the redshift distribution. Figure 1.20 [75] shows log redshift as a function of magnitude in radial zones. The central region shows general scatter around the cluster mean, shown with a short dashed line. Morphology is not distinguished in this figure. As radial distance increases the redshift pattern bifurcates in association with specific cross-bands.

Each clump associates with one element of the band substructure, the higher redshift feature associates with CU76 on the upper Coma band, the lower redshift clump with CM63 on the middle band. As one approaches the cluster core the patterns seem to 'evolve' toward lower redshift. As noted for the Perseus cluster the core extends much further toward lower redshift. There is no corresponding distribution toward high redshift which increasing core velocity dispersion requires, just another deviation from classical dynamical expectations!

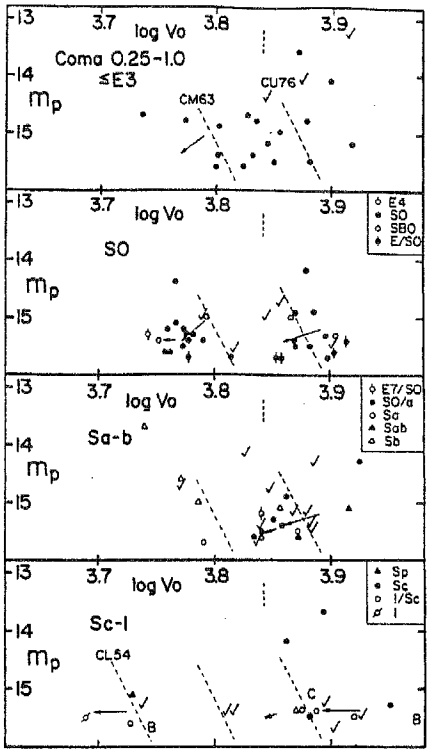


Figure 1.21: Redshift distribution according to morphology in the 1/4 to 1 degree radial zone around the Coma cluster [75]. A few galaxies with good morphology at greater radii are shown with check marks. Refer to figure 1.20 for other details. Arrows suggest possible redshift 'evolutionary' trends with redshift.

Figure 1.21 examines the splitting in the zone from 1/4 to 1 degree according to morphology

[75]. We had very good morphology for this zone from plates taken at the Kitt Peak 4-meter. I had several graduate students working for me at this time helping assemble data.

Ellipticals in the zone are well centered on the cluster mean, distributing between CM63 and CU76, right at the head of the upper band in association with partial CU65 structure which appears developed in A1367 (figure 1.19). These are all early elliptical galaxies, which, as I will discuss further, characterize cluster cores in redshift properties. As you go to So galaxies the pattern splits into two distinct groups associated with CM63 and CU76, the major structures defined within the central region at the top of the upper and middle bands. As you move to later morphologies both substructure patterns shift slightly to lower redshifts. The lowest redshift group disappears but could connect to the late spiral types in the lowest frame of the figure. The higher redshift group strengthens. This higher redshift group is characterized by later morphologies than the lower one, and shows a distinct decrease in redshift as morphology moves from So to early spirals. It then fades away or may show remnants of late spirals near the CM63 substructure. The very latest morphologies show shifts into a triple pattern. The late spiral association at the faint end of CU76 is inconsistent with the earlier population of the substructure but consistent with late type shifted remnants from a still higher redshift structure as shown with arrows. Different morphologies do not have the same redshift distribution, and multiple patterns are present within the cluster which is conventionally taken to be one dynamical unit. The redshift clumps are not spatially grouped within the radial zone hence are not readily associated with dynamical subclustering. A good example of this dispersal is shown for a group in A1367 in reference [63]. Individual dynamical units are not usually limited to very narrow ranges of morphology. The grouping and redshift changes suggests that morphology is linked to the redshift pattern in a manner unrelated to dynamics.

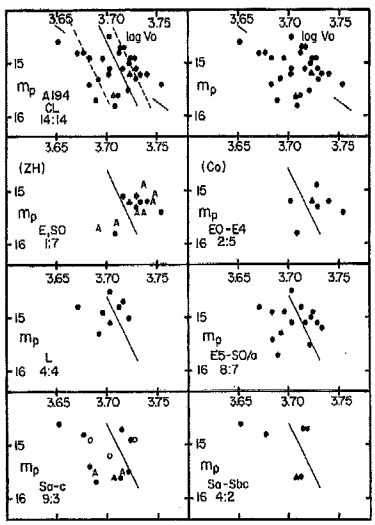


Figure 1.22: Redshift distribution according to morphology in the A1367 and A194 clusters for the CL47 and CL54 portion of the band structure (shown dashed) [75]. A1367 galaxies are distinguished using A symbols. Lines and other information are described in the text.

To further pursue questions of evolving morphology within band structure I combined data from A1367 with information on A194 which falls in the same redshift interval. The redshift-magnitude region corresponding to CL47 and CL54 in Coma is well populated with a good range of morphology. The right part of figure 1.22 shows the redshift-magnitude diagram separated by morphology for two different classifications.

The top frames show the complete sample with cross-band groups marked with dashed lines. The CL band is marked with two widely spaced dashes. A solid line between the cross-bands divides the sample into two equal groups. The three split frames below the top frames divide morphological types between earliest, middle and later (spiral) types as listed in each frame (L=lenticular, an older very flat E7 notation, now generally So). One column uses old morphology (HZ), the other modern classes (Co) (see reference [75] for details). Filled circles denote A194 galaxies, the letter A identifies A1367 objects. A ratio shown in each frame gives the relative number of galaxies on each side of the dividing line between the two subgroups. There is a clear shift in the ratio toward lower redshift as one moves from early to late morphology for both clusters, in agreement with the Coma cluster. It seems clear that cross-bands are specific regions, characterized by the lines used to define them. Within such regions systematic drifts in morphological patterns occur. There are other band properties to discuss before suggesting what this phenomenon may mean.

Is the redshift-morphology pattern in Coma, A1367 and A194 some freak accident or is it indicative of an intrinsic relationship? Figure 1.23 repeats the Coma pattern, from the top half of figure 1.21, showing the ellipticals splitting into two groups of spirals, early types at lower redshifts and later types at higher redshifts.

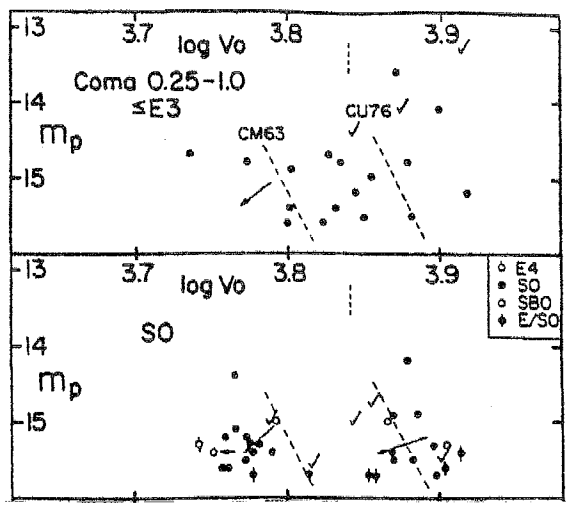


Figure 1.23: The top part of figure 1.21 [75] is repeated to show how So spirals in the Coma cluster divide into two groups, one on either side of the ellipticals in redshift. See figure 1.21 for details.

That pattern occurs repeatedly among galaxy groupings. Figure 1.24 is a morphology

redshift diagram for the A262 cluster [92]. The diagram includes galaxies down to magnitude

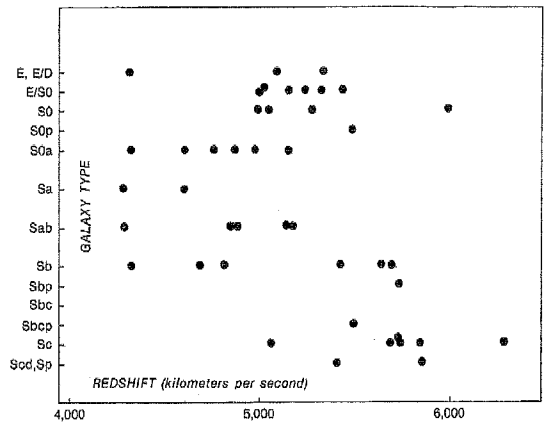


Figure 1.24: A Morphology-redshift diagram for the A262 cluster of galaxies [36]. Early type spirals distribute below the ellipticals in redshift, later types above.

15 within about 1 degree of the cluster center. The ellipticals distribute near the mean redshift as in Coma. Early type spirals are displaced distinctly to lower redshift and later type spirals are displaced to higher redshift. That is not a random pattern distributed around the cluster mean. Morphology appears to be directly related to redshift in a reproducible pattern.

Figure 1.25 shows the pattern present in the distant cluster 1358+62 [E,F], which has z near 0.33. Again ellipticals (filled symbols) distribute at mid redshift with So types (open symbols, E/So is shown with x) on either side of an So gap between magnitude 20 and 21.

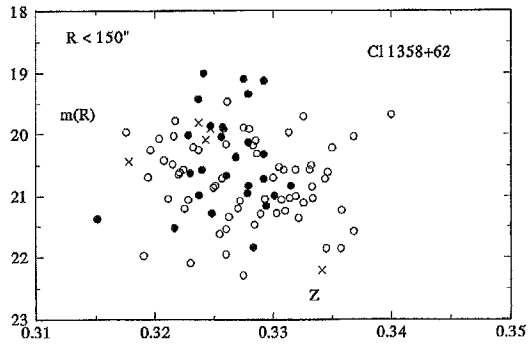


Figure 1.25: Redshift as a function of magnitude for galaxies in the 1358+62 cluster within 150 arc seconds of the cluster center [E]. So galaxies (open circles) [F] fall into two groups, one above the ellipticals (filled circles) in redshift, the other group below. x symbols denote E/So types.

The paper on 1358+62 [F] notes that the redshift distribution of the cluster is broader than

a Gaussian and identifies the So clumps as subclusters in the foreground or background. This 'standard' interpretation is untenable for several reasons not mentioned in the paper. First, the lower redshift clump in particular, and much of the higher redshift clump, is aligned quite centrally on the main cluster. This is geometrically unlikely and reminiscent of 'finger-of-god' arguments used in stellar distribution discussions. There is much more space in lateral directions: when a distribution appears spread out but points right at you, there is a good chance you have misinterpreted the data. A more telling argument against there being a lower redshift 'foreground' subcluster is the fact that there is a distinct lack of fainter galaxies below the low redshift concentration. Fainter galaxies are much more common than bright ones so such a luminosity distribution is inconsistent with the concentration being a separate group. It is far more consistent with a process associated with the cluster core itself since we see this type of pattern time after time.

The classical example of the morphology-redshift offset correlation is the well known morphological separation of redshifts in the Virgo cluster. Early studies of the Virgo cluster were disturbing because the ellipticals have redshifts which distribute around 1100 km/s while most of the spirals have much higher redshifts. If you look a bit more carefully you will find that the early type spirals are actually lower in redshift and it is primarily the later type spirals which show a high redshift. The ellipticals are in the middle. The Table in figure 1.26 includes data for Virgo, Coma and A262 along with the A1367 and Hercules clusters. The morphological splitting is seen essentially everywhere.

**Morphological Redshift Offsets**

| Cluster | Early S | Early-Ell | Ellip | Late-Early | Late S | Restrict |
|---|---|---|---|---|---|---|
| Virgo | N=24<br>S0a-Sab<br>896(790)Dbl? | -284 | N=45a<br>E-S0+<br>1180(504) | +773 | N=13<br>Sbc-Sc<br>1669(510) | To 4 degr<br>Omit Sb |
| A262 | N=13<br>S0a-Sab<br>4753(304) | -447 | N=14<br>E-S0<br>5200(353) | +933 | N=10<br>Sbp-Scd<br>5686(305) | To m=15.0<br>Omit Sb |
| A1367 | N=23<br>S0-Sb<br>6146 | -380 | N=17<br>E-E/S0<br>6526 | +1154 | N =6<br>I/Sc-I<br>7300 | To R=0.35<br>Omit Sbc-c |
| Coma | Dual<br>S0<br>5960/7580 | -960 | E-E/S0<br>6920 | +1280 | SB0-Sab<br>7240 | Also Core<br>where E<S0 |
| Hercules | N=26<br>S0-Sa<br>10704 | - 55 | N=16<br>E<br>10759 | +624 | N=11<br>Sb-I<br>11328 | Clusters |

Figure 1.26: Redshift patterns in well known clusters of galaxies. Colums 2,4 and 6 give numbers, types, and mean redshifts, some with dispersion, for early type spirals, ellipticals and late type spirals. Column 7 has comments relating to the samples. Intermediate types which do not divide clearly between the extremes are omitted. Columns 3 and 5 are the mean redshift differences between early spirals and ellipticals and between late and early spirals.

Additional data relating to morphological patterns can be found in a study of small groups of galaxies done by Jack Sulentic [G], although he compared differentially with dominant galaxies rather than general morphological types.

## 1.6 Introducing Active Galaxies

Turning now to active galaxies, galaxies which are radio sources and/or show emission lines, how do they relate to the patterns discussed? Bands, cross-bands and evidence for morphological correlations are present. Consistent patterns are seen which are difficult to explain. As one possibility I chose to look at the patterns in the context of an evolutionary model, the possibility that the redshift and/or galaxies were evolving with time. To further see why I took this approach look carefully at how Coma cluster band substructure relates to the A1367 cluster in figure 1.19. In Coma, which has a slightly higher redshift, the two upper cross-bands, the uppermost in particular, seems to roll over or fold down. In the slightly lower redshift A1367 cluster the cross-bands are well developed, and this pattern behavior continues into still lower redshift groups. Note further, in figure 1.11, that one of the galaxies at the top of the leading A1367 cross-band is a radio source. A similar association is seen in the Perseus cluster in figure 1.8. Is evolution unfolding as we step down in redshift? Are bands forming and dissolving? The rollover could relate to development of cross-bands as a function of redshift, and will be discussed further subsequently. Within classical cosmology the idea is beyond radical, but from the viewpoint of observational consistency it requires investigation. If an evolutionary model is correct then certain types of activity might be expected to correlate with the patterns in structure and morphology.

### 1.6.1 Radio Sources

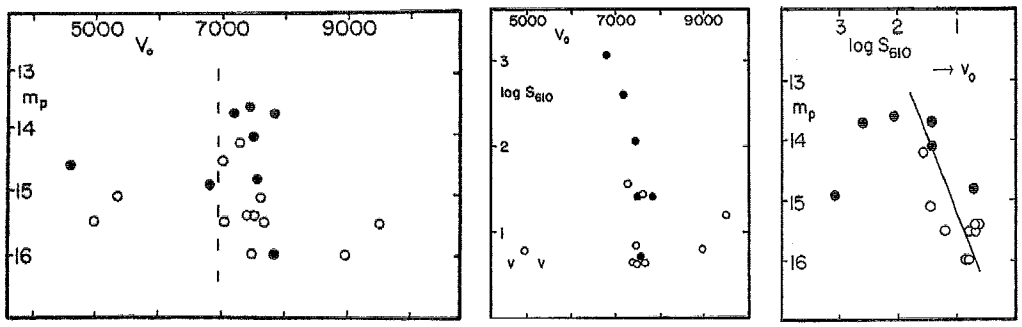


Figure 1.27: LEFT: Redshift distribution of radio sources associated with the Coma cluster [50]. The vertical line is the cluster mean redshift. Open symbols are objects with emission lines. MIDDLE: Redshift-Radio Flux at 610 MHz for Coma radio galaxies. Symbols as at left. The three strongest sources rise sharply in flux, and drop in redshift and optical brightness. RIGHT: Total Magnitude vs Radio Flux at 610 MHz for Coma radio galaxies. Symbols as at left. A line marks constant optical to radio flux. Radio flux relates to optical luminosity for the main group where all three groups superimpose.

When Massimo Teranghi was at Steward as an ESO fellow in the mid 70s, we made a study of the radio sources in the Coma cluster [50,61]. We found that radio sources were not randomly distributed, they fell into three redshift groups as shown in the left frame in

figure 1.27. The majority clump in redshift just above the mean for the cluster, they do not distribute around the mean in a normal expected dynamical pattern.

Figure 1.28 repeats the Coma radius-redshift-morphology correlation for the region just outside the cluster core in Figure 1.21 with the radio source regions indicated by marginal vertical lines. The major group of radio sources concentrate in the CU76 subgroup at the high redshift boundary of the ellipticals, which distribute between the CU76 and CM63 subgroups around the cluster mean redshift. The radio sources also fall directly between the two displaced spiral (So and Sa) groups associated with the CU76 subgroup. The So group is mostly higher in redshift, the Sa group almost entirely lower. Sc galaxies then mark the fainter end of the subgroup. Arrows denote suggested morphological evolutionary tracks. Radio sources appear to associate with a possible morphological change, becoming increasingly active and moving down in redshift as shown in the right frame of figure 1.27.

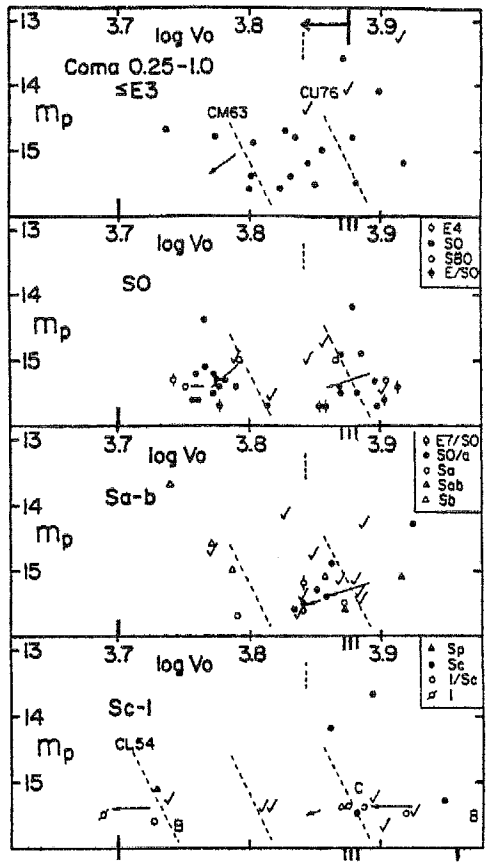


Figure 1.28: A repeat of figure 1.21 [75] showing that the dominant group of Coma radio sources associates with higher redshift spiral and mid redshift ellipticals, and between So and Sa galaxies within one subgroup, CU76, perhaps forming a link between the forms. Vertical marginal lines indicate the redshift locations of radio sources shown in figure 1.27.

Figure 1.29 repeats the A262 redshift-morphology pattern from figure 1.24 with box symbols to denote radio sources. Again the radio sources distribute above the mean and divide between the the later spirals and the ellipticals as though they link those forms.

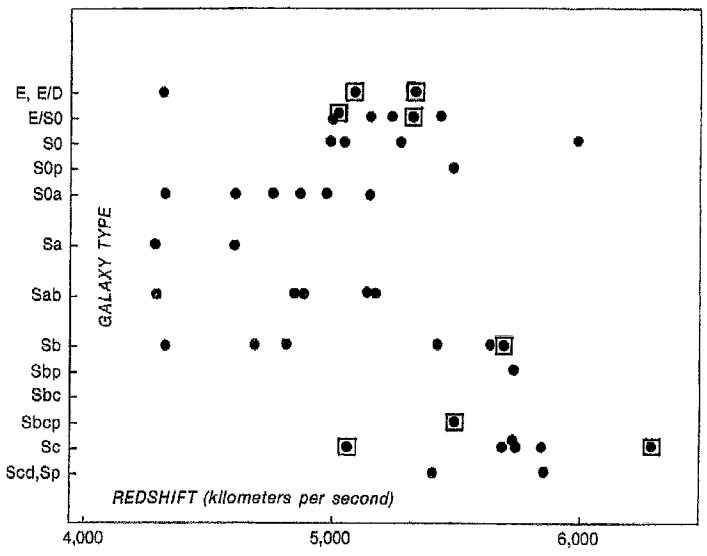


Figure 1.29: The redshift-morphology pattern of the A262 cluster in figure 1.24 [36] with radio sources marked with boxed symbols. Radio sources again distribute between the ellipticals and higher redshift spirals.

Is the activity present because these galaxies are associated with the boundary between ellipticals and higher redshift spiral forms or is it evidence of an evolutionary transition within the CU76 spirals?. We do have things like Centaurus A, and NGC 1275 in the Perseus cluster, which look like elliptical spiral combinations. Is that some kind of hybrid or transition stage? As noted earlier in figure 1.5, NGC 1275 is associated with a Perseus cluster band head as are the Coma radio sources. The A1367 cluster as well as Perseus and Coma all show such associations. The low redshift radio sources in Coma similarly associate with the CL band head.

### 1.6.2 Emission Line Galaxies

Figure 1.30 illustrates the broader class of Coma active galaxies characterized by emission lines [57]. Such galaxies to some degree overlap radio galaxies, although the strongest radio galaxies may not show emission. Emission line galaxies fall into two classes, strong emission involving high excitation lines, and weak emission usually characterized by only hydrogen or singly ionized oxygen. The heavy vertical lines in the left column mark the mean redshift of the Coma cluster, dashed lines show band locations. Filled symbols in the upper frames indicate radio galaxies (half filled for possible radio sources). The upper left frame shows all strong emission galaxies, the frame below it adds non-emission radio galaxies and one weak emission radio galaxy (square symbol). An x indicates sources more than two degrees from

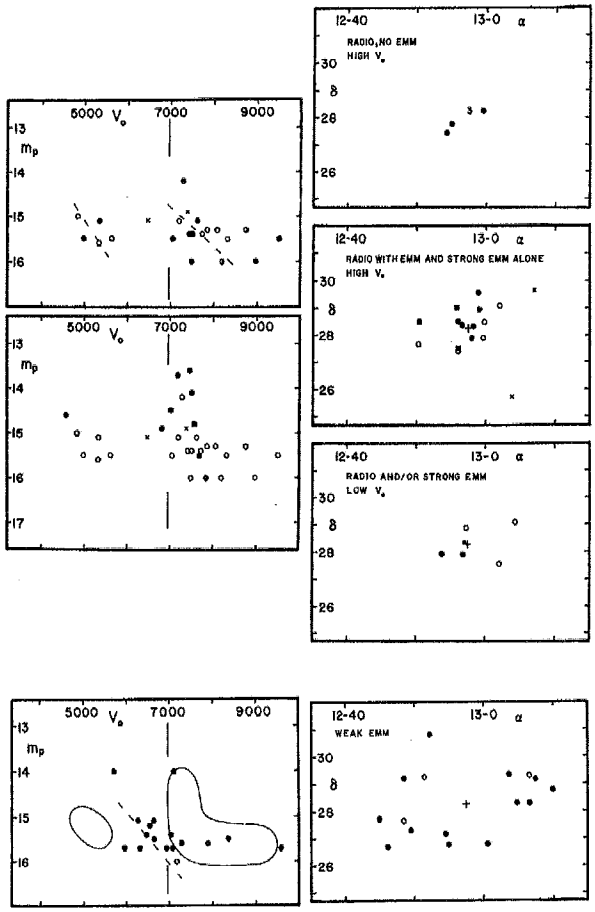


Figure 1.30: Redshift-magnitude and spatial location diagrams for emission line and radio galaxies in the Coma cluster. Symbols are defined in text.

the cluster center which may not be cluster members. The upper three frames in the right column show all the strong emission line and radio sources populate the central portion of the cluster. A cross marks the cluster core (a 3 in the upper frame should be a cross). In the lower offset frames weak emission line galaxies are shown with filled symbols (an open circle in the left frame is a faint companion of another galaxy, in the lower right frame open circles indicate the three high redshift weak emission galaxies). Outlined areas mark the location of strong emission and radio galaxies.

Some remarkable associations are shown by the diagrams. Strong emission and radio sources are clearly associated with the cluster, populate only the upper and lowest Coma bands and fall in the central regions of the cluster. Weak emission line galaxies populate the middle Coma band, avoid the strong radio and emission redshift zones, avoid the cluster center and distribute quite uniformly around the core in an outlying zone. Some may not be cluster

members, but most probably are since the distribution closely mimics the oblate form of the cluster. The strong emission and radio galaxies at both the lowest and highest redshift clearly associate with the cluster. The markedly offset distributions from the optical cluster center strongly support the finding from the radio data alone that the patterns are band associated and non-dynamical in character. The entirely different distribution of weak and strong activity will be discussed later in the context of expectations within a QTC cosmology. I presented a paper at the Haverford AAS meeting in June 1976 [56] discussing the emission and radio galaxy patterns and their redshift-magnitude band association. A brief note also appeared in *Science News* [56a] following the meeting as I continued to attempt to draw attention to anomalies in redshift patterns.

## 1.7 Cross-Bands and Vertical-Structures

As I moved into the mid to late 1970s enough evidence was assembled to begin to see relationships between the patterns within redshift-magnitude diagrams. I have introduced bands, cross-bands, morphology, emission and radio activity associated with specific redshift patterns. I was increasingly convinced that band structures, galaxy morphology, and the redshift itself appeared to be connected in some form of interrelated evolution. I will illustrate some of the evidence and further details as I close this seminar. Figure 1.31 repeats the Coma nuclear region pattern from figure 1.10.

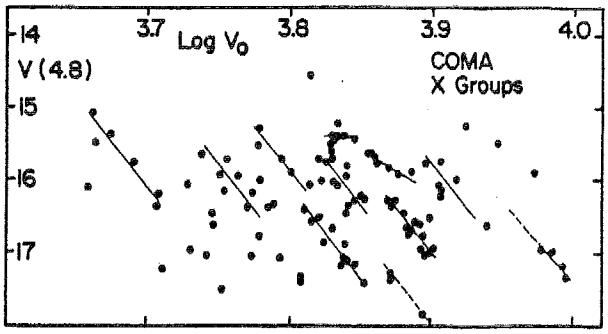


Figure 1.31: Coma cluster band substructure repeated from figure 1.18 [75] to show vertical rollover and distortion in the cross-band pattern at the low redshift end of the upper band.

The CU65 and CU76 cross-bands in Coma at the head of the upper band turn down as if they were still developing. Furthermore, the distortion occurs directly at the top of the vertical column of active galaxies shown in figure 1.27. In the slightly lower redshift cluster A1367 in figure 1.19 the two upper cross-band structures are fully developed toward lower redshift and the leading structure at $\log V_o$ of 3.8 also contains a radio source (see figure 1.11). This was highly suggestive to me of an evolutionary process of band growth toward lower redshift. Note also the extreme low redshift extent of of the Coma core redshifts. Figure 1.20 shows this low redshift extension decreases steadily outside the core, while high redshift limits remain constant. Mean cluster redshift increases with radius.

Photoelectric studies by Weedman [C], who verified the nuclear region Coma cluster photometry, included equivalent photometry in the Perseus cluster with a 6 arc second aperture. His work along with $m_p$ total magnitudes provided a means to study the Perseus cluster in detail. Figure 1.32 reproduces figure 1.8 containing my study of the core of the Perseus cluster. Scatter below and radio sources above band heads are indicated [63] and resembled the Coma cluster pattern.

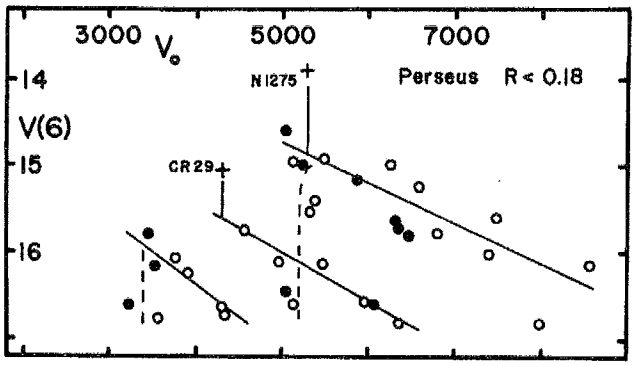


Figure 1.32: The central core of the Perseus cluster repeated from figure 1.8 to emphasize features associated with band heads.

Figure 1.33 extends the Perseus nuclear region study to the outer cluster more than 0.3 degrees from the center [63]. Two effects are easily seen. The pattern has changed dra-

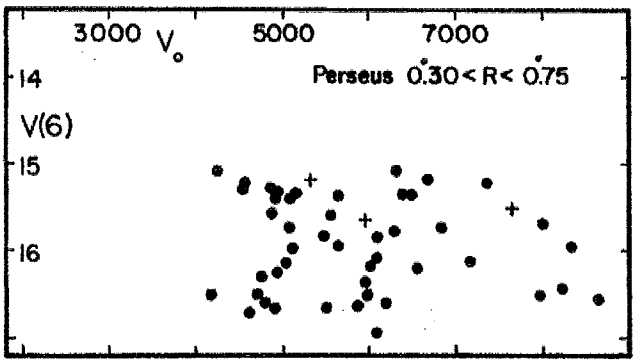


Figure 1.33: The $0.3 < R < 0.75$ degree redshift-magnitude diagram for the Perseus cluster using V(6) nuclear region magnitudes in the Perseus cluster of galaxies [57,63] to bring out the low redshift extension in the core and the presence of vertical-sequences associate with possible band structure. Radio sources are indicated with crosses.

matically. The core redshift again extends much lower in redshift while the upper bound remains constant. Two prominent vertical-sequences also appear at the head of what could be bands. Both have radio sources at the top. A detailed association of banding between

Coma and Perseus is contained in reference [63]. A study of the distribution of galaxies in the vertical-sequences [63] shows no spatial clustering, the galaxies in both columns distribute widely around the core as a property of the extended halo unrelated to any form of dynamical spatial subclustering.

### 1.7.1 Cross-Band Structure Development

Investigations using total magnitudes to examine cross-band structure in the Perseus cluster are shown in figure 1.34. They show that Perseus matches and further extends the upper Coma band including the next lower structure.

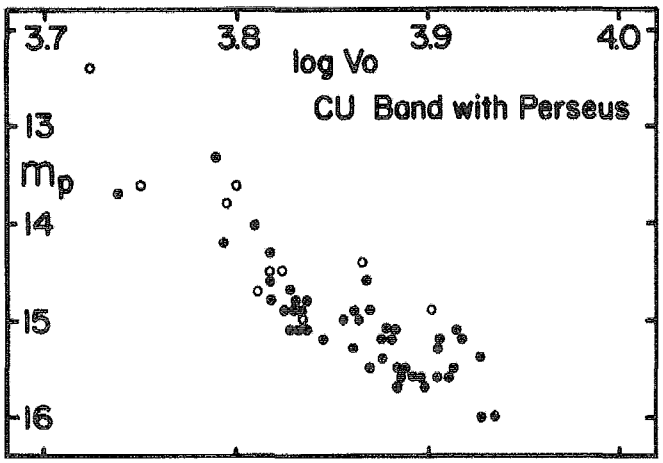


Figure 1.34: CU cross-band structure when the the Perseus cluster (open circles) is added to the Coma + A1367 pattern. The structure now extends into a new lower redshift CU55 cross-band group

Three additional clusters near the Perseus redshift, A194, A347, and the NGC 507 group further strengthen the pattern [63]. To demonstrate significance and independence of individual cross-bands figure 1.35 shows cross-band redshifts in all six clusters projected to their CU band crossing point using a slope of 12 magnitudes per factor of two in redshift.

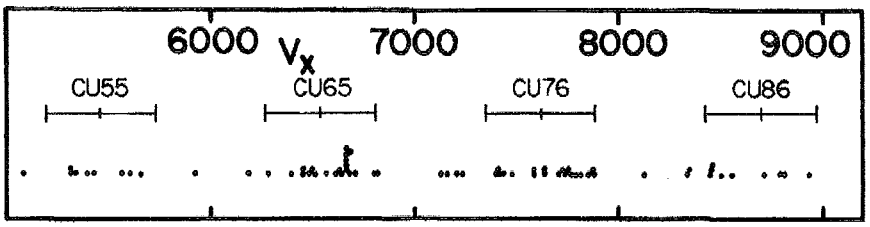


Figure 1.35: CU cross-band redshifts projected to the intersection point with the CU band at a standard slope of 12 magnitudes per factor of two in redshift and quadratically scaled to a uniform spacing for significance testing.

### 1.7.2 Associating Vertical-Sequences with Cross-Bands

Vertical-sequences appear to associate with the low ends of cross-band structures as noted in the Coma cluster. Occasional interlopers between cross-bands in the projected pattern are possible remnants of such columns, especially at the active CU76 region in Coma. Do such vertical-sequences represent structures in the process of forming, perhaps to systematically form new cross-band structures characterized by lower redshift extensions seen consistently in cluster cores? Radio sources, shown with crosses in Perseus diagrams, seem to associate with band heads and/or vertical-sequences consistent with such an evolutionary association [57,75]. Bands may also brighten with radius in clusters [57,75] suggesting that the stage or character of evolutionary development could be a function of radius as implied by changing radial morphological patterns

Further support for the evolutionary concepts is seen in the high redshift cluster 1358+62. Figures 1.36 and 1.37 repeat core and outer redshift-magnitude diagrams of the cluster.

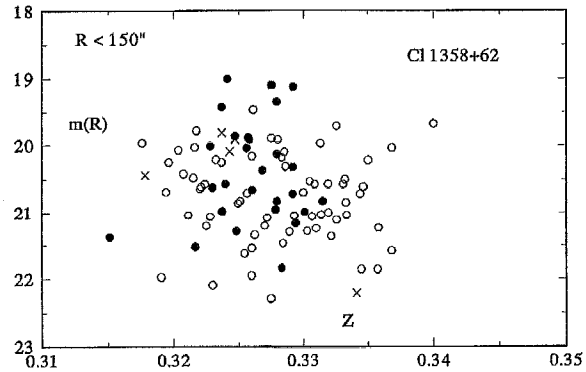


Figure 1.36: Redshift-magnitude diagram of the core of the 1358+62 cluster

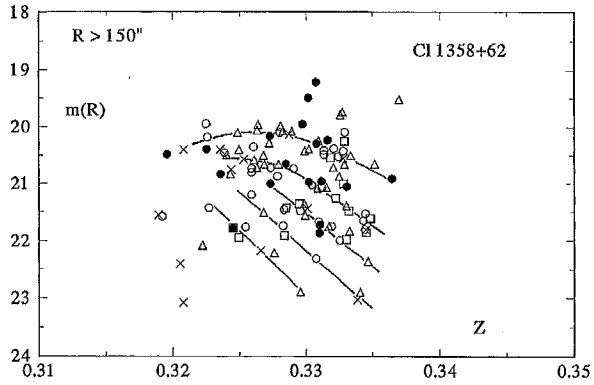


Figure 1.37: Redshift-magnitude diagram of the outer part of 1358+62.

We again see a marked lower redshift extent (to $z = 0.320$) in the core, with no corresponding excess at high redshift values, while a vertical-sequence of ellipticals (filled symbols) appears in the core between $z = 0.323$ and 0.329. In outer parts of the cluster we see a few scattered ellipticals and a well developed band system of later type galaxies mostly above $z = 0.33$ where the core has So types. In the lower redshift outer region around $z = 0.326$ the core ellipticals are replaced by by later types in what I refer to as rollover extensions of bands, and the advanced low redshift group is absent. As noted earlier, where are the lower luminosity function galaxies associated with the advanced low redshift luminous objects if subclustering is involved? What I now see is a cluster expanding and evolving in both time and space, but I will need to say much more about the redshift before I can properly explain that statement. At the time I made this analysis I was only beginning to recognize that the concept of time involves much more than a simple one-dimensional sequencing of events.

The most striking correlation I encountered connecting band structures is shown in figure 1.38, a diagram of 5 compact groups dominated by elliptical or early type galaxies [75] along with a diagram of the Coma-A1367 CM band and upper cross-band pattern for comparison.

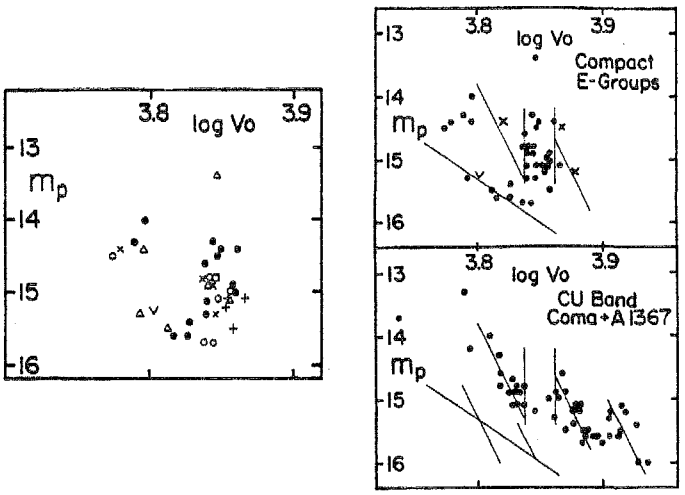


Figure 1.38: LEFT: A composite redshift-magnitude diagram of five compact galaxy groups [75] dominated by early type galaxies. Stephan's Quintet is one of the set (x symbols). See reference [75] for details. RIGHT: The set of compact groups superimposed upon the band structure pattern of the Coma + A1367 clusters [75] to show their relationship. Spirals in the compact groups are marked by x symbols.

The groups come from different locations and include groups like Stephan's Quintet. When redshifts are corrected for differences in galactic rotation to provide an equivalent set of redshifts ($V_o$), the five compact elliptical dominated groups superimpose to form a common vertical-sequence with a low redshift turn at the base in the $\log V_o$ - total magnitude diagram in figure 1.38. Each of the groups contain a 'discordant' redshift galaxy which also superimpose about 1000 km/s lower in redshift. The discrepant redshifts pose a well known stability problem in classical dynamics. The fact that five supposedly dynamically indepen-

dent groups *and* their discordant companions superimpose in a redshift-magnitude pattern poses a remarkably more serious problem. From the viewpoint of the QTC intrinsic redshift concept, however, the superimposition is precisely what is expected. Burbidge (1968) [AY] has pointed out in a similar situation I will discuss in seminar 5 (5.6.0) that such multiple superimpositions are unlikely at the $10^{-6}$ level by accident!

The right hand frame in figure 1.38 shows that the compact group vertical-sequence falls directly between cluster cross-band substructures coincident with vertical-structures within clusters. Vertical-structures of early type galaxies directly relate to the gaps between cross-bands. The compact group sequence drops down and appears to connect to the second band. Furthermore, the displaced 'discordant' group of galaxies corresponds with the location of a next lower CU band vertical-sequence or the very top of a CM cross-band. Band spacing in redshift at the redshift involved is slightly greater than 1000 km/s which equals the offset of the discordant group. Not only do five compact groups and their discordant companions superimpose but the pattern is completely consistent with what is seen within large clusters. Are we seeing redshift structure or is this an extraordinarily remarkable accident?

It may also be useful to point out that the Coma bands are separated vertically by about 3/4 of a magnitude, essentially a factor of two in luminosity. This could be significant if galaxies could fission in an active phase and transfer between bands or band structures. The issue of fissioning will be prominent in later discussions.

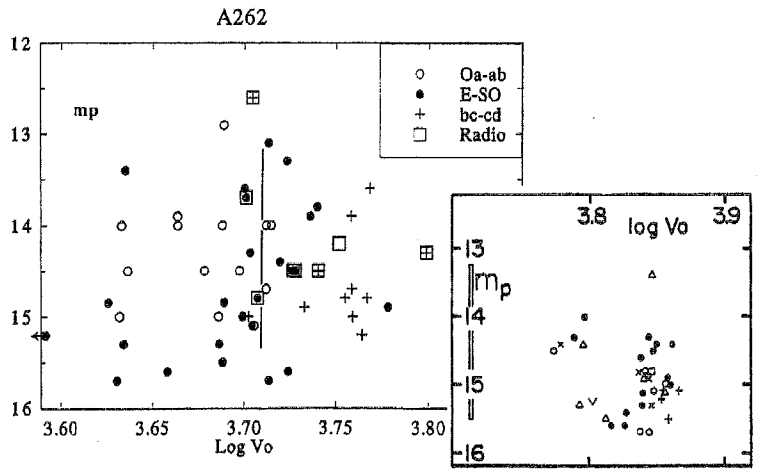


Figure 1.39: The A262 cluster redshift-magnitude pattern showing a vertical-sequence of ellipticals and characteristic split redshift locations of early and late spirals. The lower right insert repeats the compact group pattern from figure 1.38 and marks the location of the A262 vertical-sequence as a double vertical line.

There is one further example of redshift structural correspondence which involves the A262 cluster. A262 was discussed earlier as an example showing the morphological separation on either side of cluster core ellipticals. Figure 1.39 compares the redshift-magnitude properties of the A262 cluster with the set of compact groups just discussed. The split high-low mor-

phological pattern is shown using different symbols and a vertical line indicates a vertical-sequence defined by A262 elliptical galaxies. That sequence drops down and hooks around to lower redshift just as the composite compact groups do. The inset at lower right shows the compact groups. The A262 vertical pattern of ellipticals, indicated by a double line at the edge of the compact group frame, continues the pattern of 1000 km/s steps one more step toward lower redshift. This redshift spacing is, as noted earlier, the band spacing seen in Coma and the spacing of vertical-sequences shown for the Perseus cluster in figure 1.33. The A262 spirals (+ symbols) may be an extension of the band which appears at the base of the compact groups. Furthermore, the high redshift radio source in A262 matches the discordant set of galaxies associated with the compact groups. Such structures appear to be present in repetitive patterns consistent with some form of evolutionary cycle displayed in lookback time.

## 1.8 Summarizing Structures, and Changing Direction

References [57,63,75] contain further information, including extensions to local structures, and summarize my understanding of redshift structure as it stood in the late 1970s. In references [57] and [75] I proposed a provisional evolutionary model shown in figure 1.40.

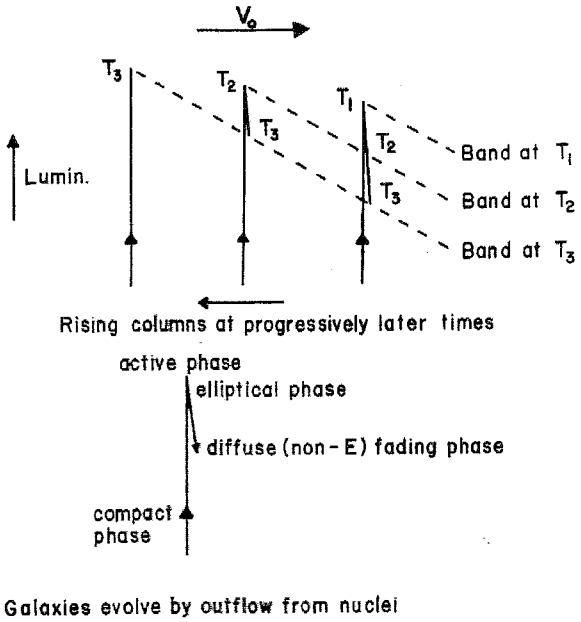


Figure 1.40: An early model of redshift and galaxy evolution

In terms of understanding as I reviewed this section of seminar 1 in 2013, I can describe the model this way. Vertical-sequences, origin to be discussed in seminar 8, which characterize columns of elliptical type galaxies, arise and outflow in cluster cores or groups. Galaxies and aggregates of galaxies are slowly growing. The columns rise to a maximum luminosity and

spawn radio and intense nuclear region activity. At band heads galaxies settle into specific cross-band subgroups where they evolve slowly down in redshift and morphology, as seen in the Coma CL76 and other subgroups. They eventually fade away or possibly regenerate (there will be much more about that later). Successive periods of activity occur at later intervals after the redshift, presumably an intrinsic property of galaxies, has decayed to lower values. An unconventional linkage of expansion of space and the flow through time is implied and at the time of most seminar 1 the flow was undefined. How such a model integrates into a broader QTC cosmology requires more discussion of redshift properties in following seminars. All the concepts in this very early model are tied closely to accurate detailed systematic observational work which does not fit within conventional dynamics.

## 1.9 Redshift Quantization

At this stage, in the mid to late 1970s, I had been pretty well typed as a non conventional astronomer. The studies were fascinating, and this period was certainly a very interesting time in my life. But by 1979 after talking about possible evolution models related to my findings concerning galaxies and the nature of the redshift it was time to shift the emphasis. I was continuing to improve the quality of redshifts, using such things as multiple observations in the Coma cluster, trying to make the data as accurate as possible. Throughout my life I have established a reputation of producing excellent redshifts; people rarely question the redshifts I produce, just the way I talk about them. But after1979 I pretty much abandoned morphology and redshift-magnitude correlation studies. Morphology and magnitudes are difficult things to measure precisely. They were what I called fuzzy variables; it was hard to get exact measures of morphology, or know just what a magnitude of a diffuse thing like a galaxy means. Furthermore, even though there is plenty of evidence, classical viewpoints are so incredibly solidly entrenched that an evolutionary view connecting galaxies and the redshift was not acceptable, much as biological evolutionary concepts are still widely rejected by society today. History is replete with such rejections, just ask Copernicus or Galileo. I therefore turned my attention almost entirely toward the redshift itself, the one quantity which could in principle be very precisely measured and studied. I will say much more about the significance and likely cause of correlations and radial dependence, but I did not understand them at the time as I believe I do now. Seminar 1 is primarily the story as of 1979, there is much more to come. QTC did not yet exist.

Figure 1.41 is an early picture of the brightest redshift-magnitude band in the Coma cluster [44]. The upper part uses original old redshift data available at the time I discovered banding. Many of those old redshifts, from Mount Wilson and Lick were very poor, containing errors of up to 300 or 400 km/s. As redshifts were progressively improved the lower diagram emerged. Uncertainties were now on the order of the symbol size. It became increasingly clear that we not only had bands, and those bands broke up into a finer cross-bands, but that substructure was now breaking up into precise redshifts. The redshift was not a continuous variable, the redshift itself was apparently quantized, a discreet quantity like spectral lines in a spectrum. At this point, in the middle 1970s, and completely by 1980 I began to concentrate entirely on demonstrating, and first convincing myself, that the redshift was really a quantized quantity. I moved from the correlation studies outlined in this seminar to the quantization studies I will develop in the next two seminars.

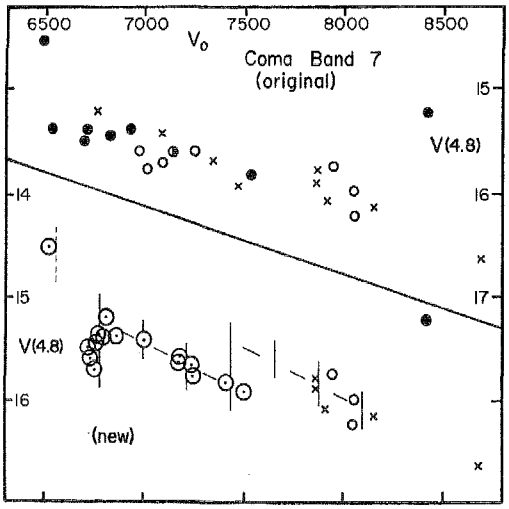


Figure 1.41: The upper frame shows the brightest Coma cluster redshift-magnitude band first seen using mostly old low precision redshifts [44]. Symbols distinguish redshift sources. Large circles in the lower frame represent newer redshifts; symbol size characterizes uncertainty. Vertical lines represent characteristic 'quantized' periodicity which was becoming apparent.

My final word (but see below) about correlations studies, redshift-magnitude structure, the correlations in morphology, the correlations with activity, and the underlying unity in some kind of evolutionary process, can be summed up fairly simply. There is something very basic going on there. I believe that follow-up of those early studies would be extremely rewarding, but it will not happen within the mindset of present extragalactic thought. I hope that some daring individuals in future generations will nevertheless pursue such ideas.

The above paragraph summarized my thoughts as I began formulating this book many years ago so I decided to leave it in the text. By 2014, now in the 8th version of seminar 1, I can and will provide consistent verifiable explanations for the above effects. Seminar 8 includes my understanding of redshift-magnitude bands for example (with verifiable analysis) as I complete the draft of this book in 2014. The last part of the paragraph, however, appears to be unchanged.

# Chapter 2

## Is The Redshift Quantized, Variable?, The Empirical Period. 1973 to 1992, Learning About z

Seminar 2 Version 5

## 2.1 Introduction

The first seminar examined correlations between the redshift and intrinsic properties of galaxies, their magnitude, morphology and activity, which provided some of the first modern tests on the nature of the cosmic redshift. Such correlations appear to require that the redshift be at least partially an intrinsic property of galaxies, rather than an extrinsic dynamical parameter as assumed in classical cosmology. Evolution of an intrinsic effect in cosmic time provides an alternative to spatial expansion of the universe to generate the observed Hubble Law. As quality and quantity of redshift data improved finer structure emerged in the correlation substructure, and by 1974 it was becoming apparent the redshift itself was in fact a quantized quantity. This seminar describes the empirical phase of development of the concept of a quantized redshift and implications concerning the very nature of galaxies and the universe they occupy.

## 2.2 The Discovery of Redshift Quantization

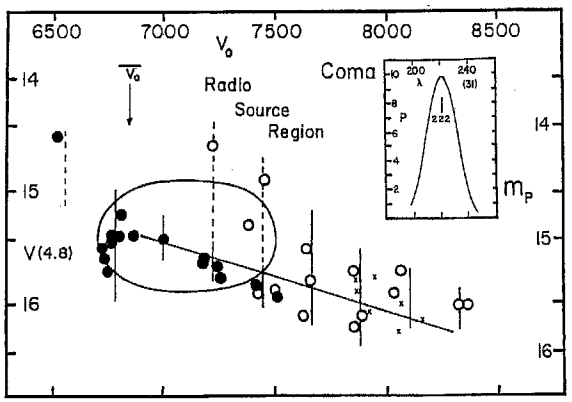


Figure 2.1: Initial redshift quantization patterns seen in the brightest Coma cluster redshift-magnitude band as quality improved. Redshift was clumped in 222 km/s intervals. This interval was later recognized to be an x3 modulation of 73 km/s which was connected to quantum substructure within galaxies

Figure 2.1 extends figure 1.41 from the first seminar to show how a finer quantized pattern within the redshift emerged from correlation studies in the Coma cluster as redshift precision improved. The initial power spectral analysis is shown as an inset to the redshift distribution on the brightest redshift-magnitude band in the cluster. An initial redshift periodicity emerged at about 222 km/s. By 1974 it was apparent the redshift was not only an intrinsic property of galaxies, but it was apparently restricted to specific values. The redshift was quantized, an idea very much at variance with any standard ideas of the time.

I had no idea initially what significance to give to the number 222 km/s. It applied to a specific set of redshifts in the Coma cluster, implied that the redshift was probably quantized, but how generally that number or concept applied to anything else was a mystery. I do not recall the details of how my work proceeded in the months that followed, but I do know quite specifically when I realized a much more important key number was one third of 222, in the 70-75 km/s range. The following paraphrased note appears in a few journal records I kept between mid 1975 and 1976.

> June 23-27 1975: Measured eleven remaining Coma galaxy spectra to complete data for a paper. Noted that the last redshifts were done in October 1974. I must have been getting into the first stages of my paper just completed ... although I did not get the two-stream idea of galaxy structure until somewhat later. The key moment came when (name omitted) gave a colloquium on the 140 km/s splitting in quasar absorption lines. I had not known about that. Suddenly I realized that the 70 km/s spacing could apply to *all* redshifts. I had previously thought the spacing got larger for larger 'systems' of redshift. Recognizing the universality of 70 and its multiples gave me a real basis to tie things together at all levels. This colloqium by (name omitted) was a real turning point.

It is ironic that the gentleman involved, the same gentleman who strongly attacked my Coma band paper at the AAS Amherst meeting in 1972, continued to play an interesting role in what was to eventually lead me to a fundamentally new cosmological model.

### 2.2.1 Introducing The Concepts to Astrophysics

For a young astronomer at the University of Arizona to propose the redshift was quantized, in the face of classical opinion, it was imperative to be sure there were no obvious inconsistencies with the concept. Consequently, in 1975-1976 I made an extensive review of what was actually known in astronomy at that time. As I noted in the first seminar, back in that era little was known about galaxies. We were dealing with limited data which was not of especially high quality; redshifts were not accurately measured quantities. It was quite possible, and proved to be the case, at that stage there was nothing in the literature inconsistent with a quantized redshift.

In the 1970s differential measurements provided some of the best data. Systematic and random errors could be very large for optical redshifts, but differential work could be done with a fair degree of precision. Such things as rotation studies therefore played an important role in early stages of development of redshift quantization. After convincing myself there was nothing inherently inconsistent with the quantized redshift idea, I published, with some difficulty, three papers in the ApJ [55, 58, 59]. They went through quite a number of

refereeings (I believe the number was about eleven). Figure 2.2 contains the essence of the first paper [55].

DISCRETE STATES OF REDSHIFT AND GALAXY DYNAMICS. INTERNAL MOTIONS IN SINGLE GALAXIES

WILLIAM G. TIFFT
Steward Observatory, University of Arizona
*Received 1975 June 20; revised 1975 October 15*

I. INTRODUCTION

In a series of papers (Tifft 1974 and references therein) evidence for a totally intrinsic redshift has been developed. The concepts are founded on the existence of correlations with the redshift of "normal" galaxies which are at variance with conventional gravitational dynamics. The tentative explanation is that multiple substates of matter exist and that matter in galaxies forms a time evolving progression of discrete states which we see displayed serially in look-back time. At a given cosmic time only a limited range (or ranges) of states is present. Our immediate solar neighborhood is representative of one specific state.

Two new observationally derived concepts will be introduced in this paper. Because of their unusual nature they will be stated in advance and should be considered as hypotheses to be tested against observations. Within observational limitations they are consistent with all new and published data known to the author. Critical examples will be used in the text to develop the ideas: first, the redshift occurs in discrete steps with a step size near 70–75 km $s^{-1}$ and/or multiples thereof; second, all major galaxies (and presumably related objects) contain *two* states of redshift which appear on opposite sides or "poles" of the nucleus. Lesser amounts of other states may be present.

Figure 2.2: Concepts introduced in the first paper on redshift quantization [55].

The redshift appeared to occur in discrete steps with a step size in the neighborhood of 70-75 km/s. It further appeared galaxies themselves had to be considered to be redshift 'dipoles', where a galaxy has two associated redshift states discontinuous across the nucleus. Implications of a quantized redshift appeared in the second paper [58], as summarized in figure 2.3.

If the redshift is quantized, you are immediately in trouble with gravitation. The appar-

ent existence of such fine structure reduced permitted velocity dispersions to too small a value, which implied that galaxies were relatively non-interactive gravitationally. That is a pretty serious statement to make in the ApJ; the editor assigned this paper a rare editorial disclaimer, admitting they could not find the paper in error, but making it clear that they were not endorsing the idea. Figure 2.3 includes the disclaimer associated with the paper. There are very few such notes in the ApJ and I have two of them.

It may be useful at this point to emphasize what a lack of conventional gravitation between galaxies implies since it will be important later in this presentation. If classical gravitation breaks down on scales larger than the scale of galaxies, but obviously applies on our local scale within a galaxy, there must be a transition zone between. Classical cosmology invokes dark matter halos (and dismisses or ignores quantization) to preserve gravitation. To look objectively at a new model one must be prepared to ignore the classical bias and look at what real observations imply. Subsequent discussion of galaxy substructure and especially galaxy pairing as a function of spacing bridges the transition zone. Take careful note of what must be invented and what will have to be ignored to preserve the classical view. I believe until we properly explore and understand this transition it is very unlikely we can develop a valid cosmology.

## 2.3 Evaluating Quantization

Well, how do we evaluate quantization? The subject developed in several stages, beginning with investigation of the nature of single galaxies. I will say a little about that stage. We will then go on to systems of galaxies, especially pairs, since the implication is the redshift must be quantized between isolated galaxies. In the interval from 1975 to 1989 important studies were carried out using pairs. I will review those investigations in some detail. At that stage I was dealing with differentials, redshift differences between objects or points close together. The final major step occurred when I took a global view, which phased redshifts together over the entire sky, work that began in the late 1970s. I will introduce the subject, which will be the major theme of the third seminar. In fact a global viewpoint was inherent in correlation studies. Pattern matching between clusters, and scaling relationships, discussed in the first seminar, implied some level of global synchronization.

I should first say something about the units of quantization. 72 km/s became the popular number describing the quantization interval, 72 km/s and various harmonics. It is widely believed the number was derived from studies of pairs of galaxies. This is incorrect. The number originated from studies of rotation curves, internal properties of galaxies, and was quantified to a fairly specific value by studies of the Coma cluster of galaxies in the second introductory paper [58]. This initial work predicated what would be found in subsequent work with double galaxies. Many people like to say quantization lacks predictions. In fact a very basic prediction was made in the 1970s - that the study of double galaxies would yield a predetermined periodicity. As you will see shortly, it did.

### 2.3.1 What Is A Galaxy?

What is a galaxy? That was the first question I asked in the 1970s, and was the theme of the first introductory paper [55] published in 1976. The paper developed what I called

# DISCRETE STATES OF REDSHIFT AND GALAXY DYNAMICS. II. SYSTEMS OF GALAXIES*

WILLIAM G. TIFFT
Steward Observatory, University of Arizona, Tucson
*Received 1975 June 30; revised 1975 December 12; revised 1976 March 2*

## ABSTRACT

In the first paper in this series, a basic model was developed, for individual galaxies, consisting of two expanding opposed streams of material differing systematically in redshift. In this paper, galaxies in pairs and groups are shown to manifest no evidence of gravitational interaction. Redshift differentials between pairs of galaxies and between galaxies in clusters are found to take on preferred values which are various multiples of a basic 72.5 km $s^{-1}$. There is also direct evidence that the redshift periodicity phases together between groups to imply that there is no large-scale motion between clusters of galaxies. The various mass discrepancies or peculiarities arising from a dynamical interpretation of differential redshifts are also shown to be of a form that no gravitational interaction and no significant motion require.

## I. INTRODUCTION

In the first paper of this series (Tifft 1976, hereafter DSR I), evidence for a two-redshift stream structure of individual galaxies was developed. In this paper, implications of that concept are extended to pairs and clusters of galaxies. In the conventional picture, such assemblies represent successive steps in extending the concept of gravitational interaction to larger scales. The introduction of a discrete redshift has direct implications with respect to large-scale gravitation. Since gravitation is viewed as the dominant large-scale force inducing "observed motion," reinterpretation of the "motion" must reduce the role of large-scale gravitation. It was originally considered possible that the intrinsic redshift effects might simply resolve the virial discrepancy problem in clusters and result in normal bound groups. The apparent existence of fine structure (Tifft 1974) in the redshift distributions, however, reduces the permitted normal velocity dispersion to too small a value. This implies, assuming the observations are correct, that galaxies are relatively noninteractive gravitationally with their more distant neighbors. Thus the discussion of double galaxies and clusters in the context of the discrete redshift cannot be separated from a consideration of gravitatio

* *Editor's note.*—The referees of this paper neither could find obvious errors with the analysis nor felt that they could enthusiastically endorse publication. The subject matter is interesting and perhaps very important. A more complete assessment of the analysis is beyond the role one normally expects of referees.

Figure 2.3: Implications of redshift quantization relating to gravitation on galactic scales as introduced in the second paper [58]. The editorial disclaimer which was attached to this paper is shown to illustrate the reaction of the scientific community to ideas which fall well outside of mainstream established physics.

the redshift dipole concept. A galaxy could be represented by two streams of material, interleaved and winding up in the case of a spiral, but with an intrinsic redshift offset between them. Figure 2.4 shows one of the first examples I used, the rotation curve for NGC 2903.

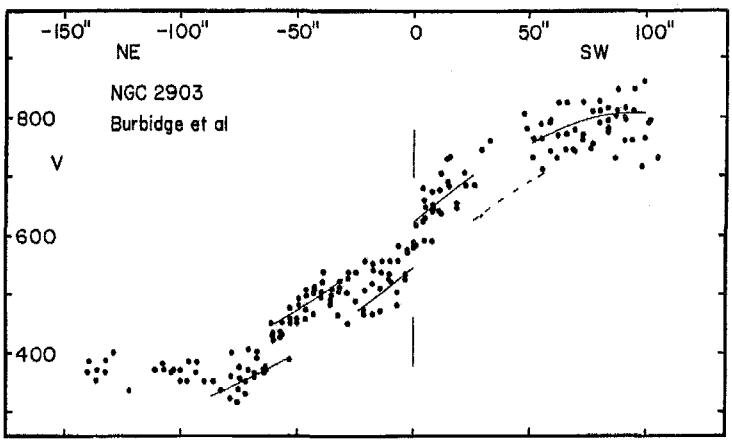


Figure 2.4: The rotation curve of NGC 2903. The alternating pattern of 70 km/s offsets corresponds to where the slit of the spectrograph crossed the two spiral arms and provided part of the original evidence for a two-stream intrinsic-dipole model of redshift structure of galaxies. The abscissa is distance in arc seconds from the nucleus along the major axis. Vertical lines mark a nuclear redshift discontinuity.

The location of the central nucleus is indicated. On either side, there is an alternating pattern of offsets, which corresponds with the crossing of the two individual spiral arms. The difference between the arms suggests an intrinsic offset, one spiral arm intrinsically shifted about 70 km/s from the other. That was the beginning of the dipole concept and the number 70 km/s.

Follow-up studies examined other galaxies [55], especially M31, the great Andromeda spiral. Figure 2.5 diagrams the M31 model, showing two interleaved intrinsically different spiral arms. Figure 2.6 contains a rotation and expansion model representing one of the redshift states which was applied to M31 to evaluate how well the two stream model represented observational data. By removing the model remaining deviations represent other redshift states present, which are indeed seen to be quantized as predicted by the dipole model.

M31 is well represented by the two stream model where the two streams (spiral arms) have an intrinsic 70 km/s different redshift. Other galaxies, including our own, were analyzed from the same perspective and discussed in the initial paper [55]. Further evidence for the dipole model will be discussed later. The two-stream terminology for the model incorporates outflow from a nuclear source which will become a key element in the QTC cosmological model with quite a variety of evidence in support of the concept. Figure 2.7 gives three examples of optical and radio data sets mapping velocity fields in M31 which were analyzed using the two stream dipole mode. Reference [55] includes many further examples. In

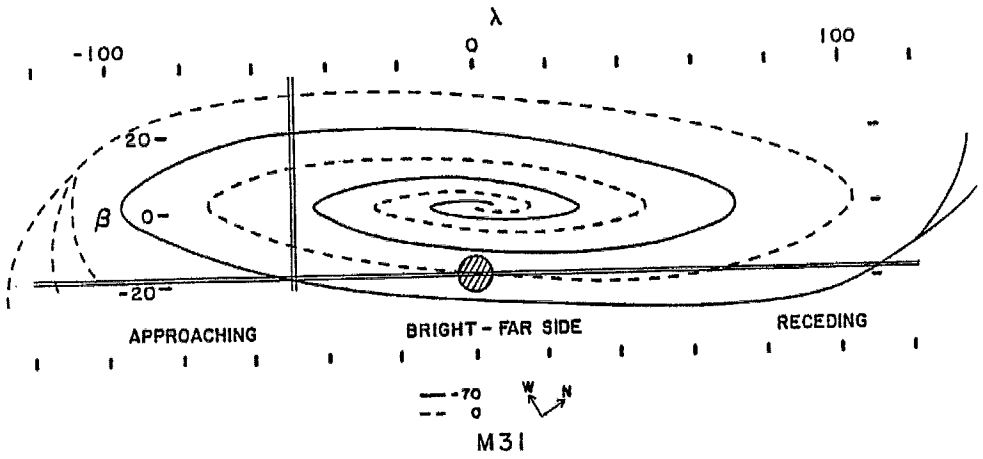


Figure 2.5: Schematic model for the Andromeda galaxy, which represents the two arms as streams with an intrinsic redshift difference of 70 km/s. Lines mark directions along which 21 cm radio scans detected anomalous redshift patterns which can be explained by the dipole model. Radio beam size is indicated; the rectangular coordinate system is in arc minutes aligned with the principal axes of M31.

ROTATION AND EXPANSION MODEL FOR M31

| $R_{kpc}$ | $R'$ | $V_R$(km s$^{-1}$) | $V_E$(km s$^{-1}$) |
|---|---|---|---|
| 0..... | 0 | 0 | 0 |
| 0.2..... | 1 | 105 | 8 |
| 0.6..... | 3 | 155 | 24 |
| 1.0..... | 4 | 175 | 39 |
| 1.6..... | 8 | 188 | 53 |
| 2.0..... | 10 | 195 | 57 |
| 2.4..... | 12 | 200 | 60 |
| 3..... | 15 | 207 | 60 |
| 4..... | 20 | 218 | 50 |
| 5..... | 25 | 228 | 40 |
| 6..... | 30 | 236 | 30 |
| 8..... | 40 | 250 | 20 |
| 10..... | 50 | 265 | 19 |
| 12..... | 60 | 278 | 18 |
| 14..... | 70 | 290 | 17 |
| 16..... | 80 | 302 | 16 |
| 18..... | 90 | 311 | 15 |
| 20..... | 100 | 316 | 15 |

Figure 2.6: Rotation and expansion model used for M31 [55]. After removing rotation and expansion using this model the residuals show the periodic pattern associated with redshift quantization.

every case strong periodic 70 km/s patterns related to the spiral structure are apparent. At this stage the model certainly was a far-out hypothesis, but an important early step toward QTC. Conventional dynamics cannot explain redshift correlations or quantization. Galaxies must in some way become quantized 'particles' on the universal scale to explain those phenomena. Later discussion and evidence will make it quite clear that the two stream dipole model plays a key role in solving major problems within classical cosmology

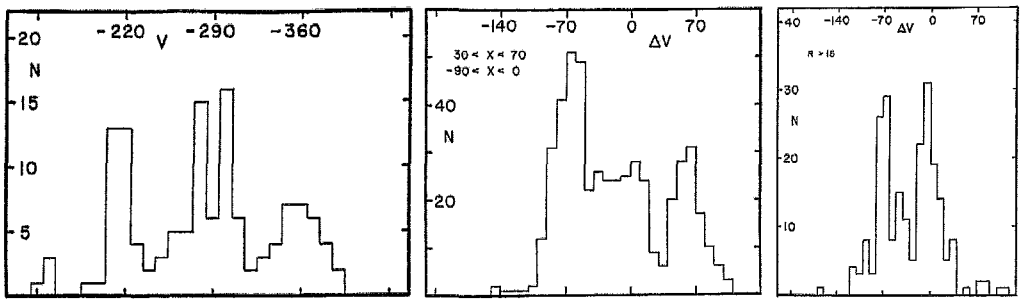


Figure 2.7: LEFT: Periodic pattern in emission line velocities for position angles near the minor axis in the central region of the M31 disk after allowing for disk expansion [55]. N is the number of measured points contributing to velocity intervals indicated. MID: Periodic differential pattern in emission line velocities in the main body of the M31 disk after removing disk expansion and rotation [55]. Points in rich emission regions near the center are consistent but omitted for clarity since they overwhelm the signal from the extended regions. RIGHT Periodic differential pattern in 21 cm velocities in the outer part of the M31 disk after removing disk expansion and rotation [55]. The central region is omitted since the 21 cm beam is too large to resolve redshift structure.

I have no significant doubt that galaxies contain an intrinsic redshift dipole structure. Based upon what I know now as I write this in 2013, structures and periods involved are more sophisticated than simply 70 km/s dipoles, but the idea that galaxies are built upon multiple intrinsic redshift states I believe to be central to understanding galaxies. A dipole model provides a natural explanation for what is commonly interpreted as warping of galaxy disks and effects such as counter rotation where the core and outer parts of galaxies appear to rotate in opposite directions. For slowly rotating systems, such as elliptical galaxies, the presence of a nuclear redshift offset (which can either enhance or reduce rotational effects) completely overwhelms rotation from a conventional viewpoint. Viewed from the dipole model, however, a clear picture emerges that yields a simple rotational pattern which connects smoothly to early type spirals. Issues related to the dipole model could provide a discussion subject in itself and after this introduction will be discussed when appropriate, especially in seminar 8 where the issue of what a dipole actually is will be addressed. I prepared and submitted a paper to the ApJ which set forth basic evidence for a dipole redshift model. The paper was rejected but the ideas are important and underlie subsequent developments. The paper, Steward Preprint 513 [85], is discussed in seminar 7 and included in its entirety as [Ap1] in the supplementary material. The third introductory paper [59], published in 1977, did look at evidence for internal effects within our galaxy, which could be ascribed to intrinsic effects. Such studies have not been pursued, but might prove very

interesting. Part of the abstract of the third paper reads as follows. The paper was entitled "Discrete States of Redshift and Galaxy Dynamics III. Abnormal Galaxies and Stars". It is remarkable how often 70 km/s appeared.

> ... Evidence is examined for effects of multiple redshift states within our own galaxy. Four possibilities are considered: interstellar material, pre main-sequence objects, rotation of massive stars, and highly evolved peculiar stars. All classes show evidence of the predicted redshift periodicity. ...

### 2.3.2 Binary Galaxies, The Perfect Test of Quantization

The most important initial tests of differential quantization utilized binary galaxies, pairs of galaxies classically in orbit around each other. The frequency of redshift differences within pairs, assuming classical theory, has a simple form which depends only upon projection angle to the line of sight. The shape of the distribution is independent of system dynamics and was derived in my second introductory quantization paper [58]. Assuming isotropic distribution for orientation of pairs in space (it is difficult to assume anything else without placing us in a unique position) differential velocities will project to form a continuous monotonic decreasing function. It should peak at zero and drop smoothly away from zero as shown schematically in the left side of figure 2.8. However, if galaxy redshifts are quantized in steps of 72 km/s, and orbital motion is absent, the differences will be quantized since intrinsic effects are unaffected by projection. The differential redshift pattern will be a histogram as shown at the right in figure 2.8. If both quantization and orbital motion are present the pattern will be severely distorted and neither pattern would be recognizable.

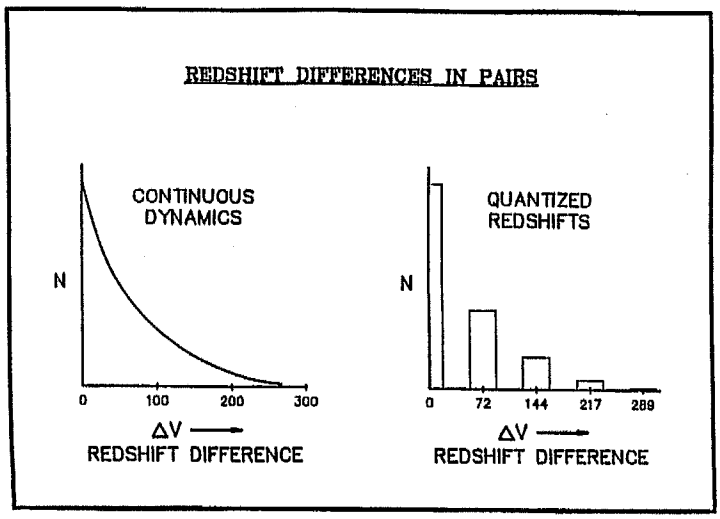


Figure 2.8: Schematic comparison of the form of differential redshift distributions for binary galaxies in classical and quantized redshift models.

There is a very striking difference between predictions arising from quantized and standard continuous models!

### 2.3.3 Karachentsev Pairs and the Peterson Sample

In the early 1970s I began two major observational programs utilizing the Steward Observatory 90-inch telescope and image tube spectrograph. The spectra were taken at 240 A/mm dispersion recorded photographically. The first program was, naturally, the study of the redshift utilizing the Coma cluster and related clusters of galaxies. This work led into my third major area involving large scale structure. The second program involved a comprehensive study of the 1972 Karachentsev [R] catalog of double galaxies. Aside from the critical role of double galaxies in the quantization study there were interesting other aspects involved. The catalog was especially interesting since it included a morphological interaction class for each pair, LIN for pairs with extended filamentary distortion, DIS for simpler distortion, ATM for a common halo (as in close E type pairs), and SEP for separate close objects with no direct evidence of connection. I later had an opportunity to work with Karachentsev to provide redshifts for a compact group of early type galaxies in the constellation Cetus which contained a discordant redshift [65]. This group is one of five such groups which appear in a later seminar which indicates that such discordant objects are expected and consistent with QTC.

The Karachentsev catalog contained 603 entries of which 324 have separations less than 80 arc seconds. The narrow spacing allows these pairs to be observed simultaneously using an oriented slit. All such pairs were observed with another 36 using separate spectra. Pairs were classified as high weight HWP or low weight LWP according to number of lines measured, line strength and clarity. Common slit pairs permitted direct redshift differentials to be measured independent of external random and systematic redshift uncertainty. Common slit measures, where only common lines were compared between the pair involved, yield especially accurate differentials. Such measures were denoted CLE, CLA or CLAE according to whether emission, absorption or a combination of lines were used. Emission line strength was noted as S, M, W or A for strong, medium, weak or absent (absorption only). A study describing the emission properties of the pairs was included in reference [86]

The basic study of pairs was published in 1982 [82] including a very extensive error analysis. All spectra (about 500) were measured manually within a 90 day period as I prepared the data for reduction and analysis on my 1978-79 sabbatical in Bologna, Italy. The early stage of reduction was greatly assisted by Professor Capaccioli at Padova University who provided computer time and assistance. Final work was done upon my return to the University of Arizona. Final uncertainties were found to be $\pm 65$ km/s for individual redshifts and from $\pm 18$ to 30 km/s for common line differentials depending upon separation. An even more significant study of pairs was presented to me while in Bologna. I will summarize the optical work after introducing the Peterson data.

Steven Peterson [H] had done a 21 cm radio studies of double galaxies. Following a colloquium I presented relating to quantization I was given a copy of Peterson's thesis by someone who remarked "look at this and you will see that your idea does not make sense". I immediately reviewed the work and found that it in fact fit the predicted periodicity pattern virtually perfectly. Apparently the gentleman who gave me the paper never bothered to check, a typical establishment response. I counted the number of pairs with differentials close to expected multiples of 72 km/s, compared with the number which fell in-between, a statistic I designated the In:Out ratio. The pattern was then formally compared against a smoothed equal area continuous pattern. Figure 2.9 [78] shows the result.

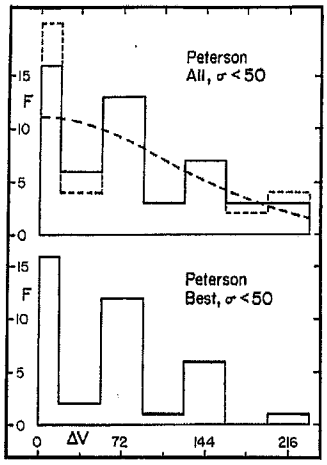


Figure 2.9: The periodic pattern [78] for differential 21 cm redshifts in galaxy pairs tabulated by Peterson. The upper part shows all but the least accurate data, the lower portion shows the effect of corrections for possible biases. Dashed lines in the upper histogram show the effect of including optical data. The smooth dashed curve is an equal area distribution of continuous type expected classically.

The result is consistent with a purely quantized redshift model, there was no evidence for any distortion due to classically expected orbital motion. The figure 2.10 table contains Chi-square evaluations of deviations from classical predictions. The result is highly significant.

SUMMARY OF STATISTICS, $\Delta V < 250$

| Parameter | Complete List | After Opt. Improvement | Corr. for Opt. Pairs | Corr. for Signal Overlap |
|---|---|---|---|---|
| Total..... | 43 | 43 | 36 | 30 |
| $N^{<18}$..... | 31 | 34 | 30 | 27 |
| $N^{>18}$..... | 12 | 9 | 6 | 3 |
| $\chi^2$..... | 7.7 | 13 | 16 | 19 |
| $p$..... | 0.006 | 0.0003 | 0.00006 | 0.00001 |
| $N^+$..... | 13 | 13 | 12 | 11 |
| $N^-$..... | 18 | 18 | 15 | 10 |

Figure 2.10: Chi-square evaluations of significance of periodic deviations in Peterson redshift differentials in galaxy pairs from a smooth continuous pattern [78]. p is the probability the pattern is consistent with a smooth continuous Gaussian curve of equal area.

With no corrections to the data set, Peterson's data shows a very significant preference for the quantized model. Improvements were made including removal of less accurate optical data, possible optical pairs and close pairs where radio beams overlap and mix signals. The initial paper was submitted to European journals but rejected twice, apparently simply because it could not possibly be correct. I then submitted the paper to the ApJ in 1980 where

it was reviewed and immediately accepted [78]. The analysis was redone in 1982 [81] with additional data from the literature and initial results from optical studies at Steward. A great effort was made to assure that uncertainties were within ±25 km/s. The quantized character of differentials was fully confirmed. In retrospect I am surprised the evidence was so strikingly clear. Neither the early 21 cm radio or the optical data had well determined uncertainties and the collection was highly inhomogeneous. There was room for improvement, but there was no doubt in my mind that double galaxy redshifts were indeed quantized.

### 2.3.4 The Karachentsev Study Findings, Evaluating I/O Ratios

Figure 2.11 [83] gives a breakdown of my study of the Karatenshev pairs. Most of the notation has been discussed in the previous section describing homogeneous morphological and spectroscopic classifications of types which permit sorting by redshift quality. Subsamples which can be measured with the greatest accuracy and are present in sufficient numbers are clearly quantized as predicted. Optical studies include many close pairs and types which cannot be studied with single dish radio telescopes. The Karachentsev pairs are clearly consistent with general quantization in pairs of all types when a proper statistical analysis is applied. Figure 2.11 will be described further after discussion of working with I/O ratios.

*I/O* Ratio Tests

| Sample | $N$ | *I:O* | *I/O* | $p_=$ | $N_{min}$ | $\sigma(I/O)$ | $\langle S'' \rangle$ | $\sigma(S'')$ | $p_=$ |
|---|---|---|---|---|---|---|---|---|---|
| HWP | 200 | 118:82 | 1.60 | 0.010 | 120 | 22.7 | 40 | 22 | 0.8 |
| LWP | 51 | 22.5:28.5 | 0.79 | ... | (>2000) | >30 | 50 | (33) | (0.3) |
| HWP, $S'' < 40$ | 101 | 64:37 | 1.73 | 0.007 | 60 | 20.3 | 23.5 | 19 | 0.55 |
| HWP, $S'' > 40$ | 99 | 54:45 | 1.20 | ... | (500) | 26.2 | 60.5 | 26 | 1.0 |
| HWP, ATM | 60 | 40.5:19.5 | 2.08 | 0.007 | 35 | 18.5 | 24 | 19 | 0.9 |
| HWP, LIN | 42 | 25.5:16.5 | 1.55 | ... | (90) | 21.6 | 35.5 | 21 | 1.0 |
| HWP, DIS | 42 | 25:17 | 1.47 | ... | (110) | 22.3 | 48 | 23 | 1.0 |
| HWP, ATM+LIN+DIS | 144 | 91:53 | 1.72 | 0.002 | 60 | 20.3 | 35 | 21 | 0.85 |
| HWP, SEP | 56 | 27:29 | 0.93 | ... | (225) | : | 53 | 24 | 0.2 |
| HWP, SEP, $S'' < 53$ | 28 | 15:13 | 1.15 | ... | (100) | 27.5 | 39 | 22 | 0.45 |
| HWP, SEP, $S'' > 53$ | 28 | 12:16 | 0.75 | ... | (750) | : | 66 | 27 | 0.25 |
| HWP, CLE | 63 | 40:23 | 1.74 | 0.03 | 65 | 20.2 | 43 | 22 | 0.6 |
| HWP, CLA | 89 | 54:35 | 1.54 | 0.04 | 90 | 21.7 | 36 | 21 | 0.85 |
| HWP, CLAE | 34 | 15:19 | 0.79 | ... | (150) | : | 45 | 23 | 0.1 |
| HWP, SS+SM | 43 | 27:16 | 1.69 | ... | (65) | 20.5 | 40 | 22 | 0.75 |
| HWP, WA+AA | 82 | 50.5:31.5 | 1.60 | 0.04 | 75 | 21.5 | 38 | 21 | 1.0 |
| HWP, MM+MW+WW | 56 | 29:27 | 1.07 | ... | (100) | : | 43.5 | 22 | 0.2 |
| HWP, CLE, $S'' < 40$ | 29 | 20.5: 8.5 | 2.41 | 0.02 | 25 | 17.2 | 19 | 18.5 | 0.7 |

Figure 2.11: Summary table of the differential redshift analysis of optical pairs observed at Steward Observatory [82] Refer to the previous discussion of the Karachensev pairs for definitions of the samples.

Proper evaluation of I:O ratios is moderately complicated and depends on size and quality of each subsample. Given a predicted periodicity, $P$, observational uncertainty, $\sigma$, will blur the pattern. As uncertainty increases sample size, $N$ must increase to establish a given level of significance for an observed I/O ratio. Attempts to disprove quantization using invalid samples were sent to me concerning both double galaxy redshift quantization and redshift-magnitude band significance levels until I published a paper [83] showing the relationship

between data uncertainty (which blurs periods or bands together), sample size, I/O ratios and significance levels. Figure 2.12 shows the relationship assuming standard Gaussian error distributions within observed data. Uncertainty, as a fraction of an interval ($P/\sigma$ in the case of a period) is plotted against a measured I/O ratio. The left scale is preset for P of 72 km/s. The curve marks the minimum sample size necessary to obtain an 0.05 probability of significance for the I/O ratio. To achieve significance, given an I/O ratio, one can determine the minimum sample size required and what the maximum sample uncertainty can be to achieve minimum significance. Both criteria must be satisfied although one can compensate for the other if they are close to the limit. A common way to use the figure is to take a sample, determine the sample size and I/O and verify that N is big enough. Then calculate what the maximum allowed dispersion is and verify that the sample matches or falls below it. If that is true the ratio will yield a valid test against a uniform distribution. It amazed me how many clearly invalid tests I received. All subsamples in figure 2.11 containing enough pairs observed with sufficient precision are consistent with 72 km/s quantized distributions at the level indicated in column 5. No valid probability can be calculated from I/O if the test is failed.

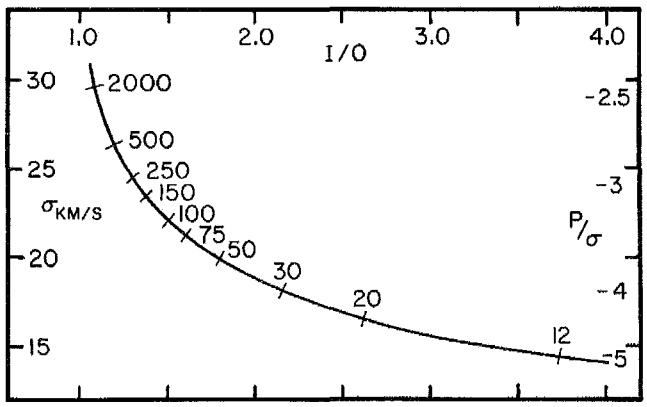


Figure 2.12: Relationship between I/O, data dispersion and sample size

The table in figure 2.11 contains the following information. Column 1 describes the sample, column 2 the number $N$ in the sample. Columns 3 and 4 give the observed I and O numbers and the ratio. Column 5 gives the significance of the deviation of the I/O ratio from unity. Column 6 gives the minimum value of $N$ required to achieve a valid significance level above 0.05. $N$ must be equal or greater than this minimum. Column 7 gives what the I/O ratio implies the dispersion must be to achieve the I/O ratio, Column 8 is the average separation of the pairs in the sample, Column 9 is the published [82] dispersion uncertainty analysis relating to separation and classes of pairs which estimates the actual observed uncertainty of the sample. The final column gives the probability that the dispersion implied from I/O is consistent with the estimate of the observed uncertainty. Consistency of the two dispersion values assures both I/O and $P/\sigma$ yield consistent evaluations. The entire set of probabilities was found to be very close to expectations. Detailed discussions of the analysis are provided with the original data paper [82] and the data analysis paper [83]. A further

detailed comparison of my measures with values from Karachentsev is provided in reference [100] which again fully verifies the Steward uncertainties.

Several other commentaries or related studies soon followed the publication of the Peterson and Karachentsev double galaxy samples. Sharp [I] initially confirmed the periodic pattern was present in several original samples using dynamical models, but later [J] attempted to ascribe the effects to some quirk in data unconnected to actual properties of the galaxies. I will comment on this point subsequently. John Cocke joined me in 1983 to examine differentials in small groups of galaxies [84]. Other studies of groups were carried out by Arp [K] and Arp and Sulentic [L]. All studies found redshift periodicities at or related to original 72 km/s predictions. However, quantization effects are more complicated in multiple systems.

Virtually all galaxies associate in groups. As separation in a pair increases accidental alignments in groups quickly contaminate binary system samples with 'optical' pairs. Redshift dispersion in groups is virtually identical to spread seen in physical pairs; group contamination effects cannot be separated from physical pairing except in close pairs where signs of direct interaction are often detectable. Since it was unclear originally how spacing and other companions would affect quantization, it was important to emphasize isolation and close pairs. A simple discriminant of physical separation in pairs uses the product of mean redshift (in km/s) and angular separation of a pair (in degrees), denoted VoS. VoS divided by the Hubble constant, and the degrees-to-radians conversion factor times 1000, is a good estimate of physical separation in kpc. Isolated pairs with VoS less than 300 (about 75 kpc) and some interaction, provide a good sample of isolated physical pairs. This is the zone investigated with the Steward sample which shows clear quantization effects. To retain compatibility, comparisons in optical data were initially limited to VoS less than 300, although the quantized 21 cm radio data extended to much wider pairs where isolation becomes especially important. I will shortly demonstrate what happens if isolation is not enforced.

### 2.3.5 Later Precision Work

Both to obtain precision 21 cm redshifts and determine what level of precision was possible with 21 cm radio redshifts John Cocke and I began 21 cm observations at the National Radio Astronomy Observatory (NRAO) at Green Bank, West Virginia in 1984 [96], and collected further optical data. In 1989 [100] we put together a paper discussing available data on isolated pairs of galaxies. Several important additional studies also existed at that time, one optical the other at 21 cm. Figure 2.13 summarizes findings of the 1989 study.

The top frame of figure 2.13 contains systems observed at 21 cm. Filled circles designate the 21 cm data obtained in my work with John Cocke. This sample was our final upgraded version of the original Peterson sample now carefully optimized for quality and isolation. Uncertainties in the redshifts should not exceed 5 km/s. The open circles are additional pairs from a Cornell study [M,N] which satisfy the isolation criteria applied to the modified Peterson sample. The original Cornell sample was very poorly assembled. Eliminating duplicates from our sample, including many we had already rejected, the Cornell sample included 70 possible new candidates. Upon examination 19 satisfied the full isolation criteria and 14 were reasonably isolated. these points are plotted in figure 2.13 as open circles. 37

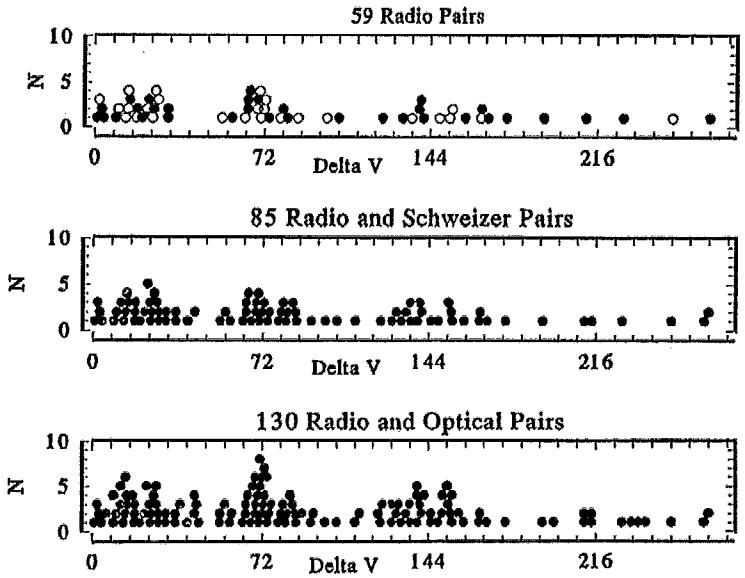


Figure 2.13: Summary of quantization testing using the best available double galaxy samples. See the text for descriptions.

of the Cornell 'pairs' were grossly non isolated triples or have prominent companions often closer than the proposed companion. Seventeen were not even considered pairs in standard catalogs. Some 24 pairs too close to avoid 21 cm overlap issues were also disregarded. The points which are actually isolated clearly agree perfectly with the Steward sample. I will show the remaining Cornell sample and another example later to illustrate distortion caused by companions when mixed into a quantum system where such effects as exclusion and degeneracy effects may apply. An intense statistical discourse concerning analysis of double galaxy quantization originating from Cornell will also be discussed below.

The second frame in figure 2.13 adds close isolated pairs Linda Schweizer observed in the southern hemisphere using high dispersion optical spectra [O]. These measures were the most accurate optical data available including a significant number of close pairs, which again reinforce the same peaks. Extremely wide pairs are omitted to keep the samples comparable. The final panel adds the most reliable data from Steward Karachentsev sample optical studies [82,83]. All reliable samples selected to maximize isolation show quantization. Figure 2.13 summarizes our view of quantization using isolated galaxy pairs, a pattern consistent with quantization, inconsistent with classical dynamical expectations.

It is useful to discuss in more detail reaction to the work, and discuss what figure 2.13 and future work may reveal. As with redshift-magnitude-morphology correlations the response was distinctly negative despite the fact that the study represents a direct test of unproven assumptions underlying classical cosmology. Although many objects in the Cornell list [M,N] are nowhere near suitable for a quantization test [100] and those that are properly isolated match the quantization concept perfectly, the Cornell group chose to dis-

agree with our findings. Newman et al [Q], in association with Cornell work, argued that small samples of data often contain random fluctuations of little significance. The Cornell studies however refused to recognize the periodicity involved was not arbitrary, it had been precisely predicted in advance based upon earlier work unconnected to pairs [58]. Work with pairs further involved multiple independent samples yielding identical results. The Cornell arguments are summarized and solidly refuted in a major 1991 ApJ paper [110] written by my very capable colleague John Cocke with my assistance to keep the facts strait. I highly recommend reference [110] to anyone who doubts the evidence for redshift quantization in pairs or beyond.

Oblique criticism by Sharp [J], that a mysterious unidentified effect may be present in data (but supposedly not in galaxies), requires further discussion. My study of pairs at Steward [82] was based upon an excellent catalog compiled by Karachentsev [R]. My differentials were measured on spectrograms oriented to include both objects; uncertainties are extensively discussed [82,83,100]. The best differentials achieve accuracies near 20 km/s, sufficient to detect quantization, and detect it consistently at levels expected from the number of pairs and data quality involved [83]. Sharp compared sets of Steward measures with data published by Karachentsev [S] and White et al [P], neither of which are accurate enough to detect quantization. (Karachentsev data is discussed by Sulentic [T] and in our 1989 summary paper [100]). One cannot invalidate effects in precision data by using lower quality data where the effect cannot be seen. A modern high precision optical study of close pairs certainly is desirable to further address uncertainties and pursue finer detail that QTC expects to be present in the redshift pattern. However, available quality data, and related studies still to be discussed, confirm quantization very clearly. We have not even begun to discuss global quantization.

To summarize and bring together the best data available at the end of the 1980s, figures 2.14 and 2.15 compare the Schweizer and Steward Karachentsev HWP samples [100] as a function of their VoS spacing out to 300. The two patterns *must* and do agree. Both diagrams show a clear three-level pattern. The mostly wider spaced radio pairs in figure 2.13 match the identical level pattern, there is no detectable change with spacing. A trace of a fourth level may be present in the combination. The Schweizer data confirms the three level pattern quite precisely. The distribution of points around predicted levels is statistically consistent with redshift error bars shown (Compare the number of points whose error bars intersect or miss predicted levels and do the same for the gaps between levels). Note especially confirmation of the zero deficiency which *only* quantization models predict.

The region around a galaxy breaks logically into several zones. In our galaxy there is an inner gravitational region about 10 kpc in radius and an extended region out to about 50 kpc which marks the extent of most visible starlight. This outer region marks the beginning of 'dark halo' effects. Close pairs in this domain show strong interactions; ordinary stars and gas clearly interact. Clear stellar interactions fade rapidly beyond 75-100 kpc, and beyond 125 kpc binaries become morphologically quite indistinguishable from optical pairs so sample contamination and isolation criteria become increasingly important.

Passing beyond separations with VoS products greater than 300-500 there is much less evidence of conventional gravitational interaction. This is the region where most radio data applies since beam sizes of single dish radio telescopes are too large to permit quality measures of close pairs. This is also where global quantization effects should become dominant

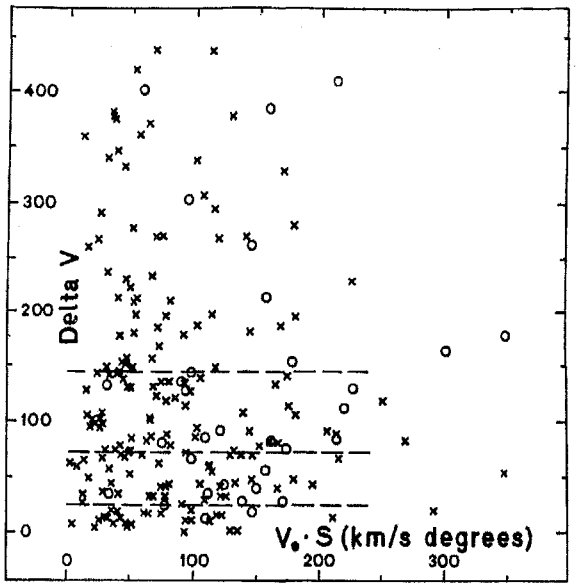


Figure 2.14: The differential redshift - projected separation diagram for the high weight Karachentsev pairs observed at Steward (x symbols) [100]. Dashed lines mark the quantized levels where points concentrate (Refer to figure 2.11 for statistics). Schweizer pairs (open circles) conform to the same pattern.

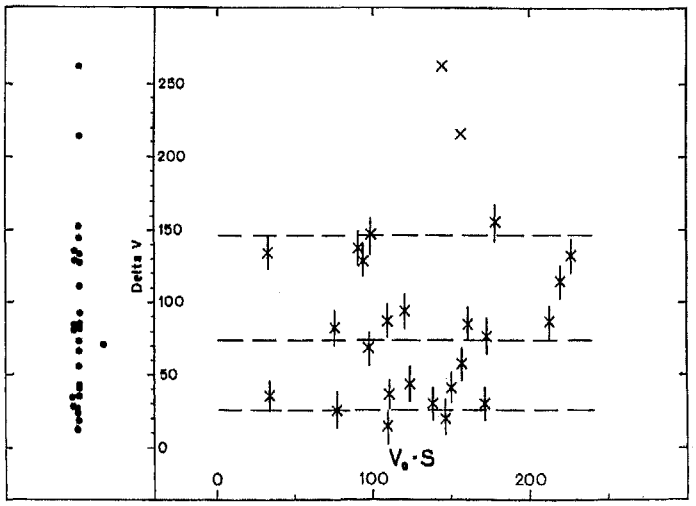


Figure 2.15: The differential redshift - projected separation diagram for the close Schweizer pairs [100]. The projected distribution at left shows expected concentrations around the predicted levels (dashed lines) consistent with uncertainties in the data shown with vertical error bars.

relative to physical pairs. Isolation of pairs becomes especially critical in this domain since, as I shall shortly show, quantum exclusion effects may distort allowed quantum levels. From the quantization viewpoint there are very basic reasons to separate the analysis of close interactive pairs, wider isolated pairs, and not-so-isolated radio samples. Lumping such samples together, as gravitationally oriented analysis does, deliberately biases against detecting quantization. Differences predicted by quantization are quite clear using appropriate sampling.

### 2.3.6 The Exclusion Principle

An important new result emerged from follow-up studies on galaxy pairs. Original prediction that peaks would occur at multiples of 72 km/s is true near 144 and 72, but not at zero. The lowest differential peak is displaced from zero by roughly 20 km/s. There is actually a dip at zero, galaxies do not appear to have very similar redshifts when close together. This by itself is indicative of quantization, suggesting an exclusion principle is operating. The deficiency is obviously inconsistent with classical dynamics, which requires a zero peak. A deficiency of small differentials was noted by White et.al. [P] in a different dynamical study, is present in the Schweizer data [O], and seen in all well studied samples. It is easily shown that the observed line-of-sight component of a randomly oriented velocity vector is uniformly distributed between zero and the full value [58]; such distributions *must* generate many values close to zero. Nevertheless It was argued that a deficiency might be caused by missing very wide pairs. To test for such an effect the Fisher-Tully catalog [V] was searched for potential very wide pairs with redshift differences less than about 50 km/s and minimum projected separations between 200 kpc and nearly a megaparsec (VoS 860 to 3600, outside the zone where pairing information is available). Figure 2.16 [100] shows the pattern of redshift differentials found.

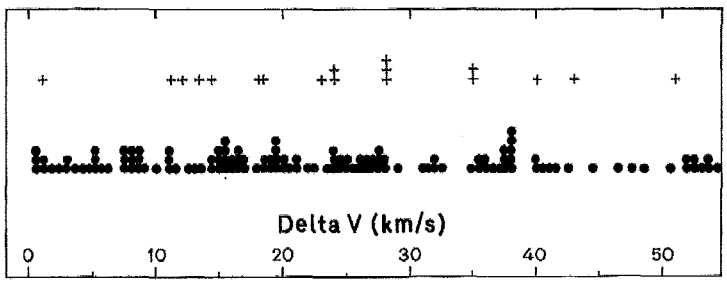


Figure 2.16: The distribution of differential redshifts from 21 cm measurements for galaxy pairings in the 860-3600 VoS range (filled circles). Crosses denote radio and Schweizer pairs which populate the offset quantum level near 20 km/s seen in close pairs with VoS less than 300

There is no excess near zero, in fact the distribution mimics the pattern for close pairs. The 14-28 km/s range is enhanced a factor 1.5 compared with the 1-14 km/s range. There is no source of widely spaced small physically associated differentials, they are simply not there. Most of the pairs in figure 2.16 should be optical pairings within group associations. The

match to the differentials for the zero-offset level in close pairs (cross symbols in figure 2.16) seems to suggest that identical redshift exclusion may extend over a considerable distance. Given that redshifts are quantized, some zero or small differences should be observable if sufficiently spaced galaxies in the identical state happen to be nearly superimposed. However, the chance of unrelated widely separated objects being in both the same state and directly in line is a rare occurrence geometrically. Such a coincidence will always produce a few non-physical differentials close to zero as seen in figure 2.16 but there is no excess related to physical pairing.

The 1989 paper [100], considers what could happen in multiple systems if an exclusion effect is present, in galaxy triplets for example, or in regions of high density as in a cluster where degeneracy may have to be considered. A 'triplets' test was carried out using galaxies within the Fisher-Tully 21 cm study [V]. There are 44 pairs with VoS less than 500 km/s/degree, (within the range that could include physical pairs), which form triple systems with redshift differences less than 108 km/s. There are two classes, reciprocal pairs where each galaxy finds its neighbor is its closest companion, and non-reciprocal pairs where one or both galaxies find the third galaxy to be closer. Reciprocal pairs include real physical pairs, but the catalog is not complete so some can be unrecognized non-reciprocal pairs. Many reciprocal pairs should fit predicted quantum levels but with contamination. Close non-reciprocal pairs, however, are unlikely to be physical pairs and are candidates to show perturbations by exclusion from the third object. Figure 2.17 compares the differential distribution for the two types of pairs.

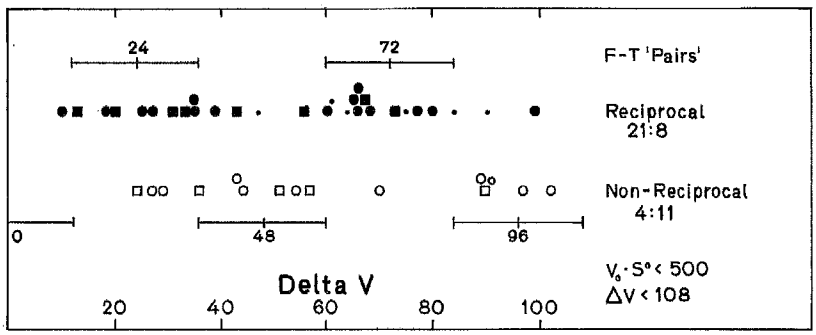


Figure 2.17: The distribution of 44 Fisher-Tully [V] pairs distinguished by reciprocity. Symbols distinguish redshift sources.

The total sample shows the expected zero deficiency but no periodicity. Periodicity appears when we distinguish reciprocity. The 29 reciprocal pairs confirm quantization at the 98 percent level despite contamination. The 15 non-reciprocal pairs are offset as predicted. It is quite clear why studies in groups or wide pairs must be distinguished from studies of isolated pairs. This test surprised even me! The data are tabulated in reference [100].

### 2.3.7 A Glance Ahead

On the basis of what we now know or suspect concerning quantization from precision redshifts involved in 21 cm global studies it seemed quite likely the differential pattern in pairs

should contain finer structure, some additional periods, and possibly depend upon the actual radial separation and character of the galaxies involved as well as isolation dependent effects. I had seen finer and finer structure emerge as precision improved. Once I realized how precise 21 cm redshifts could be I could see that the basic levels, like 73 km/s, were far wider than redshift uncertainties. Was there a finer structure? The answer is indeed yes, but I would need to understand much more about redshift quantization, discussed in the third seminar, before I could make (and verify) actual predictions.

Although this represents a considerable jump ahead, since I have been focused on redshift precision and the Cornell discussions, it is appropriate to wrap up this double galaxy discussion with a look ahead. Figure 2.18 shows the VoS-redshift differential pattern for the most isolated wider pairs with radio data from our radio work [100] and the Cornell study [M]. Note the considerable increase in the VoS range. There is a certain irony here. Just as the the early attacks on redshift-magnitude work encouraged me on to even more basic findings and finer structure, the Cornell attempts to discredit quantization in pairs materially assisted in the detection of energy level substructure within the double galaxy quantum levels. Structure should always be consistent with precision. I will return to the remaining Cornell data at the end of seminar 3.

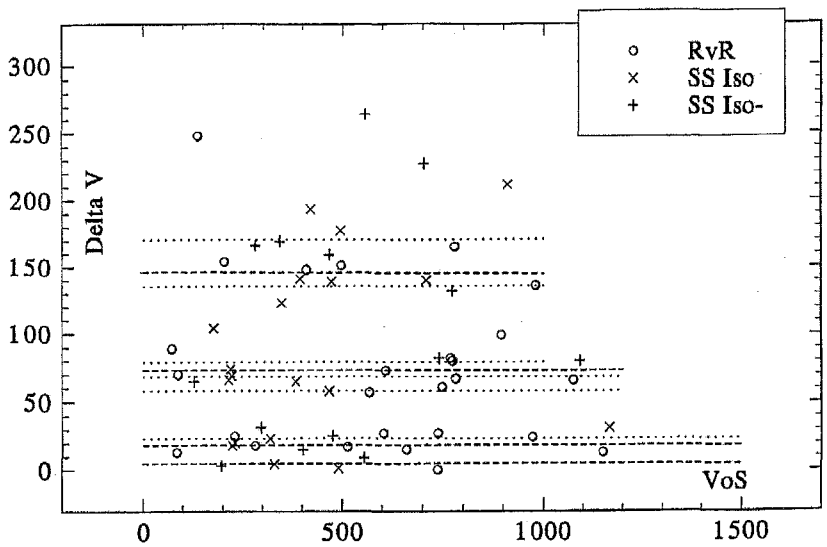


Figure 2.18: The differential redshift - projected separation diagram for the most isolated pairs which have high quality 21 cm data. RvR refers to our revised radio data related to the original Peterson sample; SS refers to Cornell data for pairs, previously discussed, which are well or moderately well isolated. Lines indicate possible levels according to recent work (discussed in third seminar as a model was developed).

The dashed and dotted lines in figure 2.18 mark what are believed to be possible allowed redshift differentials. Note that most of the data points lie close to the dashed lines, consistent with the actual measurement quality. The three well separated primary concentrations,

now subdivided, and zero deficiency are quite clear. Wide Schweizer pairs, in the isolated wide pair category, are consistent with radio pairs, but less accurate. In seminar 3, after introducing the method of level prediction, I can illustrate what appears to happen when isolation criteria are relaxed and pairs with VoS less than 200 are added. Our analysis is guided by quantization exclusion expectations which highlight clear differences from classical gravitational behavior.

If the redshift is in fact quantized with Fermionic exclusion, and there are no gravitational links between individual galaxies to induce real motion, an astute reader might realize at this point that there may be no distinction between double galaxies and any two field galaxies located in a small area of the sky within a narrow redshift range. The concept of binary galaxies may have meaning only if the pair originated from a common parent by a process such as fissioning. Perhaps I should call it quantum fissioning since the ordinary view of fissioning involves physical splitting with real motion which is simply not there. Quantum fissioning may have to involve something like fissioning in time. But why not, time is simply the inverse of energy so the fission must most likely occur in tau (the QTC 3-d domain of time). At this point I need to utilize pairs to introduce the subject of large scale structure before turning to a search for a rest frame within which galaxies can be phased together globally to reveal still more detail concerning the quantized properties of galaxies. It was apparent that such a rest frame should exist to preserve the structure we had already seen. In fact there are two such frames, a local one and a universal one.

## 2.4 Large Scale Structure, Clouds of Galaxies

Quantization of the redshift in pairs of galaxies implies there can be no classical orbital motion between the objects since it would completely obscure any intrinsic effect. Such lack of motion implies that there can be no gravity acting between individual galaxies which would generate motion. Is there any other independent test to verify the lack of orbital motion? The answer is 'yes'. As a result of the early study of pairs at Steward a large number of systems were observed over much of the sky [82].

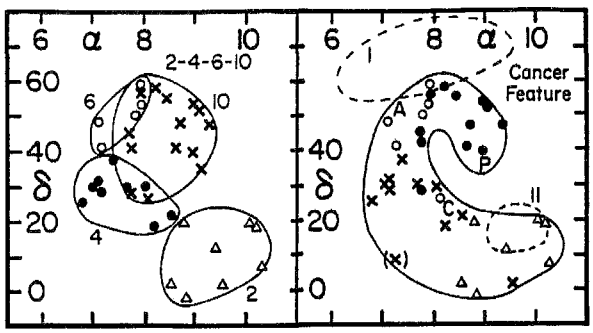


Figure 2.19: The cloud structure for double galaxies in the Cancer region [79] seen projected on the sky. Clumps of pairs with similar redshifts associate in a large filamentary structure; redshift increases from group to group along the structure. Unrelated clouds are shown dashed.

My work with pairs was done at the time astronomy was about to learn about large scale structure, how galaxies are really distributed in space. As I proceeded with redshift measurements of pairs I found regions where most of the pairs had similar redshifts. This is shown in figures 2.19 and 2.20 [79] where 'clouds' of related objects are shown. Somewhat displaced from each cloud there was usually another cloud with slightly different redshift, then another cloud shifted still further in redshift. The clouds appeared to link together into filaments as shown. This discovery contributed to the recognition, in the 1970s, that galaxies were distributed in some kind of large scale filamentary structure. There were filaments consisting of clouds of double galaxies literally strung together like beads on a string [79]. The feature in figure 2.19 appears to be twisting away from us toward higher redshift. Figure 2.20 shows clouds which appear to associate in a roughly transverse filament. Clouds were numbered for convenience, and virtually all clouds fell into such chains. I shall return later, in seminar 7, to how the cloud and filament structure relates to QTC, but initially orientation of the pairs is of interest.

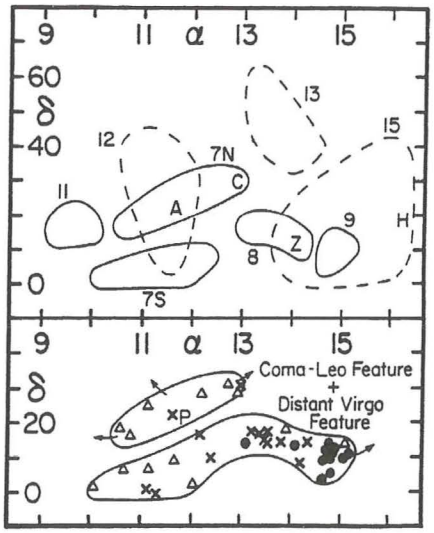


Figure 2.20: Cloud structure for double galaxies in the Coma-Virgo region [79] seen projected on the sky. The Distant Virgo feature appears to be a mostly transverse structure involving clouds 7-8-9.

### 2.4.1 The Orientation of Pairs

I noticed something strange while observing. As I moved from one pair to another nearby I rarely needed large changes in orientation to place both galaxies on the slit of the spectrograph. I therefore examined how the position angle (the angle from north through east joining pairs) related to redshift and location on the sky. Orientation for different pairs in conventional theory should be uncorrelated. Separate pairs are far apart and classically governed by individual dynamics involving different masses, periods, separations and inclinations. The dynamical state and instantaneous orientation in any pair should have no

bearing on the state or orientation of any other pair in the same cloud or elsewhere in the filament. In fact orientation was strongly correlated. Figure 2.21 shows that progressing along the Coma-Virgo filament, in both redshift or position *within and between clouds*, there is a clear systematic variation in position angle.

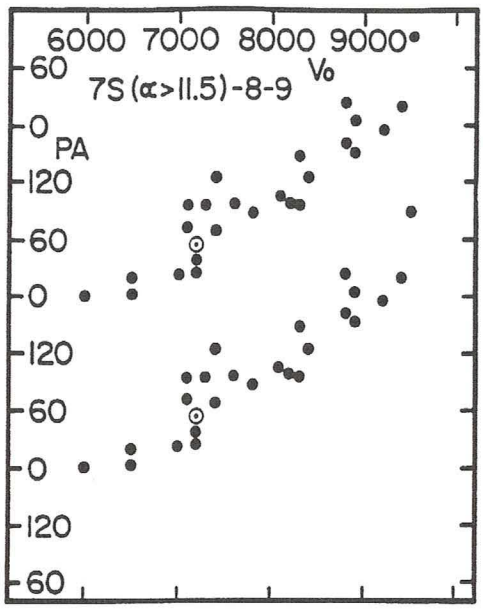


Figure 2.21: Position angle of double galaxies in the distant Virgo feature as a function of redshift [79]. Redshift increases slowly along the filament as one moves east; position angle correlates closely with both position and redshift.

Such patterns are seen in all the well defined filaments [79], and are highly inconsistent with the idea of independent dynamical motion. Orbital motion should destroy both quantization in velocity projections and randomize orientation. This finding provides a completely independent verification of the lack of motion (hence gravitation) between galaxies. It is difficult to imagine a test more fundamental than the two body problem!

My early redshift work, shared with several of my students at the University of Arizona, was pioneering work defining superclusters. Like my work in quantized redshifts it is rarely acknowledged, perhaps because it pointed out dynamically inexplicable results such as cloud and pair orientation details which to the best of my knowledge have not been examined further. There is, I believe, one statement, located at some obscure point in IAU documentation, where Professor Oort comments on the interesting orientation effects in pairs involved in large scale structure.

Orientation investigations can be carried further. Position angles for pairs are generally defined only within 180 degrees. However, if the galaxies are unequal in brightness position angle can be defined on a 360 degree basis by using the direction of increasing luminosity. When done for the pairs in figure 2.21 not only are they aligned, but the brighter object is

almost always on the same side. This is shown in figure 2.22; similar findings apply in other filaments [79]. Note the sudden reversal between clouds 8 and 9 in the Coma-Virgo filament. A similar reversal between two runs is also seen in the Perseus filament. Orientation is discussed further in seminar 7 as the concepts of flow through time are developed within QTC.

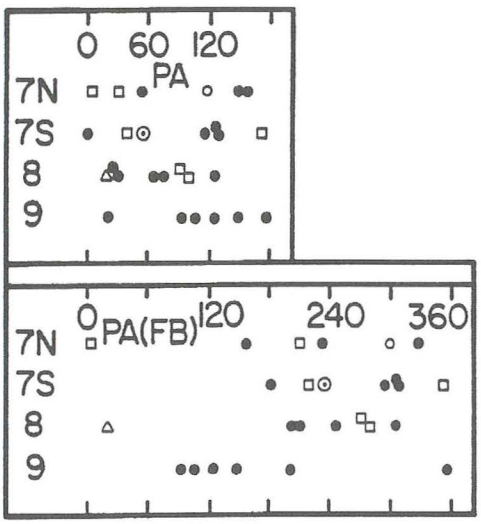


Figure 2.22: Position angle on a 180 degree and 360 degree (faint to bright) basis for double galaxies in the 7-8-9 structure. Luminous galaxies are not randomly positioned with respect to their fainter companions [121].

It also appears that cluster elongations in supercluster filaments fit the same pattern. They appear to be just another form of cloud structure within a supercluster system of apparently aligned clouds.

Orientation correlations in concert with redshift quantization suggest that an oriented fissioning process could be involved in the origin of galaxy systems. I previously introduced the concept that galaxies form from nuclear outflow associated with an underlying redshift dipole. It is not much more radical to extend the concept to fissioning of a central source structure which we happen to designate to be a nuclear supermassive black hole. Conventional models employ mergers, pieces coming together, to form galaxies. Fissioning is the inverse of merging, and can generate similar apparent interactions (run simulations in reverse). There will be more evidence for ejection or fissioning later, although not necessarily in spatial coordinates. There must be a characteristic direction involved related to large scale filamentary structure. This is a far-out concept, but is the type of model required to be consistent with large scale cloud structure, orientations and quantized redshifts. Basically, test after test finds no direct evidence for large scale motion, rather essential for an inflow merging hypothesis for galaxy or structure formation. Such motion requires normal gravitational force on the large scale. As an aside, when I discovered linked filamentary supercluster cloud structures it crossed my mind that they might be called 'God's chromo-

somes', since they were structures which appeared to define the large scale universe. Such titles are, however, not appropriate in scientific papers.

Redshift quantization combined with orientation correlations place extremely stringent restrictions on any theory which attempts to retain significant large scale conventional dynamics. A situation could conceivably exist where motion could be present but the photon unable to transmit that type of information between galaxies as 'particles' embedded in time. It takes two objects, an emitter and an absorber to define motion; the emission/reception process, not the photon, defines motion. Orientation correlations are now critical, however. Even if we could not perceive 'radial' motion (which could preserve quantization), 'lateral' relative motion, unrelated to the nature of the photon, will affect relative positions. Orientation and quantization taken together provide very powerful limits on what kind of motion is possible between galaxies. There is a flow, the flow of time, which can produce lateral displacement in conjunction with quantized redshifts. This flow is central to QTC. It is too soon to talk much about that flow although such a 'proper motion' displacement has apparently recently been observed. We need first to see what else the redshift can tell us.

## 2.5 Global Quantization, Turning to 21 cm Data

Pairs provide a very fundamental test of redshift quantization and the nature of motion on the large scale. However, further critical tests come at the global scale. On the global scale one can no longer easily obtain redshift differentials, which are generally more accurate than redshifts. We must instead have precise absolute redshifts and little optical data had the necessary precision. We need to define actual quantum states of galaxies independent of internal dynamics, literally the energy levels occupied by galaxies as the universe decays in the QTC concept. I turned to 21 cm radio redshifts since precisely controlled radio frequencies permit accurate measurements. In the middle 1980s John Cocke and I carried out a study of a large number of galaxies using the NRAO 300-foot telescope in Greenbank, West Virginia. I continued that work during my 1988 sabbatical at both Greenbank and Bonn Germany, where I demonstrated very precise redshifts can be measured using 21 cm observations [104,105].

I should first summarize what a 21 cm observation yields. The 21 cm spectral line arises from the hyperfine spin reversal transition of the electron in the ground state of neutral hydrogen. An observed 21 cm emission line line profile represents the integrated effect of all emitters within the beam of a radio telescope. The beam size of single dish radio telescopes is quite large and encompasses all or a sizeable fraction of the total signal from all but the nearest galaxies. The emission profile is spread by internal motion and, in QTC, the distribution of intrinsic redshift states present. An observation consists of measurements of signal strength as a function of frequency to map out the profile of the spectral line. There are two common types of line profiles. Relatively narrow single peaked profiles, a few 10s of km/s wide, are associated with dwarf irregular galaxies. Figure 2.23 shows such a profile. Most of the width arises from random internal motion within the galaxy. Wider, double peaked profiles, such as shown in figure 2.24, may be up to many hundred km/s wide, and are associated with rotating disk systems, the spiral galaxies, where rotation enhances the width. The peaks are due to concentrations of hydrogen in extended rotational wings. 21 cm measures are limited to galaxies with significant cold neutral hydrogen content; most 21

cm data thus comes from irregular and spiral galaxies. There is no reason to think early type galaxies behave any differently concerning quantization. Optical work with pairs or internal properties make no distinction.

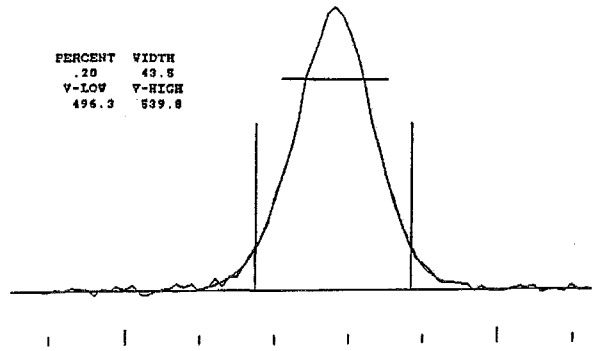


Figure 2.23: A narrow single peaked 21 cm profile characteristic of dwarf galaxies. Profile width is measured between points where the profile crosses 20 percent of average height of the central 80 percent of the distribution. Redshift is a mean of the crossing point velocities.

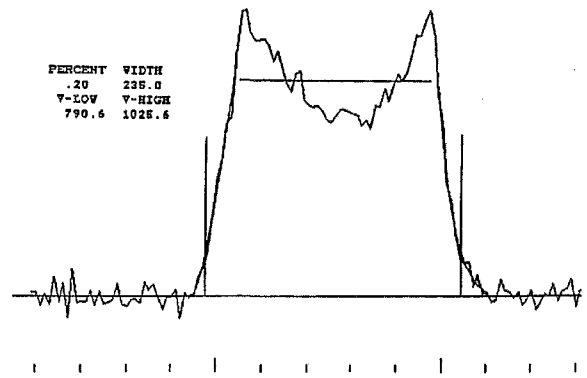


Figure 2.24: A wide double peaked 21 cm profile characteristic of spiral galaxies. Profiles are measured as noted in figure 2.23

Profile measures, as shown in figure 2.23 and 2.24, normally involves measuring profile area and two carefully defined edge points. The average of the edge points yields the redshift and the difference measures the profile width, W. Width is correlated with galaxy type and provides a discriminant for morphology. The area of the profile yields the flux, F. A shape parameter, A for asymmetry, is defined by comparing the area mean with the edge-point mean. A signal-to-noise figure, s/n, is defined by comparing a measure of signal height with baseline noise. Given adequate signal-to-noise, redshift values repeat within a fraction of a km/s. 21 cm parameters can be precisely measured and repeated [104].

### 2.5.1 The Galactocentric Rest Frame, The Solar Motion

To carry out global quantization studies redshifts must be transformed to an appropriate rest frame. Quantization is a property of galaxies - it is not sun centered. The logical initial rest frame is naturally the rest frame of our own galaxy, the galactic center, since we reside in one of the galaxies involved. Our galaxy is clearly rotating. The sun is moving in the transverse (rotational) direction at about 220-230 km/s and has small motions in the radial and perpendicular directions. This 'solar motion' generates Doppler shifts which vary from point to point and must be removed to detect quantization globally. Transformation to the galactic center requires accurate values of the three components of the sun's motion. However, since the values were not accurately known, the transformation had to be found by 'tuning' the solar motion to optimize quantization. The first study thus demonstrated that there was indeed a transformation to the galactic center that induced strong global redshift quantization.

Global redshift quantization implies that redshifts are multiples of one or more basic intervals or 'periods'. Periodic distributions involve a quantity called 'phase', where phase is a measure of where you are in a periodic cycle. A redshift, when divided by a potential 'period', yields a number of full cycles and a fraction of a cycle. Phase is the fractional part. If a set of redshifts is perfectly periodic, the phase of all the redshifts will be the same. Phase may be zero if the observer's galaxy is in phase with the period involved or a suitable harmonic. Phase shifts are important in evaluating periodicities. Our galaxy must fit somewhere within the quantized system! Phase clumping defines periods and the degree of clumping measures significance of periods. Given a range of redshifts in a sample one can carry out a standard spectral analysis, a Fourier analysis, or a 'power spectrum' analysis to see what characteristic periods are associated with the data. The stronger the clumping of phase, the greater the 'power' and significance of periods present. Power varies as transformation constants are adjusted to find values which optimize periodic properties. An early form of phase clumping utilized In:Out ratios discussed for pairs. The I:O ratio analysis is particularly useful when only a few cycles are present and the period is known.

To examine global quantization we use several types of diagrams. Contour plots of power are used to home in on the optimum transformation as we adjust the transformation constants at a given period. Figure 2.25 illustrates this type of analysis using contours of the I:O ratio from our 1984 study [87] involving transformations to the galactic center. Initial searches were made around harmonics of 72 km/s.

Figure 2.25 shows strong quantization for transformation constants near 230 km/s (transverse, denoted theta) and $-35$ km/s (radial, denoted pi). Since we reside in the galactic plane Z should be small (Z=1 km/s in this case). The initial period found was 24.15 km/s (1/3 of the basic original 72 km/s). Later diagrams of this type use power contours (from power spectra). Transformations are tuned to find maximum power to determine the optimum transformation constants. Since periods can (and do) depend upon the type of galaxy involved, samples are selected to be as homogeneous as possible by restricting parameters such as profile width. Figure 2.25 used galaxies with the narrowest profiles, dwarf irregulars. Data sets are further restricted using signal-to-noise information to control data quality. When signal-to-noise data is not available a flux-to-width ratio, F/W, may be substituted. F/W is a measure of signal height, therefore signal-to-noise if baseline noise is roughly constant.

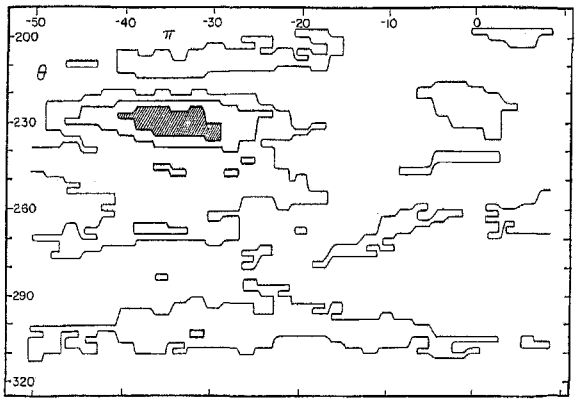


Figure 2.25: Contours of In:Out ratios as a function of the transverse (theta) and radial (pi) transformation constants for referring redshifts to a galactic center rest frame. This is for narrow profile galaxies at a period of 24.15 km/s. Maximum phase clumping (quantization) occurs for a very specific transformation [87].

Once a vertex is specified periodicities are usually examined by plotting phase against some property of the galaxies, typically profile width to define the type of galaxy related to the specific period involved. Figure 2.26 illustrates this type of analysis for the narrow profile galaxies used to generate figure 2.25. As with transformations, periods are found by adjusting the search range to find values which yield maximum power in a redshift-power spectrum or an equivalent I/O analysis. Once a period is known or suspected a phase-width diagrams is more useful for evaluation.

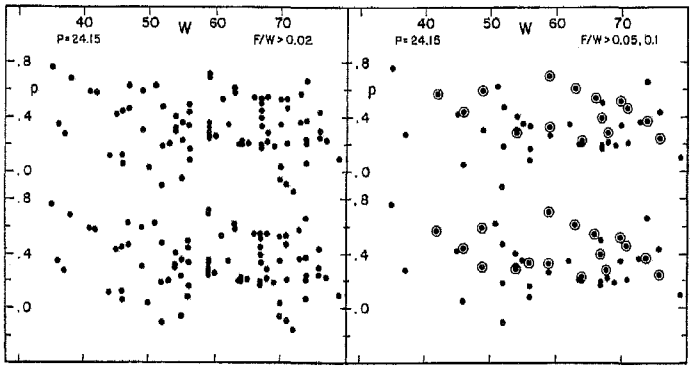


Figure 2.26: Phase-profile width diagram illustrating the 24 km/s periodicity in narrow profile dwarf galaxies in the galactic center rest frame [87]. The flux/width (F/W) ratio is used to control quality. Points are repeated in a double phase cycle.

In such diagrams phase is usually plotted through a double cycle; each point appears twice so the periodic cycle can be easily seen in the phase distribution. Figure 2.26 also shows

what happens when data quality is improved as signal-to-noise (F/W here) restrictions are imposed. Phase concentration improves as lower quality data is removed.

My first global study in the galactic center rest frame was actually done in 1978 [68,67]. This was the earliest such a study could be done. The first Fisher Tully study [U], published in the middle 1970s, contained about 100 galaxies. That study was sufficient to suggest quantization was present, but the limited sample was insufficient to properly address the problem. The study did show that profile shape, the asymmetry index A, was an important parameter in defining samples. Asymmetry appears to be associated with profile width in a nonrandom manner [68]. In 1984 [87] John Cocke and I used the second Fisher-Tully study [V], which contained more than 1000 galaxies, to show that local galaxies, those with fairly low redshifts, were clearly strongly quantized in the galactic center reference frame.

John and I found we could phase together the narrowest 21 cm profiles, as shown in Figures 2.25 and 2.26, at a characteristic period of 1/3 of 72, 24.15 km/s. The optimum set of transformation constants from heliocentric to galactocentric was $(-232, -35, 1)$, in order (transverse, radial, Z) and units of km/s. Only very minor changes to those constants have been made up to the present time, although we now know this vertex applies only to 'local' galaxies. In terms of earlier discussion in section 4 it apparently applies within our local 'cloud' of galaxies. The pi component, at $-35$ km/s, however, does imply a slow radial outflow at the sun's location. This is an important result consistent with the concept of origin of galaxies by outflow from a nuclear source, already postulated in correlation studies and used in models to map quantization within galaxies.

Since we optimized both the period and transformation to find the narrow profile quantization it is not possible to easily assess the significance of the result. We solved that problem by showing that a second class of galaxies, those with the widest 21 cm profiles, were quantized for the *identical* transformation. This is shown in figure 2.27.

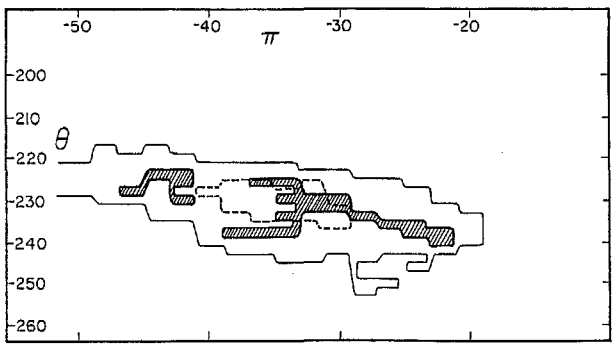


Figure 2.27: Contours of the In:Out ratio as a function of the transverse ($\theta$) and radial ($\pi$) transformation constants to the galactic center for wide profile galaxies at a period of 36.2 km/s [87]. Maximum quantization occurs at the same transformation found for narrow profile galaxies shown by a dotted contour.

The theta-pi contour plot in figure 2.27 shows the peak transformation contour for narrow W profile data with dashed lines to demonstrate the transformation match associated with

The 24.15 km/s period is indistinguishable from the transformation for the wide profile galaxies. The period found for the wide profile galaxies was 36.2 km/s. Figure 2.28 is a period optimizing plot showing how the period and theta transformation correspond.

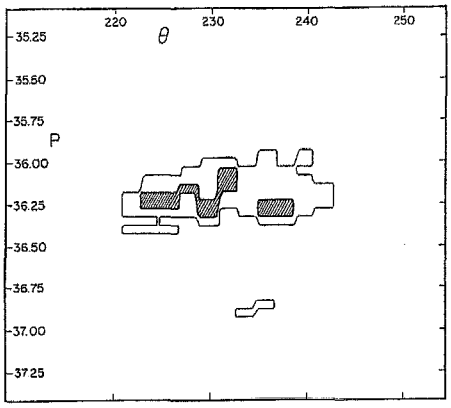


Figure 2.28: The contour diagram of the In:Out ratio as a function of the transverse (theta) transformation constant and redshift period used to optimize the wide profile 72/2 subharmonic period [87].

The 36.2 km/s period was indistinguishable from 1/2 of the standard 72 km/s period. The chance that the wide profile match could be spurious is only a few parts in a thousand. Figure 2.29 shows phase-profile width diagrams for the $W > 420$ km/s galaxies to define wide profile galaxy properties.

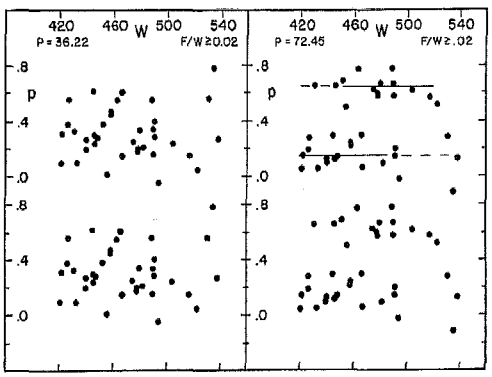


Figure 2.29: LEFT: Phase-profile width diagrams of the wide profile galaxies for the 36 km/s periodicity in the galactic center rest frame [87]. A double phase cycle shows the phase clumping. RIGHT: The same data at a 72 km/s period to show population shifts between harmonic levels.

Global redshift quantization in the galactic center rest frame had been clearly demonstrated. We were able to phase together the narrowest and widest profile galaxies, but not those in

between. At the time this seemed reasonable, quantization was a complex subject. Nature might have many ways to build galaxies. But, perhaps for the most extreme types there might be only one way to do it. That was our original suggestion in 1984 although an even more fascinating explanation was soon to emerge. Extensions in width suggested changes in harmonics and phase changes with width, a precursor of things to come later. This is illustrated in the right hand part of figure 2.29 where the width distribution changes for different harmonics.

At this stage, we had detected global quantization, had a good idea of what the galactic center transformation constants were, and had verified that the periods were related to the original 72 km/s where it all began. It was now the late 1980s and we still had important things to learn. I will focus on those problems for the remainder of seminar 2 to lay groundwork for a more detailed review of global quantization in seminar 3. There are four items to discuss: 1) redshift variability, 2) non-linearity in quantization with increasing redshift, 3) the role of the cosmic background, and 4) precise definition of periodicities.

## 2.6 Introducing Redshift Variability

Redshift variability must be present in any time dependent evolutionary cosmology, but one would not expect it to be readily detectable over ordinary human time scales. If the redshift is keyed to an intrinsic evolutionary phenomenon displayed in lookback time, rather than caused by a simple spatial expansion, the intrinsic effect must decay with time to produce the Hubble law. Further, if the redshift is quantized it must cascade down in specific rapid transitions in order to retain observed steps. To preserve both an intrinsic quantized redshift and the Hubble law one must look back in time through a quantized series of reasonably stable levels between which the redshift must be able to change. If this is correct it has profound implications. First, in order to detect a change between two closely spaced epochs the change must occur rapidly and coherently for the entire galaxy and its widely distributed photons. There can be no major effect of transit time which would prevent seeing sudden changes in objects with large spatial extent. Variation must be controlled by a process which is object related but independent of space! In the last seminars we will see how this is accomplished; just as with motion, there is a quantity distinct from space, called time. We will review observational evidence for variable redshifts here first.

As a second consideration, even if redshifts are variable in a stepwise fashion it would seem unlikely we could actually detect a change during the few years for which we have modern observations. A photon takes more than three million years to travel a megaparsec. For a Hubble constant near 70 km/s/Mpc we would expect significant steps in the redshift to occur very rarely. We might have to observe millions of galaxies to detect a few rare shifts. In fact we have evidence for much more profound effects. Either the space between galaxies as well as their individual extent is irrelevant and/or we happened to look at a very auspicious time! However, in studies of the redshift we have learned not to assume much at all.

### 2.6.1 Redshift Precision at 21 cm

Work leading to the detection of redshift variability began in 1984 when John Cocke and I began making precision 21 cm observations of local galaxies. A key question in the early

1980s was just how reliable and repeatable are 21 cm redshifts? Although both optical and radio data showed quantization effects it was essential to determine the actual precision of 21 cm work. On the basis of our 1984-86 study [96,93] and studies I carried out at both Greenbank [105] and in Bonn, Germany [104] during my 1987-88 sabbatical, I demonstrated that a single measurement at signal-to-noise of 10 or above repeated to a km/s or better. When multiple measures are averaged one can obtain sub km/s precision in work with 21 cm redshifts. Figure 2.30 contains the abstract of reference [104].

ABSTRACT

Comparison of 21-cm data from the Effelsberg 100-m and NRAO Greenbank 91-m telescopes are used to find the limiting precision for redshift measurement. At signal-to-noise levels of 10 or above random uncertainty actually achieved in a single redshift measurement is demonstrated to be 0.85 km/s at a bandwidth of 6.25 MHz. Uncertainty in other bands scales as the square root of the bandwidth relative to 6.25 MHz. Random error is also found to be independent of which telescope or software is used as long as the s/n is large. At low s/n the choice of software will affect precision. Substantial systematic errors are shown to be present in some existing systems or software, due to errors in specifying the location of the center frequency. Such errors can easily be eliminated with standardized intercomparisons. Some small residual systematic shifts, amounting to a few tenths of a km/s, are suspected and remain unexplained pending further study.

Effects of telescope pointing errors on redshifts are calibrated by comparing offset measurements. A clear correlation exists between profile shape changes and redshift differences as pointing is varied. An unavoidable minimum redshift scatter of about 0.1 km/s is shown to arise from the basic limits on telescope pointing. Profile widths, however, are very insensitive to pointing error. Overall, basic comparisons over time or between systems can be made at the 0.1 km/s level.

Figure 2.30: The abstract of reference [104] which demonstrated high redshift precision obtainable in 21 cm data.

Random error varies as the square root of the bandwidth used and is not directly related to the width of profiles; the narrowest profiles, usually observed with a 2.5 MHz bandwidth, provide the most accurate redshifts. Intermediate and wide profile galaxies usually require 5 or 10 MHz bands. Many general surveys use a single wide band for all observations.

## 2.6.2 Comparing With Older Observations, Deviations!

When we compared our new precision redshifts with older redshifts, primarily from Fisher-Tully [V] and other 21 cm investigations from the 1970s by Dickel and Rood [W] and Shostak [X,Y], there were some remarkable deviations. The oldest redshifts available for any significant number of galaxies are those from Roberts [Z] who did some of the earliest 21 cm work in the 1960s. Figure 2.31, and 2.32 show how our new data deviated from Roberts, Fisher-Tully, and Dickel-Rood, but not significantly from more contemporary data.

There is a set of objects for which redshifts agree, deviations distribute around zero, and there are parts which are displaced. The displacement is virtually always to the negative side in new-minus-old differences implying the redshift was measured to be higher in the past. The spread is leptokurtic (more skewed to the left), which is the direction in which changes should occur, but we did not expect to see this at all. The oldest data (Roberts)

shows the largest effects, the shift increases with time. Comparisons with data from Lewis [AH], contemporary with ours, showed close agreement. Several checks on systems were run; the deviations are unquestionably related to older data. No significant systematic errors between contemporary redshift measures on unresolved sources were found.

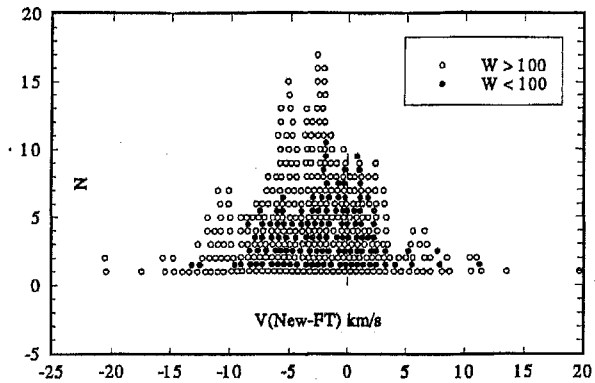


Figure 2.31: The frequency of redshift differences between Fisher-Tully (FT) [V] data from the 1970s and newer Tifft-Cocke redshifts from the 1980s. Narrow and wide profile galaxies are distinguished [111].

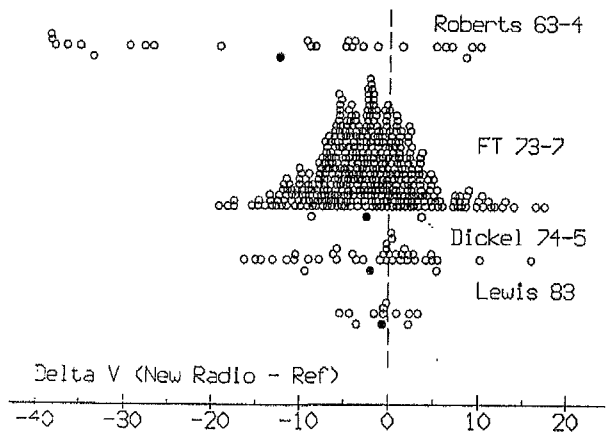


Figure 2.32: The frequency of redshift differences between Roberts [Z], Fisher-Tully [V], Dickle and Rood [W], and Lewis [AH] compared with Tifft-Cocke redshifts from the 1980s [111]. Timing for data is indicated.

### 2.6.3 Using Phase-Deviation Diagrams, Transition Cascades

Although detectors were not as good in the 70s and were quite primitive in the 60s, there are no known reasons to expect systematic shifts or even very large random scatter. I have reason

to believe that much of the early work is far better than is often assumed. Observers usually list very conservative estimated uncertainties. The real reason for doubting the deviations are systematic errors however, is because they are consistent with changes between a set of specific periodic quantized levels, they cannot be arbitrary shifts. There must be relatively stationary periodic quantum levels where galaxies reside most of the time. Changes between levels must be rapid or intermediate stages would destroy the quantized pattern. We were in fact about to find such transitional blurring in specific small harmonic steps was why we could not detect redshift periodicities in certain profile width ranges, changes were in process. To illustrate variability in quantized steps we need a new type of diagram, the phase-deviation diagram. Instead of plotting phase (in the usual double cycle) against profile width as shown earlier, we plot phase for homogeneous samples against the redshift difference between two observing epochs in the sense new-minus-old. When I did this I found as redshifts moved down, change occurred as transitions between specific periodic levels. It would be 1992, as discussed in the third seminar, before we would learn how to predict the quasi-stationary periodic quantum levels. In the late 1980s we had only the 72 km/s period and were exploring the harmonics of that level The next major step came as I explored properties of the 24.15 km/s period which is associated with dwarf galaxies in the galactocentric frame.

The first point to make is that if variability is present, what was done previously was not quite right. Periods were found by maximizing phase clumping. If transitions are occurring and phase is cascading with time periods will be biased to minimize drift. To get optimum periods and transformation constants we need a periodic phase-deviation pattern which takes time drift into account. The fact that we see stable quantum levels implies that most of the time redshifts are stable at a fixed phase. I will call these quasi-fundamental levels. Transitions occurring in a single step will yield a deviation equal to the period with no phase change. In practice, transitions appear to occur as cascades between periodic levels through intermediate smaller steps in phase. The actual step size within a cascade appears to also be periodic, some integral fraction of the larger period which is in phase with the longer period. There also appear to be modulations within cascades which can clump phase at certain fractional intermediate stages of transitions. The 24.15 km/s period is in fact such a modulation, a 1/3 interval of the basic 72 km/s period. I suspect there is a good reason for the 1/3 interval.

There are two types of phase-deviation diagrams depending upon whether the newest or oldest redshifts in a comparison are used to define phase. You can look back in time, but forward only in retrospect. Since transitions can change phase there can be a phase dependence within any sample if variability is present (and phase spread is greater than redshift uncertainty, which it is for the 24.15 km/s period). The left frame of figure 2.33 is a phase-deviation diagram for the 24.15 km/s period phased with the newest observations. There is a clear slope indicative of transitional phase drift in the sample. Variability deviations are present but the small steps within the cascade are not phased together. Earlier observations were made when the galaxies were at a different phase within the 24.15 km/s period. The change appears *before* the epoch used for phasing and the observations contain the record of the *past* phases. The 24.15 km/s period appears as a quasi stable modulation within a longer cascade pattern of small steps. If the oldest observations are used to define phase, variation will show only deviations and the deviation pattern will be horizontal as I will shortly demonstrate. The change appears *after* the epoch used for phasing so the

diagram contains only the *future* displacement information. If several levels of the cascade are occupied simultaneously there will be a *set* of transition lines either sloping or horizontal depending upon which data epoch is used for phasing.

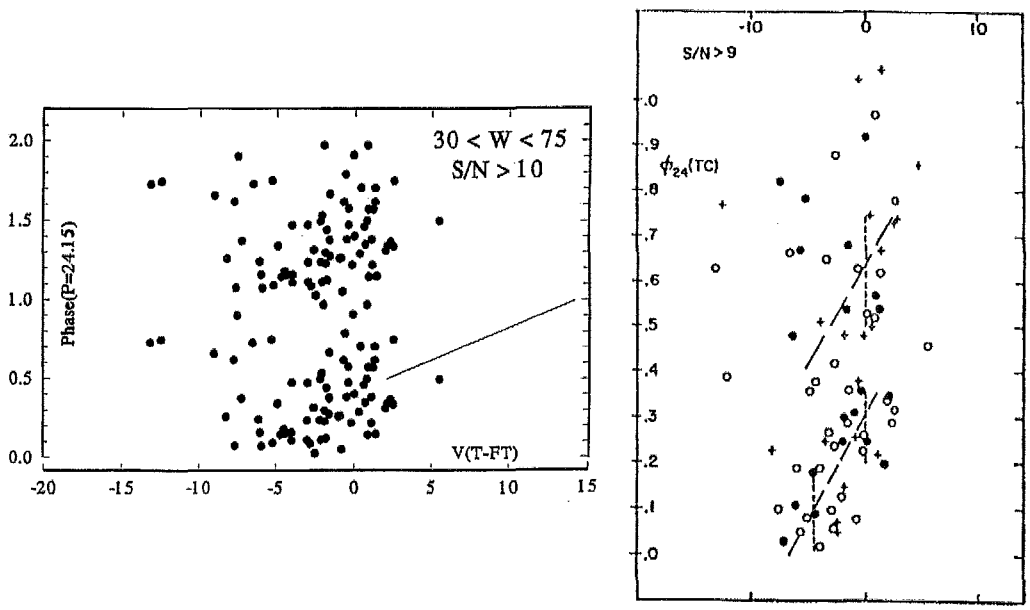


Figure 2.33: LEFT: Phase drift in the dwarf galaxy 24.15 km/s period between the Fisher-Tully (FT) and newer Tifft (T) redshift epochs [111]. Phase is determined using the new Tifft-Cocke redshifts. Only high level signal-to-noise data are shown. The sloped pattern indicates a phase dependent drift is present. RIGHT: Deviations between Fisher-Tully and mid 1980s Tifft-Cocke redshifts as a function of redshift phase (using Fisher-Tully redshifts) for the 24.15 km/s redshift period applicable to dwarf galaxies with $W < 75$ km/s and $S/N > 9$.

The implication from the left frame of figure 2.33 is that the 24.15 km/s period is not basic, but is a drifting modulation within a multi-level pattern of a shorter more fundamental period. The period involved is presumably an integer fraction of the observed period (P/n where n is the number of intermediate transitional steps).

I first demonstrated a transitional cascade process in 1987 at a symposium in Venice [94]. The first clues to the process are shown in the right frame of figure 2.33. This is a phase-deviation diagram using Fisher-Tully redshifts to set phase. There is a clear three level drift pattern which will superimpose at a period one-third of 24.15 or 8.05 km/s. The slope is considerably enhanced when shown this way since points shift down in phase and in deviation. The three groups below phase 0.7 form the much tighter sloped pattern in the left frame of figure 2.33 which splits into two groups near zero deviation and one deviated group. Weaker points now complete a picture of three sloped deviation patterns. The steep population gradient of the three levels is a clear indication the 24.15 km/s period is a modulation of shorter periods. It is also clear that without modulation the 24.15 km/s

period would probably not be detected.

Further evidence for redshift change was subsequently found in the $24/3 = 8.05$ km/s period and discussed at IAU Colloquium 124 [106] in 1989 (see also [111]). Fractional phase drift indicated the 8 km/s period was again a modulation. In 1990 the 8 km/s period was shown to contain an 8/3 km/s structure which did appear to be fundamental or close to it. The period was 2.6657 km/s, a third step in a 3-level modulation pattern beginning at 72 km/s, $72 \rightarrow 24 \rightarrow 8 \rightarrow 2.6657$.

To demonstrate the shorter period I set phase using the newest data, which was most precise, thus has the least scatter. The process is shown in figure 2.34 beginning with the 2/3 fraction of the 24.15 period, fine tuned to 15.994 km/s, to superimpose the two strongest phase clumps in the right frame of figure 2.33.

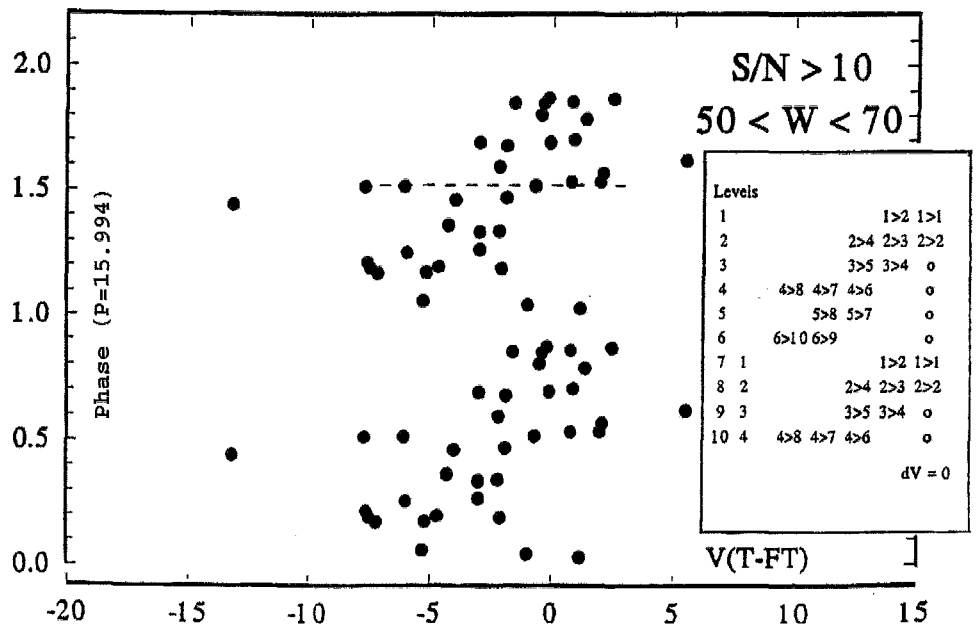


Figure 2.34: Phase-deviation diagram for dwarf galaxies at a 15.994 km/s period used to derive an underlying fundamental period (step size) by which dwarf galaxies shifted between Fisher-Tully and Tifft redshift epochs [111]. Phase is derived from 1986-1988 precision Tifft redshifts. A dashed line shows the expected direction of change. An inset shows correspondence with a 6-level model.

The horizontal line shows how a phase point should track as the redshift steps down in phase when points are plotted using the newest data to define phase. A model of the process is shown in an inset. The first number in $x \rightarrow y$ steps is starting phase, the second is the phase level it has moved to in a transitional jump (but deviation is plotted at the starting phase to generate a horizontal track). The first line in the figure and model beginning at zero deviation represents a transition from phase 0.1 to 0.2 in the 15.994 km/s period. Figure 2.34

is about a longest period clearly showing deviation tracks. There are six horizontal tracks in the figure, one corresponding to the dashed track. By shifting a transparent rule in steps of 0.167 (1/6) phase units five other horizontal features in this six level phase diagram can be seen. 15.994 divided by six is 2.6657 km/s, the period which reduces the diagram to a single distinct continuous track shown in figure 2.35. As an interesting historical aside it is worthy of note that I would not realize the significance of what I had just accomplished until about 25 years later as I was composing this book. I had transformed between two quantum states I did not yet know existed. There was still much to learn.

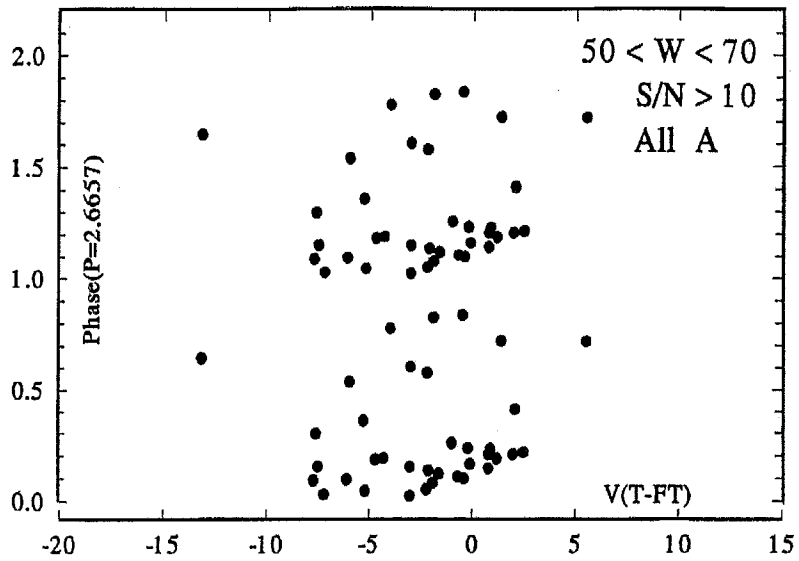


Figure 2.35: Phase-deviation diagram for dwarf galaxies at the optimum period of 2.6657 km/s responsible for the drift in the original 24 km/s period [111]. The redshift differences are between Fisher-Tully and newer Tifft data. Some points suggest that higher harmonic structure could be present.

the 2.6657 basic stable period was what we were seeking. Vertical scatter is now a measure of uncertainty in the newer redshifts, about 0.27 km/s, 1/10 of the period in case you did not believe me when I said such accuracy was possible. The phase is also near zero, another feature I would expect to see. This was the first basic period found after 72. In the third seminar, after learning to predict periods, we will see the period matches predictions within 0.003 km/s. A few points suggest higher levels but 2.67 km/s effectively accounts for a specific transition step size within the peridodity structure. The line is not quite horizontal because we are near the precision limit and profile shape (asymmetry) is beginning to matter as I can now show. This determination of an optimum fit produced almost no change in the galactic center transformation. Final values, almost unchanged since 1991, are +232.4 (transverse), −36.5 (radial) and +1.2 (Z) in km/s [111].

The 2.67 km/s period was detected through higher modulations; deviations are not uniformly spread in phase at all successive levels. By plotting the phase-deviation diagram at higher

integer multiples of the 2.67 km/s period one can assess how a cascade may proceed, as in the 6-level study just discussed. The two level cycle, the 5.33 km/s period, (which also turns out to be a basic period), is interesting in this regard and is shown in figure 2.36 [111].

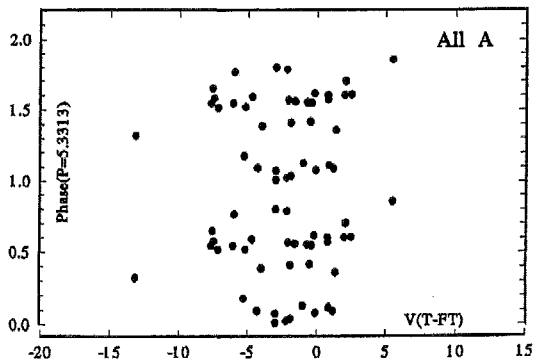


Figure 2.36: Phase-deviation diagram for dwarf galaxies at twice the optimum period of 2.6657 km/s for redshift differences between Fisher-Tully and newer Tifft data [111]. The differences between successive 2.67 km/s phase levels may be related by transition timing or rates and amounts of change at different levels.

Alternate levels of the 2.67 km/s period are quite different but can be related by diagonal transitions at the 2.67 km/s period. By separateing points by profile asymmetry the positive and negative forms may now be seen to behave differently as shown in figure 2.37.

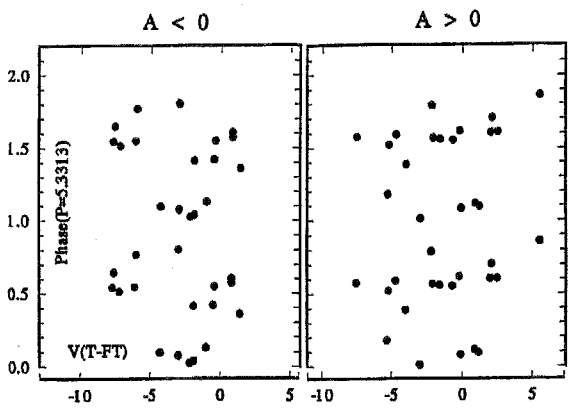


Figure 2.37: Phase-deviation diagram for dwarf galaxies at twice the optimum period of 2.6657 km/s in redshift differences between Fisher-Tully and newer Tifft data [111]. Points are distinguished by profile asymmetry to show profile shape affects phasing within the cascade.

Phase shifts appear to be related to asymmetry. Such asymmetry effects are consistent with quantization involving level transitions if profiles can be thought of as the equivalent of wave functions. The sequencing of transitions could depend upon profile shape to the

extent it modifies the overlap of redshift states which changes transition probabilities. We would therefore expect asymmetry to relate to phase sequencing as appears to be the case. We will see more dramatic asymmetry effects later.

When I first derived the 2.67 km/s period I had no idea what it meant. It was not obviously related to the original 72 km/s period but was clear in phase-deviation diagrams and power spectral analysis. The ApJ paper discussing variability appeared in 1991 [111]. Although I did not know it at the time, the 2.67 km/s period was destined to take on a much greater significance later. As noted previously, by 1993 we would be able to predict periods.

### 2.6.4 Redshift Accuracy, Consistency and Asymmetry

Before leaving this section, where very short periods and asymmetry is being utilized, I should comment further concerning 21 cm redshift precision. Two factors are involved concerning precision, the *accuracy* of the redshift derived being the true physical redshift, and the *consistency* of repeat measurements. The former is important for accurate phasing, the latter for detecting change. A measure may deviate from the true redshift slightly, but if consistent between measurements will show variation very well. My 21 cm measurement process was designed to maximize consistency. The asymmetry parameter then provides a means to evaluate the accuracy. Figure 2.36 shows remarkably level phase lines very close to cardinal phase points 0.0 and 0.5 placing the galaxies involved essentially in phase with our galaxy (the galactocentric rest frame). Furthermore the asymmetry variation in figure 2.37 is remarkably symmetric about the mean horizontal line, which confirms the meaning of asymmetry and the accuracy of the overall phase. Asymmetry in single peaked dwarf galaxies appears to introduce no more than about 0.05 km/s uncertainty in the true redshift.

There is a second aspect of redshift precision relating to the comparison of 21 cm redshifts with optical values. I use an analogy of a hollow sphere partially filled with a fluid and flowing down a turbulent stream. The edges of a 21 cm profile define the edges of the capsule, so the mean of the profile edges define the actual location (redshift) of the 'particle'. An optical redshift samples the turbulent 'dynamical' interior, which a 21 cm measure reduces to the asymmetry index. To the extent that an optical 'nuclear' redshift represents the mean of the nuclear dipole of the galaxy, it may also represent the true redshift, but the dipole is typically well obscured. In general, precise 21 cm observations appear to be an optimum means to examine the nature of the redshift. So far as I know I am the only scientist that has quantified 21 cm asymmetry. Asymmetry actually provides one of the fundamental tests of the QTC theory, but that is 20 years from where the story is at this point.

## 2.7 The Cosmological Correction

Variability was only one of the facets of quantization we needed to face before we could work effectively with redshifts globally. As we probed deeper into space, we needed to know if redshift intervals involved a dilation effect analogous to deceleration effects in conventional cosmology. We needed to detect and learn how to correct for any such non-linearity. The 2.6657 km/s period was just what we needed for such a determination. For a short period, phase drift will become apparent quickly with increasing redshift since even a small correction can be a sizable fraction of the period. At redshifts of a few thousand km/s a correction

of a few km/s will slightly bias long periods but not be apparent as a non-linearity. Figure 2.38 shows a redshift-phase plot for the narrow profile galaxy data using the 2.6657 km/s period with no correction applied. There is a distinct phase drift with z, clear evidence for non-linearity, dilation, in redshift intervals. The correction which linearizes the redshift pattern is called the 'cosmological' correction.

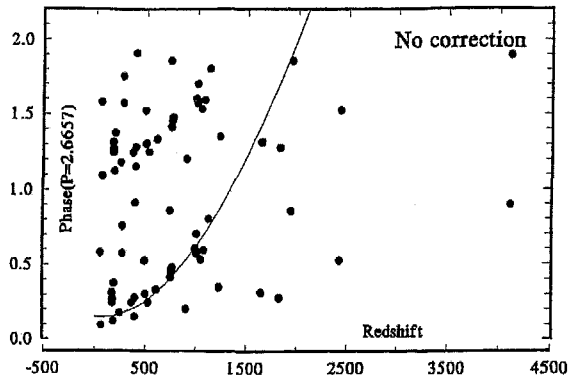


Figure 2.38: Phase-redshift diagram for dwarf galaxies at the optimum period of 2.6657 km/s in redshift differences between Fisher-Tully and newer Tifft data. Phase drifts rapidly upward [111] when no cosmological corrections are applied.

One form of cosmological correction, based upon early theoretical concepts by John Cocke [AA], had in fact been incorporated in our global studies since 1984 [87]. At the longer periods then involved the effect was of little consequence, but with the new short period this original correction can be ruled out. Figure 2.39 shows it over-corrects the data, slightly reversing the phase curvature.

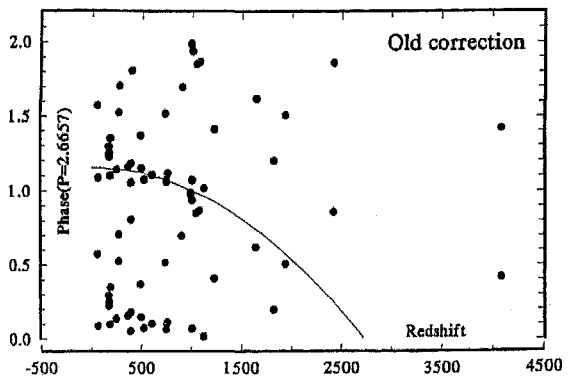


Figure 2.39: Phase-redshift diagram for dwarf galaxies at the optimum period of 2.6657 km/s in redshift differences between Fisher-Tully and newer Tifft data. Phase drifts slowly downward when original corrections are applied [111].

While I was working with variability, John was considering a number of other models. One possibility was redshift intervals might vary as the square root of the time dependent Hubble constant, H(t). I will provide a plausible reason why this should be the case in a later seminar. In conventional cosmology there is a relationship between H(t), the redshift z, and the deceleration parameter $q_o$. Using this relationship an expression can be derived for a redshift interval dz as a function of $q_o$ and z. The relationship can be integrated using a Taylor expansion about $q_o = 1/2$ to give an expression for corrected z values. $q_o = 1/2$ is an appropriate choice since it corresponds to an Omega=1 flat universe which appears to match the real universe very well. The first order term depends only on z and is followed by higher terms in $(q_o - 1/2)$. For $q_o = 1/2$ the first term gives the complete correction:

$$z(corr) = 4([1 + z(obs)]^{1/4} - 1).$$

When the new correction is applied to dwarf galaxy redshift data, as shown in figure 2.40, it removes any sign of phase drift. The correction appears to linearize the redshift intervals with z. Further discussion of $q_o$ and the correction will appear in subsequent seminars

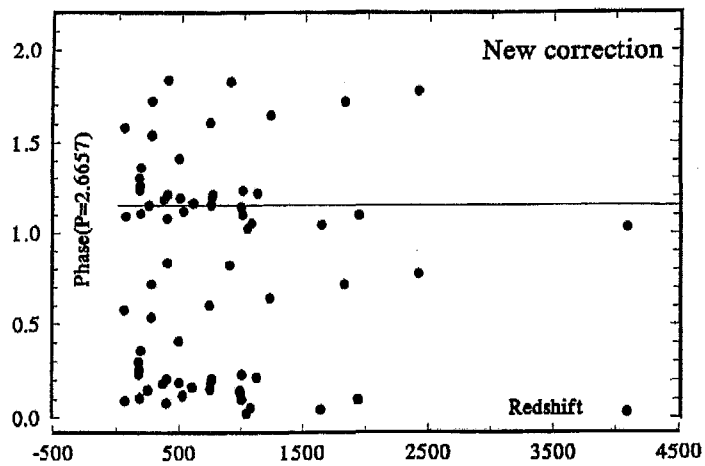


Figure 2.40: Phase-redshift diagram for dwarf galaxies at the optimum period of 2.6657 km/s for redshift differences between Fisher-Tully and newer Tifft data [111]. Phase drift vanishes when the newer cosmological corrections are applied.

When John first derived the redshift interval relationship we applied it to a study of Lyman alpha forest redshift intervals in quasars [102] and found periodicities consistent with our low redshift work. The periodicities appeared for $q_o$ near 1/2. In subsequent work with galaxy redshifts we have found no significant deviation from the exact relationship given when $q_o$ is set equal to 1/2. More background leading to the cosmological correction in the above form is contained in the quasar paper [102]. The correction has a classical basis but fits quantization. There are interesting connections between classical and quantum models. John's work in developing the correction equation was extremely important. Interplay between the variability and cosmological correction work, which developed together, made much of the more recent work possible.

## 2.8 The Cosmic Background Rest Frame

At this point we had detected global quantization, recognized variability, and had a good model for cosmological corrections. We were now prepared to look deeper into space with large samples of galaxies. Very good data was becoming available, we had precision work done at Greenbank, and deep surveys were coming from Arecibo, work by Giovanelli and Haynes and co-workers. Serious testing of global quantization was becoming possible, but a major hurdle remained. We had been working in the galactic center rest frame, but as John kept reminding me, there was a more fundamental rest frame to examine. We needed to relate quantization to the cosmic background rest frame to clearly connect to cosmology. Results from COBE were focusing attention on the cosmic background and we needed to understand the relationship between quantization and the cosmic background radiation (CBR).

COBE provided a well determined dipole component and uniformity measurements for the cosmic background. In 1991 we put together a study of quantization in the cosmic background rest frame defined by the COBE measures. The dipole component posed a serious problem for quantization. The standard explanation of the dipole is that our galaxy is moving, in some random manner, with respect to the cosmic background rest frame. The velocity involved is substantial, several hundreds of km/s. If all galaxies are actually moving randomly in this manner Doppler shifts from the motion should completely obscure any intrinsic quantization effect. However, quantization was obviously present. If we found quantization from the cosmic background rest frame we would have to find an explanation of the dipole component which did not involve the motion of our galaxy. I will provide such a model in the following seminar, but the first step was simply to see what we found when we transformed to the CBR rest frame; would we see quantization? The answer was a definite yes. When we transformed to the CBR frame we quickly found we could quantize redshifts for all types of galaxies. We would no longer be limited to the extremes of profile width. But just as variability and cosmological corrections were intertwined and developed together, so the CBR investigations and our present understanding of redshift periods are interlinked. I will take the first steps in this seminar. The next seminar looks beyond 1993 when we defined a precise period structure.

When we began investigating the cosmic background rest frame our knowledge of redshift periodicities was limited to our previous empirical determinations. We therefore looked for periodicities close to 72 km/s or its simplest harmonics. The first sample studied utilized the most reliable set of our 21 cm redshifts from the 1980s, and looked only at galaxies with profiles wider than 125 km/s to minimize effects of the shorter period we had found for extreme dwarfs. We immediately found a 72 km/s periodicity closely associated with the vertex. The upper frame of figure 2.41 illustrates our initial detection using the highest s/n data in our best data sample [124]. Details concerning this sample and others utilized are described in reference [124]

When the sample was extended to include all our new 21 cm data we could detect clear structure in the phase-width diagram. A 72 km/s periodicity was present with a distinct phase shift near $W = 200$ km/s. As with the galactic center studies we searched over a range of transformation constants centered on the COBE dipole vertex. The lower frame of figure 2.41 is a power contour diagram which shows the association of peak power with the COBE dipole vertex error box [124].

It was now perfectly clear that the CBR rest frame was a fundamental frame. It allowed us to quantize redshifts at all profile widths and provided a first glimpse of a rich phase structure. Reference [124] discusses the significance of the cosmic background association with global quantization in detail.

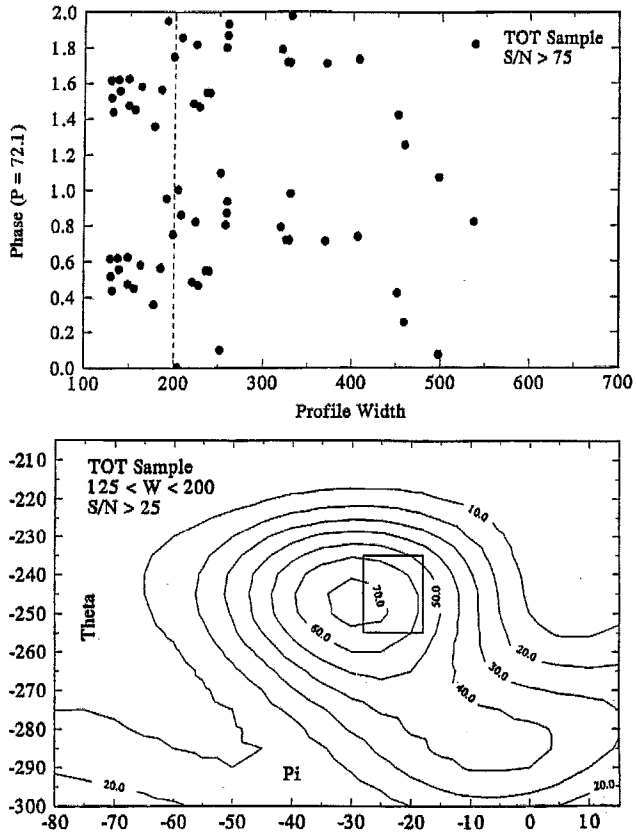


Figure 2.41: UPPER: Phase-profile width diagram for all galaxies with $W > 125$ km/s and $S/N > 75$ using newer Tifft or Tifft-Cocke redshifts as seen from the cosmic background rest frame at $P = 72.1$ km/s. The points are periodic with a distinct phase shift near $W = 200$ km/s. LOWER: Power contour diagram for galaxies with $125 < W < 200$ km/s and $S/N > 25$ with newer Tifft or Tifft-Cocke redshifts transformed to the vicinity of the cosmic background dipole vertex. Power peaks close to the COBE dipole vertex error box. The diagram refers to P=72.1 km/s at Z=272 km/s [124]. Power levels are scaled by ten for clarity.

To extend the sample of galaxies still further we turned to the complete Fisher-Tully (FT) catalog using cutoffs in the F/W ratio to control quality. Figure 2.42 shows all FT galaxies with $W > 125$ km/s and $F/W > 0.05$ [124]. The periodicity below $W = 200$ km/s was clear. To expand the sample for the rarer widest profiles we lowered the $F/W$ cutoff to 0.025 as shown in Figure 2.43. The period is again very clear with a shifted phase at 400

km/s as well. The periodic patterns above and below a 'transition' zone near $W = 200$ km/s provided independent tests for periodicity and association with the CBR dipole vertex. The contour diagrams showing the CBR association are shown in figures 2.44 and 2.45.

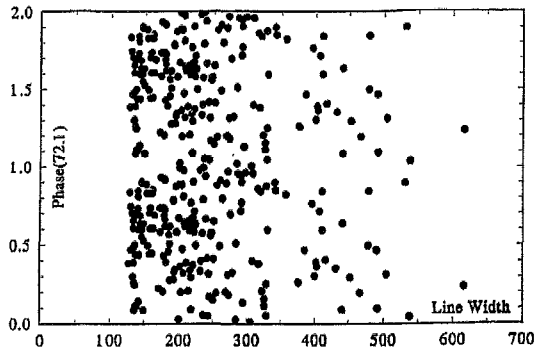


Figure 2.42: Phase-profile width diagram for all Fisher-Tully galaxies with $W >$ 125 km/s and $F/W > 0.05$ when transformed to the Cosmic Background rest frame. Points are periodic at the original 72 km/s period with a distinct phase shift near W=200 km/s [124].

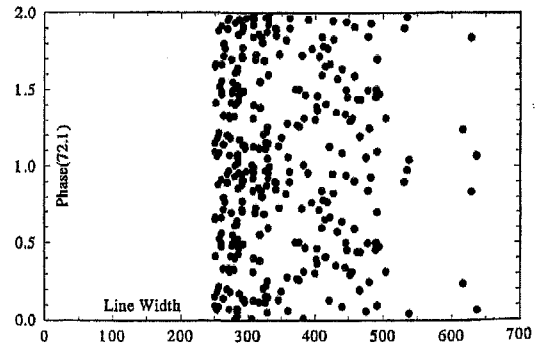


Figure 2.43: Phase-profile width diagram for all Fisher- Tully galaxies with $W >$ 250 km/s and $F/W > 0.025$ when transformed to the Cosmic Background rest frame. Points are periodic at the original 72 km/s period with a phase shift apparent near $W = 400$ km/s [124].

As a final test we utilized a sample of Arecibo redshifts by Giovanelli and Haynes [AB,AC] from their investigations of the Perseus supercluster. This was our first deep excursion outside the local domain; it returned a clear periodicity for very wide profile galaxies at a 36 km/s period, again closely associated with the CBR vertex. There appears to be a second major shift in phase beginning near $W = 400$ km/s.

The phase transition near $W = 200$ km/s is especially significant. In view of evidence for redshift variability we had reason to believe that this transition region would be a fruitful

place to examine for changes. Something clearly happens at that point, the underlying internal quantum structure of galaxies appears to suddenly change. The next seminar will indeed show evidence for variability in this region, but we would need to understand the periodicity structure better before a proper study was possible. As with the dwarf galaxy investigations from the galactocentric rest frame various periodic modulations were no doubt involved. The phase distribution far exceeded redshift uncertainty. There had to be substructure. This work was done in 1992 and first announced at the AAS Berkeley

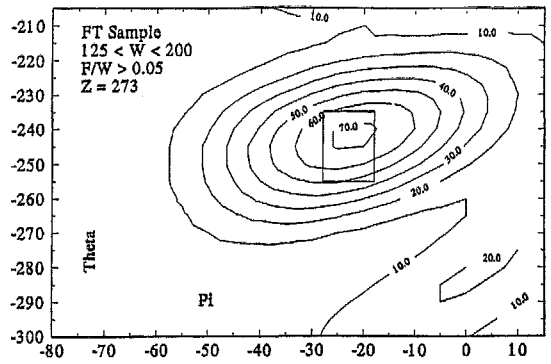


Figure 2.44: Power contour diagram for all Fisher-Tully galaxies with $125 < W < 200$ km/s and $F/W > 0.05$ when transformed to the vicinity of the cosmic background dipole vertex. Power peaks within the COBE dipole vertex error box. The diagram refers to P=72.1 km/s [124]. Power contour levels are shown scaled by ten for clarity.

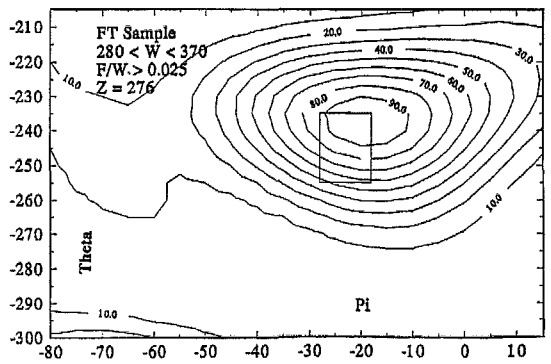


Figure 2.45: Power contour diagram for all Fisher-Tully galaxies with $280 < W < 370$ km/s and $F/W > 0.025$ when transformed to the vicinity of the cosmic background dipole vertex. Power peaks close to the COBE dipole vertex error box. The diagram refers to P=72.1 km/s [124].

meeting in 1993 [121] and the Tucson meeting in 1994 [123j. The formal paper giving details of the initial work appeared in 1996 [124].

There is one final point concerning rest frames. We had detected quantization in two different frames, the galactic center, and the cosmic background. For this to occur the frames must be related, there is a connection between them. Two such remarkable associations cannot be accidental at the level of significance we were seeing. It is therefore interesting to compare the transformation constants. As noted earlier, the galactocentric frame appears to apply to our 'local' cloud of galaxies. The cosmic frame represents the true global domain The transverse, radial, and perpendicular components with respect to the plane of the galaxy were $(-243, -31, +275)$ for the cosmic background transformation, and $(+232, -36, +1)$ for the galactic center. The tangential components are equal and opposite within uncertainty in the solar motion with respect to the local dynamical standard of rest (galactic circular motion). The radial components are essentially identical. Both imply radial expansion of the galaxy consistent with the model of dipole structures for galaxies. The perpendicular components, are very different. There are clear similarities and one important difference, which we will discuss in a later seminar. There is good reason to expect a connection between the transformations. The astute observer may notice that the sum of the CBR components is essentially zero. Is this another accident?

At this point. Coming into the early 1990s we were reaching the end of what I refer to as the empirical phase of redshift quantization work. We had resolved a number of problems. We recognized the fundamental importance of the cosmic background rest frame, and John Cocke played an important role in nudging us in that direction. We had an understanding of the cosmological correction, again very much due to my association with John Cocke while we were coping with variability. We were, however, still working with empirical periods. We did not have a theory or any means to specify exactly what periods should be present. This reminds me of the Standard Model of Particle Physics where many basic parameters, such as the particle masses and the fundamental force strengths, which are empirically defined and related. This changed rather dramatically in 1993. Both such cosmological and particle physics problems would be clarified by the same new understanding that was coming! QTC was soon to be born.

## 2.9 Independent Confirmation!

Following the original work with pairs, and early global studies, several independent studies were done by others. They were usually motivated to find what was wrong rather than to look into a new idea. Such studies are typically narrow in focus, rarely consider that new physics might be involved, and ignore broader consistencies within the work, for example, between global and differential studies. I gave a paper at the Kansas City AAS meeting in 1988 entitled "Redshift Quantization - Many Lines of Evidence" [99], to emphasize how many studies converge toward the same picture. However, no amount of ordinary evidence will apparently sway the belief of many scientists that the present classical dynamical cosmological picture is nearly complete. Quantized redshifts are simply not possible! Despite this atmosphere there were two early independent studies supporting my findings. Bill Napier presented a paper at the 1987 Venice Symposium which supported unconventional findings by Chip Arp and Tifft-Cocke [AD] that surprised a number of people. A study by Martin Croasdale [AE], published in 1989, also confirmed aspects of global quantization. A much more disturbing study was yet to come.

In 1991 Guthrie and Napier in England, made a detailed global study of spiral galaxy redshifts and found a very strong galactocentric periodicity close to our 36 km/s result [AF]. This confirmation of quantization was very disturbing to the astrophysical community, and resulted in some popular press. *Sky and Telescope* started it off with a 'news note' [115] which was picked up by the science editor of the *New York Times* [116]. This stirred *Scientific American* and *Discover Magazine* to print reviews of my work [117,118]. It is interesting to read the reviews; they contain responses by prominent astronomers regarding quantization concepts. What is more important, however, is that one of the articles came to the attention of Ari Lehto, a physicist in Finland. Lehto contacted me with news that he had developed a model which could specifically predict redshift quanta. He claimed to be able to predict exactly what periods should occur. If he was correct that would close the final missing link. Not only would we know the rest frames to use and cosmological corrections, but we would be looking for very specific predictable periods.

I was initially doubtful concerning his idea, it was fascinating, unusual, and had been published in a very obscure place - *The Chinese Journal of Physics* [AG]. But, we were on the verge of making important tests, and it was easy to check the concept. There would be important modifications, but some equations were about to emerge, the Lehto-Tifft equations, which would profoundly affect our quantization work (and particle physics). In Lehto's view it was necessary to go back to the fundamental Planck scale and envisage a decay process which would generate specific periods (and a great deal more relating to fundamental particles and forces). Many predictions based upon the idea have now been verified. I will develop and demonstrate the success of the Lehto-Tifft model in the next seminar.

# Chapter 3

## Redshifts and the Dimensions of Time, Defining the Properties of a New Cosmology, 1993 to Date

Seminar 3 Version 4

## 3.1 Introduction

The two previous seminars provided background evidence concerning correlation studies and early quantization work, which convinced me the redshift was a quantized quantity intrinsic to the nature of galaxies. By 1992 we had explored the quantization question using individual galaxies and systems of galaxies, especially pairs, and had turned to investigations on a global scale. Major steps were made globally recognizing redshift variability, including sub harmonic cascades between quantized levels, and deriving a 'cosmological correction' to correct for nonlinearity in quantized intervals as a function of z and $q_o$. Global studies began by transforming to the galactic center reference frame, but by the early 1990s it became clear the cosmic background (CBR) reference frame was far more fundamental. External verification of redshift quantization stirred up interest in the quantization issue which in turn was to lead to a breakthrough in understanding periodicities, a major step toward generating a new cosmology.

## 3.2 The United Kingdom Stirs the Pot

1992 marks a critical transition point. COBE had come on line and directed our focus toward the cosmic background rest frame. By 1992 we also had our new precision 21 cm data from Greenbank along with major surveys, which were becoming available from Arecibo. We had the accurate 21 cm data needed to make sophisticated global studies. John Cocke and I had begun to look at quantization in the cosmic background rest frame when several important events occurred. Bruce Guthrie and Bill Napier, two English astronomers, published an independent study [AF] which confirmed global periodicity. They demonstrated [AF] that nearby spirals, in the galactocentric rest frame, have redshifts which were quantized at a period close to our $72/2 = 36$ km/s interval. Figure 3.1 shows the power spectrum of their sample indicating the presence of a distinct 36 km/s periodicity.

The work by Guthrie and Napier disturbed the scientific community, which was not expecting confirmation since redshift quantization is inconsistent with present dynamical theory. I will discuss the Guthrie-Napier result in more depth after introducing Ari Lehto who heard about my work as a result of excitement that occurred as a result of the work by Guthrie and Napier. Several popular articles were published [115,116,117,118]. Some of the material came to the attention of Lehto, a physicist in Finland, who contacted me early in 1993. He developed a model [AG], which could in principle predict precise periods in redshift data.

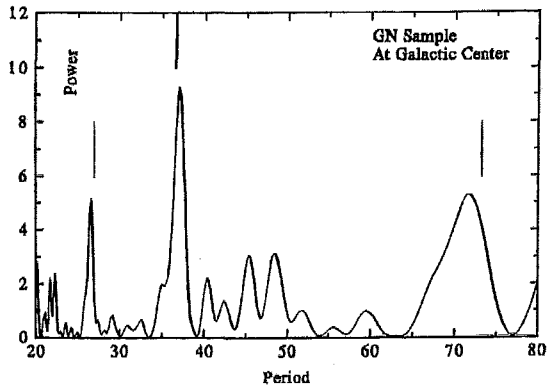


Figure 3.1: Power spectrum of the Guthrie-Napier sample of local galaxies that independently confirmed redshift quantization of local spiral galaxies in the galactocentric rest frame [125]. Vertical lines indicate predicted or possible periods.

## 3.3 Lehto's Concept

Lehto published his concept in a rather obscure place, the *Chinese Journal of Physics*, in 1990 [AG]. I have yet to find anyone who has access to that journal, so it is not surprising his idea went unnoticed until he sent me a reprint. I will review his work more specifically in the next seminar where I will look at particle physics. Lehto was originally motivated to describe properties of fundamental particles. The Standard Model of particle physics assumes many things, such as particle masses and magnetic moments along with the strength of fundamental forces, which cannot be calculated within the model. Lehto proposed a mechanism for predicting such values. His idea was to begin with the Planck units, the Planck energy, time, mass, and the velocity of light. These units can all be expressed in terms of the Planck time or Planck frequency as defined by the fundamental constants h, c and G. Present day observable properties of particles (and redshifts) are then presumed to be generated by a decay process beginning from the Planck units. Lehto proposed that the units decay by a period doubling process, essentially an action doubling process in factors of 2, a process well known in decay of systems toward chaos. If this was actually the case present day fundamental properties of matter and energy should be related to the Planck units by simple powers of 2. When Lehto explored this idea he found what appeared to be ratios involving cube-root powers of 2. Lehto then suggested a doubling process could be occurring in a 3-dimensional or 3-parameter space, which we somehow perceive as 1 dimensional; the doubling process is reduced by a cube-root transformation. I will subsequently show how this can in fact be accomplished. Lehto's process for predicting redshift periods therefore takes the basic unit, the speed of light c, and scales it by 2 to the $-N/3$ power

$$P = c2^{-N/3} \qquad P = c2^{-(3D+L)/3}.$$

We usually rewrite this in the form shown on the right, the Lehto-Tifft form. D is the doubling number, and L specifies which cube root 'family' is involved. There are 3 doubling families as L cycles from 0 to 2. The sequences are related to each other by the cube root of 2, a factor of 1.26. The pure cube root family, L=0, is presumably the most fundamental.

It contains period patterns 146.4, 73.2, 36.6, etc km/s precisely consistent with observed redshift patterns. That match provided Lehto's reason for contacting me.

### 3.3.1 Virgo Opens the Door, Expanding Lehto's Concept

Lehto's idea was certainly an unusual one; I was originally skeptical, but his particle model was rather intriguing. He provided an interesting way to calculate properties of the electron for example, which I will demonstrate and expand upon in seminar 4. However, it was easy to check his predictions since John and I were preparing to look for redshift quantization in the Virgo cluster from the cosmic background perspective. In our early work we had found quantized redshift patterns for certain types of local galaxies but had been unable to extend the findings to distant systems such as the Virgo cluster. In the context of supercluster studies it appeared that we were detecting periods within our specific cloud of galaxies and in specific clusters as seen in Coma. We needed to see if conversion from the galactic center rest frame to the cosmic background rest frame would make it possible to tune such local effects together on a cosmic scale. That did in fact prove to be the case. Figure 3.2 shows the power spectrum of one of the first Virgo cluster samples examined. Numerous periods come through strongly as spectral power spikes. Peaks are precisely defined, not shifted or blurred as seen locally in figure 3.1. Local quantization works but is somewhat distorted.

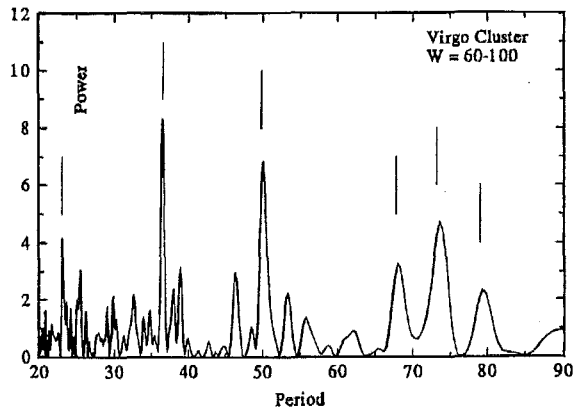


Figure 3.2: Power spectrum of Virgo cluster galaxies ($60 < W < 100$ km/s) used to demonstrate redshift quantization in the cosmic background rest frame [125]. Vertical lines indicate periods predicted by the Lehto-Tifft equation.

Periods at 36 and 73 km/s are clear and very close to locations predicted by the periodicity equation. It is important to note that the formulation leaves no room for uncertainties; possible periods are specified with the full precision of c. As will be subsequently shown, no significant deviations from the precise values predicted can be detected.

There was a problem however; there were strong peaks, especially the one in figure 3.2 near 50 km/s, which were not predicted by Lehto's original equation. Furthermore, the 2.6657 km/s period found from variability studies was not predicted by his formula. On April 30 1993 (I made note of the specific date) I suddenly realized what the pattern in the other periodicities was. A pattern incorporating but extending Lehto's predictions was what was

needed. That could be accomplished by taking an additional cube root. The periodicity equation would take the form P equals c times 2 to the (negative) ninth root of integers. With this change all the clear peaks in the Virgo spectrum were fit, most notably the one at 49.8 km/s. What really convinced me of the significance of the ninth-root rule however, was that the 2.6657 period was now explained. A period at 2.6681 km/s, indistinguishable from 2.6657 was predicted. A more detailed discussion of what I refer to as the Lehto-Tifft formulation will be developed in seminar 4 including applications to particle physics. The standard form of the Lehto-Tifft redshift period equation is

$$P = c2^{-(9D+T)/9}.$$

D is again the level of doubling and T distinguishes nine individual doubling families. They are separated by the ninth root of 2 (1.080) as compared to Lehto's original form, which has 3 families of periods separated by the cube root of 2 (1.26). Much of the remainder of this seminar will be devoted to showing that subsets of these specific periods have now been found in many samples. The fit to the formula is precise, we cannot detect significant deviations. Furthermore, we have not found any other significant periods which do not fit into the nine families. The fits are excellent, and the predicted set is uniquely present. The predicted periods, which match the peaks in figure 3.2, are shown with vertical lines. The significance of using ninth roots will be discussed after the cosmic geometry of the new Quantum Temporal Cosmology, QTC, begins to fall into place.

Power Spectral Peaks in the Virgo Sample

| | | | $-500 < V < 3500$ | | | $500 < V < 3500$ | | |
|---|---|---|---|---|---|---|---|---|
| Period km s$^{-1}$ | $P(D,T)$ | $W$ km s$^{-1}$ | Peak km s$^{-1}$ | Power | Pk/Per | Peak km s$^{-1}$ | Power | Pk/Per |
| 73.1916 | $P(12,0)$ | 50- 90 | 73.222 | 5.6(5.6) | 1.0004 | 73.719 | 6.3(5.8) | 1.0072 |
| | | 60-100 | 73.407 | 4.2(4.1) | 1.0029 | 73.645 | 4.7(4.3) | 1.0062 |
| | | 70-110 | ... | (1.0) | ... | ... | (1.4) | ... |
| | | 60-125 | ... | (3.4) | ... | ... | (3.3) | ... |
| | | 40-150 | 74.004 | 5.1(3.6) | 1.0111 | 73.530 | 5.0(4.8) | 1.0046 |
| | | all | 74.117 | 4.0(2.4) | 1.0126 | ... | ... | ... |
| 36.5958 | $P(13,0)$ | 50- 90 | ... | (2.8) | ... | ... | (2.4) | ... |
| | | 60-100 | 36.472 | 8.3(7.3) | 0.9966 | 36.529 | 8.5(8.2) | 0.9982 |
| | | 70-110 | 36.404 | 9.8(7.8) | 0.9947 | 36.460 | 10.6(9.3) | 0.9963 |
| | | 60-125 | 36.324 | 5.0(2.6) | 0.9926 | 36.439 | 5.4(4.2) | 0.9957 |
| | | 40-150 | ... | (0.7) | ... | ... | (1.0) | ... |
| | | all | ... | (0.3) | ... | ... | ... | ... |
| 67.7663 | $P(12,1)$ | 50- 90 | 67.974 | 4.6(4.3) | 1.0030 | ... | (3.5) | ... |
| 49.7992 | $P(12,5)$ | 50- 90 | 50.218 | 7.7(5.2) | 1.0084 | 50.305 | 8.3(5.2) | 1.0105 |
| | | 60-100 | 49.965 | 7.1(6.2) | 1.0033 | 50.052 | 6.8(5.6) | 1.0054 |
| | | 70-110 | 49.701 | 4.1(4.0) | 0.9980 | ... | (3.8) | ... |
| | | 60-125 | 49.694 | 7.1(6.9) | 0.9979 | 49.831 | 7.2(7.1) | 1.0009 |
| | | 40-150 | 49.675 | 6.3(6.0) | 0.9975 | 49.732 | 5.5(5.5) | 0.9989 |
| | | 100-250 | 49.363 | 4.8(1.4) | 0.9912 | ... | (1.2) | ... |
| | | all | 49.649 | 6.1(5.7) | 0.9970 | 49.702 | 5.3 | 0.9980 |
| 24.8996 | $P(13,5)$ | 100-250 | 25.081 | 4.5(3.0) | 1.0072 | 25.026 | 4.5(3.8) | 1.0050 |
| | | all | 25.031 | 4.4 | 1.0053 | ... | ... | ... |

Figure 3.3: Table of Virgo Cluster periods with T=0 to 5, and peak power greater than 4, as detected in the CBR rest frame [125]. Power is listed as at peak power and at the predicted period (in parentheses). The first set of values is for redshifts up to 3500 km/s; the second set omits possible foreground. Pk/Per measures the deviation of observed (peak) periods from predicted values.

Figure 3.3 contains a table summarizing part of the Virgo cluster investigations [125]. Spe-

cific predicted periods are listed with their D and T values, the subsample properties, and observed periods and powers (peak power is given followed by the power, in parentheses, at the precise predicted period). Only peaks reaching power 4 or above are included.

The entry Pk/Per, the ratio of the observed to predicted period, is a measure of the quality of a period fit. If observations fit a Lehto-Tifft pattern perfectly the ratio will be unity. Since the ratio between successive periods is a factor of 1.08, if fits were random the peak/period ratio should scatter essentially uniformly between 0.96 and 1.04. The numbers stay very close to unity however, indicating the periods fit the predictions very precisely. The table illustrates another important property of the periods. Power varies as the profile width range (W) is adjusted. Power switches between harmonics (compare changes at 73.2 and 36.6) but the period tracks the predicted period very consistently. Changing the sample does not provide a method to 'tune' the period as would be the case if periods were spurious noise unrelated to W. The 49.8 km/s period also appears in non-overlapping independent subsamples with W greater and less than 100 km/s. One can also see certain T values, notably T=0, are preferred. Random noise would show no T preference.

### 3.3.2 Statistical Methods

I should inject here some background concerning power spectra and related techniques for evaluating fits. In the form used, the probability (p) of finding a given power (x) by accident at a specifically predicted period (P) in a power spectrum is given by

$$p(P) = e^{-x}.$$

The mean power is unity over the redshift range involved. A power peak of 4 has a probability of 0.02 of being accidental. Only about one peak in 50 should reach above power 4, and higher peaks become very rapidly unlikely by accident. For standard error distributions the point where the likelihood drops below 0.05 (1 chance in 20) is commonly used to define where things begin to be 'interesting'. Deviations beyond this point are greater than twice the expected root-mean-square scatter (the dispersion) in a data set. Such deviations are said to exceed 2 sigma. Points in the 3-5 sigma range are exceedingly unlikely by accident.

The number of independent periods in a spectrum depends upon the redshift and period range involved. Figure 3.2 has fewer than 50 independent periods (degrees of freedom), and if random would not be likely to have more than one peak of 4 or above anywhere in the range. Peaks become broader for long periods since fewer periods fit within the redshift range of a sample; a small change in P has only a small effect on the phase distribution.

An alternative way to evaluate fits, which is independent of peak power, is to compare how peaks above some cutoff power concentrate close to the predicted periods. If you specify narrow bins around predicted periods the random likelihood of hitting predicted bins by accident depends on the relative space inside and outside the bins. One can compare the number of 'hits' and 'misses' using binomial statistics much as one would calculate the likelihood of flipping a coin N times and getting M heads. Another common test, Student's t test, uses the mean and dispersion in two samples to evaluate the likelihood they arise from the same parent distribution.

### 3.3.3 Rest Frames, The Cosmic Background Dipole Association

To demonstrate the association of periodicities with the cosmic background dipole vertex transformations are varied to generate contour maps of power to see where power is maximized. Consistent results for many independent samples indicates the association is real, but Monte Carlo simulations may be required to assess a formal significance. In most of the tests shown in this seminar even one sample match with the CBR dipole vertex by accident was unlikely. The detail nature of the contour diagrams will depend on the period involved, the redshift range, and the distribution of the sample objects on the sky.

The remainder of this seminar will use tests applied to many different samples. The procedure is 1) select a sample, 2) apply a rest frame transformation and cosmological corrections as discussed in the previous seminar, 3) do a power spectrum analysis of the sample data to determine how power is associated with periods, and 4) vary the transformation to examine how power is associated with the cosmic dipole vertex. The Virgo cluster sample provided the initial test demonstrating the importance of the cosmic background rest frame. I will spend a few moments expanding on the relationship of the CBR and galactic center rest frames since the two frames must in some way be linked. We should understand that relationship to interpret how local quantization connects to large scale cosmology.

The left frame of figure 3.4 [125] illustrates the distribution of power in the vicinity of the CBR dipole vertex for the 36.6 km/s period in the $70 < W < 110$ km/s Virgo cluster sample. The rectangular box near peak power is the COBE dipole vertex error box. The x symbol

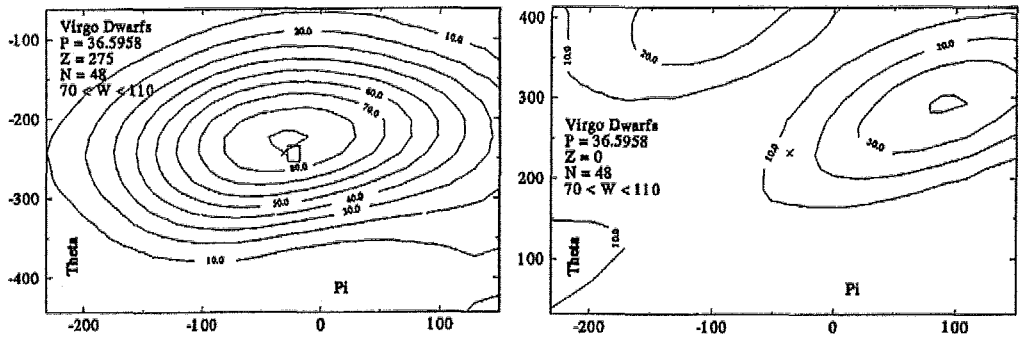


Figure 3.4: LEFT: Power distribution at the 36.6 km/s period, for Virgo cluster dwarfs, as the Theta and Pi transformation constants are varied around the CBR dipole vertex. The peak associates closely with the COBE CBR dipole vertex error box. An x marks the optimum quantization vertex adopted [125]. RIGHT: Power distribution at the 36.6 km/s period, for the same Virgo sample, as the transformation constants are varied around the galactic center transformation. An x now marks the optimum galactocentric vertex found for local galaxies [125].

is our optimum vertex over many samples. The Virgo power distribution is relatively broad since the Virgo galaxies are concentrated in one part of the sky, but there is very little doubt about the association. We will see many more examples of this association. The right frame of figure 3.4 [125] shows the same Virgo sample referred to the galactic center. The

x symbol now marks the vertex for strong quantization in local galaxies discussed in the second seminar.

There is no 36.6 km/s periodicity in the Virgo data associated with the galactic center. The 36.6 km/s period is especially significant since both Tifft-Cocke [87] and Guthrie-Napier [AF] found strong local galaxy quantization near this period in the galactic center frame. From the CBR rest frame local and external samples are consistent. The CBR rest frame provides a fundamental link, which much of the remainder of this seminar will demonstrate. The galactic center works for *local* galaxy distributions. To provide a closer look at the change as one goes from local to remote galaxies it is instructive to look more specifically at the Tifft-Cocke and Guthrie-Napier studies in the galactic center rest frame.

The original galactocentric global study by Guthrie and Napier [AF] involved about 100 local dwarf spirals with redshifts below about 1000 km/s. Guthrie and Napier, (GN), made one important change in how galaxies were sampled, they took only objects classified as spirals and omitted the more extreme irregulars. This fortuitous choice no doubt contributed to their success in finding a strong periodicity since our earlier work using profile width alone does not make this distinction. The GN sample is in fact quite homogeneous but includes only dwarfish spirals and is not representative of spirals in general. The left frame of figure 3.5 [125] shows the phase-profile width diagram for the GN sample using our galactocentric transformation and predicted 36.6 km/s period. The t notation designates morphology, t increases from early to late spiral types.

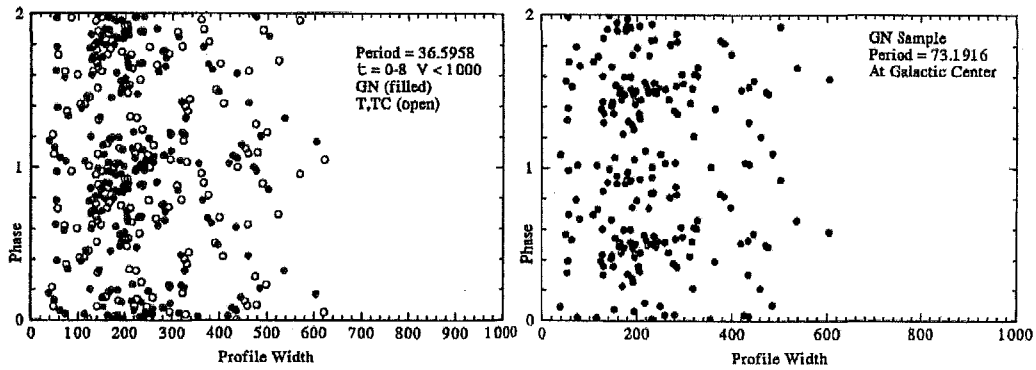


Figure 3.5: LEFT: Phase-profile width diagram of local ($V < 1000$ km/s) spirals (t=0 to 8) in the galactocentric rest frame. The original Guthrie-Napier sample [AF] is distinguished. A rather complex 36.6 km/s periodicity is present. [125]. RIGHT: Phase-profile width diagram of the same Guthrie-Napier sample plotted using the 72.2 km/s period to show longer period modulation and phase drift as a function of profile width [125].

Additional equivalent points from Tifft or Tifft-Cocke data are included in the left frame. The periodicity is apparent but arises virtually entirely from galaxies in a narrow profile width range between 100 and 300 km/s. The right frame of figure 3.5 shows the GN sample alone at the 73.2 km/s period where a modulation between successive 36.6 km/s periods is apparent [125]. As noted in the previous seminar virtually all the longer periods are now

believed to be modulations of higher harmonic frequencies, which may show phase drifts as a function of time and/or depend on specific properties of the parent galaxies.

To obtain a significant sample of earlier type and less dwarfish spirals one must go to higher redshift. Figure 3.6 [125] is a phase-profile width diagram for all Sbc and Sc galaxies in the Tifft-Cocke studies. The transformation and period are the same as used for the left frame of figure 3.5.

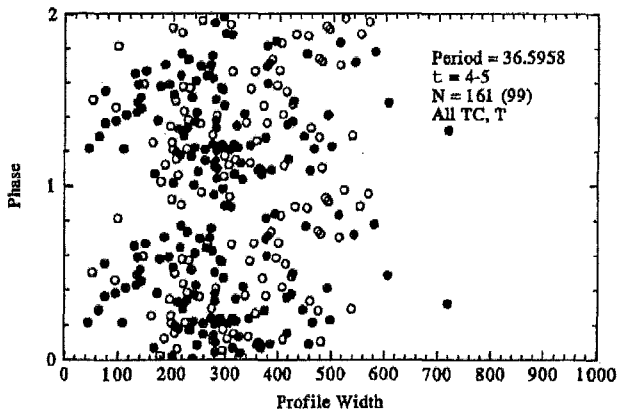


Figure 3.6: Phase-profile width diagram for spirals of type Sbc (open circles) and Sc (filled circles), from the Tifft-Cocke survey, at the 36.6 km/s period in the galactocentric rest frame [125]. The periodic pattern changes character sharply near W=200 km/s, and differs from lower redshift dwarf spirals shown in the left frame of figure 3.5.

The Sbc/Sc set of galaxies is again periodic in redshift but appears to contain two components. Both are distinct from the GN dwarfs with the component near phase 0.1 appearing as a sloping continuation of the GN sample toward greater profile width. Without distinctions by morphology and profile width the periodicities would be virtually undetectable. There are clear complex phase drifts and phase shifts due to redshift variability (2.6.3) and as selection parameters are varied in the galactic center rest frame. There is very little doubt that local galaxies have specific phase relationships to our galaxy. Such familial connections permit the detection of quantization locally but fade as redshift increases. A more detailed discussion of comparisons in the galactic center rest frame is published in reference [125].

The dual framework of quantization was what ultimately led to QTC. In retrospect it is not difficult to understand why there is both local and global quantization. For consistency on *all* scales one must turn to the CBR rest frame. From that fundamental cosmic frame quantization is synchronized, periods align precisely with predictions as seen in figure 3.2. In the galactic frame the picture is blurred with phase shifts as discussed in the previous paragraphs. Periodicities are present but distorted as in figure 3.1. From the quantization viewpoint the cosmological principle, that the universe is equivalent from all viewpoints, is clearly violated. Quantization appears to be consistent and uniform from one singular viewpoint. Locally, in structures that develop within the global framework, it is possible to

Redshift Periods $P = c2^{-\frac{2D+T}{9}}$

| $D\backslash T$ | 8 | 7 | 6 | 5 | 4 | 3 | 2 | 1 | 0 |
|---|---|---|---|---|---|---|---|---|---|
| 17 | 1.2352 | 1.3341 | 1.4408 | 1.5562 | 1.6808 | 1.8154 | 1.9607 | 2.1177 | 2.2872 |
| 16 | 2.4704 | 2.6681 | 2.8817 | 3.1125 | 3.3616 | 3.6308 | 3.9214 | 4.2354 | 4.5745 |
| 15 | 4.9407 | 5.3363 | 5.7635 | 6.2249 | 6.7233 | 7.2615 | 7.8429 | 8.4708 | 9.1490 |
| 14 | 9.8814 | 10.6725 | 11.5270 | 12.4498 | 13.4465 | 14.5231 | 15.6858 | 16.9416 | 18.2979 |
| 13 | 19.7628 | 21.3450 | 23.0539 | 24.8996 | 26.8931 | 29.0461 | 31.3715 | 33.8831 | 36.5958 |
| 12 | 39.5257 | 42.6901 | 46.1078 | 49.7992 | 53.7861 | 58.0922 | 62.7431 | 67.7663 | 73.1916 |
| 11 | 79.0513 | 85.3802 | 92.2157 | 99.5984 | 107.5723 | 116.1845 | 125.4862 | 135.5325 | 146.3833 |
| 10 | 158.1026 | 170.7603 | 184.4313 | 199.1969 | 215.1445 | 232.3689 | 250.9723 | 271.0651 | 292.7665 |

Figure 3.7: Table of periods predicted by the Lehto-Tifft model, in the D (doubling) range 10 to 17, for the nine different T families [125].

Selected Redshift Periods $P = c2^{-\frac{2D+T}{9}}$

| $D\backslash T$ | 7 | 6 | 5 | 1 | 0 |
|---|---|---|---|---|---|
| 17 | ... | ... | ... | ... | 2.2872 |
| 16 | 2.6681 | 2.8817 | ... | ... | 4.5745 |
| 15 | 5.3363 | 5.7635 | ... | ... | 9.1490 |
| 14 | 10.6725 | 11.5270 | ... | 16.9416 | 18.2979 |
| 13 | ... | ... | ... | 33.8831 | 36.5958 |
| 12 | ... | 46.1078 | 49.7992 | ... | 73.1916 |
| 11 | ... | 92.2157 | 99.5984 | ... | 146.3833 |
| 10 | ... | 184.4313 | ... | ... | ... |

Figure 3.8: Table of periods predicted by the Lehto-Tifft model which commonly occur. There are concentrations near T=0 periods, short and long T=6 values, and in T=7 [129,131]. Other periods are less common.

**4 Classes of Galaxies**

Intermediate Spirals – mostly Sc – Intermed W
T = 0 dominant, P=36,6, 18.3, 9.15 – T = 1 Shifts

Wide Profile Spirals – P=5.76 seems fundamental
T = 6 dominant, T = 0, 3 also present

Ordinary Dwarfs – t = 9,10 – 75 < W < 250
T = 6 dominant, P=46.1, 92.2 – T = 5 Association

Extreme Dwarfs – t = 9,10 – W < 75
T = 7 dominant, P=10.67, 5.33 – T = 6 Shift:

Significance testing assumes all T equally likely
T = 2,4,8 very weak, but detected occasionally

Figure 3.9: Summary of the association between galaxy morphology and the four groups of Lehto-Tifft periodicities observed to commonly occur [129,131].

recognize quantization within individual structures, especially differentially. To systematically investigate quantization we must turn to the cosmic rest frame.

## 3.4 Exploring the Cosmic Rest Frame

Armed with the background developed in investigations prior to mid 1993, detailed studies were carried out to examine properties of the redshift and evaluate significance of quantization using the Lehto-Tifft model. Following Virgo cluster work we examined two classes of data. There were precise redshifts for many local galaxies from our Greenbank work. This work provided precision comparison between new and old redshifts needed to address variability, and included information on profile asymmetry. To supplement local data, we utilized studies from Arecibo involving deep samples in the Perseus and Cancer supercluster regions. Important parts of the newer studies have been published in the 1996 and 1997 ApJ [125,138]. Reviews can be found in the proceedings of our 1996 time conference [129], and in the *Journal of Astrophysics and Astronomy* (India) [135]. I will develop evidence and use examples from those studies in the balance of this seminar.

At this stage there was no doubt in my mind that the redshift was a quantum effect, and the underlying cosmology had to incorporate some form of quantum decay through time. Dynamics played no detectable role beyond the interior of galaxies. For the benefit of readers who might like to review specific concepts discussed in earlier seminars as further studies and the development of QTC proceeds, a 'Topical Index' contained in seminar 5 (5.1.1) on page 174 provides a guide to the location of several key subjects and concepts. Many of the topics provide clear evidence of the inescapable reality and significance of QTC.

### 3.4.1 Sorting Through Lehto-Tifft Redshift Periodicity Structure

The Lehto-Tifft period structure is generated by classical period doubling, a process well known in standard physics. The formulation provides for many possible periods. The table in figure 3.7 contains predicted periods in the D=10 to 17 doubling range for the nine ninth-root T sets of predicted periods. If agreements were purely by accident there should be no preferred T or D values. In fact the observed T values are *not* random, certain values are strongly preferred. Periods divide into 4 major groups shown in figure 3.8. Periods in the T=0 family are present in nearly all samples. The T=0 family is the pure powers of 2 family containing the original 73 and 36 km/s periods. The T=6 group is also strong and appears to contain a long and short period substructure. Most remaining periods are related to T=0 or T=6 by a shift of 1, to T=1, T=5, or T=7. These periods occur moderately often with the T=7 group in particular standing out as a distinct subgroup. On the other hand, power is rarely seen in the T=2, 4 or 8 families. There are non-random specific associations with particular T values. The T=0 and 6 families also dominate fundamental particle models as we will see in the next seminar. T=0 associates with the proton, T=6 with the electron [130]. As a general rule cube-root sequences (T=0,3,6 or L=0,1,2 in 3d) dominate over ninth-root patterns and among the roots T=3 is the least likely to occur.

Given preferred sets of periods it was soon apparent the sets associated with different types of galaxies [129,135]. Figure 3.9 summarizes association between galaxy morphology and the family of periodicities involved.

### 3.4.2 Morphology and T, Intermediate Spirals, T=0

Each galaxy type appears to have a characteristic quantization pattern much as each atom has a characteristic spectrum. Intermediate spirals, primarily Sc or later, are prominent in the T=0 family with some overlap into T=1. Wide profile spirals, like our galaxy, associate preferentially with short T=6 periods while ordinary moderately narrow profile dwarf galaxies with deVaucouleurs morphological types t=9 or 10 appear to fit into the longer period T=6 pattern. This includes the 49.8 km/s T=5 period associated with Virgo dwarfs. Finally, extreme dwarf galaxies involve short T=7 periods. This class is where the 2.67 km/s T=7 period was discovered before the Lehto-Tifft rule was formulated. Association of morphology with specific periodicity families is not expected in a random process.

To bring out morphological associations with periodicity families, and show consistency between independent samples, some examples will be provided. Figure 3.10 involves local spirals with 21 cm profiles 100 to 300 km/s wide, typical of Sc galaxies.

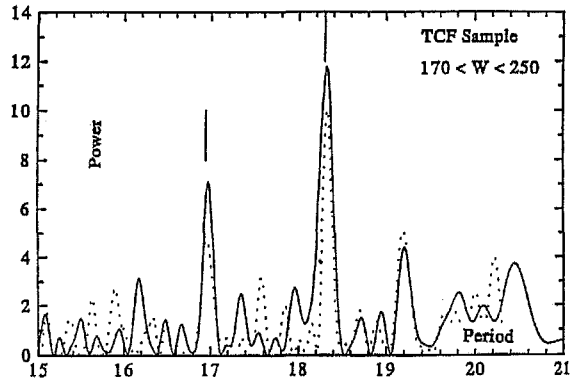


Figure 3.10: Power spectrum of local galaxies with profile widths near 200 km/s [125]. The TCF sample includes all galaxies with redshifts in common between Tifft-Cocke and Fisher-Tully. The solid line refers to galaxies with symmetric profiles, the dotted line to all forms. Vertical lines designate predicted periods; the T=0 family dominates at the 18.3 km/s period and T=1 appears near 17 km/s.

T=0 periods of 36.6, 18.3 and 9.15 km/s, are seen consistently in all studies, including work with local galaxies, Virgo cluster objects, and Cancer and Perseus data [125,129,135]. Periods are consistently matched precisely. The power spectrum in figure 3.10 shows the 18.3 km/s period in local galaxies where it is present with very high power [125]. The probability $p = e^{-12}$ is a very small number; the likelihood of getting a power peak of 12 at that specific period is extremely unlikely by accident. When T=0 periods are present associated power at T=1 may be seen. This is shown in figure 3.10 where not just some other arbitrary period appears.

Figure 3.11 shows similar data from the Cancer region. The T=0 P=36.6 km/s period is strong. The dashed spectrum applies to galaxies with $90 < W < 190$ km/s, in the intermediate W range. The solid line includes all galaxies with $V < 2000$ km/s to incorporate

all galaxies within the local supercluster. A table, shown later, shows how the T=0 family of periods pervades all the regions studied.

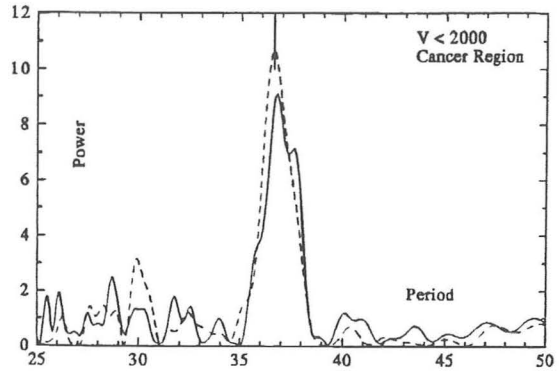


Figure 3.11: Power spectrum for galaxies, in the Cancer region, with redshift less than 2000 km/s. The dashed spectrum includes galaxies with profile widths near 200 km/s, the solid spectrum refers to all galaxies. A vertical line designates a predicted T=0 P=36.6 km/s period.

### 3.4.3 Spirals with Wide Profiles, T=6

Wide profile giant galaxies tend to show short periods in the T=6 family [129,135]. Figure 3.12 is a phase-deviation diagram for local galaxies with profiles wider than 200 km/s.

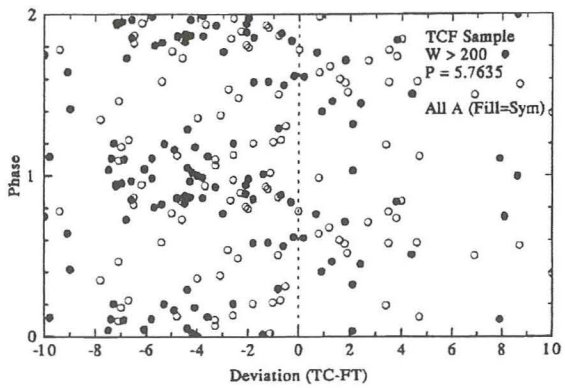


Figure 3.12: Phase-deviation diagram of local galaxies with profile widths in excess of 200 km/s [125]. The TCF sample includes galaxies in common between Fisher-Tully and Tifft-Cocke. Filled symbols show galaxies with the most symmetric profiles. The T=6 P=5.76 km/s period associates with wide profile spirals.

A periodic shifted pattern associated with variability concepts is present. Figure 3.13 shows the extraordinary periodic property of the negative wing in the deviation pattern [125].

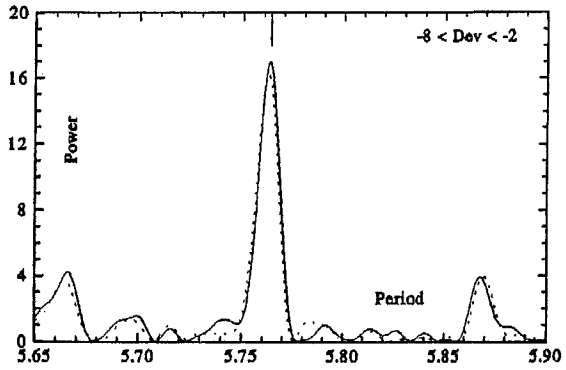


Figure 3.13: Power spectrum of the negative wing in the phase- deviation pattern for wide profile spirals in figure 3.12 [125]. The predicted T=6 P=5.76 km/s period is shown with a vertical line. The spectrum is independent of how profile asymmetry is sampled.

The power spectrum peaks at 17 precisely at the predicted period of 5.7635 km/s. To illustrate the quality of the period fit the next permitted periods are nearly twice the width of the figure away on either side of the main peak. As with T=0 periodicities T=6 periods are seen in the Cancer and Perseus regions as well. Figure 3.14 shows wide profile data in the Cancer region where the 2.88 km/s period is apparent.

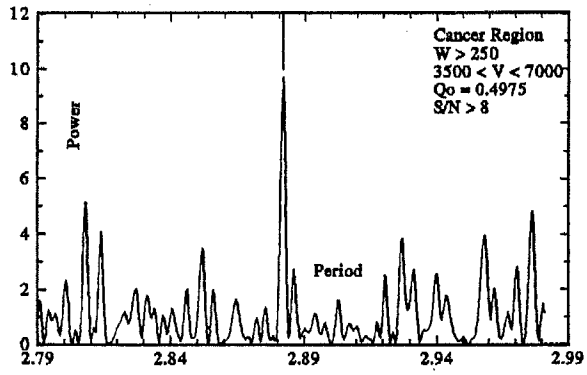


Figure 3.14: Power spectrum of redshifts of Cancer region galaxies with wide profiles and other properties as indicated. The predicted T=6 P=2.88 km/s period is shown with a vertical line. The period match occurs for a value of $q_o$ indistinguishable from 0.5.

Such short periods are particularly important for evaluating non-linearity corrections in redshift intervals as a function of redshift. Corrections are small for local galaxies but large for more distant objects. As I will show later, corrections assuming $q_o = 1/2$ appear to bring periods exactly into agreement with predicted values. My objective here however is to show how similar objects in independent samples have the same period family associations.

### 3.4.4 Extreme Dwarfs with Narrow Profiles, T=7

A third example, in figure 3.15, shows a phase-deviation diagram for local extreme dwarf galaxies ($W < 75$ km/s) where T=7 periods dominate (and were discovered) [129,135].

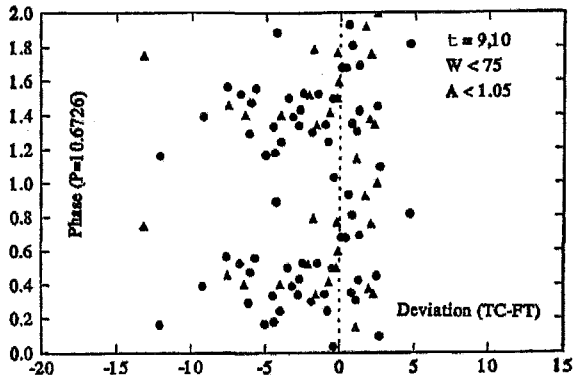


Figure 3.15: Phase-deviation diagram of local galaxies with the narrowest 21 cm profiles, $W < 75$ km/s [129]. Deviations compare Fisher-Tully and Tifft-Cocke redshifts. Triangles identify galaxies with the most symmetric profiles; positively asymmetric profiles are omitted. The T=7 periods associate with extreme dwarfs.

The effect of asymmetry restrictions in this diagram will be shown later. Figure 3.16 is the power spectrum of the negative deviation wing in figure 3.15 showing the match to the 10.67 harmonic in the T=7 series.

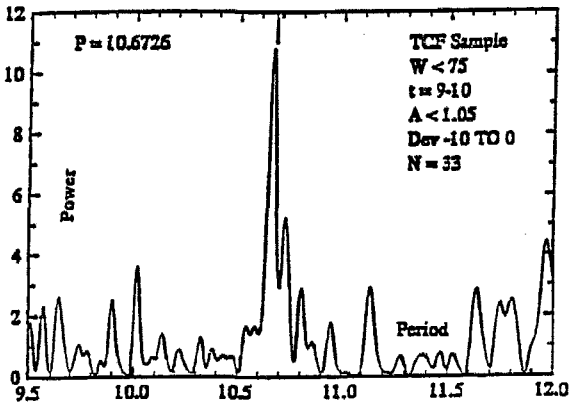


Figure 3.16: Power spectrum of the negative wing in the phase- deviation pattern for the narrow profile dwarfs in figure 3.15 [129]. The predicted T=7 P=10.67 km/s period is shown using a vertical line.

Morphology associates with Lehto-Tifft periodicity families and periods match very precisely. It is incredibly unlikely such associations and fits could occur accidentally.

The above results are taken from my 1996 and 1997 papers [125,129,135,138]. It is interesting to note the ApJ paper [125] was submitted in August 1993 and not accepted until 1996 (in a fourth revision), 3 years later. It is incredibly difficult to publish new concepts, which contradict older beliefs, regardless of the weight of evidence. To illustrate the weight of the T=0 data alone, figure 3.17 shows the T=0 part of the more than 50 periodicity examples given in the ApJ paper [125].

Summary of $T = 0$ Periodiciities

| Period km s$^{-1}$ | $P(D,T)$ | Source | Peak km s$^{-1}$ | Power | Pk/Per | N | $V$ km s$^{-1}$ | $W$ km s$^{-1}$ | $F/W$ |
|---|---|---|---|---|---|---|---|---|---|
| 73.1916 | $P(12,0)$ | Vi | 73.222 | 5.6 | 1.0004 | 54 | −500- 3500 | 50- 90 | all |
| 36.5958 | $P(13,0)$ | Vi | 36.460 | 10.6 | 0.9963 | 48 | 500- 3500 | 70-110 | all |
| | | Pe | 36.5615 | 4.4 | 0.9990 | 53 | 4500-17500 | >400 | <.010 |
| | | Pe | 36.6313 | 9.9 | 1.0010 | 31 | 0-20000 | 225-250 | S/N>4 |
| | | Pe | 36.6757 | 4.8 | 1.0022 | 89 | 2300- 8000 | 50-250 | S/N>4 |
| | | Cn | 36.7536 | 9.1 | 1.0043 | 58 | 0- 2000 | all | all |
| | | Cn | 36.5892 | 10.7 | 0.9998 | 33 | 0- 2000 | 90-190 | all |
| | | Cn | 36.2560 | 7.8 | 0.9907 | 128 | 3500- 7000 | >250 | S/N>8 |
| | | *TT | 36.5673 | 5.6 | 0.9993 | 75 | −500- 3500 | 0-150 | t =0-8 |
| | | *TT | 36.6086 | 7.3 | 1.0004 | 50 | 1000- 3500 | 0-150 | t =0-8 |
| | | *TT | 36.6852 | 6.9 | 1.0024 | 31 | −500- 3500 | 150-350 | t =4 |
| | | *GN | 37.039 | 9.2 | 1.012 | 106 | −500- 1500 | all | t =0-8 |
| 18.2979 | $P(14,0)$ | Pe | 18.3041 | 7.1 | 1.0003 | 53 | 4500-17500 | >400 | <.010 |
| | | Pe | 18.3011 | 6.9 | 1.0002 | 76 | 0-20000 | 300-400 | S/N>4 |
| | | Pe | 18.3042 | 6.0 | 1.0003 | 179 | 0-20000 | 200-400 | S/N>4 |
| | | Cn | 18.3387 | 6.6 | 1.0022 | 562 | 2000-10000 | all | all |
| | | Cn | 18.3574 | 6.9 | 1.0027 | 184 | 3500- 7000 | >250 | all |
| | | Cn | 18.3402 | 4.6 | 1.0023 | 128 | 3500- 7000 | >250 | S/N>8 |
| | | Cn | 18.3569 | 4.1 | 1.0032 | 30 | 5000-10000 | 0-175 | >.015 |
| | | Cn | 18.2979 | 7.3 | 1.0000 | 31 | 5000-10000 | 275-400 | >.015 |
| | | Cn | 18.2974 | 5.1 | 1.0000 | 71 | 5000-10000 | 170-400 | >.015 |
| | | TCF | 18.3170 | 8.8 | 1.0010 | 249 | −500-10000 | 100-300 | all |
| | | TCF | 18.3320 | 9.7 | 1.0019 | 92 | −500-10000 | 170-250 | all |
| | | TCF | 18.3253 | 12.0 | 1.0015 | 36 | −500-10000 | 170-250 | A<1.1 |
| 9.1490 | $P(15,0)$ | Pe | 9.1496 | 6.3 | 1.0001 | 25 | 4500-17500 | 510-570 | <.010 |
| | | Pe | 9.1447 | 7.5 | 0.9995 | 19 | 4500-17500 | 570-700 | <.010 |
| | | Cn | 9.1525 | 4.4 | 1.0004 | 75 | 2500- 5000 | 125-250 | S/N>10 |
| | | Cn | 9.1501 | 6.7 | 1.0001 | 40 | 5000-10000 | 175-275 | >.015 |
| | | Cn | 9.1501 | 8.3 | 1.0001 | 71 | 5000-10000 | 170-400 | >.015 |
| | | Cn | 9.1509 | 8.4 | 1.0002 | 100 | 5000-10000 | 0-400 | >.015 |
| | | Cn | 9.1474 | 4.3 | 0.9998 | 49 | 0-10000 | >400 | S/N>8 |

Figure 3.17: Table of T=0 periods [125], found in independent samples, to show the consistent appearance, and precise match with predictions, of the T=0 family of Lehto-Tifft periods. Entries with an asterisk refer to the galactic center rest frame, all others are cosmocentric [125]. TCF refers to local galaxies with both Tifft-Cocke and Fisher-Tully redshifts. Vi, Cn and Pe refer to Virgo, Cancer, and Perseus region data from Arecibo.

The abstract of reference [125], the ApJ paper containing the table, follows.

> A formula has been derived, which matches global periodicities. Observed periodicities appear to be contained within a set of integral ninth roots of 2 times the speed of light. Galaxy samples from the Virgo cluster, the Perseus and Cancer supercluster regions, and local space, are examined for periodicities as viewed

from the cosmic background rest frame. Numerous periodicities are present, most of which are coincident with periods given by the ninth-root rule; periodicities associated with previously postulated 72 and 36 km/s periods are especially strong. Some classes of local galaxies are also periodic in a galactocentric rest frame. The strength of specific periods depends upon galaxy type as characterized primarily by the width of the 21 cm profile. Variation of the width range shifts power between harmonics but does not induce new periods. Using a previously predicted dependence of periodicity on z and $q_o$ we confirm $q_o$ is consistent with a value of 1/2.

Entries in the table are similar to entries in the Virgo table in figure 3.3. The Pk/Per ratios track predicted periods precisely, and equivalent results are found in independent regions, locally and Virgo, Cancer and Perseus. The number of galaxies involved is large, with several subsamples containing more than 100 galaxies and one incorporating 562. These are not small numbers. Two examples compare results on either side of $W = 400$ km/s showing continuity across phase discontinuities. There will be further comment about this later. The t in the final column of the table refers to morphology class not redshift family.

### 3.4.5 The Consistency of Cosmic Vertex Transformations

I will now address a different question, how consistently various samples associate with the cosmic background dipole vertex. Figures 3.18 shows two sets of four power contour diagrams relating to the association [135]. The upper figure relates to Virgo or local samples, the lower frame includes samples from the Cancer and Perseus regions.

A box (or portion thereof) in each frame represents the COBE dipole vertex error box and x marks the adopted best vertex from many quantization studies. Contours are scaled by a factor of 10 and are shown for a Z=275 km/s transformation. Z has proven to be very stable, consistent within 1 km/s. The vertex determinations repeat very well, matching COBE closely in Z and theta. The radial transformation term, pi, is consistent with the galactocentric value confirming radial expansion of the galaxy as noted in seminar 2. The consistent displacement of the cosmic vertex from the CBR dipole vertex was initially surprising. The QTC cosmological model described in later seminars will explain why the lateral transformation might be expected to deviate slightly due to an evolutionary fissioning process. Our lookback timeline may not point quite directly at the dipole vertex, which could possibly produce a very small lateral CBR temperature gradient. A comment in the October 2013 *Scientific American* 'Advances' column refers to studies relating to such a gradient.

The upper group in figure 18 repeats the Virgo diagram in frame C from figure 3.4 and shows results from local galaxy studies. The T=7 narrow profile study, shown in figure 3.15, generates the map in frame A, while a comprehensive T=0 study of 249 intermediate profile width galaxies (related to figure 3.10) yields the map in frame B. The wide profile local study shown in figures 3.12 and 3.13 results in the map in frame D. There is a small amount of overlap between the intermediate and wide profile samples; the period transition is not sharply defined by W. Short period studies define the vertex very precisely. Local galaxies are consistently periodic in the CBR rest frame, but one *must* recognize and separate different classes of galaxies.

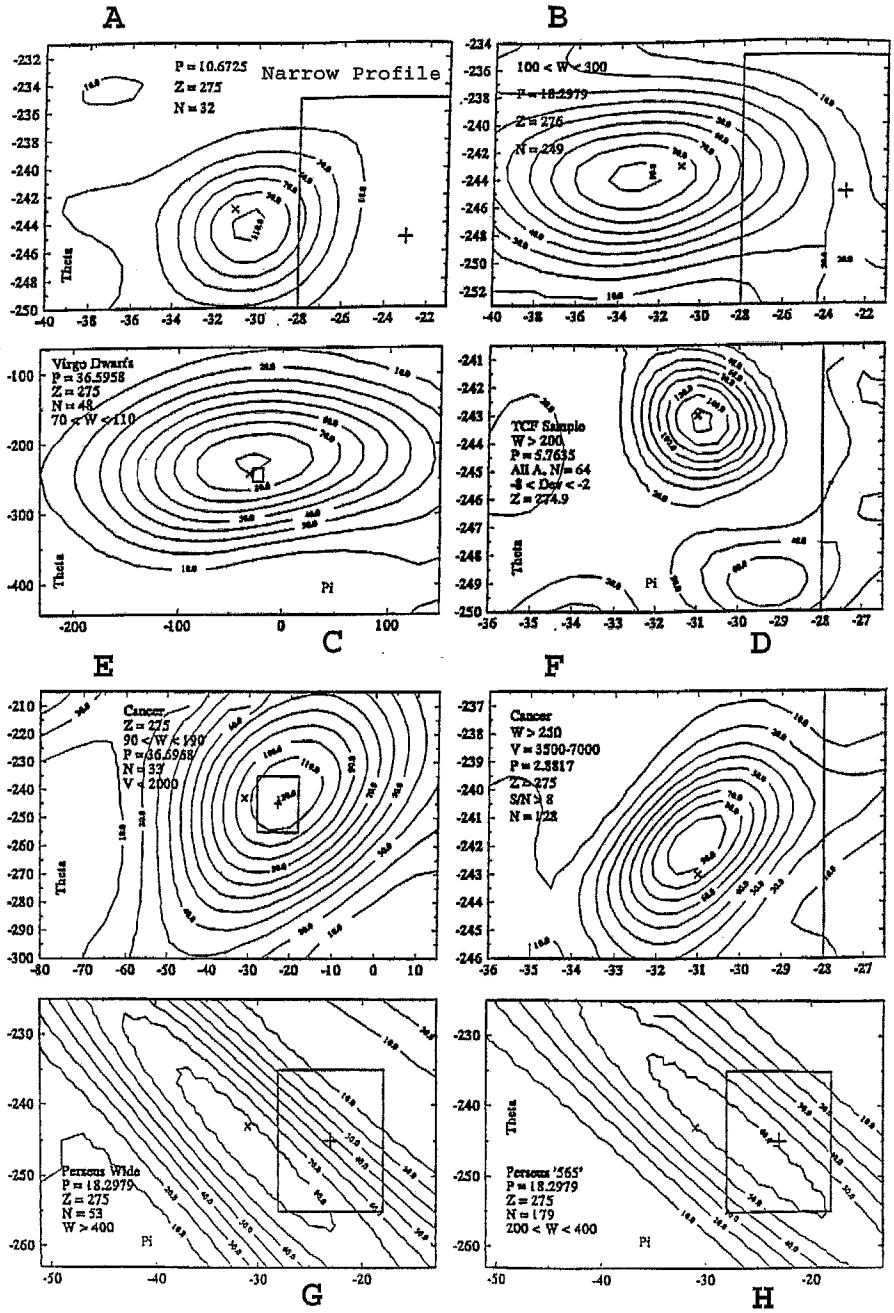


Figure 3.18: UPPER (A-D): Power distribution of local and Virgo cluster samples [135] for transformations related to the CBR dipole vertex. LOWER (E-H): Power distribution of four independent Cancer and Perseus samples [135].

The lower group in figure 3.18 shows the vertex match for samples from the Cancer and Perseus regions. Diagram E corresponds to the Cancer study, shown in figure 3.11, at the 36.6 km/s period for intermediate width galaxies. Diagram F is a map from the independent 128 Cancer galaxy sample of wide profile objects, shown in figure 3.14, plotted for the 2.88 km/s period. Note the very close agreement with the short period study in frame D. The Perseus diagram in frame G relates to the 18.3 km/s period present in wide profile galaxies ($W > 400$ km/s), while frame H utilized 179 independent Perseus galaxies with narrower profiles ($W < 400$ km/s) at the same period. The maps are virtually identical (the elongation is due to the elongated distribution of Perseus galaxies on the sky). These two diagrams sample the same periodicity on opposite sides of a major phase shift, which occurs close to $W = 400$ km/s (as noted earlier in the table in figure 3.17). One distribution concentrates near phase .0, the other near .5, but that boundary is crossed with the same period and vertex. Periodicities and transformations are unaffected by such phase shifts.

### 3.4.6 Phase Relationships

This brings me to the next point where I will look at phase relationships. If observed periodicities were accidental, concentrations should not occur at any particular phase. In fact phase concentrations occur primarily at or near specific cardinal values 'in phase' with the cosmic background. Figures 3.19 illustrates this for intermediate and wide profile local galaxy samples used to generate power spectra in figures 3.10 and 3.13. The right hand frame of figure 3.19 also shows a precursor set of galaxies at phase 0.5 one P=2.88 km/s above and to the right which may at some point transition to extend the phase 0.0 group as the galaxies evolve down in redshift. A potential transition line may be seen extending further on up to the right. This is a good illustration of the QTC variability concept.

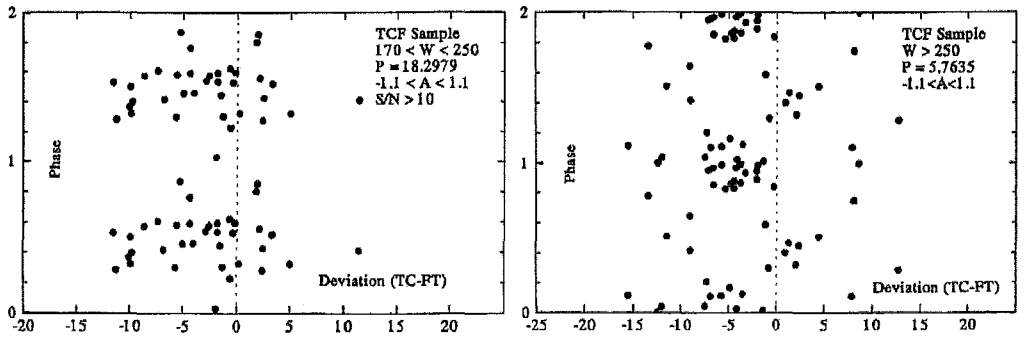


Figure 3.19: LEFT: Phase deviation diagram, for the sample used to generate the spectrum shown in figure 3.10, to show how phase concentrates around simple cardinal phase fractions, near 0.5 here [125]. RIGHT: Phase deviation diagram for a high signal-to-noise sample, related to the spectrum in figure 3.13, to show how phase, in this case, concentrates around cardinal phase fraction 0.0 [125].

As a further illustration of phasing it is instructive to look at samples near critical profile widths, including 200 km/s or 400 km/s, where sudden phase changes occur with no, or simple harmonic, period changes. The left frame of figure 3.20 is a Cancer region phase-profile width diagram, which shows changes between the 18.3 and 9.15 km/s periods [125].

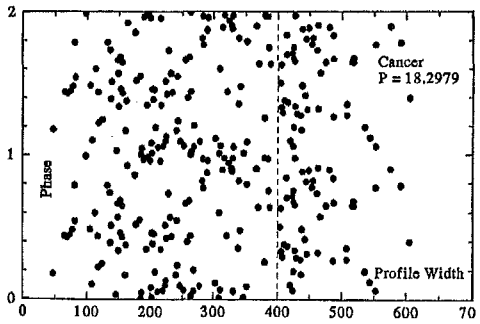


| | W | N | Pk/P | Pow |
|---|---|---|---|---|
| Per(18) | >400 | 53 | 1.0003 | 7.1 |
| | 200-400 | 179 | 1.0003 | 6.0 |
| Cnc(9) | >400 | 49 | 0.9998 | 4.3 |
| | <400 | 100 | 1.0002 | 8.4 |
| Cnc(9) | 175-275 | 40 | 1.0002 | 6.7 |
| (18) | 275-400 | 31 | 1.0000 | 7.3 |

Figure 3.20: LEFT: Phase-profile width diagram for Cancer region galaxies to show how phase concentrates around simple cardinal phase fractions with sudden shifts at critical profile widths near 200 and 400 km/s [125]. The 400 km/s point is shown dashed. Tables in figure 3.17 and the right frame of figure 3.20 define the sample properties. RIGHT: A table of periodicity properties for Perseus and Cancer region samples involving transitions across phase discontinuities copied from the general list in figure 3.17. Periods track across such phase transitions unperturbed or show simple harmonic shifts [135]. The 400 km/s transition point is the same in all samples.

At W=200 km/s the 18.3 km/s period doubles to the 9 km/s periodicity and then back to 18.3 at W=275 km/s. Phase tracks closely around .0 and .5 until another shift occurs at W=400 km/s to phase .25 and .75 at P=9.15 km/s. The Table on the right [135] in figure 3.20 summarizes data at transition points in both Cancer and Perseus regions from the more general table in figure 3.17.

As you cross transition boundaries there are phase shifts between simple cardinal fractional values. For the Perseus region frames G and H in figure 18 show how the transformation vertex is also not significantly affected. Sample sizes are large, and periodicities track across phase changes as though they were not there.

### 3.4.7 What Could Cause the W=N00 Phase Breaks?

Although I will not discuss the subject in detail here, phase shifts which occur at certain critical profile widths are directly related to the quantized substructure of galaxies I introduced in the second seminar. The width of a profile determines what kind of intrinsic redshift 'dipole' can fit within a galaxy. A profile that is narrower than 75 km/s (or somewhat wider to allow for natural internal velocity spread) cannot readily contain a 73 km/s dipole. It is an interesting fact that double peaked profiles appear at about that width [67], while narrower profiles are single peaked. As you approach W=200 km/s you can accommodate a 146.4 km/s dipole, twice the 73.2 T=0 state, along with some natural kinematic width. Except for some early speculation on this point in 1978 [67,68] this subject has not been pursued. One important application involves the coupling of expansion and rotational velocities with the dipole offset. This coupling modifies the 'apparent' rotation and expansion pattern and generates two distinct families of nuclear rotation and velocity dispersion for certain classes

of galaxies. I was unable to publish a paper on this subject [85] relating to motions in elliptical galaxies, although some of the concepts appear in my Venice symposium paper [94]. The paper, which exists as Steward Preprint 513, is reproduced as supplement [Ap1] of this book. The study provides a powerful demonstration of the reality of nuclear dipoles and is discussed in seminar 7 in that context. Such dipole structural changes with profile width appear to be clearly related to galaxy morphological changes. Failure to recognize the dipole offset has dramatic effects if modeled dynamically, including the dual family patterns, apparent warps and counter rotation.

## 3.5 A Little Cosmology, $q_o$ and the Cosmic Correction

It is useful here to introduce some basic cosmology and terminology. There are three dynamical geometries in Newtonian cosmology depending upon the net energy (kinetic + potential) within the system. If the net energy is negative the system is 'closed' and can expand only so far before falling back, like tossing a ball up which will eventually fall back. If the net energy is positive the system is 'open' and will expand without limit, the motion exceeds the escape velocity. In between if the total energy is exactly zero the system will just manage to expand to infinity but will take an infinite time to do so in what is denoted as a 'flat' system. In any cosmic geometry the flow lines of photons or the surfaces containing them will be curved by the mechanisms that define the geometry, General Relativity or its equivalent in classical cosmology, or the flow of time in QTC for example. 'Curvature' can be defined at a point on a surface as zero, positive or negative by placing a tangent plane at the point. If all lines in the surface passing through a point lie in the tangent plane at the point, the surface has zero curvature at that location. If all lines in the surface through the tangent point deviate to one side of the tangent plane the surface is locally 'positively' curved. If some lines deviate to different sides the local curvature is negative. If positive curvature is uniform at all points on a surface the structure is spherical (and for practical purposes lets stay in three dimensions). Curvature of a surface can be determined by drawing triangles; a triangle drawn on a zero curvature surface (flat plane) has angles that add up to 180 degrees. On a positively curved surface the sum is larger, the sides of the triangle bow out. For a negatively curved surface the sides pinch in and the sum is less than 180 degrees. Our universe is observed to be 'flat' or very close to flat (which could be an extremely large sphere which is locally *very* flat.

There are two media within which a cosmology can be constructed, space and time. In classical cosmology space and energy appear and evolve under the control of the standard known forces. Time is involved as a one dimensional sequencing parameter of events and gravitation is presumed to be in control on the large scale through General Relativity or equivalent theories. Key parameters involved in the classical expanding universe are the mean density of matter and the 'deceleration parameter' $q_o$ which define the flow of spatial evolution. In classical cosmology effects such as dark energy and dark matter also enter so $q_o$ is a function of time. If ordinary gravity was the overall controlling factor, in the scale free notation where mean density is 1.0, $q_o$ would be equal to 0.5. $q_o$ is effectively a measure of curvature caused by whatever actually causes the curvature. Light paths then conform to the curvature of space. Actual deceleration could be anything, including zero if gravity is not involved in producing curvature, but curvature could still exist for some other

reason. In QTC there is curvature, the universe is an expanding sphere of time, but no deceleration is present. Classical cosmology is a continuous dynamical theory which cannot generate observed quantized redshifts or large scale non-dynamical structures. They fall in the domain of QTC, but large scale curvature and its $q_o$ notation are still involved.

Seminar 2 demonstrated that curvature does enters into QTC hence $q_o$ must be known to work within QTC. The cosmological correction in QTC removes period dilation in redshifts caused by curvature in the expanding cosmic geometry involved. Although curvature has a very different explanation it has the same effect on photons. The geometry and evolution of QTC is defined in seminars 6 to 8 after its physical properties have been defined. A preview here is intended to define (and verify) the value of $q_o$ needed to utilize the cosmological correction. There are two expansions in QTC, a radial expansion of time which incorporates quantization and a lateral effect involving curved photon paths between objects within 3-d time which defines the cosmic arena. The cosmological correction compensates for the (continuous) energy loss (slight redshifting) due to curvature in lateral photon flow. Contrary to space, time in QTC has a unique origin, $t = 0 = t_o$. Time may have no physical character, it is an action which I will refer to as decay or aging, but it does have a fixed geometry and origin.

In all respects I have examined, QTC leads to the real perceived universe. To reach that end the QTC interpretation of $t_o$ is that $t_o$ is a 'split in time' and time is *conserved.*

$$t_o = -t \leftarrow 0 \rightarrow +t.$$

The universe has a net zero sum temporarily *at all times.* I will indicate later that $t_o$ can never be reached looking backwards in time. It is and always was or will be nothing, *but its components are real and finite (since they clearly exist).* $t_o$ in QTC appears to be a zero value aggregate of dipoles of time anti-time, which exists in what I define as tau-space. Each component ('instant') of a temporal dipole is displaced in time from zero and the other component, hence finite (and isolated). As QTC has developed the dipole structure has been demonstrated to exist along with its consequences *in both dipole and evolved form.* There is much more evidence to discuss before saying more about the nature of QTC. Various aspects of QTC will be discussed further in seminars 6 to 8. Returning to the definition of $q_o$, given that the components of a temporal dipole are 'instants' of time, QTC presumes there is a reciprocal transformation between time and energy (the reciprocal of time is frequency, which scaled by Planck's constant is energy) QTC presumes that the evolution of the universe could be driven by a decaying oscillation in a reciprocal link between time and energy. There could be two temporal dipole domains evolving in superimposition, a possible oscillation between a continuous spatial form (sigma) and a quantum temporal form (tau). This is possible in QTC because the dipole components are isolated in time. All evidence is consistent with this model. Time anti-time is equivalent to energy anti-energy, both conserved. The expanding universe thus has zero net energy (is cosmologically flat) in an isotropic spherical expansion with zero deceleration. Based on the opening paragraphs of this section it should have $q_o = 0.5$. The immediate task in QTC was to prove $q_o$ actually is 0.5. That is discussed below. No deviation from the value of 0.5 has been detected and by using that value no deviation from linearity in redshift periodicities with lookback time has been detected. I should note that several diagrams comparing QTC predictions with observations contain curves marked with *classical* $q_o$ curves for comparison to point out where QTC falls among them. $q_o$ in QTC is a constant 0.5 for spherical expansion of time.

### 3.5.1 Verification of $q_o = 0.5$

The initial determination of $q_o = 0.5$ in QTC involved the detection of a 24 km/s periodicity in redshift intervals in Lyman Alpha Forest spectra of quasars [102] as noted in seminar 2. This test was based upon the presumption the Lyman Alpha clouds might be equivalent to or predecessors of dwarf galaxies which show the 24 km/s periodicity locally. A more local test using ordinary galaxies involves the use of galaxies with short periods, which are very sensitive to the cosmological correction over wide redshift ranges. The effect stretches or compresses the redshift interval involved and therefore shifts power spectrum peaks slightly. As noted previously the cosmological correction has been derived as a function of $q_o$. As $q_o$ is adjusted, power peaks will slowly shift. As $q_o$ is changed, near the value 0.5, the Pk/Per ratio will vary. The ratio is observed to pass through unity, an exact fit to predicted periods, when $q_o$ passes through 0.5. Figure 3.21 contains a table [125] [129] showing the Pk/Per ratio dependence on $q_o$ in power spectra for three independent samples in the Perseus and Cancer deep redshift studies.

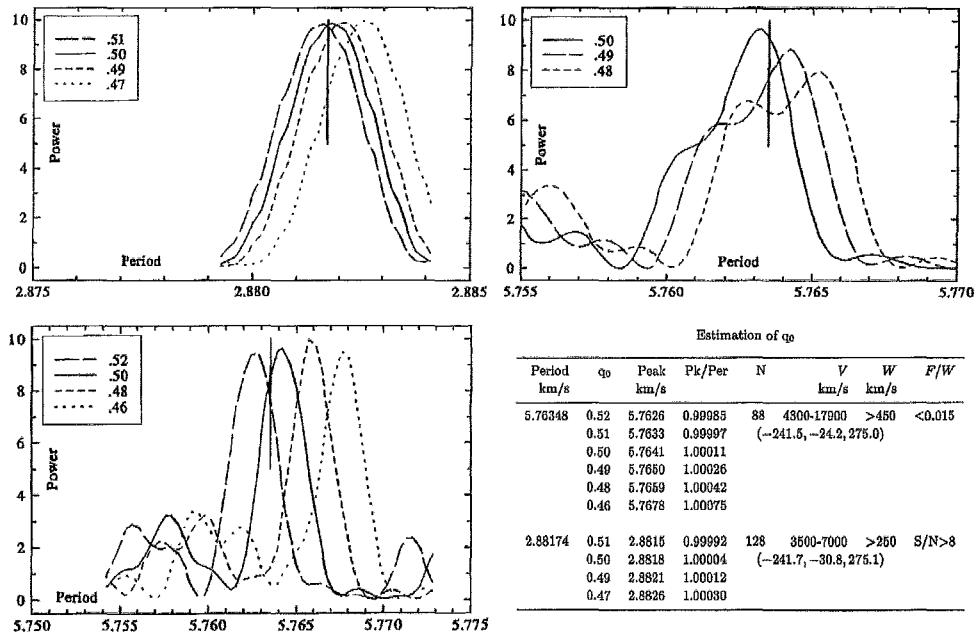


Estimation of $q_0$

| Period km/s | $q_0$ | Peak km/s | Pk/Per | N | V km/s | W km/s | F/W |
|---|---|---|---|---|---|---|---|
| 5.76348 | 0.52 | 5.7626 | 0.99985 | 88 | 4300-17900 | >450 | <0.015 |
| | 0.51 | 5.7633 | 0.99997 | | (−241.5, −24.2, 275.0) | | |
| | 0.50 | 5.7641 | 1.00011 | | | | |
| | 0.49 | 5.7650 | 1.00026 | | | | |
| | 0.48 | 5.7659 | 1.00042 | | | | |
| | 0.46 | 5.7678 | 1.00075 | | | | |
| 2.88174 | 0.51 | 2.8815 | 0.99992 | 128 | 3500-7000 | >250 | S/N>8 |
| | 0.50 | 2.8818 | 1.00004 | | (−241.7, −30.8, 275.1) | | |
| | 0.49 | 2.8821 | 1.00012 | | | | |
| | 0.47 | 2.8826 | 1.00030 | | | | |

Figure 3.21: A table [125] [129] and power spectra [125] show periodicities for three deep samples in Perseus and Cancer regions. They come into close agreement (Pk/Per passes through 1.000) with predicted Lehto-Tifft periods when $q_o$, used to correct for redshift dilation (the cosmological correction), passes through 0.50 [129]. The upper left frame is from Cancer, the others from Perseus. Only the left frames, showing symmetric profiles, are listed in the table.

The value $q_o$=0.5 tunes periods precisely to predicted values within our ability to measure them. $q_o = 1/2$ corresponds to a flat cosmology,which is basically what is observed for the real universe. It is highly unlikely such a match can be accidental.

## 3.6 Uniqueness of the Set of QTC Redshift Periods

A number of relationships concerning phase, T associations and nonlinearity have now been discussed. These relationships are very unlikely to be accidental, nor are the highly significant power levels detected at predicted periods. A few things remain to be demonstrated, beginning with the uniqueness of the period set involved. Are other periods detectable above noise levels or is the Lehto-Tifft set complete? To test for power at unpredicted frequencies we looked for power shifted away from predicted periods. The first test done used Virgo cluster samples. The average power and power dispersion was measured for all allowed periods in a specified range. For Virgo the 25 periods falling between 23 and 126 km/s were involved to cover the range of well known periods consistent with the quality and redshift range available. The period set was scaled by factors ranging from 0.96 to 1.04, in steps of 0.01, to shift periods away from the predicted set and distribute them over the factor of 1.08 interval between predicted values. The average power and power dispersion was then recalculated. Figure 3.22 displays the power pattern, figure 3.23 the power dispersion.

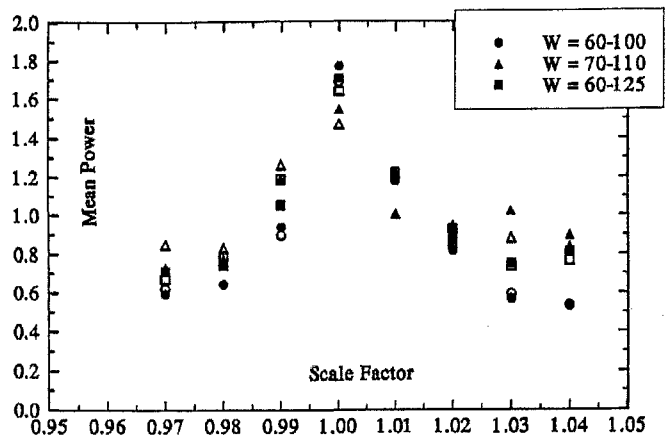


Figure 3.22: Average power over all predicted Lehto-Tifft periods between 23 and 126 km/s in several Virgo cluster samples. Periods are scaled by factors shown on the abscissa to move periods away from the predicted set. Power peaks for the predicted set; there is no evidence for power at other frequencies.

If the predicted period match was just an accident one should see distributed power and scatter regardless of what period set was utilized. In fact power and dispersion peak sharply at the predicted period set, the predicted set uniquely accounts for all the excess power detectable. To formally test significance we can compare the power distribution at and between the predicted set using the Student's t test. Average power at the predicted set is $1.7 \pm 1.75$. In between (shifts $> .02$) it is $0.8 \pm 0.75$. These numbers yield a Student's t of 4.1, or a probability $p = 10^{-4}$ that the two distributions come from the same population. Not only do we have a set of periods that fit the data, we have a unique set. Later I will show a second such test where the signal can be specifically extracted from underlying noise.

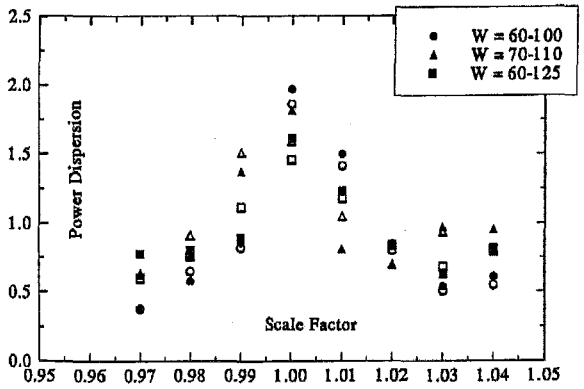


Figure 3.23: Power dispersion for all predicted Lehto-Tifft periods between 23 and 126 km/s in several Virgo cluster samples. Periods are scaled by factors shown on the abscissa to move periods away from the predicted set. Scatter peaks for the predicted set; there is no evidence for signals at other frequencies.

### 3.6.1 Binomial Testing

We can carry the test of how well the predicted periods are fit further by analyzing the peak distribution with binomial statistics. The upper frame of figure 3.24 is a summary diagram of period detections between 20 and 100 km/s in the Virgo cluster region. The abscissa is Pk/Per minus 1; detections which fit periods concentrate around zero. Halfway to the next period is $\pm 0.04$. Detections with power greater than 4, in profile width ranges, are shown with filled symbols; open symbols characterize the 14 'distinct' periodicities seen in the Virgo data. Vertical lines define bins containing 1/8, 1/4 and 1/2 of the range between predicted periods. The curved line marks the separation of independent degrees of freedom (the minimum distinct peak spacing), which is period dependent and set by the redshift range of the sample. Points separated by more than this spacing are independent periods; there may be more than one association with the nearest predicted period, shown on the vertical scale, when this spacing is less than 0.04.

For longer periods, scatter and concentration around predicted values is much less than the spacing of the degrees of freedom. Random noise should spread points uniformly. Quantization does not require absolutely precise fits. Deviations may represent real drifts since periods are apparently modulations of higher harmonics and not strict periodicities. The slight diagonal concentration suggests such modulation is indeed present. The spacing of degrees of freedom sets a lower value for effective detection of periods. A lower limit for periods is required or noise will quickly dominate small signals. Note that non-randomness of detected T values is apparent. Three of the five most deviant detections are weak and in rare T classes; they are quite possibly noise since random noise peaks with no concentration are expected. Only one of the rare T classes is likely to be real. The strongly concentrated peaks include T=0, 1, 5, and 6, confirming the nonuniform T preference. Evaluating the concentration using binomial statistics, 8 of the 14 detections have at least one 'hit' within the central 1/8 of the overall period range. The probability of 8 hits in 14 random trials within 1/8 of the range is 0.00008. A more conservative assessment using mean values (open

circles) is 9 hits in 14 trials within 1/4 of the range, which yields p=0.002. Allowing for modulation trends and T associations a realistic likelihood for accidental clumping is perhaps 0.0005. The table in figure 3.24 summarizes the Virgo study and includes binomial evaluations for samples from the Perseus region.

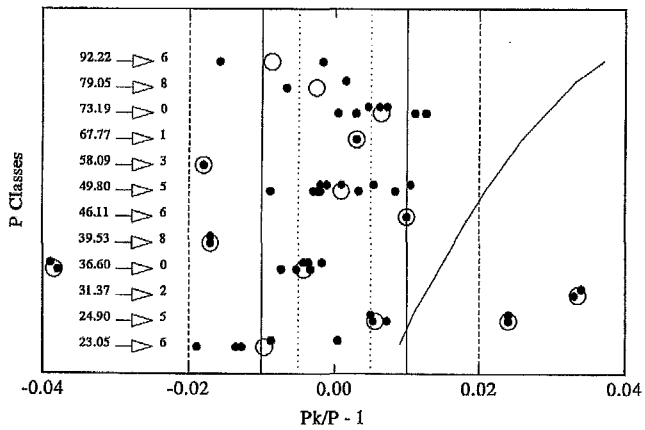


Binomial Tests of the Distribution of Power Peaks

| Sample | N | V km s$^{-1}$ | W km s$^{-1}$ | P km s$^{-1}$ | Fit | Pk>4 | Hit | Prob |
|---|---|---|---|---|---|---|---|---|
| Virgo | 137 | All | All | 20-100 | 1/8 | 14 | 8 | 0.00008 |
| | | | | | 1/4 | 14 | 9 | 0.002 |
| Per(W) | 53 | All | > 400* | 17-250 | 1/10 | 27 | 9 | 0.0009 |
| S/N>4 | F/W<0.01* | | | 36-250 | 1/10 | 10 | 6 | 0.0002 |
| | | | | 17-250 | 1/10 | 18† | 9 | 0.00002 |
| | 28 | All | > 400* | 17-250 | 1/10 | 9 | 4 | 0.008 |
| | F/W>0.01* | | | | | | | |
| Per(565) | 179 | All | 200-400 | 16-250 | 1/5 | 21 | 10 | 0.004 |
| | 79 | All | 300-400 | 16-250 | 1/6 | 18 | 6 | 0.08 |
| | 31 | All | 225-250 | 16-250 | 1/4 | 10 | 7 | 0.004 |
| | 56 | 6-8000 | 50-250 | 10-100 | 1/16 | 8 | 4 | 0.0009 |
| | 34 | 6-8000 | 200-350 | 10-100 | 1/16 | 9 | 3 | 0.02 |

* Predetermined †Corrected for clumping

Figure 3.24: UPPER: The (Pk/Per-1) distribution for samples studied for binomial testing in the Virgo cluster. See the text for details. LOWER: Binomial test table showing concentration of Pk/Per around predicted periods for the Virgo and individual Perseus samples. 'Fit' is the test fraction of the interval between periods. 'Hit' is the number of all periods with $Pk > 4$ within the fit zone.

Binomial testing has the advantage of being independent of power level. The statistical meaning of high power can be questioned since extreme peaks are unstable. The binomial test is independent of interpretation of high power; the number of peaks exceeding a conservative cutoff power near 4, is quite reliable. However, The result is the same yielding consistent results indicating peaks uniquely concentrate around Lehto-Tifft periods. A more extensive detailed discussion of several forms of binomial evaluation is contained in an appendix to reference [138]. In the final analysis there is extremely strong evidence that the redshift is a quantized quantity. The concept, however, continues to be ignored.

## 3.7 Applications of QTC, Phase-Deviation Waves

For the rest of this seminar I have selected some examples of findings when QTC was applied to interesting data sets. The The first example concerns a connection between galaxy morphology, periodicities and redshift variation. Figure 3.25 [138] is a phase-deviation diagram for galaxies with $100 < W < 300$ and morphologies in the t=8 to 10 range.

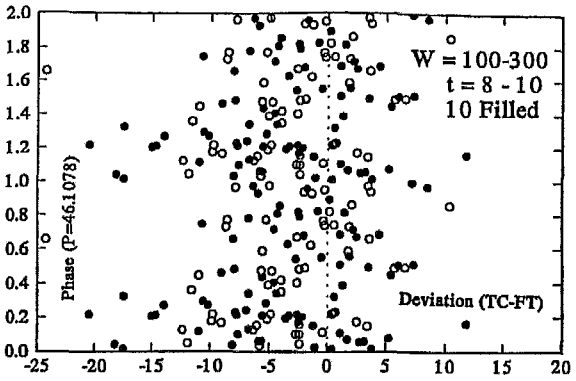


Figure 3.25: A Phase-deviation diagram of local galaxies with $100 < W < 300$ km/s [125] and morphology of t=8 or later; t=10 dwarf irregulars are shown with filled symbols. Without using variability periodicity is easily masked at intermediate widths. Deviations compare Fisher-Tully and Tifft-Cocke redshifts. The amplitude of the deviation wave, at the T=6 P=46.1 km/s period, depends upon morphology as shown in the table in figure 3.26.

The 46.1 km/s T=6 period characterizes ordinary dwarf irregulars in the t=8-10 morphology range. The offset phase wave caused by variability is obvious. The second line in the figure 3.26 table [138] shows, by t test, that the offset between phase intervals 0.0 to 0.5 and 0.5 to 0.0 is significant at the 99.8 percent confidence level.

DEVIATION PATTERNS IN DWARF GALAXIES

| Morphology | $N$ | Mean (0.0–0.5) (km s$^{-1}$) | Mean (0.5–1.0) (km s$^{-1}$) | Dispersion (km s$^{-1}$) | $t$ | $p$ |
|---|---|---|---|---|---|---|
| 10 ..... | 45/29 | $-5.14 \pm 1.07$ | $-0.06 \pm 1.21$ | 7.04/6.28 | 3.12 | 0.005 |
| 8–10 ..... | 90/63 | $-4.57 \pm 0.66$ | $-0.88 \pm 0.68$ | 6.22/5.34 | 3.80 | 0.002 |
| 8–9 ..... | 45/34 | $-4.00 \pm 0.81$ | $-1.59 \pm 0.77$ | 5.29/4.35 | 2.13 | 0.02 |
| 1–8 ..... | 67/64 | $-4.04 \pm 0.65$ | $-2.32 \pm 0.79$ | 5.24/6.25 | 1.70 | 0.05 |
| 1–7 ..... | 44/46 | $-3.44 \pm 0.79$ | $-2.55 \pm 1.03$ | 5.10/6.81 | 0.69 | 0.25 |

Figure 3.26: Table comparing deviation distributions, in half phase intervals of figure 3.25, for local dwarf galaxies. Galaxies with morphology class t=8 or greater show a T=6, P=46.1, association and significant phase dependent deviations. Spirals with t=7 or less show little or no phase dependence for deviations. They associate with T=0 periods rather than T=6.

Figure 3.26 includes a breakdown of offset properties by morphology, including data for

earlier type spirals. The offset is clearly a function of morphology, reaching a maximum for t=10 irregulars, and essentially vanishing for spirals earlier than t=8. The table further shows the numerical division of objects between the two phase intervals is different for irregulars and spirals. Spirals divide evenly and show minimal offset differences. They in fact associate primarily with the T=0 family of periods, which will be examined later. The irregulars show a marked offset and uneven phase distribution associating them with the T=6 family. This confirms the finding by Guthrie and Napier [AF] that spirals and irregulars have different quantum properties, and shows that many factors must be combined to isolate unique subsamples. Periodicity would not be easily recognized in this sample without using variability offsets. Correlations within broad morphological samples are easily masked but highly unlikely to occur by accident.

We can learn a little more about variability from the irregular galaxies. The upper frame in figure 3.27 is a phase-deviation diagram, at the 46.1 km/s period, for t=9 and 10 dwarfs in the profile width range 75-250 km/s.

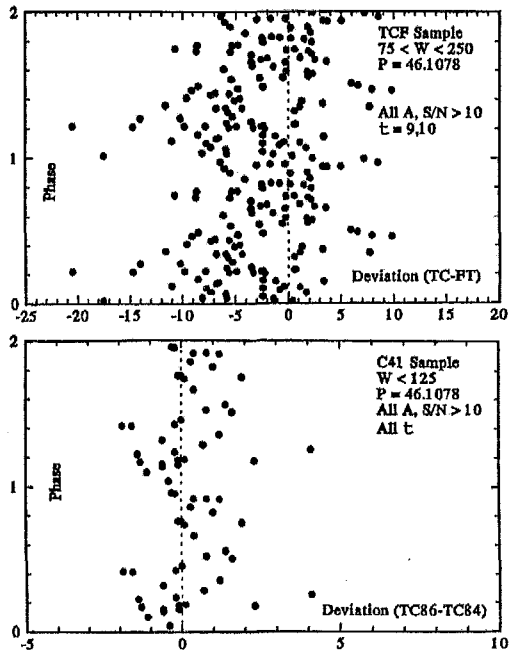


Figure 3.27: UPPER: Phase-deviation diagram for local galaxies with $75 < W < 250$ km/s [129] and morphology of t=9 or later using Fisher-Tully and Tifft-Cocke redshifts, a time base of 10-15 years. The deviation pattern has an amplitude of about 7 km/s. LOWER: Phase-deviation diagram for local galaxies with $W < 125$ km/s [129] comparing Tifft-Cocke redshift between 1984 and 1986. A small amplitude deviation pattern is consistent with the longer time baseline pattern in the upper frame.

The slight shift to narrower profiles in the lower frame increases the percentage of irregulars but still avoids extreme narrow profile dwarfs. The upper diagram compares Fisher-Tully

redshifts from the early 1970s with Tifft-Cocke measures made in the mid 1980s, about 12-13 years later. The lower frame compares data entirely within the Tifft-Cocke study, over a two year span from 1984 to 1986. The same wave is present with a smaller amplitude consistent with the shorter time involved. Evidence for variability does not rest entirely on older data. The slight positive shift at zero could be due to a negative shift by our galaxy! More recent data from the late 1980s into the mid 1990s (based on more limited but precise data from the NRAO 140-foot telescope) is less clear, but see [Ap2]. No other explanation of the older deviation patterns appears possible. Change appears to be rapid between quasi-stable modulations. Many questions relating to variability remain open.

## 3.8 Metallicity and T in Local Dwarfs

As a second example, a recent review paper by Mateo [AI] concerned Local Group dwarf galaxies of all types including dwarf ellipticals (dE) and spheroidals (dSph) as well as dwarf irregulars (dIrr). Mateo notes that for the majority of galaxies the metal content is dependent upon the luminosity of galaxies. However, the dE, dSph, and certain transition classes appear to follow a different luminosity-metallicity relationship than the dIrr types. Mateo then asks "If dIrr and dSph galaxies represent fundamentally different objects, why does a protodwarf galaxy choose one type rather than the other?" He notes that rotation has been suggested, but most of the galaxies show very little rotation. Since good redshift data on these systems is now available I looked for redshift periodicities to check possible T family associations. Figure 3.28 shows phase-morphology diagrams I found. The ordinate

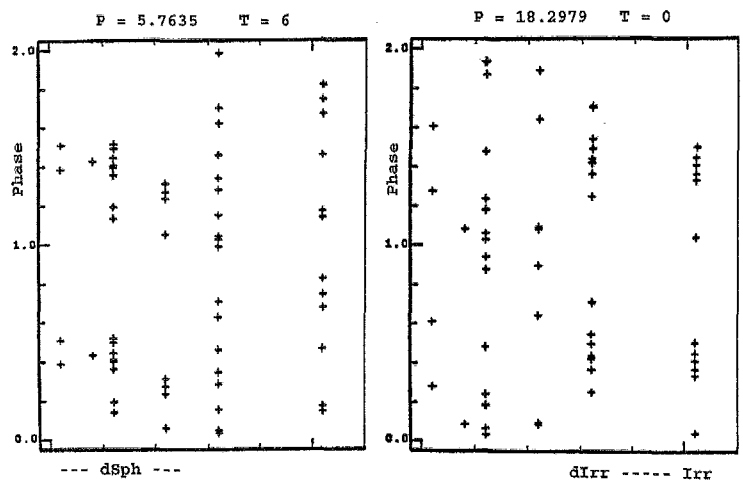


Figure 3.28: Phase patterns for Local Group dwarf galaxies. Dwarf spheroidals (dSph) and dwarf irregulars (dIrr) have different metallicity properties [AI]. The dSph objects appear to be members of the T=6 family while irregulars are T=0 systems. This is previously unpublished work.

in the left frame is T=6 phase at the P=5.76 km/s period and the right frame ordinate is T=0 phase at the P=18.3 km/s period. The first columns in both frames refer to dSph

related objects while the last two main columns contain dIrr and Irr types. The redshifts (referred to the CBR frame) of the dSph galaxies are nicely quantized in the T=6 mode (left frame) with perhaps some weak association with T=0 (right frame). The Irregulars behave differently. The Irregulars are well quantized in the right frame T=0 mode but not at all for T=6 in the left frame. The two classes appear to be in different quantization families. Can properties like metallicity be associated with quantization families? Is there something subtle about the makeup of matter and/or the nature of forces that drive different lines of evolution in different families? Alternatively different families may form galaxies at different times so we see them now at different evolutionary stages. This finding provides an important illustration of the potential for quantization work to provide some exciting new answers in galaxy evolution. Note that, as before, the basic T=0 and T=6 families stand out, and phase concentrations occur at different fractional phase values. Another accident?

## 3.9 A close Look at $W = 200$, Phase Cascades

As a third example I will discuss what seems to be happening in the vicinity of the $W = 200$ km/s 'phase break'. Details of much of the following material appear in the 1997 ApJ [138]. The work touches on morphology, variability, profile asymmetry and interrelationships between T families. The break near $W = 200$ km/s is quite universal. It is easily seen in the Cancer region (refer to figure 3.20), and locally in both the galactic center rest frame (refer to figure 3.6) and the CBR rest frame (refer to figure 2.41 and 2.42 in the second seminar). The existence of the phase break indicates something interesting and important is happening there. It is a good place to look for variability, and represents a transition region between well defined spiral morphology and more nondescript dwarf irregulars. Spirals dominate at greater widths, dwarf irregulars at narrower values, although the transition is fuzzy.

In the intermediate width range we have strong T=0 family dominance. Figure 3.29 duplicates figure 3.19 (left), to show the strong T=0 P=18.3 km/s periodicity present.

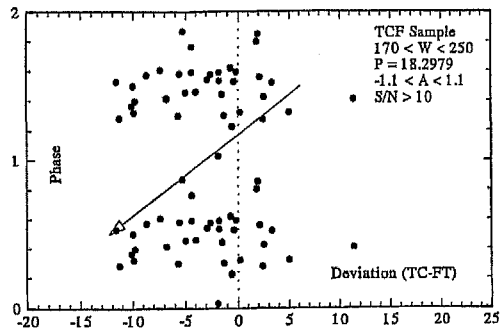


Figure 3.29: Phase-deviation diagram, for local galaxies with $170 < W < 250$ km/s [138], indicating variability associated with the $W = 200$ km/s phase break. Deviations compare Fisher-Tully and Tifft-Cocke redshifts. The T=0 P=18.3 km/s period is dominant in this profile width interval.

The profile width range is offset to the wide side ($170 < W < 250$) km/s to assure spiral

dominance, and the sample is limited to the most symmetric profiles. Figure 3.30 repeats the power spectrum of this sample from figure 3.10.

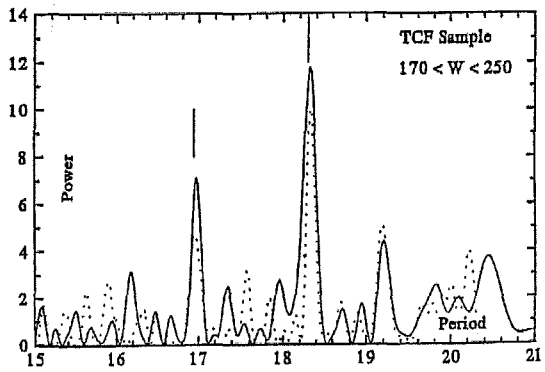


Figure 3.30: Power spectrum of local galaxies with profile widths near 200 km/s [125]. The TCF sample includes all galaxies in common between Fisher-Tully and Tifft-Cocke. The solid line refers to symmetric profile galaxies, the dotted line to all forms. Vertical lines designate predicted periods; the T=0 family dominates at the 18.3 km/s period and T=1 appears near 17 km/s.

The spectrum shows the T=1 family periodicity makes its appearance along with marked evidence for variability. Samples offset toward wider profile width ranges will be referred to as 'spiral dominated'.

Figure 3.31 shows a more general phase-deviation diagram at the T=0 P=18.3 km/s period for all 249 galaxies with $100 < W < 300$ km/s for which Tifft-Cocke minus Fisher-Tully redshift deviations are available.

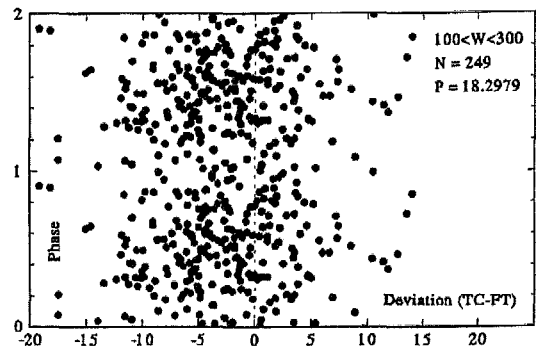


Figure 3.31: Phase-deviation diagram for the 249 local galaxies with $100 < W < 300$ km/s and both Fisher-Tully and Tifft-Cocke redshifts [138]. The T=0 P=18.3 km/s period is dominant in this profile width interval. Phase scatter is due to underlying substructure.

This 'mixed' sample is nicely periodic (power 8-9) in the CBR frame (see the TCF samples

in the figure 3.17 table), but there is considerable phase scatter. The scatter is not due to uncertainties, it arises from intrinsic structure within the diagram and mixed morphology. (I previously showed dwarf irregulars favor a T=6 period for example.) Figure 3.32 shows what happens when the $100 < W < 300$ km/s sample is limited to spirals (t=1 to 8). The diagram shows what appear to be three sloping phase 'cascades'. Figure 3.33 shows t=8,

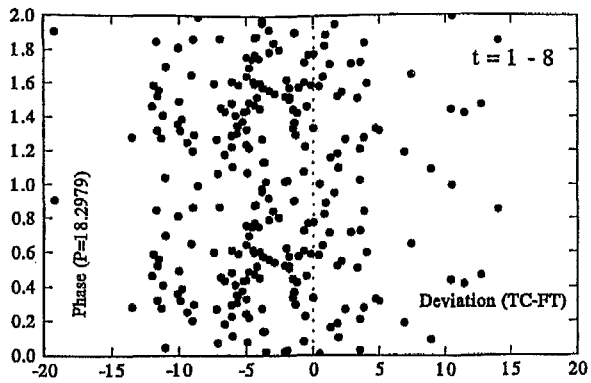


Figure 3.32: Phase-deviation diagram for local spiral galaxies with $100 < W < 300$ km/s and both Fisher-Tully and Tifft- Cocke redshifts. The T=0 P=18.3 km/s period, shown in figure 3.31, contains a 'phase cascade' substructure associated with spiral galaxies [138].

Scd, objects alone. The structure is specifically spiral related, it persists through all spiral types but drops out quickly for t greater than 8. Morphology relates to structure on the deviation axis, but does not affect phase.

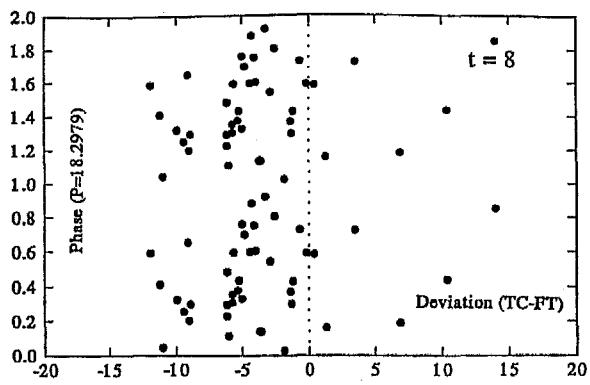


Figure 3.33: Phase-deviation diagram for local t=8 spiral galaxies with $100 < W < 300$ km/s and both Fisher-Tully and Tifft-Cocke redshifts. The phase cascade substructure associated with spiral galaxies in figure 3.32 extends through all spiral types but not into the later type irregulars [138].

### 3.9.1 Enter Asymmetry

It is here asymmetry enters, asymmetry does distinguish by phase. This is shown in figure 3.34 for the spiral dominated side of the intermediate profile range related to the $W = 200$ km/s phase transition.

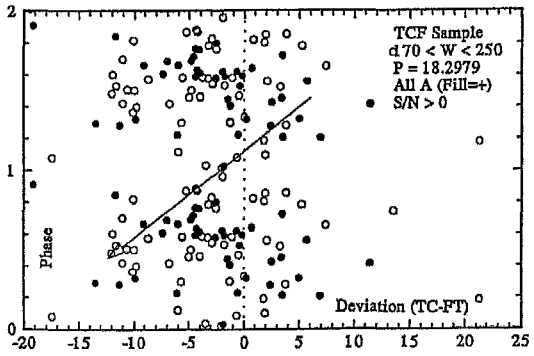


Figure 3.34: Phase-deviation diagram for local galaxies with $170 < W < 250$ km/s and both Fisher-Tully and Tifft-Cocke redshifts. The T=0 P=18.3 km/s period, shown in figure 3.31, contains a higher harmonic pattern characterized by alternating profile asymmetry [138]. Filled symbols for positive asymmetry, open symbols for negative.

The figure shows the 18.3 km/s phase structure is broadened by interleaved asymmetry shifts, and is in fact a modulation of the next doubling period, 9.15 km/s. Figures 3.35 and 3.36 show positive and negative asymmetries separately.

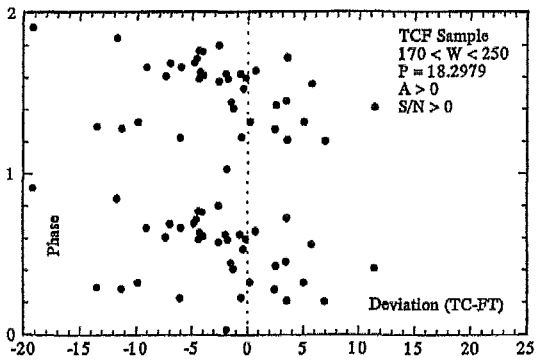


Figure 3.35: Phase-deviation diagram for local galaxies with $170 < W < 250$ km/s and positively asymmetric profiles in figure 3.34. A 9.15 km/s harmonic pattern is apparent within the 18.3 km/s period [138].

Alternating and interleaved offset patterns are apparent at the 9.15 km/s period. The shift between the two patterns, the asymmetry shift, is consistent with half of 9.15 km/s, the 4.57 km/s harmonic.

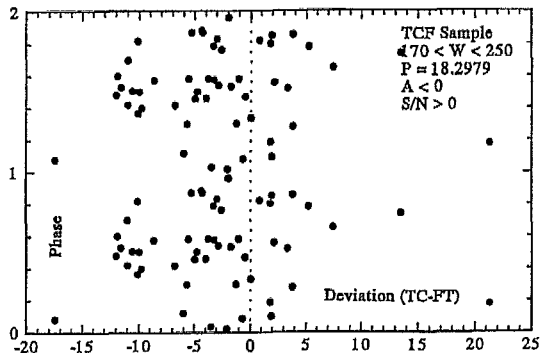


Figure 3.36: Phase-deviation diagram for local galaxies with $170 < W < 250$ km/s and negatively asymmetric profiles in figure 3.34. A 9.15 km/s harmonic pattern is apparent within the 18.3 km/s period with a phase shift from the positive asymmetry pattern in figure 3.35 [138].

Asymmetry appears to relate to phasing of objects between quantization states. Quantized transitions occur in general because distribution functions overlap, and overlap determines transition probabilities. As profile shape varies, the amount of overlap between quantum states changes and affects the timing of decays. It is quite reasonable to expect profile asymmetry to relate to phasing in quantized data.

Phase structure at the 9.15 km/s period is quite sharp for positively asymmetric profiles. Figure 3.37 is a phase-deviation diagram at the 9.15 km/s period for galaxies with $150 < W < 300$ km/s, a slightly augmented spiral dominated sample, with positive asymmetry.

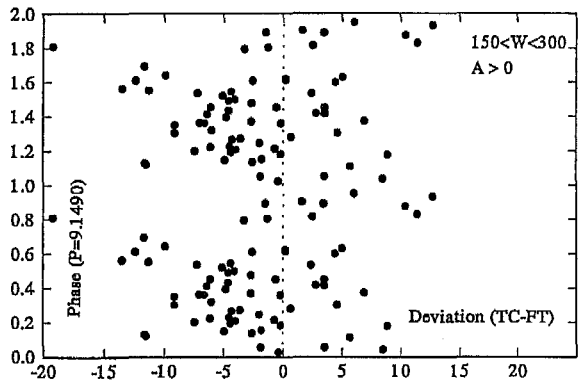


Figure 3.37: Phase-deviation diagram, for a spiral dominated sample of local galaxies with positively asymmetric profiles, to illustrate the stong T=0 P=9.15 km/s periodicity present in the deviation pattern [138].

Figure 3.38 shows how the pattern can be fit with a cascade structure of the type described in figure 2.34 in the second seminar. The power spectrum of redshifts in the negative wing,

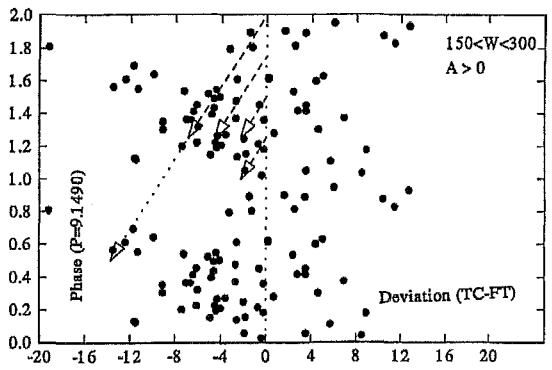


Figure 3.38: Phase-deviation diagram, for a spiral dominated sample of local galaxies with positively asymmetric profiles from figure 3.37, to show how the stong T=0 P=9.15 km/s periodicity present can be represented as a series of phase cascades [138].

between deviations of +1 and −10, exceeds power 9 and maps precisely into the CBR rest frame figure 3.39).

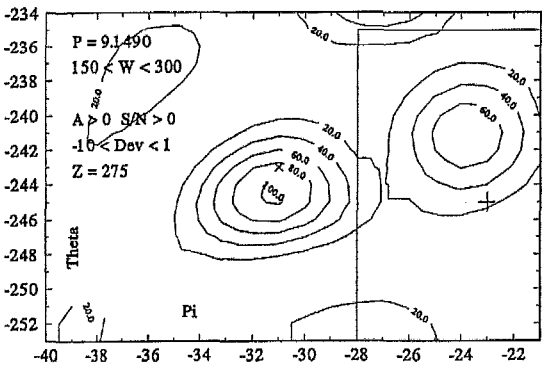


Figure 3.39: Power distribution, for the local spiral dominated . galaxy sample in figure 3.34 [138], for transformations related to the CBR dipole vertex. The edge of the COBE CBR dipole vertex error box is shown; x marks the adopted quantization vertex [125]. Compare with figure 3.18 to verify consistency (this sample is a subset of the upper right panel B).

### 3.9.2 Transition Step Patterns Within Deviations

A careful look at the deviation pattern, expanded in figure 3.40, suggests a finer deviation pattern laterally between cascades. A power spectrum of the deviation pattern shows power greater than 4 at 2.31 km/s, consistent with the expected P=2.2872 associated with D=17 level of the T=0 family. The sample shows evidence for four doublings, 18.3, 9.15, 4.57, and

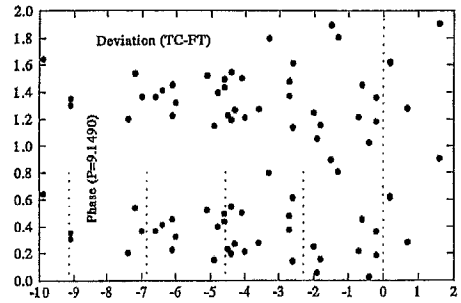


Figure 3.40: Expanded Phase-deviation diagram of the negative wing, in figure 3.37, to show fine structure in deviations at the T=0 P=2.29 km/s period [138]. The period corresponds to lateral spacing of the cascades shown in figure 3.38.

2.29 km/s in the T=0 family. Figure 3.41 contains the power spectrum of the galaxies in the negative wing of figure 3.37 between deviations of +1 and −10. The 18.3 km/s period, 1/2 of it, 9.15 km/s, and 1/4 of it, 4.57 km/s can be seen [135]. The 6.1 km/s 1/3 harmonic of 18.3 km/s is also present since, even if not directly generated in a doubling process, a chain of shorter fundamental intervals will induce it.

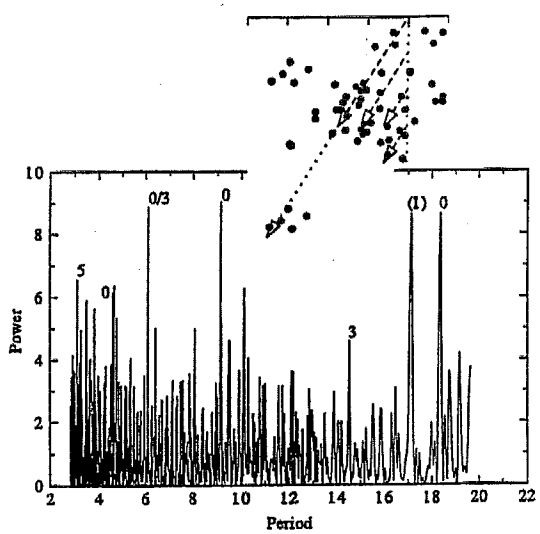


Figure 3.41: Power spectrum of the negative deviation wing in figure 3.37 between deviations of +1 and −10 km/s, to show the multiple T=0 harmonics present [135]. The inset shows possible cascade structure from figure 3.38.

A table in figure 3.42 [135] lists peaks with power greater than 4 in the period range 3 to 20 km/s, including various misfits. T preference for pure cubes, T=0,3,6, stands out among the peaks which fit, followed by T=1,5,7, and avoidance of T=2,4,8 as previously seen.

POWER PEAKS IN THE V9P SAMPLE

| Period (km s$^{-1}$) | $T$ | $w$ | $P_{pk}$ (km s$^{-1}$) | $w_{pk}$ | Pk/Per |
|---|---|---|---|---|---|
| | | | | $T = 0, 3, 6$ | |
| 18.2979..... | 0 | 4.4[a] | 18.3681 | 8.7 | 1.0038 |
| 14.5231..... | 3 | 4.6[a] | 14.5234 | 4.6 | 1.0000 |
| 9.1490..... | 0 | 8.6[a] | 9.1441 | 9.0 | 0.9995 |
| | ... | ... | 9.1786 | 5.3 | 1.0032 |
| 6.0993..... | 0/3 | 2.1 | 6.1084 | 8.9 | 1.0015 |
| 4.5745..... | 0 | 0.3 | 4.5825 | 6.2 | 1.0017 |
| | | | | $T = 1, 5, 7$ | |
| 16.9416..... | 1 | 0.9 | 17.1374 | 8.7 | 1.0116 |
| 3.1125..... | 5 | 0.1 | 3.1195 | 6.6 | 1.0022 |
| | | | | $T = 2, 4, 8$ | |
| None..... | ... | ... | ... | ... | ... |
| Misfits with $w > 6$ | | | | | |
| 9.8814..... | 8 | ... | 10.1251 | 6.3 | 1.0247 |
| 4.5745..... | 0 | ... | 4.6609 | 6.4 | 1.0189 |
| Misfits with $5 < w \leq 6$ | | | | | |
| $P_{pk} = 4.7617, 3.8411, 3.5089$ | | | | | |
| Misfits with $4 < w \leq 5$ | | | | | |
| $P_{pk} = 19.1915, 10.2854, 9.5226, 8.0870, 6.4285, 3.2829, 2.9250$ | | | | | |

Figure 3.42: Table of power peaks, including misfits, in the power spectrum of the P=9.15 km/s negative deviation wing shown in figure 3.40. Peaks with power (w) greater than 4, in the period range 3 to 20 km/s, are listed [138].

### 3.9.3 Separating Signal from Noise

We can demonstrate the presence of a signal distinct from background noise by showing the power distribution is non-exponential. The degrees of freedom of a power spectrum (the number of independent periods or 'peaks') is determined by the redshift and period ranges involved. This particular sample, over the period range from 3 to 20 km/s, has 770 degrees of freedom. By multiplying 770 times the probability of seeing a peak greater than 4, 5, 6, or 7 you can calculate the number of expected periods that should show up in the data by noise alone in those power ranges. The figure 3.43 table indicates for the example under consideration 14, 5, 2 and 0 peaks are expected above the indicated power levels.

The actual frequencies are, 20, 12, 8, and 4; there is a consistent excess of about 6. Now compare the number of misfits in the figure 3.43 table with the number of expected random periods – there is a near perfect match. There are 12 with power greater than 4 and you expect 14, there are 5 with power greater than 5 with 5 expected, etc. The misfits account precisely for expected noise and leave a consistent excess signal. The table in figure 3.43 includes a more restricted test in the range P=4 to 20 with the same result. One can directly account for noise and verify a real non-exponential signal is present.

| | Non Exponential Signals | | | | |
|---|---|---|---|---|---|
| Power> | 4 | 5 | 6 | 8 | Indep P |
| $e^{-P}$ | .018 | .0067 | .0025 | .0003 | |
| Obs/Expec | 20/14 | 12/5 | 8/2 | 4/0 | 770(P=3-20) |
| Exc/Misft | 6/12 | 7/5 | 6/2 | 4/0 | Excess = 6 |
| Obs/Expec | 15/9 | 9/3 | 7/1 | 4/0 | 500(P=4-20) |
| Exc/Misft | 6/8 | 6/3 | 6/2 | 4/0 | Excess = 6 |

Figure 3.43: Table used to demonstrate the presence of a non- exponential signal in the distribution of power peaks listed in the table in figure 3.42 [135]. Refer to the text for descriptions. Obs = observed number, Expec = expected number, Exc = excess number, Misft = number of misfits from the table in figure 3.43.

We can also carry out a uniqueness test similar to what was done in Virgo by comparing the number of peaks that match periods predicted or scaled away from predictions. The table in figure 3.44 shows the result assuming cube roots are dominant. In the period range 2.8 to 20 km/s, of the 63 possible periods in the 7 loations scaled away from the 9 predicted Lehto-Tifft periods, only 1 returns a power in excess of 4. The probability of 1 success in 63 trials is 0.7, there is no evidence for periodicity away from predicted periods. For the 9 trials at the 1 set of predicted periods 3 return power greater than 4, a match which has a random probability of 0.0005. Figure 44 also shows a Student's t test comparing mean power and power dispersion for the on and shifted matches. The result, t=3.5, implies $p < 0.001$ consistent with the binomial statistic. A unique set of periods is present.

| (V9P | P = 2.8-20 | | T = 0,3,6) | |
|---|---|---|---|---|
| N | Pow>4 | <Pow> | Sig | p |
| 63(7-Off) | 1 | 0.9 | 0.8 | 0.69 |
| 9(1-On) | 3 | 2.5 | 2.9 | 0.0005 |
| | | t = 3.5 | | <0.001 |

Figure 3.44: Table summarizing binomial and Student's t statistical tests of the non-exponential signal and unique set of periods present in the power spectrum shown in figure 3.41 [135]. Refer to the text for description. V9P is the name of the data sample involved.

### 3.9.4 The Dwarf Side of $W = 200$, T=1

While discussing effects in the vicinity of the 200 km/s profile width phase break it is instructive to look at the dwarf dominated side as well. We can select a dwarf dominated sample by choosing a profile width range below the 200 km/s break while still excluding the extreme dwarfs. Figure 3.45 shows a table of power peaks greater than 4 in a sample with

$90 < W < 180$ km/s. Several things are apparent. The 18.3 km/s T=0 peak remains but

A DWARF-DOMINATED SAMPLE

| Period (km $s^{-1}$) | $P(D, T)$ | Peak (km $s^{-1}$) | Power | Pk/Per |
|---|---|---|---|---|
| 18.2979..... | $P(14, 0)$ | 18.2921 | 4.4 | 0.9997 |
| 16.9416..... | $P(14, 1)$ | 16.7471 | 4.9 | 0.9885 |
| 8.0043..... | $P(16, 7)3$ | 8.0049 | 5.0 | 1.0001 |
| 7.8429..... | $P(15, 2)$ | 7.8000 | 4.9 | 0.9945 |
| | ... | 5.9801 | 4.7 | ... |
| | ... | 5.5732 | 4.2 | ... |
| 5.3363..... | $P(15, 7)$ | 5.3003 | 6.0 | 0.9933 |
| ..... | ... | 5.0208 | 5.1 | ... |
| | ... | 4.4695 | 4.2 | ... |
| | ... | 4.2933 | 6.4 | ... |
| 4.2354..... | $P(16, 1)$ | 4.2378 | 6.3 | 1.0006 |

Figure 3.45: Table of power peaks, including misfits, in the power spectrum of a dwarf dominated sample with $90 < W < 180$ km/s, on the low side of the $W = 200$ km/s phase discontinuity [130]. Peaks with power above 4 with periods 4 to 20 km/s are shown. Periods associated with T=1 and 7 are present.

drops in power. The secondary T=1 peak, already seen in figure 3.30, remains clear and a shorter T=1 period at 4.24 km/s now stands out. The T=7 family, associated with the extreme narrow profile dwarfs, also makes its appearance. States below the phase transition point seem to display T states shifted by +1 from the common T=0 and 6 family modes. This could be indicative of quantum structural changes occuring near such a boundary, or during transitions between quantized levels. To bring out the apparent importance of the T=1 states, figure 3.46 shows a phase-deviation diagram for $t > 8$ dwarfs, in the $90 < W < 180$ km/s range, at the T=1 P=4.235 km/s period.

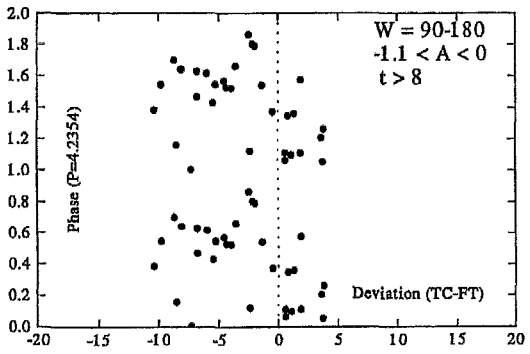


Figure 3.46: Phase-deviation diagram for a dwarf dominated sample (galaxies with $90 < W < 180$ km/s), on the low side of the $W = 200$ km/s phase discontinuity [130]. Late type dwarf irregulars ($t > 8$) with moderately negative asymmetric profiles conform to the T=1 P=4.24 km/s period.

There is a restriction to mildly negative asymmetries as well, related to phase shifts, which I will return to shortly. The usual alternating offset pattern is quite apparent. What is especially interesting however, is what happens when dwarf spirals in this profile width range are added. Figure 3.47 shows $t < 8$ objects as open circles.

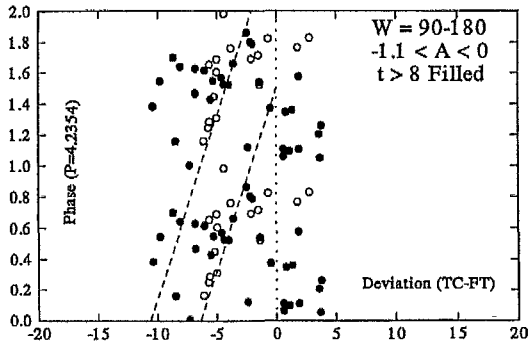


Figure 3.47: A duplicate of the figure 3.46 diagram. As noted dwarf irregulars (filled symbols) conform to T=1 P=4.24 km/s phase levels. When spirals (open symbols) are added they associate with dashed phase cascade lines [130].

As seen in the general diagram in figure 3.34, the spirals also spread along cascade lines, in this case cascades associated with the same T=1 period related to the dwarf levels. Notice phase clumps occur around 0.0 and 0.5. Phasing at stable predicted levels normally occurs at simple fractional values; phasing is not arbitrary.

### 3.9.5 The Extreme Dwarfs

Finally, passing to the extreme dwarfs, figure 3.48 repeats figure 3.15 for $W < 75$ km/s dwarfs (t=9 and 10) at the T=7 10.67 km/s period. Negative asymmetry objects are shown

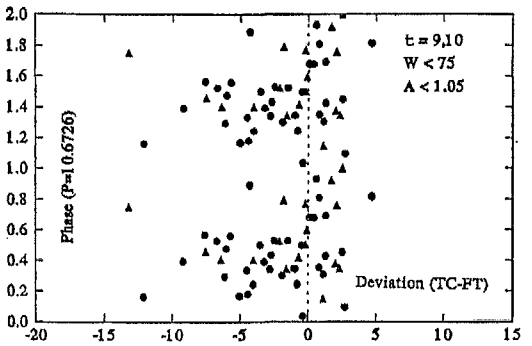


Figure 3.48: Phase-deviation diagram for local galaxies with the narrowest 21 cm profiles, $W < 75$ km/s [129], previously shown as figure 3.15. Triangles identify galaxies with the most symmetric profiles and positively asymmetric profiles are omitted. T=7 periods appear to associate with extreme dwarfs.

with filled circles and symmetric profile objects with filled triangles. Positively asymmetric objects are added as + symbols in figure 3.49 to show the dramatic half cycle phase shift of the type shown earlier for the intermediate profile width galaxies in figure 3.34.

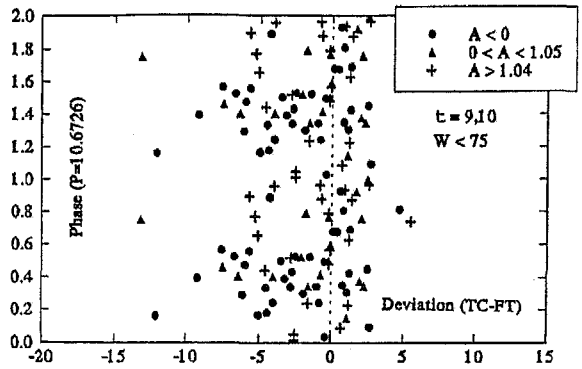


Figure 3.49: Phase-deviation diagram for local galaxies with the narrowest 21 cm profiles, $W < 75$ km/s [129], as shown in figure 3.48. Profile asymmetry is distinguished as indicated. Galaxies with positively asymmetric profiles are now included and are shifted one half cycle from galaxies with symmetric or negatively asymmetric profiles.

Cascade lines at this D=14 T=7 10.67 km/s period are suggested in figure 3.50. The cascade lines are spaced by the D=16, T=7, 2.67 km/s period.

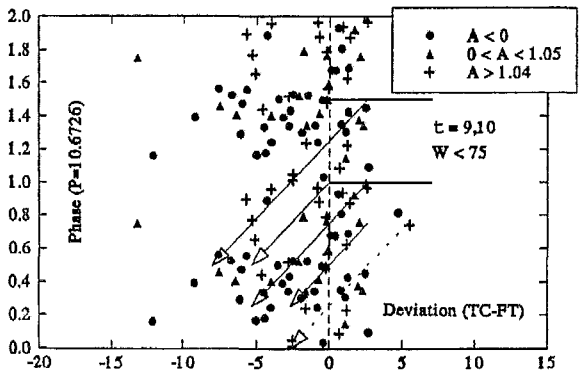


Figure 3.50: This figure repeats figure 3.49 and adds possible cascade lines. Asymmetry alternates between consecutive levels of the 5.33 km/s harmonic [129].

Asymmetry alternates between levels and the levels can be associated with cardinal phase values as shown at 0.0 and 0.5. The phase patterns are clearest in the extreme dwarfs for negative asymmetry, for the intermediate dwarf dominated sample at mildly negative asymmetry, and for the spiral dominated samples at positive asymmetry. There seem to be intimate interrelationships between profile width, asymmetry, T states, morphology, and what appears to be transitions between states.

## 3.10 Exclusion and T Levels in Pairs

As a final example I will comment briefly on some recent work, which may relate to preferred D (doubling level) and T values. This involves double galaxy data, which was introduced in the second seminar before the T structure was defined. Figure 3.51 is a version of figure 2.18 from the second seminar. The figure contains differentials for the most isolated binary

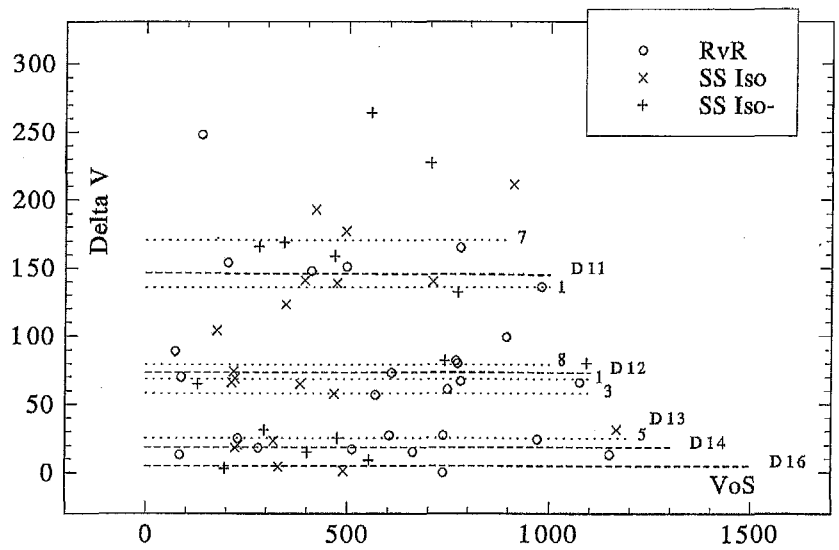


Figure 3.51: Redshift differentials for well isolated double galaxies are shown as a function of minimum physical separation (proportional to the mean redshift times the separation in degrees, $V_oS$). Isolated pairs associate with specific D and T ranges.

galaxies. The original hypothesis, that the differentials should be multiples of a single basic interval, originally 72 km/s, can now be expanded to incorporate a set of levels associated with the Lehto-Tifft predictions. The spread in differentials is real, it well exceeds the redshift uncertainties. The differentials distribute over at least three distinct ranges. The dashed levels mark T=0 Lehto-Tifft intervals for D values as shown. Dotted levels mark intervals associated with other T values. Isolated pairs appear to concentrate in T ranges closely centered around T=0. An association with specific odd numbered T values is suggested, but redshift measures are not precise enough to distinguish between specific closely spaced levels in individual cases. It is clear, however, that certain D values are absent. The conspicuous gap below the D=12 concentration is due to the essentially complete absence of D=13 levels. On examination there is also no evidence for D=15. Isolated pairs seem to prefer even D levels, including possible D=10 levels above the barely developed beginning of D=11 structure. The lack of higher D=11 levels generates the gap below the 140 km/s levels. If we view the diagram as an energy level diagram of redshift decay, then, at the current epoch, states have not progressed much beyond D=16. The observed zero deficiency can be explained as a result of the lack of higher orders of large-scale doubling decay.

We can now perhaps see what happens when we consider less isolated pairs and more complex systems. Figure 3.52 displays pairs from the Cornell sample [M], which were rejected either because of non-isolation, or very close association. Generally speaking such galaxies

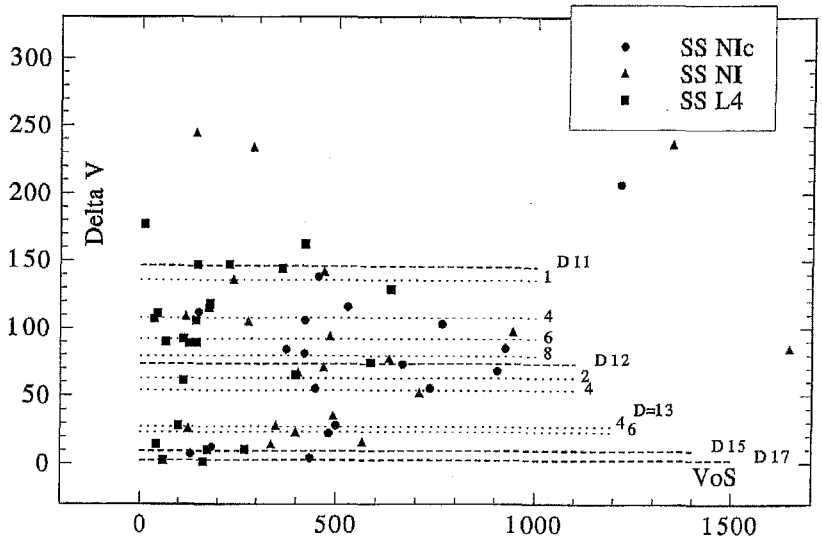


Figure 3.52: Redshift differentials for non-isolated double galaxies are shown as a function of minimum physical separation (proportional to the mean redshift times the separation in degrees, $V_o S$). As galaxies become more crowded together there are changes in the populated D and T ranges compared with isolated systems shown in figure 3.51. This is previously unpublished work.

find themselves in a higher density environment, which can potentially affect the quantum state. The pattern appears to be shifted toward slightly higher T states. The later D=11 states appear above D=12, late D=13 states appear in place of D=14, and D=15 replaces D=16. The pattern is dominated now by odd numbered D concentrations. The gap around differentials of 40 km/s remains clear and the gap below 140 km/s is more restricted. The pattern is shown with even T dominance, but specific associations are not really reliable. What can clearly be said is there is an apparent shift toward higher levels from the pattern in the isolated pairs. In a quantum mechanical model this may make sense, it relates to degeneracy. Decay is retarded at higher density if lower states are already occupied. I might not make such a radical suggestion if this was the only evidence for such an idea, but two other related studies exist. If the level structure for isolated pairs is represented as a rough 72 km/s periodicity, as originally proposed, then the density shift will appear as a phase shift at that periodicity. We can see that phase shift here comparing figures 3.51 and 3.52. You can also see such a shift in the 'triplets' test discussed in reference [100] (2.3.6), and by comparing the denser cores and diffuse structure of superclusters discussed in reference [94]. There is indeed evidence that at higher density, states are forced into or held longer in higher levels. We conventionally interpret greater redshift spread as greater 'velocity dispersion', and invoke dark matter to explain it. A lack of independent quantum states in QTC is more likely what causes or enhances redshift spread in denser regions.

This seminar completes the review of the three phases of my involvement with the question of the nature of the redshift, the correlation phase, the empirical quantization phase, and the directed Lehto-Tifft quantization work. I have summarized a lot of evidence the redshift is quantized, that unique predictable intervals are present, and that quantization is related directly to intrinsic properties of galaxies. The redshift is trying to tell us what galaxies are, and apparently how a progressive quantized decay process is operating. We must pursue such lines of research more deeply to construct a proper cosmology. We will not get there until we really understand the redshift. As a final comment with respect to the redshift, it is *precision* data that is needed, not the rather coarse low precision values currently being produced in vast quantities! Further, although very high z data is certainly needed most of the answers needed in QTC will probably be found at z values less than 2.

The Lehto-Tifft model goes beyond the redshift question however, it probes the nature of time, matter, energy and the fundamental forces as well. In the fourth seminar I will discuss particle physics, and how it prepares us to look at an alternate quantum cosmology.

# Chapter 4

## Particle Physics and the Dimensions of Time, New Viewpoints on Matter and Energy

Seminar 4 Version 8

## 4.1 Introduction

Three previous seminars traced the development of redshift quantization from early correlation studies through later work involving precisely predicted periods and early particle studies. The later work is based upon a semi-empirical association of redshift intervals with physics at the Planck scale, a connection originally noted by Lehto [AG]. Lehto's suggestion has wide consequences relating to the underlying structure of matter and energy and opens the door to an alternative cosmology. This seminar is a current version of an original seminar given in November 2000, supplemented with subsequent investigations.

## 4.2 Begin at the Beginning

Lehto was originally motivated to describe properties of fundamental particles. The Standard Model of particle physics assumes many things, such as particle masses and magnetic moments, which cannot be calculated within the model. Lehto proposed a mechanism for predicting such values from first principles. We reiterate his concept here as initially described in the third seminar. Begin at what is called the Planck scale which is considered to be the beginning of physics as we know it where key fundamental constants, the Planck units, were defined including the Planck energy, time, mass, distance and the velocity of light. These units can be related to the Planck time or frequency as defined by the fundamental constants $h$, $c$ and $G$. Present observable properties of particles (and redshifts) are then presumed to be generated by a decay process beginning at or near the Planck scale. Lehto proposed that the Planck units decay by a period doubling process, essentially an action doubling process in factors of 2, a process well known in decay of systems toward chaos. Note this implies (although Lehto never specifically stated it that way) that there is an underlying cyclical (wavelike) driving process involved. In classical physics this is the quantum mechanical wavelike nature of energy (action) in space whether in active energy form (light) or passive form (matter). If the doubling process is actually the case present day fundamental properties of matter and energy should be related to the Planck units by powers of 2. When Lehto explored this idea he found what appeared to be ratios involving cube-root powers of 2 instead. Lehto then suggested that a doubling process could be occurring in a 3-dimensional or 3-parameter space which we somehow perceive as 1-dimensional; the doubling process is reduced by a cube-root transformation. We will subsequently see how this can be accomplished.

Lehto's original work [AG] examined primarily how properties of the electron and the electromagnetic force strength might be generated by his process. I have subsequently expanded this work to incorporate all the 'stable' particles and known forces. This seminar develops many of the essential ideas, only parts of which are formally published [125,130,AJ]. The stable particles are those which cannot decay by the strong force. They constitute the ground-state energies of particle physics, including the basic baryons, bosons, mesons and leptons, along with the quarks, which make up the visible matter of our universe. The Standard Model effectively describes particle interactions but provides little guide to why the particles and forces have the specific properties, such as the actual masses of particles, that characterize them. A common element linking matter and energy is time; energy can be expressed as $h\nu$ where frequency, $\nu$, is the inverse of time. Matter and energy are two forms of the same thing, and even distance can be expressed as a time delay while force is energy expended per unit distance. All the basic elements or actions in the universe can be tied to the units of time.

Since modern known physics emerges, becomes distinct or even possible, at the Planck scale, the Planck units form a logical starting point which could link to, or relate to, the generation of the present day particulate structure of the universe. Further, since one of the fundamental processes which drives evolution in the universe is decay from high to low energy status, it is not surprising that some decay process beginning at the Planck scale should be involved. String theory, a current popular approach to particle theory, is also linked to the Planck scale. In string theory one views particles as resonant excitation modes of energy loops associated with the Planck scale which provides an underlying quantum 'froth'. In Lehto-Tifft concepts particles are products of a quantized decay cascade originating at the Planck scale. Particle energies do in fact have a special decay relationship with respect to the Planck energy. Particles seem to exist at decay levels (energy levels) where a specific 'stable' configuration or resonance occurs in the doubling process.

### 4.2.1 The Planck Units and the Doubling Decay Process

The Planck units are readily derived from a dimensional analysis of equivalent energy forms. Expressed in terms of the Planck time they are

$$t_o = \sqrt{\frac{hG}{c^5}} \qquad d_o = ct_o \qquad E_o = \frac{h}{t_o} \qquad m_o = \frac{h}{t_o c^2}.$$

The Planck unit for speed is $d_o/t_o = c$. Using $c = 2.997929 \times 10^{10}$ cm/s, $h = 6.6252 \times 10^{-27}$ erg s, $G = 6.668 \times 10^{-8}$ dyn cm$^2$ g$^{-2}$ the quantities, in cgs units, are

$$t_o = 1.3506 \times 10^{-43}\text{s} \quad d_o = 4.049 \times 10^{-33}\text{cm} \quad E_o = 4.905 \times 10^{16}\text{erg} \quad m_o = 5.458 \times 10^{-5}\text{g}.$$

The Planck distance and time are extraordinarily tiny quantities; reaction times and scales in particle physics are many orders of magnitude larger. The Planck mass and energy, inversely related to time, are correspondingly large, quite logical candidates for 'decay' (in the case of specific objects I will often use the term 'aging'). Modern physics has not even begun to probe nature at the Planck scale. It seems unrealistic to assume that present day 'fundamental' particles contain no further substructure within which aging could proceed.

In its simplest form the period doubling process should generate levels related to the Planck scale by progressive factors of two. The Planck energy (or mass) will decay, or the Planck time (or distance) extend as

$$E = E_o 2^{-N} \quad t = t_o 2^N,$$

where $N$ is any positive integer. In the volume doubling form perceived as one-dimensional the process takes the form

$$E = E_o 2^{-N/3} \quad t = t_o 2^{N/3}.$$

The domain involved in this process is energy, or, through its intimate association with time, temporal. Time could have an underlying 3-dimensional character although it is perceived as 1-dimensional.

### 4.2.2 Two Spaces, Tau and Sigma

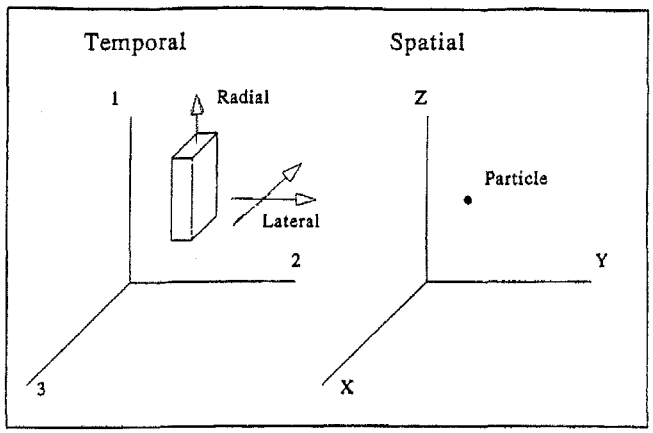


Figure 4.1: Defining two linked three dimensional spaces, Three dimensional time (Tau), and three dimensional space (Sigma).

Figure 4.1 introduces a conceptual picture of the process which may be involved. The figure portrays two three dimensional spaces, a temporal (or action) space on the left (which will be called $\tau$ (tau) space) and a spatial space on the right (which will be called $\sigma$ (sigma) space). A three dimensional tau-space 'structure' is represented by a volume where the three dimensions can be interpreted to indicate the degree of 'doubling' on each axis. The volume of the structure represents the total mass (or mass-equivalent energy) of the structure. In three dimensional sigma-space the structure is manifest as a particle whose properties are defined by the character of the tau-space structure. Relative flow of one space with respect to the other, at the speed of light, will cause either space to perceive the other space as 1-dimensional by aberration, hence provide the perceived geometrical reduction of each 'structure' as either a 3-space or 4-space with respect to observers in the other space, depending upon the role the space-time link plays in the structure. The temporal structure and the associated particle have this link in common. When the particle is created, in a transformation process between tau and sigma-space, they have the birth time 'coordinate'

in common, a term I refer to as 'temporal commonality'. Except for certain relativistic effects, which apply only within sigma-space due to motion within and by the particle in sigma-space, this commonality is retained no matter how the particle moves within sigma-space. Spatial locations cannot be perceived by its tau partner (although relativistic effects which change the rate of passage of time in sigma-space will be detected). This distinction and the properties of tau and sigma-spaces play a central role in the cosmology developed in this book.

The fact that the transformation of pure mass-energy involves a cube root has special significance. At first sight, when presented with the cube-root rule, most people think the relationship is rather unusual, although it is effectively a reduction of an energy volume to an energy density. In fact such a rule is very well known, Kepler's third law of orbital motion where distance is related to a two thirds power of a temporal term. If energy action perceived in sigma-space has its basis in actual dynamics, or an equivalent analog in 3-d tau-space, a form of Kepler's third law is precisely how it could be detected. Lateral action involved in Kepler's first and second laws could at most provide some blurring if it could be observed at all. Kepler's laws exist because space is three-dimensional, hence the cube root rule potentially associates three dimensions with time. The association provides symmetry between space and time and gives us a means of separating quantum and spatial dynamical physics. Quantum physics associates with three dimensional tau-space while continuous conventional dynamics can occur in sigma-space. Special relativity is consistent with such a picture. Subsequent discussion will expand further on this model.

### 4.2.3 Early Studies, Representing Particle Forms

Table 1
Fit Quality According to Lehto [AG]

| Electron Properties | Observed | Model | % Diff |
|---|---|---|---|
| Rest Energy | 0.511 | 0.510 | 0.1 |
| Magnetic Moment | $9.283 \times 10^{-24}$ | $9.285 \times 10^{-24}$ | 0.007 |
| Charge | $1.602 \times 10^{-19}$ | $1.602 \times 10^{-19}$ | 0.003 |
| Spin | $5.273 \times 10^{-35}$ | $5.273 \times 10^{-35}$ | 0.000 |
| (Fine Str Const)$^{-1}$ | 137.036 | 137.045 | 0.007 |

Figure 4.2: Lehto's match to the properties of the electron

Using his original concepts Lehto was able to model the properties of the electron, and the electric force strength, to within a small fraction of one percent of their measured values. We will look at this process in some detail below. Figure 4.2 contains Table 1 showing the quality of fit Lehto achieved. The success of the model, and Lehto's suggestion that redshift quanta might be similarly calculated, led to the precise fitting of redshift periodicities (125,138)

described in the third seminar. Lehto originally suggested that redshifts might be some form of quantized velocities. However, since projection alone will destroy quantization involving spatial motion (as discussed in double galaxy work) something much more subtle must be involved. To pursue this issue I extended particle physics investigations and turned to models involving 3-dimensional time in cosmology. Before discussing particle modeling I should expand upon the set of 'Lehto-Tifft' (LT) equations involved.

Lehto's original cube-root expressions were applied to defining mass-energy for specific particles, the electron in particular. I quickly found that we needed to be more explicit to distinguish fermions from bosons. The cube-root rule describes scalar properties associated with mass-energy independent of spatial distance. Cube-root reductions apply consistently to fermions. Force, associated with bosons, involves energy operating over distance which adds a fourth dimension to the 3-d concept. Therefore boson characteristics and forces consistently require a fourth root reduction associated with the doubling process. In addition, as discussed for redshifts in the third seminar, it is important to distinguish the separate families of cube or fourth roots involved. We do this by expanding the integer power $N$ as $N = aD + n$ where $D$ is the amount of doubling, $a$ is the dimensionality involved, 3 or 4 (or 9 in the case of redshifts), and $n$ is the fractional doubling or doubling 'family' involved.

The Lehto-Tifft decay equations thus take the general form

$$X = X_o 2^{\pm(aD+n)/a},$$

where $X_o$ is a particular unit at the Planck scale. The specific form used for redshifts from the previous lecture is

$$P = c2^{-N/9} \qquad P = c2^{-\frac{9D+T}{9}}.$$

$T$ specifies which of 9 possible ninth root 'families' is involved. The 9 appears to apply only to photons; particles require only one cube-root (or fourth-root) operation as we shall demonstrate. The implications of this distinction will be briefly discussed later. In a very similar construct we write the expressions for the mass-energies of fermions or bosons as

$$E_f = KE_o 2^{-\frac{3D+M}{3}} \qquad E_b = KE_o 2^{-\frac{4D+F}{4}},$$

where $M$ and $F$ distinguish cube or fourth root families, and $K$ is a scaling constant (1.0 or $1/\sqrt{\pi}$) which we will subsequently define.

From the very onset, I should point out that although there appear to be many possible doubling 'families' described by $T$, $M$ or $F$, in fact certain values are strongly preferred. Random accidental matches should favor no specific families. $T = 0$ and 6 are dominant redshift families as discussed in the third seminar. These correspond to pure doubling and the 2/3 power. We will shortly see that particle masses relate dominantly to $M = 0$ or 2, again pure doubling or the 2/3 power. It seems likely to be more than a curious coincidence that 2/3 is also the relationship involved in Kepler's third law which describes stable dynamics in three dimensions.

I will now turn to the actual description of particle properties beginning with the characterization of the electron. We require only the pure cube root rule and set $K = 1.0$. This fundamental energy doubling sequence is called the 'gamma' sequence since the $K = 1.0$ condition also completely describes redshift (photon) energies when using the ninth root

form of the equation. The description actually begins with electron-positron pair formation, a fundamental junction point between matter and energy domains. The mass-energy of the electron-positron pair is given to a fraction of one percent by the expression

$$m_{e\bar{e}} = m_o 2^{-\frac{224}{3}}.$$

Note that 224/3=74.67 and the electron alone is one factor of two smaller at 75.67; the fundamental stable lepton fits the dominant 2/3 power pattern, $M = 2$, as noted above. Now 224 may look rather arbitrary but it is not. 224 is the sum of 32 + 64 + 128, all powers of 2 generated within a doubling sequence, $2^5$, $2^6$, and $2^7$. If each term is associated with a 3-d direction, as shown in figure 4.1, we define a volume which can evolve naturally through the doubling process.

$$m_{e\bar{e}} = m_o 2^{-\frac{224}{3}} = m_o 2^{-\frac{32+64+128}{3}} = m_o 2^{-\frac{l+m+n}{3}}.$$

The picture is consistent with representing action space (tau-space) as having three dimensions, $(l, m, n)$, within which a doubling process proceeds. This unique type of relationship appears to be basic in defining properties of the stable particles. Further, the number 64, central to the process, is itself a very special number as we will subsequently see. The fact that particle properties relate to the Planck units in such a unique way is very difficult to dismiss as accidental.

The gamma sequence describes the electron, redshifts (photons), and certain other particles very well. However, it does not describe various other basic particles including the proton. To fit proton properties a second energy sequence is required. The necessary sequence (called the pi sequence) is generated when $K$ is set equal to $1/\sqrt{\pi}$ in the previous definition of permitted energies. Along with the gamma sequence this is all we will need to describe basic properties of the stable particles. The proton mass in particular is closely described by

$$m_p = \frac{m_o}{\sqrt{\pi}} 2^{-\frac{192}{3}} = \frac{m_o}{\sqrt{\pi}} 2^{-\frac{64+64+64}{3}}.$$

We note again the remarkable fact that the N value involved, 192, is the sum of three perfect squares, 64+64+64, in this case the key number 64 itself. Furthermore the fit occurs in the $M = 0$ family, the pure doubling family, which along with the 2/3 family dominates observed patterns in both redshifts and particle physics. We should also point out that the patterns, 64+64+64 and 32+64+128 involve the same degree of doubling; we have just slightly changed the synchronization. Properties of the electron and proton, the two most basic stable particles, appear to be intimately connected and revolve around the number 64.

The scaling constant $K = 1/\sqrt{\pi}$ is the factor which relates the area and radius of a circle. This is the type of relationship we might expect if one structure involves azimuthal (angular momentum) and the other radial quantization, the two basic modes which permeate quantum theory. We will subsequently see how calculations of magnetic moments provide a confirmation of such an interpretation. Neutron structure suggests another aspect of what may be involved in the link between the sequences. Neutrons have nearly the same mass-energy as the proton and, consistent with its decay process, can be represented as an electron-proton combination. Neutron decay involves the weak force and connects the proton and electron which fall in different sequences. Weak decay involves transitions between two patterns, again implying some characteristic 'structural' change between quantization

modes. This is schematically illustrated in figure 4.3 and certainly suggests the existence of a finer structure within particles as one approaches the Planck scale. I shall in fact demonstrate what that structure may be later in this seminar. Both quantization mode differences and the weak force appear to be involved in generating the two energy sequences.

Other important associations are present. Baryons are three quark hadrons. One can associate the three quarks with the three dimensions (or three degrees of freedom) of tau-space. Extending this concept to mesons requires incorporating an additional spatial term. If the spatial term were to nullify a temporal term two effective dimensions would be consistent with the two quark meson structure. Such a combination involves three temporal terms minus a spatial term, which resembles the standard metric seen from a *temporal* viewpoint. Standard 4-space proper distance involves three spatial terms minus a temporal term and corresponds to the distance between two simultaneous events. The analog in tau-space is the temporal separation between two *cospatial* events, in this case particles (3-d tau structures), which certainly describes bosons and Bose-Einstein statistics. There is a clear potential symmetry between processes in a spatial (sigma-space) domain and a linked temporal (tau-space) domain which relates intimately to the distinction between fermions and bosons.

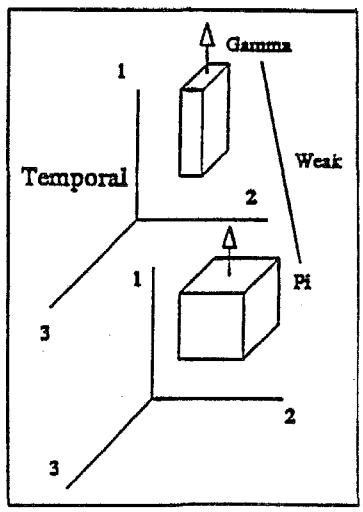


Figure 4.3: There is a very interesting relationship involved in the distinction between the Pi and Gamma energy level scales. See the text for discussion. One important factor is the role of the weak force connecting 3-d and 4-d spatial-temporal structures and their statistical behavior.

As a commentary on the statistical distinction (exclusion properties) between fermions and bosons, the 3-d vs 4-d Lehto-Tifft model indicates how this is accomplished. Fermions, as pure 3-d spatial structures have no means to escape spatial exclusion and cannot occupy the same space. From the spatial viewpoint they correspond to specific spatial constructs flowing along a timeline. Bosons on the other hand can remain distinct in their fourth temporal property, appearing spatially superimposed while temporally distinct, distributed along a timeline within a range set by the uncertainty principle relating space and time

intervals. I will expand further on the uncertainty concept which involves a fuzzy overlap between space and time which QTC provides.

### 4.2.4 Assigning Vector Modes, Magnetic Moments

Having associated protons and electrons with different quantization modes, we may now specify which mode applies to each particle. The key comes from examining magnetic moments of the electron and the proton, as described by Lehto in 1996 [AJ]. The procedure is summarized in Table 2 within figure 4.4. The first part reiterates the structure of the underlying Lehto-Tifft mass energy equations. Magnetic moments involve a current loop, a circle, the area of which is $\pi r^2$. Solving for r shows a $1/\sqrt{\pi}$ relationship with the lateral area and associates radial quantization with the proton. The inverse product $r\sqrt{\pi}$ associates the lateral (azimuthal) effects with the electron. The radial and azimuthal dimensions of a current loop are its radius and circumference. Magnetic moment units at the Planck scale are found by setting the circumference or radius equal to the Planck length $d_o$, (or $ct_o$ in terms of Planck time), and multiplying the associated area by the current involved.

**Table 2**

Properties of Electrons and Protons

| Energy Sequence | Gamma | Pi |
|---|---|---|
| Energy Equation | $E_o 2^{-N/3}$ | $(E_o/\sqrt{\pi})2^{-N/3}$ |
| Basic Fermion | Electron | Proton |
| Rest Mass | $m_e = m_o 2^{-75.67}$ | $m_p = (m_o/\sqrt{\pi})2^{-64.00}$ |
| Quantum Basis | Azimuthal | Radial |
| Loop Equation $A = \pi r^2$ | $\sqrt{A} = r\sqrt{\pi}$ | $r = (1/\sqrt{\pi})\sqrt{A}$ |
| Quantized Quantity | Circumference | Radius |
| Unit | $2\pi r = d_o = ct_o$ | $r = d_o = ct_o$ |
| Current | $i = e/t_o$ | $i = e/8t_o$ so $v < c$ |
| Unit Moment $\mu = iA$ | $\mu_{oa} = (e/t_o)\pi(d_o/2\pi)^2$ | $\mu_{or} = (e/8t_o)\pi(d_o)^2$ |
| Magnetic Moment | $\mu_e = \mu_{oa} 2^{75.67}$ | $\mu_p = \mu_{or} 2^{64.00}$ |

Figure 4.4: Properties and magnetic moments for electrons and protons

The current in the circumferential mode is the unit electric charge divided by the Planck time, $e$ circulating at the speed of light. The loop radius is $d_o/2\pi$, hence the moment, the current times the area, is $\mu_{oe} = ec^2 t_o/4\pi$. The subscript $e$ associates this unit azimuthal mode moment with the electron. Evolving this unit through the same decay process which yields the electronic mass-energy now generates the magnetic moment of the electron very closely. Both the magnetic moment and mass of the electron are found to high precision

by raising the corresponding Planck unit to the same power (with opposite sign since time grows as mass-energy decays). This remarkable result connects two fundamentally distinct properties of the electron and suggests that the electron structure may involve some form of azimuthal quantization.

To examine the radial mode set the loop radius equal to the Planck distance. The circumference now exceeds the Planck length by a factor $2\pi \approx 6.28$. Since the circulating charge cannot exceed the speed of light, it must take more than 6.28 Planck times to make the circuit. The lowest number generated by a doubling sequence of permitted steps meeting this restriction is eight. The maximum allowed current is thus $e/8t_o$, so the unit radial mode moment is $\mu_{op} = ec^2t_o\pi/8$, where the subscript $p$ associates the unit moment with the proton and the radial mode. Evolving this unit through the same decay process which yields the proton mass-energy closely generates the magnetic moment for the proton just as occurred for the electron. In classical physics the magnetic moments cannot be accurately predicted. An empirical factor, the Lande g factor, is required to explain the moment. The observed moment comes out directly in the Planck decay model, and may associate the proton with some form of radial quantization. Magnetic moments provide a strong argument that two modes equivalent in some form to radial and azimuthal quantization underly the structure and properties of the stable particles. There is no certainty that all particles in a particular sequence follow the same structural pattern, but structure should relate to magnetic properties

### 4.2.5 Summarizing the Gamma and Pi Energy Levels

Having demonstrated that the electron and proton occupy specific energy levels described by the Lehto-Tifft 3-d and 4-d decay process it is useful to provide a general tabulation of the comprehensive pattern of permitted levels as I turn to discussing the remaining stable particles. Table 3 tabulates the energy levels in MeV for compound dimensionally reduced doubling levels N $= (l + m + n)/3$ or $(l + m + n + i)/4 = 55$ to 80 including the K and $E_o$ scaling constants to convert to MeV using 1998 constants. The electron energy level of 0.5104 will be found at level 75.67 in the Gamma table, the proton or neutron at 64.00 in the Pi table. In case you are interested the Higgs is there, as it should be, at 126277.7 MeV at Gamma 57.75, but I will get to that later.

## 4.3 Baryons

We will now look at other stable particles beginning with baryons, which are fermions. Fermions should be represented by 3-d cube-root modes since they involve pure mass-energy and obey Fermi statistics. Each particle should associate with a specific energy level in one of the sequences. These levels appear to be at least quasi-stable locations which associate with stable ground states represented by the proton and electron. In order to connect in weak decays the mass-energies should also be consistent with possible difference energies *between* the sequences which match particle mass-energies involved. For various reasons the matches need not be exact. Different charged forms of the same particle go together although they may differ slightly in mass-energy. Table 3 provides a complete list of possible cube and fourth root levels between doubling levels 55 and 80. As with redshift periods specific levels are present relating to all the individual stable particles. Tabulated values are based

Table 3a Gamma Energies (1998 Constants)

| N | N.00 | N.25 | N.33 | N.50 | N.67 | N.75 |
|---|---|---|---|---|---|---|
| 55 | 849491.5347 | 714334.4 | 674241.9 | 600681.2 | 535146.1 | 505110.7 |
| 56 | 424745.8 | 357167.2 | 337120.9 | 300340.6 | 267573.1 | 252555.3 |
| 57 | 212372.9 | 178583.6 | 168560.5 | 150170.3 | 133786.5 | 126277.7 |
| 58 | 106186.4 | 89291.80 | 84280.23 | 75085.15 | 66893.27 | 63893.84 |
| 59 | 53093.22 | 44645.90 | 42140.12 | 37542.58 | 33446.63 | 31569.42 |
| 60 | 26546.61 | 22322.95 | 21070.06 | 18771.29 | 16723.32 | 15784.71 |
| 61 | 13273.31 | 11161.47 | 10535.03 | 9385.644 | 8361.658 | 7892.354 |
| 62 | 6636.653 | 5580.737 | 5267.515 | 4692.822 | 4180.829 | 3946.177 |
| 63 | 3318.326 | 2790.369 | 2633.757 | 2346.411 | 2090.414 | 1973.089 |
| 64 | 1659.163 | 1395.184 | 1316.879 | 1173.206 | 1045.207 | 986.544 |
| 65 | 829.582 | 697.592 | 658.439 | 586.603 | 522.604 | 493.272 |
| 66 | 414.791 | 348.796 | 329.220 | 293.301 | 261.302 | 246.636 |
| 67 | 207.395 | 174.398 | 164.610 | 146.651 | 130.651 | 123.318 |
| 68 | 103.698 | 87.199 | 82.305 | 73.325 | 65.325 | 61.659 |
| 69 | 51.849 | 43.600 | 41.152 | 36.663 | 32.663 | 30.830 |
| 70 | 25.924 | 21.800 | 20.576 | 18.331 | 16.331 | 15.415 |
| 71 | 12.962 | 10.900 | 10.288 | 9.1657 | 8.1657 | 7.7074 |
| 72 | 6.4811 | 5.4499 | 5.1441 | 4.5828 | 4.0828 | 3.8537 |
| 73 | 3.2406 | 2.7250 | 2.5720 | 2.2914 | 2.0414 | 1.9268 |
| 74 | 1.6203 | 1.3625 | 1.2860 | 1.1457 | 1.0207 | 0.9634 |
| 75 | 0.8101 | 0.6812 | 0.6430 | 0.5729 | 0.5104 | 0.4817 |
| 76 | 0.4051 | 0.3406 | 0.3215 | 0.2864 | 0.2552 | 0.2409 |
| 77 | 0.2025 | 0.1703 | 0.1608 | 0.1432 | 0.1276 | 0.1204 |
| 78 | 0.1013 | 0.0852 | 0.0804 | 0.0716 | 0.0638 | 0.0602 |
| 79 | 0.0506 | 0.0426 | 0.0402 | 0.0358 | 0.0319 | 0.0301 |
| 80 | 0.0253 | 0.0213 | 0.0201 | 0.0179 | 0.0159 | 0.0151 |

Table 3b Pi Energies (1998 Constants)

| N | N.00 | N.25 | N.33 | N.50 | N.67 | N.75 |
|---|---|---|---|---|---|---|
| 55 | 479274.2752 | 403020.0 | 380400.2 | 338898.1 | 301923.9 | 284978.2 |
| 56 | 239637.1 | 201510.0 | 190200.1 | 169449.0 | 150961.9 | 142489.1 |
| 57 | 119818.6 | 100755.0 | 95100.06 | 84724.52 | 75480.97 | 71244.55 |
| 58 | 59909.28 | 50377.50 | 47550.03 | 42362.26 | 37740.48 | 35622.27 |
| 59 | 29954.64 | 25188.75 | 23775.02 | 21181.13 | 18870.24 | 17811.14 |
| 60 | 14977.32 | 12594.38 | 11887.51 | 10590.57 | 9435.121 | 8905.568 |
| 61 | 7488.661 | 6297.188 | 5943.754 | 5295.283 | 4717.561 | 4452.784 |
| 62 | 3744.330 | 3148.594 | 2971.877 | 2647.641 | 2358.780 | 2226.392 |
| 63 | 1872.165 | 1574.297 | 1485.938 | 1323.821 | 1179.390 | 1113.196 |
| 64 | 936.083 | 787.148 | 742.969 | 661.910 | 589.695 | 556.598 |
| 65 | 468.041 | 393.574 | 371.485 | 330.955 | 294.848 | 278.299 |
| 66 | 234.021 | 196.787 | 185.742 | 165.478 | 147.424 | 139.150 |
| 67 | 117.010 | 98.394 | 92.871 | 82.739 | 73.712 | 69.575 |
| 68 | 58.505 | 49.197 | 46.436 | 41.369 | 36.856 | 34.787 |
| 69 | 29.253 | 24.598 | 23.218 | 20.685 | 18.428 | 17.394 |
| 70 | 14.626 | 12.299 | 11.609 | 10.342 | 9.2140 | 8.6968 |
| 71 | 7.3131 | 6.1496 | 5.8044 | 5.1712 | 4.6070 | 4.3484 |
| 72 | 3.6566 | 3.0748 | 2.9022 | 2.5856 | 2.3035 | 2.1742 |
| 73 | 1.8283 | 1.5374 | 1.4511 | 1.2928 | 1.1517 | 1.0871 |
| 74 | 0.9141 | 0.7687 | 0.7256 | 0.6464 | 0.5759 | 0.5436 |
| 75 | 0.4571 | 0.3843 | 0.3628 | 0.3232 | 0.2879 | 0.2718 |
| 76 | 0.2285 | 0.1922 | 0.1814 | 0.1616 | 0.1440 | 0.1359 |
| 77 | 0.1143 | 0.0961 | 0.0907 | 0.0808 | 0.0720 | 0.0679 |
| 78 | 0.0571 | 0.0480 | 0.0453 | 0.0404 | 0.0360 | 0.0340 |
| 79 | 0.0286 | 0.0240 | 0.0227 | 0.0202 | 0.0180 | 0.0170 |
| 80 | 0.0143 | 0.0120 | 0.0113 | 0.0101 | 0.0090 | 0.0085 |

upon 1998 values of the fundamental constants. Uncertainty is is almost entirely due to uncertainty in the gravitational constant. Changing G by its 1 sigma uncertainty will scale numbers up or down by 0.0015, 0.15 percent. Numbers are given to higher precision for consistency.

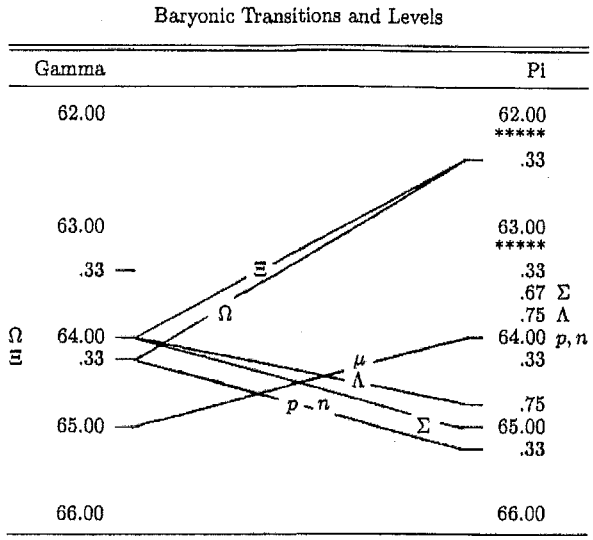


Figure 4.5: Energy levels and transition paths for the fundamental baryons. A transition for the muon connecting to the basic 64.00 level is also shown. All levels either reside at or connect to level 64.00. Fermions always associate with 3-d levels with one exception. The fourth root association of the Λ baryon (which has bosonic associations in QTC) is discussed at length later in the text

Fermion structures distribute around level $N = 192 = 3 \times 64$ as shown in figure 4.5. Various cube and fourth roots are indicated by decimals. Gamma sequence fits are shown to the left, pi sequence fits to the right. Particle symbols are shown at *levels* which correspond to their mass-energy, and on lines where a connecting *transition* energy difference matches the mass-energy involved. Certain limits, shown with asterisks, will be described subsequently. Specific mass-energy fits are summarized in subsequent tables. The basic baryons shown are the $p, n$ = proton/neutron, and $\Lambda$, $\Sigma$s, $\Xi$s, $\Omega$ = lambda, sigmas, cascades, and omega, along with the muon, $\mu$. A specific muon transition is shown for reasons discussed later. The muon lepton level (68.00 in the gamma sequence) and the electron level (75.67 in the gamma series), are off scale at the bottom. We will have much more to say about leptons, which have a specific function in QTC.

Although fits to energy levels are unique, fits to transitions are not independent. Since the scaling factor between the sequences is specified, as are the ratios between levels in each sequence, transition energies are completely defined by the choice of levels. We will show later that several transitions can be associated with any cube or fourth root level. The few most appropriate fits form an interesting pattern which we will look at more carefully after introducing the general pattern of fits.

With the exception of the lambda particle, which we will discuss separately, all the baryons occupy 3-d, (cube-root), levels and match transitions between 3-d levels which we associate with fermions. Further, all particles either occupy a basic level 64.00 or connect to it by transitions (including the lambda and the muon). Not shown, but obvious from the factor of two connections within energy families, all particle anti-particle pairings are equally well fit one integer level higher. Transition fits connect the two sequences, a process we have associated with the weak force since when certain particles decay they can generate particles falling on the other sequence. Decay or excitation which does not involve both sequences can be associated with the strong (or electric) force, for example photon-photon decay or particle anti-particle formation. Such processes represent excitation changes within individual quantization modes. Fits are generally within one percent of the mass-energies involved. Exact fits are not expected since relativistic and charge related effects no doubt enter as corrections for any particles having mass. Different charged forms, including the proton-neutron pair, associate with the same levels and transitions. In this context we note that redshift fits appear to be exact within our ability to measure the energies involved. The photon, uncharged and massless should not and does not show any significant deviations from observed states. We will return for a more detailed look at fermion level structure when quarks are discussed after examining mesons.

## 4.4 Mesons, the Common Bosons

Mesons are bosons, two quark hadrons. As noted earlier bosons relate at some level with force. Forces involve a four-dimensional association of space and time. The reduction of bosons to perceived particles in space should therefore involve fourth roots where bosons involving mass (mesons and later gauge bosons) are associated with weak force interactions. Figure 4.6 shows that this is consistent with findings. Figure 4.6 is similar to figure 4.5 showing level and transition matches. The pion ($\pi$) and kaon ($K$) occupy the lowest levels (66.75 and 65.75) of the pi and gamma sequences. Their particle pairs and the eta ($\eta$) and $F$ (or $D_s$) mesons form direct doubling patterns above them, except that the $\eta$ pair is replaced by the $\Lambda$ particle, which as noted earlier serves an interesting dual function. The pattern again revolves centrally around level 64. Both the $\Lambda$ particle and $\eta$ meson are linked to level 64 by transition energies equal to each others mass-energy. The $\Lambda$ particle has both baryon and meson properties, a point we shall return to when looking at relationships between particle structures. Sequences may be extended to the heavy $D$ and $B$ mesons, but the patterns become more obscure when the heavy quarks are involved. The horizontal line above level 67 and certain other features of figure 4.6 will be discussed subsequently.

The light meson states not only occupy fourth root levels, they all occupy the same fourth-root level, 3/4. This is unlikely to be a random association, and will be seen later to relate to properties of forces and transitions. Transition energies link 3-d to 4-d level in the opposite sequence, although .00 levels can match either root. The significance of 64 in this regard will be relevant later; 64 is the smallest number above unity which is both a perfect cube and square. The number 64 provides a junction point between fermion and boson mass-energy structures, a resonance which may explain why matter exists at this level. The 3-d to 4-d boson linkage suggests a force to mass-energy linkage, and may provide insight into the role of neutrinos. I will return to this point in later discussion.

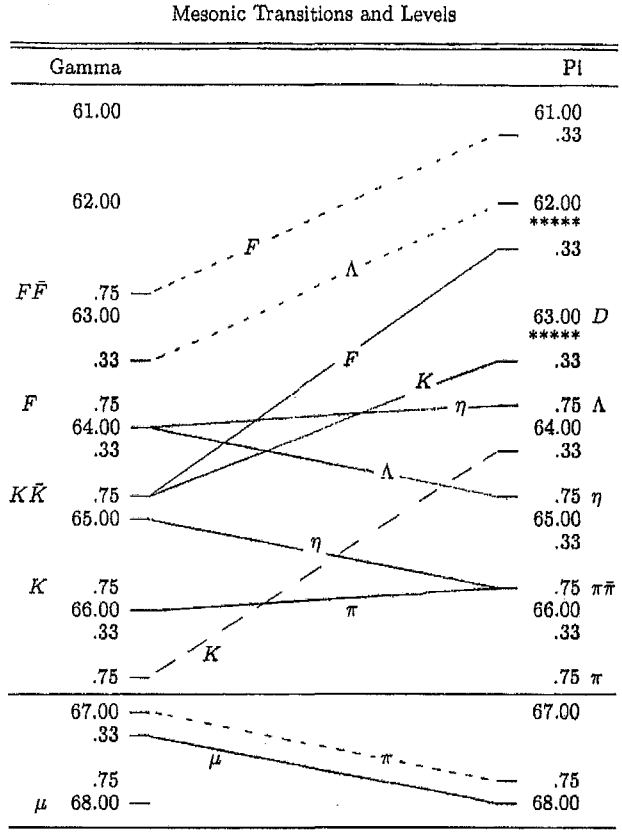


Figure 4.6: Meson levels and transitions. All meson particles occupy the unique set of N.75 levels, including the multifunction Λ particle. Each meson has two possible transitions indicated, some using dotted or dashed lines for reference. The muon, which plays a special function related to the light mesons in QTC is shown at the bottom below a horizontal limiting line for mesons.

## 4.5 Summary and Discussion Concerning Transitions

Figure 4.7 combines the fermion and boson diagrams. Membership in four doubling families occur, 0.75, 0.00, 0.33, and 0.67, with links to level 64. Certain hypothetical particles and quark mass fits are also shown and will be discussed later. Table 4 compliments the diagram and tabulates mass-energy fits involved. The first column lists particles, distinguishing neutral and charged forms where appropriate. The second and third columns give measured masses for charged and neutral forms respectively. Charged particle anti-particle pairs have equal mass. Baryons differ by charge and are separated. Column 4 gives mass-energy level fits; column 5 shows deviations from measured masses. The last columns list key transitions matches and deviations.

As noted earlier, transition matches are not independent of level choices. Table 5 summa-

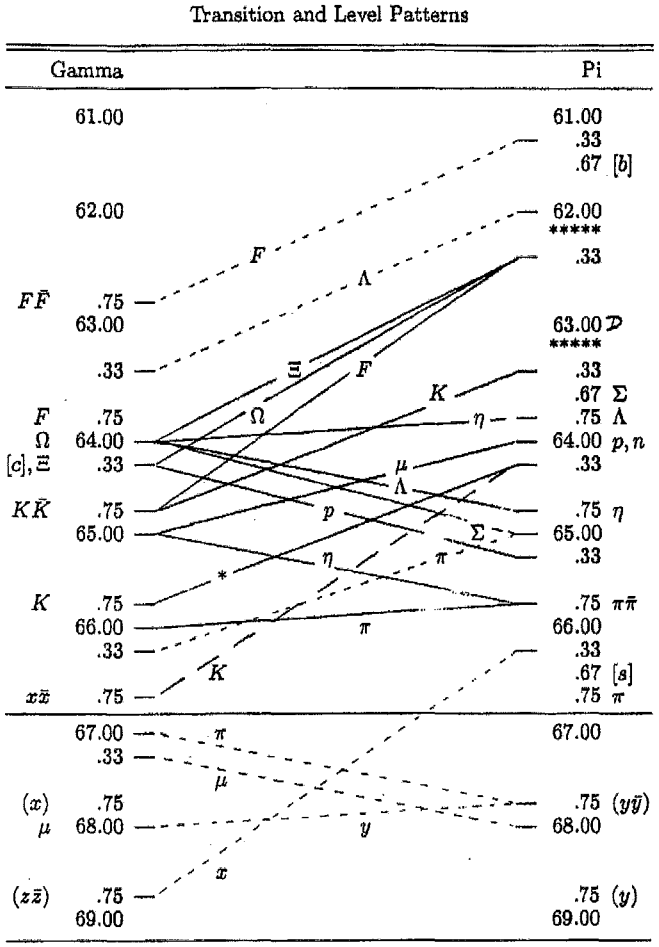


Figure 4.7: Transition and level pattern for both baryons and mesons.

rizes transitions which match energies within about 2% and closely associate with levels involved. More complex matches are possible but involve connections which have little or no association with the energy level being matched. The table is divided into four parts to distinguish 3-d and 4-d level matches in each of the energy sequences. The first column in each table defines a transition match where $\pi$ or $\gamma$ indicates the energy sequence and a subscript (or subscript combination) gives level difference with respect to the level being matched. For example, the first line for 3-d gamma level fits, when applied to the electron (which matches level gamma 75.67), refers to the transition $\pi_{73.67} - \gamma_{75.33}$. The second column shows the percent deviation of transition energy with respect to the level energy being matched. If negative the transition is slightly less energetic than the level. Note this is not a measure of deviations from actual mass-energies of particles since they differ slightly from level energies. Subsequent columns refer to individual particles. Different forms are distin-

Table 4
Level and Transition Matches

| Particle | Mass Mev | Mass Mev | Level | Dev Mev | Transition | Dev Mev |
|---|---|---|---|---|---|---|
| $p^+$, $n$ | 938.3 | 939.6 | $\pi_{64.00}$ | 2.2, 3.5 | $\gamma_{64.33} - \pi_{65.33}$ | 7.1, 5.8 |
| $\Lambda^o$ | ··· | 1115.7 | $\pi_{63.75}$ | 2.5 | $\gamma_{64.00} - \pi_{64.75}$ | −13.1 |
| | | | | | $\pi_{62.00} - \gamma_{63.33}$ | −5.1 |
| $\Sigma^{\pm}$, $\Sigma^o$ | 1189.4 | 1192.5 | $\pi_{63.67}$ | 10.0,13.1 | $\gamma_{64.00} - \pi_{65.00}$ | 1.7, −1.4 |
| | 1197.4 | | | 18.0 | | −6.3 |
| $\Xi^-$, $\Xi^o$ | 1321.2 | 1314.9 | $\gamma_{64.33}$ | 4.3, −2.0 | $\pi_{62.33} - \gamma_{64.00}$ | −8.5, −2.2 |
| $\Omega^-$ | 1672.5 | ··· | $\gamma_{64.00}$ | 13.3 | $\pi_{62.33} - \gamma_{64.33}$ | −17.5 |
| $\pi^{\pm}$, $\pi^o$ | 139.6 | 135.0 | $\pi_{66.75}$ | 0.4, −4.2 | $\gamma_{67.00} - \pi_{67.75}$ | −1.8, 2.8 |
| | | | | | $\gamma_{66.00} - \pi_{65.75}$ | −3.1, 1.5 |
| $K^{\pm}$,$K^o$ | 493.7 | 497.7 | $\gamma_{65.75}$ | 0.4, 4.4 | $\pi_{63.33} - \gamma_{64.75}$ | 5.7, 1.7 |
| | | | | | $\pi_{64.33} - \gamma_{66.75}$ | 2.6, −1.4 |
| $\eta^o$ | ··· | 547.4 | $\pi_{64.75}$ | −9.2 | $\gamma_{65.00} - \pi_{65.75}$ | 3.9 |
| | | | | | $\gamma_{64.00} - \pi_{63.75}$ | −1.4 |
| $F^{\pm}$ | 1968.5 | ··· | $\gamma_{63.75}$ | −4.6 | $\pi_{61.33} - \gamma_{62.75}$ | 29.1 |
| | | | | | $\pi_{62.33} - \gamma_{64.75}$ | 16.8 |
| $Z^o$ | ··· | 91187 | None | ··· | $\gamma_{57.00} - \pi_{57.00}$ | 1367 |
| $W^{\pm}$ | 80220 | ··· | None | ··· | $\gamma_{58.00} - \pi_{59.25}$ | 778 |
| $e^{\pm}$ | 0.511 | ··· | $\gamma_{75.67}$ | 0.0006 | $\pi_{73.67} - \gamma_{75.33}$ | −0.0023 |
| | | | | | $\pi_{74.00} - \gamma_{76.00}$ | −0.0020 |
| $\mu^{\pm}$ | 105.7 | ··· | $\gamma_{68.00}$ | 2.0 | $\pi_{64.00} - \gamma_{65.00}$ | 0.8 |
| | | | | | $\gamma_{67.33} - \pi_{68.00}$ | 0.4 |

guished when they differ in mass-energy. The transition energy is given for each particle or set of particle forms. Asterisks mark transitions which appear to be most appropriate. Deviations from actual particle masses are shown on the line below transition energies; parentheses distinguish less likely associations. The last column refers to notes associated with subsequent discussion. Actual particle mass energies are shown above each particle column. Associated levels and level energies are listed above the particle mass-energies.

The first part of the table concern 3-d gamma levels which apply to the basic leptons and the $\Xi$ and $\Omega$ baryons. The first two transitions listed connect to the gamma sequence symmetrically around the gamma level involved and match the level very closely. Actual particle masses are well matched, especially for the electron and the neutral cascade particle (where charge related corrections might be expected to be less important). The first transition also connects the cascade particle to level 64, the key level associated with all particle structures. Except for the muon, energies match within about one percent. The last two lines in the 3-d gamma level table show much better fits to the muon. The first of these transitions provides a direct connection to level 64 for muons, completing an association of level 64 with all the low energy stable fermions. The final line, which also fits the muon well, is a unique fit directly involving the particles own level in the opposed sequence. As discussed

## Table 5 Transition Matches

| 3-d Gamma Level Matches | | | | | | | |
|---|---|---|---|---|---|---|---|
| Level Energy | | 0.5104 | 103.70 | 1316.88 | ← | 1659.16 | |
| Level Fit | | 75.67 | 68.00 | 64.33 | ← | 64.00 | |
| Mass Energy | | 0.5110 | 105.7 | 1314.9 | 1321.2 | 1672.5 | |
| Transition | %Dev | $e^{\pm}$ | $\mu^{\pm}$ | $\Xi^{o}$ | $\Xi^{-}$ | $\Omega^{-}$ | Notes |
| $\pi_{-2.00} - \gamma_{-0.33}$ | −0.3 | 0.5087 | 103.37 | *1312.71 | ← | 1653.9 | note 1,2 |
| | | −0.0023 | −2.3 | −2.2 | −8.5 | −18.6 | |
| $\pi_{-1.67} - \gamma_{+0.33}$ | −0.25 | 0.5090 | 103.44 | 1313.57 | ← | *1655.0 | note 2 |
| | | −0.0020 | −2.3 | −1.3 | −7.6 | −17.5 | |
| $\pi_{-4.00} - \gamma_{-3.00}$ | +2.7 | 0.524 | *106.50 | 1352.5 | ← | 1704.0 | note 3 |
| | | (+0.013) | +0.8 | (+38) | (+31) | (+32) | |
| $\gamma_{-0.67} - \pi_{+0.00}$ | +2.3 | 0.522 | 106.10 | 1347.4 | ← | 1697.7 | note 4,5 |
| | | (+0.011) | +0.4 | (+32) | (+26) | (+25) | |
| 3-d Pi Level Matches | | | | | | | |
| Level Energy | | 936.08 | ← | → | 1179.39 | ← | |
| Level Fit | | 64.00 | ← | → | 63.67 | ← | |
| Mass Energy | | 938.3 | 939.6 | 1189.4 | 1192.5 | 1197.4 | |
| Transition | %Dev | $p$ | $n$ | $\Sigma^{+}$ | $\Sigma^{o}$ | $\Sigma^{-}$ | Notes |
| $\gamma_{+0.33} - \pi_{+1.33}$ | +1.0 | *945.39 | ← | → | *1191.12 | ← | note 6 |
| | | +7.1 | +5.8 | +1.7 | −1.4 | −6.3 | |
| $\gamma_{+0.00} - \pi_{+0.33}$ | −2.1 | 916.19 | ← | → | 1154.33 | ← | note 7,8 |
| | | (−22) | (−23) | (−35) | (−38) | (−43) | |
| 4-d Gamma Level Matches | | | | | | | |
| Level Energy | | 493.27 | ← | 1973.09 | | | |
| Level Fit | | 65.75 | ← | 63.75 | | | |
| Mass Energy | | 493.7 | 497.7 | 1968.5 | | | |
| Transition | %Dev | $K^{\pm}$ | $K^{o}$ | $F^{\pm}$ | | | Notes |
| $\pi_{-1.75-0.67} - \gamma_{-1.00}$ | +1.2 | *499.39 | ← | 1997.58 | | | note 2 |
| | | +5.7 | +1.7 | +29.1 | | | |
| $\pi_{-1.75+0.33} - \gamma_{+1.00}$ | +1.2 | *496.33 | ← | *1985.33 | | | note 2 |
| | | +2.6 | −1.4 | +16.8 | | | |
| 4-d Pi Level Matches | | | | | | | |
| Level Energy | | 139.15 | ← | 556.60 | 1113.20 | | |
| Level Fit | | 66.75 | ← | 64.75 | 63.75 | | |
| Mass Energy | | 139.6 | 135.0 | 547.4 | 1115.7 | | |
| Transition | %Dev | $\pi^{\pm}$ | $\pi^{o}$ | $\eta^{o}$ | $\Lambda^{o}$ | | Notes |
| $\gamma_{+0.25} - \pi_{+1.00}$ | −1.0 | 137.82 | ← | *551.28 | *1102.57 | | note 9,10 |
| | | −1.8 | +2.8 | +3.9 | −13.1 | | |
| $\gamma_{-0.75} - \pi_{-1.00}$ | −1.9 | *136.49 | ← | 545.97 | 1091.93 | | note 10,11 |
| | | −3.1 | +1.5 | −1.4 | −23.8 | | |
| $\pi_{-1.75} - \gamma_{-0.75+0.33}$ | −0.2 | 138.82 | ← | 555.29 | 1110.57 | | note 12 |
| | | (−0.8) | (+3.8) | (+7.9) | −5.1 | | |

Note 1: Connects $\Xi$ to level $\gamma_{64.00}$.
Note 2: Symmetric about $\gamma$ level.
Note 3: Connects $\mu$ to level $\pi_{64.00}$.
Note 4: Relates to $\mu$ and (t,c,d) quarks.
Note 5: Connects $\Omega$ to level $\pi_{64.00}$.
Note 6: Connects $\Sigma$ to level $\gamma_{64.00}$.
Note 7: Relates to (b,s,u) quarks.
Note 8: Connects $p, n$ to level $\gamma_{64.00}$.
Note 9: Connects $\Lambda$ to level $\gamma_{64.00}$.
Note 10: Symmetric about $\pi$ level.
Note 11: Connects $\eta$ to level $\gamma_{64.00}$.
Note 12: Allows $\Lambda$ as a 3-d to 3-d transition.

later this match may be associated with quarks as well as the muon lepton.

The second part of the transition table concerns 3-d pi sequence matches corresponding to the basic nucleons, protons and neutrons, and the sigma baryon. One transition fits these baryons and matches the pi energy level within one percent. This transition also links sigma particles to level 64. As with cascade particles, the transition fit to the neutral sigma is very good. A second transition listed resembles the last gamma match by connecting to the particles own level in the opposite energy sequence. These transitions do not closely match the baryons, but may associate with quark energies and certain properties of leptons. This transition does however connect the proton and neutron to level $\gamma_{64.00}$. All the baryons have such a connection (or occupy) this remarkably central level in the gamma sequence.

If the $\gamma_{64.00}$ level represents a mass-energy limit for ordinary stable particles the corresponding limit in the pi sequence should fall somewhat below level $\pi_{63.00}$ This limit is shown in figures 4.6 and 4.7 as a row of asterisks. Indeed, the next more massive particle, the D meson which occupies level $\pi_{63.00}$, requires the introduction of the charmed quark to create a new hierarchy of particles. An additional limit, shown below level $\pi_{62.00}$ restricts transitions. All transitions from above this level to below $\gamma_{64.00}$ will exceed the $\gamma_{64.00}$ level energy. Figures 4-6 and 4-7 show that the $\Xi$ and $\Omega$ transitions fall within this limit as required. The F meson transition, shown in figures 4-6 and 4-7 with a solid line, exceeds the limit and therefore also involves the charmed quark. Certain transitions which may be forbidden or fall out of the normal particle range are shown with dashed lines.

The third part of the transition table concerns the $K$ and $F$ mesons associated with 4-d levels in the gamma sequence. Two transition symmetries about the gamma level involved provide satisfactory fits, again especially good for the neutral particle, the $K_o$. The significance of the 3/4 (0.75) levels occupied by the mesons is now apparent. To generate a 3-d level, in this case in the pi sequence, a level shift of $-M.75$ (or $+M.25$) is required. Any other 4-d shift will not allow one to generate a 3-d level with a simple N/3 level shift, in this case to the 1/3 (N.33) 3-d level. The levels remain 4-d in the gamma sequence so the transitions are 3-d to 4-d consistent with boson properties.

The last part of the transition table concerns the $\pi$ and $\eta$ mesons, along with the $\Lambda$ baryon, which occupy what appear to be 4-d levels in the pi sequence. We again see two transitions symmetric about the pi sequence level involved. This dual transition symmetry applies to all the particles except the pi sequence baryons which are the lowest level ones. The best fit (by percent deviation) is again a neutral particle, the $\eta_o$. We again see a $-M.75$ or $M+.25$ level shift necessary to provide a 3-d connection, in this case at the N.00 level on the gamma end. The pi level remains at 4-d, hence these transitions connect 3-d to 4-d (or 4-d to 4-d but there is no apparent role for such transitions). These transitions link both the $\Lambda$ and $\eta$ particles to the key level 64. The fit is not especially good for the $\Lambda$ particle and the presence of this particle in the 4-d pattern appears to violate the expected 3-d character of fermions. The last transition shown in the transition table may resolve this issue. The pi level involved resides at N.00 which may be either 3-d or 4-d while the end is set to a 3-d N.33 level. This transition will accommodate both 3-d to 3-d or 3-d to 4-d connections to complete the baryon 3-d symmetry. We further see that this transition is now an excellent fit to the $\Lambda$ mass energy as seen for other neutral particles. We will look more closely later at the character of the $\Lambda$ particle in relation to the distinction between fermion and boson structures.

To summarize, we can represent virtually all the low energy particles. Level 64 is central, and the region around it contains no obvious gaps. The pattern contains two energy sequences of the form expected from period doubling. The basic fermions fill, and transitions connect, 3-d levels. Since fermions involve only mass-energy they should be, and are, consistent with three dimensions. The mesons, as bosons, populate fourth root levels associated with a force related 4-d geometry. They associate specifically with the three-quarter power of two, and transitions can connect 4-d to 3-d levels. The weak force is central to stable particle decays involving transitions between the gamma and pi energy mode sequences where azimuthal and radial quantization forms appear to be involved. Such decays can relate four dimensional forces and bosons to three dimensional fermionic mass energy. The neutrino appears to be what accounts for the odd fourth temporal dimension involved in such transitions. The strong force is not directly involved in energy mode transitions between the pi and gamma patterns, it is involved primarily with excitation within the individual energy modes. Certain issues remain for discussion, for example what exactly are the leptons, and what function do they fulfill in the particle game.

## 4.6 Energy Levels, Moving up to Level 56

As the higher energy domain and more exotic particles are considered, including gauge bosons, the Higgs resonance and quarks, a few points should be clarified. One issue involves the meaning and significance of specific doubling levels in QTC. I will use the tau lepton and gauge bosons to introduce the subject. The tau lepton was not found to associate with a specific level or transitions in the stable particle low energy discussion. The muon and the electron have been associated with appropriate levels and transitions, but there is much more to come. In QTC leptons appear to serve certain limiting functions related to other classes of particles and may not be structurally similar. They will be discussed in detail later. Table 4 contains the gauge bosons, the $Z_o$ and $W$ particles, which are only moderately well represented in the Lehto-Tifft model. The weak force has been associated with transitions between the gamma and pi energy sequences. The gauge bosons confirm that association. As with the tau lepton there are no level fits for the gauge bosons, but there are adequate transition fits as though the particles exist only in relation to transitions, not as stable particles of the Lehto-Tifft class. One very interesting relationship does connect the $Z_o$ particle with the electron, the stable end result of weak decays. The electron-positron mass energy is represented by the power ratio $224/3 = 74.67$. An equivalent $Z_o$ pair is matched between between levels 56 in both sequences. At $56 = 224/4$ the $Z_o$ boson appears to be a different arrangement of the same $N = 224$ level which defines the electron, a fermion. Levels 56 and 74.67 also associate with quark properties and the Higgs resonance. We will subsequently see that these levels mark upper and lower bounds for quark rest masses.

What then is a Lehto-Tifft energy level? There appears to be one or more basic energy structures which exist at the Planck level. They will be introduced in subsequent discussions of quarks, the Higgs resonance and the nature of the fundamental forces. Lehto-Tifft levels represent, or at least include, specific quantized energy levels generated by a basic doubling process. It appears that as universal energy density decay proceeds, the closer an energy structure or resonance matches a L-T level the more likely it can successfully transform, at least briefly, to a sigma-space particle. Many energy 'resonances' may exist but only those

close enough to, able to transform to, or with long enough lifetimes, can enter an L-T level as a particle in sigma-space. Also, as energy increases L-T level spacing increases limiting eligible energies. Finally there must be compatible stable spatial structural configurations possible at the energy involved in sigma-space, for example a stable form of 3-d dynamics or its equivalent. There appear to be at least two doubling levels possible where these conditions can be met, level 64 and 56 around which known particles or at least transient resonances can exist. The role of level 64 has already been discussed. The possible role of level 56 will be discussed subsequently in relation to quarks and the Higgs resonance.

### 4.6.1 An Overview of Two Spaces

Since the original version of seminar 4 was written before certain findings, such as the Higgs discovery, a brief review of aspects of QTC is useful before discussing some topics which were added to seminar 4 later. A summary of the structural model of QTC and the mechanism that appears to reduce time or temporal structures to the 1-d or particle form perceived in sigma-space may be useful.

As introduced in section 2.2 (4.2.2), two three dimensional spaces have been proposed, one temporal and one spatial, moving relative to one another at the speed of light. This results in each space perceiving the other as one dimensional by the action of aberration. Physics in such spaces will develop in a form locally consistent with conventional 4-space. Since photons are stationary in time the model is consistent with special relativity and constancy of the speed of light. Time will be perceived as a one dimensional flow from within space. A basic symmetry exists between time and space, each being three dimensional but perceiving the other as one dimensional. There is no reason to limit time to a one dimensional format, and observations turn out to be inconsistent with that concept or require complex 'patches' (such as dark energy) to make it work. In the 3-d mode of time quantum physics may be associated with 3-d time (or the actions within it) and continuous dynamical physics with 3-d space. Both domains of physics may co-exist. QTC cosmology based upon this concept is the subject if seminars 6 through 8

Three dimensional volumes of temporal (tau) space are associated with energy (the reciprocal of time) which can be spatially perceived as particulate mass traveling with space. Mass is a 'passive' form of energy, a manifestation of a form of 3-d stable action or resonance in temporal space. In this view what is a photon? The photon is a massless action; since we associate the three dimensional concept with passive mass-energy the photon cannot be a three dimensional entity. QTC therefore views the photon, a form of 'active' energy, as a two dimensional 'lateral' action, energy without volume. The jump between temporal and spatial space effectively adds (or deletes) a third 'radial' component related to the relative spatial flow. The photon form of active energy, not having made this transformation, resides in the temporal space and is perceived as photons moving through space at the speed of light. Matter having made the jump acquires the third radial dimension and is characterized as energy volumes appearing as particulate mass. Particles also have kinetic energy associated with excess energy from formation or interaction, which appears as continuous spatial motion. This in-space motion is subject to the rules of special relativity and is distinct from flow *between* spaces in tau. Flow of sigma-space through tau is a temporal flow, decay or aging in time, not a spatial flow. More formally it is the rate of change of time in sigma.

Important properties of space-time follow from the above structure. In seminar 2 the Cosmic Background effect was introduced (2.8.0) as being caused by lag in the temporal flow of matter with respect to empty space due to retardation of time by relativistic motion within constituent particles, primarily protons. The precise match between predicted and observed global redshift quantization rules out the conventional explanation of the CBR dipole being caused by random motion of galaxies since that would destroy redshift quantization. The lag has other important consequences. Aberration is not quite complete in folding temporal space to a one dimensional timeline, or from the temporal viewpoint folding space into a spaceline. The connection between space and time is therefore slightly fuzzy, an admixture which provides an origin for the uncertainty concept. The mixture assures that energy levels will be diffuse making transitions possible, explains simple effects such as why a photon cannot distinguish between slits in double slit experiments, and more complex things such as why particle interaction effects have to allow for all possible trajectories in Feynmann diagrams or their newer simplified versions. The diffuse association of space and time plays an important role in QTC.

Interactions within and between particles, or between particles and active energy, involve forces. Force involves energy operating over distance hence is four dimensional in the Lehto-Tifft model. Pair formation can be understood in dimensional terms in such a model. Two dimensional active photon energies, interacting and distributing over a third spatial component, generate 3-d particles (or particle anti-particle pairs inversely annihilate to photons) by adding or deleting the radial dimension. The standard pair formation process from the point of view of QTC is discussed in seminar 6. Ordinary particle reactions differ. Three dimensional passive energy (particles) acting over distance produce other three dimensional particles. If interactions involve both 4-d and 3-d particles, in weak transitions between the pi and gamma energy sequences, the odd fourth dimension must be accounted for. As noted earlier the neutrino enters as a product in such interactions. The neutrino as a particle must involve three dimensions, yet be massless (or nearly so), to leave 3-d mass but take away or nutralize an associated fourth dimension. This is equivalent to pair annihilation *without* destroying mass, a particle equivalent of a pair annihilation photon. A planar (volume-less) action is suggested which involves three dimensions. Such an action might be provided by a diagonal plane in a 3-d energy structure. It could also perhaps be a 3-d particle with a mix of spatial and temporal dimensions. I will later introduce a concept of triads involved in particle structure. Like photons, neutrinos propagate through space at near light speed, but unlike photons participate in weak structural interactions.

A possible further commentary regarding the neutrino may be warranted. In QTC the perceived speed of light is the reflex of the temporal flow of matter through tau-space. As noted previously the flow (aging) of matter is retarded from the flow of massless space. To the extent that the neutrino may be structurally different from normal 3-d mass its apparent spatial flow rate could conceivably be different from ordinary matter. It is conceivable that the lightest neutrinos could appear to move slightly faster through sigma-space than photons.

## 4.7 Quarks and Lepton Limits

Before discussing fundamental forces I will probe a bit further into the substructure of matter. Leptons behave essentially as point particles, but hadrons contain quark substructures.

Free quarks are never seen but masses of particles constructed from quarks may be described as the rest mass of their quarks plus relativistic corrections from quark motion and other possible contributions to the binding energy. As noted earlier, such sources of mass-energy make it impossible to precisely predict composite particle masses from the first order Lehto-Tifft model. Photon energies involved in redshift measurements are fit precisely, perhaps because such corrections do not apply to massless photons. I will begin by introducing a model of quark masses within the Lehto-Tifft model then consider their relationship to the Higgs resonance and concepts regarding the substructure of matter at the Planck level. The results provide insight into interrelations between particles.

I did not try to model quark rest masses originally because relativistic corrections involving the low mass quarks dominate the ordinary stable particle masses. However, an adjunct faculty member at Pima Community College, Jerry Long, had derived an empirical relationship between various particles, including quarks, which somewhat resembled a Lehto-Tifft series. Expanding upon Long's work I developed a logical pattern of possible rest masses for quarks. In conjunction with investigations at energy level 56 the quark study led to important insight relating to finer substructure within matter.

To be consistent with Lehto-Tifft, quarks, which are fermions, should fit within gamma and pi sequence cube root patterns. Figure 4.8 and Table 6 illustrate and list level and transition energies found. Cube root classes are indicated at the top of figure 4.8 and transitions are shown between asterisks. Level and transition matches are given in Table 6. Figure 4.7 also shows quark levels in square brackets for the strange, charmed and bottom quarks. Other features in figure 4.8 are discussed below. Masses for the heavy quarks are reasonably known since relativistic corrections are fairly small. The charmed and bottom quarks can be assessed using charmonium and bottomonium spectra, which are excitation spectra of bound charm anti-charm or bottom anti-bottom quark pairs where energy levels correspond with specific hadrons of known mass-energy. The charmonium spectrum is shown below figure 4.8. The lowest level, the singlet $s$ state, is the $\eta_c$ boson. The charmed quark energy level should be less than half of the $\eta_c$ mass to allow for relativistic corrections. A consistent Lehto-Tifft level places the charmed quark in level 64.33 of the gamma sequence. By a similar process the bottom quark appears to be consistent with level 62.67 in the pi sequence. Direct estimates of the top quark match gamma level 57.33 quite unambiguously. The three low mass quarks are more problematical; typical estimates [AK] place the strange quark somewhere near 150 MeV and the down and up near 10 and 5 MeV. Levels consistent with these numbers place the strange quark in pi level 66.67 and the down and up in gamma level 71.33 and pi level 71.67. If we examine the overall pattern in these level matches we discern an interesting pattern. The gamma sequence quarks, the top, charm, and down quarks, are separated by factors of $2^7 = 128$. The pi sequence quarks, the bottom, strange and up quarks are separated by factors of $2^5 = 32$. These connections are shown symbolically in figure 4.8 between related quarks. It is interesting to note that if these relationships had been seen prior to detecting the top quark its mass could have been predicted in advance.

Why does the quark sequence not continue to lower energies consistent with further decay? If you go another step two things happen, the gamma level drops below the pi level and the electron is encountered. The electron seems to terminate the quark series. The next level in a quark pattern would be $\pi_{76.67}$, shown with an $(X)$ in figure 4.8. The electron pair was shown to be represented by a 128-64-32 doubling structure. The pattern incorporates the

Quark Levels and Transitions

| Level | $\gamma_{.00}$ | | $\pi_{.00}$ | $\gamma_{.67}$ | | $\pi_{.33}$ | $\gamma_{.33}$ | $\pi_{.67}$ |
|---|---|---|---|---|---|---|---|---|
| 56 | | | | * | | | | $(X)$ |
| | | | | | $t$ | | | |
| 57 | * | $Z$ | * | | | * | $t$ | |
| 58 | | | | | | | | |
| 59 | | | | | | | | |
| 60 | | | | | | | | |
| | | | | | | | $\downarrow 2^7$ | |
| 61 | | | | * | | | | $b$ |
| | | | | $b$ | | | | |
| 62 | | | * | | | | | |
| 63 | | | | * | | | | |
| | | | | | $c$ | | | $\downarrow 2^5$ |
| 64 | | | | | | * | $c$ | |
| 65 | | | | | | | | |
| 66 | | | | * | | | | $s$ |
| | | | | $s$ | | | | |
| 67 | | | * | | | | | |
| | | | | | | | $\downarrow 2^7$ | |
| 68 | | | | | | | | $\downarrow 2^5$ |
| 69 | | | | | | | | |
| 70 | | | | * | | | | |
| | | | | | $d$ | | | |
| 71 | | | | * | | * | $d$ | $u$ |
| | | | | $u$ | | | | |
| 72 | | | * | | | | | |
| 73 | | | | | | | | |
| 74 | | | | | | | | $e\bar{e}$ |
| 75 | | | | | | | | $e$ |
| 76 | | | | | | | | $(X)$ |

Figure 4.8: Energy levels and transitions of quarks showing their relationship to level 56, the $Z_o$ gauge boson and the electron.

Charmonium Energy Levels

| Part | $s=0$ $l=0$ $j=0$ | E(Mev) | Part | $s=1$ $l=0$ $j=1$ | E(Mev) | Part | $s=1$ $l=1$ $j=0,1,2$ | E(Mev) |
|---|---|---|---|---|---|---|---|---|
| | | | $\psi(2s)$ | ——— | 3686 | | | |
| $\eta_c(2s)$ | ——— | 3594 | | | | | | |
| | | | | | | $\chi_{c2}(2p)$ | ——— | 3556 |
| | | | | | | $\chi_{c1}(2p)$ | ——— | 3511 |
| | | | | | | $\chi_{c0}(2p)$ | ——— | 3415 |
| | | | $\psi(1s)$ | ——— | 3097 | | | |
| $\eta_c(1s)$ | ——— | 2980 | | | | | | |

**Table 6**
Quark Level and Transition Energies

| Particle | E(lv) Mev | Level | E(tr) Mev | Transition |
|---|---|---|---|---|
| $Z\bar{Z}$ | ··· | None | 185109. | $\gamma_{56.00} - \pi_{56.00}$ |
| $t$ | 168560. | $\gamma_{57.33}$ +7 | 172473. | $\gamma_{56.67} - \pi_{57.33}$ |
| $c$ | 1317. | $\gamma_{64.33}$ +7 | 1347. | $\gamma_{63.67} - \pi_{64.33}$ |
| $d$ | 10.3 | $\gamma_{71.33}$ < 7 | 10.5 | $\gamma_{70.67} - \pi_{71.33}$ |
| $e\bar{e}$ | 1.0 | $\gamma_{74.67}$ | | |
| $b$ | 4718. | $\pi_{61.67}$ +5 | 4617. | $\gamma_{61.67} - \pi_{62.00}$ |
| $s$ | 147.4 | $\pi_{66.67}$ +5 | 144.3 | $\gamma_{66.67} - \pi_{67.00}$ |
| $u$ | 4.6 | $\pi_{71.67}$ < 5 | 4.5 | $\gamma_{71.67} - \pi_{72.00}$ |
| $e\bar{e}$ | 1.0 | $\gamma_{74.67}$ | | |

two quark scaling numbers symmetric abound the key number 64. This certainly suggests a relationship between quarks and the electron. Since the gamma and pi sequences may include vector model structures it also implies that electrons and quarks may have finer structures. Note I am not associating leptons in general with the quarks, just the electron. I will shortly explain why.

Table 6 summarizes level and transition fits for quarks. Each level has a matching Fermi transition involving cube-root levels. The transitions were identified in Table 5 as ones connecting to a given particles level in the opposite sequence. No attempt has been made to model electric charge for quarks, but the quark matches involve only occupation levels and level changes of 1/3 or 2/3 and all transitions involve $\gamma_{N.67}$ levels.

If the electron defines the lower bound for the quark pattern, what defines the top? The answer is particles associated with L-T level 56 including the gauge bosons and the recently defined Higgs boson. I have already noted that the electron-positron pair has an interesting structural relationship to the $Z_o$, both appear to relate to forms of N=224 configurations. The quark sequence falls within these limits, extending only one cycle above or below the central level 64. Extensions above or below these limits change the mass-energy relationship between consecutive quark pairs. The upward extension of the pi sequence is shown with an $(X)$ symbol (where a $Z_o$ pair transition would fit the pattern in figure 4.8 at level 56). Figure 4.9 contains a more detailed picture of levels at the top of the quark sequences. The top quark occupies the 57.33 gamma level whereas the $Z_o$ appears to be represented by the transition between levels 57.00 in both sequences.

## 4.8 The Structure of Fundamental Particles

At this point it is useful to bring together all the particle types to examine and relate them in terms of possible multi axial structure. Studies during 2012, including the Higgs

Gauge Boson Transition Energies

| Level | Particle | $E_\gamma$ Mev | Trans | $E_\pi$ Mev |
|---|---|---|---|---|
| 56.00 | | 424746 | | |
| .25 | | | | |
| .33 | | | | |
| .67 | | | | |
| .75 | | | | |
| 57.00 | | 212373 | $\leftarrow Z_o \rightarrow$ | 119819 |
| .25 | | | | |
| .33 | $t$ | 168560 | | |
| .67 | | | | |
| .75 | Higgs | 126278 | | |
| 58.00 | | 106186 | | |
| .25 | | | ↓ | |
| .33 | | | ↓ | |
| .67 | | | $W^\pm$ | |
| .75 | | | ↓ | |
| 59.00 | | | ↓ | |
| .25 | | | | 25189 |
| .33 | | | | |

Figure 4.9: Relationships of the Gauge Bosons, the Higgs Resonance and the top quark just below level 56

resonance and properties of quarks led to the present concept of particle structure within QTC. The first part of Table 7 introduces some basic energy level components relating to doubling levels 56 and 64. The table then summarizes proposed structures related to the Higgs resonance, quarks, light mesons, baryons, and within them the two lightest leptons. There are some remarkable patterns present.

Table 7 begins with the number 7 which appears to be quite basic to QTC. It represents the smallest non-degenerate tri axial doubling pattern, 4 2 1, which appears to play a central role within possible $l, m, n, i$ structures and actions. I will refer to the pattern as a 'triad'. The significance of the triad will become especially clear in relation to quarks and the fundamental forces. The numbers 56 and 64 are basic doubling levels from which L-T structures are constructed. 56 is a multiple of 7 hence multiplets of 56 contain exact multiples of the base 7 structure. The 4-d and 3-d multiplets of 56 and 64 are the base templates for Bose (boson) and Fermi (baryon, quark and lepton) particles. The final arrangement shown, the electron pair structure, is an alternate 3-d arrangement of the $4 \times 56 = 224$ boson pattern. 64 and its multiplets are not multiples of 7 but provide the powers of two patterns basic to the doubling process by which energy degrades as matter flows through time. Subsequent columns at the top of Table 7 provide the total doublings involved, the doubling or multiplet level notation, the binary representation of the total doubling and a description or designation of each feature.

# Table 7 Structural Patterns

| Pattern | Sum | Level | Binary | Description |
|---|---|---|---|---|
| 7 | 7 | 7.00 | 4 2 1 | quantum base structure |
| 56 | 56 | 56.00 | 32 16 8 | 8 base sub structure |
| 64 | 64 | 64.00 | | smallest cube and square |
| 56 56 56 56 | 224 | 56.00 | 128 64 32 | 4-d Higgs neutral base |
| 56 56 56 | 168 | 56.00 | 128 32 8 | 3-d Quark neutral base |
| 64 64 64 64 | 256 | 64.00 | | 4-d hadron base |
| 64 64 64 | 192 | 64.00 | | 3-d hadron base |
| 128 64 32 | 224 | /3=74.67 | | Electron pair $e\bar{e}$ |

Higgs structure

| Chg | Pattern growth | | | | Properties | | | Comments |
|---|---|---|---|---|---|---|---|---|
| | 56 | 56 | 56 | 56 | +224 | | | 4-d form 32-16-8 |
| +3 | 1 | 1 | 0 | 1 | | | | |
| | 57 | 57 | 56 | 57 | gamma | 2->S | /4=56.75 | Sum = 227 |
| +4 | 3 | 3 | 0 | 0 | | | | |
| | 59 | 59 | 56 | 57 | gamma | 6->P | /4=57.75 | H E=126778 Kaon-like |

| Quark structure Chg | Pattern growth | | | | Gamma set Base mult | Pi set Base mult | Binary form |
|---|---|---|---|---|---|---|---|
| | 56 | 56 | 56 | 56 | 32x7 | 224 4-d form | 128-64-32 |
| 1 | | | <- 1 | | | | |
| | 56 | 56 | 56 | | 24x7 | 168 3-d form | 128-32-8 |
| 3 | 1 | 1 | 1 | | | | |
| 21- | 57 | 57 | 58 | | 172 Top quark /3=57.33 24x7+4 | | 128-32-8-4 |
| \| | | | | | | | |
| 15- 7 | 61 | 62 | 62 | | | 185 Bottom quark /3=61.67 26x7+3 | 128-32-16-8-1 |
| \| \| | | | | | | | |
| 5 - | 64 | 64 | 65 | | 193 Charm quark /3=64.33 27x7+4 | | 128-64-1 |
| \| \| | | | | | | | |
| - 7 | 66 | 67 | 67 | | | 200 Srange quark /3=66.67 28x7+4 | 128-64-8 |
| \| \| | | | | | | | |
| 5 - | 71 | 71 | 72 | | 214 Down quark /3=71.33 30x7+4 | | 128-64-16-4-2 |
| \| | | | | | | | |
| - - | 71 | 72 | 72 | | | 215 Up quark /3=71.67 30x7+5 | 128-64-16-4-2-1 |
| 3 | 3 | 3 | 3 | | | | |
| - | 74 | 75 | 75 | | 224 $e\bar{e}$ pair | | 128-64-32 |
| 1 | 1 | 1 | 1 | | | | |
| - | 75 | 76 | 76 | | 227 Electron | | |

Meson structure

| Chg | Pattern growth | | | | Properties | | | Comments |
|---|---|---|---|---|---|---|---|---|
| | 64 | 64 | 64 | 64 | =256 | | | 4-d Hadron base |
| | 0 | 0 | 0 | -1 | | | | |
| | 64 | 64 | 64 | 63 | | | /4=63.75 | $\bar{E}$taEta form |
| \| +1 | 0 | 0 | 0 | 1 | | | | |
| \| | 64 | 64 | 64 | 64 | =256 | | | 4-d Hadron base |
| \| +3 | 1 | 1 | 0 | 1 | | | | |
| | 65 | 65 | 64 | 65 | pi | 2->S | /4=64.75 | Eta |
| +4 | 3 | 3 | 0 | 0 | | | | |
| | 67 | 67 | 64 | 65 | gam | 6->P | /4=65.75 | Kaon |
| +4 | 5 | 5 | 0 | 0 | | | | |
| | 69 | 69 | 64 | 65 | pi | 10->D | /4=66.75 | Pion |
| +1 | -1 | -1 | +4 | -1 | | | | restructure |
| | 68 | 68 | 68 | | gam -> muon | | /3=68.00 | Muon |
| | 4 | 4 | 4 | | | | | |

Baryon structure

| Chg | Pattern growth | | | | Properties | | | Comments |
|---|---|---|---|---|---|---|---|---|
| | 64 | 64 | 64 | 64 | | | | 4-d hadron base |
| | 0 | 0 | -1 | 0 | | | | |
| | 64 | 64 | 63 | 64 | pi | =255 | /4=63.75 | Lambda (hybrid form) |
| | 0 | 0 | -1 | | | | | |
| | 64 | 64 | 63 | | pi | =191 | /3=63.67 | Sigma |
| +1 | 0 | 0 | 0 | | | | | |
| | 64 | 64 | 64 | | pi | =192 | /3=64.00 | Proton,neutron (symmetric) |
| | | | | | gam | | | Omega |
| +1 | 0 | 0 | 1 | | | | | |
| | 64 | 64 | 65 | | gam | =193 | /3=64.33 | Cascade |

### 4.8.1 Making Mesons, With A Lepton Limit

Before discussing the Higgs and quarks it is useful to review the light mesons and the baryons in the two lowest sections of Table 7. Multiplet structural patterns are shown at the left, beginning with a 4-d hadron base defined at the top of the table. Cumulative changes to multiplet terms to generate the next lower particle are given below each term. When in 3-d form the changes are consistently put in the third column. Total step by step changes to a line are offset to the left. The top line in each lower section, the 4-d hadron base, is a representation of a 4-d metric structure of 64. The first three figures represent temporal terms, the fourth number the spatial term, of a 4-d temporal metric. This 4-d basic pattern never appears as a particle although it may be involved in a particle anti-particle pair process. It is useful to point out that the four 64 terms sum to $256 = 36 \times 7 + 4$, a common variant ($\pm 1$) of multiples of 7 which will be frequently seen. To generate mesons now reduce the spatial term by one to generate the unstable 4-d $\pi_{63.75}$ eta anti-eta meson level. A pair formation process can now produce eta mesons by adding four more axial units, two returning to the uniform 64 state and advancing one beyond, a process symbolically neutralizing one temporal unit, leaving two active (boson-like) terms. Advancing each of these terms by one will generate (symbolically) the neutral two quark S-state eta meson. Subsequent additions in steps of four (two in each of the two active terms) generates successive P and D radial shell vector states to represent the kaon and pi mesons. I use the convenient S, P, D vector shell notation since the successive 2-6-10 net doubling change in steps of 4 per level could indicate that such underlying real structural changes occur.

Why does the process not continue to produce still lighter mesons? At the kaon the pattern is 11 units in advance of the neutral 4-d hadron state. Addition of one more unit permits the system to transform to the symmetrical 68 68 68 3-d energy state, terminating the light meson sequence by generating a muon. The muon lepton appears to terminate the light meson series just as the electron lepton terminates the quark sequence. Each step in the light meson sequence also involves the number 4 as indicated in the left margin of figure 4.7. Successive additions of 4 generates the eta S state, then successive higher meson forms, and finally terminates the series by redistribution to a symmetric 3-state muon. The last step is reminiscent of the termination of the Carbon-Nitrogen energy sequence when the 4-nucleon helium nucleus splits from carbon, and symbolically suggests the presence of underlying structure within the particles. The distinctly different structures of the electron and muon also indicate that leptons are not a structurally similar family, if they are a family at all. We will shortly see further examples of the role of 4. A line above level 67.00 in figures 4-6 and 4-7 represents the muon 'limit'. Certain hypothetical meson and meson pair extensions below the limit are shown in figure 4.7 for later use concerning meson decay patterns. Although symbolic the process does generate proper masses and realistic structures in metric form.

### 4.8.2 The Lambda Anomaly and Other Baryons

There is one further item to address. It was noted previously that the eta anti-eta occupies the same 4-d energy level, 63.75, as the Lambda baryon. The final section of Table 7 addresses this issue. Suppose the final stage of the 4-d hadron base consisted of a deficiency of one in a temporal rather than the spatial term. This is now the energy level of the Lambda particle before transformation to 3-d, a hybrid form of a 4-d meson state. There are indeed two forms of this state. Additional changes in steps of one unit can now generate

all the baryons as normal 3-d fermions. Baryons show no deviations greater than 1 from 64. They are characterized by zeros in all, or all but 1, of the 3-d multiplet index. The 4-d hadron basic template resides in the 64.00 energy level which, as shown in Table 5, contains or relates by direct transitions to all the baryons and the muon.

The baryons obviously provide an upper limit to the light meson pattern at the $\eta\bar{\eta} \approx \Lambda$ shared level which appears to explain the unique character of the $\Lambda$ baryon. Two quarks, the strange and charmed, also fall in the baryon and light meson range. The strange quark is at level $\pi_{66.67}$ just below the kaon. The charmed quark appears at level $\gamma_{64.33}$ at the point necessary to produce the higher energy $D$ meson.

### 4.8.3 A Glimpse Of Where Particles Begin

As the physics of QTC and particle physics steps back in time to level 56 and beyond I sensed a change. At the energies involved, stable things like ordinary particles struggle to even exist. It seemed to me that it was time to shift to a more basic mode and ask just what came before stable particles could be built. We see energy resonances. Is that tau knocking on the door saying there is something more basic? In 2012 I opened that door and entered the world of fundamental triads. As I shall subsequently describe, I had already glimpsed a basic triad in the definition of force, but it would take the quarks to recognize what basic triads probably were. A few final comments within the high energy particle domain provides a preparation for discussing quarks.

Since QTC provides no certain L-T level to associate with the gauge bosons I will not attempt to discuss those particles beyond presuming they are products of the the 4-d 56 level. That level can be associated with the Higgs resonance which falls at level $\gamma_{57.75} = 126278$ MeV slightly below the top quark at $\gamma_{57.33} = 168560$ MeV. The M.75 level identifies it as a boson and places it $2^8 = 256$ times more massive than the kaon although structurally it resembles the eta meson. I will return to the Higgs after discussing the structure of quarks.

The first part of Table 7 reiterates that the electron pair is represented as a rearrangement of doubling containing the same number of operations as the 64-64-64 structure. The table also illustrates how the 3-d 224 structure of the electron-positron pair can be related to the 4-d 224 structure of the $Z_o$ pair by either redistributing 224 or removing a $4 \times 8 = 32$ pattern from a 64 quartet, 8 being the smallest perfect cube. Since $224 - 32 = 192$ such an operation generates $192 = 3 \times 64$ structures. As discussed later, an extra 32 as a spatial interval associated with the electric force may relate to how electric charge is linked to triads. In the same sense linking a 64 triad with a 64 spatial term may involve the weak force.

56, associated with the gauge bosons, is in itself a rather unique number, $56 = 8 + 16 + 32$. Superposition of four such structures (or adding two doublings to each term) generates the 32-64-128 electron pair structure directly. It seems quite clear that nature has discovered a very effective process of utilizing triad arrangements of doubling structures. How much further can that process be carried? As noted earlier, the different structures and roles, at least for electrons and muons, suggest that leptons may not be a simply related family. Lehto [AJ] has made a similar comment in discussing magnetic moments. Lehto also pointed out that if you carry the redistribution of doubling numbers one step further, the energy involved when the exponent of 2 is $(16 + 64 + 256)/3 = 112 = 224/2$ matches the energy of

the 21-cm electron spin reversal in neutral hydrogen. Perhaps it should be no surprise that quarks have a close relationship to triads as well.

### 4.8.4 It Seems that Quarks Are Made of Triads

Turning now to the issue of the symbolic axial representation of quarks in the third section of Table 7, I will begin by introducing the apparent role of the base 1 2 4 = 7 triad in quark structure. The gamma and pi sets are distinguished with particle name, doubling sum, fractional level form and multiple form of 7 in the middle columns. A binary representation is provided in the final column. There is an interesting way to see how to transform between the 4-d 56 neutral base and the 3-d Fermi 56 structure. Dividing the128 64 32 form of 4-d 56 by the 1 2 4 triad term by term yields 128 32 8 = 168 = 56 56 56. The division shows that it takes three doublings, one in the second binary term and two in the third. 168 is three fourths of 224 which is the 3-d form of 56. A few doublings in the right places provide very interesting transformations. Now add one more unit to each of the three temporal axes to add to the one that triggered the dimensional transformation (conservation of dimensions from the 4 to 3-d conversion?) to symbolically generate the top quark at level 57.33 in the gamma sequence.

$$172/3 = 57.33 => 57\ 57\ 58.$$

Both the starting configurations 4-d and 3-d 56 structures are multiples of the 1 2 4 = 7 structure, thus the top quark can be represented in triad form as

$$57\ 57\ 58 = 24 \times 7 + 4.$$

This level cannot be represented by a uniformly spaced 3-d set of powers of two, as the proton and muon are. However, it differs only with the addition of a 4 which seems to be a key to maintaining triad structures. The appearance of the 4 is seen in the binary column of the quark section of Table 7. Note that the 3-d top quark symbolic axial triad, 57 57 58 differs by only 1 from a uniform set, a pattern all fermions must have (or all equal for the central uniform $T = 0$ level 64 or the muon at 68 = 64 + 4) to fit the cube root rule. Mesons differ from one another using the 4-d multi-level +4 vector shell S,P,D pattern change per level to fit the 4-d role.

Continuing down in the gamma column, the charmed quark is generated by adding 7 to each axis, $3 \times 7 = 21$, one basic 1 2 4 structure in each axis, to drop to gamma level 64.33.

$$64\ 64\ 65 = 27 \times 7 + 4$$

This places the charmed quark centrally in the quark pattern around 64, basic to all known particle structures. An identical step now leads to the down quark to complete the gamma sequence at level 71.33.

$$71\ 71\ 72 = 30 \times 7 + 4$$

The basic 1 2 4 structure is easily seen to be a fundamental component of quark and possibly all fundamental particles.

Returning to the top quark, the complete sequence of quarks may be generated sequentially. This is the beginning of a pattern which leads to the electron. The pattern development

is illustrated in three forms, the 3-d axial doubling form, the structure in terms of the 1 2 4 basic 7 triad, and the binary powers of two required to represent the total number of doublings involved in each quark. There is no implication that the sequence represents the actual process by which quarks evolved. It is intended only to show relationships between the quarks. Binary combinations used are symbolic of the real task of constructing a quark, but show the powers of two process and the 3-d tri axial form. As noted above the top quark takes the following form.

57 57 58 $\quad 24 \times 7 + 4 \quad$ 128 32 8 4

The $3 \times 7 = 21$ step through the bottom quark to the charmed quark does not divide in multiples of 7. It divides into 13 and 8, both deviating by one from multiples of 7 (which is possible for fermions). The 13 provides one 1 2 4 structure and with a 2 and 4, an 8 4 1 binary pattern, which with the top quark 8 4 yields 16 8 1 to generate the bottom quark. The base triad multiplier grows by two and the extension drops to +3, staying within one of the common $N \times 7 + 4$ pattern.

61 62 62 $\quad 26 \times 7 + 3 \quad$ 128 32 16 8 1

The step to the charmed quark adds the 8 to combine with the bottom quark 8 yielding 16. This chains up to 64 through the binary 32 16 pattern in the bottom quark, and adds one base triad multiplier returning it to +4 form. Note that this is a shared level with the Cascade particle as noted in figure 4.7, but now presumably in a triad format.

64 64 65 $\quad 27 \times 7 + 4 \quad$ 128 64 1

The 21 doubling step through the strange quark to the down quark divides as 7 and 14. Adding the 7 triad to the charmed quark cascades the binary 1 up to 8 and raises the base triad count by one while retaining the +4.

66 67 67 $\quad 28 \times 7 + 4 \quad$ 128 64 8

Addition of a dual 7 base now generates an 8 4 2 pattern to combine with the strange quark binary 8 to yield the down quark pattern and advance the base triad count by two.

71 71 72 $\quad 30 \times 7 + 4 \quad$ 128 64 16 4 2

The addition of a single doubling now generates the up quark. The base triad increments to +5, still within one of the +4 pattern.

71 72 72 $\quad 30 \times 7 + 5 \quad$ 128 64 16 4 2 1

The consistency of the formulation of the structure in terms of the 1 2 4 basic triad is clearly indicative of the importance of this 3-d structure in the actual structure of matter at the quark level. Now continuing to develop a subsequent structure the addition of 9 doubling steps leads to an interesting result. 9 = 3 3 3 or 7 2 or 8 1. All three lead to the electron pair at 128 64 32.

74 75 75 $\quad 32 \times 7 = 224 \quad$ 128 64 32

The first increments the symbolic 71 71 72 3-d fermion up quark pattern to 74 75 75 = 224 = 128 64 32 = $e\bar{e}$, the 8 1 does the same thing as a cascade within the powers of two pattern, and the 7 2 as a change of the 7 structure to exactly $224 = 7 \times 32$. All paths lead to the electron pair. The quark series is clearly bounded by the 4-d and 3-d forms of the $7 \times 32$ structure. Such exact multiples of 7 structures do not appear to exist as stable particles. The $e\bar{e}$ pattern decays immediately to the electron and positron, a split in time in QTC.

### 4.8.5 And What About the Higgs?

The development of quark structures beginning with the 56 56 56 3-d fermion base demonstrates the apparent importance of the 1 2 4 basic triad structure. One further illustration of this basic structure involves the Higgs resonance. The Higgs is a boson as attested to by its presence in the $N.75$ 4-d family of particles. Beginning with the 4-d 56 56 56 56 = $224 = 32 \times 7$ symbolic neutral base and adding 7 doublings, one 1 2 4 = 7 triad structure, generates the Higgs structure (shown in Table 7 in boson vector form).

59 59 56 57 $\quad 33 \times 7 = 231 \quad = 57.75$ level

The Higgs structure is a precise multiple of the 1 2 4 triad 7 structure, and falls below the 4-d 56 base in the gamma series by exactly one triad 7 pattern. This pattern is nearly identical to the pattern formed around the kaon by the light mesons below the 4-d 64 base. The Higgs occupies the position of the kaon in the 64 base gamma pattern. To illustrate the relationship the two patterns are illustrated below, beginning with the light mesons. The first three columns give the 4-d fractional doubling level, the energy level in MeV, and the level structure in triad multiples. The next columns give a picture of the pi energy structure (on the left) followed by an offset to the gamma structure (on the right). Each line gives a symbolic temporal metric energy form and the particle it represents below which doubling changes are shown to generate the pattern in the alternate energy sequence indicated by the arrow. The arrows are not indicative of transitions, only of changes in doubling content since the two columns have different quantum form scaling constants (4.2.3).

| | | | | | | | |
|---|---|---|---|---|---|---|---|
| 63.75 | 1113.2 | 37x7+3 | 64 64 64 63 | $\eta\bar{\eta}$, $\Lambda$ | | | |
| 64.00 | 936.1 | 37x7+4 | 1 | | $\rightarrow$ | 64 64 64 64 | 64 Gamma Base |
| 64.75 | 556.6 | 36x7+0 | 65 65 64 65 | $\eta$ | $\leftarrow$ | 1 1 1 | |
| 65.75 | 493.3 | 37x7+4 | 2 2 | | $\rightarrow$ | 67 67 64 65 | K |
| 66.75 | 139.2 | 38x7+1 | 69 69 64 65 | $\pi$ | $\leftarrow$ | 2 2 | |
| 68.00 | 102.7 | 29x7+1 | -1 -1 +4 -1 | $\mu$ | $\rightarrow$ | 68 68 68 | |

| | | | | | | | |
|---|---|---|---|---|---|---|---|
| 55.75 | 284978 | 31x7+6 | 56 56 56 55 | $X\bar{X}$ | | | |
| 56.00 | 424726 | 32x7+0 | 1 | | $\rightarrow$ | 56 56 56 56 | 56 Gamma Base |
| 56.75 | 142489 | 32x7+3 | 57 57 56 57 | $X$ | $\leftarrow$ | 1 1 1 | |
| 57.75 | 126278 | 33x7+0 | 2 2 | | $\rightarrow$ | 59 59 56 57 | H |
| 58.75 | 035622 | 33x7+4 | 61 61 56 57 | $Y$ | $\leftarrow$ | 2 2 | |

The meson pattern has been discussed (4.8.1) although the pattern shown here includes the triad aspect and shows the association of 4-d energy levels with exact multiples of 7+0 or 7+4 $\pm 1$. The pattern follows an energetically possible decreasing sequence and energy changes from pi to gamma are consistently smaller than gamma to pi as expected from direct or inverse use of the scaling constant connecting the energy sequences. Further commentary concerning actual meson decay will follow discussion of fundamental forces. Meson patterns develop below the eta in steps of 4 leading to the kaon and pion and, as noted previously (4.8.2), are associated with baryons through the lambda particle at level 63.75.

The Higgs development is essentially identical to the kaon within the mesons. The Higgs as a 7 structure below the 56 neutral base resembles the kaon meson below the 64 neutral base. The role of an equivalent 'X boson' replacing the eta meson is unclear since the initial step involving an equivalent of the lambda particle is energetically not possible. Beyond that,

equivalent developments related to the Higgs and resonances at X and Y may be possible as the 56 base is not affected by omitting the initial step. There is a pattern shift in the +4 part of the triad count, the Higgs is +0. a pure 7 multiplet, while the kaon is +4. This is a result of the 64 to 56 base switch, but both patterns define clear bosonic patterns. Particles in the high energy domain are complex. There is too little data to say much more than the similarity of the patterns, which could produce the Higgs as simply a higher level boson. The Higgs then might decay in a pattern similar to the kaon (which, as noted above, I will subsequently discuss).

I have now seen four patterns beginning at 3-d or 4-d basic binary doubling or triad structual points, the 56 3-d fermion quark association, the 3-d 64 level baryon association, the 4-d 56 light meson association and the 4-d 56 Higgs association. Three of them I have developed to closely represent the existence of most known common particles including the leptons. I have little doubt that the Higgs path should develop similarly, but that is for future study. What is clear is that the 1 2 4 triad has appeared which along with the basic doubling concept, perhaps provides one more step towards understanding the basic structure of matter. I believe that there may need to be much more thought given to the role of the triad and related developments in the early universe. In the final seminar I will provide some commentary relating to that period.

## 4.9 The Fundamental Forces

At this point I have shown that the Lehto-Tifft model can represent many properties of fundamental particles rather well, but several fundamental questions remain to be addressed. To go beyond a static description the model must be able to describe the fundamental forces and beyond that, explain why the number 64 plays such a central role in the model. One key to addressing such questions involves the fine structure constants, designated as $\alpha$, which measure the relative strength of forces. $\alpha$ measures the ratio between the interaction strength of a force and a fundamental reference strength. Interaction strength is the product of energy times distance and reference strength is the product $hc$. $hc$ is an energy-distance product since $hc = h/t_o \times ct_o = E_o \times d_o$. The subscript refers the products to the Planck scale to show the fundamental character of $hc$ as the Planck energy times the Planck distance. The Lehto-Tifft decay concepts may now be utilized to examine the fundamental forces.

In the Lehto-Tifft model mass-energy involves a three dimensional temporal volume. $\alpha$ therefore has a 4-dimensional form, as a product of three dimensions associated with energy, and one associated with space. Force has an underlying 4-dimensional structure acting in one spatial direction. The Lehto-Tifft description of forces therefore involves fourth roots to reduce to a one dimensional perceived form as required for bosons. Decay proceeds by the growth of volume which degrades (literally redshifts) energy density within the volume. The total energy of an evolving volume is assumed to remain constant (assuring conservation of energy). In Lehto-Tifft evolution of force we presume that although volume grows it is the total energy of the unified acting volume that generates force. Distinction between forces is then due only to distance over which total energy acts. If this were not the case force strength would decay with time, which while perhaps possible, has not been explored. The three dimensional form of the spaces within which the force originates and operates is also consistent with the observed inverse square divergence of force.

To derive the expression for $\alpha$, in order to discuss the fundamental forces, equate $E_o$ with the Planck volume $V_o$ and write a general Lehto-Tifft form for interaction strength as

$$V_o 2^{(l+m+n)} \times d_o 2^i.$$

$(l+m+n)$ defines an *invariant* minimal Planck volume and $hc = V_o d_o$. The values of $l, m, n,$ and $i$ must be powers of two, with $l, m,$ and $n$ set to minimal values. The fine structure constant is defined as $2\pi$ times the force strength ratio. The factor 2 comes from the $2\pi$ that relates the forms of Planck's constant $h = 2\pi\hbar$. Since the $V_o d_o$ product cancels in the force ratio the fine structure constant is a dimensionless number

$$\alpha = 2\pi 2^{-\frac{l+m+n+i}{4}}.$$

The negative power indicates that strength decreases with distance.

To evaluate $\alpha$, values of $l, m$ and $n$ must be specified. There are two possibilities for the minimal *temporal* $(l, m, n)$ triad, (1,1,1) or (1,2,4). The significance of the basic 1 2 4 triad developed in discussion of quarks is now quite clear, 1 2 4 is indeed a fundamental unit within the structure and properties of both matter *and time*. Fermi exclusion applies. Adopting the 1 2 4 form gives a verifiable correct answer and yields an expression for $\alpha$ as

$$\alpha = \pi 2^{-\frac{1+2+4-4+i}{4}} = \pi 2^{-\frac{i+3}{4}}.$$

The final form incorporates the external factor of two into the power term.

**Table 8**
Fine Structure Constants
$\alpha = \pi 2^{-(i+3)/4}$

| $i$ | Sq | Cu | $(i+3)/4$ | F | $\alpha$ | Force | |
|---|---|---|---|---|---|---|---|
| 1 | | | 1.00 | 0 | $1.57 = \pi/2$ | | |
| 2 | | | 1.25 | 1 | 1.32 | | |
| 4 | $2^2$ | | 1.75 | 3 | 0.934 | Str at $E_\pi$ | Boson-like |
| 8 | | $2^3$ | 2.75 | 3 | 0.467 | Str at $E_p$ | Kepler-like |
| 16 | $4^2$ | | 4.75 | 3 | 0.117 | Str at $E_Z$ | Boson-like |
| 32 | | | 8.75 | 3 | 1/137.045 | Electric | Lepton-like |
| 64 | $8^2$ | $4^3$ | 16.75 | 3 | $2.8 \times 10^{-5}$ | Weak | Composite |
| 128 | | | 32.75 | 3 | $4.4 \times 10^{-10}$ | | Lepton-like |
| 256 | $16^2$ | | 64.75 | 3 | $1.0 \times 10^{-19}$ | | Boson-like |
| 512 | | $8^3$ | 128.75 | 3 | $5.5 \times 10^{-39}$ | Gravity | Kepler-like |

Table 8 tabulates $\alpha$ and associated parameters as a function of the distance factors $2^i$. At $i = 32$, previously associated with electronic structure, the fine structure constant for the electromagnetic force is generated. Lehto [AG] originally derived this result, showing the high degree of agreement with the observed value. This derivation relates more generally to all known forces. At $i = 512 = 2^9$ we find $\alpha$ for the gravitational force between nucleon masses which dominate ordinary (visible) matter. $\alpha_g$ at the mass of the proton is $2\pi$ times the force coupling ratio $Gm_p^2/hc$. This evaluates to $5.9 \times 10^{-39}$, a remarkably good match to the value at $i = 512$. Note that the agreement using the proton mass implies that

no large quantity of any other significantly different 'dark' particle mass can contribute to gravitation, a point discussed later in seminar 7. In QTC dark matter is ordinary matter most of which is simply out of temporal communication range. At $i = 64 = 2^6$ we find a value close to the fine structure constant for the weak force. The close association of 64 and the 32-64-128 structure of the electron pair is certainly consistent with a unified theory for the weak and electromagnetic forces. Referring back to discussion of 3-d and 4-d particle structures in Table 7, it is now apparent why 32 and 64 4-d extensions relate to electric and weak force properties of basic stable particles.

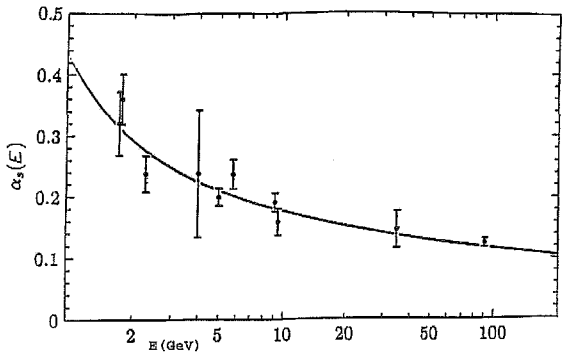


Figure 4.10: The fine structure constant as a function of energy in the strong force domain according to the Standard Model.

$\alpha$ values for $i = 4, 8$, and 16 appear to relate to the strong force. The strong force fine structure constant is distinctly energy dependent as shown in figure 4.10. The number 0.117 at $i = 16$ corresponds very precisely with the strong force strength at the mass-energy for production of the $Z_o$ gauge boson. The value of 0.467 at $i = 8$ in turn corresponds well with the force strength at the mass-energy of the basic baryon, the proton, while 0.934 at $i = 4$ matches $\alpha$ at energies associated with the light mesons. Each critical i value appears to relate to a distinct class of particles. The Lehto-Tifft model differs from the Standard Model at low mass energies. In the standard representation $\alpha_s$ diverges to infinity around the mass-energy of the lightest mesons. In the Lehto-Tifft model there is no divergence. As one passes to smaller and smaller scales the force increases but remains finite. The agreement in the observable region is very good. In Table 8 the value for $\alpha$ at $i = 4$ actually matches the standard formula near the kaon mass-energy but smaller Lehto-Tifft values suggest that this level should be associated with pions, the lightest mesons. The fact that the strong force spans several scales may imply that the strong force is actually a composite effect with a sub-structure related to the classes of particles involved. Unless there are classes of finer structures it is quite possible that no force exists at smaller scales. No three dimensional substructure may now be possible closer to the Planck scale. Within the quark and fine structure constant discussion the minimal Planck 3-d structure appears to be the basic 1 2 4 triad implying that it is indeed a minimum structural temporal scale. The triad is a unit I now call the chronon.

Table 8 contains more information. The fourth-root, combined with the three in the numerator of the power term defining $\alpha$, results in force constants which are 3/4 powers. As

previously seen, 3/4 levels ($F = 3$) are the fourth-root levels populated by the light mesons. There is complete consistency between how force is defined and energy levels occupied by related bosons, rather remarkable if accidental.

Table 8 also contains an important clue potentially related to the nature of matter and force. Whether $i$ is a square, cube, or neither is related to the character of the particles or forces involved. $i$ is a perfect cube when mass related properties are involved. $2^3 = 8$ is associated with the strong force at the level of the baryons, $4^3 = 64$ with the key level where baryon (3-d Fermi) matter exists as particles, and $8^3 = 512$ associates with gravity where mass is the charge. This is where Keplerean cube-root relationships can exist with integer quantum numbers and associate with 3-dimensional space where stable dynamics is possible. Such dynamics may exist in both quantized and continuous domains at this level. It may be no accident that stable matter exists only near this 'resonance'.

When $i$ is a perfect square bosonic properties are seen. $i = 2^2 = 4$ associates with light meson production, while $i = 16 = 4^2$ is related to the $Z_o$ gauge boson and the Higgs resonance. $i = 64 = 8^2 = 4^3$ is both a perfect square and cube, a unique common point between cubes and squares. It is here that we find the $\Lambda$ baryon as the equivalent of an $\eta$ particle pair consistent with a bosonic level. 64 is the smallest integer which is both a square and cube, a point where Bose and Fermi physics are compatible. We earlier noted that the 3-d baryon structure provided an *upper* bound to the light meson sequence much as the muon lepton defines the lower bound.

Finally there is the electron pair, It links together 32 and 128, which are neither cubes nor squares of integers. They are, however, the products of cubes and squares. $32 = 2^3 \times 2^2$ and $128 = 2^3 \times 4^2$ two odd powers of two which are associated with quarks and also centered on the key number 64. The three types of relationships correspond directly with three basic types of particles, In Table 8 I refer to the fermion mass related cubic stage as Kepler-like, the boson related square stage as boson-like, and the cube-square combination as lepton-like, (although this may apply only to the electron). 64 is the unique level where these relationships become compatible, and that is where matter exists. No other theory or idea, to my knowledge, provides a rational for why matter takes this form.

The association of force with specific Planck scale distances has certain implications relating to unification and singularities. It also opens the possibility for forces (and particles) at larger $i$ intervals, although the forces and mass energies involved will be extremely small. In classical unification it has always seemed somewhat illogical to me that gravitation would be the first distinct force, followed by the strongest and then the intermediate forms. In the force relationship implied in the Lehto-Tifft model the situation is quite different. As one approaches a singularity, one conventionally should enter a black hole. At the ordinary Schwarzschild black hole scale there is no problem with gravitation in the Lehto-Tifft model. Black holes, or what looks like such classical anomalies, can certainly exist. However, there should be no gravitational anomaly at the center. Once matter compacts within a $512d_o$ scale gravity should weaken or disappear. New compact stable or quasi-stable structures may exist at very small scales. If enough matter is so compressed external matter, under reduced gravitation, may emerge from a black hole. A second, perhaps more important aspect of gravitational decoupling relates to temporal coupling, the loss of temporal commonality. The gravitational binding force for galaxies can potentially decrease resulting in slow expansion as discussed in earlier seminars. Violent internal instability could perhaps generate 'active'

nuclei. A new approach to understanding the origin of galaxies, and the universe as a whole is possible. Cores of such Lehto-Tifft black holes may contain a new form of singularity. I will later refer to such or related structures as 'sigma-sources', origin points for 3-d material sigma structures such as galaxies. Aspects of these concepts will be discussed in the final seminars.

## 4.10 Particle Generation and Decay

The structural patterns in Table 7, along with earlier figures and tables describing level and transition energies, suggest that certain particle generation and decay processes may be discernible. Light mesons in particular are of interest, particularly the kaon. Although I have no experience dealing with particle decay the following pattern may suggest a possible solution to aspects of kaon decay. There appear to be two decay modes which is unique to this particle. Figure 4.11 diagrams modes and levels ordered by energy across both energy sequences.

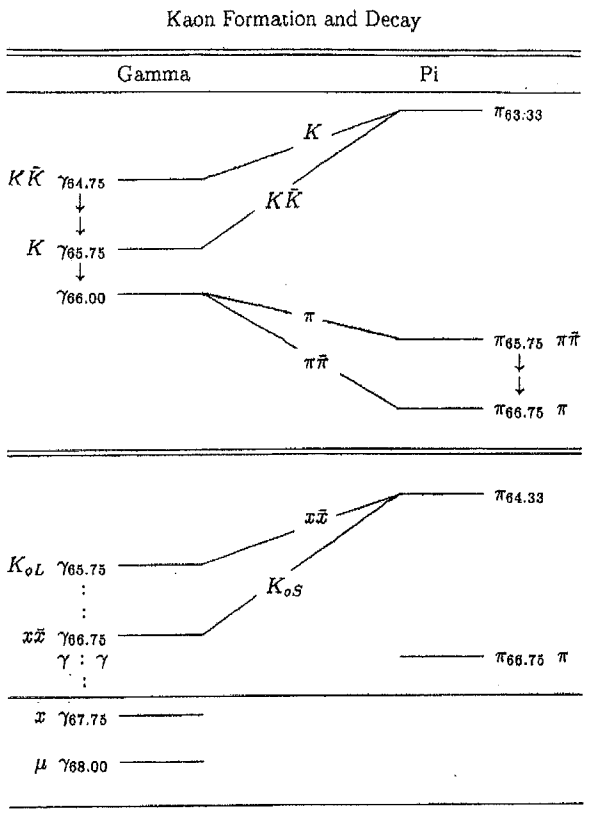


Figure 4.11: Decay modes for the kaon. There appear to be two possible decay modes for this meson.

A transition from $\pi_{63.33}$ deposits one kaon of energy into level $\gamma_{64.75}$ (level $K\bar{K}$) which presumably drops to $\gamma_{65.75}$ yielding a kaon pair. Alternately a transition from $\pi_{63.33}$ drops to $\gamma_{65.75}$ yielding a kaon pair directly. These processes seem indistinguishable and presumably generate $K^+, K^-$ pairs. This is the point where the strange quark enters (the $s$ enters at (64+64+64+8)/3, the kaon at (64+64+64+64+7)/4 making kaons possible. Energy at level $\gamma_{66.00}$ can then generate two pions and account for the two pion charged kaon decays. This step is identical to the final step on $\eta$ decay with one less pion energy. Alternately the muon replaces the pion and a neutrino enters.

The second kaon process involves transitions from level $\pi_{64.33}$. Before tracing these processes some commentary on transitions is warranted. Transitions involve energy differentials which do not directly involve electric charge. Charge is presumably a property of particles generated and residing at energy levels. The kaon and kaon pair energies arising from transitions from level $\pi_{63.33}$, discussed in the previous paragraph, effectively deposit a kaon pair energy in level $\gamma_{65.75}$. Charge conservation implies that a pair of charged kaons will result (unless a $K_o$ pair can be generated). Transitions from level $\pi_{64.33}$, shown in the lower part of figure 4.11, are not energetic enough to produce kaon pairs. They should generate only neutral particles, providing a route for $K_o$ production. The drop to level $\gamma_{66.75}$, previously shown dashed in figures 4.6 and 4.7, involves one kaon energy and should result in a $K_o$. The transition terminates on a level corresponding to a hypothetical meson pair, denoted $x\bar{x}$, a neutral combination. $x$ mesons, and others (see figure 4.7) which fall below the 'muon limit' previously discussed, may not exist. However, the $x\bar{x}$ energy level falls above the limit. It should provide a valid path for $K_o$ production. The $x\bar{x}$ energy (247 MeV) is equivalent to a pion + muon combination (140+106 MeV), consistent with the muon as a limiting particle for the light meson pattern. The second transition, from level $\pi_{63.33}$ to level $\gamma_{65.75}$, delivers one $x\bar{x}$ energy and should contribute to $K_o$ production since it connects to the $K$ energy level itself with insufficient energy to produce charged kaon pairs. The levels discussed in charged kaon production communicate since the upper level represents kaon pair production. In the lower different particles are involved. Ordinary direct connection between the levels is presumably forbidden in such a metastable relationship. Unlike the situation for production of charged kaons, two independent routes for $K_o$ production appear to be possible. This is interesting since the $K_o$ is well known to have two distinct decay modes.

The upper transition deposits excess energy directly into$\gamma_{65.75}$, the same level involved with charged kaon decay. Decay may now proceed in the same manner and rate with an extra pion from the $x\bar{x}$ energy. (The $x\bar{x}$ state may be a different vector form of a pion state.). This well describes standard 3 pion decays of the $K_{oL}$ which proceeds only slightly slower than 2 pion charged kaon decays. We therefore associate this path with the $K_{oL}$. The lower transition connects to a presumably highly unstable pair formation state and should decay much faster. Since one kaon of energy is involved the result should be a 2 pion decay similar to the charged kaon process. This associates the transition with the $K_{oS}$ which decays 100 times faster than the $K_{oL}$. It is also consistent with rare electromagnetic decays of the $K_{oS}$ that should associate with annihilation processes at the unstable $x\bar{x}$ level. Rare, normally forbidden transitions between the levels will cause some $K_{oL}$ particles to transform to the $K_{oS}$ state. This will yield the 2 pion CP violation decays associated with the $K_{oL}$. Re-excitation of $K_{oL}$ particles in interactions with matter should repopulate the $\pi_{64.33}$ level and regenerate both decay states as observed. The Lehto-Tifft model appears to be able to at least symbolically describe aspects of meson formation and decay.

A few final comments relate to meson properties. The association of only charged meson pairs with pair formation levels is consistent with there being no charged forms of the $\eta$ meson. A hypothetical $\eta\bar{\eta}$ state may be prevented by the formation of the $\Lambda$ at the baryon limit. This further illustrates how baryons cap the light meson sequence. In a similar sense the $F$ meson can have no neutral state. Differences in connecting and populating gamma and pi levels suggest that the next meson which might show CP violation properties would be the $B$. However, no attempt to further describe high energy meson properties has been made at this time. The $K_o$ meson relationship with a hypothetical $x$ meson may suggest that very rare $x$ meson events might be detectable. The $x$ meson mass-energy should be close to 123 MeV which may be difficult to separate in a maze of pion events of nearly the same energy.

## 4.11 Introducing Cosmology

I will close this seminar by summarizing some ideas as an introduction to seminars 6 through 8 related to cosmology. I assume there is a 3-dimensional temporal space which we view from 3-dimensional spatial space as 1-dimensional due to aberration caused by relative flow of space through time at light speed. Temporal space is a quantum domain containing 'active energy' derived from conditions at the Planck scale. Decay from the Planck scale proceeds by dimensional doubling which generates quantized redshifts, the quantized structure of matter (a passive form of energy) and related effects as energy transforms between temporal and spatial domains. Matter resides in three dimensional spaces, home to continuous dynamical physics where we reside. Such spatial units flow outward through temporal space along *timelines* and experience passage of time as a temporal flow driven by energy density decay as the universe expands.

In three-dimensional Euclidean space flux diverges as the square of distance. Inverse square force laws result and yield Keplerean physics. In 3-d temporal space there might be some form of dynamics but it is difficult to conceive of motion without invoking space. Since particles appear in space as quantized 3-d spatial structures I prefer an alternate view of what produces what looks like underlying Keplerean physics within time. The physical process of generating particles in a transformation from tau to sigma is presumed to be pair formation and is discussed in seminar 7. The process adds the third radial dimension to an incipient particle's temporal energy form making it a part of the aging flow of matter through time. Aging (temporal flow) enters at the time of birth. The flow of 3-d action through temporal (tau) space must include a process which can *induce* spatial (sigma) space much as electric flow induces magnetism. Quantized particles must possess space as a *property* of the particle, much as redshift is a property of galaxies. From a practical viewpoint 'p-space' travels with a particle and can support 3-d continuous dynamics internally. Mass motions, kinetic processes, occur only spatially. No 'motion' appears temporally where active energy exists without ordinary dynamical form. Redshift quantization insists on such a picture. On the large scale galaxies appear to be individual aggregates of quantized particles with spatial motion defined only within their individual 'g-spaces'. Classical motion between g-spaces cannot be perceived or exist to preserve redshift quantization in photon exchanges between galaxies. Motion between g-spaces must be temporal not spatial flows. Universal expansion is really a temporal expansion, time grows as energy decays. Time provides the

grand domain, space provides the temporal tool for the actual aging (decay) in the form of matter (energy's passive form) with its own internal motions as its g-space envelope flows as a temporal particle through time

Dynamics, driven by three-dimensional action where only specific energy units are possible, should still produce quantized Keplerean physics. In ordinary continuous space and time Kepler's laws have continuous solutions. One side of the equation is spatial, the other temporal, and both parameters can adjust for any specific action. Where action units are quantized, so both sides of the equation are temporal, only specific energies can occur, restricting solutions of Kepler's laws. A 1-d linelander's perception of such a quantized domain, which is providing his action, can detect only the quantized energy permitted by Kepler's third law; The full set of Kepler's laws must be inferred in reverse order. The third law is all that can be seen directly. That is what the Lehto-Tifft rule is, a quantized form of Kepler's third law. The rule paints a picture of 3-d time containing quantized action, time controls both sides of the Lehto-Tifft form of Kepler's equation. However, that does not prevent dynamics in sigma, dynamical life begins at birth into sigma.

**Keplers Laws**

Kepler #3 $a^3 = (GM/4\pi^2)P^2$ (Circular orbit)
$a$ = length ($r$) = RADIAL term
$P$ = time = $1/\nu$, lateral energy = AZIMUTHAL term
$r \propto (\nu^2)^{-1/3}$ A CUBE ROOT rule
In 3-d time distance $r$ becomes a 1-d time interval

Kepler #2 Angular momentum (Circular orbit)
$P = 2\pi r/V = (2\pi r^2)/(rV) = (2A)/(r^2\dot{\theta})$
For fixed $P$, $r^2\dot{\theta}$ = Fixed fract of A = Law of Areas
Azimuthal quant is equivalent to areal quantization
In quantized 3-d time $r$ and/or $A(r^2)$ must quantize

Kepler #1 The S-state circular orbit relates $A, r$
$A = \pi r^2$ $r = (1/\sqrt{\pi})\sqrt{A}$
Which is observed to relate the $\gamma$ and $\pi$ energies

Figure 4.12: Keplers Laws, the classical connection between cubes and squares

As a kind of appendix to this seminar, for persons not actively familiar with Kepler's laws, it may be useful to take a quick look at the laws. You cannot have dynamics in one dimensional space; it becomes effectively possible only in three dimensions. Figure 4.12 shows the form of Kepler's third law for circular orbits. It is derived by equating the gravitational force, the restraining force at the scale of orbiting masses, to centripetal force which balances gravity. The radius of an orbit is denoted 'a' and the orbital period $P$. Period is a time, an inverse frequency, and frequency is related to energy. The Lehto-Tifft rule is the same with the spatial distance replaced by a time interval. If temporal actions are quantized only specific solutions are now possible. You may quantize either time intervals ('radial quantization') or energies ('angular effects') related to Kepler's law of areas.

Kepler's third law implies Kepler's law of areas. Figure 4.12 shows that a circular orbit period equals circumference divided by velocity. Put in an additional $r$ factor in the numerator and denominator to see that the numerator is twice the orbit area. The denominator is the angular product $rV$ which is the angular momentum. For any fixed period the angular momentum must be a fixed fraction of the area, which is Kepler's second law. The law is commonly stated by saying that the object sweeps out equal orbital areas in equal times. The law is general for any orbit and is simply a statement of conservation of angular momentum. Turning to Kepler's first law, orbits are closed ellipses, or in the limiting case circles. The 's' state circular orbit is described by the equation for the area of a circle. Radii are related to area properties by a $1/\sqrt{\pi}$ factor. This is the factor connecting the Lehto-Tifft particle energy sequences.

There is a consistent logic connecting a three dimensional temporal/energy space with some form of quantized Keplerean physics. Everything revolves around the 64 level of doubling, the special integer which is both a square and a cube, where Keplerean dynamics becomes possible in a quantized domain.

# Chapter 5

## Turning to High Redshift, Connecting Galaxies With Quasars

Seminar 5 Version 3

## 5.1 Introduction

I was not directly involved in most quasar and active galaxy studies for several reasons. There was little I could contribute observationally and controversy arising from work by scientists like Geoff Burbidge and Halton Arp involved dynamical concepts such as violent ejection inconsistent with redshift quantization which was emerging in my work. There were two facets of early quasar and active galaxy work which did draw my attention since they appeared to be clear observationally. One was nonuniformity in quasar redshift distribution, most notably peaks found near $z$ of 0.30, 0.60, 0.96, 1.41, 1.96, (and 0.061 including active galaxies), that were debated since the 60s [AM]. The other concerned galaxy systems with dynamically inconsistent redshifts. That was referred to as the discordant redshift problem and also dated from the 60s [AN]. My work, beginning in the early 70s, was not far behind [55]. In this seminar I will discuss lines of study including the characteristic peaks in the redshift distribution of quasars and the issue of discordant redshifts as noted above along with aspects of redshift quantization related to the above problems and galaxies in general.

The Hoyle Memorial Conference held in the U.K. at Cardiff in 2002 provided the perfect time to enter the higher redshift domain (and incidentally enter retirement). The conference was held in honor of Fred Hoyle, a man who unhesitatingly pursued new and exciting ideas well ahead of scientific views of his time. I was pleased to know Fred and in some respects to follow his path. As an invited participant there was an opportunity to present some ideas that might help understand the cosmos that Fred so loved. High quality data sets from the Hubble Deep Field were becoming available along with basic deep surveys of quasars (primarily identified as radio sources at that time) and a variety of active galaxies. The following abstract of my presentation [151] summarizes much of what I will discuss in this seminar along with more recent understanding which emerged as QTC developed.

> The Lehto-Tifft redshift quantization model is used to predict the redshift distribution for certain classes of quasars, and for galaxies in the neighborhood of $z = 0.5$. In the Lehto-Tifft model the redshift is presumed to arise from time dependent decay from an origin at the Planck scale; the decay process is a form of period doubling. Looking back in time reveals earlier stages of the process where redshifts should correspond to predictable fractions of the speed of light. Quasar redshift peaks are shown to correspond to the earliest simple fractions of $c$ as predicted by the model. The sharp peaks present in deep field galaxy redshifts surveys are then shown to correspond to later stages in such a decay

process. Highly discordant redshift associations are expected to occur and shown to be present in the deep field surveys. Peaks in redshift distributions appear to represent the spectrum of possible states at various stages of the decay process rather than 'dynamical' physical structures.

My original Cardiff presentation included examples of my findings relating to redshift quantization and discussed the concepts behind the Lehto-Tifft formulation of the nature of the redshift (along with matter and energy in general). Since most of that background has been covered in detail elsewhere in the seminar series I will minimize repetition here. However, many details are important and not widely known. As the seminars developed I had numerous occasions to refer to earlier discussion. Since I will increasingly refer to such items, particularly as I begin to develop a cosmology, I developed a 'topical review' outline as an index to the seminars using the (seminar, section, subsection) notation defined in the preface. This seminar is a transition point where I move from describing my work to discussing mostly external data to synthesize an alternate cosmology. References to earlier work will be more common. To avoid repetition and make back referencing convenient, I belive topical reviews should be quite useful. The summary in the following section is incomplete but should provide a useful guide to much of the important early work.

### 5.1.1 When Did I Say That?

**Redshift-Magnitude Bands:** Discovery (1.3.1), Morphology-redshift correlation and convergence toward zero redshift (1.3.1), Data verification (1.3.2), Other clusters, A2199, Perseus (1.3.2), Total Magnitudes, outer Coma (1.4.0), Correspondence between clusters Coma and A1367 (1.4.1), Standard total magnitude slope 4.3 magnitude (1.4.1) (1.4.3), High redshift cluster Cl 1358+62 (1.4.2), Quasar banding (1.4.3), Active and emission galaxy association (1.6.2), Quantization discovery in upper Coma band (1.9.0).

**Cross-Bands:** Structure within bands (1.5.0), ApJ editorial disclaimer (1.5.0), Relation to morphology (1.5.1), Drift suggests morphological evolution (1.5.1), Radio galaxy associations (1.6.1), Relation to compact groups (1.7.2), Cross-Band development (1,7,1).

**Morphological Patterns in Clusters:** Systematic morphology pattern in Coma (1.3.1), General redshift patterns, Early spirals low, E galaxies at core, Later spirals high (1.5.1), A262, 1358+62 morphological offset examples (1.5.1), Table of morphological offsets (1.5.1).

**Vertical-Sequences:** Relationship to cross-bands, band heads, activity (1.7.0), Perseus examples (1.7.0), As compact groups (1.7.2), Discordant redshift association (1.7.2), Periodic spacing in redshift for A262 and compact groups (1.7.2), Early model (1.8.0).

**Double Galaxies:** A basic quantization test, dynamics vs quantum (2.3.2), Karachentsev pairs defined (2.3.3), Peterson 21 cm pairs and results (2.3.3), Karathensev pairs study results (2.3.4), Evaluation of I/O ratios (2.3.4), Cornell and Schweizer data analysis and commentary (2.3.5), Best summary diagram (2.3.5), Distinction by radial zones (2.3.5), Zero differential exclusion (2.3.6), Wide pairs do not resolve zero deviation (2.3.6), The importance of pair isolation, effects of contamination, a study of 21 cm triplets (2.3.6), Best data from current work (2.3.7), Orientation in pairs, large scale alignment! An independent test in violation of dynamics (2.4.1), Alignment by luminosity as well (2.4.1).

## 5.2 Preparation for High Redshift and Quasars

Despite what I say earlier, relating to repetition, since each seminar needs to some extent to stand alone some brief initial summary review is necessary. My work and data with local redshifts provided the basis for seminar 3, which in turn provided the basis for the steps to high redshift. Work prior to 1992 employed empirical periodic intervals studied differentially or globally within a galactic center rest frame. Independent confirmation work was carried out in the 90s by Guthrie and Napier [AF], and continued by Napier [AO]. In 1992 emphasis shifted to the cosmic background rest frame, seminars 2 and 3 provided key information regarding double galaxies, superclusters and global redshift properties. Lehto's basic concept of links to the Planck scale for both particle physics and redshifts entered in 1993. Subsequent testing, Tifft [125,138], confirmed and extended concepts leading to the current Lehto-Tifft quantization model. Lehto's concept developed in two directions, into particle physics in original 3-d form which I expanded to include 4-d leading to seminar 4, and with my ninth root expansion into the cosmic side of seminar 3 and now seminar 5. The 3-d (and 4-d) form is discussed in depth in (4.2.0 to 5) and requires little further discussion. That form is linked specifically to 3-d sigma-space. There are no known example of ninth root forms in 3-d space (except perhaps photons passing through). The ninth root form appears to apply only to active energy in tau-space. Except for details relating to the Planck association provided in seminar 4 the ninth-root form was developed very simply in (3.3.0,1) (and in the Cardiff presentation). For internal consistency the underlying concept, described in the Astrophysical Journal [125], follows

Lehto [AG] was originally motivated to describe properties of fundamental particles from first principles. Begin with Planck units, the Planck energy, time, mass and light speed. These units can be related to the Planck time or frequency as defined by fundamental constants $h$, $c$, and $G$. Observable properties of particles (and redshifts) are then presumed to be generated by a decay process beginning at the Planck scale. Lehto proposed that the Planck units decay by a period doubling process, an action doubling process in factors of 2, a process well known in decay of systems toward chaos. If this was the case present day fundamental properties of matter and energy should relate to the Planck units by simple powers of 2. When Lehto explored this idea he found what appeared to be ratios involving cube-root powers of 2. Lehto suggested that doubling could be occurring in a 3-dimensional or 3-parameter space which is perceived as 1-dimensional through the action of a cube-root transformation. A brief summary of the formulation which developed is warranted.

### 5.2.1 The Lehto-Tifft Equations

Lehto's initial form for permitted redshift intervals (periods) follows from the above,

$$P = c2^{-N/3}.$$

$N$ is an integer $\geq 0$. A form applicable to particle physics replaces $c$ with the Planck mass or energy. The equation is a general form of Kepler's third law. In ordinary space spatial distance relates to the 2/3 power of a time interval, a relationship unique to 3-d space. The existence of this pattern involving only temporal terms raises the possibility that temporal/frequency/energy space is actually 3-dimensional. If 3-d space is flowing relative to such a 3-d temporal space the flow will by definition be the speed of light, a

constant. Time will be reduced to 1-d by aberration and generate perceived 4-space. The model automatically provides constancy of $c$ and preserves special relativity. Temporal space must be quantized since it involves a stepwise decay (redshift quantization) from fixed units. Dynamical 4-spaces flowing through time are not so restricted. Quantum and continuous physics can co-exist. Redshift data are consistent with such a periodicity formulation.

The basic cube-root equation is rewritten to distinguish cube-root doubling 'families'

$$P = c2^{-N/3} = c2^{-\frac{3D+L}{3}}.$$

$D$ is the number of doublings, and $L = 0$ to 2 specifies which root is involved. The above equation accounts for most redshift periods, however, the complete set of periods requires a second cube root operation to yield ninth-root families distinguished by an index $T$ which ranges from 0 to 8.

$$P = c2^{-N/9} = c2^{-\frac{9D+T}{9}}.$$

The ninth-root equation completely and uniquely describes all presently found redshift periods [125,138]. $T$ values do not occur randomly. Pure doubling, $T = L = 0$, dominates, followed by the 'Keplerian' $T = 6$ ($L = 2$) value. Odd $T$ values shifted by 1, ($T = 1, 5, 7$) are less common, while even values ($T = 2, 4, 8$) are rare or absent. $T$ families also relate to galaxy morphology [138]. At high redshift, the $T = 0$ family appears to become even more dominant.

A second relationship is required to assess redshift quantization. Redshift intervals dilate with distance due to geometric effects which must be removed to evaluate quantization. In classical cosmology geometry, 'curvature', involves the 'deceleration' parameter $q_o$. The Hubble 'constant' is a function of time, $H = H(t) = f(z, q_o)$ where $q_o = 1/2$ corresponds to Euclidian geometry. Such a relationship must exist in any cosmology. $q_o$ need not be uniquely associated with gravitation but $H(t)$ will be described much the same way. The $z$-dependent distortion in redshifts is called the 'cosmological correction'.

The cosmological correction was investigated by Tifft and Cocke [87] for application in global quantization studies. A correction assuming redshift intervals dilate in proportion to $\sqrt{H(t)}$ was shown by Tifft [125] to linearize redshift periodicity to well beyond 10,000 km/s if $q_o$ is set equal to 1/2. In this seminar no deviation from the correction is seen within $z = 1$ or 2. The relationship is discussed in seminar 2 (2.7.0). For $q_o$ exactly equal to 1/2 the derivation yields a closed relationship between $z$(observed) and $z$(Lehto-Tifft) which fits all data examined [125,138].

$$z_{obs} = \left[\frac{z(LT)}{4} + 1\right]^4 - 1 \qquad z(LT) = 4[(1 + z_{obs})^{1/4} - 1].$$

These equations are used to convert observed redshifts to $z(LT)$ for quantization evaluation.

The formulation is easy to understand. The equations are consistent with the 3-d temporal concept where energy is associated with temporal volumes which vary as $t^3$. If photon redshifts relate to energy density, which varies as volumes evolve, the rate of change is perceived as $H$. Volume evolves as $t^2$ so $H$ should depend on $t^2$ and redshift intervals vary as $\sqrt{H(t)}$ as observed.

## 5.3 Progressing In Time, Characteristic Redshift Peaks

The Lehto-Tifft model involves the evolution of galaxies and the redshift through an energy decay process based upon period doubling. Looking back in time from our advanced stage should reveal earlier redshift doubling stages and precursor processes that generate galaxies. To be consistent with the decay process higher redshift data should contain predictable early doubling stages. Table 1 shows that this is indeed the case. The table demonstrates that very early doubling and perhaps mixing, involving the simplest fractions of c, (the T=0 pure doubling series), when converted to Lehto-Tifft format generates the observed quasar redshift peaks quite precisely. The table contains the basic D=2 doubling patten and two early possible mixings to complete a remarkable series of 1/4 fractions of c. The pattern then continues the T=0 doubling sequence, a rather remarkable result if accidental. The quasar connection also makes it quite clear to me, if there really was much doubt, that quasars are the precursors, the source functions from which galaxies developed. Peak locations have also been described by Karlsson [AP] using an empirical logarithmic series. The doubling process within the ninth root rule format provides a much more complete and precise fit as subsequent discussion will demonstrate. The process links directly to galaxy periodicities.

**Table 1**

Quasar redshift peaks

| z(LT) | D=2 | z(obs) | z(peak) |
|---|---|---|---|
| c/16 | | 0.064 | 0.061 |
| c/8 | | 0.131 | |
| c/4 | 1/4 c | 0.274 | 0.30 |
| c/2 | 2/4 c | 0.601 | 0.60 |
| | 3/4 c | 0.989 | 0.96 |
| c | 4/4 c | 1.441 | 1.41 |
| | 5/4 c | 1.968 | 1.95 |

The reality of significant peaks in the quasar distribution has been actively disputed in the framework of conventional dynamical cosmology. Even in QTC where peaks are both expected and confirmed, by no means do all quasars conform to the pattern. It seemed quite likely early in the study of quasars that the distribution depended upon the type of quasar involved. Burbidge [AQ] and Burbidge and Napier in Hoyle, Burbidge and Narlikar [A] indicate that the peaks appear when quasars which are strong radio sources are involved. This is consistent with QTC where a regular pattern of radio and active emission occurs within the redshift distribution of clusters of galaxies (1.6.1,2). Until photometric processes were developed to detect quasars most were located as radio sources. As I will shortly discuss, other Lehto-Tifft T values play an important role in defining the quasar peaks. One of the best examples showing the association with radio frequency activity is illustrated in figure 5.1, which shows the complete set of 3c quasar radio sources. Other redshift T

states expected within QTC are shown (Vertical lines), which considerably enhance the peak association. T=0 marks the points of the peak locations listed in Table 1.

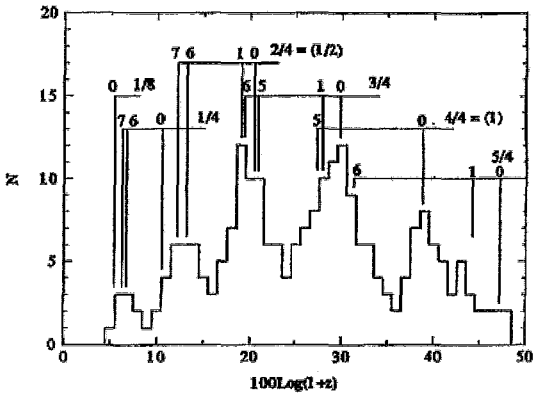


Figure 5.1: The redshift distribution for the 3C radio survey showing peaks potentially due to an intrinsic redshift component. Redshifts predicted by the Lehto-Tifft model are shown with doubling stages and $T$ values

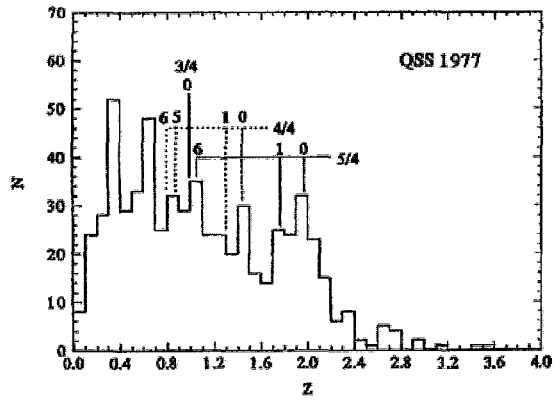


Figure 5.2: The redshift distribution for quasars, mostly radio sources, known by the mid 1970s. This figure shows the higher redshifts clearly. Redshift peaks are indicated in Letho-Tifft notation as in figure 5.1.

Figures 5.1 and 5.2 show how the extended set of common T values reinforce the redshift peaks. The least likely or absent T forms associate with the gaps. An interesting feature of the higher T value association with T=0 is readily seen. At highest redshift T=0 appears to associate with T=1. At lower redshift T-6 appears and progressively T=5 and 7. The higher T values proceed ahead to enhance a subsequent peak. This process is apparently one aspect of redshift decay and galaxy evolution displayed over time.

There may be other classes of quasars which associate with the peaks. Burbidge and Napier

[AM] associate quasars close to low redshift galaxies and many pairs at high redshift. This could be an index of recent activity, but initial numbers were small. Studies based upon large optically selected samples do not confirm redshift concentrations or associations [AR]. This is not surprising as early samples were primarily radio selected objects. In the Lehto-Tifft model active objects concentrate in redshift and/or phase together periodically. As discussed for galaxies, objects appear to decay toward lower redshift as they age, which can displace them from newer active areas. Such a decay pattern will be shown later in this seminar using Hubble Deep Field high redshift galaxies presumed to be evolutionary products of quasars. Similar studies could be carried out to investigate phasing between different quasar categories if suitable categories can be defined. The question of physical association in the presence of redshift descrepancies is an open question. In QTC physical association and which step in a periodic redshift pattern an object occupies are two different questions. That issue will be addressed subsequently using HDF redshifts.

A study by Arp et.al. [AS], based upon quasars selected by radio flux, was used to further investigate the association of radio emission with the quasar redshift distribution. Filled symbols in figure 5.3 show the distribution present in the southern galactic hemisphere field investigated. Two assistants, N. Jobson and L. Lippiello, slightly extended the sample (open symbols) using the Veron-Cetty and Veron 1996 quasar catalog [AT]. As in previous diagrams the distribution of common T and D states is indicated.

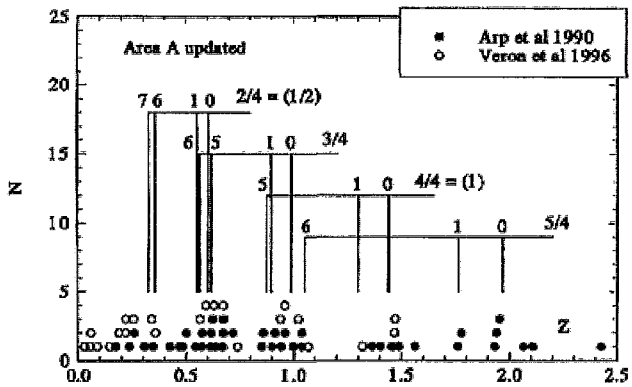


Figure 5.3: The redshift distribution of quasars and active galaxies in a south galactic field [AS]. The study was augmented using additional data to compare with redshift peaks predicted by the Lehto-Tifft model.

A peaked distribution identical to and extending the pattern in figure 5.1 is apparent. The association with T=1 and other common T values is especially notable as are the gaps where rare or absent T values should occur. Such predicted features are unique to the Lehto-Tifft model. In view of the clear apparent pattern match the entire southern hemisphere south of the initial field was added to generate figure 5.4. The associations are strikingly clear.

To extend studies to lower redshift, including the $c/8$ peak predicted at $z(obs) = 0.131$, the quasar and active galaxy redshift distribution was extended to low redshifts using the Veron-Cetty and Veron 1996 catalog [AT]. Since many redshifts were preliminary or of low

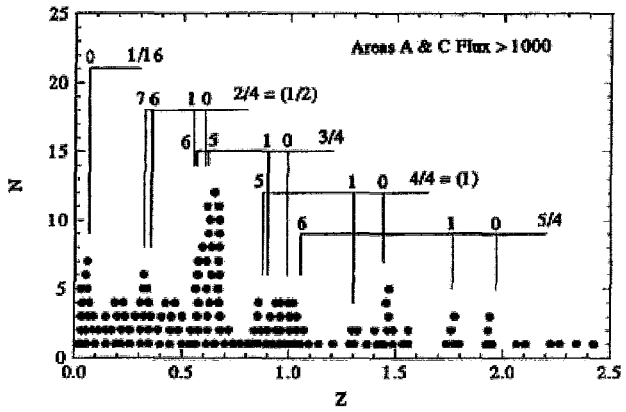


Figure 5.4: The redshift distribution, shown in figure 5.3, augmented with with a large portion of the south galactic cap to further verify predicted redshift peaks.

quality only objects with redshifts listed to three or more significant figures were used. This is a serious problem in quantization work. Classically precision is of little import, a serious oversight arising from preconception that the redshift is a simple dynamical quantity despite a great deal of evidence to the contrary. Figure 5.5 shows the lower redshift distribution.

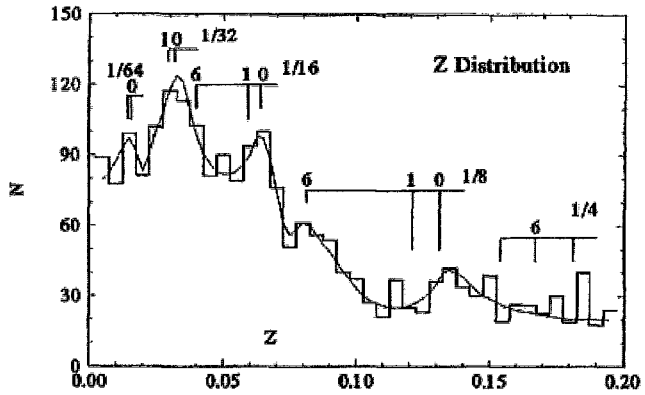


Figure 5.5: The general redshift distribution for quasars and active galaxies, as known in 1996, compared with redshift peaks predicted by the Lehto-Tifft model.

The $c/8$ peak is present. The peak is an x2 multiple of the $c/16$ peak at $z = 0.06$. The c/8 peak is not predicted by Karlsson [AP], however, Burbidge [AY] has noted multiples of the 0.06 period which is the Lehto-Tifft c/16 state. The Schmidt and Green [AU] bright quasar sample also shows small concentrations at $c/8$ and $c/16$ locations. A figure for that study is included in my Cardiff paper [151]. When limited to active objects the low redshift Lehto-Tifft fit is remarkably clear. For ordinary galaxies high doubling patterns can be quite complex [125, 138]. Quasars and active galaxies are consistent with Lehto-Tifft predictions.

## 5.4 Connecting Galaxies to Quasars

To maintain the Hubble law and sharp redshift quantization, objects must cascade down through sets of specific related redshift levels. The principal peaks in the pattern of quasar redshifts appear to represent an active stage of the earliest doublings. States such as 3/4 and 5/4 might represent early frequency mixing or, as I will indicate for the HDF galaxies, intermediate evolutionary stages in a harmonic cascade decay between primary doublings. In such a model secondary decay may produce less active quasars and ordinary galaxies forming a redshift 'spectrum' between primary doubling peaks. Much shorter redshift periods found locally imply doubling and harmonic redshift evolution is much more advanced now than seen in quasars. The obvious place to look for earlier stages of decay is at high redshift. Decay from $c/2$, the first T=0 doubling located at the $z = 0.6$ quasar peak, should be especially clear. The redshift spectrum should show a strong $T = 0$ dominance, 'phased' decay products, and discordant redshift associations where physically related objects occupy different but related, periodically phased, harmonic redshift states at any given time. Decay locally has reached the $D = 11$ to 17, (c/2048 to c/131072), P=146 to 2 km/s range. At the $z = 0.6$ peak we would expect periods in the $D = 4$ to 9 range ($c/16$ to $c/512$) with redshift intervals in the 20,000 to 500 km/s range. That is indeed what we find.

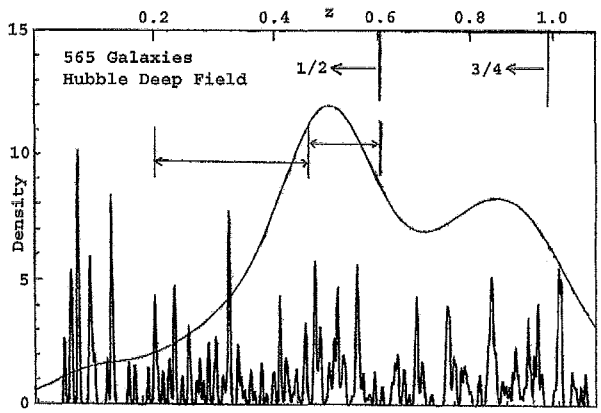


Figure 5.6: Smoothed galaxy density (curved line) and local overdensity fluctuations associated with redshift clumping in the Hubble Deep Field region according to Cohen et.al., [AX]. Broad density peaks below the $c/2$ and $3c/4$ quasar peaks are shown as are intervals used for detailed redshift comparisons.

To compare with predictions I utilized excellent accurate redshift surveys done in and around the Hubble deep field (HDF) and a southern deep field (SDF) by Cohen et.al. [AV,AW,AX]. Figure 5.6, adopted from Cohen et.al., [AX], shows an HDF region overdensity redshift spectrum. The sharp spikes are classically interpreted as unusually low velocity dispersion clouds or 'cell wall structures'. The smooth curve shows the heavily smoothed overall galaxy density distribution. From the QTC viewpoint the peaks displaced below $z = .6$ and $z = .96$ are consistent with being evolved harmonic decay remnants of early $c/2$ and $3c/4$ doublings having little or nothing to do with dynamics. To investigate, the redshift pattern was studied in two segments marked below $c/2$ and around $c/4$ which falls at z of 0.3.

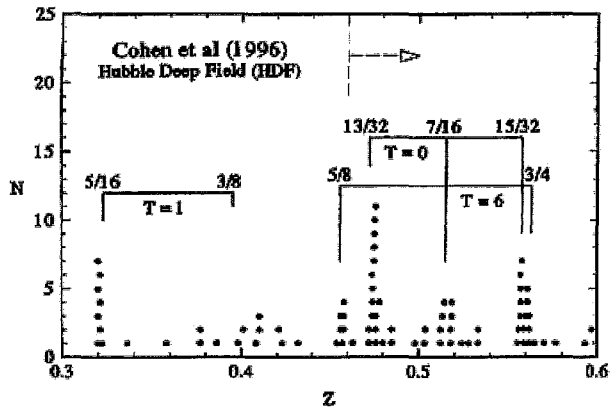


Figure 5.7: The redshift distribution in the Hubble Deep Field region, below the $z = 0.6$ quasar peak. The relationship of the pattern to several T values is shown. The study was subsequently divided at $z = 0.46$.

A 1997 study utilized an early HDF study by Cohen et.al., [AV]. Figure 5.7 is a redshift frequency diagram with predicted Lehto-Tifft T=0 redshifts for fractions of $c$ expected in the interval. Possible T=1 and 6 values are also marked. Three strong T=0 peaks below $z = 0.6$ fit 'harmonic' decay patterns in $c/16$ and $c/32$. Such harmonic decay below doubling levels provide the strong periodicities observed in QTC. *Galaxies appear to be found at nodes of harmonic decay induced by period doubling.* This is shown in figure 5.8 where the $c/16$ phase distribution is plotted against right ascension for the three main peaks above $z = 0.46$ in figure 5.7. A few hundred km/s phase trend is present. Such phasing is far from expectations for dynamical aggregates of galaxies spread over 25,000 km/s in redshift.

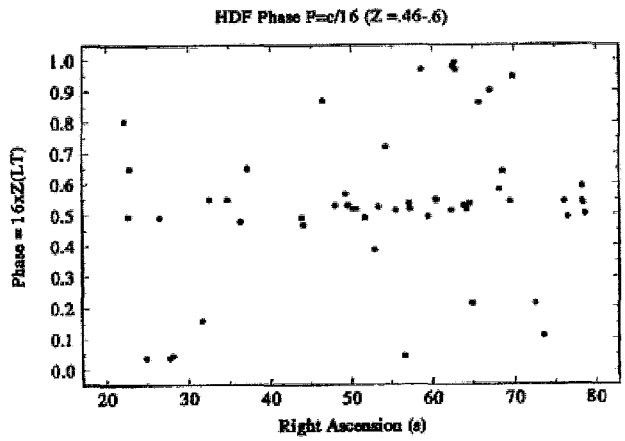


Figure 5.8: The redshift phase distribution for the $c/16$ period using the 1996 [AV] Hubble Deep Field sample with $0.46 < z < 0.6$ shown in figure 5.7.

### 5.4.1 Redshift Patterns

To extend the study of the three related peaks below $z = 0.6$, figure 5.9 shows the redshift distribution from the complete HDF catalog by Cohen et.al., [AX]. Figure 5.10 shows that the two lower main peaks and satellites are slightly offset from $c/32$ or $c/16$ locations.

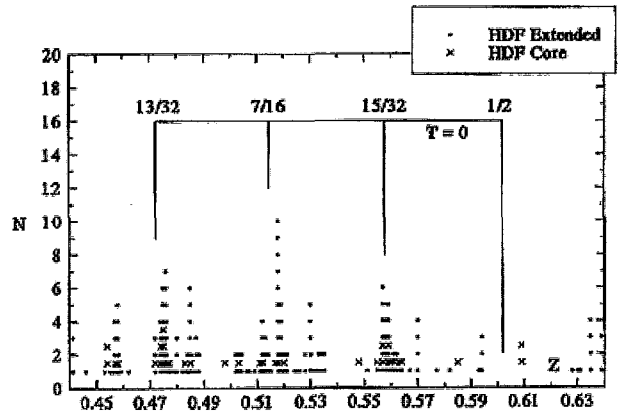


Figure 5.9: The redshift distribution in the Hubble Deep Field region below the $z = 0.6$ quasar peak using the complete catalog [AX]. The three major $c/32$ periodic peaks immediately below the $z = 0.6$ quasar peak are indicated.

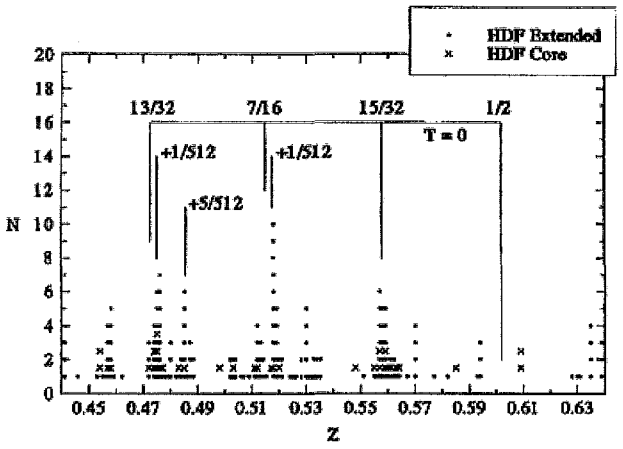


Figure 5.10: Fine structure and offsets above the three major peaks in figure 5.9.

Offsets may be consistent with higher harmonic fractions of $c$ between peaks and increase in complexity with decreasing redshift. Further, fractions involved are all *odd* fractions. Additional examples of this pattern will be seen shortly. This is the signature of a decay process which has proceeded to a specific harmonic level within a doubling but not beyond

D=5, $c/32$. The small offsets in steps of $n/512$ suggest there could be finer structure within the harmonic decay process which is increasingly incomplete toward lower levels.

### 5.4.2 Planes of Time

At this point I need to jump conceptually ahead. In the following section I will describe a test which QTC predicts (and passes). The objective of the test is to show that the three redshift peaks I have been discussing are three distinct 'planes in time' which constitute a single aggregate of sigma-spaces. QTC is a quantum theory which superimposes two spaces. In tau-space individual points in time are unique (fermionic), but events can be simultaneous (bosonic) by distributing in sigma-space. In sigma-space points of space are unique (fermionic) but can be coincident (bosonic) if distributed in time. QTC presumes the flow of time is a 3-d energy (a temporal inverse) oscillation. A 3-d oscillation is something like a 2-d sound wave which bunches together periodically at its nodes. Galaxies appear at the nodes and generate observed periodic quantized redshift pattern characterizing QTC. Such a wave pattern can decay by doubling, generating two superimposed wave patterns where alternating nodes will be harmonics of one another spread in time. In QTC a quantum transition is a forward jump in time from node to node within such a picture. This has been directly demonstrated by showing variability in the redshift (2.6.2), in cascades (2.6.3) (3.9.0), involving specific forward steps (3.9.2) as shown in figure 3.40 and appendix (Ap2). More about how such transitions may occur is deferred to the cosmological discussion in seminars 6 through 8. At this point it is sufficient to show that they occur. Galaxies appear to be just another form of particle which can undergo quantum transitions.

What is a node in QTC? In QTC a node must be a sigma-space where time can compress and superimpose events by dispersing them in space. Time flow continues in sigma as aging. From a node it is possible to look back to earlier synchronized nodes, which photons allow since by redshifting they stay synchronized with their parent node, they have temporal commonality. Nodes resemble the observer's node and contain a series of superimposed 'planes of time' which appear to be traveling together. If successive doubling levels corresponds to common spatial distance an aggregate of objects should be seen. The group can contain several temporal planes that travel together in redshift steps. The redshifts will be greater the earlier in time the parent synchronized node created a given plane. If you look back far enough to spread out the doubling fraction intervals the individual planes of time will therefore be seen as individual redshift peaks within the synchronized doubling aggregate.

Turning now to the view from within our particular node containing local planes of time, photons can be collected by lookback from earlier nodes within an aggregate where the temporal planes are distinct as redshift peaks. Patterns within such synchronized peaks may then be examined to see how they correlate temporally (older nodal forms should be more evolved). The HDF set of redshift should extend back to a time period when decay had proceeded only so far, to the maximum $D = 5$ doubling or $c/32$ level for the three peaks in the HDF sample below c/2. The aggregate should contain a range of related harmonic doubling fractions related to different evolutionary stages. I am far ahead in discussing this concept, but I introduce it here to demonstrate the actual apparent relationship of doubling and redshift to distance and aging. The demonstration will provide the verification test of the prediction.

Doubling sequences overlap. Even fractions correspond to earlier doubling levels (i.e.14/32 = 7/16) which by being earlier can be presumed to be older and may have decayed. The most prominent example of a missing higher state is the $c/2$ state itself which is associated with a much earlier quasar era. That level is completely absent in figures 5.9 and 5.10. Observed doubling chains cover only a few consecutive doubling states. Harmonic pattern segments appears to represent aggregates related to later doubling stages than the quasar doubling point where it begins, although the (odd) harmonic fractions are numerically consistent with the (empty) quasar and earlier doubling harmonic fractions. Another way of describing the pattern is to note the spacing between the two odd outlying c/32 peaks is equal to the spacing of c/16 intervals, *the c/32 pattern is 'phased' into the previous c/16 period to generate the next harmonic of the c/16 period.* All the peaks (except for the quasar) could be at the same lookback (distance) as a single aggregate of synchronized doublings! The slight phase drift within figure 5.8 can be due to redshift evolution delays caused by the true distance range present within a single aggregate of galaxies characterized by a specific doubling. Distance appears to be characterized by closely related doubling level harmonic patterns, redshift concentrations which are planes of time that characterize the development of the aggregate.

### 5.4.3 Spatial Correlations Between Harmonic Levels

As noted above, a common doubling decay level for the three $c/32$ peaks suggests a common spatial (distance) association despite a wide redshift spread. To test for associations, the correlation between galaxy positions and redshift peak membership was examined.

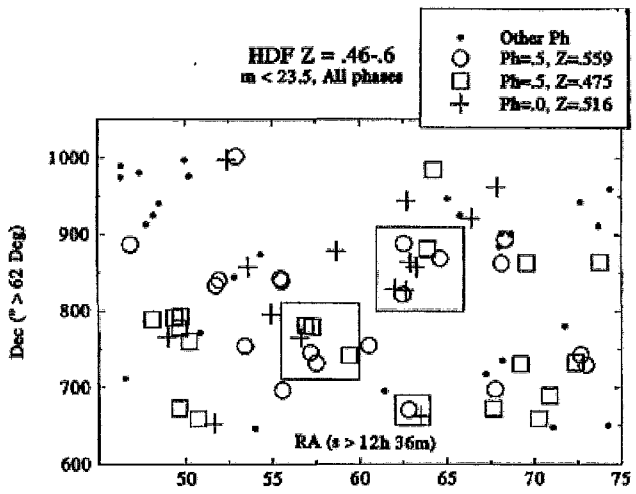


Figure 5.11: Positions for HDF objects, with $0.46 < z_{obs} < 0.6$ and $m < 23.5$, according to redshift peak membership. Large boxes denote aggregates comparable to local galaxy groups. A small box indicates a discordant redshift pair.

Figure 5.11 is a diagram of the positions of galaxies with $0.46 < z_o < 0.6$ in a rectangular region within the HDF extended study [AX]. Symbols distinguish the three dominant red-

shift peaks and objects in between. The sample was cut at a uniform magnitude of 23.5 to account for deeper sampling in the central field, although few galaxies in the $z$ range being studied were involved. The galaxies appear to contain groupings. At the distance associated with $c/2$, 1 Mpc has an angular scale close to 100 arc seconds. The larger boxes in figure 5.11 thus correspond with typical group sizes locally (although the two scales in figure 5.11 are different, declination is in arc seconds, right ascension in seconds). However, what appears to be spatial clumps are composites of the three different harmonically related redshift peaks. In addition there are numerous pairings of galaxies associated with different peaks. One such pair is enclosed within a small box in figure 5.11.

### 5.4.4 Discordant Redshifts

To assess the significance of the discordant associations, one of the Steward graduate students, D. Christlein, carried out Monte Carlo evaluations of the angular separation distribution between pairs which combine different redshift peaks. The number of pairs between specific peaks, in ranges of separation, were counted for the observed distribution and compared with 1000 samples generated by random wrapped displacements in RA and Dec of the objects in one peak relative to the other. Block displacements were used to preserve any real clumpy structure. Figure 5.12 shows the result for associations between the two extreme c/32 peaks separated by 25000 km/s in redshift, and for associations with objects which are not in peaks. The two odd fraction c/32 peaks phase together well, showing significant excess associations for both close pairs and groupings. Objects which do not associate with the peaks do not phase together significantly, they show no significant associations. Figures 5.13 and 5.14 show comparisons between adjacent peaks, odd c/32 and c/16 pairings which have redshift differences in the 12000-13000 km/s range. There are differences in the patterns but still significant evidence for physical association. Galaxies widely discordant in redshift appear to associate together in periods corresponding to simple fractions of the speed of light. The temporal planes are almost certainly spatially associated and the correlations tell me much more.

There are important differences between the correlations. To facilitate intercomparisons I can refer to the three peaks by redshift, their c fraction or their symbol in figure 5.11,

0.559 as circle or 15/32
0.516 as cross or 7/16 or 0.516 as cross or 14/32
0.475 as square or 13/32

I will refer to correlations by figure number, redshift difference or c fraction difference

F12 as 0.475-0.559 or 13/32-15/32
F13 as 0.516-0.559 or 7/16-13/32 or 14/32-13/32
F14 as 0.516-0.475 or 7/16-15/32 or 14/32-15/32

As a basis of temporal *quantum* evolution I have suggested that two processes are operating, period doubling followed by harmonic sequencing. Galaxies exist at the nodes of these processes. The process is readily observable and verifiable via consistent patterns within quantized redshifts as referenced in (5.4.2). The three HDF redshift peaks contain a mixture of two doubling D levels, the 4th and 5th. Is the 7/16 D fraction a 14/32 harmonic level, an older left over 7/16th level laid down earlier, or a mixture? As noted earlier doublings normally occur sequentially, and galaxies can move down in redshift in quantum aging steps,

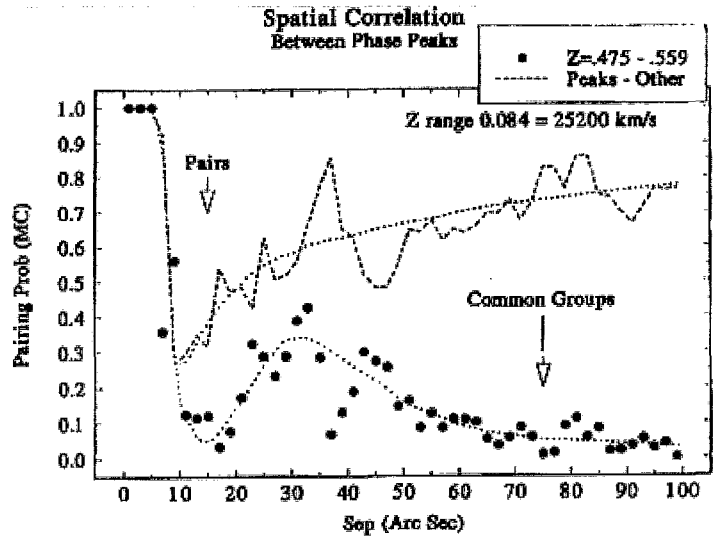


Figure 5.12: A Monte Carlo evaluation of the significance of the discordant redshift associations between the $z = 0.475$ and $z = 0.559$ redshift peaks in the Hubble Deep Field, and between these peaks and objects with redshifts in between the three major peaks. Physical association is indicated for both discordant pairs and groups.

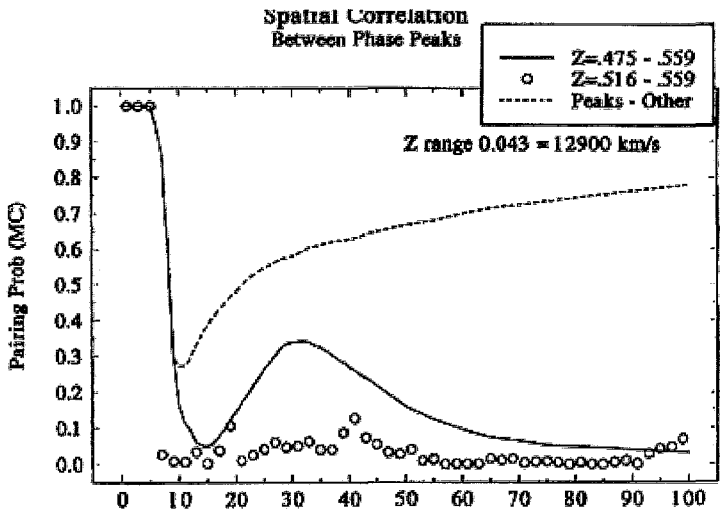


Figure 5.13: A Monte Carlo evaluation, similar to figure 5.12, of discordant physical associations between the $z = 0.516$ and $z = 0.559$ peaks. Results from figure 5.12 are shown for comparison.

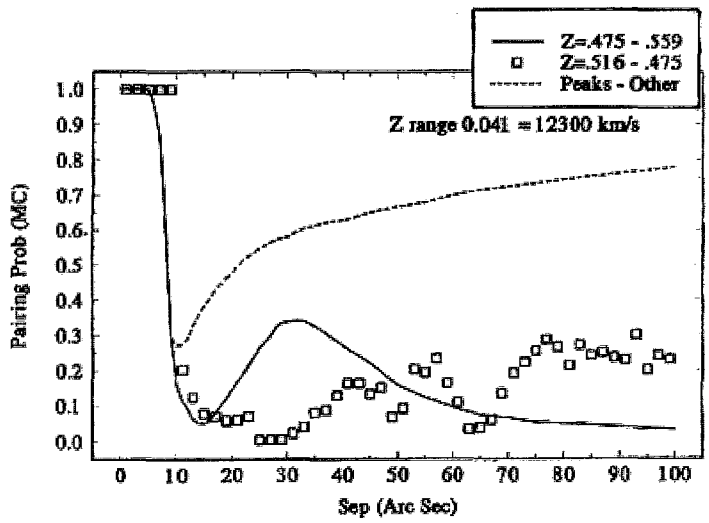


Figure 5.14: A Monte Carlo evaluation of discordant associations between the $z = 0.516$ and $z = 0.475$ peaks. Figure 5.12 results are shown for comparison.

literally within planes of time. Spatial distance to an aggregate may be the same but what is the actual sequence of the different temporal redshift planes defined by the three peaks? Basically, is the middle peak the oldest (did the D=4=n/16 doubling actually precede the D=5=n/32 pattern), or is it really in the middle, part of n/32?

There are two notable changes between the three correlation diagrams, and both yield the same answer. The evolution of the scale of close pairing and the deterioration of compact grouping appears to proceeds as f13 to f12 to f14. f13 shows highly significant pairing of galaxies below 10 arc seconds when the middle 7/16 peak is compared with the highest redshift 15/32 peak. The pairing drops to a less significant level and moves out to 15 arc seconds when comparing the two widest spaced n/32 peaks in f12. Significant pairing then moves out to nearly 30 arc seconds when the mid 7/16 peak is compared with the most recent (lowest redshift)13/32 peak in f14. Grouping follows the same pattern, highly significant between the mid and highest redshift peak, drops within the internal n/32 sequence and is absent in the mid to lowest redshift interval. The f13 segment must be the earliest interval, the D=4 mode must slightly precede the oldest D=5 state to depict the earliest evolution. The two n/32 states in f12 cover a later intermediate period and the f14 diagram contains the longest interval from the old n/16 state to the most recent n/32 state. Not only is the redshift not a measure of relative distance, within doubling overlaps it is not even a measure of relative aging.

QTC is highly verifiable. I recently realized I had already encountered an earlier test of doubling sequence evolution in seminar 1, was puzzled by it, but had not learned enough yet to recognize it. Check out figure 1.30. The middle band of the Coma redshift-magnitude diagram is completely different with respect to emission line galaxy activity. Such activity associates with an older outlying more evolved population. There is much more to say before

I can discuss redshift-magnitude bands as I develop QTC cosmology in subsequent seminars, but doubling and planes of time are clearly involved. A related important conclusion should also now be apparent. By collapsing a wide range of redshift to a common distance within one aggregate of galaxies with minimal redshift spread, the use of redshift 'dispersion' as an argument for dark matter would seem to be in question. The same thing will happen to the Coma cluster where Fritz Zwicky first noted excess dispersion. Along with the fundamental fact that the cosmic redshift is quantized, how much evidence is required to demonstrate that the cosmic redshift has nothing to do with motion of galaxies (except internally where it is caused by an entirely different spatial effect)?

## 5.5 The Southern Deep Field

To compare with the HDF study the Southern Deep Field (SDF) investigated by Cohen et.al. [AW] was utilized. Figure 5.15 shows the redshift distribution in the $0.3 < z < 0.6$ range. There are clear periodicities in both $c/64$ and $c/32$ directly related to and extending the HDF pattern in the $T = 0$ family. $c/32$ and $c/64$ states are marked. The $c/32$ harmonic pattern seen in the HDF is present but considerably weakened and extended to a second pattern headed by the 3/8 state. The later $c/64$ doubling harmonic pattern is also present headed by a very strong 31/64 state directly below the empty 1/2 quasar D=1 doubling level. Within the higher redshift pattern of alternating 64 and 32 doubling fractions the 64 pattern is stronger than the earlier (older) 32 levels. The reverse applies in the lower redshift pattern. The entire pattern is a clear confirmation of the QTC evolutionary process, seen in the HDF, toward lower redshift through harmonic steps beginning at quasar decay points. The D=5 10/32 and 14/32 doubling fraction states can also be associated with earlier D=4 5/16 and 7/16 $c/16$ levels although those levels may have decayed away at the later evolutionary stage present in the SDF field.

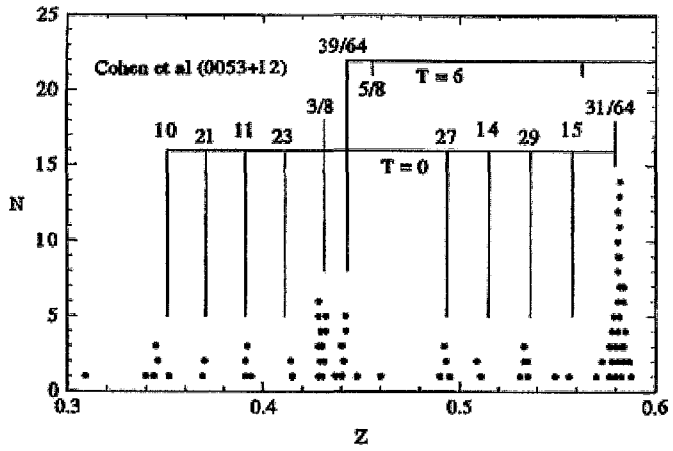


Figure 5.15: The redshift distribution in a southern deep field region (Cohen el.al., [AW]) for $0.3 < z < 0.6$ to illustrate the association of redshift peaks with specific values predicted by the Lehto-Tifft model.

Each harmonic pattern is headed by either a level consistent with the T=0 quasar decay chain (3/8) or a later D=5 or D=6 harmonic pattern doubling fraction directly below an empty higher quasar chain point (31/64 below 1/2). This was true in the HDF (15/32 below 1/2), and is present in the T=6 series in figure 5.15 (39/64 below 5/8), which is empty or nearly so. The higher series doubling and harmonic levels appear to be what generates the later harmonic patterns. These harmonic doubling level patterns then appear to be what is seen at lower redshift as redshift-magnitude band patterns. The five peak patterns in figure 5.15 are consistent with the five band pattern seen in the $z = 0.33$ 1358+62 cluster (1.4.2, figure 1.14) discussed in seminar 1. Further discussion relating to the nature of redshift-magnitude bands is deferred to seminar 8.

Figure 5.16 is a phase diagram constructed for the $c/32$ period. The diagram contains a strong concentration around 0.5 (odd $c/64$ states) and a weaker concentration around 0.0 ($c/32$ states). This pattern is consistent with expectations for objects at or approaching the $D = 6$ ($c/64$) doubling level. The phase distribution around 0.5 may contain a spatially dependent stepped pattern at still higher fractional intervals, as also seen in figure 5.8 within the HDF data, but more data are needed. Extended studies using *accurate* redshifts in the $z$ interval between 0.3 and 0.6 should be very interesting and could provide a basic test of QTC concepts.

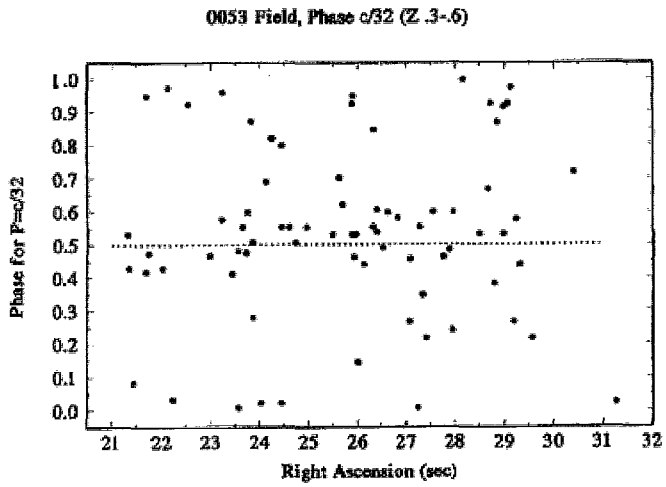


Figure 5.16: The redshift phase distribution (at the $c/32$ period) for the 1999 southern deep field sample shown in figure 5.22.

The break near $z$=0.46 suggests that the $z$ range above and below $z = 0.46$ should be separated as was done for the HDF. Above this level the $c/64$ period is very strong with a trace of $c/32$ and perhaps some 7/16 state remaining. The n/32 fractions also show the largest offsets in the decay direction toward lower redshift. As noted in the HDF study the state adjacent to the empty $c/2$ state is strong and accurately matched. The QTC model suggests this harmonic pattern could be a single aggregate at a distance corresponding to $D = 6$ decay, closer than the similar HDF association in the $D = 4$ to 5 range.

The lower redshift region is more difficult to assess. The T=0 $c/64$ states are barely represented while the $c/32$ states are stronger. The offset points below the 10/32 level mark could be a 5/16 level remnant and the leading 3/8 state is strong. With other patterns discussed (and more to come) the higher (earlier) leading state is empty. The 3/8 state is the first eighth state below $c/2$, is well fit and consistent with a D=3 system associated with the higher doubling pattern. Figure 5.15 also shows a possible T=6 state connected to a D=3 $c/8$ pattern at 5/8. The 5/8 state is apparently empty but the 39/64 state 1/64 below it is populated giving some support to the presence of a weak D=6 structure. However, two different T states are involved at c/64. The $D$ range involved suggests the pattern could be a composite structure or complexity at a doubling level. The objects below the 3/8 state associate primarily with the $D$ = 5 n/32 levels since few occupy the $D$ = 6 n/64 levels. If $D$, the number of doublings, is associated directly with distance, some objects could be more distant than the higher T=0 redshift group. As previously noted individual redshifts may not relate closely with actual distance. Much more study is required to find, map and understand such structures to determine if and how $D$ levels relate to actual distance. The SDF is consistent with QTC quantization patterns seen in the HDF. There appear to be redshift patterns potentially consistent with large associations at various stages of doubling and harmonic decay. It also seems much more likely that sharp redshift structures relate to patterns in energy levels of decay than to forms of physical structure.

## 5.6 Extensions To Lower Redshift

Further investigations of the deep field work used the lower redshift extension in the extended HDF catalog by Cohen et.al., [AX]. Figure 5.17 shows three prominent narrow redshift peaks in the $0.2 < z < 0.46$ interval below the HDF region previously discussed. Many other redshifts distribute within the interval. The pattern may look random but it is not.

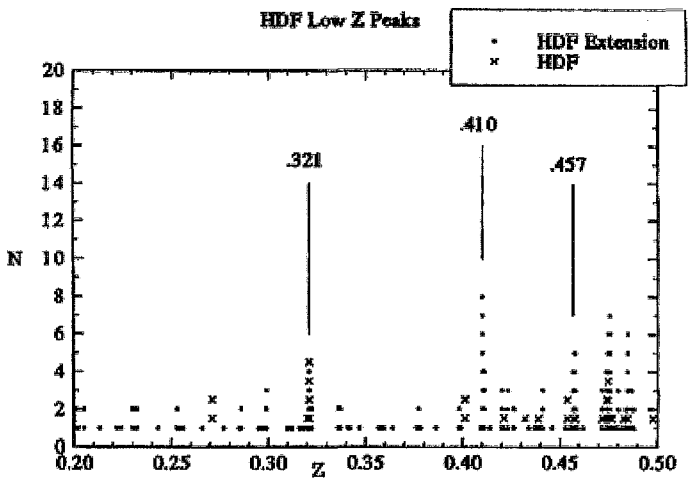


Figure 5.17: The redshift distribution in the Hubble Deep Field region below $z = 0.5$ using the complete catalog [AX]. Three peaks are present below $z = 0.46$.

The redshift pattern is easily interpreted using phase relationships with the D=4 $c/16$ period. Figure 5.18 is a phase plot, the decimal part of $z_{LT}$ divided by 1/16. The three peaks now appear at phase 0.314 ($z_o = 0.457, z_{LT} = 0.395$), 0.613 ($z_o = 0.321, z_{LT} = 0.288$) and 0.740 ($z_o = 0.410, z_{LT} = 0.359$). The peaks correspond to doubling fractions of 5/16, 39/64, and 95/128 within a few parts in a thousand, and are shown with solid lines identified by the fractions. Each fraction is the first odd doubling fraction below an empty doubling or harmonic fraction in the basic T=0 quasar pattern. They are offset by D=4=1/16, D=6=1/64 or D=7=1/128 from 3/8=6/16, 5/8=40/64, and 3/4=96/128 as shown with dashed lines. The phase diagram shows that high level quasar levels are empty. There are clear gaps at phase 1/2, 3/8. and 1/4. The missing $c/32$ redshift pattern below the absent 1/2 level is filled by the HDF three peak pattern beginning at 15/32 below 1/2=16/32 and the SDF pattern beginning at 31/64 below 1/2=32/64. These patterns are absent in figure 5.18 since they are generated from redshifts above the range used in the figure.

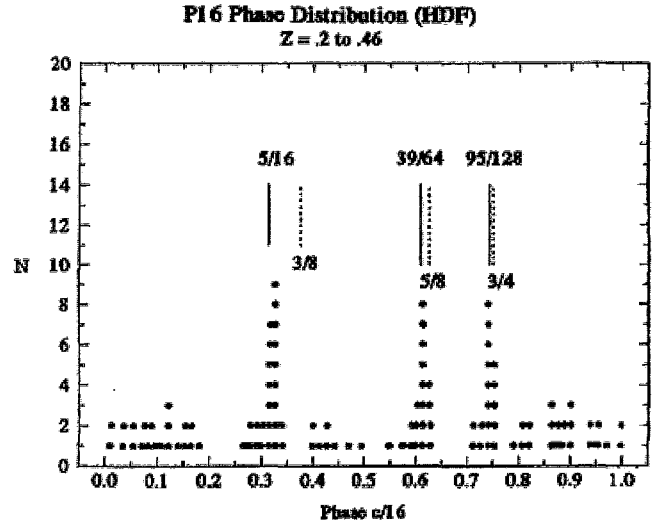


Figure 5.18: Redshift phase at the $c/16$ period for Hubble Deep Field objects with $z$ between 0.2 and 0.46. The peaks in figure 5.17 fall at 5/16, 39/64 and 95/128 doubling fractions directly below empty key quasar D=2 or 3 doubling or harmonic levels and are reinforced by objects at c/16 redshifts in phase with them.

Peaks in figure 5.18 have sharp upper bounds and bases sloping to slightly lower phase. The sloping base implies the presence of redshifts at small fixed intervals below the peak at the same higher level of doubling, almost certainly due to the presence of small harmonic cascades seen below the leading c/2 peak in the HDF and SDF patterns. Points within the peaks and base need not arise from the same aggregate providing the main peak. Points from redshifts periodically spaced in c/16 have the same phase and can represent synchronized aggregates or single objects widely linked within a quasar level doubling pattern. This could relate to large scale supercluster structures. The 17 points in the $z = .457$ peak, at phase 0.314, are enhanced by 11 points from $z = 0.376$, 0.298, and 0.224 to generate the sharp

clear peak and contributions to the sloped base. Such points represent the same feature within different c/16 cycles. Additions are normally at or below the peak, the upper bound remains sharp, decay is always toward lower redshift. The other two peaks are also slightly enhanced. Figure 5.19 shows the $c/16$ couplings for the three peaks. Formulas describing the $z(LT')$ couplings for the three phase peaks are $(16n+5)/256$, $n = 3-6$, and $(8n+5)/128$ or $(4n+3)/64$ for $n = 3-5$. Certain other related features may be present in the phase diagram, but the sample is too small at this time to comment further. A wider search using precision redshifts around the HDF and in other areas is needed to pursue such questions.

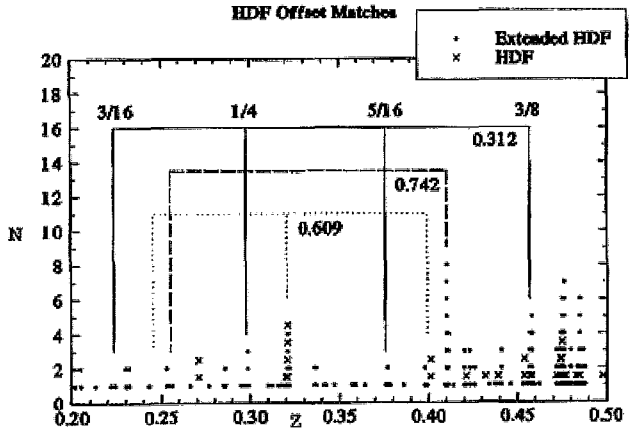


Figure 5.19: The redshift distribution in the Hubble Deep Field region below $z = 0.5$, as shown in figure 5.15, with $c/16$ phase linkages marked for the three reinforced phase peaks in figure 5.19.

The $c/16$ period pervades the region below $z = 0.5$. A very large fraction of the HDF and SDF redshifts below $z = 0.6$ are accounted for in this analysis. All significant features are accounted for. There is no significant evidence for redshifts inconsistent with QTC predictions. The cosmic rest frame and the cosmological correction, which linearizes the doubling and harmonic periodicities, are critical in high redshift work. The correction is relatively small at low $z$ which apparently explains why the $z = 0.06$ quasar related period was found previously by Burbidge (1968). There is a story about that which is appropriate to relate at this point.

I will begin with two quotations from Burbidge(1968), the first concerning the announcement of the $z = 0.061$ periodicity.

> I believe that we are now separating out a class of object which in no case is a normal galaxy of stars. The idea underlying this separation is that, while we have no reason to question the well-established conclusions that the normal cluster galaxies give a tight Hubble relation ... and that the redshifts are to be interpreted simply as Doppler expansion shifts, this wide class of peculiar emission-line objects may have a redshift component which is not of this kind. It can be seen by inspection ... that there is some rather surprising effects. The most remarkable feature is that there is a cluster of six objects widely distributed

> in the sky with $z = 0.061$ with a total spread of 0.004, and five of them have $z$ equal to 0.060 or 0.061. the probability of this occurring by chance is ... exceedingly small [$4 \times 10^{-6}$]. I conclude that this is a highly significant result. On the basis of this observation, it appears that there may be a significant pattern in the redshifts of the form $z_{obs} = 0.061n$, which is particularly pronounced for some values of n.

Burbidge goes on to discuss a variety of possible interpretations including that the redshift is an intrinsic effect. One statement of interest appears as follows.

> Alternatively, we might argue that these redshifts are of the form .... In this case the Universe must have the property that the formation or evolution of these peculiar objects is concentrated about epochs spaced in this way, i.e., it must have some sort of "crystalline" structure. If this were the case, we might ask whether normal galaxies show similar peculiarities in their distribution of redshifts. As was mentioned ..., no effect of this kind appears to be present.

The first quotation clearly credits Burbidge as discovering the c/16 quasar level periodicity, although not recognizing it as c/16. You need cosmocentric redshifts and the cosmological correction to establish that relationship and detect the periodic properties of galaxies in the same D=4 c/16 pattern. The second quotation is a remarkably good description of what QTC implies, but provides no information concerning its underlying structure. Both statements also demonstrate the deep seated conviction that there is no problem regarding the conventional dynamical structure of the expanding universe concerning ordinary galaxies.

Burbidge became well aware of my work with quantized galaxy redshifts, including the 2003 Cardiff paper relating to quasars, but never elected to become involved in a quantum based cosmology. I was not directly involved in the issue of the nature of quasars which was one of Burbidges major concerns. As my work developed it was not readily compatible with quasar models being discussed. I may say more about this period in my personal bio if I ever complete it, but it is appropriate to note that Burbidge recognized what turned out to be a true form of quantized redshifts and conceptually understood what that could imply.

There are a few points to make before summarizing the quasar and high redshift investigations and moving on to cosmology. The fact is that only odd multiples of a given $D$ level are seen with certainty. For example, as indicated in the HDF analysis, the 7/16 redshift peak may not be equivalent to 14/32. The absence of even forms could be related to the absence of even $T$ values in the Lehto-Tifft formulation of redshift families, or more precisely the absence of $T$ values which are direct powers of two, 2, 4, and 8. Six divides only once to the odd value of 3. $T$ =1, 5, and 7, with 6, and sometimes 3 related values are what is seen in addition to the pure $T = 0$ patterns. A discussion of how T values are potentially formed (in seminar 8) may provide an explanation of why T values are not equally represented.

To complete the study of the lower redshift sample, spatial associations were examined. Figure 5.20 shows the spatial location of galaxies in the $0.2 < z < 0.46$ range. Separate symbols are used to identify objects in the composite pattern containing the $z = 0.457$ peak. Clumping appears to be present, now on a larger angular scale as expected from the lower redshifts involved. The concentration in the northeast part of the figure and the general contrast between the east and west halves suggest a possible large scale physical association

of discordant redshifts as seen in the HDF. However, a much larger sample will be required to properly test this possibility in the lower redshift range.

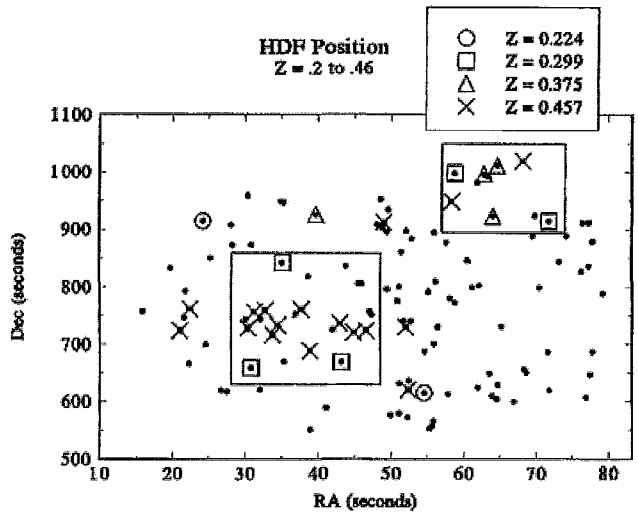


Figure 5.20: Positions for Hubble Deep Field objects with $0.2 < z < 0.46$, distinguished by redshift, for objects in the 0.3125 phase peak of figure 5.16. Boxes indicate possible physical concentrations including possible discordant redshift associations.

## 5.7 Summary

In this seminar concentrations in the redshift distribution of quasars at $z = 0.061$, 0.3, 0.6, 0.96, 1.41, and 1.95 have been shown to correspond very closely with Lehto-Tifft predictions of 1/16, 1/4, 1/2, 3/4, 1.0, and 5/4 of the speed of light, $c$, ( z= 0.064, 0.274, 0.601, 0.989, 1.441, and 1.968). The decay is presumed to be a period doubling process, beginning at the Planck scale, characterized by an index $D$ which indicates the number of doublings which have occurred. These doubling stages then appear to provide focal points below which harmonic decay patterns of galaxies develop. The redshift peaks, especially at the highest redshifts, appear to associate with an active stage where radio emission or other indications of activity are apparent. The doubling levels associated with this stage of quasar activity are $D = 0$ to 4, with the $T = 0$ ninth root family dominant and $T = 1$ and 5, 6 and 7, believed to be the next most likely values, present in increasing numbers at lower redshift.

Peaks immediately below quasar doubling levels are consistently found to correspond to more advanced doubling fractions. They form harmonic patterns at the advanced doubling level. The patterns appear to represent aggregates of galaxies at distances corresponding to the advanced D level. The harmonic patterns begin at the odd D fraction immediately below the quasar level (which is normally empty) and continues down through a cascade of three to five steps of alternating odd D fractions. For example the empty HDF D=2=1/2=16/32

state is followed by a 15/32 peak then 7/16 and 13/32. The SDF pattern begins with 31/64 one doubling higher and alternates with n/32 fractions. Correlation analysis indicates that such periodically phased peaks, although significantly different in redshift within the cascade, appear to be strongly associated spatially. The coupling generates highly discordant redshifts within pairs and groups but indicates the different peaks form one aggregate. The common advanced D values, not redshift, appears to indicate distance. Within the aggregate the lowest D fraction set appears to be older than later higher D fractions, again despite the different ordering by redshift. Monte Carlo evaluations of the discordant redshift patterns below $z = 0.5$ in the HDF show significant associations between redshift peaks which differ by 12,000 and 25,000 km/s between doubling fractions.

There is also evidence that such aggregates can chain together at the wider spaced successive quasar doubling levels to form supercluster-like chains between the galaxy aggregates. Figures 5.21 and 5.22 illustrate doubling and harmonic patterns, discussed in this seminar to illustrate the structures.

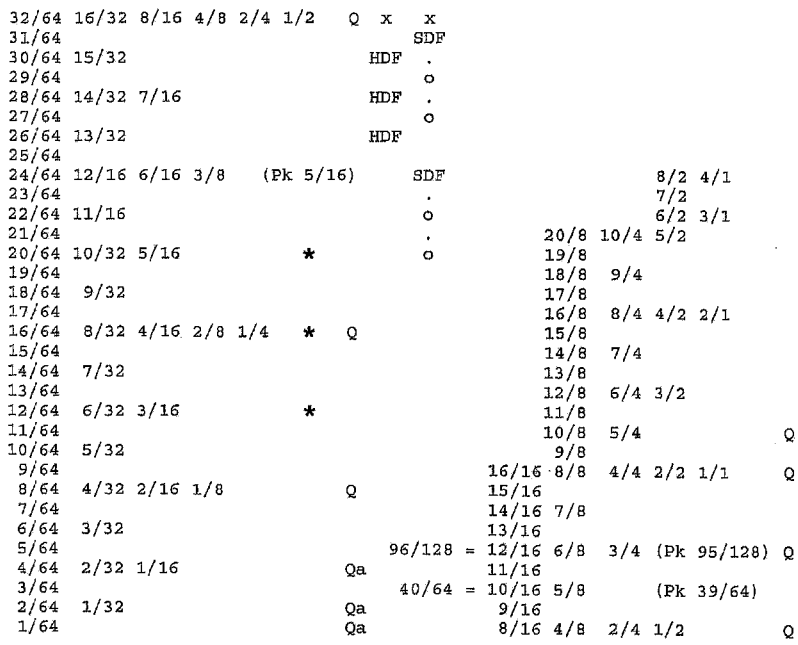


Figure 5.21: Doubling patterns showing links to higher doubling harmonic series forming galaxy aggregates and quasar level doubling chains potentially forming superclusters. Patterns are traced from D=6=c/64 at left to to D=0=c at right.

Figure 5.21 shows the c/64 harmonic pattern vertically beginning at upper left in the quasar D=2=1/2 doubling decay chain shown horizontally. Subsequent vertical steps decay through the patterns of prior doubling chains showing the quasar decay chain marked Q. Galaxy aggregate chains marked HDF and SDF are shown linked to the HDF and SDF c/32 and c/64 harmonics discussed and the c/16 supercluster-like chain beginning at D=4=6/16=3/8

and descending to D=4=3/16 is marked by asterisks. Qa denotes where the quasar chain merges with active galaxies. The higher quasar chain from D=4=c/16 to D=0 is shown at the right. The pattern extends the quasar doubling chain to the $z$=1.95 peak and shows the D=2 and D=3 decay chains leading to the D=7=96/128 and D=6=39/64 low redshift galaxy peaks.

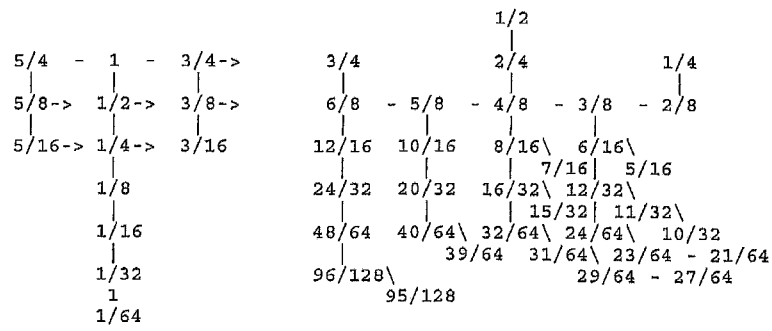


Figure 5.22: Doubling patterns showing linkage to higher doubling harmonic series leading to the formation of galaxy aggregates and quasar level doubling chains potentially forming superclusters. Patterns at left trace the standard quasar doubling chain. At the right a harmonic process is diagrammed leading to the formation of initial odd doubling fraction states which lead and interleave below the previous (empty) quasar doubling level to form galaxy aggregates. Space prevents including all links following the first two.

Figure 5.22 shows quasar doubling decay chains at the left with vertical bars, a harmonic-like link at the top line and arrows directed to the diagram at the right. The right pattern shows a vertical doubling pattern that generates *even* harmonic fractions which are coincident with the quasar fraction until visibly decaying into a higher advanced doubling fraction to produce an odd advanced doubling fraction redshift peak. These peaks then lead harmonic patterns seen directly below advanced quasar doubling levels. The doubling process appears to extend across several doubling fractions when it occurs. The step to the odd fraction is shown with a diagonal connection. All of the harmonic patterns and supercluster-like patterns present in the data can be traced in this diagram. The D=2=3/4, D=3=5/8 and D=3=3/8 superchain descents to 95/128, 39/64 and 5/16 are shown. The HDF 15/32 to (older) 7/16 (above 15/32) and the SDF 31/64 to (older) 15/32 (above 31/64) begin the HDF and SDF advanced doubling patterns and such dual patterns can continue to complete sequences of redshift peaks. Redshift and aging sequences are readily intermixed which appears to be what correlations show. Further discussion of underlying cyclical processes is deferred to the cosmological seminars which follow.

Extended studies using precise redshifts, especially below the $z = 0.6$ active quasar peak, can provide critical, perhaps definitive, information relating to the nature of the redshift. Strong T=0 states at low doubling levels should be prominent. Photometric redshifts are not suitable to detect the fine structure expected. Equivalent local studies require much higher resolution since doubling appears to have proceeded to D=16 or beyond. Precise 21-cm redshifts are required for most local quantization work.

# Chapter 6

## Introducing Quantum Temporal Cosmology

Seminar 6 Version 5

## 6.1 Introduction

As I have developed my biography I have learned a great deal. The personal timeline has involved mostly collecting and synthesizing a lot of old records and putting them together in a logical flowing pattern. The scientific timeline has been different. It does require recalling and synthesizing many of my specific scientific investigations, but it has also involved a much more significant element, a growth of understanding. As I have written various sections I find I am suddenly asking why or how I should say something, do I understand why that is the right thing to say, what does what I am saying really mean, what deeper meaning or explanation lies under or within the thought. And every so often my mind takes the hint and suddenly there is a realization that I missed or neglected something important, and a deeper insight dawns. I keep a journal of some of those insights, and one that came on May 23, 2012 said to me "you have an inconsistency". I have been saying that time does not pass for photons, but time must pass for everything, think about it, and suddenly I realized that time does pass for photons, but not in a classical sense. In QTC tau-space you can have it both ways. I introduced the concept of tau and sigma-spaces in 1993 as described in seminar 4, primarily in relation to properties of fundamental particles, but had not considered them in detail from the cosmological viewpoint. It appears that a more careful analysis of tau-space is apparently where the answer to the question of how time passes for photons resides. The answer may be quite simple but has significant consequences.

Many of the bits and pieces that have been developed through the earlier seminars, and even my social timeline, represent the history of a developing story. I intend to leave it that way and not go back and change the story by inserting some of the later insights because that is not the way it happened, and a biography should tell the story as it happened. Instead, as I construct a cosmology, I will introduce new concepts as they come, at least what I realized on May 23, 2012. I may insert a note that a deeper insight relating to tau-space will be provided later, but not change the learning curve at that point. Still, I freely admit I may be wrong, I follow the scientific method to the letter, but May 23, 2012 added a very significant bit of understanding from my point of view.

Some review and background development is needed to prepare the framework of QTC. The early developments regarding the nature of the redshift, discussed in seminars 1 and 2, made it clear that classical cosmology, based upon General Relativity, was almost certainly wrong, but it clearly presented a useful laundry list of things that were linked to understanding the redshift. I invented the tau-space/sigma-space concept in 1993 as a place to hang the 3-d concept of time and energy (action) which Lehto handed me. It was a handy construct where matter and the redshift could be represented, and provided a framework

to distinguish between quantum and continuous physics. For subsequent years that served well to represent matter and redshifts, and led to precise development of 'properties' of the redshift (quantization, variability, structure and evolution of galaxies, etc), as spelled out in seminar 3, and the representation of matter and the fundamental forces discussed in seminar 4. The basic elements of this seminar were presented in a colloquium on March 31, 2000 but the concepts needed to incubate. My final publication [151], an invited paper at the Hoyle Memorial Conference in Cardiff U.K., before my retirement in 2002, extended the concepts to high redshifts incorporating quasars and is summarized as seminar 5. After my retirement I retained close contact with Dr. Anthony (Tony) Pitucco, now retired but at that time Chairman of Physics and three other departments at Pima Community College. Tony has been one of my key supporters. Tony keeps reminding me how physics has become increasingly frustrated in trying to make progress in understanding current major problems like dark energy, dark matter, the failure to unify gravitation with the other forces, etc. He deserves credit for urging and encouraging me to undertake this biography to bring the QTC story together since it addresses many of those problems from a new perspective.

## 6.2 What Is Space and Time?

How is the space we occupy perceived by a photon? The answer is aberration folds it up to a one-dimensional line. Aberration is the effect you see when moving through a rainstorm. The faster you go the steeper the slope of the falling rain, and if you traveled at the speed of light all of space would fold up to a straight line coming directly at you at the speed of light, c. The aberration equation which describes this effect is easy to derive if you assume c is a constant and use a little trigonometry. The equation is shown in figure 6.1.

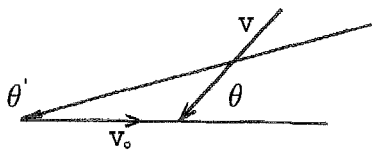


$\theta \rightarrow \theta' \rightarrow 0$ as $V_o \rightarrow c$

$$\cos\theta' = \frac{\cos\theta + \beta}{1 + \beta\cos\theta} \qquad \beta = \frac{V_o}{c}$$

Figure 6.1: The aberration equation describes the angle ($\theta'$) at which an incoming item (light or a raindrop traveling at velocity V and angle $\theta$) appears to be approaching if the observer is moving at velocity $V_o$. As $V_o$ approaches the speed of light the forward view folds up to a 1-d line straight ahead.

Special Relativity gives the same result in a more complicated way. Relative motion distorts perception of space and, at the speed of light, an observer will perceive any space he is moving relative to as one dimensional – a straight line coming right at you. Now in the case of space and photons does it matter which of these is actually moving? In some absolute sense is the photon moving through space or is space moving past the photon? We perceive we live in a three dimensional space and since motion is relative we naturally choose our space as

the reference frame and assume photons move through space. But, what kind of a space do you suppose photons live in, and what would they think?

Photons moving through our 3-d space are perceived to come from all directions at the constant speed c, and it does not matter how you are moving since your motion changes how time passes in such a way that you always see photons moving at constant speed c. The constancy of c is basic to special relativity which relates motion to time. If you think about it, motion can be defined as moving in time. For a moment consider a point in space. All directions into or out of a point are radial by definition. The direction of any action at a point is radial and coincident with the flow of time. Since photons take greater amounts of time to reach an observer the more distant their starting point, one is perceiving what was happening at earlier and earlier times when one looks out in any direction from any point in space. I will refer to such a perspective as lookback time along lookback lines. Motion in any direction can be thought of as moving along a lookback line or simply moving in time. The 'distance' to any point can be replaced by a transit time to the point, so why worry about space? So, what is space? In the sense of this book space is simply where matter and energy exist and interact. Matter, energy, and time are tangible related and observable things. Space has no known property beyond dimensions. Distance is not a physical thing. As noted above it can be defined in term of transit time intervals. For example, in the cosmology developed in this book increasing photon transit time between divergent timelines provides the observed expansion of space. Space requires no particular properties, and the redshift is also linked to temporal not spatial properties. Time, not space, is basic to relativity, time is conveniently converted to a spatial coordinate, ct, by multiplying by c to work with spatial 4-space. Time plays a very basic role, so why is space given primary consideration when developing a cosmology? Space could be nothing more than the empty arena within which the tangible quantities matter, time and energy play their games. Space exists in the sense that matter and energy reside in it but is it really anything more than a name for the territory that matter and energy do not happen to occupy at any particular time? For reference, this viewpoint in physics is referred to as the Newtonian approach.

### 6.2.1 Matter, Energy and Time

Photons are a form of 'action', light radiation is a form of pure 'active' energy. As a related idea matter is a form of 'passive' energy and the two forms are related by Einstein's relationship where a given active energy is equivalent to a specific passive mass times the square of c. Light, the active form we perceive is carried by an energy field oscillating at some frequency scaled by a fundamental constant, Planck's constant, $\hbar$. Frequency is simply the number of oscillations per second which is simply the reciprocal of time 1/t. There is that funny thing time again. Time and energy are fundamentally related, they are real things! Time cannot change for a photon or its frequency would change (we will readdress that point later when we discuss the redshift). Photons have a specific energy at birth, which can be related directly to their frequency. Time slows on an object's internal clock as the velocity of any object with mass increases, and ceases to pass when V=c. Mass also increases for moving masses and diverges to infinity when V=c. The situation is a bit different for photons which can indeed move at c but are massless. However, time passes or it does not for a photon, depending on your point of view.

### 6.2.2 Now Define Spaces and Timelines

To set a clear theoretical stage to ultimately permit mathematical modeling, I will begin rather formally. (My mathematical colleagues insist on it). Imagine a line with uniformly spaced marks, called timemarks, set in a region of usual Euclidean 3-space. Any collection of such timelines shall constitute a space called tau-space. Now any individual or set of associated timelines and the related Euclidean space within which the timelines are embedded will be referred to as a sigma-space. Both tau-space and sigma-spaces are characterized by ordinary real numbers, and no other properties such as 'length' or 'orthogonality' are initially imposed. Now consider a region of sigma-space 'flowing' along a timeline such that the space flows past the timing marks recording the passage of 'cosmic' time. This is not a flow in the sense of motion in sigma-space, in QTC it is a flow in time, which I shall refer to as 'aging' or a temporal flow. Now associate a photon with the line. It must associate with a fixed point along the timemark sequence since, as we shall see, cosmic time does not pass for photons, no flow, no passage in time. The space will be flowing past the photon. An observer within the flowing sigma-space will detect photons passing through space at velocity c, the reflex of the space flowing at c. One does not actually see photons moving through space, we know nothing of their existence until they interact with something and transfer energy and/or momentum through an absorption, reflection or scattering process. Without such an interaction process it follows that all photons will automatically pass at c. We have constancy of c for all photons, a single flow rate of space along its timeline. This makes the constancy of c perhaps simpler to understand. We must, however, now make some important distinctions. As noted above the flow is a temporal flow, not a spatial flow, and we will need to distinguish between the flow of empty sigma-space and matter. In QTC the passage of cosmic time (and photons) is simply the constant temporal flow rate of our portion of sigma-space. If, in addition, a portion of sigma-space is endowed with matter then the combination will be called a g-space (the g will be explained later.) Special Relativity, known to apply within a g-space, will still maintain the constancy of c for real motion of mass within sigma-space, but does not apply to the temporal flow. All we have done is postulate a different explanation for the constancy of c. We will discuss the distinction between matter and empty space further subsequently, but broaden the discussion of timelines first.

Timelines have interesting properties, but just what is a timeline? Let us assume for now that 'time' has the same character as our usual concept of space i.e., that it has a geometric structure which can be considered 3-dimensional. Any number of bits of sigma-space and g-spaces along with their associated timelines are embedded within tau-space, and have temporal flow along their timelines . How will a massless sigma-space observer perceive tau-space? Recall the opening discussion of what aberration does to spaces when moving at c, it folds them up to one dimensional lines. From the observer's sigma-space, tau-space will appear one dimensional and will be perceived as the (classically one-dimensional) arrow (flow) of time. If you ask where does one look to 'see' our timeline the answer is given below. You can actually detect on the sky the direction of the timeline through our g-space. Before I discuss that point I need to make an important distinction. Our timeline is specific to our g-space, and is distinct from the general concept of looking back in time along what we previously defined as 'lookback' lines which are paths that photons follow to communicate between timelines. They may be formally defined as transit pathways between

timelines. A lookback line is not a timeline, it is a path through tau-space laterally between timelines. From our sigma-space viewpoint lookback lines radiate outward isotropically from any stationary point within our g-space since you can look in any direction in g-space and a photon coming in from any spatial direction must have started at some earlier point in time. You look back in time in all directions from any point in sigma-space, All those lookback lines must track back through tau-space to the origin point of the universe. The properties of lookback lines will be discussed in part 3 of this chapter. It is on lookback lines that we will encounter the redshift issue.

### 6.2.3 Transforming Between Tau and Sigma

To consolidate the timeline concept from the viewpoint of both a sigma and a tau-space observer, and introduce some additional terminology, begin in sigma-space. A massless observer in sigma-space is flowing along his timeline, which by aberration is a 1-d line (in some as yet unspecified direction) of the folded up dimensions of tau-space. Photons are flowing in from his array of lateral lookback lines carrying signals from other timelines. Reciprocally, the sigma-space timeline, from the viewpoint of an observer at a fixed point in tau-space associated with the timeline, will call the flowline his 'spaceline' since from tau-space it is sigma-space which is folded up to a line as sigma-space flows by. An isotropic array of lateral 'spaceback' lines (paths) analogous to lookback lines in sigma-space will radiate outward from his point in tau-space. If there is a sigma-space containing matter (a g-space) flowing by the tau-space observer it will be sending photons out along the spaceback lines. To visualize what happens when you transform between tau and sigma-space, let the tau observer step off his fixed temporal point and enter the sigma-space flow associated with his spaceline. As the observer adjusts to the flow along his one-dimensional spaceline associated with sigma-space the spaceline opens like an umbrella, unfolding as aberration fades away to reveal 3-d sigma-space. The observer becomes a point in sigma-space with an isotropic array of radial lookback lines around him with photons coming in from g-spaces on other timelines. What was the spaceline that the observer stepped into has become the timeline of his associated sigma-space. That line remains defined as a specific directed line in both spaces, it has just changed its character along with the observer's original isotropically distributed spaceback lines, which are now lookback lines. If the observer stepped off his spaceline as tau-space energy structures related to mass were flowing along his spaceline he will emerge in sigma-space in a region containing matter and sigma energy, most likely a galaxy. If he stepped off when only empty sigma-space was flowing by he will emerge in an empty sigma-space void, although other g-spaces on other timelines may be sending photons along his lookback lines through his massless point. If he has the right kind of receptor to intercept those photons he will see the visible spatial universe around him, at the point in time he chose to step out of tau. If the tau observer has the option to choose different cosmic times to transform he can sample the state of the universe at different cosmic times. As noted, the observer is massless. The injection of mass into sigma-space involves a conversion from energy to mass and is discussed separately.

### 6.2.4 Mass in Sigma-Space

Now reconsider physical mass motion within our g-space. Motion within sigma-space dilates (retards) time, a consequence of special relativity which I will describe in more detail later.

In QTC or a standard relativistic model motion slows the rate of passage along the associated timeline. This creates a relative drift in temporal flow for matter vs massless empty space. The cosmic background photon sea defines this massless spatial frame which is observed to be anisotropic. The distortion is classically interpreted as a Doppler induced dipole due to systematic motion of our galaxy in space. Such an interpretation is neither allowed or necessary in QTC since such random motion is apparently negligible as is demonstrated by the observation of redshift quantization which random motion would destroy (refer to discussion of global redshift quantization). In QTC it is the relative drift in temporal flow of matter and empty space which induces the dipole which will be oriented along the timeline of our g-space. The lag is not caused by ordinary mass motion within our g-space either. It is the internal motion within matter itself, the relativistic motion of quarks within protons and neutrons which induce the baryon masses making up virtually all ordinary mass in the universe. It is this relativistic motion that slows the flow of g-space matter with respect to the flow of massless sigma-space. Using the rest mass of quarks and the common baryons it is not hard to show that the delay in fact matches the scale of the CBR dipole. I will show this later in seminar 7 where the transfer of mass-energy between tau and sigma-spaces will also be discussed. The delay has other effects, if g-space time passes slightly slower than it does for massless sigma-space, tau-space may not be completely aberrated, and a g-space timeline will be a little fuzzy. Time and space may be slightly mixed, which I suspect is related to the uncertainty principle, and such things as why a photon cannot distinguish between the slits in a two slit diffraction experiment. I may comment further on related points later in the text. Since the direction of our g-space flow is defined by the CBR dipole, it might be of interest to probe the apex points in the sky. The effect should also apply to the speed of neutrinos which by being massless or nearly so could have temporal flows closer to the speed of massless sigma-space than our g-space (remember, we and our laboratory equipment are made of the very material lagging slightly in the flow rate and it is this slower flow that we define as c). This point might also be approached through the 4-d structure of bosons discussed elsewhere in this book. Neutrinos are involved in transitions which convert between 3-d and 4-d temporal structures where they presumably associate with the fourth dimension as a spatial-temporal link.

### 6.2.5 Why Choose 3-d for Time?

Aberration will fold up any number of dimensions to 1-d, so why specify that tau-space should be 3-d? Basically, it provides a symmetry with sigma-space as we know it, although certain mathematical theories suggest space could have hidden dimensions. The model for matter, energy and time proposed herein has no need for such dimensions however, and is vastly simpler. A 3-d space permits conventional dynamics, Keplerian forms with minor modifications imposed by relativity. Kepler's third law directly relates inverse square divergence of forces to the 3-d volume of space. Without that 3-d structure dynamics would be totally chaotic. The formulation of fundamental particle physics discussed in this book, using the Lehto-Tifft relationship, is a 3-d model with a 1-d spatial-temporal link. The model appears to be highly successful in describing particle properties which have to be assumed in the Standard Model, including particle masses, exclusion properties, strength of the basic forces and how photons and forces can communicate instantaneously across spatial distances (which are temporally in common). As noted in seminar 4, QTC may provide a glimpse of the basic structure of matter itself. The 3 and 4-d based Lehto-Tifft relationships

provide the basis for Quantum Temporal Cosmology (QTC) which explains major problems found in classical cosmology, such as dark matter, dark energy, and horizons (the latter two do not exist in QTC, dark matter does). Predictions of redshift states appear to yield precise fits to observed data. (For a particularly good discussion of the precision of fits to redshift periodicities refer to reference [127].) Particle masses are very close but not as precise, but there are good reasons for the difference. Particles have mass where internal dynamics of some form is presumably involved so relativistic and charge related effects enter, which are imperfectly known. Redshifts have no such problems, they relate to the massless photon which has no mass dependent internal effects. The redshift can be affected by real dynamical motion between galaxies, so far totally undetected in quantization studies. The understanding of forces provided by the model readily explains the lack of large scale gravitational links between g-spaces, there is no current temporal link as we look back in time (this point will be discussed further after defining lookback lines). The model is remarkably internally consistent, and readily testable. In my mind unless serious flaws with QTC can be demonstrated it should be actively pursued. The model provides a possible answer to the relationship between classical continuous physics and quantum physics, including the dilemma at gravitational singularities. Quantum physics provides the rules for tau-space and microscopic spaces (called p-spaces) where fundamental particles reside. The electric force, which QTC describes as a kind of hybrid force, allows the construct of larger structures, including us, who play their games in classical continuous 3-d sigma-space g-space structures within which conventional physics, including relativity, appears to apply.

## 6.3 Now Construct a Cosmology

To proceed with developing a QTC cosmological model we begin by defining the basic geometry of tau-space. To do that we conceptually look back along our timeline to $t = 0$, the point of origin. Some event occurred as time began which led to our expanding universe. Classical cosmology with its focus on space adopted the expansion as a creation and subsequent expansion of space using apparent one-dimensional time as simply a sequencing parameter. Spatial expansion spreads parallel timelines. Gravity provides dynamical control based upon General Relativity where the range of gravity is unlimited. The model has led to serious observational problems, inflation, dark matter, dark energy, gravitational singularities and other subtle problems with gravity which have not been resolved. Figure 6.2 illustrates the classical structural framework. The cosmology is a mathematically continuous theory presuming large scale dynamically controlled motion.

This is inconsistent with redshift quantization and observed spatial alignments between galaxies, discussed in earlier seminars, which deny the existence of such motion. Established astrophysics dismisses quantization evidence and pursues programs to find classical answers to the growing set of problems while rejecting almost any effort to pursue the quantum model. So much for the scientific method.

The observational data relating to quantization, as summarized in this book, is strong enough that I long ago dismissed General Relativity (except locally) and classical cosmology (almost entirely). Working with a few colleagues, it has been possible to develop an alternative quantum based model consistent with essentially all the evidence I know, both in astrophysics and the basic physics of forces and fundamental particles. It is possible to

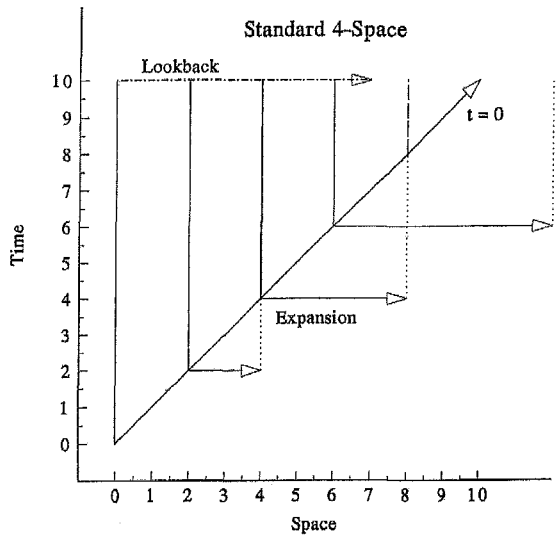


Figure 6.2: A standard classical space-time diagram. Time increases vertically, space horizontally. Timelines remain parallel and space expands horizontally at a rate proportional to distance as shown by expansion arrows.

resolve many problems inherent in classical cosmology, such as dark energy, and suggests potential answers to many more. This book has been written to bring together and summarize the observational evidence in one place. Individual studies divided may be argued, but the consistent united program is, I believe, undeniably successful. I believe it should be carefully considered and tested since it is highly verifiable. The following paragraph defines the geometry of QTC which appears consistent with the quantum picture presented in the five prior seminars.

### 6.3.1 The Origin of Time and Birth of QTC

Returning to the one item that virtually all scientists accept, our universe appears to have been initiated in a singular or near singular event billions of years ago. I will address a specific possibility consistent with QTC in seminar 8 where I will explore the very early universe. There is a clear distinction between classical and QTC cosmology with respect to the origin. QTC presumes that the event took place at or close to a near singular point which defines the origin of 3-dimensional time (tau-space). Based upon violent explosive events known to me, everything flies out radially from such points like a 4th of July firework. Space will automatically exist as a consequence of the divergent geometry of three dimensional time itself since distance can be defined in terms of transit time between radial flowlines (timelines) within an expanding three dimensional time sphere. Energy will also exist as a direct consequence of time in a reciprocal relationship. An oscillation in this relationship incorporating the well known equivalent reciprocal process, pair formation and anihilation, can then exchange active tau-space quantum energy with a passive particle (p-space) quantum form of energy as matter. The matter evolves, continuing temporal flow,

as aging in spatial sigma-space, under control of larger scale continuous physics. Emerging classical *spatial* forces now confine passive matter, *within finite temporal ranges*, as g-spaces on timelines with naturally occuring empty voids between them. The transformation provides a means for decay of tau while conserving both time and energy. Matter may, in effect, be a passive dustbin product of the active expansion. Examining how well this conceptual picture fits real evidence is the function of remaining seminars. Figure 6.3 shows a simplistic picture of energy structures diverging on timelines within tau-space. From a sigma viewpoint there are two expansions, radial in time and and transverse in space. Figure 6.4 shows a basic QTC time-time diagram where diverging timelines are characterized by angles in radians, while segments of constant cosmic time are shown dashed.

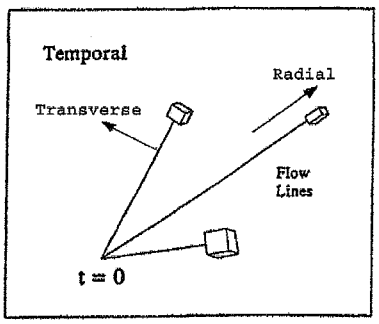


Figure 6.3: A schematic time-time diagram showing the 3-d outflow divergence of temporal energy structures from a near-singular origin at $t_o$.

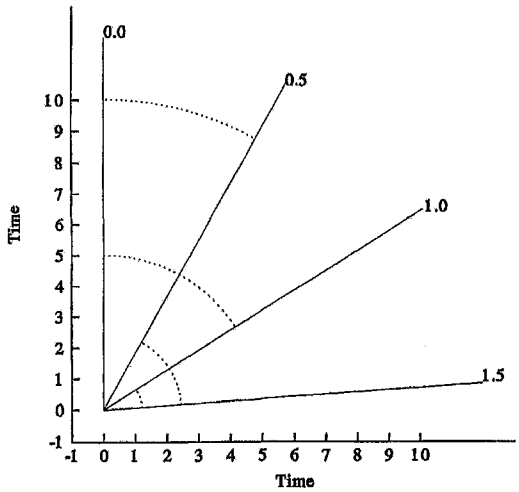


Figure 6.4: A formal time-time diagram where divergence angles are specified in radians and segments of equal time, spherical 'now surfaces', are shown dashed. The time scales are arbitrary to indicate increasing time (age) since origin.

The major geometrical difference from classical cosmology is that time runs in a radial pattern about t=0, $t_o$, and timelines diverge. Transit times between divergent timelines grow with time. From any developing sigma-space on a timeline an observer will perceive (via lookback *time*) what appears to be an expanding spatial universe. It will in fact be an expanding secondary pattern superimposed on an expanding sphere of time. This incidentally resolves the classical 'flatness' problem. In classical dynamical theory the universe appears to be at a mass density where $q_o(t)$ is precisely 1/2. Space is very flat so ordinary local 3-d geometry is essentially undistorted. In classical cosmology this is a remarkable accident often linked to the anthropic principle which attempts to couple ideal conditions for humanities' existence to cosmology. In QTC $q_o$ is always precisely 1/2. Relativistic gravitational physics plays no large scale cosmological role, only a local one where gravity can actually operate. Dynamical forces cannot be transmitted between objects significantly distinct in lookback time (on different timelines). Temporal commonality is required to transmit forces (in fact in QTC that is how it is done). This is especially clear in studies of double galaxies in seminar 2. One can look back in time (via the redshift), but not transmit force back through real physical 3-d time. I will discuss this further when examining lookback time.

At this stage the possibility of differing radial flow rates along timelines will not be considered, although some possibilities have been briefly examined [130, 131] Different flow rates along timelines may not apply to time since active energy has no mass and c is a singular Planck unit. However, branching with slight deflections can presumably occur at fissioning points along timelines. Otherwise temporal regions are spherically expanding shells, designated as 'now zones'. Locally space and time are orthogonal. Special Relativity applies and General Relativity, or equivalent, applies locally within g-spaces where matter comes into existence and gravitational dynamics emerges. Between galaxies on individual timelines the quantized redshift indicates that gravity does not apply. There is no evidence of acceleration or deceleration, the radial expansion rate is constant. Tau-space, as represented by our now zone, is considered Euclidean in structure, a finite sphere, expanding to infinity in an infinite time. The parameter $q_o$ is 1/2, but relates to spherical curvature not deceleration. There are two expansions, temporal (radial) and spatial (lateral). Both will affect energy decay related to such issues as dark energy which appears to be absent in QTC. Many of the above aspects of QTC will be discussed in the remaining seminars.

### 6.3.2 Introducing the Redshift

We now come to the question, what is the redshift, and why is it quantized? There are a number of things I need to discuss before we can directly address that issue. Basically the redshift is a measure of the change in frequency of a photon between its value at emission compared to its value at absorption, an energy ratio called the Lemaitre relationship. In cosmological models it is simply the ratio of the scale of the universe at emission and absorption, the degree of dilution of energy density. In classical cosmology the scale factor (the degree of expansion) is called R and Ra/Re = 1+z where e denotes emission, a denotes absorption and z is the redshift (z is expressed as a fraction of c, multiply by c to express it in velocity units). The observed z is denoted $z_o$. In QTC the scale ratio is simply the ratio of the age of the universe (the radius of the expanding tau-sphere) at emission and absorption, Ta/Te = 1+z.

### 6.3.3 The Cosmological Correction

In classical cosmology the dilution of energy density is determined by the expansion of space as modified by gravitational deceleration denoted by the symbol $q_o$. The curvature of space induced by gravitation (General Relativity) is specified by $q_o$. The expansion rate, the Hubble 'constant' H, is a function of $q_o$, hence time, H = H(t). Redshift z is in turn a function of H. In QTC there is no detectable deceleration but there is curvature, Photons must travel in curved paths to remain within their spherical now surfaces but the curvature has no relationship to gravity. A term equivalent to $q_o$ enters but is a constant 1/2 set by the expanding spherical geometry as noted above. Energy density dilution in QTC includes two effects, the expansion of time from radial temporal flow simultaneously with the transverse divergence of timelines as shown in figure 6.3, An observed redshift, $z_o$, in QTC is affected by both, but the intrinsic quantized part of z is presumably related only to the temporal expansion. There must be a correction applied to remove the second presumably continuous expansion effect in order to detect quantization over large photon transit times (distance). The correction, called the cosmological correction, is essential to extend quantization studies to higher redshifts. The correction is very small for nearby low redshift objects. Locally sigma-space is very 'flat'. Early studies quickly discovered quantization, readily seen locally without correction. Early global quantization studies also quickly discovered the distortion. Theoretical forms for the correction were explored, as discussed in the second seminar. The final form proved to work essentially perfectly. It opened the full range of redshifts to quantization studies, which verified and extended the local discovery. The underlying undistorted redshift was quickly shown to be quantized in the predicted Lehto-Tifft format. The following paragraph provides a simple explanation of the effect and the approach to correcting for it.

The volume enclosed by a spherical expanding now surface grows as the cube of its radius, cosmic time. The energy dilution (expansion) rate of the volume is the derivative (rate of change) of the volume, therefore varies as the square of time. (this is just the relationship between the volume and surface area of a sphere). This rate of change is H, the Hubble constant, thus H must depend on the square of time. The distortion should consequently depend on the square root of H. Using the Lemaitre relationship $z_o$ can be related directly to H providing a relationship between $z_o, q_o$ and the corrected redshift. The classical relationship between H and $q_o$ can presumably be used since $q_o$ is $q_o$ regardless of its cause. The correction is demonstrated in seminar 2 and was derived by expanding the expression for the square root of H($q_o$) in a Taylor series about $(q_o - 1/2)$ to evaluate $(1+z_o)$ in terms of $q_o$ and the corrected undistorted z, ($z_{LT}$ using a subscript LT for Lehto-Tifft). The expression for the correction including the first high order term of the expansion in $(q_o - 1/2)$ is

$$z_{LT} = 4[(1+z_o)^{1/4} - 1] - 2(q_o - 1/2)[(1+z_o)^{1/4} + 1/3(1+z_o)^{-3/4} - 4/3] + \ldots.$$

If $q_o$ is exactly 1/2 all higher terms vanish and the first order term provides an exact correction. The following equations now provide the conversion between observed ($z_o$) and Lehto-Tifft ($z_{LT}$) corrected redshifts.

$$z_{LT} = 4[(1+z_o)^{1/4} - 1] \qquad z_o = \left[\frac{z_{LT}}{4} + 1\right]^4 - 1 \qquad (1)$$

The correction was tested and proved to work perfectly for $q_o = 1/2$. No drift from an exact fit to the Lehto-Tifft predictions has been detected. The effect provides a direct test

of the spherical expansion underlying QTC. Figures 2.38 to 2.40 in seminar 2 demonstrate how an observed periodicity for short periods found in local dwarfs drifted in phase without correction, for an early model and with the model just described. A test using quasar Lyman alpha forest data [102] demonstrated that predicted periods appeared at high redshift when $q_o$ was set equal to 1/2. Later tests [125], discussed in seminar 3 (3.5.1), using deep galaxy surveys and allowing for small changes in $q_o$, showed that precise matches to Lehto-Tifft periods were found when $q_o$ was exactly 1/2 within very small uncertainties. Equation 1 provides the means to convert observed $z_o$ to $z_{LT}$ which represent the undistorted redshift pattern associated with QTC. The effect implies that photons do travel between timelines along curved paths to remain within spherical now surfaces. How curvature may be achieved without gravitation will be discussed in a later seminar.

### 6.3.4 Classical Lookback Structure

To address the redshift the geometry of how a photon approaches an observer within a now zone must be developed along with certain properties of photons. At this point QTC and classical cosmology take different paths. There is an inconsistency in classical cosmology from the point of view of QTC. Relativistic physics implies that time does not pass for photons, yet the light cone picture of classical cosmology, the space-time diagram shown in figure 6.5, shows a photon proceeding upward in cosmic-time and laterally in classical space (the classical equivalent of sigma-space). This creates a 45 degree light cone (the 45 degree photon track rotated about the vertical time axis). All world lines (time tracks for physical objects) must lie within the cone.

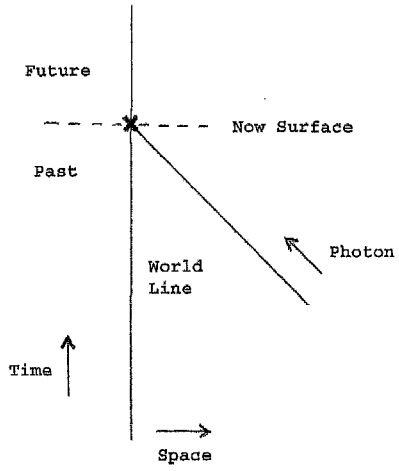


Figure 6.5: Classical space-time diagram. World lines proceed upward in time and laterally in space within a 45 degree cone determined by the speed of light. Photons approach and intersect an observer by moving up along the surface of the light cone. The apex of the cone defines the boundary between past and future events. The vertical line is the 1-d timeline of classical cosmology.

An incoming photon comes in on the past light cone redshifted continuously by classically

smooth spatial expansion. Classical cosmology says that cosmic time does pass for a photon, it simply does not know it. This is explained in Special Relativity by the motion of the photon through space retarding the photon's clock, but not the photon's location (flow) in cosmic time. Well, in QTC that works for matter with mass, but not for massless photons.

### 6.3.5 Defining the Task of QTC

In classical cosmology redshifts must be continuous variables, but they are not, and large scale dynamics must apply, but there is no evidence it does outside of galaxies. How is this possible? In QTC the radial expansion coordinate is not a velocity, sigma-space is aging by flowing *in* time. Photons come in along lookback lines in sigma-space where matter, which is aging by flowing radially, collides with them. At the same time, in QTC, photons do move at the speed of light and they do age, but not by means of continuous radial flow (although that is what drives aging of matter). If they did redshifts would not be quantized. Photons, and radiant energy in general, can be affected by motion, but that happens only within g-space. Cosmologically between g-spaces photons must advance (age) in quantized steps of radial cosmic time under control of their parent source *as they are actually seen to do.*

There are several topics which require discussion. What are photons and what distinguishes them from matter, what is the redshift, and what are lookback lines in QTC? Other issues are also involved: what is temporal commonality, how is it accomplished, and how are sigma and tau-spaces connected as energy and matter transform? These latter issues will be discussed in more depth in the following seminars in conjunction with dark matter. A continuous cosmic time flow applies to matter and sigma-space, but not to photons. This distinction is inherent in the 3-d modeling of energy and mass in tau-space. The model provides the means to predict many quantities defined empirically within the Standard Model of particle physics, explains redshift quantization, its precise observed values, and offers explanations for many problems in classical cosmology.

### 6.3.6 Structures and Processes Within QTC

The previous sections of this seminar presented the broad structure of QTC which differs in important ways from classical cosmology. Seminar 8 will examine the early universe from the viewpoint of QTC, but at this point it is sufficient to note a few key aspects. At the origin of cosmic time the Planck structure came into existence at a near singular point. This is apparent since characteristics of both the active (light) and passive (matter) forms of energy have been shown to conform with simple doubling decay patterns derived directly from Planck units. Two things must have emerged from the initial event, radiant energy units, photons or their precursor elements, and incipient higher energy resonance structures with the potential to become matter by transforming into sigma-space. In QTC the initial event is considered to perhaps have induced an oscillation between time and its inverse, energy. In any case expansion (decay) involving a period doubling process began (as demonstrated for both redshifts and matter within QTC). The model of matter which was developed in seminar 4 predicts properties of particles rather well. As an example of the success, the Higgs resonance, announced in April, 2012, was immediately integrated into QTC. The energy level of the Higgs boson at gamma level 57.75, precisely eight doubling levels above the kaon, was there waiting to be recognized. The Higgs led to an analysis of

quark structure and recognition of the 1 2 4 doubling triad as a basic structural element relating to the nature of both matter and the forces. Two basic structures appear to underly QTC from the beginning. They are a basic dipole, a bosonic structure consisting of two fermionic instants of time, and the basic triad, which I call the chronon, that QTC suggests underlies the structure of both matter and photons. Clear evidence for an underlying dipole structure has been presented, directly as a redshift offset in galaxy nuclei, in galaxy pairing and in a two stream pattern of outflow structure which forms galaxies. The significance of the triad has been demonstrated both within possible structure of quarks and as the basis of the fundamental forces. More detail of the origin of structure is deferred to seminar 8, but to begin, a simpler picture provides a distinction between matter and photons.

### 6.3.7 Photons and Redshifting

A concise summary of matter and energy within the structure of QTC indicates that the basic structure of matter, discussed in seminar 4, is 3-d with the radial component linking matter to the temporal aging flow. The generation of matter will be discussed in seminar 7. A 3-d structure defines a specific passive energy content, mass. The photon however is massless, an active energy construct. To be massless the photon must be a 2-d lateral plane of energy. It has no radial component, no volume, hence no mass and no flow in radial cosmic time. It does flow laterally since it passes between timelines. However, the photon can only communicate between that portion of timelines with which it has temporal commonality. Radial aging flow involves 3-d energy density decay. Particle structure itself is, however, maintained by internal p-space binding forces even as overall g-spaces slowly expand by outflow and evolve as proposed in the two stream model. Lateral photon flow involves no change in cosmic time. Time is conserved although energy is expended. The curved path necessary to remain within a spherical temporal now surface requires redshifting, the *observed* continuous cosmological correction.

By not flowing radially the photon will lag behind the parent structure that generates it. However, when born within a now surface a photon acquires temporal commonality, it remains linked with its parent now zone by skipping ahead periodically radially in cosmic time (age) by redshifting in quantized steps 'allowed' by certain periodic processes including doubling. This is shown in the right portion of figure 6.6 by dashed lines. How this can be accomplished and certain consequences of the effect are discussed in seminar 8. The incentive for such steps is in the radial direction of time governed by energy density decay coupled with transition restrictions. The decay process in QTC has such restrictions, a periodic flow pattern with harmonic doubling, a process with specific energy states. Just as an electron cannot spiral into the nucleus of an atom in a continuous way, the photon is a 2-d energy resonance which has a specific frequency that can make only specific changes in energy determined at some executive temporal level. It is regenerated, not re-emitted, to keep up with its now zone. Temporal commonality must control since all photons shift together no matter where they are, there is no transit time delay, simply a change of state. Such energy decays provide a means for galaxies to age, like stars, by dissipating energy. Galaxies and their photons age together, the kids never really break their ties to home. Those few redshifted photons which are actually absorbed on other timelines provide communication links which allow us to look back in time. They are immigrants which actually

leave home. Certain aspects of neutrinos could also be linked to planar or near planar structures involving the fourth dimensional link, which the neutrino appears to carry away in weak force interactions. Figure 6.6 illustrates three aspects of QTC: photon paths, temporal commonality, and dark matter. For the moment look at the upper right portion where a temporally linked photon is approaching an observer's timeline where it is absorbed within the observer's now zone. The photon travels laterally with forward steps in cosmic time for which it drops in energy yielding quantized redshifts.

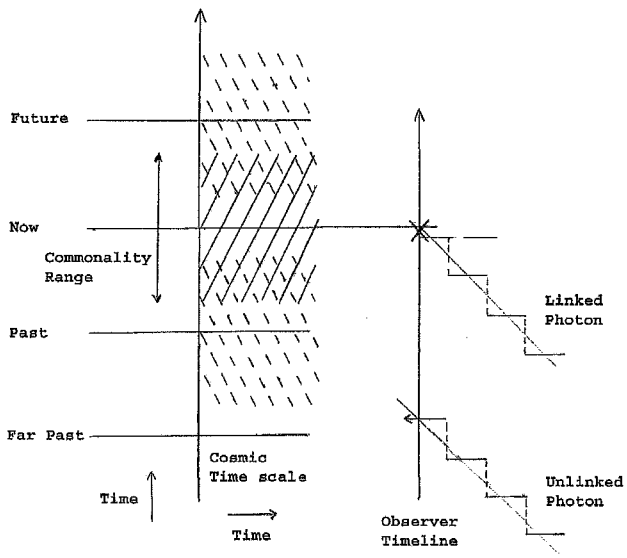


Figure 6.6: Quantum Temporal Cosmology time-time diagram. The left side illustrates the flow of a now zone. The right side shows the approach of photons to an observers timeline where absorption is dependent upon temporal commonality.

In QTC one clock is needed which relates to the radial flow, defines a real function, aging, and drives a real action, period doubling quantization in response to evolving energy density and/or temporal separation. Lateral flow in space needs no clock. Energy is expended to retain curvature (the cosmological correction), which will be further discussed in subsequent seminars. However, radial cosmic time is conserved during lateral segments of transverse flow with changes for the photon only in radial quantization steps.

There is another interesting aspect of flow in lateral time. Interactions at a timeline are orthogonal. The photon has two transverse axes, orthogonal to each other and cosmic time. This may be related to polarization, existence and orthogonality of electric and magnetic fields and play a role in pair formation, annihilation and entanglement. In pair formation both axes must transform simultaneously, there must be two equivalent particles and photons, and both time and energy are conserved. Particle anti-particle pairs are involved so there is only a tau-sigma transition with no change in temporal commonality, only the form of energy. Photon pairs and particle pairs are always in communication through a *real common point in time* although they can separate in space. Commonality involves a fuzzy point, mixing space and time since the temporal lag of matter prevents a

complete folding of dimensional axes. In QTC this is the essence of an uncertainty zone of temporal commonality through which information and force can be instantly transmitted. 3-d time in tau is an integral part of the universe locked in a partnership with 3-d sigma, which QTC suspects has a great deal to do with the distinction between Fermi and Bose statistics. Pair formation is discussed in seminars 7 and 8. The process generates two opposed patterns of particle anti-particle matter with no net change in time at conversion. Further details of matter anti-matter production requires knowing more about both dipoles and photons. Particle pairs are apparently isolated by being separated in time after formation. Locally produced anti-matter normally rapidly annihilates. The story is different for anti-matter arising from decay of nuclear g-space dipoles which formed earlier. That matter apparently exists in plain sight within the dual redshift stream pattern. Further information about the early universe, photon structure and dipole decay is needed before addressing that issue.

It is important to note that the lateral axes of tau are perpendicular to the radial flow along our timeline, the radial axis. However, we do not perceive it that way. Aberration folds up the axes, they will be indistinguishable in a fuzzy radial line blurred by incomplete aberration. Our timeline has a triple structure. Neither space can distinguish separation within the medium of the other. I will return to this point in subsequent seminars.

### 6.3.8 Communication Through Lookback Time

Lookback in QTC requires a light cone structure involving photons which cannot move smoothly forward in cosmic time, but only in quantum jumps between periods of lateral flow. Figure 6.7 repeats figure 6.6, a diagram schematically showing such an incoming path for photons. Three horizontal lines with hatched zones around them represent temporal stages of a now zone flowing upwards in cosmic time, the lower region where it was at some point in the past, the middle one where it is now, and the upper one where it will be at some point in the future. The hatching represents the fuzziness of the zone (temporal commonality range) where a mixture of space and time allow transmission of incoming information, a mixture where photons resonate with matter and can be absorbed. The thickness of this zone defines the range of time within a now zone between the 'dark' zones of the past and future. Passage across this zone (which does occur within QTC) is referred to as 'lateral evolution' contrasted with lookback along the zone toward $t_o$ denoted as 'cosmic evolution'. The QTC sphere includes the past and may or may not be bounded by *our* future or a zone that emerged earlier. The vertical line to the right represents the timeline of an observer in synchronization with the now zone locally.

Two photons are approaching the observer's timeline. The upper one from a now zone which retains commonality with the observer's surface, a distant part of an earlier epoch of the observer's now zone or one sufficiently synchronized or overlapping. The lower one is from a now zone with no temporal commonality with the observer. The photons are traveling on lateral paths at constant cosmic time, with vertical quantum redshifting jumps forward to maintain synchronization with their parent surface. When the upper photon reaches the observers timeline it is within the observer's now zone, is sufficiently synchronized and absorbed (x symbol). When the lower photon arrives at the observers timeline without commonality it passes or interacts in the past. An equivalent situation applies to the future. Generation of such unsynchronized photons is possible depending upon the character and

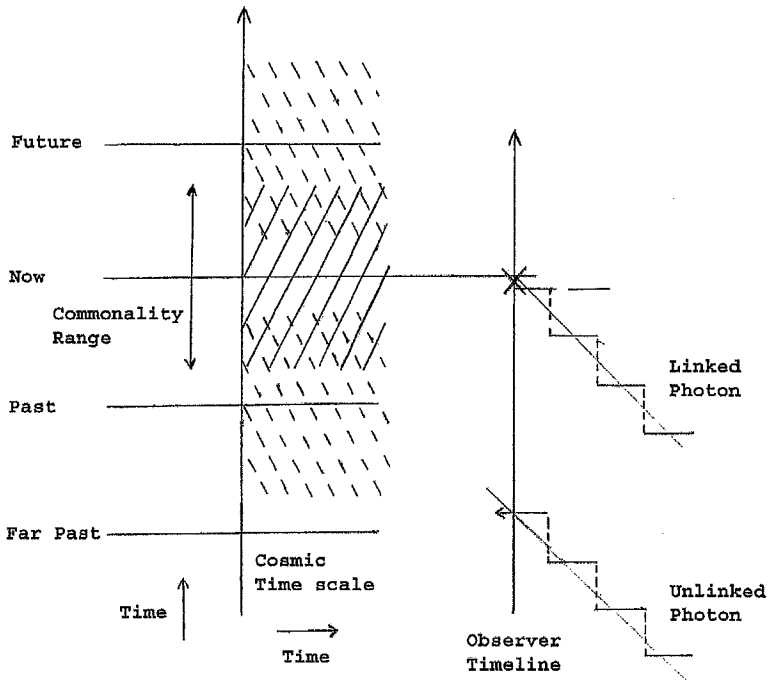


Figure 6.7: Quantum Temporal Cosmology time-time diagram. The left side illustrates the flow of a now zone. The right side shows the approach of photons to an observers timeline where absorption is dependent upon temporal commonality.

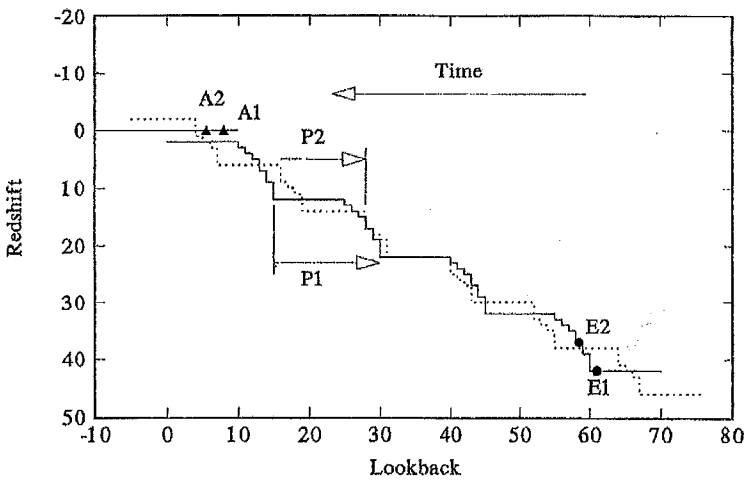


Figure 6.8: An extension back in time between synchronized now zones showing photon path linkage with quantum cascade transitions between more stable longer term resonances which appear to be characteristic of redshift quantization.

duration of the creation process at $t_o$. Aspects of lateral evolution within our now zone will be discussed in the coming seminars. Figure 6.8 shows a wider temporal range of photon evolution with redshift 'cascades' connecting more stable resonances as discussed previously in seminar 3.

Everything decays or ages in some way. The flow of time in increasing divergent timelines is a natural route of energy dilution. The QTC energy decay process involved provides stepwise period doubling harmonics. Photon transitions occur since the redshift is observed to be quantized. As noted earlier quantized redshifting is analogous to cascading decent of electrons through lower permitted energy states. Such cascades are seen in redshift variability data previously discussed. In a particle cascade the transition can generate a photon, in a redshift change the transition can regenerate a photon to equalize energy densities. Unlike a particle transition where we see the energy change (a photon), with the redshift we see the actual energy level structure. In that sense redshift variability decay cascades may be somewhat analogous to radioactive decay chains where we see actual intermediate unstable levels between longer more stable period resonances that seem to characterize redshift quantization. Redshift quantization involves an exchange of energy for time, apparently driven by evolving energy density, to maintain global energy conservation.

What triggers a quantum step in redshift, how is the energy involved actually dissipated, and how is the process perceived? Photons, just as particles, retain temporal commonality (essentially a birth time record). Photons leave a g-space travelling in lateral time and maintain a record of the emission point in cosmic time. The g-space which generates the photon continues to flow (age) in cosmic time. Any external g-space which receives a photon will perceive the source at the lookback cosmic time the photon left its source including intenal dynamics in g-space up to the moment of emission. A photon conveys the state of its parent at the moment it is emitted. When it steps forward in time the photon's energy is redshifted, but the temporal link remains unchanged. Tau-space is unaware of changing photon location after emission. Matter is bound by the fundamental forces within sigma-space, and exists in a specific quantum state within a decay pattern from the Planck stage. The flow through time continues and appears as aging of matter but not of photons that carry their cosmic time of origin (unless absorbed and reemitted so the parent changes). Timelines continue to diverge and energy density continues to drop. This generates or contributes to slow expansion of g-space, not fully confined by the fundamental forces which operate only within sigma-space. Some 'new' matter may be introduced by outflow as well.

In QTC the progress of time initiated at $t_o$ appears to be or resemble a periodic oscillation in a reciprocal relationship between energy and time. The periodic redshift states of a galaxy in QTC appear to correspond to nodes in that oscillation for reasons to be discussed in seminar 8. Consider a galaxy flowing in time as perceived by an observer on another timeline. The external observer is watching by intercepting photons from the galaxy. Now let the temporal divergence stress within the galaxy being observed reach a tipping point where massless quantum tau switches the energy balance to the next lower state (or alternatively the driving oscillation enters a new cycle). All the photons of the parent sigma-space involved, which still carry their origin record (or its previously periodically incremented record), obligingly update their origin memory one quantum step. They correspondingly pay the price by redshifting by the equivalent energy. This applies no matter where photons wandered off to since tau makes no distinction of lateral offsets from timelines. As far as the external

observer is concerned, subsequent photons received indicate the redshift and perhaps even the apparent position of the galaxy has shifted discontinuously. Well, what happens within the galaxies continuous g-space, and how and why? Probably very little, an electron after a quantum energy jump is still a normal electron and so is a galaxy. I will address that issue and the internal lateral evolution within a galaxy in subsequent seminars. An energy state instantaneous jump in QTC means only a switch was thrown in quantum tau. That is a different three space. Like changing your TV station, it does not tell you anything about what happened or why at the TV station at that moment. Perhaps it is time to recognize that galaxies are simply a larger type of quantum particle communicating using photons in a space-time linkage. Continuous existance within an aging particle may or may not be affected when the particle changes its energy state unless it happens to involve an event in the other space as well, like a timeline fission or doubling. A change of state is a quantum update in tau, including the lookback temporal time sheet photons carry. The first updated photon seen will pass the new tau status to an observer, but only a significant tau event will appear in sigma. Keep an eye on that 'sigma-source' (as QTC refers to it) in your galaxies nucleus where the two stream flow forming galaxies originates. QTC suspects that is the horizon of the future.

In QTC quantum transitions involve a change within an existing information train of carriers which already exists. It is instantaneous because neither tau or sigma can distinguish locations within the lateral medium of the other. In effect the lateral trail is folded up along the cosmic time axis (recall the fuzzy triple structure of a timeline previously noted). Any temporal commonality gap is essentially zero within the uncertainty fuzz of the foldup. Photons never leave home until they transfer within a g-space or to another timeline. There is no transit time delay in temporal information.

Although there is no apparent delay in transmitting information and forces, it is possible for *matter* to lose contact with its birth now zone. Temporal separation of mass and massless photons occurs due to relativistic retarded flow of passive energy (matter) vs active energy. This continuous lag generates lateral evolution within a now zone such that matter can drift beyond the boundaries of its birth zone. In QTC this defines the passage into dark matter. Force and communication linkage with the matter's birth temporal zone will be progressively lost. Lateral evolution and certain cycles of time within the history of a galaxy will be discussed in subsequent seminars. This transition provides the QTC distinction between past, now and future which defines the width of now zones. There is a clear distinction between communication and forces. Photons have the unique ability to move forward in time, hence we are able to *look* back in time to study the evolution of our universe (up to a point perhaps). They pay a price, redshifting from both the cosmological correction due to tau space spherical curvature and the quantized jumps to maintain ageless temporal commonality. Matter moves forward in time by aging but lags active energy with no means to advance. Forces operate only within the width of a now zone, and range depends upon the force (which is why QTC utilizes p, e, and g-space notation). There is no dynamics between g-spaces, as is quite well demonstrated by the studies of double galaxies. Forces can transmit within sigma (local space), but not through tau, (time intervals which exceed temporal commonality) We can see galaxies back in cosmological time, but commonality is updated only for photons. Forces require commonality within matter which can be lost through temporal drift that photons do not experience. I may have more to say about that subsequently, it appears to involve a distinction between Fermi and Bose statistics.

### 6.3.9 Derivation and Properties of a Lookback Line

Successive timelines tilt progressively as lookback time increases in QTC, so the lookback line must tilt to maintain appropriate light cone angles. In QTC the lookback angle may not be precisely 45 degrees with respect to a timeline, but should be close. The perceived speed of light within a g-space is the temporal flow rate of the g-space. It is conceivable that could differ between timelines, but as noted previously that seems unlikely because of the uniformity of quantum states linked to a single set of Planck units. Such differences could shift relative locations of temporal now zones which would have different Hubble constants [130,131]. In addition the lateral speed of light between timelines could be slightly faster since flow rates of g-spaces are retarded by relativistic motion within matter. If matter in all g-spaces is equivalent relativistic lag time could be the same, which could make light cone angles similar for all g-spaces. These issues may be areas for study, but until better understood a classical light cone approximation will be assumed.

The lookback equation is a function of the divergence angle $\theta$ between timelines. If $t_e$ is the time of emission of a photon at its timeline and $t_a$ is the time of absorption at an observer's timeline, the equation of the light cone is

$$t(-d\theta) = dt \qquad dt/t = -d\theta \qquad ln(t) = -\theta$$

$$t = e^{-\theta} \quad = \quad t_e/t_a \quad = \quad t_e/1 \quad = \quad t_e$$

where we have normalized to here and now $t_a = 1$. Now using Lemaitre $t_a/t_e = 1 + z$

$$z_{LT} \quad = \quad t_a/t_e - 1 \quad = \quad 1/e^{-\theta} - 1$$

$$z_{LT} \quad = \quad e^{\theta} - 1 \qquad (z_{LT} + 1) = e^{\theta}. \qquad (2)$$

The path, shown in figure 6.9, is a natural logarithmic spiral leading back to t=0.

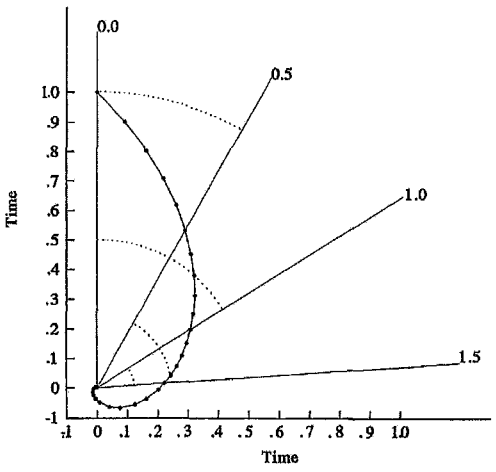


Figure 6.9: The lookback line shown in steps of 0.1 radians for a 45 degree crossing angle at timelines. The track is a logarithmic spiral crossing all timelines.

Note that although there is a clear limit at $t = 0$, it can never be reached, the track loops closer and closer but never reaches $t_o$. The nature of $t_o$ will be discussed in seminar 8.

To perceive the lookback line as a complete lookback surface, including all possible lookback directions, rotate the path around the vertical time line. Note that this lookback surface intersects all possible timelines, the entire universe is in communication with any point within it, there are no lookback horizons. This is one of the interesting properties of QTC. Our universe has a finite expanding temporal volume of interconnecting points. The surface is somewhat equivalent to the past light cone in classical cosmology (except this is a diagram in 3-d time, not space-time). Matter and events inside and outside this fuzzy now zone cannot communicate with our now zone using photons as discussed in the previous subsection (6.3.8). As noted there, it is a zone of finite temporal thickness defined by the range of temporal commonality. The inner zone is presumed to contain dark matter which has drifted far enough behind current time to be out of temporal commonality. It would presumably be sufficiently older ordinary matter. The zone could also contain matter from a later event at $t_o$ which has not expanded as far in cosmic time. Such matter could presumably never enter or reenter our now zone. The outer zone could contain matter produced by an earlier event at $t_o$, which has expanded further in cosmic time. Conceivably very high energy particles from such a zone, which may drift much faster back in time, might drift into our now zone as *very* high energy cosmic rays! There appears to be no reason this could not happen.

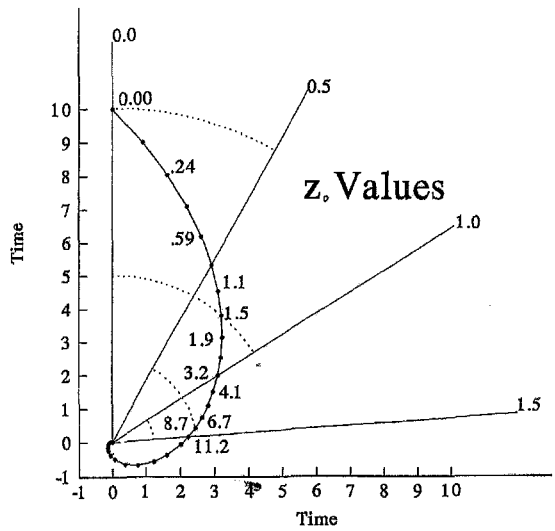


Figure 6.10: The lookback line in QTC including $z_o$ values showing that observed values at $z$ near 10 are still far from the time of origin

To visit another surprise, utilize the equations from the cosmological correction discussion (6.3.3) and lookback line derivation to derive $z_o$ and $z_{LT}$ values at points along the lookback line. Figure 6.10 shows observed $z_o$ values along the lookback line. Present day observations have reached observed z values in the vicinity of 10. In classical cosmology theory we are getting remarkably close to the classical origin time but are encountering problems since we

still see remarkably normal objects. If QTC is correct you can see that $z_o = 10$ is nowhere near the origin, only about 3/4 of the way back, leaving plenty of time for galaxy formation (which is quite different in QTC since there is no evidence gravity applies on the large scale). Why is this? Classical cosmology has only one expansion correction to redshifts, QTC has two. Classical cosmology does not account for expansion of tau-space. Table 1 is a table of $z_o$ and $z_{LT}$ as a function of divergence angle $\theta$ in radians. At theta of 1.5 radians $z_o = 11.2$ but $z_{LT}$ is only 3.48, nowhere near the origin time. T in the table is the fractional age of the universe. Things get fainter faster than classical cosmology predicts, exactly what one would expect in QTC where there is more (but predictable) expansion. Perhaps you can see in advance why classical dark energy appears to go away in QTC as will be shown in the following section. Supernovae around $z_o = 1$ should look too faint.

Table 1: $z_o$ and $z_{LT}$ values as a function of $\theta$

| Angle (Rad) | T (fract) | $z_{LT}$ | $z_o$ | Angle (Rad) | T (Fract) | $z_{LT}$ | $z_o$ |
|---|---|---|---|---|---|---|---|
| 0.0 | 1.000 | 0.0000 | 0.0000 | 1.3 | 0.273 | 2.6693 | 6.728 |
| 0.1 | 0.904 | 0.1052 | 0.1094 | 1.4 | 0.247 | 3.0552 | 8.678 |
| 0.2 | 0.819 | 0.2214 | 0.2405 | 1.5 | 0.223 | 3.4817 | 11.24 |
| 0.3 | 0.741 | 0.3499 | 0.3985 | 1.6 | 0.202 | 3.9530 | 14.63 |
| 0.4 | 0.670 | 0.4918 | 0.5902 | 1.7 | 0.183 | 4.4739 | 19.14 |
| 0.5 | 0.607 | 0.6487 | 0.824 | 1.8 | 0.165 | 5.0496 | 25.20 |
| 0.6 | 0.549 | 0.8221 | 1.112 | 1.9 | 0.150 | 5.6859 | 33.38 |
| 0.7 | 0.497 | 1.0138 | 1.468 | 2.0 | 0.135 | 6.3891 | 44.51 |
| 0.8 | 0.449 | 1.2255 | 1.913 | 2.3 | 0.100 | 8.9742 | 109.7 |
| 0.9 | 0.407 | 1.4596 | 2.471 | 2.5 | 0.082 | 11.183 | 206.6 |
| 1.0 | 0.368 | 1.7183 | 3.177 | 2.7 | 0.067 | 13.880 | 398.2 |
| 1.1 | 0.333 | 2.0042 | 4.077 | 3.0 | 0.050 | 19.086 | 1108. |
| 1.2 | 0.301 | 2.3201 | 5.232 | pi | 0.043 | 22.141 | 1823. |

For a more far-out surprise, since it even impressed me, if you trace back to $\pi$ radians (180 degrees) you see that all lookback lines intersect. That corresponds to $z_o$ about 1,800, $z_{LT}$ about 22, still well after $t = 0$. Note that this common lookback point at pi radians, which I refer to as a Pi point, repeats every 180 degrees on the track back toward $t_o$. It is a periodic event. A much more significant point in lookback occurs much further back in time at what I call the 'opacity' point where the redshift reaches a value near 1000. In QTC this point lies beyond the second Pi point and marks the stage of the early universe when space became transparent as matter and energy 'decoupled'. I will address this point and the issue of 'uniformity' in the cosmic background in later seminars. I do not think the inflation concept used to achieve uniformity in classical cosmology has any meaning in QTC since it applies to space which has little meaning in QTC. Seminar 8 will address a QTC view of $t_o$ and stages of the early universe.

## 6.4 Some Basic Tests and Illustrations Using QTC

There are still numerous issues to discuss. One trivial one worth illustrating briefly is to show geometrically that the Hubble Constant has the value 1/t as previously stated. Figure 6.11 is the standard QTC time-time diagram showing one way to define H(t). H is basically the observed velocity divided by the distance to the source. Distance is a strange quantity

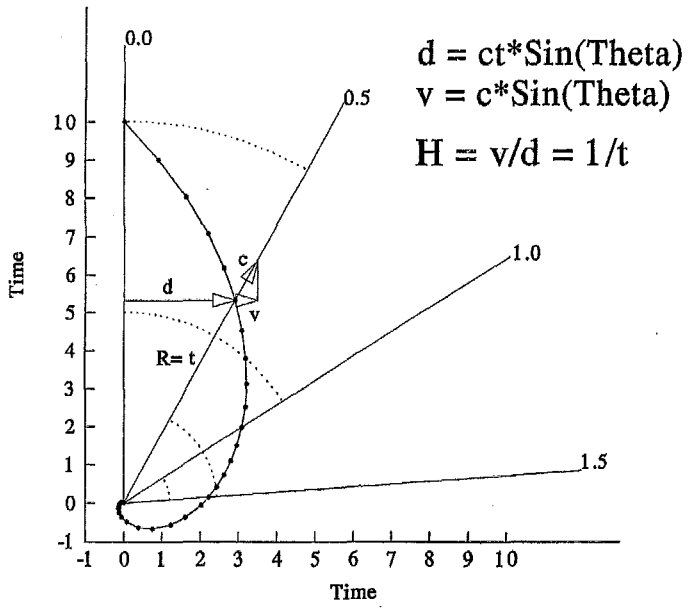


$$r=\text{Distance on arc} = ct\theta = c\theta e^{-\theta}$$

$$V=\frac{dr}{dt} = c\theta$$

$$H=\frac{V}{r} = \frac{c\theta}{ct\theta} = \frac{1}{t}$$

Figure 6.11: Derivation of H(t) in the geometry of QTC

in cosmology, it can be defined several different ways (which is why I prefer to ignore space and speak in terms of transit times). In the figure d is the perpendicular distance from our (the observers) timeline to a point on another timeline. In QTC the end points, unless very close together, need not be on the same now surface. The radial expansion rate at the external point is c in QTC so the observed line-of-sight velocity, V, is c times the sine of the deviation angle theta as shown in the diagram. Likewise the distance d is the radius R to the observed point, which is ct, again times the sine of theta. The V/d ratio is once more simply 1/t. Note it makes no difference where you put the end point of d on the observers timeline since the geometry involves similar triangles so the ratio will always be 1/t. As a second illustration, equations below the figure show the computation assuming distance follows the curved now surface implied in QTC. The result is again the same simply because velocity is just the rate of change of distance and distance on an arc is directly proportional to the radius, t. It is simply t times the velocity, which therefore cancels in the ratio leaving 1/t. The result is generally independent of the path chosen within QTC geometry.

Rather than make the content of this seminar too diverse, I will close this presentation with illustrations of two cosmological tests, the standard tests of variation of angular size and luminosity with redshift. Seminar 7 will then discuss transformation between tau and sigma, the apparent cause of the cosmological correction, temporal commonality, and other effects which can occur within QTC and relate to actual observations or predictions. This includes dark matter, various anomalous redshift effects, structural aspects of large scale structure, and communication between past, present and future, which I will denote as Langolier effects in recognition of the "Four Past Midnight" story "The Langoliers" by Steven King. Only my story is possibly not fiction.

### 6.4.1 Angular Size as a Function of z

The following derivation describes an angular size parameter for a metric rod of length $D$. The angular size is $D/d_e$ where $d_e$ is the distance at emission. As the light sphere grows the flux drops but the angle ($\angle$) in Euclidean space is unchanged. The classical equation is given at the lower part of the derivation.

$$\angle = \frac{D}{d_e} \qquad d_e = ct_e\theta$$

$$\frac{t_a}{t_e} = 1 + z_{LT} \qquad t_a = \frac{1}{H_o} \qquad t_e = \frac{1}{H_o(1+z_{LT})} \qquad d_e = \frac{c\theta}{H_o(1+z_{LT})}$$

$$\angle = \frac{DH_o(1+z_{LT})}{c\theta} \qquad \frac{c\angle}{DH_o} = \frac{(1+z_{LT})}{\theta}$$

$$(1+z_{LT}) = e^{\theta} \qquad \theta = ln(1+z_{LT})$$

$$\frac{c\angle}{DH_o} = \frac{e^{\theta}}{\theta} = \frac{(1+z_{LT})}{ln(1+z_{LT})} \qquad \text{Plot vs } z_o$$

---

$$\text{Classically} \qquad \frac{c\angle}{DH_o} = \frac{q_o^2(1+z_o)^2}{q_o z_o - (1-q_o)[\sqrt{(1+2q_o z_o)}-1]}.$$

Figure 6.12 shows the expected QTC behavior compared to classical predictions. Figure 6.13 shows a comparison with data by Gurvits [AZ] of active nuclei sizes. $z_{LT}$ is used in the calculation which is plotted against $z_o$ (observed z). The QTC calculation is close to the $q_o = 0.1$ classical prediction in the redshift range involved and is quite a good fit to the Gurvits data in the higher redshift region.

### 6.4.2 Dealing with Dark Energy

The dependence of magnitude upon redshift is somewhat more complicated. Given a standard candle, such as type 1a supernovae, one needs to calculate the light sphere area at time of absorption, $t_a$, apply the inverse square and $(1+z)$ factors for the redshift and time dilation. In the Lehto-Tifft formulation the $(1+z)$ factors must be applied for both the

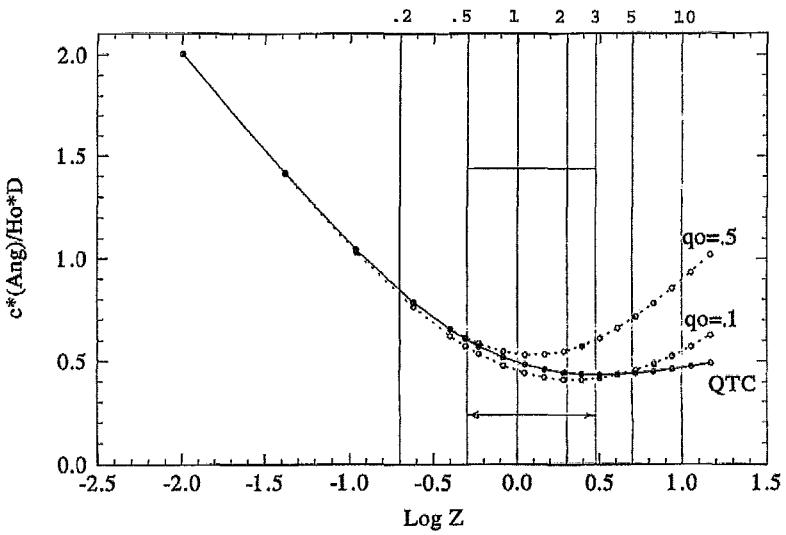


Figure 6.12: Predicted behavior of angular size in QTC and classical cosmology as a function of observed redshift. QTC tracks close to the classical $q_o = 0.1$ line. Values of z are shown at the top with the range 0.5 to 3 marked.

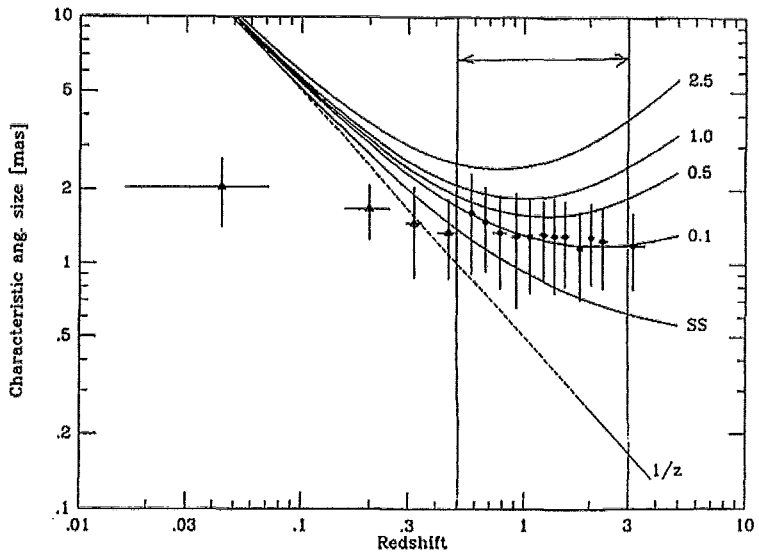


Figure 6.13: Comparison of classical predictions of angular size dependence on observed redshift according to observations from Gurvits [AZ]. The range of z from 0.5 to 3 is indicated. QTC closely tracks classical $q_o = 0.1$ as shown in figure 6.12.

temporal and spatial expansions. The following derivation shows the magnitude parameter utilized, with the classical relationship shown at the bottom. The flux is the source luminosity ($L$) divided by the surface area of a sphere at the distance to the absorber ($d_a$) and the four energy dilution factors.

$$\text{Flux} \;=\; \frac{L}{4\pi d_a^2(1+z_{LT})(1+z_{LT})(1+z_{LT})(1+z_o)}$$

When I originally did this study I was unsure of the cause of the spatial part (the reason for the cosmological correction) hence I left one of the factors as $(1+z_o)$ to split the difference. For small $z$ it will make little difference. That term should most likely also use $z_{LT}$, however, the principal effect arises because there are two sets of expansion factors. This fact alone assures that the fit will be at a fainter level compared with classical predictions. Now convert to luminosity distance which takes out the inverse square.

$$\text{Luminosity distance} \;=\; d_L \;=\; d_a(1+z_{LT})^{3/2}(1+z_o)^{1/2}.$$

Normalize to $c=1$ and $t_a=1$ in QTC (refer to the lookback equations)

$$d_a \;=\; 1-e^{-\theta} \;=\; \frac{1+z_{LT}}{1+z_{LT}} - \frac{1}{1+z_{LT}} \;=\; \frac{z_{LT}}{1+z_{LT}}.$$

Which in observed units is (multiply by $c/H_o$)

$$d_a \;=\; \frac{c}{H_o}\,\frac{z_{LT}}{1+z_{LT}}.$$

Which converts $d_L$ in normalized units to

$$d_L \;=\; z_{LT}(1+z_{LT})^{1/2}(1+z_o)^{1/2}.$$

Now convert to a relative distance modulus using

$$(M-m) \;=\; 5\;log\;\frac{d_L}{10\;pc} \qquad h=100\;H,$$

And convert to magnitude units

$$(M-m\;+\;5(log\;h)) \;=\; 42.386\;+\;5(log\;z_{LT})\;+\;2.5(log(1+z_{LT})\;+\;log(1+z_o)).$$

---

The classical equation 1s

$$(M-m\;+\;5(log\;h)) \;=\; 42.386\;+\;10(log\;q_o)\;+\;5(log\;[q_oz-(1-q_o)(\sqrt{1+2q_oz}-1)].$$

A good review of classical cosmology is contained in chapter 27 of "Modern Astrophysics" by Carroll and Ostlie [BA], however the derivations in QTC are much simpler compared to classical relativistic theory. Figure 6.14 shows the theoretical comparison of the classical and QTC expectations, where the QTC values again track close to classical $q_o=0.1$ in the observed range of supernova luminosities. Figure 6.15 shows a detailed plot of the actual fit to supernova data available at the time the seminar was given in March 2000.

QTC matches the supernova data very well suggesting that there is no significant evidence for dark energy. A more careful comparison with more recent data is clearly warranted, but again we find that QTC appears to fit all cosmological tests far better than present classical cosmological theory. Seminar 7 will continue discussions of observational effects predictable within QTC, including dark matter.

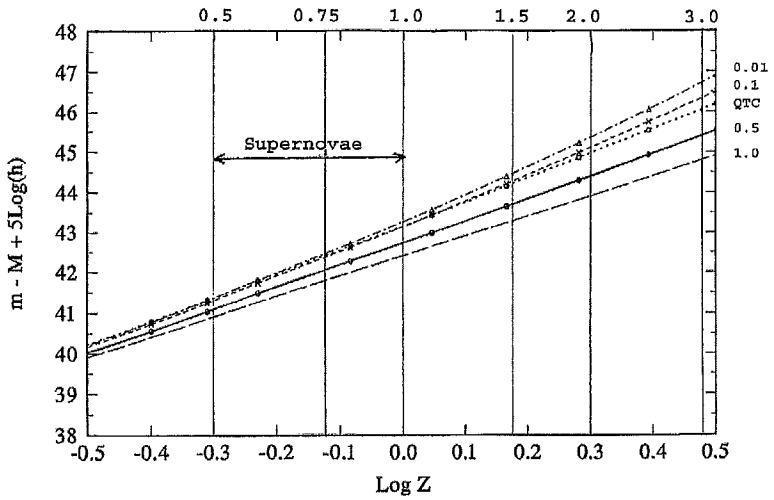


Figure 6.14: The theoretical pattern for the dependence of the distance modulus of type 1a supernovae as a function of observed redshift for classical and QTC cosmologies.

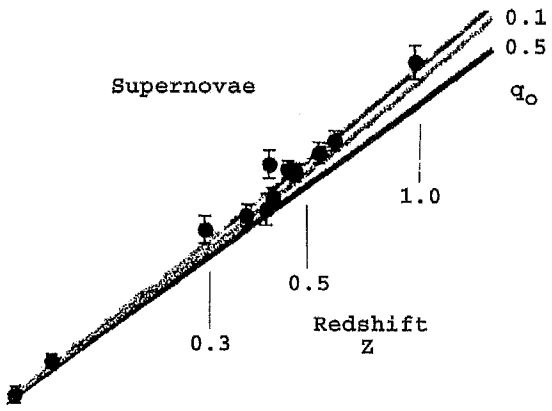


Figure 6.15: A comparison of the magnitudes of high redshift supernovae known in 2000 with the predictions in figure 6.14.

# Chapter 7

## Quantum Temporal Cosmology, Langolier Effects

Seminar 7 Version 5

## 7.1 Introduction

The previous seminar developed the basic structure of QTC, and earlier seminars discussed observations and inferences which underlie its development. There are many other important cosmological problems which can be approached to expand the scope and definition of QTC. Issues include the origin of the cosmological correction, the origin of matter, singularities including black holes and event-one, dark matter and galaxy origin and evolution, aggregates and voids, and observed effects that occur between and along timelines and within galaxies. Aspects of the early universe and matter anti-matter will be deferred to seminar 8, but many other observed phenomena related to the structure and flow in time are consistent and predictable within QTC. I refer to them as Langolier effects in recognition of Steven King's literary probe the vagaries of time [DA]. The issue of dark energy has been addressed in the previous seminar (6.4.2). A dual growth pattern involving expansion in radial time combined with lateral expansion of space appears to be able to account for the phenomenon. Any scientific theory may be incorrect and QTC is certainly incomplete, but if QTC is wrong classical cosmology has a real problem ahead to explain the growing list of Langolier effects. Some discussion is more speculative and represents suggested approaches to certain fundamental problems which are conventionally discussed only in terms of large scale gravitational dynamics. Redshift quantization implies a dynamical approach is incorrect, but more information is needed to fully discuss many aspects of QTC. Much of the work is intended to point the way toward better alternative answers to such problems. Many QTC concepts are new, and while tied closely to precise statistically sound observations require an open mind willing to try to understand reality even where it requires giving up long cherished older ideas. That is the way science should be built. Section 2, following this introduction, attempts to describe the essence of QTC up to this point in a few paragraphs. Section 3 follows with a broader discussion of where QTC is and where it is heading as the properties of active energy (photons), the properties of passive energy (matter) and the nature of the forces upon which QTC is built are integrated into a consistent cosmology. QTC offers a possible, and perhaps long overdue, way to link quantum and classical physics. That link appears to exist within the properties of time.

## 7.2 Just What is Quantum Temporal Cosmology - QTC

QTC invokes a model of time (tau) and space (sigma) as 3-dimensional coupled domains. Tau is defined as a spherical temporal domain extending radially from a near-singular point of origin. Tau is also the domain of 'active' massless energy which is the inverse of time.

The origin of time and its inverse, energy, is discussed in seminar 8. In QTC the quantized decay of the (finite) energy involved at 'event-one' occurs in tau. As energy decays its inverse, time, grows. The outflow from event-one can be represented as a wave form involving energy and time to both define quantum physics which governs tau and provides the quantum decay processes, involving harmonic period doubling, which underlies QTC. Quantized decay generates the specific energy levels which define masses and properties of the known fundamental 'particles', including the boson form where the Higgs was found. Particles occur where the existence of matter is compatible with classical 3-d Keplerean physics. Still deeper clues to internal structure of matter and the fundamental forces are readily demonstrated. The radial coordinate of tau defines cosmic time with respect to an origin referred to above as event-one. Radial flow in tau is transport *in* time, aging, a non-dynamical flow. Physically it represents a progressive drop in cosmic energy density, not by expanding in space, but by expanding in time, its real physical partner. Sigma-spaces then develop as transformed individual spatial domains within tau where energy can take a passive form as matter and within which classical spatial motion and dynamics apply. Galaxies are essentially a higher form of 'particles' flowing through tau. Radial flow in tau of sigma-spaces along 'timelines' at light speed provides the cosmic density drop and perception of aging with the passage *through* tau - an expansion in time. Divergence of timelines provides a second perceived lateral expansion, which I often refer to as expansion in space since it appears to be a continuous process. The dual expanding geometry provides an explanation of dark energy and generates a non-decelerating temporal sphere with a constant $q_o = 1/2$. This pattern resolves the cosmological 'flatness' problem. Equal-temporal spherical surfaces or zones covering small radial intervals of time are referred to as 'now surfaces or zones'.

Matter in QTC is a form of 3-d temporal resonance containing the radial component which associates it with the radial aging flow. Radiant active energy, photons, are massless hence are two dimensional resonances which flow only in *lateral* time. They are never-the-less an intimate part of the quantum structures which generate them and are linked to that structure by temporal commonality. The are in effect a wave function form of a dipole construction much as timelines are. As a consequence, although photons wander away through tau and sigma traveling in lateral time, in QTC they must advance in time by quantum jumps (the observed redshift quantization) to retain their sigma-source commonality. Photons provide the means for tau to pass energy (decay) into sigma both through redshifting in precisely defined quantum steps and the cosmological correction continuous leakage to retain now-zone curvature as they turn the decay problem over to sigma by transformation into matter. They accomplish this while conserving the reciprocal global constancy of energy and time (which appears to sum globally to zero as considered in seminar 8).

Conventional forces exist and bind matter within sigma-spaces, but do not apply within tau. Force can be transmitted across space which is sufficiently co-temporal (sigma), but not across time (tau). The four forces are defined and related in terms of characteristic powers of Planck scales which along with temporal range define their physical range limits. There are no singularities associated with forces in QTC. Tau and sigma-spaces perceive each other as essentially one dimensional since the flow of sigma through tau at speed c, by aberration, causes each space to perceive the other as one-dimensional. Tau perceives matter in sigma as co-spatial, and sigma perceives lateral time, in a specific range of radial time, in tau as co-temporal. A joint co-relationship is actually true only at connection points between the spaces where matter and energy are exchanged, the points of pair formation or

annihilation. This is where co-spatiality and co-temporality occur in a small but finite fuzzy overlap of space and time. Simultaneity is an individual property of the two spaces and distinguishes Fermi and Bose statistics. Matter and space flow at slightly different rates in sigma which appears to generates this overlap. Matter lags slightly behind massless space due to temporal lag caused by internal relativistic motion within particles, dominantly the proton. The lag generates the cosmic background dipole and results in incomplete aberration. A temporal-spatial mixture zone exists from the point of view of matter. This zone is identified in QTC as the origin of uncertainty and the juncture point between tau and sigma. Within this zone matter and energy can exchange, and force and communication can connect instantaneously. There is no transit delay (as directly observed in redshift variation). Both time, energy (active and passive) along with momentum are conserved. In QTC this fuzzy region provides the connection between Fermi and Bose statistics and tau and sigma-spaces, one ruled by quantum physics, the other by continuous physics.

## 7.3 Where QTC Is and Where It Is Going

Along with the above concise summary I will review aspects of QTC in preparation for further discussion of what they imply. As noted, QTC invokes time as 3-dimensional radiating from a near singular point. The radial outflow of energy from the event defines cosmic time (the inverse of energy, scaled frequency) for an expanding (aging) time sphere where equi-temporal surfaces or zones are referred to as 'now zones or surfaces'. Redshift quantization implies that there is no gravitational action between g-spaces (galaxies) which flow along individual timelines. All forces have both large and small range limits. Small scale limits are set by the force strength definition characterized by minimum spatial Planck intervals. This limit should prevent singularities although temporal commonality must also be maintained. A large scale force range is also defined by a temporal limit beyond which force cannot connect. The electromagnetic limit leads into dark matter and a larger gravitational limit leads to dynamical decoupling. The existence of the upper limit is confirmed from the observation that redshifts transformed to the QTC cosmological frame are quantized, showing no hint of conventional dynamical blurring. Other tests demonstrating geometrical large scale alignments, differential quantization, and exclusion properties in differentials, especially in galaxy pairs, confirm inconsistency with large scale classical dynamics. Precisely defined redshift states superimpose globally (as seen from the cosmic, CBR, rest frame) as do structures including redshift-magnitude bands and substructures within bands. Gravitation cannot be a factor in cosmology beyond the local scale of individual galaxies. There is a transition zone as one passes into dark matter where force linkage and ability to communicate is progressively lost. This is due to a lack of a common temporal link, temporal commonality, as introduced in seminar 6. Forces cannot connect through time beyond a limited range within sigma. Force and local perception clearly cannot connect 'now' with its *local* past or future, which in QTC co-exist side by side in 3-d time. We can look back in time *only* through the logarithmic lookback path corresponding to our specific now zone with which we have commonality in origin time. This lookback commonality is possible only because photons generated within our now zone on other timelines can redshift forward in time to maintain that commonality with its parent source, us, and others that fall within our common now zone. Continuous physics is contained within a 'particle', a sigma-space, defined by a temporal shell within which its fundamental and continuous forces are defined.

The radial outflow from event-one is a temporal process, an expansion in 3-d time (tau), not a velocity in a spatial sense which is applicable only within sigma-space. An observer in tau will note that sigma-spaces are flowing radially at c. Within sigma the observer will perceive the flow as aging of the sigma contents equivalent to the outflow in tau. The observer will also experience real spatial motion, arising from excess energy transmitted when passive energy (matter) was transformed into sigma. Sigma flow on diverging radial timelines in tau-space provides the actual energy density decay corresponding to the expansion of tau, a mutual 'aging' process. Each galaxy flows independently along its own timeline. The flow, whether temporal as radial redshifts or spatial as aging, should be detectable by proper-motion parallactic displacements as timelines extend and change photon transit times between timelines. (I call the aging effect spatial expansion, although it may not actually change our sigma-source scale as sources slowly diverge in tau; it may appear as radial redshifting). The flow rate will be registered to be the speed of light by observers within whatever sigma-space they occupy. The speed is the reflex of the radial flow of their outflowing g-space matter, including the observer, at the invariant Planck rate c as they receive lateral flowing photons. The radial flow makes time appear to be 1-dimensional from sigma by aberration and produces observable evolutionary effects including changing morphological patterns and redshift changes due to the cosmological correction and radial quantization. Redshifts evolve to lower values as observable outflow within galaxies, driven by relativistic lag in the flow of time for matter, appears to replace older matter which passes out of communication into dark matter. Galaxies change in morphology and redshift as temporal aging proceeds. *Spatial aging directly relates to quantum decay.*

Time does not pass continuously for photons, they do not age that way. In QTC they are two-dimensional active energy structures in lateral time with no projection or direct link to the orthogonal cosmic time axis hence no continuous temporal flow. They move in transverse time orthogonal to cosmic (radial) time. (A wave translates within the plane about and within which it is oscillating). Advances perpendicular to the plane (in cosmic time) then occur for photons by quantum energy decay in exchange for an aging step in cosmic time involving a period doubling harmonic process. Time is the reciprocal of energy, an energy loss buys a step forward in time and redshift quantization is the consequence. Photon travel between timelines laterally is a curved path with radial redshift steps to maintain association with its parent now zone. Both the curvature and steps require energy. The energy loss due to lateral curvature is analogous to classical deceleration, essentially a continuous 'spatial' effect corrected by the QTC cosmological correction (2.7.0),(3.5.0),(6.3.3). I will discuss the underlying physics of this important effect subsequently (7.7.2),(8.2.7). The effect arises due to timeline divergence and resultant now-surface curvature. With this correction for spatial (lateral) expansion no deviation from predicted period doubling redshift quantum levels in the radial temporal flow is currently detected. There is no detectable radial acceleration or deceleration. It is the lateral effect which maintains a spherical geometry ($q_o$ at precisely 1/2), which resolves the flatness problem and the overlooked quantized temporal radial expansion which leads to the dark energy problem in classical cosmology.

Allowed quantum steps associate with galaxy morphology. Timing of quantized redshift changes appears to be reflected in the shape (asymmetry) of 21 cm profiles consistent with quantum transition expectations between overlapping quantum states (3.9.1). The greater the overlap the more likely the transition. Transitions are simultaneous for all photons associated with a galaxy. Spatial separation is a property of space not time, all of sigma is co-

spatial from the viewpoint of tau. If this were not the case different transit-time delays would destroy observed quantization. Quantization allows photons to advance in cosmic time and retain temporal commonality with its parent structure's now zone regardless of where they are. The lack of spatial location influencing force or information exchange between points which have temporal commonality is illustrated (but not caused by) aberration. Aberration appears to be a spatial manifestation of temporal commonality. In the aberration picture lateral temporal axes are folded up coincident with the radial axis of the parent, space goes away for time. No matter how photons diverge in sigma that does not change their commonality in tau. Force and photon properties are transmitted by temporal quantum links which have nothing to do with space. Removing spatial information has no effect on temporal unity. From the temporal viewpoint photons never leave home. The temporal tau-state of the parent retains control of all its parts, including spatially dispersed photons which never separated in cosmic time, only in irrelevant space. Photons emitted from an external source in the *same* now zone as a receiver do leave home when absorbed and can transmit some information. They have sufficient spatial temporal commonality (sufficient simultaneity from the tau viewpoint) to allows the receiver to look back and communicate at least visual (massless) information across time. Quantum transitions via photons apparently allow a link with the past to be retained for near simultaneous events via photons.

Temporal commonality is also critical to describe the behavior of passive energy, matter, as fundamental particles in sigma-space. However, behavior differs dramatically from active energy, photons, associated with tau-space. Photons are stationary in cosmic time and maintain temporal commonality with their source and now zone by quantum steps forward in time. Matter is flowing in time but slower than massless space or energy due to internal relativistic retardation of time. It is not an ejection effect, it is simply the slow drift relative to free space; matter drifts *through* sigma. Direct evidence for such a constant drift rate behind the flow of massless sigma-space is provided by the CBR dipole, as discussed in the following section (7.3.1), and can be related directly to properties of the common proton. Passive energy (matter) progressively drifts across its now zone in what I refer to as 'lateral evolution' since, unlike photons, matter has no means of compensating for falling behind. Evidence for drift associated with redshift patterns related to morphological evolution (1.5.1) and redshift patterns inconsistent with dynamics (throughout seminar 1), culminating with redshift quantization, were introduced very early in redshift studies. Evidence for the presence of a radial outflow within galaxies, shifting older material sufficiently out of temporal communication and into dark matter, was also clearly seen. Those evolutionary stories underlie much of the remaining text. We can perceive the form of sigma structures at earlier time, but not interact with the structure. We can read a massless photon message (information) but not connect to the material itself (force). Forces generated by matter in a sigma-space do not connect beyond the boundaries of the sigma-space. You can see and feel the effects of the forces only *within* their finite force designated spaces and can neither see or interact with our local past or future, or with older or newer now zones that may border our now zone. (Well some super energetic particles might possibly drift back from the future.) If tau is a continuous three dimensional space it is clear that its spatial inclusions (sigma particles) *must* have such limits to isolate now from the past and future. Inversely the existence of such boundaries demonstrates that tau is multi-dimensional and affects the potential interpretation of event-one and the meaning of $t_o$ which will be considered in seminar 8. It is interesting to note that we call nuclear forces short-range forces. We

accept that their force range is limited, which is why I call their domains distinct p-spaces. The forces that control us we *presume* are long range in classical physics because that is what does work locally. The commonality requirement for the electrical force ends as we encounter dark matter, a zone I sometimes call e-space, and gravity ends at the boundary of g-spaces which are simply larger particles where gravity works within a universe controlled by time. The photon fooled us because of misunderstanding the redshift. In QTC the scale of temporal commonality depends upon the scale of the particle type you choose. Further discussion relating to temporal commonality is examined in section 7.4.

As noted above, in QTC photons are modeled as lateral 2-d massless active energy structures. Mass requires the addition of the third 'radial' axis to define 'passive' energy (as fundamental particles) and link matter to the radial flow in the direction of the third axis (cosmic time). All the basic 'stable' particles are modeled in QTC as 3-d energy structures (fermions) or 4-d energy-spatial structures (bosons). The photon as an active energy entity may be described structurally in QTC but is not restricted to a specific energy. The potential structure of a photon as a boson is discussed in seminar 8. In QTC bosons as particles (mesons) with mass appear in weak force related actions in sigma, and contain a 4-d temporal link of a specific fourth root force-related form (4.4.0). Bosons provide a means of conserving the temporal link involving transitions with 3-d fermions by producing neutrinos. Weak force transitions involve the neutrino whenever fermion-boson changes are involved. The neutrino must provide or preserve the temporal link. In QTC the definition of forces implies that action through a common temporal link is what characterizes actual transmission of force, not a physical presence of bosons. There is no transit time delay.

Just as redshift energy changes occur in harmonic ninth-root doubling steps from an initial Planck unit c, permitted energy levels for particles are specific cube-root or fourth-root doubling steps from the Planck energy or mass. There are two basic structural quantization modes in three dimensions, radial and angular. There are two, apparently corresponding, energy level patterns for particles within QTC denoted as gamma and pi. The gamma pattern may involve radial quantization as found in the classical vector model while the pi pattern may relate to the vector model azimuthal picture of angular momentum. This is indicated by the calculation of magnetic moments of the electron and proton (4.2.4). The two energy patterns are related by the standard $1/\sqrt{\pi}$ factor connecting the scale of the circumference and radius of a circle. Such a relationship implies some form of substructure. Different particles must have specific substructures which are energetically consistent with cosmologically allowed energy doubling levels. Structural forms can differ, but total and transitional energies between states must closely match permitted energies. Seminar 4 demonstrated such structural aspects using quarks which provide substructure for hadrons and noted that the Higgs resonance is consistent with a specific QTC energy level.

In QTC allowed stable particle energies are centered around energy doubling level 64 which is the smallest integer above unity which is both a square and a cube. 64 is conceptually related to three dimensional Keplerean dynamics where 2-d, 3-d and 4-d spatial dynamics are compatible. This suggests that structure within matter existing in 3-d sigma-space has a relationship to classical dynamics. Inverse square force divergence couples with 3-d space to permit stable dynamics slightly modified by special relativity. Since particle structures are multi-axial, slight variations in doubling structure near 64 are possible and match all ordinary stable particles. Furthermore, all the closely associated energy levels are

found to be occupied, with different classes of particles falling in different cube or fourth root structural categories. Quarks match 1/3 and 2/3 cube root levels, the light mesons populate the 3/4 fourth root levels (including the Higgs) while baryons match the pure 64.00 (0/3) doubling level or levels within one cube root of pure doubling. (Except the $\Lambda$ which appears to provide a bridge to the mesons at level 63.75, a level which can satisfy both 3-d and 4-d properties). Leptons are found to serve a unique function of providing lower limits to the quark pattern (the electron) or the light mesons (the muon) and are fermions with potentially quite different structural forms. Higher energy particles and resonances associate with level 56 which has some unique relationships with level 64. There are good reasons in QTC why matter can exist as particles at or near doubling levels 64 and 56.

Force is energy displaced over spatial distance, a four dimensional construct in QTC. The fundamental forces are therefore defined in QTC. Force strengths, the fine structure constants, are represented by a minimal basic Planck unit, the 1 2 4 triad introduced in seminar 4, displaced over successive spatial doubling intervals (4.9.0). The same basic triad was later found to apparently be an elementary structural element within certain particles (4.8.0). The forces are simply related in order of strength and tabulated in seminar 4. The light mesons as force related particles have the same types of structure at doubling levels of the particles near 3-d structural doubling level 64. In QTC at least gravitational and electrical force must be transmitted instantaneously through a temporal commonality link, as demonstrated by the lack of transit time effects in quantum transitions. Force linkage issues appear to involve temporal commonality, or lack of it and is discussed further in section 7.4

### 7.3.1 The Cosmic Background Dipole Form

To conclude the summary of earlier discussions of aspects of QTC, one of the most important effects present is the relativistic lag of the temporal flow of matter within a now zone. The effect, a well known aspect of special relativity, indicates that mass increases and time slows as spatial motion increases. The relativistic motion of quarks within fundamental particles presumably generates the mass of the composite hadrons, and determines their temporal flow rate. That flow rate will be slower than the flow rate of massless energy and empty space. Matter, dominated by protons and neutrons as the basic stable particles, must lag behind the massless energy pattern defining the decoupling era. We see that pattern as the Cosmic Background radiation field detected by looking back along lookback lines mapping the past evolution of our now zone. The differential flow should define the amplitude and direction of the CBR dipole associated with our sigma-space as it flows along its timeline. I will demonstrate that here as a direct example of one effect of the flow and lag. The components of the differential flow are provided by the transformation constants to the CBR and galactocentric rest frames. The constants in km/s galactic coordinates to transform to the CBR frame are

$$\theta = -243, \qquad \pi = -31, \qquad Z = 275.$$

The galactic center transformation is

$$\theta = 232, \qquad \pi = -36, \qquad Z = 1.$$

The zero sum of the CBR transformation is presumed to be an example of conservation of time within QTC. The agreement of the radial $\pi$ terms confirms slow outflow within our

galaxy. We may now use these values to determine the effective mass of any and all particles contributing to the drift including dark matter. In QTC the value should correspond to what we see as visible matter since dark matter is the same without temporal commonality. This should essentially match the proton when we apply relativistic corrections to the rest mass of the quarks which make up the proton. The rest mass energy of the up and down quarks are taken from QTC values in seminar 4 (in $MeV/c^2$). The proton mass energy is 938.272.

$$m_u = 4.61 \qquad m_d = 10.30.$$

The lateral transformation constants are real velocities, rotation and outflow motions in our galaxy. They combine vectorially to 245 km/s although the outflow term is of little significance in the computation. The effective cancellation of the spatial lateral component indicates that rotational terms may not exist in tau-space. The $Z$ component in QTC involves the temporal reference frame and represents the flow of our g-space in time, a flow *of* sigma-space, not a flow *in* sigma-space. Relativistic transformations to the galactic center improve quantization as expected for real velocities, however such corrections do not appear to apply to the CBR transformation. We therefore treat the $Z$ effect separately as a non-sigma temporal flow and do not combine it directly vectorially with real internal sigma motion in QTC. Temporal and spatial terms appear to act independently. Now subtract the spatial and temporal components from $c = 299792.958$ to account for the g-space lag and form two $\beta = v/c$ factors, t for temporal, s for spatial,

$$\beta_t = 0.999082699 \qquad \beta_s = 0.999182768,$$

and form mass scaling factors $1/\sqrt{1-\beta^2}$,

$$temporal = 23.3522 \qquad spatial = 24.7401.$$

Combine them additively as independent effects and scale by the sum of the rest mass of two up and one down quark,

$$(4.61 + 4.61 + 10.30) \times 48.09 = 938.76,$$

which does indeed generate the mass of the proton. In fact 938.76 is essentially precisely the total mass energy of a proton plus an electron (938.27 + 0.51 = 938.78). This is the maximum possible energy that can be extracted from the most basic particle combination responsible for most photons used to define motions. Could it be instrumental in defining the range of visible perception within a sigma-space? Although this could be an incredibly remarkable agreement there certainly appears to be a conceptual agreement with QTC. Such an agreement is necessary since there is no evidence of real relative motion between galaxies, and rotation velocities level off (flat rotation curves) such that it seems that some limit cannot be exceeded (be perceived or possible).

The effect of timeline flow lag is central to the QTC explanation of dark matter and the detection of such things as galaxian proper motion. However, before discussing these phenomena I should develop some other aspects of QTC beginning with the QTC process for transforming from active energy into mass as particles.

## 7.4 The Origin of matter, Pair Formation

There are two known methods of converting energy into mass, one involves rapid motion of matter through space used above to illustrate the slowing of the flow of time. This process has no bearing on the initial production of matter. The second process is pair formation where radiant energy (a pair of photons) is converted into a matter anti-matter particle pair. This process is rejected as the mechanism to explain the matter now present in the classical view of cosmology since the mechanism is presumed to produces an equivalent mass of anti-matter which would annihilate any matter produced. A third hypothesized process involves the growth of mass by flow through the Higgs field espoused by particle physics. However, it is unclear how to associate this with initial matter formation. The pair formation process in QTC begins with active energy and directly generates specific known particles. QTC provides a solution to the anti-matter problem by separating the two forms of matter in time at formation. They can then flow in time together distinct but in plain sight. This has been noted in early seminars and relates to the dipole structure and two stream redshift pattern within galaxies. Before that is discussed in seminar 8 I need to develop more concerning the apparent structure of matter and photons within QTC along with the large scale flow pattern of sigma-spaces in time.

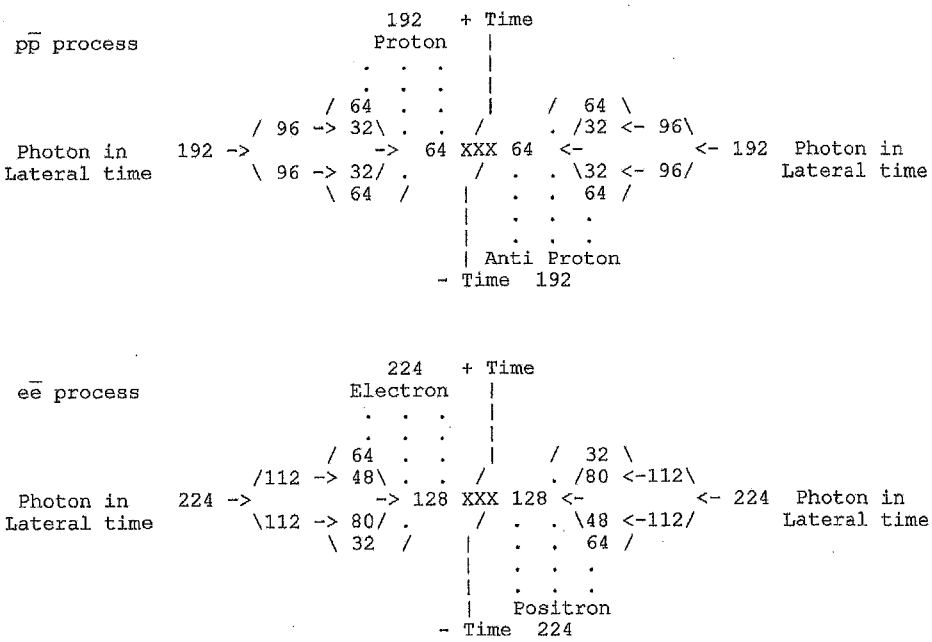


Figure 7.1: Schematic diagram of pair formation where lateral flowing photons interact generating radial opposed axes and redistribute their doubling structure to generate a particle and anti-particle pair.

Pair formation is assumed to be the means by which matter is created within QTC beginning with an illustrated summary of what is known, or I presume, about the process. As a

general rule since time is the inverse of energy (scaled frequency), both energy and time must be conserved in pair formation and annihilation processes. Only equivalent particle anti-particle pairs can form although excess kinetic energy can be present and appear as a range of kinetic energy above the particle mass equivalent energy. In the inverse pair formation process, annihilation, specific photon energies are again produced. Since only specific passive mass-energy levels exist in QTC only specific particles consistent with the doubling process can exist. QTC thus provides uniquely for the basic set of stable particles by defining the possible energies where pair formation is possible. Formation can occur at any cosmic time and there is no apparent reason why the pair process cannot proceed at any energy, but can produce a particle only at specific energy levels. Pair formation at other energies may proceed but produce only short lived noise, potentially generating the underlying quantum vacuum fluctuation noise.

Figure 7.1 is a conceptual picture of the pair formation process in slow motion for protons and electrons using doubling numbers that will match those permitted energy levels. Two photons with energies compatible with such an energy, expressed in doubling numbers, are encountering each other at nearly the same point in space-time. Recall the QTC properties of photons, they are moving in lateral constant time. Photons are bosons. In some sense the photons resonate together transforming their lateral flow into a rotating dipole. the rotation generates opposed axes perpendicular to the lateral flow, which associates them with the radial flow of cosmic time as particles. They redistribute their total energy structure into particle anti-particle structures of 64-64-64 for the proton or 128-64-32 for the electron) as shown schematically. The particles are now separate and flowing in radial cosmic time.

### 7.4.1 Temporal Commonality

Observationally QCT has demonstrated numerous key properties of the universe. At this point it is useful to introduce some of the conceptual concepts of what the QCT time anti-time dipole structure established at the origin of the universe appears to be. The universe is consistent with being a quantum structure based upon an expanding three dimensional sphere of time. The origin at $t_o$, further discussed in seminar 8, is hypothesized to be a 3-d split in time which defined the Planck units and established an initial spherical shell of time anti-time dipoles based upon the Planck units. The shell essentially defined a quantum ground state energy level. The basis for this concept is the dipole structure observed to exist in the nuclei of sigma-spaces where continuous physics applies and galaxies emerge by outflow from the dipole structure. The dipole consists of instants of time separated by an energy interval. The initial interval is presumed to be the Planck time representing a very large binding energy (its inverse). It is the decay of this energy state which we observe via redshift evolution. The wave function of this energy level can decay through a period doubling process and radial expansion. Time and anti-time cannot move in opposed directions, there is no negative radial direction. The instants initially reside in the same 'plane of time'. The anti aspect of the dipole is a property of the split interval, it defines a quantum energy level with respect to $t_o$ at zero in tau, and serves as a temporal shield against the casual recombination if the instant anti-instant pair. The instants have the same value of radial time, call it level 1. That birth time equivalence provides their temporal commonality (equal energy split above zero). Once a radial flow is established through a pair formation process the instants can separate in space, enter a rotating radial aging flow by winding up

together maintaining their temporal isolation interval (in tau which is unaware of spatial separation in sigma). This is directly observed in the dual redshift streams which form sigma structures such as galaxies and their precursors. The decay of the excited energy spacing interval is what constitutes the aging evolution of sigma-spaces and presumably the universe, again as seen in the systematic decay of redshift intervals. The anti interval is now radial, distinguishing 'planes of time' within a timeline which may mix with closely related planes since tau has no awareness of mixing of spatial locations within sigma. With this preview we can say a bit more about photons and temporal commonality.

As a boson in QTC a photon in tau must possess a bound temporal structure. In QTC a time anti-time dipole is a symmetric Bose time anti-time temporal structure. The initial dipole shell essentially defines an energy level. It has no radial extent (mass or cosmic temporal flow). Pair formation then provides a process that can split initial photons that have such a dipole structure into its sigma (Fermi) form as matter anti-matter pairs. In tau the components form a bound Bose form. Once in sigma they maintain their temporal interval distinction as matter anti-matter but are free (Fermi) particles since tau will not recognize separation in space. Pairs newly formed from a sigma-source will flow outward within their specific dual stream pattern, moving and aging, displaced in temporal commonality from their companion stream which characterized the dipole source which generated them. The temporal displacement of the two streams involved makes little difference since the spin of the sigma-source dipole winds outflowing paths together slightly spaced physically and the sigma flow has no effect on the dipole temporal spacing. I will return to the issue of planes of time and matter anti-matter in seminar 8. An astute reader may already see where this may lead, but I need to develop timeline structure further first. At this point I will comment a bit further to summarize the QTC interpretation of temporal commonality somewhat more formally at the particle level.

When a particle is born into sigma-space it joins a sigma-space flow, as just hypothesized, at slightly less than the speed of empty space because of internal relativistic delays. At that speed the particle perceives time as virtually but not quite one dimensional. Mathematically stated other nearby particles in its immediate space are nearly 'co-temporal', which means traveling along nearly the same timeline at nearly the same point in cosmic time. They are still separated in two ways, a small transit time between individual timelines due to spatial distribution, and radial location along their timeline, their degree of temporal 'simultaneity'. With incomplete folding of space and time there may also be some non-zero fuzzy range for interaction. Since particles within a sigma-space interact by forces their individual timelines are continually interwoven. Sooner or later a particle is likely to reach an intersection with one of its anti-particles, especially if the separations are very small. In classical cosmology the separation in time has no meaning. If they are sufficiently co-spatial the game is over, back to a role as active energy. Co-spatiality alone is all that is required for annihilation. In QTC co-temporality (which is distinct from spatial simultaneity) is also required, temporal separation is real and particles can disconnect in time. This is an an aspect of temporal commonality, initially defined by the time/energy interval defining the source dipole involved in the formation of a galaxy. As discussed in seminar 8 particles of matter anti-matter may have different degrees of temporal commonality.

In the pair formation/annihilation process, a reversible process, temporal commonality must act in coordination with co-spatiality. The range of temporal simultaneity over which the

process is effective is subject to discussion in seminar 8 and presumably includes the uncertainty mixture between space and time. As noted previously space and time are intermingled in QTC since matter and massless space flow at slightly different rates, causing aberration to be incomplete. The mixing also relates to the actual structure of time, a subject discussed in seminar 8. This is an area within QCT which can be investigated observationally. Temporal commonality links with other properties, time-energy in the case of the redshift. In that case since both space and the photon are massless, temporal commonality may be all that is required to generate redshifts (and provide the perfect matches found with Lehto-Tifft predicted values). The concept of temporal commonality is a central part of QTC.

### 7.4.2 The Higgs Resonance

Before leaving the subject of the generation of mass it is appropriate to briefly discuss the recent announcement of a potential Higgs particle which could play a role relating to mass generation in the Standard Model of particle physics. In fact QTC predicts that a resonance or potential particle should exist at the announced energy level near 126 GeV. The level involved is 57.75, a 4-dimensional (boson form) level in the Gamma energy doubling sequence in Table 3a of seminar 4 (4.3.0). It is $2^8 = 256$ (eight doubling levels) above the kaon. Such repetitive doubling patterns are present elsewhere among particles, in the top-charmed-down heavy quark sequence ($2^7$) and bottom-strange-up quark sequence ($2^5$). Particle structure patterns repeat in scaled patterns. If a more complete higher pattern related to the pion-kaon-eta meson pattern is actually present involving the Higgs then bosons might exist in the Pi energy sequence near level 56.75 (142.489 GeV) analogous to the eta, and 58.75 (35.622 GeV) analogous to the pion. A detailed discussion of such a pattern is contained in section 8 of seminar 4 (4.8.5) following the discussion of the potential role of the 1 2 4 doubling triad in particle structure. The fact that the 57.75 energy level is a precise multiple of 1 2 4 triads ($33 \times 7$) exactly one triad below the level 56 4-d Gamma base structure may also be a good reason to expect a detection of a resonance at that level. Particle anti-particle resonances should also occur at twice the energy of each boson. The significance of the association with a pattern of energy doubling levels centered around level 56 was also discussed in seminar 4 in relation to gauge bosons and quarks (4.8.3, 4.8.4). If the Higgs is a kaon equivalent in a higher energy version of the pion-kaon-eta meson sequence around level 64 the pion and eta equivalents should probably be present along with a muon equivalent which terminated the meson sequence. An equivalent Higgs pattern would terminate at level 60 in the Gamma structure, but no 3-d doubling structure is available at that level. The particle/resonance structure above the stable particle range and below the Higgs is very complex. In QTC the level 56 patterns appear to be more related to electronic and quark structure discussed in seminar 4 rather than the composite hadronic stable particles.

There is an alternate explanation for the discovery of the Higgs resonance. The mass being searched for was known only within a wide range, and the Higgs was in fact found at nearly the limit of the expected range. That range included one or more Lehto-Tifft levels. Was the resonance found because it is the Higgs, or because there happens to be a Lehto-Tifft level at that point? It also took an immense effort to accumulate a sufficient number of events. It would never have been found any other way. Is it really the Higgs, which just happens to match a Lehto-Tifft predicted level? If QTC is correct I would quite likely expect to see a few excess attempts to build a boson-like particle there. This is in no way meant

to downplay the magnificent successes of particle physics and high energy collider research, but it is a legitimate question. Perhaps QTC should include the Higgs, although I have no reason to think that at the moment. There may be merit in combining the concepts.

An early version of the second paragraph above was written on September 6, 2012. On September 10th I received my copy of *Physics Today* for September 2012 which contains a very nice "Search and Discovery" article by Johanna Miller [BC] discussing the discovery of the Higgs resonance at 125 GeV. The second to last paragraph in the article is quite remarkable in the context of QTC. It reads as follows.

> The Standard Model has done an excellent job of predicting how the known particles interact via the strong, weak, and electromagnetic forces, but it's incomplete. It has nothing to say about gravity, dark energy, or dark matter, and it offers no insight into why the particle masses are what they are, or why the forces have the relative strengths they do. Any deviations between the newly discovered boson's behavior and the Standard Model's predictions could open the door to new physics that might help answer those questions.

The paragraph is a remarkable summary of what QTC does do. QTC provides the levels where particles or major resonances may exist, the essential scaling pattern defining the forces and a lot more in astronomy and cosmology. The Standard Model describes how matter and energy interact given the structure but not defining it. QTC defines the basic structures. Many higher energy resonances are possible which do not match possible stable doubling levels, hence can only exist very briefly as unstable resonances. The tau lepton may be such an example as may be the newly found Higgs resonance and perhaps the Gauge Bosons. The tau lepton could represent a limiting form to a set of higher energy boson forms as the muon relates to the lower energy meson forms. Much may be learned by combining QTC with the Standard Model, and replacing large scale dynamics and concepts of force transmission by involving temporal concepts. The consistency of patterns and spacings, and especially the match of the hypothetical Higgs resonance, which had to fit within the N.75 4-d category, is a clear confirmation that the QTC n'th root period doubling concept at 3-d and 4-d is an important part of understanding both particle physics and cosmology.

## 7.5 Singularities, Supermassive Black Holes and Outflow

To proceed further it is useful to peer within the structure of supermassive black holes and later (seminar 8) event-one as well. A key element within QTC, which has been invoked in earlier discussion, involves systematic outflow within galaxies, nuclear outflow or streaming, and redshift offsets/discontinuities at nuclei. There are several aspects to examine beginning with removing the nuclear singularity, generating outflows and looking at consequences of outflow on galaxy evolution and the redshift.

The fine structure constants, derived and discussed in seminar 4, define the forces (4.9.0). Each contain a spatial interval which characterizes the force, 512 Planck units for gravitation. As one approaches a singularity in a galactic nuclear supermassive black hole, or even in a stellar black hole, matter must compress beyond the limit. As such a limit is

exceeded gravity should presumably fade away and some alternate form of stability potentially achieved. Remaining forces are available at smaller scales and some form of evolution may conceivably be possible. Since the effect occurs within sigma it is not clear how time is affected, however loss of temporal commonality will also disconnect gravity. As overall gravitational force weakens the exterior galaxy should slowly expand. Such an expansion effect is present in both the galactocentric and cosmocentric transformation constants and in two stream modeling of internal redshift structure of galaxies discussed in seminar 2. One of the most striking examples is included in the first supplement to this book where expansion effectively combines with nuclear redshift offsets to clarify anomalies in rotation patterns within ellipticals along with applications to spirals. The *Astrophysical Journal* declined to publish this article [85].

Coupled with the issue of the disconnection of forces within black holes is the observation that nuclei of galaxies appear to contain a temporal (redshift) dipole structure which in itself denies the existence of a singular center and provides the dual source for outflow observed in the two stream model (2.1.0). The initial evidence for the dual stream was discussed and illustrated (2.3.1) in reference [58]. The *Astrophysical Journal* attached my first of two editorial disclaimers to this paper. The note reads as follows.

> *Editors note.* — The referees of this paper neither could find obvious errors with the analysis nor felt that they could enthusiastically endorse publication. The subject matter is interesting and perhaps very important. A more complete assessment of the analysis is beyond the role one normally expects of referees.

Some of the more striking illustrations of the two stream model and direct evidence for the nuclear dipole are included in this seminar (7.5.6). The remaining portions of section 5 of seminar 7 discuss various forms of direct verifiable evidence in support of outflow, the dipole structure, and redshift along with morphological evolution within galaxies.

A more detailed discussion of what a singularity appears to be and how it relates to the nature of redshift dipole structures and the two stream outflow seen in galaxies will be discussed in seminar 8. At this point there is more to say about outflow and how it relates to dark matter and the evolution of galaxies in QTC.

### 7.5.1 Dark Matter

In QTC the classical process of forming galaxies by mergers and sweeping up intergalactic debris is not possible as demonstrated by redshift quantization and redshift correlations with galaxy properties. There is simply no evidence of large scale dynamics. The alternative appears to be formation and evolution by outflow from nuclear quasi-singularities seen in galactic nuclei. Evidence of systematic outflow within galaxies has been found in both galaxy modeling and global redshift periodicity transformations. Periods of nuclear activity are known including early nuclear color patterns of activity in my thesis work [9] and Lowell photometry [20]. There is evidence for both outflow and cyclical activity in nuclei. The evidence suggests successive younger zones could be generated and evolve radially as shells or spiral streams, the latter corresponding to outflow from the decay of the nuclear dipole associated with nuclei. Each generation could have more time for metal enrichment in agreement with radial metallicity gradients in galaxies, supermetallicity toward nuclei and low metallicity into halos and outward in disks. As outflow exceeds the range of *past*

temporal commonality for an inner region 'younger' observer, older matter should pass into dark matter. Gravitational coupling extends further than electromagnetic coupling since its larger spatial definition scale implies a larger coupling scale. This is consistent with the observation of extended flat rotation curves but no visible presence of mass. There is no reason to believe that dark matter differs from ordinary hadronic matter. In QTC dark matter is ordinary matter out of electromagnetic commonality, although part of it may still be within gravitational range. In fact, the CBR dipole scale computation in section (7.3.1) indicates that the temporal lag that leads to dark matter is consistent with the proton mass which dominates visible matter. That match is direct evidence that no significantly different particles are involved. The passage into dark matter is only a loss of temporal connection, not evidence for any alternate matter.

I will continue the discussion of relatively *old* dark matter in the following section to present further direct observational evidence, but first I should briefly introduce a concept of relatively *young* dark matter. In QTC there is matter which entered our temporal commonality window later than us, so there is a younger boundary to our now zone of visibility. A temporal commonality linkage extends both backward and forward in time. We are currently drifting across our now zone as a part of 'lateral' evolution of our galaxy, in what I shall refer to subsequently as one aspect of a series of evolutionary 'cycles in time'. There is one way to look forward in time. If the radial outflow concept of galaxy evolution is correct looking radially in toward a galaxy's nuclear outflow source, which I will designate as a 'sigma-source' should lead us towards a younger 'future' boundary. The forward flowing visible (but not gravitational) outer boundary of the expanding cosmic sphere defining our now zone must in some sense reside at our nuclear sigma-source horizon. In general, this boundary point in galaxies is quite possibly the common temporality limit in the direction of future galaxy development in QTC and may relate to correlations being found between supermassive nuclear black holes and galaxy properties. In QTC galaxy nuclei appear to represent or 'enclose' a break point in time. As noted earlier, discussed in seminar 2, and especially well shown in the first supplement (Ap1), [85], in this book, QTC involves the presence of a redshift offset discontinuity in galaxy nuclei. This may be difficult to comprehend but is easily seen observationally and discussed in (7.5.6) and (7.7.1). In QTC nuclear structure appears to play a basic role in the evolution of galaxies and systems of galaxies.

### 7.5.2 Flowing Through Time

There are two means to look back in time within QTC. First, one can look back *longitudinally* through the lookback corridor which, with the assistance of redshift quantum steps out of the past, allows us to map how *our* now-zone developed as far back in time as we can see, which I suspect will be nowhere near the real beginning, event-one. I will use the term 'now surface' to refer to the outer, younger, and inner, older, surfaces of 'now zones' outflowing in time. The lookback corridor has a finite width in relative cosmic time (the thickness or interval of time taken up by our now zone) and does not allow access to now zones which may have proceeded or followed our now zone with respect to their emergence at event-one. These domains lie outside the communication zone which defines the width of our logarithmic lookback track in cosmic time derived in seminar 6. The width of our lookback zone is limited by the range of temporal commonality. I will discuss the internal evolution of now zones in general beginning from event-one in subsequent sections of this chapter. In

a sense our now zone fills a *lateral* portion of cosmic time between older and newer now surfaces which are separated by its width. There is therefore a second means of looking at an interval in time *laterally* across our lookback zone by looking at evolution radially within galaxies, including our own. What happens during the interval of time (now) between non-communicating now-zones (future and past)? That is the subject I will pursue first. There are two correlated stories, the evolutionary history of the universe and the evolutionary history of now structures, beginning with galaxies. Earlier (older) outflow from event-one may form now zones outside our now domain while later (younger) zones may line the inside. This introduces some ambiguity in the use of terms past (old) and future (young) between the two approaches. The history of a galaxy begins at a particular radial point in cosmic time which is the young outer edge of its personal now zone at its sigma-source (which may reside at the older inner edge of a still earlier now-zone). It then evolves away from that entry edge (which is what I mean by laterally) toward what will eventually be the inner old edge of its personal now zone (and the young edge of a later inner now zone). There appear to be two aging cycles, a cosmic cycle of now zones and an internal cycle within the time interval defining each now zone. Temporal commonality presumably applies to the cosmic zone since we appear to see both the entry (sigma-source) and exit (old dark matter) edges from within our now zone. Each individual galaxy appears to enter its now zone at its sigma-source on the leading surface of now and leaves its zone on the following edge as it moves into dark matter. Internal aging fills the lateral time gap between external older and younger zones, a rather familiar 'generational' life cycle pattern!

### 7.5.3 Lateral Evolution, Galaxy Aging

If QTC is correct, and galaxies arise by outflow from a nuclear sigma-source function, the radial pattern observed within galaxies should map its evolutionary 'aging' traverse across the visible width of our now zone's lookback corridor. Further discussion of the step through a sigma-source, other than its generating expansion of galaxies will be deferred to a later section concerning generation and evolution of now zones. I am introducing some new concepts in physics, but they are inferred from real observations. Until we carefully follow the thread of real observations I believe we have no chance of understanding our universe.

In this section I will discuss the inner (older) fringe of our lookback zone beginning with a general prediction. The prediction is a fundamental test of QTC although at the time I carried out the initial work I had only a general idea of what to expect.

> P7.1: If objects are outflow products from sigma-sources the outer portions of objects (including but not limited to galaxies) which contain sigma-sources should be systematically redshifted, or conversely the cores should be systematically blueshifted.

This follows from the fact of the earlier emergence of the older portions, their systematic lag in time flow and photon redshifting through which photons (but not the matter) maintain temporal commonality with their parent source.

Although redshift accuracy has been discussed in earlier seminars, since small but important significant effects are involved using 21 cm redshifts I will begin by demonstrating the precision of 21 cm redshifts obtained at Greenbank and Effelsburg in the 1980s and 90s using the Greenbank 300-ft and 140-foot telescopes and the 100-m Effelsburg instrument.

Figure 7.2 contains a sample of some of the redshift standards generated at that time. Mean

Typical standards and comparisons

| Identity | V-140ft | MeanErr | N | Wid | V300ft |
|---|---|---|---|---|---|
| UGC0192 | −347.78 | +/−0.16 | 9 | 081 | −347.8 |
| UGC0668 | −232.37 | +/−0.04 | 7 | 037 | −232.3 |
| UGC1201 | +851.48 | +/−0.44 | 5 | 325 | +850.8 |
| UGC2080 | +904.11 | +/−0.27 | 7 | 137 | +902.8 |

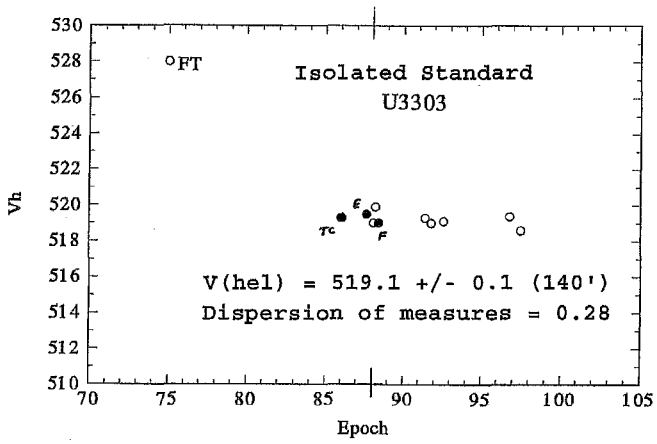


Figure 7.2: Illustrations of the precision of redshift data utilized in this book

heliocentric redshifts and profile widths with uncertainties from multiple (N) observations are shown in the table and redshifts are plotted in a time drift diagram for UGC3303. The filled symbols in the diagram represent special comparisons done in 1986-88 intercomparing 300-foot (TC or T), 140-foot (F) and Effelsburg 100-m (E) observations. There are no significant differences between instruments (although several errors in systems and software were found and corrected first to establish this). Open circles represent later 140-foot observations after the loss of the Greenbank 300-foot instrument. (FT) is an older Fisher-Tully data point for UGC3303 from 300-foot data. It is one of the many comparisons discussed in seminars 2 and 3 relating to redshift variability where redshifts shift down virtually instantaneously between periods of stability. Studies found no reason for Fisher-Tully 300-ft observations to be significantly less accurate than my later data. Redshifts can be consistently reproduced within a fraction of a km/s for objects unresolved within different telescope beams (true for UGC3303) or spaced only slightly in time. Effects I am presenting involving 'resolved' sources cannot be due to redshift measurement uncertainty. Extensive references to 21 cm data, provided in earlier seminars, are not repeated here. Unpublished lists of my redshift data are included as supplements in this book.

21 cm parameters measured are the heliocentric redshift $V_h$ (corrected to the stable center of mass of the solar system), profile width $W$, a profile shape (asymmetry) index $A$, and signal to noise $S/N$ for uncertainty measurements. There are two methods to define the redshift. I measure profiles by finding the frequency (linked to precision atomic standards) at two

edge points where 21 cm frequency profiles cross the 20% point of the average height of the central 80% of the profile. I found these measure to be highly stable and reproducible using reduction software I developed and tested extensively to optimize precision. The difference in redshifts at these points define the profile width and their average defines one highly reproducible measure of the redshift, which is the value I utilize. A second redshift value is derived by finding the profile area midpoint. The difference between the edge point and area measures is used to calculate the asymmetry index. I will define this index, unique to my measures, in a figure later in the discussion.

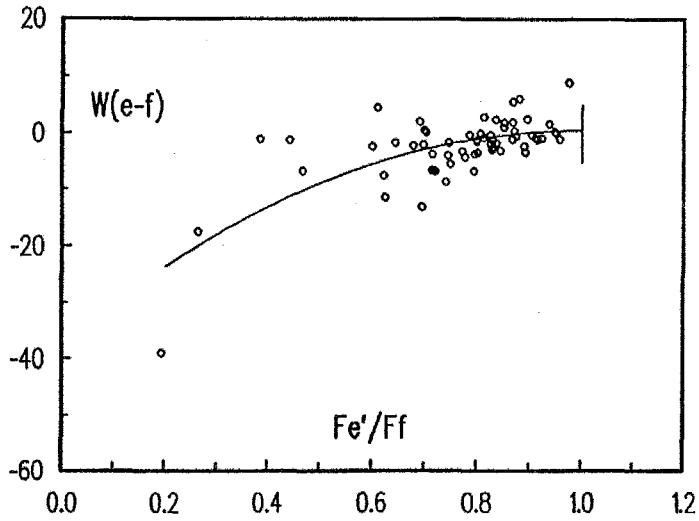


Figure 7.3: The change in profile width between Effelsburg and 140-ft Greenbank observations when plotted against relative flux. The difference goes to zero for unresolved systems indicating there is no systematic distinction between measures from different radio telescopes.

The beam sizes of the three radio telescopes used for 21 cm work are 9.0, 10.8, and 21 arc minutes for the 100-m, 300-ft, and 140-ft respectively (symbolically designated e, t or f). Radial trends in redshift parameters can be detected by comparing parameter differences between telescopes. Since observed flux grows with beam size the observed flux ratio provides a suitable radial index to detect such changes. The flux ratio is relatively insensitive to galaxy size since the ratio changes only if there is a real change in flux somewhere outside the smaller beam, allowing one to easily compare the relative character of outer and inner regions. For clearly resolved objects differences may also be compared against optical size to distinguish changes. In making comparisons a distinction must be made between small non-nucleated dwarfs and clearly nucleated rotating disk systems. This is effectively accomplished by dividing samples at profile width 100 km/s. Figure 7.3 shows the change in profile width between Efflesburg and 140-foot Greenbank measures. The figure indicates that the neutral hydrogen disk extends well beyond the visible stellar disk illustrating how the flux ratio provides a simple and effective index distinguishing between inner and outer structure.

### 7.5.4 Radial Redshifting

Figures 7.4 and 7.5 show Effelsburg minus 140-foot Greenbank measures of redshift for both the nucleated disk systems and minimally or non-nucleated dwarfs.There is a clearly significant excess redshift in the outer portion of the disk systems which is absent in the narrower dwarf galaxies. Tabulated values show the flux ratio division point for equal

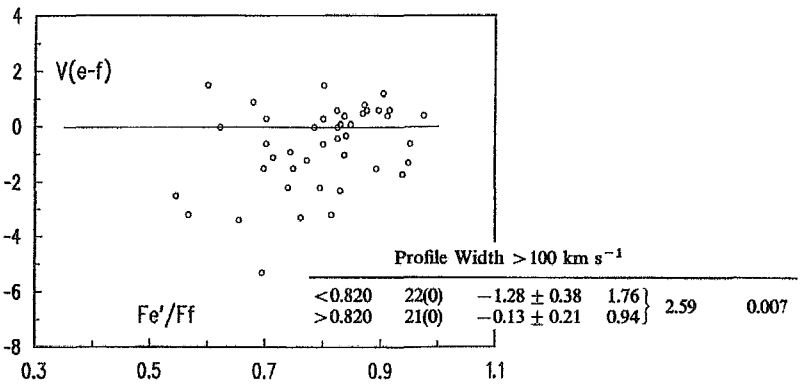


Figure 7.4: The change in redshift between Effelsburg and 140-ft Greenbank observations for galaxies with $W > 100km/s$ when plotted against relative flux. Redshift systematically increases for the outlying hydrogen. A t-test distinguishing between the outer and inner regions shows the significance of the change.

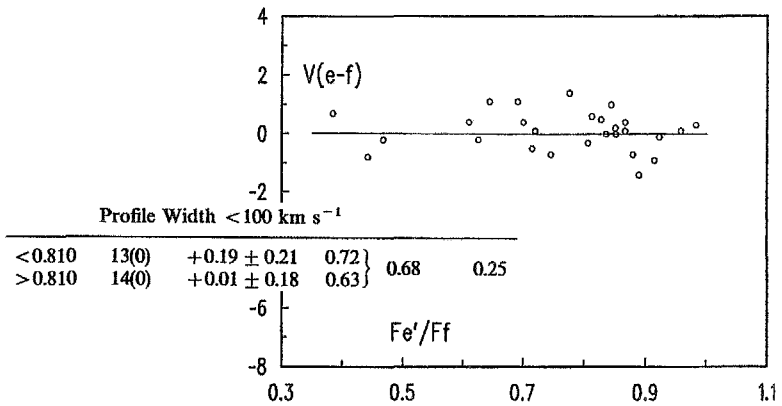


Figure 7.5: The change in redshift between Effelsburg and 140-ft Greenbank observations for galaxies with $W < 100km/s$ when plotted against relative flux. There is little if any change in redshift with radius. A t-test dividing the inner and outer sample shows no significant difference.

in/out sampling (0 = no omissions), t test parameters and probability that the samples come from the same population. The importance of the $W = 100$ km/s division point has been mentioned several times in earlier seminars. It essentially distinguishes the point at

which a 72 km/s redshift interval becomes possible within the 21 cm profile width, and the profile structure changes from single to double peaked. There is a clear structural and dynamical change at this point. Before pursuing the significance of the radial redshift excess in nucleated systems figure 7.6 illustrates the same effect comparing 140-foot minus 300-foot Greenbank redshifts plotted against galaxy major axis optical size for resolved disk systems. The effect is clearly present. Symbols distinguish 10 MHz (filled) and 5 MHz band measures.

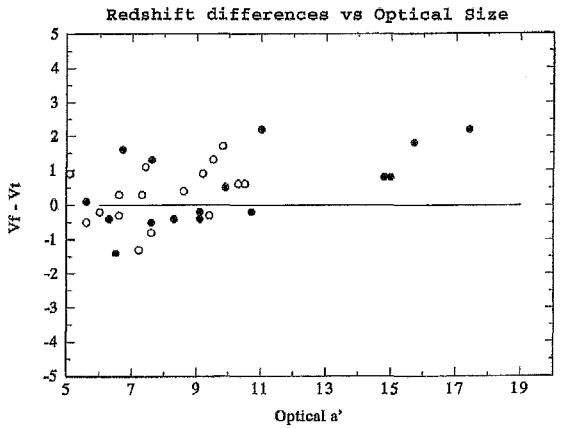


Figure 7.6: The change in redshift between 140-ft and 300-foot Greenbank observations for galaxies with $W > 100$ km/s when plotted against the optical size of the galaxies. Redshift systematically increases as outlying hydrogen is included in the signal. Symbols distinguish bandwidth used, 10 MHz for larger galaxies, 5 MHz to give higher resolution for smaller ones.

Since neutral hydrogen is optically thin (negligible internal re-absorption), especially in outer parts of galaxies, neither systematic expansion or asymmetric hydrogen distribution can produce systematic radial changes. Such effects can increase scatter but not generate systematic shifts. Increased scatter is seen in figure 7.4. Radial effects confirm the prediction of QTC that older outlying nuclear outflow has lagged behind at higher redshift and been replaced internally by lower redshift younger material. The radial redshift difference is greater than shown since the larger beam includes the lower redshift material. If the redshift increase is expanded linearly to a scale of a megaparsec it grows to essentially the scale of the Hubble constant suggesting the outflow rate effectively matches the rate of lateral universal expansion. In QTC this is the rate of divergence of radial timelines (the spatial part of QTC expansion), just as QTC predicts. The radial redshift effect vanishes for non-nucleated dwarf galaxies as shown in figure 7.5. Such galaxies nave no current (or currently active) nuclear sigma-source and show no radial redshift gradient in QTC. Only galaxies with a currently active sigma-source appear to show such effects. I will suggest a possible different nature of dwarf systems further in the cosmic evolutionary section to follow studies of radial evolution in 21 cm profile asymmetry within galaxies. At this point I need to turn to a discussion and test of the radial properties of the redshift within galaxies provided by the asymmetry parameter. The tests related to radial redshifting and asymmetry are fundamental tests of QTC totally unpredicted or expected within the domain of classical cosmology.

### 7.5.5 The Asymmetry Parameter

To begin I need to define the asymmetry parameter $A$, which defines deviation of a 21-cm profile from symmetry. Figure 7.7 illustrates the effect where redshift increases to the right. The parameter uses the average of redshifts defined by profile edge measures, which determines the heliocentric redshift $(V_2 + V_1)/2 = V_H$, and the mid profile area redshift $V_a$. In double peaked profiles $A$ basically notes whether the high or low redshift peak is dominant.

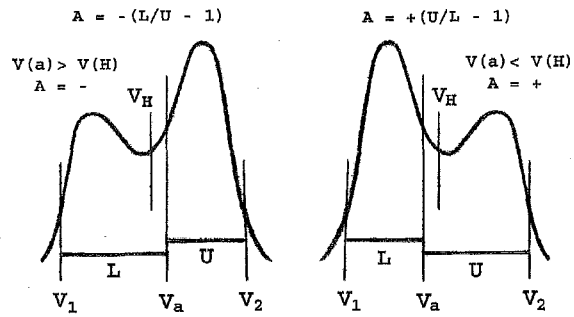


Figure 7.7: The definition of the asymmetry index in redshift measurements.

In single peaked profiles it reflects profile tilt. The parameter is defined by the ratio of the redshift intervals between the edge and area redshifts, the upper and lower intervals $U$ and $L$. Rather than making asymmetry continuous about symmetry I chose a signed form by dividing the larger interval by the smaller, subtracting unity and attaching a sign to make $A$ a directional asymmetry percentage. The choice of sign is quantum mechanical related, an enhanced or retarded probability of a redshift transition occurring. Evolution is toward lower redshift over time (to the left in figure 7.7). The likelihood of transitions between states is enhanced as overlap of wave functions (in this case 21 cm profiles) increases, and decreases as overlap is reduced. The probability of a change is therefore enhanced if the wave function 'leans' in the decay direction. The right hand side of figure 7.7 is dominant on the low side therefore has an enhanced transition probability in QTC to move to lower redshift so has positive (+) $A$. The left 21 cm profile is retarded (high redshift dominant) and has a reduced transition probability hence negative (−) $A$.

Asymmetry provides a critical test of QTC theory although in classical cosmology it is of little interest. The classical explanation of double peaked 21 cm profiles is quite simple. In rotating disk systems neutral hydrogen concentrates in outer disks where star formation is active and extends out from there. Rotation of the disk provides two velocity concentrations where the rotation velocity peaks or levels off, one approaching the other receding. In between rapidly changing rotation spreads the velocity pattern producing a dip in the profile. The core region also often contains little neutral hydrogen. Asymmetry then arises if neutral hydrogen is unevenly distributed between the two sides. Either peak can be dominant or they can be symmetrical. This explanation may be generally correct, but in QTC is incomplete. Rotation effects due to uneven distribution can slightly increase or decrease asymmetry values. This will produce scatter about $A = 0$ but cannot cause systematic drifts from zero. QTC predicts a systematic radial drift should be present.

### 7.5.6 Redshift Dipoles and Asymmetry in QTC

I have mentioned that single peaked profiles are replaced by double peaked ones when profile widths exceed 100 km/s, marking the transition between simple dwarf galaxies and rotating dwarf spirals. This is the minimum width which can accommodate a 72 km/s redshift interval, fundamental to QTC, after allowing for typical internal velocity dispersion. It is also where redshift variability appears to be active as discussed in seminar 3. A similar interval is seen at $W = 200$ km/s where a 140 km/s dipole can be accommodated. Early

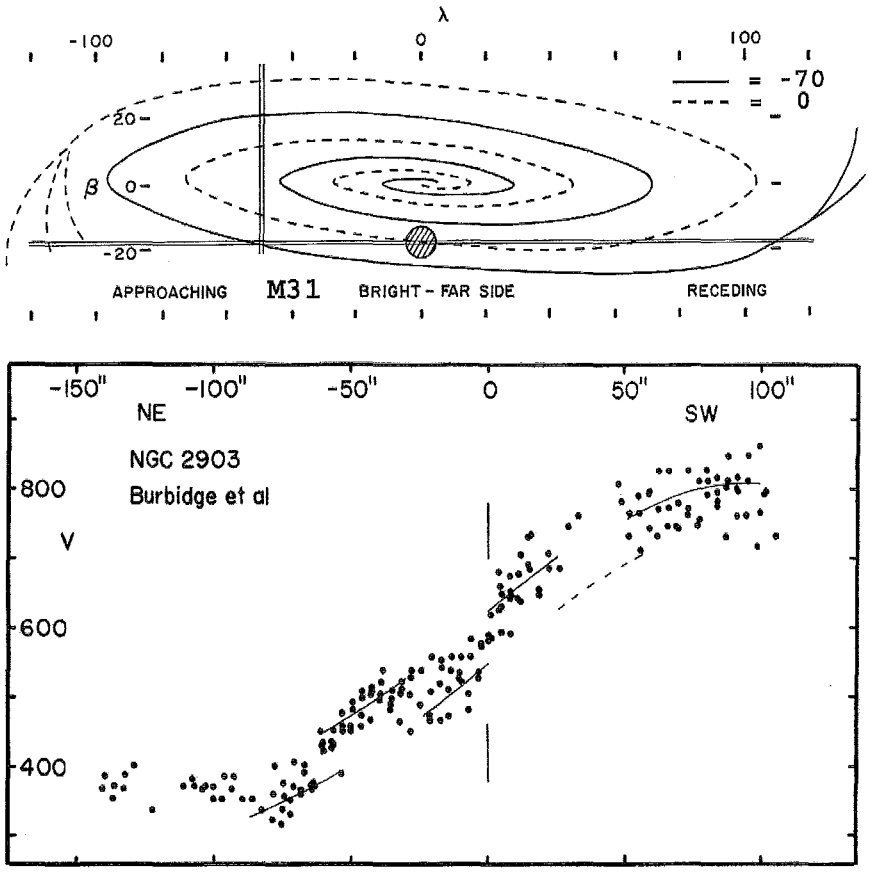


Figure 7.8: The Two-stream Nuclear Redshift Offset Model in QTC.

in redshift quantization work I recognized galaxy nuclei contained such a redshift 'dipole', a discontinuous 72 km/s redshift offset [55]. Studies indicated the rotating nuclear dipole appeared to provide the origin of two spiral streams (arms) offset in redshift for disk galaxies. Figure 7.8 shows the two stream representation of M31 and a major axis rotation pattern in NGC2903 which shows alternating offsets at arm crossings [55]. The dipole concept was introduced in seminar 2. Because of the importance of the dipole and streaming effect in subsequent discussion I will dwell briefly on the nuclear offset.

In QTC galaxies are treated as *particles* in tau-space where particle 'spin' can be related to rotation in sigma-space. Dipoles associate directly with double peaked profile structure. They can add or subtract to observed rotation or expansion values to generate behavioral 'families' such as rapid or slow rising rotation, counter rotation or apparent disk warping. The effects are most notable in ellipticals where small rotations will be strongly affected. In 1984 [85] I made a study of ellipticals and further studies of M31 to detect dipole effects. Figure 7.9 is a composite of figures from that study (which was rejected by the *Astrophysical*

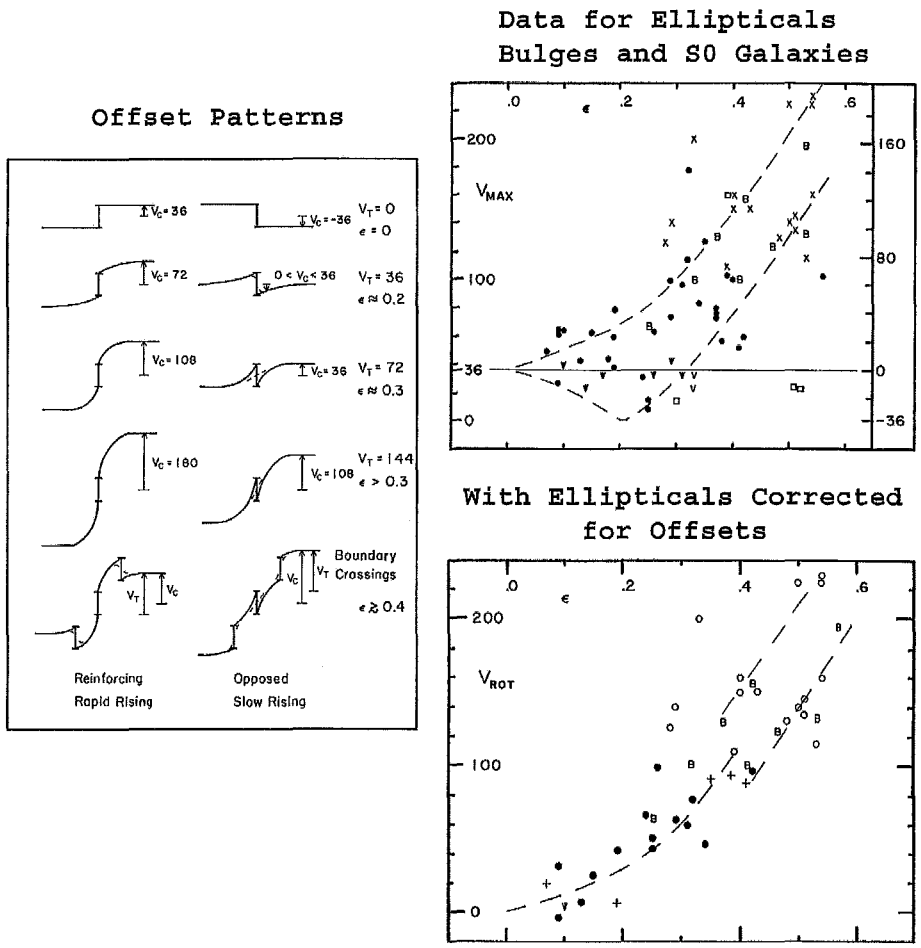


Figure 7.9: Nuclear redshift offset Effects

*Journal* as too controversial) but beautifully illustrates the effects. The paper is included as the first supplement (Ap1). Doubters of the nuclear dipole concept may find it disturbing.

The left frame illustrates rotation patterns for dipoles reinforcing or opposing true rotation to produce rapid and slow rising rotation families (bear in mind that an intrinsic offset does not project). $V_C$ is the 'apparent' rotation including the offset, $V_T$ the true corrected

rotation and $\epsilon$ the ellipticity of the galaxy which should be a measure of expected rotation. Opposed patterns can be seen to be consistent with nuclear counter rotation effects and larger rotations provide two stream offset patterns (compare the lower left reinforcing pattern with the center of the NGC2903 pattern in figure 7.8). The upper right frame of figure 7.9 plots rotation measures available for ellipticals, spiral bulges and So galaxies as a function of ellipticity (indicative of rotation). Slow and rapid rising rotation branches are shown dashed, spaced by the 72 km/s dipole interval. The lower right frame shows ellipticals with the dipole removed when the 'orientation family' (opposed or reinforcing) could be confirmed from related dispersion information (discussed in the supplement and section 7.7.1). A smooth rising rotation pattern against galaxy eccentricity now merges perfectly with the mean rotational properties of uncorrected So galaxies (which directly show the split pattern). The analysis of dispersion measures included in section 7.7.1 reveals a banded structure directly related to redshift-magnitude banding along with correlations distinguishing between reinforcing and opposed dipole orientations. Newer 21 cm data associated with the M31 pattern, shown in the upper part of figure 7.8, is also discussed in the supplement. I consider this paper to be remarkably good evidence in support of nuclear temporal dipoles. The result is fully verifiable and none of the data are mine.

### 7.5.7 Asymmetry Trends in QTC

The dipole along with redshift variability and evolution by outflow are keys to galaxy evolution and understanding radial trends in asymmetry. The following premise sets forth the expected behavior of asymmetry as a function of radius for nucleated disk galaxies.

> P7.2: Asymmetry measures should trend positively in inner minus outer differentials for nucleated disk galaxies (using comparisons between telescopes, small beam minus large beam). The outer part should be systematically retarded relative to the inner value.

Conventional rotational models cannot produce such trends. The following paragraphs and illustrations demonstrate that the correlation is present and further discuss why it is expected. Assuming an association of the nuclear dipole spacing with the dual redshift

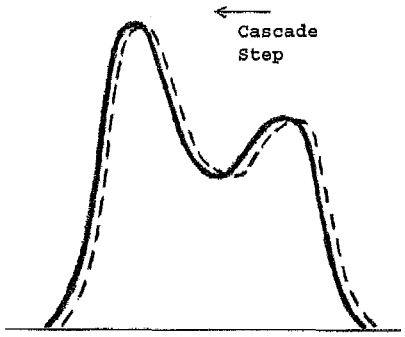


Figure 7.10: A radial redshift fringe develops in outer older material as it begins to lose temporal commonality with the core and drift into dark matter

peaks in a 21 cm profile and related two stream structure provides the first element of an association with asymmetry. One item remains. There are two ways to produce a redshift excess at the visible edge of a galaxy. As outflow brings new material into the nuclear region it may already be slightly blueshifted. For example we see a blueshifted 'expanding' structure in our galaxy. Alternatively the fact that we see clear global 72 km/s periodicities in redshifts implies that redshift multiples of 72 km/s are quite stable. It is also clear that transitions must occur as we look back in time. From studies discussed in seminar 3 it seems likely transitions can occur in a smaller cascade of harmonic substeps. As material emerges and moves outward in the disk a radial temporal if not redshift gradient should appear. The oldest outer material will be the first to get out of temporal synchronization with inner material and begin redshifting to maintain temporal commonality before drifting out of temporal range to become dark matter. Either process would produce an outlying small redshift gradient in figures 7.4 and 7.6, and provide the mechanism to generate dark matter. Outer materials become systematically retarded, more relatively negative in asymmetry (tending toward higher redshift). Figure 7.10 schematically illustrates such a redshift fringe.

Now if we compare the asymmetry parameter measured in the inner region (using a small beam larger telescope) with a value from a large beam smaller telescope a radial trend in asymmetry should be seen. Regardless of the overall asymmetry of a disk caused by material distribution, the greater negative asymmetry in the outer part, when subtracted from (added positively to) the inner region value will produce a positive drift in the differential. Figure 7.11 shows the positive differential drift is indeed seen in the Effelsburg minus 140-foot Greenbank observations on disk galaxies with $W > 100$ km/s.

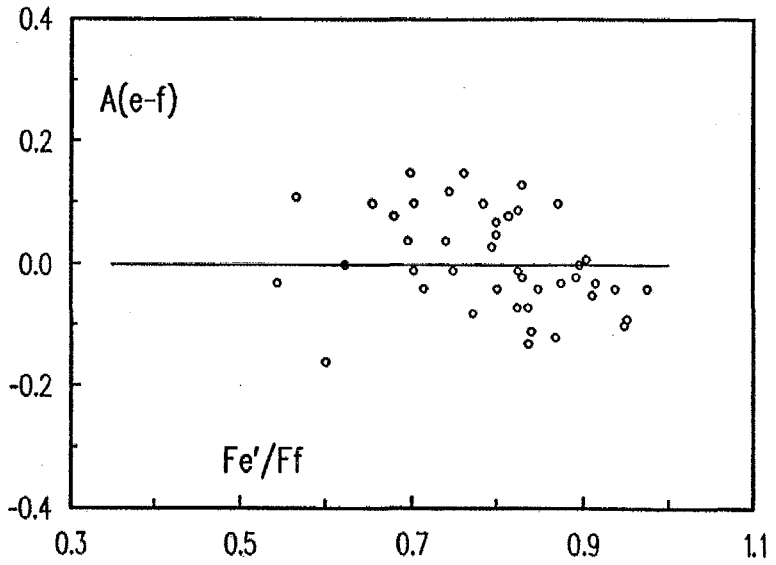


Figure 7.11: The change in asymmetry between Effelsburg and 140-ft Greenbank observations for galaxies with $W > 100$ $km/s$ when plotted against relative flux. Asymmetry systematically decreases (becomes systematically more negative, more retarded) for outlying hydrogen, thus driving the differential positive.

Figure 7.12 provides a general schematic illustration of various effects. The general lookback effect to higher redshift is shown at the top along with an arrow indicating the general trend of evolution (decay) toward lower energy (redshift) states. The double dipole structure indicates a shift between newer material entering the outflow at the left replacing older outer material. The older material is either slightly redshifted because it entered at an earlier time or as it drifts out it redshifts slightly to maintain a common link to newer material before passing into dark matter. Either process produces a redshifted outer fringe and a flow into dark matter. The larger telescope small beam sees less of the older outlying fringe (sees more of 'what is now') while the large beam sees both the young and more older 'what was' material to generate the asymmetry gradient. The overall picture of real observed radial redshift and asymmetry gradients along with evidence for redshift dipoles and variability properties make a remarkable case for taking a serious look at QTC.

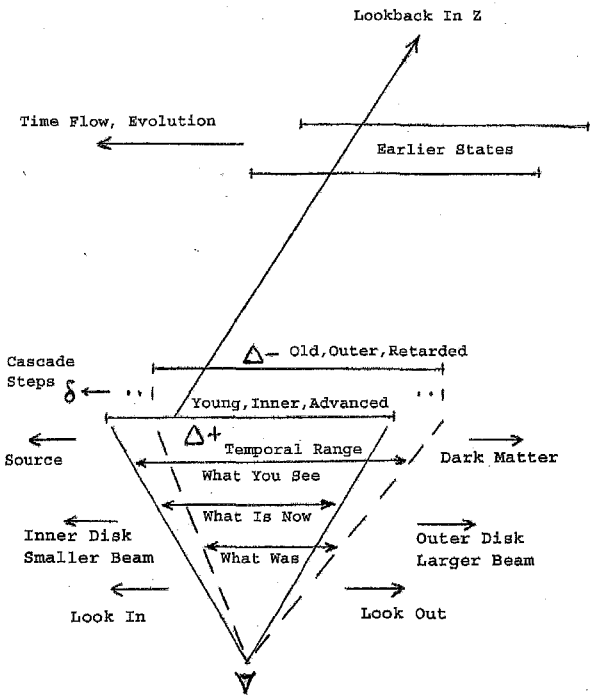


Figure 7.12: Model illustrating how asymmetry measures from outer older material in disk galaxies will trend negatively from inner measures

There is one further aspect of asymmetry to discuss. Figure 7.13 illustrates the radial properties of asymmetry for the narrow profile dwarf galaxies with $W < 100$ km/s. Although there is no significant radial change the kink for barely resolved systems at flux ratio 0.85 could easily be a remnant of the disk system trend if a minimal nuclear remnant is or was present and still detectable using the very outermost parts of nearly unresolved systems. The

very outermost trend to a slightly more negative differential (more positive outer asymmetry) in well resolved systems (small flux ratio) might be inferred to be present in the few scattered outlying resolved points in the disk systems in figure 7.11, however, much more data is needed to properly explore dwarf galaxies or very outer visible fringes of disks. There is much to be learned within QTC concerning the radial gradients of redshift and asymmetry within galaxies at the dark matter boundary. Slight effects from outlying beam structure and non-isolation may also have to be investigated.

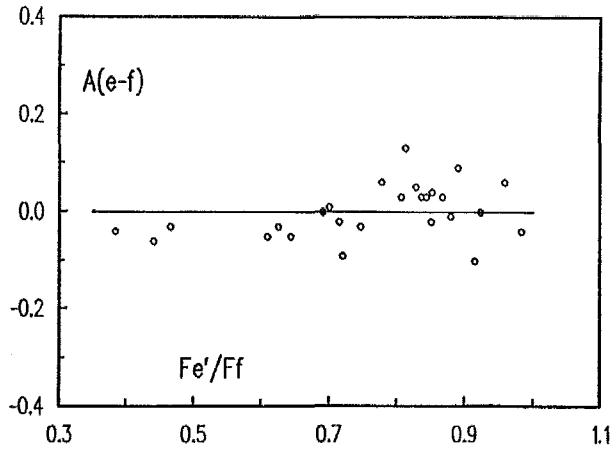


Figure 7.13: The change in redshift between Effelsburg and 140-ft Greenbank observations for galaxies with $W < 100$ km/s when plotted against relative flux. There is little if any change in redshift with radius. A t-test dividing the inner and outer sample shows no significant difference.

## 7.6 Introducing Origin and Evolution of the Cosmos — Early Physical Findings and Premises.

The story has reached a point where it is appropriate to bring results together into a summary of findings and premises which define the basis of Quantum Temporal Cosmology. The picture is largely empirical. Many aspects are beyond current standard models, although most critical concepts have been verified several times, and are consistent as a group. This listing will summarize key observables and premises derived primarily from early studies in seminars 1 to 4 which laid the groundwork for seminar 6 to introduce QTC. Certain effects developed in seminar 7 proceeding this summary, which utilize basic 21 cm data will also be included. More advanced finding in seminars 4 and 5 began to add more detailed features as analysis was integrated into the cosmic picture. Since there is more to say about deep space, early cosmology and evolutionary development, most of seminar 5, and subsequent discussion in seminars 7 and 8 will be introduced as individual premises or summarized in text. In the following summary an asterisk flags statements based on observed or modeled findings which appear well founded. Items marked P are inferred premises developed from the findings. Back references are included for many of the items.

A.) **The Redshift:**

1.*) The redshift is an intrinsic property of galaxies as demonstrated by detailed correlations between the redshift and properties specific to galaxies. This includes redshift-magnitude bands (1.3.1,2),(1.4.0,2), crossband structures (1.5.0),(1.7.1), morphological associations (1.5.1), relationships with internal activity (1.6.1,2), and vertical structures (1.7.0,2). A detailed topical reference to the above subjects plus double galaxies is provided in (5.1.1).

2.*) The redshift is a quantized quantity (1.9.0),(2.2.0). The basic periodicity involved is seen as the redshift interval between the dual quantized streams within galaxies (2.3.1), which equals the nuclear dipole differential, and as quantization within double galaxies (2.3.2-5,7) which indicates there is no sign of dynamical motion between galaxies. This is confirmed by orientation studies which show large scale alignment properties (2.4.1) inconsistent with any detectable large scale gravitational interaction between independent galaxies. Global studies at 21 cm extend local all sky quantization to the galactocentric rest frame (2.5.0,1) and to unrestricted all sky quantization from the cosmocentric rest frame (2.8.0),(3.3.0,1),(3.4.5). Galactocentric quantization has been independently confirmed (2.9.0),(3.3.0).

3.P) Since the redshift is quantized and increases with lookback, transitions between permitted doubling levels must occur and are the origin of the redshift (6.3.7). An equivalent amount of energy is exchanged for a shift in cosmic time (aging). Large scale dynamics is not involved.

4.*) Transitions must be instantaneous for all photons associated with a galaxy since no transit time delays or local smearing are detected (3.9.2).

5.*) Quantization values are defined by a period doubling process originating at the Planck scale (3.3.0),(4.2.0,1). Periods are precisely defined by the Lehto-Tifft equations (3.3.1),(5.2.1) which apply globally with respect to the 'cosmic' rest frame. Quantization also applies less precisely locally within regions which have a common origin, such as our local 'cloud' of galaxies (3.3.3).

6.*) Redshift periods are members of doubling families of ninth root powers of two scaled by the fundamental Planck unit c. Ninth root families are designated by T values 0-8 and doubling levels D (3.3.1). T values of 0 and 6 are common, 1, 5, and 7 occur less frequently, and 2, 4 and 8 are rare or absent (3.4.1).

7.*)Morphology and 21 cm profile widths of galaxies relate to T values (3.4.1-4).

8.*) The ninth-root set of periods forms a unique and complete set of possible redshift states (3.6.0,1).

9.*) Given the correct period redshifts are consistently in phase with the rest frame from field to field (3.4.6).

10.*) An exclusion principle applies to redshifts, identical redshifts in neighboring galaxies are not permitted as illustrated in binary pairs (2.3.6),(3.10.0). Galaxies appear to be a form of higher order fundamental particles.

11.*) The redshift is observed to be variable (2.6.0,2), cascading to lower frequency in allowed finer structure three dimensional doubling decay steps (2.6.3),(3.9.0-2),(6.3.8). Direct step patterns may be seen (3.9.2). Changes can be seen in recent data alone (3.7.0) as temporal expansion (aging) proceeds.

12.*) The differential redshift between the core and outer parts of disk galaxies with well developed nuclei increases slowly with radius (7.5.4). Narrow 21 cm profile dwarf galaxies without clear nuclei show little radial change. This effect provides a unique test of QTC.

13.*) 21 cm profile asymmetry is related to the timing of transitions between redshift states (3.9.1,4-5).

14.*) asymmetry differentials in 21 cm profiles between the core and outer disk increases systematically for disk galaxies with developed nuclei (7.5.7). Narrow profile dwarf galaxies with little nuclear development may show related effects. This is a unique test of QTC.

B.) **Time and Space.**

1.P)The origin of time at $t_o$ is represented as a zero fluctuation (split) of zero into time, anti-time and its corresponding inverse, energy anti-energy, such that both time and energy sum to nothing (zero) and are conserved in subsequent fundamental decay operations of the fluctuation. The split defines the Planck time/energy interval and related units involved in the subsequent quantum decay process we perceive as the expanding universe. Time is represented structurally as a time anti-time dipole (a boson structure) defined energetically as the decay state or states of the initial Planck temporal/energy 'interval' involved. Several states (planes of time) appear to exist simultaneously within sigma.

2.P) Time, as now perceived, consists of a three-dimensional spherical domain (tau space)(3.3.0),(4.2.2),(4.6.1) decaying by radial expansion from its near singular origin (6.3.1).

3.P) Matter, as passive energy, established by the pair formation transformation process from active energy in tau-space, resides in three-dimensional spatial (sigma) domains, where it 'ages' in time under the action of continuous physical processes to provide the physical decay driven by the radial expansion of time. Sigma-spaces flow radially along 'timelines' (4.2.2),(4.6.1) which provide the routes and mechanisms for decreasing energy density (decay) within tau-space.

4.P) Sigma-spaces flow radially outward (4.2.2),(4.6.1),(6.2.2) at light speed along timelines. Tau and sigma view each other as one dimensional by aberration (4.6.1),(6.2.0). There is no detectable acceleration or deceleration of sigma-space. The flow of matter within sigma is considered in section C. The flow from within sigma is perceived as aging, the passage through time, not as motion.

5.*) The lookback line in QTC is a logarithmic spiral leading to, but never reaching, $t_o$ which is its limiting zero point (6.3.9).

6.*) All lookback lines come together at multiples of $\pi$ radians of lookback in QTC, referred to as Pi points (6.3.9). Rotating any lookback line about our timeline generates a surface which intersects all timelines as they pass through all the observers lookback lines. The integrated signal back to the first Pi point includes information from all possible timelines distributed over the time interval from the Pi point time to now. Each successive Pi cycle again samples all timelines at an earlier time cycle, but never actually reaches $t_o$, the mathematical limit of the logarithmic cycle. The classical redshift at the first Pi point is 1823, but only 22.14 in QTC. The maximum observable lookback point is presumed to occur at the point where the universe becomes opaque, which is not likely to be a Pi point. This point is denoted as the opacity point and samples a ring of timelines corresponding to the divergence angle corresponding to the opacity point. Further commentary regarding lookback properties is deferred to seminar 8.

7.*) Tau and sigma perceive each other as one dimensional. There is no lateral awareness of the other space (6.3.7) as demonstrated by no transit time delays in redshift transitions. Temporal commonality determines transition timing, not a photon's spatial location.

8.*) The Hubble constant $H(t)$ is a function of the passage of time since $t_o$, $H = 1/t$.

9.*) Since timelines diverge there is a second lateral expansion perceived as spatial expansion. A continuous divergence driven 'cosmological' correction is required to distinguish doubling driven temporal radial quantization (2.7.0),(6.3.3). The correction arises from spherical temporal curvature, which requires $q_o = 1/2$. Quantization tests using quasars [102] and later more precisely using galaxies (3.5.1) verify that $q_o$ is 1/2 within a high degree of certainty.

10.*) Constant $q_o = 1/2$ in QTC resolves the cosmic flatness issue in QTC.

11.*) Not allowing for a dual expansion causes observed redshifts to increase too rapidly, overestimating how far back in time observations have penetrated. (6.3.9).

12.*) Dark energy in classical cosmology appears to be due to failure to allow for both a temporal and spatial expansion. (6.4.2). There is no significant evidence for accelerating expansion in QTC.

C.) **Matter as Fundamental particles.**

1.P) Matter in the form of fundamental particles is produced from energy or reverts to energy by the pair formation/annihilation process (4.6.1),(7.4.0), which conserves time, energy and momentum, or by interaction or decay processes between such particles. Matter then exists in defined (sigma) spaces.

2.P) Matter flows along timelines at light speed reduced by lag induced by relativistic motions within fundamental particles, essentially protons.(6.2.4).

3.P) the relativistic lag in the flow of matter in time (tau) results in incomplete aberration between space and time. The fuzzy overlap is presumed to be the origin of the uncertainty principle (4.6.1),(6.2.4),(6.3.7).

4.*) The relativistic lag in flow of matter with respect to massless energy is observed to generate the Cosmic Background (CBR) dipole (4.6.1),(6.2.4),(7.3.1).

5.*) The scale of the CBR dipole depends upon the amount of relativistic lag provided by matter, primarily protons, and is apparently fully accounted for by protons (7.3.1). There is no need or evidence for 'dark' particles. See B12 concerning dark energy.

6.*) Only specific particles can exist as matter, or as certain transient energy resonances, which correspond closely with cube or fourth root period doubling decay levels derived from the Planck energy (4.2.3). See tables (4.2.5). The 'stable' particles further occupy levels which are consistent with forms of three dimensional spatial dynamics (4.11.0).

7.*) There are two energy level series within the doubling pattern which relate to apparent vector substructure, one in radial quantum mode the other azimuthal (4.2.3) as indicated by the ability to directly derive magnetic moments (4.2.4). Internal decay within each series involves the strong and electromagnetic forces. Transitions (4.5.0) between the series, denoted Pi and Gamma, involve the weak force and allow the tracing of certain particle decays such as the kaon (4.10.0), which has two modes of decay for the neutral form.

8.*) Fermions are three dimensional spatial particles including baryons (4.3.0) and quarks (4.7.0) which match unique cube root levels. Bosons are four dimensional, including the light mesons (4.4.0),(4.8.1,5), which have a one dimensional temporal link that relates them to Bose statistics. The Lambda particle provides a unique link between baryons and the light mesons (4.8.2).

9.*) Leptons appear to be fermions which serve as lower limits to other types of particles, electrons for quarks (4.7.0), muons for the light mesons (4.8.1).

10.*) Neutrinos appear to associate with the bosonic fourth dimensional temporal link, preserving it in transitions (4.6.1).

11.*) Quarks and potentially all fundamental particles can be modeled from a basic doubling structural 1 2 4 triad (4.8.4) at the Planck scale (4.7.0),(4.8.0),(4.8.3,4), and/or characteristic doubling structures based upon patterns of 56 (4.6.0),(4.8.3) or 64 doublings. The basic doubling triad is the same 1 2 4 doubling triad which defines the fundamental forces (4.9.0), and is initially referred to as a chronon. The Higgs is an excellent example of a higher energy triad based boson (4.8.5). The Higgs is a $2^8$ scaled version of the kaon.

D.) **Matter In the Form of Structures.**

1.*) Matter at the cosmic form exists in the form of galaxies, clouds (2.4.0), clusters, or pairs of galaxies, superclusters, and presumably precursor dark units. The forms are embedded in associated dark matter, essentially empty cosmic voids, free flowing photons and possible high energy free flowing particles (as p-spaces) which fall within the temporal communication range of local observers.

2.*) Galaxies evolve by outflow from a nuclear source function (sigma-source), presumably associated with what are referred to as supermassive black holes.

3.*) Galaxy nuclei appear to contain a temporal dipole structure (which drives an outflow of matter appearing in disk systems as two interleaved spiral streams.

4.P) Matter 'born' at different times is separated by relativistic drift and the older will pass into dark matter with respect to the younger if temporal drift separations exceed communication ranges (denoted as temporal commonality) established by common origin.

5.P Unlike photons, matter which temporally drifts behind newer matter entering its parent has no means to advance and passes into dark matter as it looses temporal commonality and its corresponding force linkage.

E.) **Energy**

1.P) Photons are 2-d temporal energy structures restricted to flow in lateral time (4.6.1).

2.P) Photons are a form of energy anti-energy dipole characterizes by the binding energy interval of the dipole structure involved. Pair formation is the process by which photon pairs can be split into matter anti-matter particle pairs, which in turn can be seen as the nuclear dipole and two stream differential redshift outflow in galaxies.

3.P) In tau the dipole energy level intervals represent quantized energy levels in the decay of time/energy as the the universe ages. In sigma these energy levels appear as distinct 'planes of time' within which they appear as temporally distinct standard energy distributions governed by classical continuous physics. It is this spread that provides energy level overlap which permits quantum transitions.

4.P) Photons, active massless energy, retain temporal commonality (energy interval) with their now zone of origin by redshifting to remain linked to their parent source. Since distribution in space, lateral distribution from a spaceline, has no temporal distinction, photons never effectively leave their parent unless externally intercepted.

F.) **Forces.**

1.*) Fundamental forces and the fundamental substructure of matter appear to be based upon a specific energy/temporal structure, the minimal degenerate triad doubling structure 1 2 4 at the Planck scale. Structure scaled by successive spatial doubling scales beginning at 4 Planck distances define and directly relate the known fundamental force strengths (4.9.0).

2.*) All forces have a minimum spatial range which characterizes the force, and a maximum temporal range defined by the ability to remain in communication.

3.*) The existence of precisely quantized redshifts implies that gravitational dynamics does not apply between galaxies. There is no observational evidence for dynamical motion and considerable evidence for its absence.

4.*) Fundamental forces transmit instantaneously between matter within temporal communication. Redshifts of entire galaxies change immediately for all widely dispersed photons at redshift transitions. There are no transit time delays.

5.*) Normal conventional continuous acting forces apply only within sigma-spaces.

6.P) Matter which falls outside the defining limits of forces constitutes 'dark' matter. Forces in general do not apply beyond individual force communication limits which define the boundaries of sigma-spaces.

Additional findings or premises relating to quasars, large scale structure and other aspects of global cosmology are considered in the remainder of this seminar. Subsequent statements and premises will be stated in text. The above statements and premises have been observationally demonstrated or inferred from observations presented or described in previous discussion. By stating them as premises I can relate the concepts within a consistent cosmological picture while presenting further evidence and examples along the way. Some implications of what may be coming are noted in seminar 6 (6.3.5,6) as interpretation of the findings discussed up to this point are integrated into a quantum cosmology.

### 7.6.1 Moving to Higher z, Quasars

Important issues relating to the nature of the redshift were known well before my work with redshift quantization. The discovery of quasars and the opening of studies at high redshift led to several questions discussed in seminar 5, most notably the recognition that groups of galaxies sometimes contained galaxies with highly discordant redshifts, and that quasars seemed to concentrate at certain specific redshifts rather than having a smooth distribution. I was not especially involved with these questions initially until after 1970 when I began my work leading to redshift quantization using ordinary low redshift galaxies. The redshift controversy that developed in the late 1990s between new ideas and classical dynamics was not an especially pleasant time. I never could quite understand why new ideas were quite so unwelcome considering that problem after problem kept appearing.

No one seemed to be trying to unify some of the redshift problems in the late 1990s. With low redshift quantization developing nicely I turned to new precision data becoming available to see if some high redshift problems could be related to local work. It proved to be surprisingly easy as already discussed in seminar 5. The work was presented in 2002 as an invited paper at the Fred Hoyle memorial conference at Cardiff, U.K. [151], although the concepts still remain of no interest within classical dynamical cosmology or even within other schools of redshift controversy. Since several findings are important to present a smooth picture of the QTC model I will summarize and illustrate some key findings.

The quasar redshift peaks near z of 0.30, 0.60, 0.96, 1.41, 1.96, and a more local periodicity near z of 0.061 have been discussed since the 1960s [AM]. In QTC redshifts are basic fractions of c which decay in a doubling process. If the quasar peaks represented early stages of galaxy formation consistent with QTC the quasar peaks should correspond with earlier, larger, fractions of c *after applying the QTC cosmological correction.* The cosmological correction was known by the mid 1990s and when applied to the quasar peak redshifts did

Quasar redshift peaks

| z(LT) | D=2 | z(obs) | z(peak) |
|---|---|---|---|
| c/16 | | 0.064 | 0.061 |
| c/8 | | 0.131 | |
| c/4 | 1/4 c | 0.274 | 0.30 |
| c/2 | 2/4 c | 0.601 | 0.60 |
| | 3/4 c | 0.989 | 0.96 |
| c | 4/4 c | 1.441 | 1.41 |
| | 5/4 c | 1.968 | 1.95 |

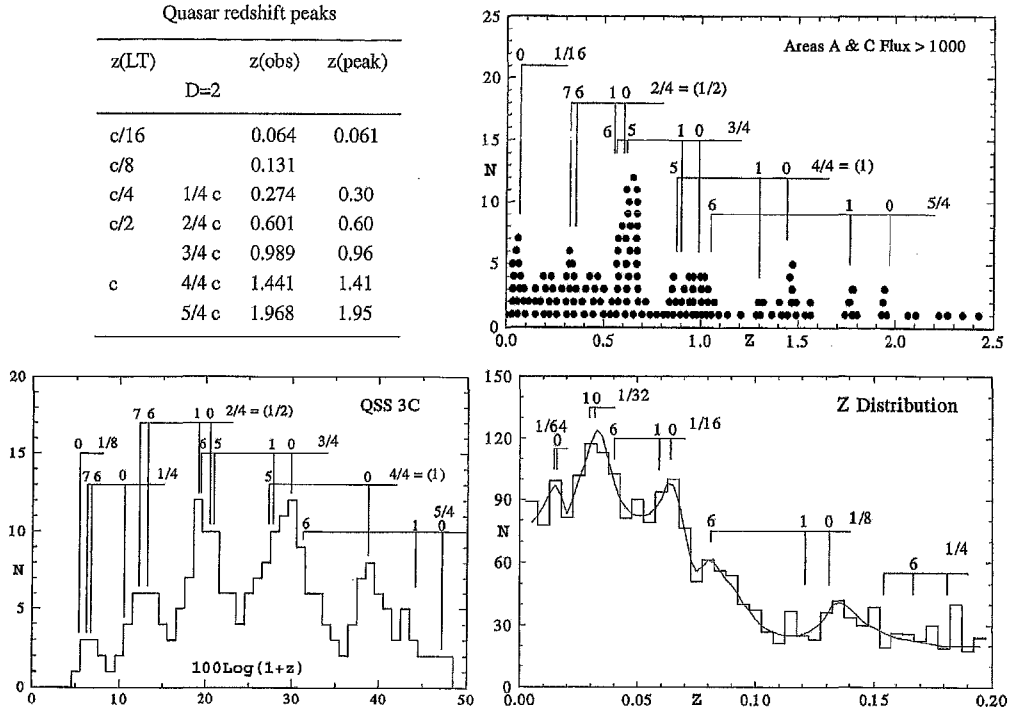


Figure 7.14: Quasar periodicities in QTC. Frames are discussed in the text.

indeed convert them to simple fractions of c in the very first D=1(c/1) series beginning with $1 \rightarrow 1/2$ as shown in the upper left table in figure 7.14. Well, not quite, it is necessary to presume that different timeline structures may have formed earlier (this will be discussed in seminar 8) as some form of mixing occurred in the earliest high density environment to produce 3/4 and 5/4. Such mixing is a known process, and the match to quasar peaks is essentially perfect. Note that without the cosmological correction uncorrected standard redshifts will not be periodic and hard to detect. The QTC ninth root T state splitting and T state preferences were already known however so it was immediately possible to examine quasar samples for expected doubling decay products. Most of the early quasar discoveries related to objects seen as radio sources. Active quasars appear to relate most closely to the quasar peaks. The upper right frame is a sample of radio selected quasars, the lower left frame is the third Cambridge catalog set of radio quasars, and the lower right frame extends to lower redshift using active galaxies as well. All the samples show a very marked association with the predicted expected periods associated with the quasar peaks. Seminar 5 includes further information. The redshift distribution of active quasars associates very well with early doublings predicted by QTC.

Proceeding to greater doubling at lower redshift the population rapidly changes to galaxies. Here the Hubble Deep Field and similar deep studies with precision redshifts become of primary interest. The early work by Cohen et al [AV,AW,AX] is particularly informative. They find remarkably sharp redshift patterns, a perfect example of distinct energy states

expected in QTC. Further, corrected for the cosmological correction distortion they match QTC predicted values very closely. Before commenting on the matches the upper left frame of figure 7.15 looks at the general pattern of the redshift distribution. Two lines along the top redshift scale mark the location of the 1/2 and 3/4 quasar doubling states discussed above. Arrows toward lower redshift mark the direction of redshift state decay. The curved line through the figure shows the smoothed galaxy density indicating two density peaks below the quasar energy states. Such an excess is consistent with QTC if a fissioning event occurred at the quasar state producing multiple sources which developed into galaxies. The two bracketed lines around the peak below the basic 1/2 quasar decay state mark intervals examined for matches to predicted redshift states.

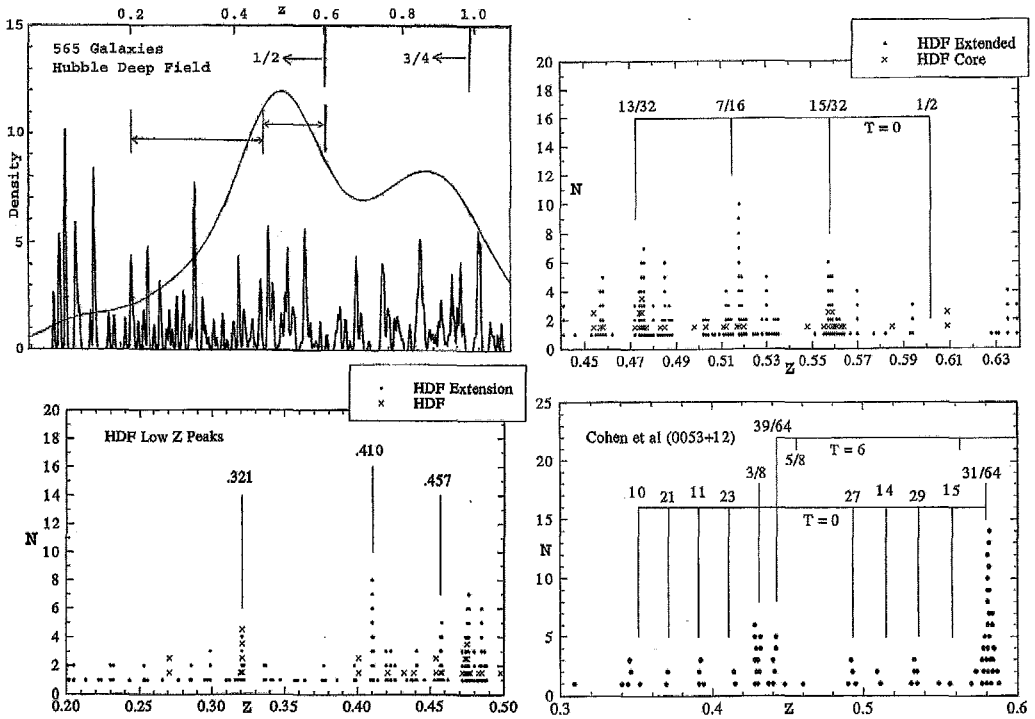


Figure 7.15: High z galaxy periodicities in QTC. Frames are discussed in the text.

The upper right frame shows the redshift pattern directly below the 1/2 state. A four energy state periodicity pattern in the D = 5 (c/32) state is shown corresponding to redshifts at 16, 15, 14 and 13/32 fractions of c. For this set, level decay has proceeded to the D = 5 level. At this point it may be effective to shift into a QTC analysis mode to bring out certain properties of the pattern for consideration. Look at the redshifts as representing energy states that galaxies occupy. The 16/32 = 1/2 state is actually a D = 1 level, therefore empty as it should be since that quasar state decayed at a much earlier time. The modulation of the three levels below 16/32 is uneven. Two odd levels must be actual D = 5 (c/32) levels. The even level with a different population is divisible by two hence actually a D = 4 (c/16) level. Do consecutive doubling levels decay smoothly together or does modulation indicate

otherwise? This even odd modulation will be seen again shortly. Another interesting effect is present. The two lower redshift peaks are slightly offset from predicted values. The offset is in fact 1/512 of c, a D=9 value in both cases. In seminar 3, I found that changes in state appeared to involve small harmonic steps. A QTC interpretation would suggest that the transition to the lower D=5 (c/32) state is incomplete (and to the D=4 (c/16) state as well). Furthermore the taller spike above the 1/512 item for the lowest peak is offset 5/512. Offset numbers 1 and 5 (along with 7) are odd number offsets we have seen before when discussing T values deviating from the dominant 0 and 6 values. Are we seeing some property of harmonic cascades? Finally note that the first peak below 1/2 is a precise 1/32 fit. The triplet shows progressive retardation and terminates in about 3 steps. The next step would be 12/32 which reduces to 3/8. Is it absent because it is an earlier quasar state? Keep such notes in mind. This illustration is an example of how to search for clues about what is actually happening. Nothing definitive yet, but worthy of note!

The lower left frame of figure 7.15 shows the lower redshift interval between redshift of 0.2 and 0.5. Three distinct redshift peaks are present below the group discussed above. To understand the significance of these peaks it is useful to look at their phase distribution within the D = 4(c/16) periodicity. Since all redshifts in a standard z peak are very similar, the peak will appear in QTC redshifts at its cosmologically transformed redshift. Dividing the QTC redshifts by a predicted period will then place the peak at a phase which describes how the peak relates to the particular period involved, and also add objects to the peak at other redshifts in phase with the period. When this is done using D = 4 (c/16) the peaks all fall at phases directly related to the D = 4 period and strengthen by adding phased points from other redshifts. The peak at z = 0.457 falls at phase 0.312 and adds 11 points to its original 17. Phase 0.312 = 5/16 and the other peaks correspond to 10 and 12/16 which associate with 5/8 and 3/4. The exact fits to the last two are actually 39/64 and 95/128, one step in the D=6(c/64) and 7(c/128) states below the lower D = 3(c/8) and D = 2(c/4) states. This is exactly as seen in the previous paragraph, 15/32 in the D = 5(c/32) series is just below the D = 1 c/2 state. In all cases have the absent lower quasar D states decayed at earlier higher redshift stages? Do earlier quasar states generate later galaxy cascades? Levels appear to spawn advanced D fraction harmonic cascades of levels just below them. The 1/16 c period was already seen and discussed in the 1960s since the QTC cosmological correction is small enough to not mask it. In QTC this cascade process is now seen to be much more general. It may be worthy of note that locally the 73 km/s period corresponds to D = 12. Is this our present decay level in the aging process of the universe?

The lower right frame of figure 7.15 is the redshift distribution for an alternate field studied by Cohen et al [AW]. We again see periodic patterns of the same type. A major concentration occurs at 31/64 of c below the empty c/2 location. Below the peak we see a two stage modulation of 29 and 27/64 interlaced with galaxies close to 14 and 15/32. A second series begins at 24/64 = 3/8 and continues through 23 and 21/64 interlaced with 10 and 11/32. One other peak in the T = 6 system appears to follow the same pattern at 39/64 just below an empty 5/8 of c location. The numbers are too small here to consider higher offsets but it appears impossible to me that such periodic patterns at predicted QTC locations can possibly be accidental. Quasars appear to me to represent an early cycle or stage of development underlying the order within an evolving aging universe. I will return to the issue of evolutionary cycles in section 7.

Relationships between redshifts in peaks within the distribution have been considered, but what is the spatial relationship between galaxies in the peaks? Degree of decay increases with doubling. Are redshifts states with a common D level physically associated and simply in different quantum states of that level? Figure 7.16 examines that question using the three

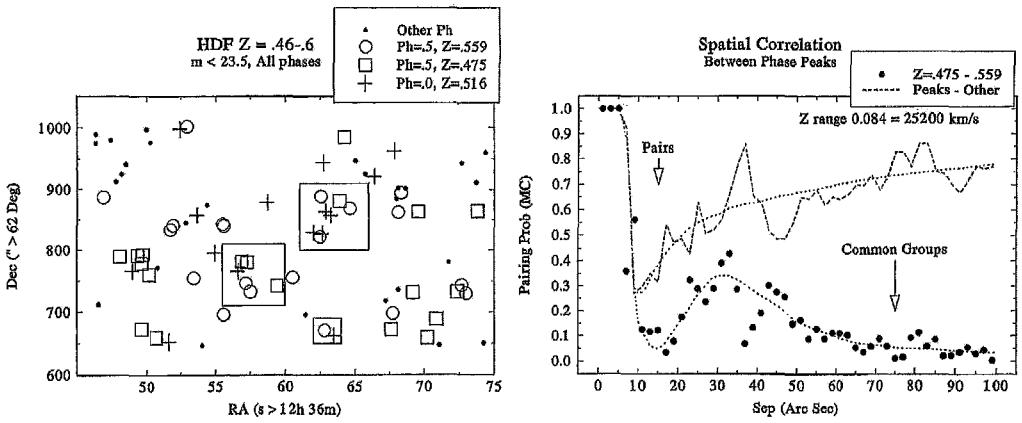


Figure 7.16: Distribution and grouping of galaxies in the Hubble Deep Field between closely related redshift peaks. Frames are discussed in the text.

dominant peaks in the D = 5 c/32 group at upper right in figure 7.15. The left frame of figure 7.16 shows position on the sky of galaxies with $0.46 < z < 0.6$ and $m < 23.5$ in a rectangular region around the Hubble Deep Field. (Seminar 5 provides full details). Symbols distinguish the three peaks and objects between. Galaxies appear clumped as both pairs and groups without regard to redshift peak membership. Two larger boxes represent the size of local galaxy groups at the redshift involved. A spacing of 100 arc seconds corresponds to about 1 Mpc. The right frame of figure 7.16 is a Monte Carlo analysis, done by a graduate student, Daniel Christlein, working with me on the likelihood that clumping between two widely spaced peaks (a redshift difference of 25000 km/s in figure 16) is accidental. For spacings up to 100 arc seconds there is clear evidence for both pairing and grouping of galaxies widely spaced in doubling related levels. The upper curve shows galaxies between peaks are not significantly grouped. D appears to be a far more reliable distance and association indicator than redshift. Discordant redshifts within both pairs and groups of galaxies are a natural consequence of QTC. Another example of the role of both D and T in redshift intervals (for local galaxy pairs) is shown in (3.10.0).

## 7.6.2 Constructing Superclusters

Superclusters are the largest known cohesive visible structures in the universe. They appear to be filamentary structures separated by vast empty voids. Since supercusters play a significant role in aspects of QTC I will discuss them in some detail. In the early period of describing the large scale universe, galaxies were presumed to be more or less uniformly distributed with density fluctuations providing clusters and groups interspersed with a general field of isolated objects. Galaxy group and cluster formation was presumed to be a

large scale dynamical process (and still is in classical cosmology). Present day supercluster structure was unknown, especially existence of vast empty voids. I was apparently the first person to recognize cosmic voids. As one of the first to pursue systematic redshift surveys, initially in the region around the Coma cluster, I quickly became aware that the foreground of the Coma cluster (at a redshift of 7000 km/s) was 'devoid' of galaxies beyond a few well defined groups. The left side of figure 7.17 is the original 'cone' diagram published in 1976 [52] defining the foreground of the Coma cluster and the empty void it contains. The right side of figure 7.17 is a view of the contents of the cone between redshift 4450 and 4930 km/s to define one of the isolated groups in the foreground. The compact spike in the center is the low redshift end of the Coma cluster. The inner zone is complete to $m_p = 15.7$ to 3 degrees radius, the outer zone is complete to $m_p = 14.9$ out to 6 degrees.

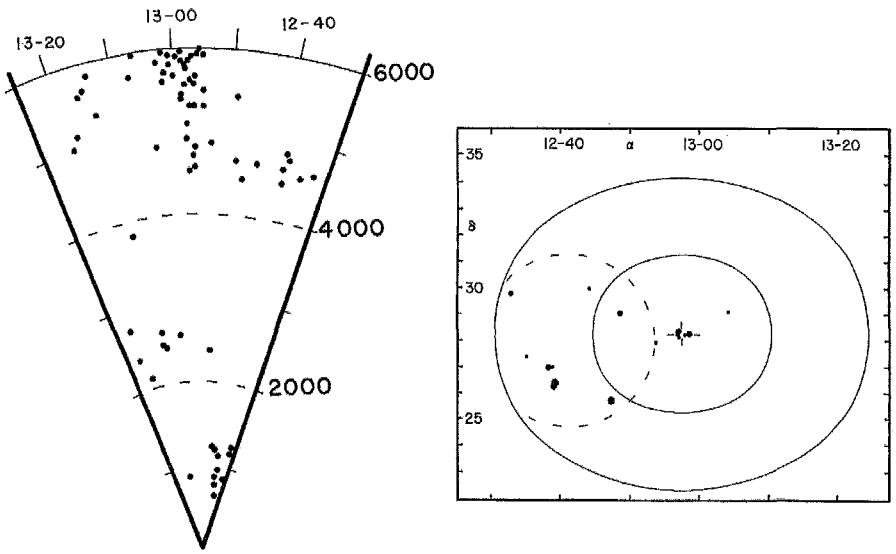


Figure 7.17: LEFT: A 12 degree cone diagram of the foreground of the Coma Cluster showing a vast void and isolated foreground groups. No more than one percent of space appears to contain galaxies. The radial coordinate is redshift in km/s, the lateral coordinate is right ascension. RIGHT: a slice through the cone near redshift 4650 to show a foreground isolated cluster and the low redshift tip of the Coma cluster. The inner zone shown is complete to magnitude 15.7, the outer zone to 14.9.

Figure 7.18 shows the distribution of galaxies within a cone slice from redshift 6000 to 7800 km/s covering the mean redshift range of the Coma cluster. The left frame shows the entire 12 degree cone sample complete to magnitude 14.9. The right frame shows the central 6 degree zone, containing the cluster, complete on down to magnitude 15.7. The cluster is seen to be a well defined flattened ellipsoid with little evidence that it extends significantly beyond three degrees. A second small cluster falls in the dashed zone to the northeast and an extended sample to the west was studied to examine the remarkably well defined 'cloud' of

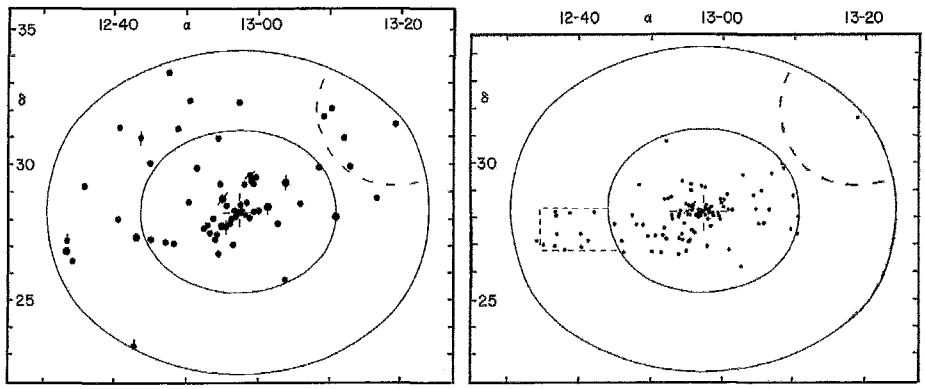


Figure 7.18: The distribution of galaxies in a cone slice including the Coma Cluster between redshift 6000 and 7800 km/s to illustrate the cluster structure and an extended cloud of associated galaxies. LEFT: the twelve degree zone complete to magnitude 14.9. RIGHT: The central six degree zone and a west extension complete on down to magnitude 15.7. Galaxy pairs have a line through the symbol

galaxies extending northwest from the cluster. The cloud has a well defined edge and depth. The study of this structure was subsequently extended by two of my graduate students to link it to the NGC1367 cluster and begin the demonstration of the existence of large scale supercluster structures which rapidly became an important field of study. My early work with students in this area will be described in more detail in my general biography.

This early paper, perhaps the first clear direct evidence for superclusters and voids, can be summarized in one paragraph. Two major structures can be tentatively identified as populating intergalactic space. The first feature is small groups of galaxies which appear to occupy perhaps 1 percent of space in fairly well-defined volumes. The galaxies in the groups show a low redshift dispersion, relatively little concentration, and tend to show emission lines suggesting a primarily spiral morphology. The density in such groups is near $10^{-30} gm\ cm^3$. Sizes generally are less than 10 Mpc. Truly isolated galaxies are very rare or non-existent. The second structure is the major cluster complex which tentatively consists of one or more major clusters in an extended cloud or wisp of material. The outlying material may extend several tens of megaparsecs and have various sub concentrations.

With the discovery of redshift quantization and clearly non-dynamical structures and correlations within the Coma and other clusters it became immediately clear to me that dynamics could not possibly be the process by which cosmic structures or even galaxies formed. The year 1976 marked my turning toward a quantum theory for cosmology beginning with the development and publication of three introductory papers [55,58,59] discussed in seminar 2. Once redshift quantization was discovered in the Coma cluster I actively turned to studies of double galaxies as a fundamental test of large scale dynamics. Double galaxies were about to provide not only critical aspects of redshift quantization and a final death knell for large scale dynamics (for me), but also basic properties of superclusters [79].

### 7.6.3 Double Galaxies, and Large Scale Structure

In 1972 Karachentsev [R] published a useful catalog of northern hemisphere double galaxies complete to magnitude 14.5 including a classification system relating to various types of interaction. I coordinated with him in a study of a group containing a discordant redshift galaxy (Karachentsev and Tifft, 1978 [65]) and developed a spectroscopic program using the Steward 90-inch telescope to provide redshifts for catalog pairs close enough together to obtain spectra of both objects on a single oriented slit. Most reduction and analysis was done in 1978 while on sabbatical in Bologna, Italy. The main data was published in 1982 [82] along with several related studies [79,83,86]. While at Bologna I was introduced to 21 cm work on pairs by Peterson [H] that led to my 21 cm investigations of redshift quantization, discussed in seminars 2 and 3, leading to global quantization and redshift variability.

From the viewpoint of supercluster studies my optical double galaxy work soon proved to be important in the development of Quantum Temporal Cosmology. The study includes nearly 300 pairs extending in depth to 10,000 km/s over the entire northern hemisphere providing a nearly complete sample of a specific class of objects. Several aspects of their distribution and properties appear to be critical to understanding large scale structure. By using an oriented slit I was able to obtain quite accurate differential redshifts as well as orientation information. Very early in the work I noted that within certain areas both redshifts and orientations were surprisingly similar. The abstract of the 1980 paper titled "Double Galaxies as Indicators of Large Scale Structure" (Tifft 1980 [79]) provides a concise summary of the findings. With that introduction I will develop distribution and orientation information in more detail.

> Northern hemisphere double galaxies are shown to contain large-scale clumping in the form of clouds associated into four or five large-scale filamentary structures. The filaments are on the order of 10 Mpc thick and 100 Mpc long. Position angles of the doubles are aligned regionally, and the alignment varies in a regular manner within the large-scale structure. Clusters within the structures appear to have elongations which fit the orientation pattern defined by doubles. Sections of the structures, where the viewing angle is largely transverse, show an asymmetry where the brighter, more nucleated component is preferentially on one side followed by a reversal and a section with opposite orientation. In structures seen nearly radially a regular pattern of orientation change of $180^o$ appears to occur every 3,000 km/s in redshift. Both clockwise and counterclockwise rotation are present, but otherwise the pattern of change appears identical.

As the abstract indicates the subject of double galaxies is complex. To begin, cloud structure will be discussed, then followed by a close look at orientation. Figure 7.19 shows cloud structures, designated by serial numbers, and a supercluster pattern for the 2-4-6-10 Cancer cluster cloud structure at 8-10 hours of right ascension. Redshift ranges (in km/s) with a few exceptions (see changes in right frame) are cloud 2=3200-4400, cloud 4=4500-5500, cloud 6=5600-6600, cloud 10=8000-9500. Letters refer to clusters, C = Cancer, A = A569, ( P = pair). The 7-8-9 cloud structure and features near the Coma cluster around 13 hours have redshifts, triangles = 6000-6900, x = 7000-8000, dots = 8100-9500. The extension into the cloud 15 Hercules region have redshifts, open triangles = 6500-7500, x = 7500-8500, open dots = 8600-9500, dots = 9600-10900, filled triangles = 11000-13000. Letters refer to clusters, C = Coma, A = A1367, H = Hercules, Z = unnamed.

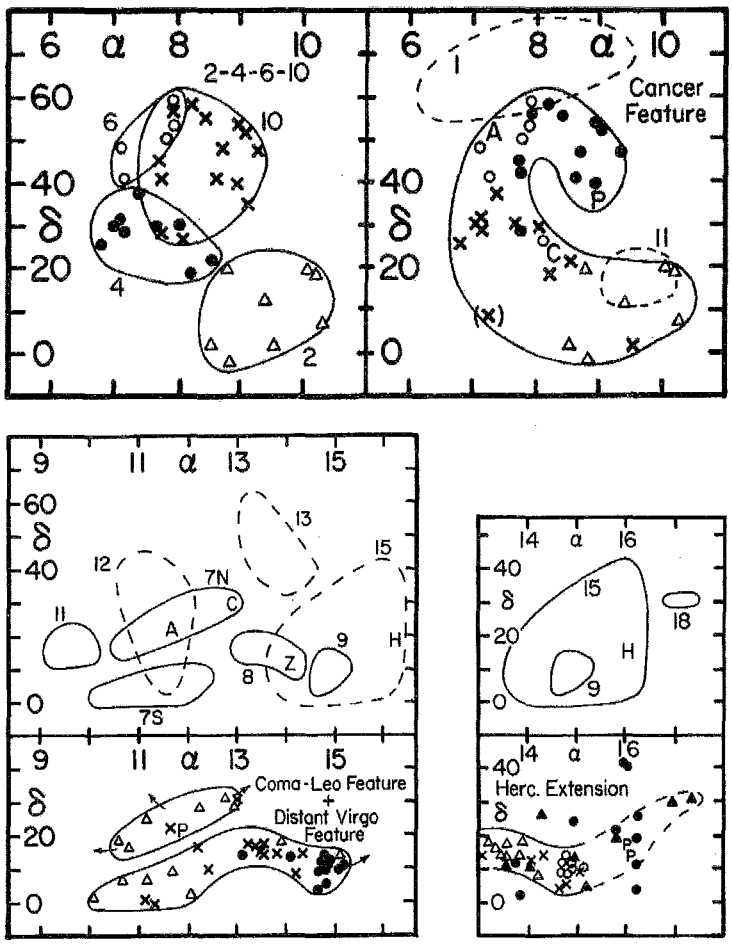


Figure 7.19: Cloud structure in the Cancer and Coma supercluster structures.

Figure 7.20 shows the structure of the Perseus cluster region and an equal area plot extending east into the Cancer region across the Milky Way. Symbols indicate redshift, open dots = 4400-6100, x = 6700-7700, dots = 8000-9700, filled triangles 10200-11800. Three crosses = 2000-2400 are foreground or a possible low redshift extension. The track across the Milky Way indicates a possible connection to the low redshift cloud 1.

To determine actual scales and demonstrate that the overall pattern of clouds and filaments is consistent, a simple statistical analysis was carried out. A distance independent parameter $V_oS$ was found for each pair in the survey. $V_o$ is the average redshift of a pair in km/s, proportional to distance, and $S$ is separation in degrees, inversely proportional to distance. The product is thus proportional to the minimum true separation independent of distance. The frequency of occurrence of $V_oS$ globally provides the spacing and size of characteristic clumping within supercluster structures. Excluding pairs with redshifts less than 2000 where

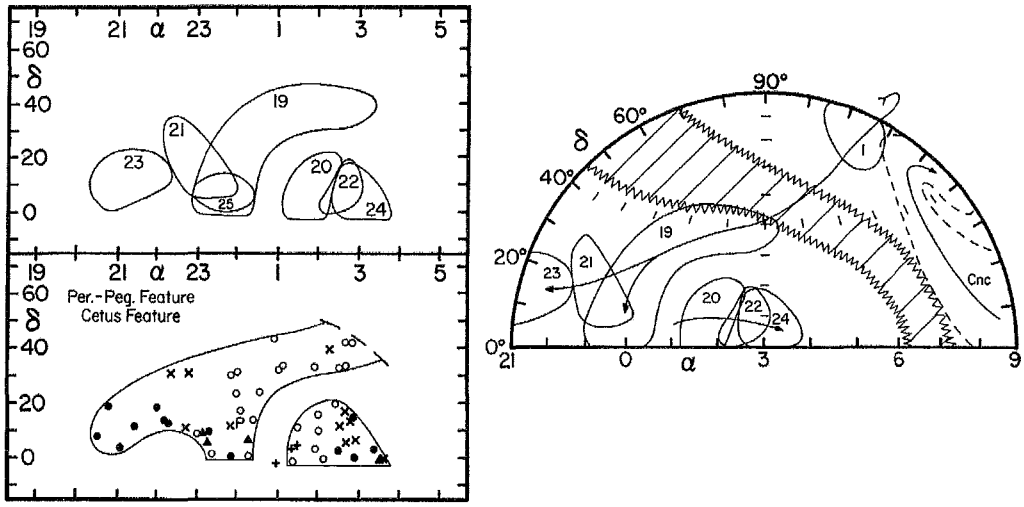


Figure 7.20: Cloud structure in the Perseus supercluster region and a global view east across the Milky Way.

the sample is incomplete, 281 pairs are available which generate 39,621 combinations. Of these 4395 have $V_oS < 1.6 \times 10^5$ and $\Delta V < 3000$. At this scale 42 pairings exceed $45^o$ and only two exceed $60^o$ where the error in the small angle approximation for the separation parameter is only 5%, but the sample begins to be incomplete due to declination and Milky Way spacing limitations. We therefore expect the analysis to be reliable up to between $V_oS = 1.0 \times 10^5$ and $1.5 \times 10^5$.

Figure 7.21 presents key elements of the analysis. Assuming a uniform homogeneous sample and uniform space density of galaxy pairs, the number of pairs should be a linear function of $V_oS$. The upper left frame of figure 7.21 shows counts, N, in $V_oS$ intervals of $2 \times 10^4$ (20 on the figure scale where $V_oS$ is scaled down by 1000) for two 500 km/s $\Delta V$ ranges, 1500-2000 (dots) and 2000-2500 (open dots) between pairs. Two lines are fit depending upon the weight given to the 100-150 range. The relationship is linear to between 100 and 150 where incompleteness should appear. There is no excess below 150 implying no evidence for clumping at any scale for pairs differing in redshift by more than 1500 km/s. Studies for differences up to 4000 km/s again show only increasing incompleteness without clumping. The lower left frame of figure 7.21 shows the $V_oS$ distribution for redshift differences between pairs of 1000-1500 km/s. An excess appears around $V_oS$ of 50 corresponding to a scale of 10-15 Mpc for the Hubble constant of 75 used for this work. This represents the lateral scale of the individual clouds in figures 7.19 and 7.20. Since no clumping appears at larger scales this is also the maximum scale of significant *radial* clumping, the depth of any larger structures (for example edge-on disk structures). The right hand frame in figure 7.21 examines three redshift intervals less than 1000 km/s between pairs. Two characteristic scales of clumping are now present indicating strong lateral clumping which increases progressively with $\Delta V$. This corresponds to dimensions up to at least 35 Mpc as indicated by the scale at the bottom of the frame. This confirms the multiple cloud association chains seen in figures

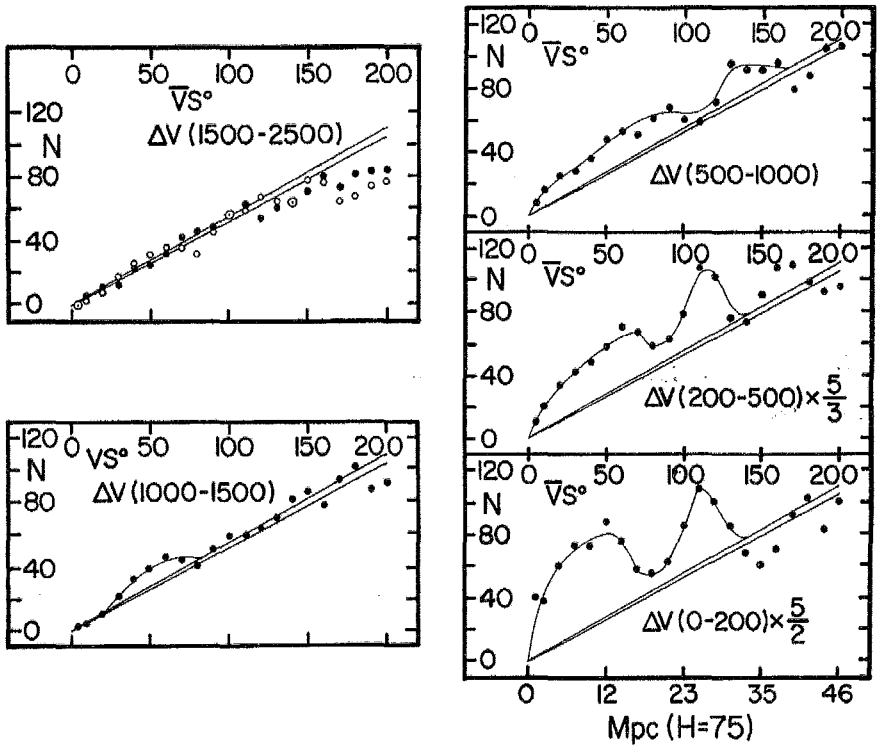


Figure 7.21: Tests for structure and scale within superclusters. Within diagrams the redshift within $V_o S$ is expressed in thousands of km/s and N is number counts. Individual frames are discussed in text.

7.19 and 7.20 which define supercluster structures. The distinct dip between the two cloud scale structure peaks imply that supercluster structures are not simple continuous objects, but have a clear individual cloud substructure.

Only one type of structure appears to explain the geometry of superclusters, isolated filaments. The observed lateral to depth scales immediately rule out large spherical distributions, not surprising since the earliest surveys [71 and other references] of superclustering indicated they were flattened. Since the preferred orientation of flattened disks is edge-on the depth limits of the present study makes pancaked disks unlikely. However, for linear features or thin filaments, long in only one dimension, preferred orientation is sideways. Observed depth will be much less than lateral extent as found herein. Also, with increasing $\Delta V$ one will be comparing portions of filaments further apart which will increase the correlation range with $\Delta V$ as observed. Finally, structures built from sets of individual characteristic cloud forms will generate the dual peak pattern seen in figure 7.21. Superclusters therefore appear to be filamentary structures consisting of individual clouds. This is inconsistent with collapse structures proposed within classical cosmology, but consistent with successive steps along individual developing timelines as proposed within QTC.

This is perhaps a good point to make an important distinction between three dimensional space and time. Supercluster structures seem to be filamentary but are not straight lines. Timelines are straight lines except for small deviations at certain points which I shall discuss momentarily. Time is steady and linear, but flow in space is not. Tau-space has no perception of lateral space (remember, there are no transit time delays in redshift quantum steps within a galaxy), it perceives space as a slightly fuzzy linear flow, a spaceline. Just as space perceives time, lateral effects in time have no perceivable meaning in space (beyond a fuzzy uncertainty zone thanks to special relativity). Space still flows linearly through time (sigma through tau) but matter in sigma has no such restriction *within* sigma. Sigma, and the redshift, age linearly (except for relativistic drifts) but matter moves about governed by classical continuous physics within *individual* distinct sigma *particles* called galaxies. Superclusters in QTC are simply clouds of such sigma particles which develop as a tau-space timeline grows. I will return to the alignment property of galaxy pairs discussed in the 1980 double galaxy paper [79] after looking at the issue of timeline development.

### 7.6.4 Timeline Development, Lets go Fissioning

How does nature make galaxies and aggregates of galaxies beginning with pairs then compact groups, groups, clouds,and finally superclusters? Classical cosmology assumes large scale continuity in gravitation and motion which can produce things like large scale gravitational collapse and dynamical merging. However, the quantized redshift rules out continuous motion on the large scale. Going further, continuous motion produces continuous patterns, not correlated reproducible quantized relationships we see. Yet the redshift is the basis for essentially all classical cosmic dynamics, and every critical test for classical dynamics in my studies fails. Not a single study is consistent with classical dynamics beyond the scale of individual galaxies. Still, somehow the cosmic structures must grow and propagate by some mechanism to generate the structures and relationships we see. One proposed means for formation of structures is outflow from an internal source as developed and modeled for galaxies in section 5. A second mechanism involves fissioning of a source function with a successive generation of a pattern of objects on related slightly divergent timelines. Such a process produces striking observational effects, may relate to event-one itself and is the topic of this section. Fissioning and successive fissioning along timelines appears to produce what we see on the cosmic stage. The process is illustrated in figure 7.22.

As we look back in time we encounter the products of other timelines within our now zone as they were one lookback time ago. The lookback zone is our now zone displayed in lookback time - the cosmic time radial location of our now zone as we look out laterally in sigma and radially back in tau. Photons we receive now were generated within our now zone when it was one lookback time younger. If they left heading laterally toward our timeline they will step in redshift and be received one lookback time later. We can see any galaxy at some stage in its history but nothing directly about its past or future. If the source function on another timeline fissioned at an earlier time it presumably formed a narrow forward divergent flow pattern (sigma flow through tau is at c and fissioning is a sigma-source process at much smaller speeds). What will we see? A pair, a compact group, a group or a cloud depending on how much earlier it shattered and how many subcycle events occurred subsequently. This raises two questions. What evidence exists for a fissioning process, and what evidence allows us to infer the existence of temporal flows?

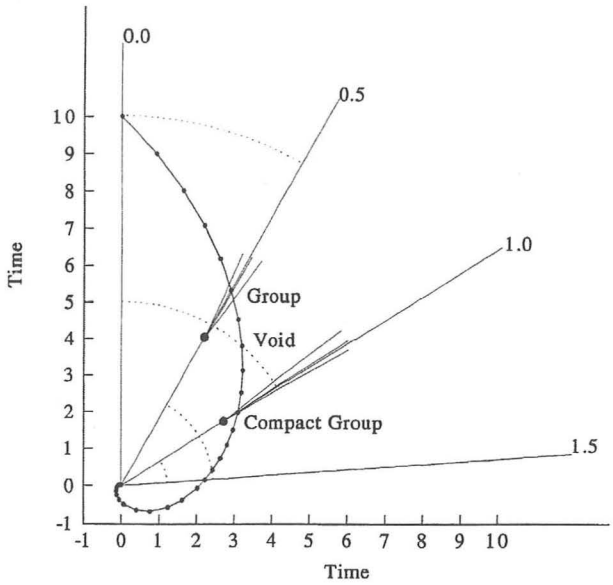


Figure 7.22: QTC time-time diagram illustrating the effect of fissioning along other timelines at cosmic times within our lookback surface We see a later stage of evolution of the event as it appeared one lookback time ago.

### 7.6.5 Alignment

The concept of a timeline fissioning into a narrow forward cone of associated timelines, as discussed in the prior section, was developed after my detection of orientation effects. Alignment was first discovered observationally when I noted that I often needed to make only minor adjustments in the spectrograph slit orientation regionally. Once recognized, however it provided a direct observational demonstration of timeline flow where it is sigma-space that is actually flowing. Certain dynamical collapse situations might occasionally generate an orientation pattern locally, however, aside from the fact that quantization rules out such dynamics, the effect is clear within all the structures defined in section 6.2. Like most of my quantization work which violates dynamical theory the effect is, however, largely ignored. I know of only one clear reference, somewhere within IAU documentation, where a comment by Professor Oort refers to "interesting alignments of double galaxies".

Orientation for spectroscopic purposes is the position angle of the spectrograph slit measured north through east from $0^o$ to $180^o$. The angle has local relative meaning but includes the rotation of the east-west coordinate system. When there is a clear distinction between the two galaxies, orientation on a $360^o$ basis has been defined using relative nuclear faint-to-bright (FB) dominance. Within classical dynamics there should be no significant correlation of $180^o$ orientation and no correlation at all for $360^o$ orientation between independent pairs. To minimize east-west coordinate effects I distinguish between superclusters with a wide (transverse) or narrow (radial) east-west distribution. Perseus and Coma are transverse, while Cancer and Cetus features are more radial.

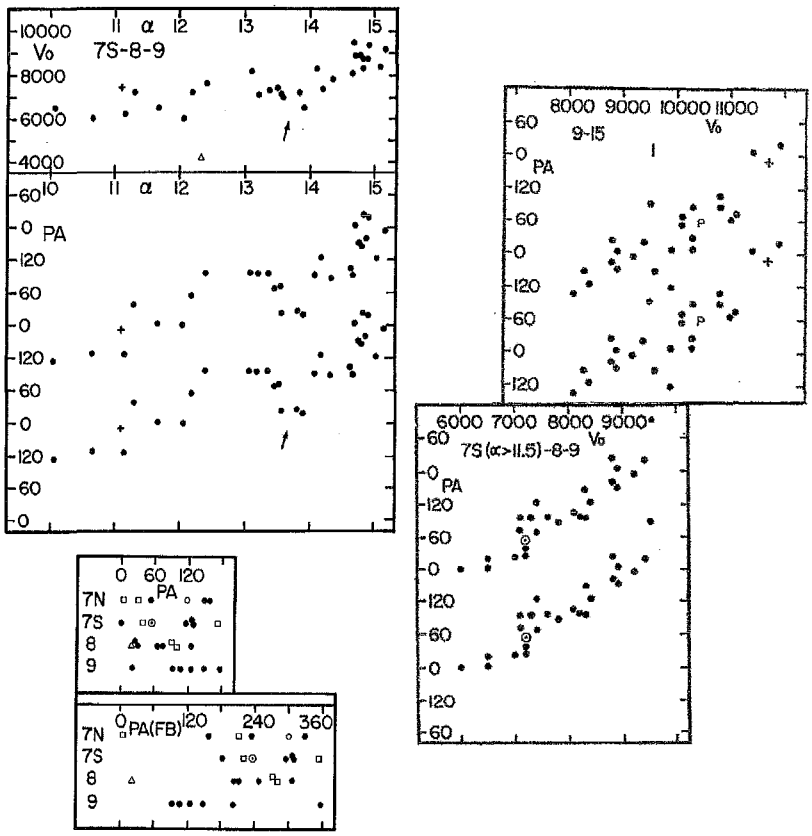


Figure 7.23: Orientation correlations within the Coma supercluster structure. Individual frames are discussed in text.

Figure 7.23 examines the 7S-8-9-15 transverse Coma structure. The upper left frame shows the east-west distribution of both redshift and position angle. Position angle, shown in a double cycle to clearly show its periodic form and continuity, tracks the redshift pattern precisely including the sharp kink through group 8 shown with an arrow. The figure at right shows the remarkably tight correlation between position angle and redshift including a connection into the Hercules region (cloud 15) as the filament turns more radial. These figures totally defy dynamical explanation in my mind. Furthermore, the small figure at lower left shows a strong one sided FB luminosity orientation with an apparent reversal at group 9. Open symbols represent objects which slightly overlap in redshift between group definitions. Virtually all the pairs in groups 7N, 7S and 8 have the dominant galaxy on the west side. The 14 to 1 imbalance in groups 7S and 8 is unlikely at the 0.001 level by accident. The spatially distinct groups form a clear filamentary temporal related chain. The transverse 19-21-23-25 Perseus-Pegasus filament in figure 7.24 has similar properties. Position angle follows both sky position and redshift. The upper right frame in order left to right defines the symbols used to distinguish clouds SW19-21-23-25. The left frame plots

the 180° and FB 360° patterns separately to illustrate an apparent systematic FB reversal by 180° involving group 21 and the west end of group 19. The small figure at lower right shows the orientation distribution patterns for individual groups. Starting from the east

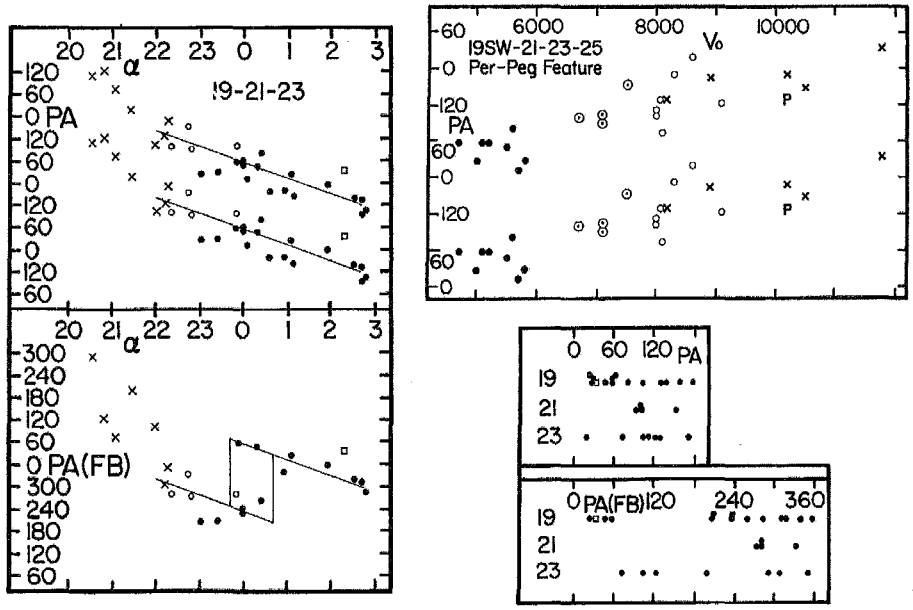


Figure 7.24: Orientation correlations within the Perseus supercluster structure. Individual frames are discussed in text.

end of region 19 (basically the Perseus cluster itself), there is a run of 7 FB aligned pairs, followed by a 180° FB reversal and a run of 9 more aligned FB pairs, (basically group 21). The probability of either run alone by accident is about 0.01. The chance of seeing two such runs consecutively is vanishingly small. Not only are pairs (and clusters) aligned within the large scale structures, but over large portions there is also correlated luminosity ordering. Incidentally, zone 1, possibly associated with Perseus on the the other side of the Milky Way also shows a tight internal clumping of position angle.

Luminosity ordering is aligned with filaments and 180° FB reversals seem to occur where structures are transverse. If this is the case such alignments might be less obvious in more steeply inclined structures. Figure 7.25 contains position angle plotted against redshift for the more radially oriented 2-4-6-10 and 20-22-24 structures. The lower right frame summarizes orientation information for the 2-4-6-10 Cancer structure. Groups 2 and 4 may show some FB clumping but it is much less marked. On the other hand redshift - position angle correlations remain clear. This more radial viewpoint effectively incorporates a twisting of filaments along with reduced longitudinal changes.

The left hand frames of figure 7.25 show the individual redshift - position angle correlations for the Cancer and Cetus structures. Symbols change in order of group number and redshift. A rather striking repetitive pattern is immediately apparent. Of the four major filaments the

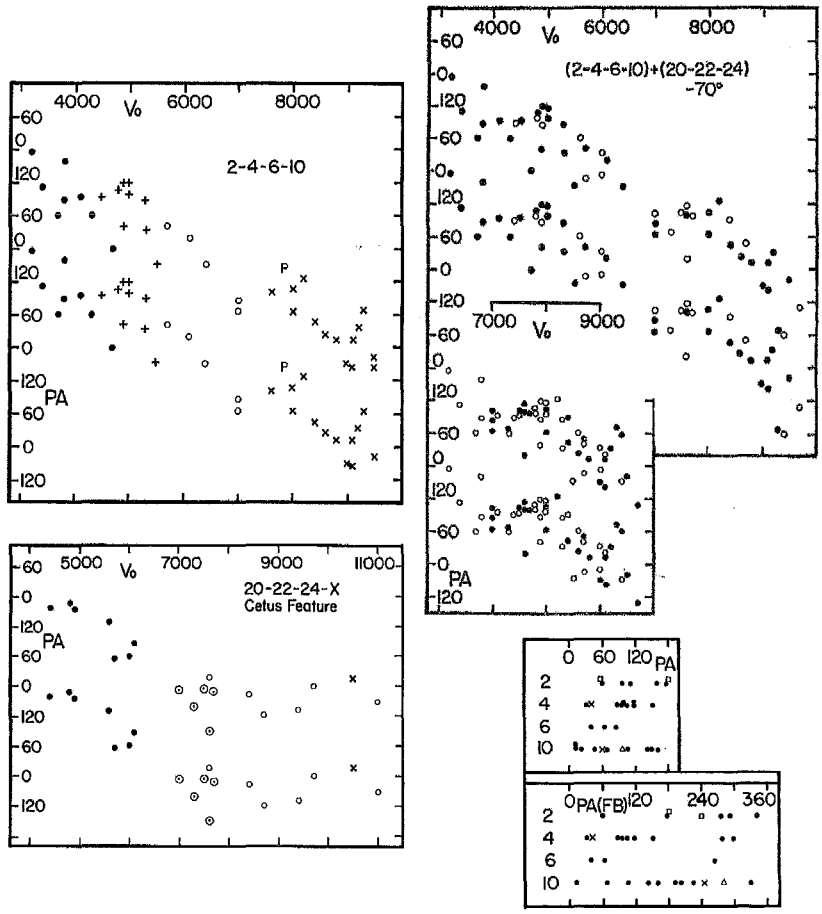


Figure 7.25: Orientation correlations within the Cancer and Cetus structures. Individual frames are discussed in text.

two more transverse features appear to show position angle increasing with redshift while the two more radial ones show a decreasing trend. There is therefore no unique counterclockwise or clockwise variation with redshift. The same cannot be said for the change of twisting angle. The upper part of the upper right frame of figure 7.25 superposes the Cetus and Cancer features after allowing for a position angle shift of $-70^o$ in the Cetus structure. The correlations superpose closely. Both show a variation close to $180^o$ degrees per 3000 km/s change in redshift. The increased point density makes the zone of avoided angles very clear and suggests a break at 6000 km/s. Furthermore the pattern now repeats on 3000 km/s steps. Since the position angle change per 3000 km/s is $180^o$ there is no phase shift in the position angle repeat. The lower left inset to the upper right frame in figure 7.25 shows the result of superposing the part of the redshift pattern with $V_o < 6600$ on the high redshift part by adding 3000 km/s to $V_o$ and making no shift in position angle. The agreement is remarkable. We may now describe the behavior more precisely as consisting of a change of

$180^o$ over about 2000 km/s plus a slight reversal of the trend in the preceding or following 1000 km/s. The reverse slope falls near $V_o = 7600 \pm 3000n$ km/s while the gaps where we separate the distributions for overlay fall near $V_o = 6600 \pm 3000n$ km/s

To further test the reality of the redshift position angle correlations I examined the more nearly radial parts of the other large scale features beginning with the 7S-8-9 feature in the lower right frame of figure 7.23. Except for the fact that the position angle variation is clockwise with redshift we see that the change is again $180^o$ per 3000 km/s. The endpoints correspond to the above defined gaps near 6600 and 9600 km/s and an offset or flattening is seen near 7600 km/s. The flattening or offset points correspond to group boundaries.

Although Cancer and Cetus features contain no information above 9600 km/s we can project that higher cycles might occur. The upper right frame of figure 7.23 includes the possible Hercules extension (group 15) of the 7S-8-9 feature. The region 15 position angle change is also $180^o$ in a 2000 km/s interval and the steep slope is preceded by an offset about 1000 km/s long. Although region 7S represents a transverse segment (in the lower part of the upper left frame of figure 7.23 it appears as nine points between 10 and 12.5 hours of right ascension) it again spans $180^o$ of position angle. Region 7N is identical with the Coma cluster at the upper end and the A1367 cluster falling at its midpoint (see figure 4 of reference [79] along with other individual groups). There appears to be little question that filamentary superclusters consisting of intricately linked related clouds of galaxies exist. They presumably bear a relationship to specific timelines, but details are unclear. Is there a connection between the 'beads on a string pattern' in superclusters and the three or four associated quasar cascade steps of evolving decay discussed in section 6.1? Magnitude limits of present research should be extended. We have barely scratched the surface of lookback time. Detailed astrophysics of superclusters, as seen in the Coma foreground, needs to be extended. The deeper and deeper push with costly massive surveys is actually taking away resources from detailed local studies needed to understand the nature of the local cosmos. My work was done with modest telescopes. We have skipped over and perhaps misinterpreted much of the very territory we need to study. Many of the answers to understanding cosmology are likely to be found within z = 1. I do not believe answers will be found within dynamics at high redshift, rather within 'timely' studies locally.

I first detected the intricate filamentary structure of clouds linked by detailed repetitive orientation patterns in the late 1970s. They represent an important aspect of large scale structure and timelines currently well beyond even my imagination. Is it cosmic chemistry, molecular structure? I once briefly thought it might be possible to call the structures God's Chromosomes but quickly decided to stay out of that domain. We need many detailed local studies, but for my story now it is time to move on to probing evidence for sigma-sources and early phases of galaxy evolution by outflow.

## 7.7 Sigma-Sources and Cycles

Redshift quantization and large scale redshift and orientation related structures, such as redshift-magnitude banding and double galaxy properties, leave no room for dynamics as a mechanism for galaxy formation on the large scale. Evidence for outflow and radial correlations of redshift along with patterns of morphological evolution appear to indicate

that objects are actually formed by evolution from nuclear sources which generate the sigma-space 'particles' we call galaxies. These 'sigma-sources' flow outward on timelines, perhaps as a wave-particle structure, which I will consider in seminar 8, originating at event-one or certain subsequent events within the flow. The basic divergent outflow and dilution of energy is what drives the dual temporal and spatial expansion of the universe in the QTC model. Much of the rest of this seminar is devoted to summarizing evidence for sigma-sources and flows along with events within the flow including redshift doubling, fissioning, and harmonic redshift patterns. These periodic patterns represent cycles between generations of objects. Several generations can exist simultaneously, just as humans cycle through generations with overlapping individual boundaries. An observer can see all stages of many generations, but the observer exists only during his individual life cycle. The personal cycle I am dealing with cosmologically is perhaps defined by the 'life' cycle of our specific cosmic passage from sigma-source to dark matter described in section 5. We may perceive all stages of a complete galaxian existence cycle but our time within that long period may be a much shorter sub cycle of the evolution of the galaxy such as the flow time from sigma-source to dark matter. The width of this latter sub zone seems to be defined by the communication range of the fundamental forces that define matter, not the lifetime of matter. The time to cross this shorter interval is unclear. We may have successive generating events from a sigma-source shedding bits and pieces in doublings (fissioning bangs). Nature may build quasar doubling chains this way in long term cycles. In the meantime we may cycle galaxies through internal harmonic doubling fractions in supercluster chains or by outflow (outflow burps) in much shorter cycles within correlated redshift structures. To understand the cosmos we need to study interleaved generational cycles. Where evidence exists some inferences can be drawn.

If we accept the above picture, and In QTC there seems no way to avoid it, we may ask the next question, just what is a sigma-source? A sigma-source may be defined as the origin point of a physical cycle in time. A cycle is a period, a time interval, beginning at transition points for a packet of energy, whether it be the birth of a child, a galaxy, or a universe. It seems to take two forms, an outflow point in space or a fission point in time, which may be two forms of the same thing. I believe they can be recognized as points where something appears from nothing visible (a sigma-source) or vanishes into nothing visible (a sigma-sink dark zone), which depends upon which side you view it from. Matter and energy evolves from an entry point to an exit point, which are both points of time in QTC, a flowing entry *point* in sigma, and a flowing exit *point* in tau. Recall that tau has no perception of lateral space, the dark matter exit act may enter a single flowing point of time in tau. If you look carefully there is real evidence such sources and sinks exist. I will summarize some of the evidence and introduce a few further examples.

An introduction to what I refer to as event-one, the apparent origin of our visible universe, provides one way to begin. That point may or may not be the 0,0 point in figure 7.26, which reproduces figure 7.22 for reference purposes. Seminar 8 will attempt to discuss the early history of QTC in more detail.

As a starting point for 'our' now zone in QTC, which I have noted several times is all we can possibly see, I need to first define just what that point in time is spatially because it is probably *not* a point in space. The lookback line was derived in seminar 6 (6.3.7) as a logarithmic spiral converging on $t_o$ as a mathematical limit it never reaches. If we rotate that line about our timeline we see that our lookback zone is a thin 3-d shell bounded by

the past and future. There are two interesting points along a lookback line. As noted in seminar 6 (6.3.7) all lookback lines converge at multiples of pi radians of the divergence angle of timelines, $\theta$, from $t_o$. These points are designated as Pi points. Our complete lookback shell crosses all possible timelines once in each cycle of pi radians about $t_o$. Starting at zero we cross our own timeline every $2\pi$ radians of lookback! In seminar 8 I will say more about Pi points. A more important observable point is what I call the opacity point, which falls at a timeline divergence angle, $\theta_o$ in lookback, where the universe became transparent after early stages of formation. It is presumably at this decoupling lookback location in $\theta$ that the present family of timelines could become established. So much for $t_o$ which is probably of only philosophical import. In QTC the opacity zone, which generates the CBR, is a circular ring around the 3-d lookback shell at the opacity angle, a ring in time which could be a point only if it occurred at a Pi point. In classical cosmology the opacity point is a point straight back along our timeline closely surrounding $t_o$ supposedly tremendously expanded by inflation. In QTC the first Pi point is at the intersection of our lookback line with what would be our anti-timeline, if there was one, at $\theta = \pi$ radians on the far side of $t_o$.

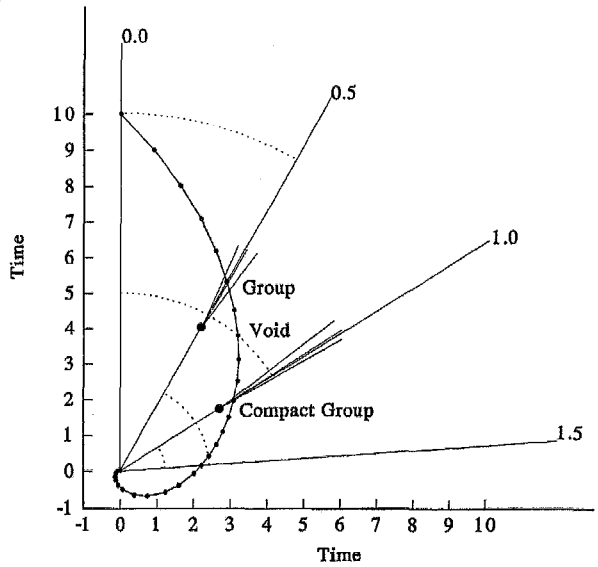


Figure 7.26: QTC time-time diagram illustrating the lookback line to illustrate Pi points and the approach to $t_o$. The timeline angle, $\theta$ is indicated in radians.

In classical cosmology the CBR decoupling point occurs in the neighborhood of redshift $z = 1000$ when the universe was (classically) about 0.001 of its present scale (ignoring inflation). In fact at the first Pi point in QTC the redshift $z_{LT}$ is only 22, after disposing of dark energy, and we are nowhere near $t_o$ at about 1/25 ofthe present scale. Values are shown in Table 1 of seminar 6 (6.3.7) which shows both $z$ and $z_{LT}$ as a function of the cosmic divergence angle $\theta$. It is interesting to note that the QTC model provides a simple method of indicating what the classical redshift must be at decoupling without bothering with the physics! The two models should be and are consistent. The classical redshift reaches 1000 at $\theta = 3$ radians, just short of straight back. In QTC to reach $z_{LT} = 1000$ it is necessary

to proceed to $2.2\pi$ radians, slightly past our own timeline on the near side of $t_o$ where at $2\pi$ $z_{LT}$ is still only 535. In QTC we look back enough to cross all timelines twice, and a few nearby ones a third time. What we might expect to see at this first opacity point will be deferred to seminar 8. Even in QTC, where we see only a small part of the time sphere around $t_o$, a small circular region around $t_o$, the origin of timelines should still be close to radial with a small dispersion. The model of tau as a spherical expansion about $t_o$ is very close to correct. In QTC the origin of timelines is nearly a point in 3-d time. Note our timeline Pi point center could be slightly offset from the opacity point defining the CBR due to fissioning effects. This can be seen in the redshift transformation to the cosmic background rest frame in the ($\pi$) component. We may not, and apparently do not, look quite straight back at the CBR dipole. There should perhaps be a small tilt.

The opacity zone in QTC represents some form of emergence point, a visible origin point of timelines that make up our now zone. A set of discrete sigma-sources defining and flowing on major independent timelines with voids in between must appear since by this stage large scale force linkage appears to be fading away. This is what is indicated in figure 7.26. Secondary fissioning or action develops the structure we see today. Voids will develop naturally between timeline bundles in tau-space since no forces exist outside of sigma-spaces. Without large scale forces structures can exist only along sigma-source timelines, leaving natural voids between. There is no evidence that long range forces and dynamical actions exist in tau-space outside of sigma-spaces, but plenty of evidence they do not. The redshift is clearly quantized. In QTC voids are a generated aspect of 3-d tau-space, not sigma-space. It may be useful to recall again that all that can be seen in principle at the inner end of our lookback shell is what our now slice of time appeared to be at decoupling time. Sigma-spaces as we know them as galaxies do not yet exist, but the sources that will generate them apparently did. QTC deals with time and its inverse energy. Perhaps it could look something like a very high energy pattern or resonance event which will eventually decay into lesser *particles* which QTC calls galaxies - or earlier precursors. QTC is a quantum theory with a quantum based origin. Initially there need be no general diffuse medium other than energy, and that may be confined in early forms of sigma-sources. Matter as p-space particles may already exist within early sigma-spaces, perhaps much as conventional cosmology indicates, but g-spaces as we know them are yet to come. I will briefly return to early stages at the end of this section to introduce seminar 8.

### 7.7.1 Timeline Growth, Fissioning, Sources and Flows

There is evidence for sources, but more directly for structural growth, as systems evolve, involving flows operating within tau and sigma-space or geometrical consequences of a fissioning process. Fissioning (7.6.4) and flow are signs of decay, generating galaxies and groups where energy degradation can occur by redshifting and thermal or kinetic processes as matter appears on the scene. Section 5 of this seminar discussed evidence for radial flow and internal evolution of galaxies where radial redshifting (7.5.4) and systematic radial trends in asymmetry (7.5.7) provide direct evidence for passage of inflow from the nucleus into dark matter outflow as large scale temporal force and communication linkage is exceeded. Supermassive nuclear black holes are presumed to represent sigma-sources for galaxies arising from small scale or temporal limitations of gravity inherent in QTC (7.5.0). The dipole structure discussed as residing in galaxy nuclei, and demonstrated observationally in (7.5.6)

and the first supplement (Ap1), is inferred to potentially be a binary sigma-source. It is an origin of two differential redshift streams (2.3.1) which provide direct evidence of a dual outflow (7.5.6). Sigma-sources appear to be doorways into time connecting to matter and energy. I will proceed by summarizing evidence for fissioning and flows before introducing further evidence for sigma-sources and evolution.

The apparent existence of timelines is the first basic demonstration of flow. All relevant tests of the tau-sigma model attest to the concept of the flow of sigma through tau. As noted in the prior section (7.7.0) the model incorporates an implied demonstration of early fissioning. The logarithmic lookback path, leads to the opacity point (or small region) representing the emergence of timelines. The opacity region provides a consistent origin for both timelines and cosmic voids. It is not quite $t_o$ but is as far back as we can go experimentally.

Beyond timeline formation of precursors the next observable step involves the formation of the first generations of galaxies or precursor including quasars. In section (7.6.1) and seminar 5 there is evidence that at certain quasar redshifts related to simple fractions of c excess numbers of galaxies appear (5.4.0) and periodic doubling patterns (5.4.1) analogous to local supercluster filament chains are seen. In QTC the galaxy stage appears to require a precursor sigma-source function which can produce showers of galaxies. Such a source function is suggested, actually required, by several observed effects if we accept the key premise that large scale dynamics is ruled out by quantum properties of redshifts and the QTC properties of forces. Successive fissioning and secondary timeline forward divergence provide an explanation of compact groups (7.6.4) and quantized oriented pairs (3.4.1) leading to groups then clouds and oriented structured supercluster filaments (7.6.5), each step of which is quantum consistent and dynamically inconsistent. We see a consistent pattern of fissioning, divergence, timeline flow and structure development including such features as cross-band development (1.7.1) in redshift-magnitude bands. Such examples are evidence of a flow and/or fissioning mechanism producing a forward narrow flow or evolutionary development. Other examples and details relating to these issues are developed below.

The final transformation constants used to transform to the galactic center and cosmic rest frames are $(\theta = 232.2, \pi = -36.5, Z = 1.2)$ and $(\theta = -243, \pi = -31, Z = 275)$ km/s [125] while the original CBR vertex transformation used is $(\theta = -245, \pi = -23, Z = 275)$ km/s. The constants to transform observed redshifts to the cosmic reference frame differ from the transformation to the CBR vertex in only one coordinate, the lateral ($\pi$) value. In QTC The cosmic radial ($Z$) term is due to our sigma relativistic lag in time flow which is consistent with the scale and direction of the CBR dipole. The angular ($\theta$) term nullifies our sigma particle spin (galactic rotation). The lateral ($\pi$) term represents both real expansion of our galaxy in sigma and the equivalent tau temporal divergence from the fissioning event that generated (or recycled) our galaxy. We do not look quite straight back to the CBR. This could perhaps produce a slight gradient in the CBR. The $\pi$ coordinate is, and should be, the only common coordinate in the transformations to the galactic center and cosmic frame. This relationship also explains why we have local global quantization within our local cloud (including our Local Group) and the cosmic frame. There is no spatial bulk motion in tau, only in sigma, but expansion in sigma, equivalent to divergence in tau, is in common. We can see local cloud quantization from the galactic center, with some distortion, and true overall global quantization from the cosmic rest frame. Time is conserved in transformations between the frames, the cosmic transformation sums to zero.

Many observations are directly consistent with a concept of a non-velocity flow through tau, a process representing the outflow and degradation of energy. The redshifting of photons (6.3.7) is a major aspect of that decay and provides direct evidence of the flow. Redshift variation, actual changes in the redshift, is observed as a one way decay towards lower redshift (2.6.0-2),(3.7.0),(3.9.0-5),(Ap2). The flow provides separation of clouds in redshift between successive fission events (7.6.2,3) which can generate the filamentary 'beads on a string' supercluster structure (and quasar doubling cascades) or separate and align double galaxies (2.4.1). Within sigma it appears as a radial flow generating the dual redshift streams (2.3.1) from nuclear dipoles which are well illustrated observationally by elliptical galaxy rotation studies and spiral modeling discussed in section (7.5.6). This outflow is seen directly in the radial expansion terms in the cosmic and galactocentric (2.5.1),(2.8.0) transformation constants and generates a systematically blueshifted core and outlying radial redshifting (7.5.4) in galaxies as older outflow material drifts toward and into dark matter due to its lagging temporal flow.

The most fascinating apparent example of a temporal flow is the direct observation of the proper motion of the Large Magellanic Cloud nicely reviewed in the Sky & Telescope October 2012 article by R. Zimmerman [BD]. Independent galaxies cannot move about in terms of velocity in QTC , but temporal flow does produce relative displacements which will appear as proper motion. The discovery in the LMC played havoc with existing dynamical models of the clouds, quite consistent with the QTC concept of the absence of conventional dynamical interaction between galaxies. QTC suggests our galaxy and Andromeda are quite likely a fissioned pair with objects such as the Magellanic Clouds perhaps present as distorted outlying fragments of the event. Andromeda and the Milky Way differ in redshift by the standard 73 km/s with Andromeda in the lead. The entire Local Group forms an internally quantized group [58].

The flow also produces the striking low redshift excess in the cores of clusters of galaxies shown in seminar 1 (1.5.1). See for example seminar 1 figure 1.20 showing the marked lower redshift distribution in the Coma cluster with decreasing radius (and no equivalent change at the high end which classical dynamics should produce along with destroying observed internal quantization and structured patterns). Section 7 of seminar 1 (1.7.0-2) discussed the low redshift excess in detail found in all clusters examined, including the growth of cross-bands (1.7.1) and includes the remarkable correspondence of discordant low redshift galaxies in compact groups (1.7.2). The shift is always one way. Cluster cores appear to be the equivalent of galactic nuclei as outflow sigma-sources at a much larger scale. The corresponding morphological shift, with low redshift for early type galaxies and higher redshift for older spirals is the evolutionary result of the same 'radial redshift' effect caused by lagging temporal flow discussed within galaxies. Older stages of galaxy evolution lag behind the newer cycles and appear at higher redshift approaching dark matter. This aspect will be developed further later involving vertical evolutionary redshift patterns in early type galaxies as examples of sigma-sources in action.

## 7.7.2 Dispersion Bands and Vertical Input

At this point I have introduced several possible sigma-sources: Event-one and the opacity lookback point potentially related to the basic origin of the universe, timeline fissioning, and a substantial summary of evidence for flows. Galaxy nuclei and cluster cores potentially

represent input sources within structures conceivably associated with dark matter exit points connected by radial flow. There is, however, another way to see an input point connected with vertical-sequences seen in clusters and groups as suggested in the early evolutionary model for redshift-magnitude banding in seminar 1, figure 1.40 (1.8.0). The study of nuclear dipole structure and rotation in elliptical galaxies described in (7.5.6) led to remarkable evidence associating vertical structures of ellipticals with galaxy source functions. The reference is Steward Observatory Preprint 513, rejected by the Astrophysical Journal, but contained herein as the first supplement [85] (Ap1).

Any bulk motion in galaxies, rotation or expansion, will be augmented or reduced by a nuclear dipole offset (7.5.6). Measures of expansion combined with velocity dispersion and rotation in ellipticals fall into two families, changing slowly or rapidly with radius. Such a dipole induced effect is expected in QTC, but is one of the puzzles in classical dynamics. High quality dispersion measures became available in the early 1980s. The data, discussion and references are given in full in the first appendix (Ap1), however key figures and commentary will be introduced at this point. Ellipticals are considered to be effectively optically thin (transparent). Dispersion is measured as central ($\sigma_o$) or overall averaged ($\bar{\sigma}$). The difference $\sigma_o - \bar{\sigma}$ is a good measure of expansion or dispersion after modification by a nuclear dipole offset. Since dispersion is luminosity sensitive, especially at high luminosity, the less sensitive difference is used to detect the dipole. For the same reason galaxies fainter than $M_B = -21.5$ were studied initially. Typical dispersion measures are several hundred km/s. The ellipticity of a galaxy, $\epsilon$, is a flattening measure which increases with rotation. Absolute blue magnitudes are used in diagrams. None of the data are mine.

The left portion of figure 7.27 contains the absolute magnitude - mean dispersion diagram of the sample. It is a banded diagram which closely mimics redshift magnitude bands in slope and spacing (except for the $90^o$ rotation) complete with a form of cross-band structure. The clarity of the pattern surprised me initially. It must be a global effect, as redshift-magnitude banding was found to be, since the galaxies are widely distributed between different but similar types of structures. Galaxies are apparently built to very specific designs and seem to evolve, like stars, within a very specific pattern analogous to the stellar HR diagram. The data, projected to $M_B = -21$ at the marked slope, is shown below the main frame with equal interval counts to evaluate the significance of the primary gap. The gap is significant and discussed in (Ap1). Open dots identify galaxies observed to show steep dispersion gradients, filled dots have small gradients. Bands are identified using + and − notations. Note the cross band association and continuity of the solid dot pattern. The pattern switches between bands at the breaks between cross-bands which we are about to see correspond to vertical-sequence locations.

Before turning to vertical-sequences, the right hand frames of figure 7.27 bring out the dipole effect hidden within the nuclear excess dispersion, $\sigma_o$ reduced by the mean $\bar{\sigma}$. The sample, especially fainter galaxies, divides clearly into two families, the reinforcing (R) and opposed (O) dipole sets. Since the division is essentially entirely due to the nuclear dipole offset it should not, and does not, show any relationship with galaxy luminosity or shape The split is very close to the expected 36 km/s fully accounting for the different velocity dispersion patterns with radius. The split provides the orientation information needed to derive the clear corrected rotation pattern for ellipticals shown in figure 7.9 of (7.5.6). The dipole concept completely resolves the dual rotation and dispersion pattern problem, a rather

powerful confirmation of the dipole concept. Further details illustrating the dipole rotation correction in relation to eccentricity, which again clearly distinguishes the rotation families, are given in the first appendix (Ap1). In the upper right frame of figure 7.27 filled circles designate + and open circles ++ band objects. A + symbol marks galaxies with $M_B$ above $-21,5$. In the lower frame circles refer to + and triangles to ++ band galaxies with a colon for the two brighter galaxies. Open and filled symbols distinguish reinforcing and opposed dipole families. The + symbol object is uncertain as to orientation.

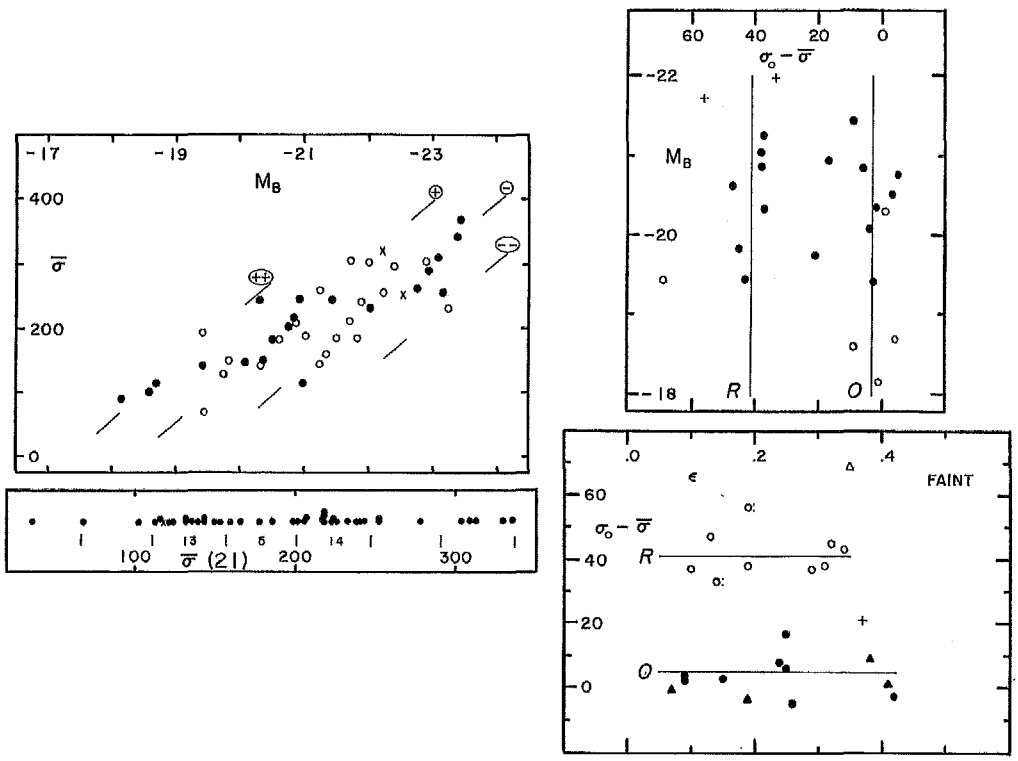


Figure 7.27: Dispersion banding and dispersion correlations for elliptical galaxies. Individual frames are discussed in text.

The left frame of figure 7.28 shows actual magnitude - morphology band structure for the dominant + and − bands as a function of ellipticity used to represent morphology. For eccentricity greater than 0.19 there is a distinct progression of eccentricity with fainter absolute magnitude exactly as seen in redshift magnitude bands. Even when E and So types dominate there is the same distinct ellipticity trends in redshift-magnitude diagrams [34]. On the other hand, the nearly spherical galaxies with $\epsilon \leq 0.19$ shift dramatically into a vertical column aligned at the head of each band. They appear to be sequential in eccentricity with the morphological band pattern but not in luminosity. Faint and bright galaxies have completely different eccentricity distributions highly suggestive of a different origin and evolution. A rank sum test on the two main bands indicates only a few parts in

1000 chance that the fainter galaxies on either band have the same eccentricity distribution as the brighter galaxies. Seen in magnitude - eccentricity (or redshift-magnitude) diagrams vertical patterns of early E galaxies appear to arise from nowhere as fainter spherical systems which connect to bands of evolving later type galaxies.

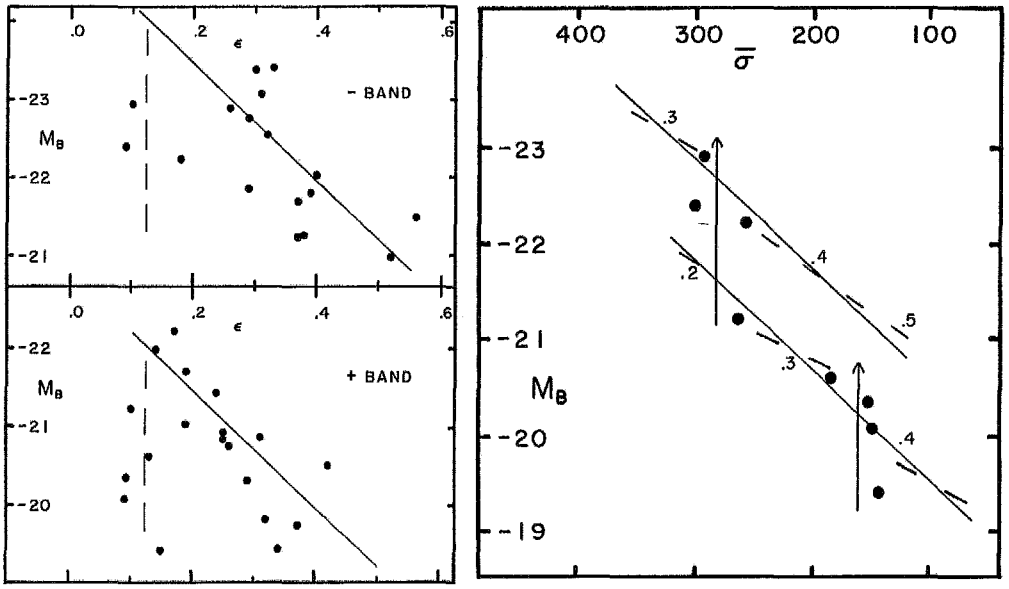


Figure 7.28: Vertical-sequence effects associated with elliptical galaxies. Individual frames are discussed in text.

Returning to a (now rotated) magnitude - mean dispersion pattern shown in figure 7.27, the right frame of figure 7.28 shows the location (filled circles) of the + and − dispersion band ellipticals, having $\epsilon \leq 0.19$. The cross-band structure from figure 7.27 is shown dashed and progressive eccentricity values from the left frame of figure 7.28 are shown. The vertical-sequence low eccentricity galaxies now split and appear precisely at cross-band junctions generally consistent in both luminosity and velocity dispersion but now not in eccentricity. This is consistent with the staggered track of filled symbols noted in the left frame of figure 7.27. In effect, vertical-sequences appear to relate to injecting 'new' galaxies into or removing old ones from junction points between cross-bands. Cross-band structures appeared to be individual evolving packets of galaxies in seminar 1 (1.5.1) beginning with figures 1.20 and 1.21. Further discussion of possible evolutionary patterns involving cross-bands will be summarized in seminar 8. It is increasingly clear that vertical-sequences and cross-bands play an important related role in the evolution of galaxies and redshift-magnitude bands.

To continue an examination of vertical-sequences, figure 7.29 duplicates figure 1.38 from seminar 1 showing five compact early E dominated groups which superpose exactly forming a vertical-sequence which falls precisely between the leading cross-bands of the upper band within the Coma plus A1367 cluster complex. Now recall that in the Coma cluster and most clusters investigated, a vertical early E type galaxy luminosity pattern connects to the

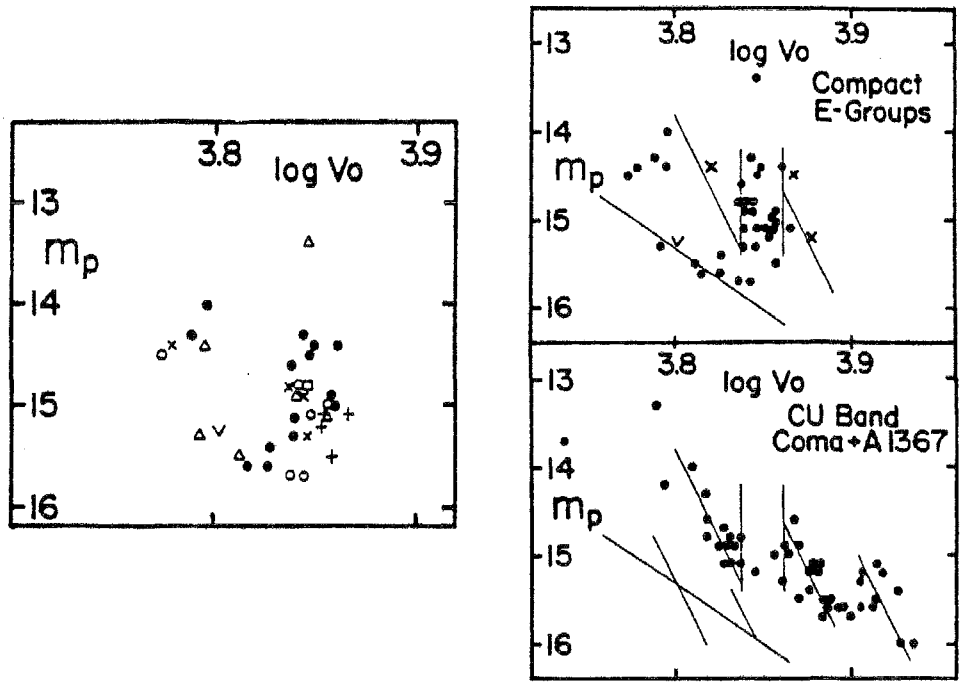


Figure 7.29: Five Compact groups.

cluster core where QTC proposes a sigma-source resides. This source along with temporal flow and lag processes distributed over time generates the cluster of galaxies. The source and objects associated with it should be in or near the cluster core but may be dispersed in magnitude and redshift (and properties correlated with redshift) to relate the objects to other parts of a diagram. A redshift-magnitude diagram does not indicate where any object is spatially located. Figure 7.17 in section (7.6.2) illustrates this well in Coma. The long low redshift spike associated with the Coma core extends below redshift 5000, corresponding with the lowest redshift cros-band in the lower Coma band. In QTC this low redshift excess, found in all clusters studied, represents redshift decay evolution, not velocity dispersion in the core. There is a consistent low redshift excess toward cluster centers with no corresponding high redshift tail required by a velocity interpretation. Such a sigma-source, flowing in time, generates lower redshift early type galaxies, and leaves a wake of evolved galaxies of later morphological types, which is precisely what is implied by the morphological distributions both radially and in redshift. This systematic shift also explains the oval shape of clusters which align with the associated supercluster pattern. The shape has nothing to do with cluster rotation. Individual cross-band packets appear to be factories within which life cycles of individual galaxies play out. Young cross bands appear at lower redshift and old ones die off at higher redshifts. To me this looks like the internal cycle within a galaxy described in section 5 on a much larger scale, now perhaps recycling entire galaxies.

### 7.7.3 Lets talk about $t_o$

What have we learned at this point about the origin of the universe? As we look back along our lookback line we see evidence for interesting cycles which define our status of evolution within a galaxy, the status of galaxies evolving within cross-bands, the status of clouds of galaxies evolving within supercluster structures and those structures evolving from quasar doubling patterns. Each step leads us back toward the opacity point from which timelines emerge. $t_o$ appears to lie beyond. Note, however, we have worked back only to $z_{LT}$ of about 3, the opacity point is near 1000! We have seen that QTC evolutionary procedures involve a systematic energy density decay driven by doubling and harmonic action displayed along lookback lines. That fits the data well, but if QTC is correct and all the above is true we are a long way observationally from, and can never actually get to $t_o$

The lookback line, according to QTC, is a logarithmic spiral. It spirals around $t_o$ continuously but never connects. The lookback 3-d shell passes through all timelines every $\pi$ radians, generating progressively smaller cycles in an infinite progression towards $t_o$. The doubling pattern is mathematically an infinite series which converges to a finite lower limit of zero, an infinite series between zero and infinity. A QTC cosmology has no reachable origin or end. Mathematically It is a closed periodic form of an evolving cosmology without beginning or end. We can see back to the opacity point slightly past the second Pi point. The lookback shell crosses all timelines every pi radians passing alternately through a point on our timeline or anti-timeline. Matter and energy appear to oscillate between tau and sigma in various cycles. The periodic redshifts of galaxies suggests an oscillation in time where galaxies can exist at nodes of the oscillation which progresses and evolves in time. I will discuss such a model in seminar 8. It may have a lot to do with a distinction between Fermi and Bose statistics. Time and energy are reciprocals, if both time and energy are strictly conserved, the process can potentially recycle indefinitely. Of course mathematics and reality may be quite different but it looks like the opacity point is our visible origin. The Planck point, $t_o$, which lies within that point has long been considered the origin of modern physics. If it is the only meaningful origin point then from the QTC point of view I think of $t_o$ as a zero sum fission in time generating its reciprocal, energy, and the decay begins. QTC begins with a finite dipole of time, which relates to the dipole that galaxies appear to harbor in their nuclei. Such a zero sum split can resolve the matter anti-matter problem and many other items via QTC. There are still a few early tales to tell about QTC.

From the beginning the universe must have been a quantum structure, call it infant tau at conception. Its initial temporal dipole evolved rapidly, formulating timelines, and if QTC is right the timelines, its dipole structure and their components (call them instants of time/energy) developed (decayed) rapidly by period doubling. As early sigma-space substructure developed at least one 2-d structure apparently formed, the 1 2 4 doubling triad which QTC recognizes as the basis for the fundamental forces and a basic structural component of fundamental particles discusses in seminar 4. I elected to call this structure a chronon. Individual instants must be fermions since the minimum triad is a degenerate structure (4.9.0). The chronon structure requires an internal binding force. In QTC this is presumed to be the birth point of the strong force, or its temporal equivalent, internal spring-like bonds binding the structure and ultimately quark structures. As discussed in seminar 4 (4.8.4), quark structure appears to be constructed from a progressive superposition of chronons. It is also of interest to note that this progression appears to lead directly

to the electron as a quark limit (4.7.0). A second possible initial structure uses time itself to distinguish instants of time/energy as a time anti-time dipole. This temporal dipole linkage provides for Bose statistics and is the basis for the weak force. This appears to be what requires splitting the QTC particle doubling process into the two (pi and gamma) interconnected energy level patterns (4.2.3) and involves neutrinos which are needed to account for and preserve the 4-d temporal link as discussed in seminar 4. The light meson structure (4.4.0) in turn leads to the muon lepton limit (4.8.1) which terminates that structural process as the electron terminates the quark pattern. These processes of binding chronons appears to be the way QTC begins to formulate p-spaces of matter.

Photons are basically a product of sigma-spaces. The earliest structures in the universe are presumed to be temporal dipole structures in tau-space, bosons constructed from fermi temporal instants (a zero sum split in time), which interact and bond to generate a fundamental triad structure and begin generation of timelines and early radial sigma patterns where forces, unique to sigma, can begin to develop. This is necessary to define and generate photons which QTC defines as 2-d boson structures confined in planes of lateral time involving the triad. The triad is a basic temporal/energy package needed to define both force and structure. A rough concept of the early QCT universe is discussed in seminar 8. Classical cosmology simply assumes photons were there from the beginning.

A 2-d triad structural form provides a very thin layer of phased temporal commonality. An internal strong force, or temporal equivalent, is the force which appears to bind triads. It has a very short range in time, a few Planck distances in the QTC force definition. Larger spatial intervals are involved in generating of successive forces which presumably develop successively as passive energy structures (matter) become possible by pair formation. An underlying triaxial temporal dipole substructure within timelines and photons in QTC can also account for the ninth root pattern of redshift decay compared to more restricted 3-d states available to passive energy structures forming 3-d fundamental particles. A triad pattern may also relate to the 1/3, 2/3 character of quark electrical charge.

The triad strong restraining force appears to explain the cosmological correction to photon energies. Laterally moving photons passing between timelines are moving through a spherically curved tau-space, not curved by gravitation as classically assumed, but by the spherical geometry of expanding time. There are no long range forces acting on them in tau. As a photon attempts to travel straight it will rises above its now surface. That stresses its triad restraints and the structure is pulled back, presumably in a slow oscillation about its allowed laterally curved plane. This expends energy which progressively produces a slight continuous redshifting. This is similar to forced curvature in General Relativity but for a different reason potentially related to the photons internal strong force binding. This explanation came to light during a discussion with my colleague Dr. Pitucco, so we call it the PT effect, an explanation consistent with the QTC planar model of photons. Photons are restricted to planar structure and lateral flow in time except when buying quantized radial redshift steps forward (in allowed doubling steps) to retain temporal commonality with their radial flowing 3-d sigma parent sources. The correction is precisely defined assuming spherical curvature, $q_o = 1/2$. Gravitational curvature of photon paths within sigma-space, where gravitation operates, retains its relativistic explanation (recall again that tau has no awareness of motion in sigma-space), but on the large scale the PT effect applies and may need to be considered in such effects as lensing.

With the growth of the photon population, which also apparently completes the triad of forces, strong, weak and electric related to energy in the active form, a foundation has been laid establishing sigma-space and passive energy as matter. It does not seem surprising that the first three closely interlinked forces can and have been theoretically related. The rules now change a bit and I am not surprised that gravitation stands apart from the other forces as sigma-space emerges and constrains the p-spaces that must have evolved earlier. QTC provides direct structural hints in seminar 4 that quark triads and doublets can be constructed from chronon triad structures, and the pair formation process can generate the radial axis and initiate the flow of sigma through tau. The triad and doublet patterns are present on both sides of the tau-sigma transition and energy level doubling patterns are clear and fit very well. However, the detailed steps to get from there to here will require much more study and experiment. QTC lays a groundwork, and if it is at least roughly correct I believe the details can be developed. I sincerely believe that QTC can open a path to a far better understanding of both cosmology and particle physics. Seminar 8 provides discussion and illustrations, and fills in various details, as a summary guide of evolution from $t_o$ to 'now'.

# Chapter 8

## Summarizing QTC, The Early Universe and Cycles in Time

Seminar 8 Version 4

## 8.1 Introduction

This book has been written to reach a wider audience than just professional scientists. Although many of the ideas are new and complex they can often be illustrated by simple analogues to make a point more clearly. As I use this seminar to bring together an overview of Quantum Temporal Cosmology, including a guide for back reference to key developments in the earlier text, I may use that approach. As an example, think of a time anti-time or matter anti-matter dipole as a male-female couple where the two parts are both the same (people) but differ in a specific way (sex) and can wear different costumes (time or matter) while their relationship slowly becomes less exciting (aging) etc. Using familiar characteristics may make it easier to understand how different properties may or may not affect other properties. A case in point relative to QTC concerns the 'anti' property in anti-time or anti-matter. Time and anti-time are both time, the fact that one is anti of the other only means they cannot touch or they will annihilate. In QTC the anti concept deals only with existence or existence in a particular form. In QTC time and anti-time do not flow in opposed directions, as is commonly assumed, time is in fact a dimensional property, it does not flow at all, aging is the flow. To represent dipoles in text or figures a short dash (-) denotes the anti property *not* charge or the, always positive, sign of time. The split in time provides a dipole structure which initially defines Planck units and can evolve from that point but retain a dipole coupling without touching. Now let the intensity of our hypothetical couple's involvement be another property, the binding energy to represent the spacing of the dipole, an interval of time, which can change with time in certain ways. As the dipole widens energy decays and the relationship fades, while going to zero or reaching some lower limiting spacing means touching. Such examples may make it easier to see how features like anti properties can be integrated with other properties.

New aspects will be introduced as questions are raised about the birth of time, implications involved, and connections to the picture of how the universe and its families of galaxies evolved and are continuing to evolve. As I review the nature of energy and the energy level structure upon which our universe operates I will discuss three broad subject areas: the early universe, the universe since it became visible, and life cycles that appear to define individual galaxies. A few key figures are used to illustrate points, but seminar 8 is intended for persons who have read the text, wish to see how it can be pulled together into a cosmology, and perhaps refer back to specific subjects as developed in earlier parts of the text to refresh impressions as the subject develops. Familiarity with many of the concepts and the dual 3-d tau-sigma time-space structure (6.2.2) and [130] is assumed. References in the

(Seminar.Section.Subsection) form are provided, for example (8.1.0) for this section, (6.2.2) for seminar 6, section 2, subsection 2. (Ap#) refers to appendices. References to my or external publications appear in brackets, [#] or [Letter], and refer to numbers or letters assigned in appendix 4, (Ap4). A letter or number may be combined with the year.

## 8.2 Some Starting Premises, and Objectives

Much of the discussion in earlier seminars provides evidence for effects which must be integrated together to synthesize a consistent overview of QTC. As evidence is pulled together several interrelated key issues emerge as I attempt to address the very early universe. Concepts related to singularities and dipole structures will be developed. There is the issue of development of early energy structure, fundamental forces, and evolution of matter and energy while incorporating the tau/sigma distinction. Related to singularities, there is time anti-time/matter anti-matter, and the earliest forms of the units of energy. As noted above later sections will summarize development of observed structure and cyclical patterns that emerge within visible structures. Where I begin is obviously speculative, but it leads, and is based upon, what I see and have demonstrated in the visible universe. I begin by presuming the universe in QTC *is a quantum based structure.* Galaxies are quantized particles in a non-dynamical domain of 3-d time (tau-space) where dynamics is limited to the interior of the particles (3-d sigma-spaces). The origin of time is a near-singularity of zero. Upon these and other observationally based premises I will step back in time to $t_o$

### 8.2.1 $t_o$, The Early Universe, with Temporal Dipoles

The upper right corner of the entries in figure 8.1 shows $t_o$, which was defined previously (7.7.3) as a finite split in time leading to a dipole structure of time. Mathematically $t_o$ is an unreachable limit, zero, the beginning of a series of cycles of doubling decay of time. There is no singularity or 'physical' origin, just a limit, a representation of a fluctuation (split) of 'nothing' perceivable, into a real time anti-time dipole structure which is a perfectly good alternate form of nothing (it sums to zero) but forms a temporary form of something anti-something which is still a form of nothing. Is that any different than energy changing its form from passive matter to active energy? A fair answer to the question of how the universe began in QTC may be simply, "well, 'nothing' happened". Existence is simply an interval of time, and that is all QCT needs, a split in time which which sums to nothing and will subsequently decay back toward nothing as an existence anti-existence pairing. The concept of nothing is a philosophical issue beyond the scope of this book, although the concept of different forms of nothing certainly seems conceivable. The sum of anti properties does yield nothing = 0 within QTC, however transitions of form may occur at limiting physical values which approach but do not reach zero. From the very beginning to the very end the dipole concept is central to QTC. Relative to 'now', if scale has any absolute meaning, the temporal dipole zero sum components are initially very small but finite, defining what can be called the beginning of the 'Planck time phase' of the universe. The concept may pose interesting philosophical questions, probably already well known, but is linked to real present day observations. Does zero require an origin if, as only a limit, it is unreachable? Or, how does an unreachable limit affect the physics of its finite components? Can reality consist of an unending series of cycles between two unreachable limits (zero and infinity)?

I have been impressed, as QTC has emerged, that the observable universe contains what seems to be some form of unending interconnected cycles in time. QTC is a study of some of the cycles we happen to be experiencing that relate well to the dipole of time concept.

```
------------------------------------------------------------------------
                        Energy Level Patterns
                                                                  0
Patterns in 7                                   Split-in time  +1  to -1
                                                                Instants
1   7 7x2^0          Basis of force scaling                     1   2   4
                     Minimum Non-Degenerate Energy unit     =    Chronon
                     Basis of particle structure
2  14 7x2^1                                                     2   4   8
                     All fermions match 3-d energy levels
                     and 3-d to 3-d Gamma-Pi transitions
3  28 7x2^2          All Bosons match 4-d energy levels         4   8  16
                     3-d to 4-d transions involve neutrinos

4  56 7X2^3          56 level patterns     64 level patterns    8  16  32
                        56                       64
                                               8^2 4^3
5 112 7x2^4                                                   16  32  64
            168  24x7  56 56 56 2/3 112
                       Quarks  1/3  56
                       Nx7+4 +/-1
                       -> e limit              Kepler
            192                      27x7+3    64 64 64  2/3 128
                                               ->  Proton 1/3  64
                                              Baryons +1,0,-1
6 224 7x2^5       32x7  56 56 56 56                          32  64 128
                  33x7   -> Higgs                              e+e-
                         2^8 kaon     37x7+3  Eta/Eta, Lambda   electron
                                      37x7+4    64 64 64 64
                                                 Mesons
                                      36x7        Eta
                                      37x7+4      Kaon
                                      38x7+1      Pion
                                       +1     -> Muon limit 68  68  68
------------------------------------------------------------------------
```

Figure 8.1: Summarizing From $t_o$ to Matter.

### 8.2.2 Lets Talk About Dipoles

Dipoles in QTC are described as the number of doublings, powers of two, involved in generating them. They consist of equal 'instants' of 'time' and 'anti-time' which define an interval. The reciprocal of either instant of time is energy or anti-energy which add together as zero. The time split between the components can be thought of as representing a form of temporal potential energy much as separating masses to generate potential gravitational energy. However, there is no evidence for a 'continuous' exchange of energy. Instead, specific 'quantized' decay through a harmonic doubling process is seen globally. Furthermore, to mention two observed facts. double galaxies ignore Kepler's laws and do *not* orbit each other, while galaxies in clusters line up morphologically segregated in redshift-magnitude bands and *refuse* to scatter in redshift as dynamics requires. It seems quite clear that time and large scale physics knows a lot about quantum physics and properties of active energy, but nothing about dynamics and gravity. This is the 3-d domain that QTC defines as tau-space. On the other hand, when two photons join hands, spin around and merge into their 'matter' form, they can pass into a spatial domain flowing through time as matter ages.

Kepler and Einstein wake up, let gravity loose, and dynamics begins. QTC provides that opportunity, it locks up continuous action and its driving forces, including gravity, within sigma-space 'particles'. Gravity does not have a quantum form in QTC, so QTC provides for it within a g-space. Note that the forces appear when sigma-space is entered, they do not exist in tau. I will return to that specific point subsequently. QTC then demonstrates that there is a quantized dipole sigma-source locked into the heart of g-spaces, out of which continuous physics flows to build the galaxies. What else can nuclear redshift dipoles and the offset redshift streams they generate be? The (Ap1) story convinced me to seriously study the problem, although seminar 2 already made the issue hard to avoid. The *Astrophysical Journal* published a disclaimer for the paper that introduced the nuclear dipole (2.3.1), but declined to publish the (Ap1) evidence. However, the question remained, what is a galaxy if it has such properties? I have thought quite a bit about the beginning.

The reciprocal of time is frequency, the number of cycles per unit of time of a wave form of energy. At the split in time QTC presumes a finite initial instant of time was established which defines the Planck time along with corresponding Planck energy and related units. Simultaneously an anti-instant was established such that the *sum* of time and energy for the initial instant pair was zero. Time with its connected energy, represented as an oscillating wave function or functions, can represent the dipole of instants. The nature of the event which formed dipoles of time may be of interest, but that is a philosophical issue I will not pursue, although QTC can provide a good description of the real universe which appears to add up to nothing. Time can increase and energy decrease together to maintain their reciprocal relationship in a decaying universe, but not proceed the opposite way since at the split point would require more energy than existed. The limit in that direction is infinity, the reciprocal of zero. Time may be free to diverge toward infinity and energy density to approach zero in the decay direction while both continue to sum to nothing globally. Alternately the Planck units may be involved in some inverse fashion to define that limit. Philosophers may discuss that issue. In the meantime the universe exists.

In the previous paragraphs a concept is developed which can lead to and be consistent with what is known from observation. We know we live in a domain where continuous physics applies. We also know and accept that at the very small scale (relatively) a different form of physics applies, quantum physics. Local physics is striving very hard to connect the processes entirely at the small scale with very little evidence that is possible. QTC has shown me that is a futile effort, especially since QTC has shown that quantum physics is perfectly happy at all scales, large and small, including aspects of the galaxy we live within. QTC implies continuous physics is not workable at any but a remarkably small local scale. Continuous physics exists in only small galaxian laboratories where I hope scientists can work to bring together both quantum and continuous physics in a picture of how both processes are necessary and must work *together* in an even grander pattern. At this point I will introduce a QTC premise applicable to past and subsequent discussion.

> P8.1: Within a limited range of uncertainty in quantum tau or any sigma-source or g-space concordant with continuous physics, the total energy and anti-energy in all forms sums to zero.

Using dipoles and evolution by harmonic period doubling QTC can resolve the flatness problem in cosmology. Observations, including precise demonstrations within QTC, have

shown that the universe is indeed 'flat', $q_o = 1/2$. QTC generates and maintains that condition from its origin as a split in time. At the split, using a normalized scale, opposed instants appear at t = 1 and -1. The dipole scale, representing an opposed pair, has twice the scale, a total energy anti-energy differential of 2. Twice the energy is what a system requires to drive its components exactly to escape. For example to launch a satellite into a circular orbit. Or, in this case a 3-d expansion of temporal dipoles into a spherical shell (a *stable* energy level) creating tau-space and generating a set of Planck units appropriate to the particular split involved. The energy presumably populated the first generation shell (energy level) for dipoles of unit energetic length. The temporal bond between 'instants' of time which define the dipole is presumed to be a temporal form analogous to the strong force. Instants are presumably fermion class structures, the dipole an initial boson form.

While we have factors of two in mind, think about what my imaginary couple might have continued to learn if they could not resist trying to touch. As zero is approached time shrinks and its energy inverse grows as it approaches infinity. Suppose when it reaches a critical value, perhaps twice the Planck energy, that energy is sufficient to stop or *reverse* the flow. Is that what the split in time is? Perhaps there is a recycling point, perhaps two (I may return to that possibility later in seminar 8) between which the universe can oscillate forever. If total energy and time are really conserved (as appears to be the case). There never need be an original event, just an endless oscillation of nothing. Just a thought provoking suggestion for philosophers to contemplate.

### 8.2.3 Dipole Bonding, Generating Photons

Initially we are concerned with the origin of tau, not space with its classical thermal properties. The earliest conditions are likely to be quite non-classical. Discussion at this point is highly schematic, but the objective is to generate products which emerge including photons, forces, timelines and sigma-sources. In QTC classical forces do not exist initially. Some form of sigma structure involving spatial intervals and triads is required to define them. The dipole shell about $t_o$ at birth was presumably a thin shell of time containing dipole (bosonic) structures consisting of instant anti-instant pairs. The wave function of a time anti-time dipole is presumed to be a lateral bosonic form since the instants in each dipole have the same value of time. The instant anti-instant form represents an interval of time at the temporal value of the instants. Since the interval represents the energy involved, defined by the inverse of the very small temporal value involved, the initial wave functions are extremely energetic. The pattern as QTC develops appears to begin with extremely energetic boson structures which will generate very massive sigma-sources. These sources will subsequently progressively decay toward lesser structures. Very major sigma-source energy structures may exist before gravity unlinks around the time of emergence of timelines at the opacity (decoupling) point. There is no evidence that gravity plays any role at the large scale cosmic scale much beyond the opacity point.

To accommodate the anti property the wave function presumably consists of linked perpendicular components which will travel laterally in the temporal tau shell generated (since instants belong to a specific plane of time). This looks a lot like a photon related structure in QTC. The dipole structure (wave function) can presumably double (the interval and doubling is observable as quantized redshifts now) and, if not present initially, generate a cloud containing a range of doublings. Fermi exclusion between instants should prevent bonding

of identical dipoles but successive doublings and inverted ordering should be able to bond in the early cloud. Early structures including 1, 2, 4 triads of dipoles should be able to form. Since there are several ways to link pairs, triads and timelines this is an especially critical point in time. Although at this point we are very early in the birth of the universe, real observations *now* should allow us to infer what presumably occurred earlier. There are direct consistency tests in QTC related to what happened then and what we see now.

### 8.2.4 Triads, Quads and Photons

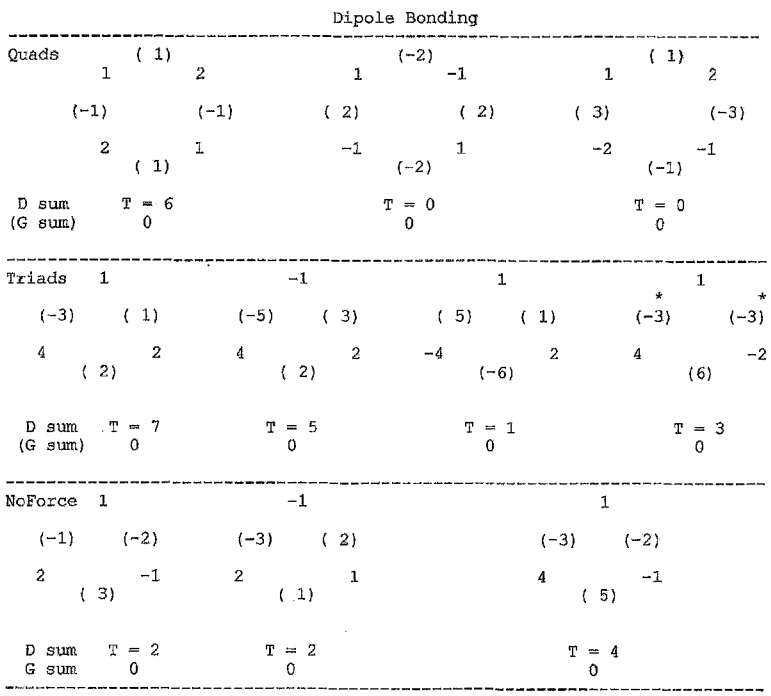


Figure 8.2: Early dipole binding where 4 dipole (quad) and 3 dipole (triad) units are viewed end on. The other end consists of the equivalent set of anti-instants to each instant set shown. Binding G (glution) intervals are shown (parenthetically) between each pair of instants. The central quad in the top row can represent, in a general way, the split at $t_o$ itself (see text).

Characteristic dipole energy intervals within sigma-sources determine the T value periodic redshift pattern a given timeline can generate (3.3.1),(3.4.1). Since the fundamental forces depend upon space and the initial triad or equivalent structures which do not yet exist at the beginning dipole split, the first question to ask is what can be generated initially leading to triad and timeline generation. As noted above the unit 1 -1 dipole cannot bind with itself directly, but should bind with its reverse -1 1. Figure 8.2 shows early types of 4-way (quad) and 3-way (triad) dipole sets. The view is end-on with the opposite end containing the same number and opposite anti sign since each dipole is an instant anti-instant pair. Each

diagram shows a quad or triad structure defined by the pattern of the levels of doubling of its component dipoles, 1, 2 or 4. Between doubling levels, in a clockwise sense, doubling differences are shown in parentheses to represent binding links. Binding involves 'glutions' in analog with gluons with 'ti' inserted to apply to binding of temporal instants. The two most common redshift patterns associate with T = 0 and 6. The central diagram in the upper segment of figure 8.2 represents the split in time symmetrical about zero. It can be generalized to represent a full 3-d action generating a spherical ground state energy level. The four dipole states add to zero and represent the pure doubling T = 0 state. Individual or composite wavestates may decay by doubling, collide, and possibly bond. The cosmic time within a related range of doublings defines 'commonality'.

This is no thermal environment at this initial stage and effectively illustrates the concept of temporal commonality. Dipoles carry time 'levels', the instant value, but also their commonality 'link', the cosmic time about which dipoles spread, zero in this initial case. The T distribution is the one end sum. Bosons can distribute differently within the same commonality. There is a range of time within which bosons can interact. This is their Bose statistical property. The sets within the figure are T state populations within the zero now zone. As noted previously, a now zone has a width, a property of Bose statistics, Bosons incorporate a range of 'planes of time' within which continuous action is possible. That range is, however, a limited range. 'Now' must be distinguished from its own past and future. For the same reason *all* forces must have limited ranges, force cannot transmit across unlimited ranges of time! Galaxies are particles in time! Only the photon, a temporal messenger for *individual* now zones allows one to look back in time *and only in their own commonality time*, They do that at the price of quantum redshifting, trading 'aging' decay for a step forward in cosmic time. We do the same thing in sigma, except we age continuously between the ticks of the quantum clock. We live in Fermi-land where instants within dipoles decay smoothly between the clicks. We are the product of the Fermi instants set free to move (briefly) about in a continuum called space. Temporal commonality does not change in space, tau has no awareness of locations within sigma. Fermi-land (sigma) is the medium through which Bose-land (tau) connects the quantum planes of time. At the early stage of the universe it appears commonality extends over at least three doubling stages. This probably sets the interaction range between timelines and the scale of sigma-sources. The sigma-source dipole itself appears to represent the commonality doubling level ground state. I will discuss excitation later.

Returning to the top frame of figure 8.2, using only the 1 and 2 doubling states there are three other quad forms with T = 0, one shown at the right end of the upper frame. Each of these types have both a right handed and left handed form. The original set of four level 1 dipoles is symmetrical. All forms may be further extended by adding the 4 -4 doubling while retaining their 0 commonality state. It seems clear why T = 0 is the most common T state. The binding G states always sum to zero, but it is not clear if there are limits on the G values. It is not obvious that all combinations are actually allowed although equality of adjacent states is presumably forbidden. Multiple combinations of the same T state may contribute to the presence of harmonic cascade decay seen between full doubling states. Commonality of 0 is retained in all the T combinations.

The left quad example generates the T = 6 state. This form is the lowest possible state using only 1 and 2 level dipoles, and has the minimal G sum which is perhaps why the T =

6 state is the most common after T = 0. There is one other quad state for T = 6, using the 4 -4 dipole in a 4 2 1 -1 quad set. These quite different forms of the zero commonality level may be why there are two different redshift periodicity patterns at T = 6. This is shown in seminar 3 (3.3.3) figures 3.8 and 3.9. There are two quad state forms (not shown) that relate to T = 1 and 3 which use only dipoles of level 1 and 2. The T = 1 state uses a -1 1 -1 2 arrangement and the T = 3 involves 1 2 -2 2. It is possible that such arrangements are forbidden or rare. Using the 4 -4 dipole it is also possible to generate T = 8, and T = 7, 5, 4 and 2 with appropriate combinations. However, T = 0, 6, and 8 can be generated only with quad structures. T appears to be defined by the doubling pattern involved.

The second section of figure 8.2 shows triad structures. Combinations of 1, 2, and 4 doubling states readily produce 1, 5, and 7 T states. The triad can also generate 3, as shown, which is not seen or is rare. This may be forbidden since two adjacent binding G states are identical as flagged by asterisks. All triads have both right and left handed forms. The lower section of figure 8.2 shows that triads can generate T = 2 and 4 at the expense of omitting one of the three dipoles which may affect generating the appropriate 1 2 4 force triad. However, a second form of the final triad is a 2 -2 4 form. Such forms could combine to include all three doublings, perhaps replace quad forms and provide the extra 4 seen in seminar 4 particle structures. Such combined patterns could generate timelines and sigma-sources. All states are shown at the same commonality level which advances with cosmic time.

The discussion of T states should clarify several important aspects of QTC. Although many details are clearly ill defined, the QTC concept of $t_o$ and the subsequent development of tau-space leading to galaxies is consistent with T classes, forces and particle structure observed. The success of generating appropriate forms demonstrates consistency all the way back to $t_o$. There is no difficulty in generating T values, and important avenues to explore cosmologies recognizing the structure of time are clearly possible. It is also apparent that the frequency of different T forms is consistent with observations and quite likely determined from the initial formation process and less likely by subsequent evolution. Especially important is the clarification of the limited range of temporal commonality. The wave function required must contain only a limited range of frequencies and retain the structure of a limited spread of planes of time as the commonality index grows and older levels decay.

### 8.2.5 Photons and Timelines

Dipoles or dipole structures in the early universe are effectively photons. Photon interactions in the pair formation process are the key to transforming into sigma-space as discussed in seminar 7 (7.4.0 ). In the process the anti forms are split, presumably into highly excited forms to begin the process of generating the fundamental forces beginning with the strong spatial form. In the process radial flow begins in characteristic T forms. In the new pattern generated, the doubling process can proceed as a new black-body thermal environment forms, and expands radially as it begins to cool. The commonality aspects remains, however, the anti forms are isolated within distinct planes inhibiting if not eliminating annihilation. Note that in the table of forces, (4.9.0) table 8, the spatial $i$ interval of 4 is where the forces begin with the strong boson form. That 4 is available to couple with the 1 2 and 1 2 4 medium of instants, a natural transition point, just as they enter and begin generation of forces and structures within sigma. Now there is a continuous thermal medium to begin a continuous decay process where spatial triads can begin to double and link. As the process

continues, *now within the sigma framework* it begins to look very much like the classical picture of early evolution with one important difference. Now the essential triad structures can exist to begin the building process. The triads are available to provide the strong force at triad level, begin evolution of forces as longer range forces become established in turn, opening the path to eventually generating matter. Spatial photons can form and a timeline structure begin. The tau sphere can begin expanding as the forces develop and triads begin to combine within the chaos of intense interaction between initial timeline structures. What QTC has provided is the initial link to build forces and structure consistent with the non-dynamical large scale universe we see today. We see the dipole, the triad, the ordered forces, the pattern of T and D energy levels which define the particles of matter and that fundamental quantized messenger, the redshift. It is just a sketch, but a consistent if crude one, of how QTC may begin to generate the universe. Since in tau there are no restraining forces, expansion can continue through a quantum doubling process within a wave driven form of energy, to generate successive spherical shells of time, the continuously 'flat', zero total energy, universe within which we reside.

### 8.2.6 Some Premises, and Moving On with Cosmic Time

At this point I will introduce three premises which collectively relate to much of what has been stated in section 8.2 so far, but for convenience jumps well ahead in certain aspects to cohesively link with the coming discussion. Premise 8.2 refers primarily to the basic dipole structure within a sigma-source. Premise 8.3 refers to temporal commonality and aspects of the dipole structure and its evolution. Premise 8.4 relates the wave function of a timeline to statistical properties of the energy flow it represents. As I summarize, expand and develop some subsequent concepts the thrust of the premises should be clear.

> P8.2: A dipole within a sigma-source defines a commonality now zone temporal state about which a distribution of doubling planes of time and anti-time exist, typically two or three. Within this pattern in sigma-space continuous physics applies. Ends of the dipole represent matter and anti-matter which progressively decays producing two outflowing (aging) streams of fermionic matter which generate a visible galaxy. The streams are normally isolated from one another by the differential temporal interval characterizing the commonality dipole.

> P8.3: A galaxy, defined by its commonality source, normally occupies the ground state of its sigma-source temporal planes, and defines the observable redshift state of the dipole (and galaxy). Under certain conditions excited states may occur near the source and at junctions of temporal planes. The slow decay, seen as radial expansion within a galaxy, generates observable radial redshifting and a radial asymmetry correlation. As the degree of decay reaches a critical level the system can decay and drop into the next lower energy doubling pattern, or more likely adjust in a higher harmonic transition cascade step. Sigma provides the decay phase which prepares tau to decay in quantum jumps. Tau ticks when sigma has provided sufficient continuous decay.

> P8.4: The wave function involved in galaxy formation and decay involves a statistical pattern. In the temporal form (tau), energy is bosonic (dipole-like) which

> can distribute in planes of time to avoid simultaneity while at a common point in space. As the 3-d temporal wave function approaches a node (where fermionic matter appears) time becomes too compressed for its fermionic instants. By passing into sigma as matter anti-matter they can distribute in space while they retain the commonality value of time. Tau retains commonality and makes no distinction between location in space. In QTC the wave function can be called, or be recognized as, an oscillation between Fermi and Bose statistics. Galaxies exist because of a periodic compression of time. They appear as an outflow from the commonality sigma-source dipole as matter anti-matter streams isolated by layers of time and pass back into tau as they pass into what sigma perceives as dark matter as the wave function expands.

The initial split in time does not generate a hot thermal soup in QTC. That is the classical picture. There is no consideration given to the nature of time, particles are formed without regard to how forces and structure develops and energy begins as photons with no real picture of what they are. Such an origin does not lead to any of the early observed patterns or a large scale quantum structure. That approach is inconsistent with QTC where a picture relating to time and an actual pattern of observed particle structure and evolution of the observed forces can be generated, *and actually compared with verifiable observations.* The pattern of a dipole split at the beginning and consistent evidence leading to the quantized dipole structure within galaxies (7.5.6) seems to leave no alternative option to a quantum origin form. Energy involved in the early dipole split is incredibly large which implies that early sigma-sources will be extremely massive. This is not inconsistent if rapid evolutionary cycles follow the origin. As the lookback cycle approaches $t_o$ the logarithmic wrap around $t_o$ shortens rapidly as is apparent in seminar 6 (6.3.9) figures 6.9 and 6.10. The nature of cycles of early development is discussed in seminar 7 (7.7.0). There is some evidence that the lookback pattern through quasars leads to more and more massive sources (coming in (8.3.1)). It seems quite likely that much of the evolution of matter, such as early element formation and perhaps some enrichment of metals, was set in motion within such unseen structures. Once the gravitational force emerged within very early sigma sources there must have been active interaction between timelines. It is not until after the opacity point (decoupling) that timelines diverged enough to decouple all forces including gravity. Recent observations of polarization patterns within the CBR are possibly indicative of the large scale gravitational decoupling phase in QTC since there is no indication of gravitational interaction between sources beyond that point. There are striking triad patterns in the first images [BE] (*Physics Today*, May 2014) and [BF] *Sky & Telescope*, July 2014).

At some point triad patterns can begin to link. We know within QTC that quarks (4.8.4) appear to form a series of structures differing by specific triad doubling steps (4.8.0), although they are too complex to form in the earliest period of development. It is incredibly unlikely that their structure would emerge by accident and link together with all the other aspects of particle structure known in QTC. Very early forms of interaction must induce an active exchange between tau and sigma. Exchanges should generate mostly noise and some very brief unstable high energy resonances until a stage is reached matching allowed more stable doubling levels at a low enough energy. At this point basic p-state particles should begin to form both matter and anti-matter appropriately isolated in planes of time. Some aspects of the classical picture of early particle formation may be relevant except for QTC restrictions to allowed energy levels and annihilation. A high degree of uniformity exists

initially. Again, as noted above, the bubble structure shown in CBR polarization studies look much like sigma-source timelines emerging while gravitation can still relate adjacent structures at the opacity point. Maintaining CBR uniformity is not a problem in QTC, especially since lookback involves *only* the emergent portion defining the region around our own now zone lookback line (7.7.0), a quite limited portion of the entire opacity zone. Our timeline has no perception of the total distribution of the opacity zone around $t_o$ although timelines arising from other segments intersect our lookback shell in later stages in their development. There is no role for the classical concept of spatial inflation in QTC.

Basically, the early universe development in QTC breaks into three stages: the split in time with the early Bose phase: the early timeline phase where sigma begins well mixed with tau through the decoupling opaque stage: and the beginning of the isolated non-dynamical phase from the lookback angle $\theta = 2\pi$ to $\pi$. Most of the previous paragraphs referred to the first two stages. Beginning with the third interval we are concerned primarily with the exchange of information between other timelines within our now zone or the remnant of the background radiation directly associated with our now zone. We have no contact with the very early universe other than advanced segments of other timelines where they intersect our lookback shell (6.3.9). In QTC we appear to receive little recognizable information between $z_{LT}$ about 10 and the opacity zone (between $z_o$ of 200 and the same presumably restricted CBR). I will call this zone the 'black forest' since I believe it is probably well populated. As noted earlier I will address that issue subsequently. There are, however, a few basic topics which can be expanded upon now.

To accomplish the tau-sigma transformation, tau must package its property, energy, in pieces that can exist in both tau and sigma, transform between the two domains and retain their anti relationship as they age. The grand total of energy has to be zero internally, it is simply in two different anti forms. Antimatter has to be there and is there in plain sight in QTC, isolated within appropriate planes of time. A first step in QTC is apparently to establish a passive form of energy, matter, that can provide a *continuous* aspect of the decay process where *time (as aging)* can grow smoothly while tau and sigma work out the decay process for their individual energy forms. The decay process appears to have three aspects. The expansion of tau steadily increases the volume of time and therefore decreases the overall energy density *but not its localized density or total energy.* That must also decay to reduce the total energy to pay for the growth of time. Total energy approaches zero as time approaches infinity. The expansion of tau provides the means to decay, but not the actual energy decay. The second factor involves the period doubling decay of the quantum oscillation of the timeline wave function which reduces photon energy observed as the redshift effect. The third effect, which triggers or is triggered by, the second effect is the slow continuous decay of the sigma-source dipole structure as the two stream decay outflow works its way back into tau via the dark matter process. Total energy decreases to retain the reciprocal relationship with the growth of tau, all of which actually adds to zero. Another factor that illustrates the same zero level concept is the strong force which binds temporal dipoles (or quarks), a temporal form presumably equivalent to the strong spatial nuclear force, with time itself as the charge. That unbreakable bond if about to break generates a new partner instead so the energy sum remains unchanged. This is presumably what may have happened to generate what I called the initial Bose dipole cloud containing pairs of Fermi instants, a fissioning event, all of which continues to sum to zero. Time and energy are conserved on the grand scale as zero in QTC.

There is considerable evidence that galaxies must contain dipole structures (7.5.6). Now we add the fissioning concept as an expansion on the simple doubling process. Fissioning generates two or more objects (such as double galaxies, and compact groups). The total population grows at successively lower energy levels as each distinct object contains a complete independent dipole structure. A dipole is a specific interval of time between time and anti-time (a symmetric fission in time which conserves time and sums to zero). In QTC such a dipole can, and I believe did, provide the singularity at $t_o$. That effectively is what matter anti-matter bosons are and in QTC can avoid the singularity in sigma-sources such as galactic supermassive black holes. In addition to avoiding singularities, that type of structure provides the origin of the two evolving opposed outflows observationally demonstrated in QTC as two expanding discontinuous redshift streams within galaxies. The streaming was introduced with figure 2.4 in seminar 2 and discussed in depth in (7.5.6) and the first appendix (Ap1). Based upon what is seen in QTC, it appears each pole of a dipole can decay (when within sigma) and generate an outflow stream as the dipole evolves. I think of the outflow process as 'sigma aging' and the fission and doubling process as 'tau aging'. There is clear evidence in support of such a picture, represented as a wavefunction cyclical oscillation (6.3.6), which passes through actions induced at doubling points. As a key example, chains of quasar and galaxy development in redshift patterns are seen where galaxies appear at periodic 'nodes'. That is what galaxies distributed periodically in redshift, or in redshift variability steps appears to imply. This concept is summarized in premise 8.4 which is essentially a model for a QTC timeline. Events, such as the formation of galaxies, occur at the nodes in periodic patterns as energy oscillates and flows in cosmic time. Oscillations are presumed to be 3-d since they relate to the interaction of two 3-d spaces. Such 2-d oscillations exist, (Kundt's effect) where pressure waves sent through tubes focus nodes of dust particles in a medium. In QTC this could represent compression of time in a transition into space, an exchange of active for passive energy states, literally Bose for Fermi states as in pair formation in QTC. Sigma may be thought of as the 'internal' life cycle structure of a dipole evolving in tau. What we observe may be the decay process of a split in time where galaxies are one minor stage in a very long term cyclical process.

Turning briefly to fundamental particles and forces in QTC, the lower part of figure 8.1 shows patterns and properties of doubling concepts. The figure then summarizes the four particle classes (five including leptons as limiting forms) built upon 4-d quartets and 3-d triplets of 56 and 64 doublings discussed in seminar 4 (4.8.0-5). In QTC it is highly likely that matter and energy exist, and take the forms they do, because of close matches to properties of the numbers 64, 56 and 7. As energy levels drift away from forms closely consistent with internal structural dynamics matter simply cannot form. Interactions unable to form particles or brief resonances just produce the underlying noisy quantum 'foam'

Concerning specific forces, the electric force is unique in that it is built upon a *product* of the two most basic components within the force structure (4.9.0). The characteristic spatial scale of the electric force involves the simplest square and cube (4 and 8) and is the first structure consistent with long range action and 3-d dynamics (3-d space and inverse square divergence). This is also, as noted above, why QTC presumes that stable matter exists very close to doubling level 64, the first integer which is both a cube and square involving the two key numbers 4 and 8. However, force linkage is also dependent upon temporal commonality. Time is a real 3-d domain within which matter can exist within encapsulated spatial spaces. Force can link over only limited ranges of temporal separation which define the upper limit

to the scale of individual e and g spaces in QTC. This must obviously be true or we could link to our own past or future. If there is a force beyond gravity, and the QTC model says there conceivably could be, it could have an immensely long range. I prefer not to go there, but it is an interesting thought. May the force be with you!

The three forms of the strong force in table 8 of seminar 4 (4.9.0) are not individually compatible with both spatial long range dimensional conditions, cubes and squares, hence must be short ranged and limited to the internal structure of matter configurations. The three initial levels of force strength (alpha) also refer to different subclasses of particles (4.9.0), light mesons, baryons and gauge bosons, none of which yet exist at the initial event. Although the weak force definition includes both square and cubic factors it accomplishes that with a time anti-time link (4.2.3) which appears to limit the force to short range and invokes the neutrino which is associated with the temporal link. This association, which links planes of time, quite likely provides the mechanism which involves neutrino oscillation. The transfers may be excitation effects which I will discuss in (8.2.8). The short range forces require a different space to define their domains, so QTC calls their domains p-spaces. The neutrino with its temporal connection should perhaps be given its own unique space, perhaps an n-space. To consider long range forces operating beyond the range of short range particle spaces it is necessary to turn to sigma-spaces.

### 8.2.7 Matter - Antimatter

A fission in time produces bound time-antitime dipoles. Each instant and anti-instant in a dipole is reciprocally equivalent to a large amount of energy, but in QTC it appears that energy is available only upon transformation to sigma-space. In the transformation an aging temporal flow can begin, permitting separation into matter and anti-matter (7.4.0). In QTC while time and anti-time are locked in a bound dipole, or any structure constructed of such dipoles including the photon, there is no free matter or anti-matter. We should still refer to it as temporal and anti-temporal. The force which binds a time anti-time dipole, where charge is presumably time itself, is very strong. Instants within dipoles are presumably replicated (as in strong force separation of quarks) and cannot separate in tau-space.

In the transformation from active to passive energy (matter) in pair formation the temporal force link appears to be exchanged with the strong nuclear force. In tau, time and anti-time are opposed but bound, they do not separate, there are no temporally opposed universes. Once in sigma the components are still bound but in a continuous domain and can evolve. They appear and flow as separate inter-wound streams in two (or more) non-interacting *planes* of time retaining their temporal dipole nature. (Recall that a distribution in sigma is a point in tau and remains that way until reentering tau after passing into dark matter.) Sigma *as a whole* 'flows' providing internal 'aging' until reaching the next evolutionary temporal node when the tau dipole pattern can pass into its next cycle. In sigma the streams reside within a single spatial structure. They respond normally to *long range* sigma forces and look and act almost normal, except there is a time shift between them. There is a differential redshift, the *observed* two stream QTC pattern. That will and clearly does complicate dynamics within a galaxy if not recognized and corrected for as discussed and illustrated in seminar 7 (7.5.6) and (Ap1). But, whether in dipole form in tau or streaming in sigma, the two forms co-exist. There is no critical matter anti-matter problem in QTC.

The forms can interact under certain conditions discussed in the following section. Pair formation within each individual temporal plane can occur normally and interact as conventional matter anti-matter since such pairs will be temporally identical. Otherwise it is apparently possible for the temporally displaced steams to mix since they are not shifted completely out of *our* range of temporal commonality. We can see them and gravitation applies. As particles they are confined within a short range of temporal commonality defining p-spaces where their short range forces define *their* 'dark' boundaries. They cannot 'see' us. My third defining ApJ paper [59], which introduced quantization in 1977, looked for and found evidence of predicted periods in interstellar material and certain classes of stars. Much of the stellar data applies to excitation rather than matter anti-matter. I particularly recommend looking at the accurate B star rotation data shown in figure 7 of paper [59]. That subject was not pursued, it was too far outside of my time, but such mixing of excited states quite likely exists and has real consequences if interpreted as motion.

The net result is that there is no global matter anti-matter crisis in QTC. In temporal mode matter does not yet exist and its precursor forms are locked (eventually if not initially) in unbreakable dipoles. In sigma mode matter and anti-matter may mostly coexist as time and anti-time in distinct temporal planes. We simply define our plane to be the one containing 'ordinary' matter. If created locally within one temporal plane the real anti form of matter for that plane quickly annihilates or possibly moves out of temporal contact (7.7.0) The portion present in particle boson forms in sigma can decay into normal matter. This is where the neutrino enters to dispose of the leftover 4-d link (4.6.0). The dipole distinction could possibly relate to the handedness of local neutrinos and an excess positron density observed in local space. Clearly much in this stage of QTC is speculative, but there is clear evidence for both tau and sigma domains and pair formation appears to be the basic means of linking the domains. If QTC is basically correct (and there is a lot of evidence to explain if it is not at least partly correct) ultimate details of the tau-sigma link remains for future astrophysicists to work out. Before moving on I can say and illustrate what might be excited states of dipoles and observable consequences of mixing.

### 8.2.8 Excitation and Mixing

Dipole decay or interaction in the environment of a supermassive black hole sigma-source or even a stellar black hole occurs in a rather violent place. It is quite reasonable to expect some visible QTC effects to emerge. Lesser effects may also be seen from mixing at dipole stream boundaries. Figures 2 and 3 show data from the core of M31 used in 1976 to introduce the concept of discrete redshift states [55]. A very rapid change and complex patterns of spectral displacements commonly appear in the spectra of galaxies as one approaches the nucleus. This is also the region where my early photometric work on galaxy nuclei [9,18,20] shows anomalous nuclear color patterns and correlated radio properties [22]. With the addition of the redshift those early studies are what led me to investigate the redshift in detail. Figure 8.3 (upper) shows major axis emission line data from the core of M31 from Rubin and Ford [1971 BH]. Figure 8.3 (lower) shows the absorption line differential pattern shift in the central arc minute of the nucleus from Walker [1974 BI] and Morton and Thuan [1973 BJ]. The location of the data in the lower frame is shown dashed in the upper frame. The vertical line marks the standard nuclear dipole and five dashed lines show the rotation pattern of M31 divided into five QTC redshift states spaced by 70-75 km/s. For a detailed

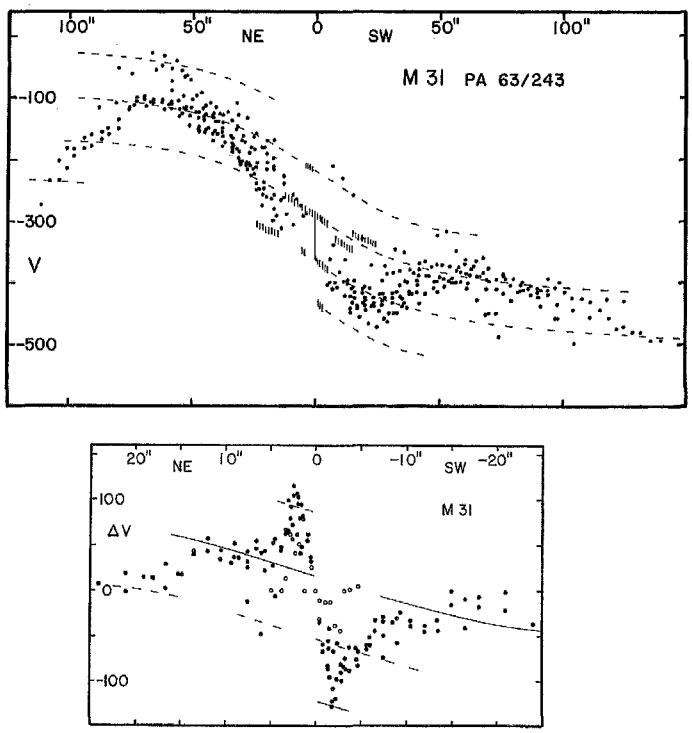


Figure 8.3: M31 major axis rotation patterns

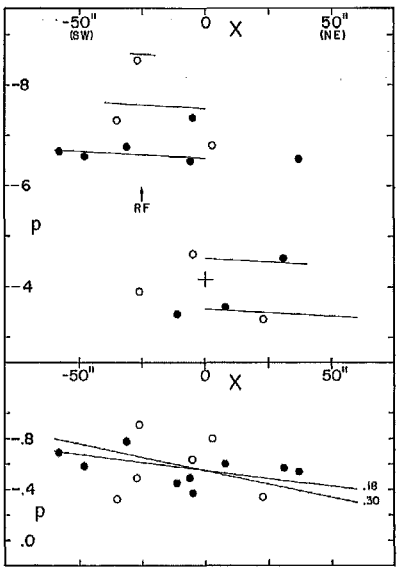


Figure 8.4: Planetary nebula redshifts in the M31 core

description of the figures refer to reference [55]. The offsets to the southwest presumably represent alternate windings of spiral arms. The large major northeast offset at 50 arc seconds is a well known anomaly. Real velocities and spectral blending contribute to the pattern, however the multiple state patten, confirmed in many later studies is remarkably apparent. Note especially that occasional data points inconsistent with a smooth velocity pattern fall directly on the multi state pattern as they should if the multi excited state pattern is correct.

Figure 8.4 shows data from Lawrie [1983 BK] for planetary nebulae in the nuclear bulge of M31. Discussion of this figure is given in appendix (Ap1). Solid dots show data with uncertainties less than 20 km/s, open circles up to 35 km/s. X identifies location along the M31 major axis. The data are superimposed at a period of 72.5 km/s in the lower frame to show a smooth unperturbed rotation gradient over six periodic levels. The arrow marked RF indicates the location of a strong negative surge in emission line measures. The smooth periodic pattern is significant at the 0.005 level and scatter drops smoothly as data quality improves. A cross marks the M31 nuclear redshift and p denotes cycle count (upper frame) or periodic phase (lower frame) at 72.5 km/s. Is this velocity dispersion at a remarkably periodic special period? Or is this evidence of excited or multiple states which may rapidly decay and not be seen later as the system slowly expands in the dual stream model of QTC? The redshift has been demonstrated to rapidly decay under certain conditions using 21 cm measures (seminar 3, figure 3.27 (3.7.0)). Although any rate of decay is unpredictable it might be of interest to remeasure some of these 'velocities'. For further details and examples see reference [55].

One especially interesting bit of evidence of mixing between the two offset redshift streams appears to exist. Although the two streams are isolated in time and do not routinely interact they do differ in matter anti-matter character as particles. Protons may be anti-protons and electrons may be positrons. Away from the high density nuclear regions, where as noted above there is evidence of activity, the streams become relatively isolated forming distinct spiral arms (I will return to morphological evolution later). In the outer regions with well defined distinct arms we could expect to see evidence of diffusion. We apparently do. Our plane of ordinary matter is characterized by electrons at the low mass end. Diffusion from our companion dipole stream should presumably provide positrons if the QTC picture is correct. Space experiments do show a clear excess of positrons in the solar vicinity. There is an interesting article by Steven Blau in the June 2013 issue of *Physics Today* [BG] discussing the excess. Figure 3 in Blau's article shows an intriguing pattern in experimental data. There is a clear excess and in Fermi data there are three peaks (admittedly of low significance) spaced by factors of two in the positron fraction excess. These peaks correspond to three QTC permitted particle energies in the N.33 column of the seminar 4 Table 3b Pi energies indicating where particles can exist. The levels are 185.7, 92.9, and 46.4 Gev possibly related to the hypothetical x meson discussed in seminar 4 (4.10.0) in conjunction with kaon decay. The energies are consistent with allowed levels in the 1/3 power of two family of fermions and certainly could accommodate energetic positrons. It might be interesting to see a power spectrum of the Fermi data.

The premise that dark matter decay could be related to the positron excess is not possible within QTC. Dark matter is possible in QTC because it has drifted back in time beyond our temporal communication limit. Any energetic product of our dark matter decay will drift

even further out of detection range. In QTC the positron excess is predicted to be present, not from dark matter, but most likely by diffusion from the flow pattern of the decay stream arising from our dipole partner. It can arise from matter that is quite visible. While on the issue of matter drifting into our now zone from dark matter there is one strange if highly unlikely possibility. If there is a now zone from a cycle proceeding us 'laterally' in the time sphere (nominally our 'future' direction) conceivably extremely high energy particles might be able to drift back into our now zone. If so they might provide a few extremely high energy cosmic rays. There actually could be a few such events. The possibility of such a future now zone boundary was noted in seminar 7 (7.5.2).

### 8.2.9 Just What Is the Nature of Our Universe?

If QTC provides even a partially correct model of our universe it is very different from the standard dynamical model. Born as the origin of time, a fission of nothing into dipole pairs of instants of time and anti-time, the universe emerged as a quantum domain constructed of time and its inverse partner energy. Where you go from there depends upon what the anti property is. If anti applied to time represents existence then if the time interval gets small enough perhaps the universe can actually return to zero. We know if applied to matter that when anti meets its mate they simply change form, that is not existence. Even though the anti sum is zero QTC implies that the initial zero event apparently cannot be reached. But, we seem to be here and QTC seems to fairly well describe how the ride proceeds.

Accepting that we exist, out of that incredibly active first moment of time, the dipoles must have interacted to generate the several forms which could bond, grow and interact further to generate the various forms of radial timelines we see today. The forms we see appear to be consistent with the early structure generated, and allow the decay of energy density by the expansion of tau. The timelines then carry the mechanisms, sigma-spaces, where dipoles can decay gracefully to begin a long road back toward zero using physical continuity within 3-d space. By employing two linked domains it may be easier to understand how matter can appear to jump between quantum states. The constant c is recognzed as the rate of change of time as matter is injected into sigma, drifts slowly out of contact with now to change the wave function shape so time can slip into the next lower quantum slot.

Timeline structure appears to have a triple structure consisting of three consecutive period doublings which define the T values in the redshift patterns. The midpoint of the doublings appear to define cosmic time and the point of temporal commonality of the set. A visible galaxy appears to occupy the ground state doubling which defines the redshifts of the galaxies with extraordinary precision. This 1 2 4 pattern in a tightly bound pattern, probably as two anti forms, defines the forces applicable to sigma and the basis of the structure of matter and anti-matter. This picture is based directly on observed patterns within force relationships, particle physical properties, and the energy level patterns the particles occupy. It forms a remarkably consistent picture, including the apparent function of leptons as limiting particles. The triad itself and the fundamental particles it generates are bound by the strong force, which may have three forms relating to particle type. The electric force is what binds larger assemblies of fermions, and, with the addition of the 4-d temporal link apparently associated with neutrinos, the 4-d bosonic particle types. Particle properties and the short range and electrical forces are well described by QTC. Gravity then goes on to bind large sigma-space structures together and finally sigma-space itself. The pair formation

or annihilation process provides the link between tau and sigma. The cycle between entry and dark matter exit to sigma-space then provides tau with the means to expand and slowly decay. Overall the system is remarkably consistent.

One of the more obscure aspects relates to dark matter. There seems to be little question about what it is. In QTC it is ordinary matter which has moved out of lateral commonality. Exactly what happens to it is less clear. What happens when one passes out of commonality with newer matter entering sigma? Is dark matter recycled in an overall conservation of energy and time? I will comment further on these issues in subsequent discussion.

I always wondered what a photon is. My understanding has been built upon observations and resolving real effects. The cosmological correction to a photons redshifted energy was introduced in seminar 2, formally derived in (6.3.3), and its explanation was discussed in (7.7.2) as involving an internal restraining force on the photons structure within the expanding geometry of spherical time. As the observational properties of dipoles were examined, and recognized as bosons joining time and anti-time, it became apparent that photons must contain a dipole form. Thus the restoring force maintaining travel in a spherically curved lateral surface must be the temporal tau force. As the boson character splits to form fermionic matter in pair formation it must contain or generate the strong force to assume a particulate form. The strong force must be there to link the basic triad lateral structure. A model of a photon appears to be an oscillation of an electric charge within a strong force latent particulate structure confined to flow within a spherical plane under the control of time. As timeline flow of the internal latent sigma structure of the boson diverges and stresses the structure it occasionally jumps ahead in time and generates the redshifted photon.

## 8.3 From Two Pi To Now

Section 2 of this seminar explored the earliest stages of QTC up to the point where photons existed and matter as fundamental particles could begin to exist. This section will carry the evolution of that infant matter up to the present time. The pre-matter stage served to tie observed dipole structure of galaxies to a consistent beginning. In QTC the universe appears to evolve in a cyclical pattern containing discrete temporal (tau) dipole structures which evolve within spatial (sigma) domains in a cyclical process. There are potentially two or three forms of cycles. Looking back from 'now', from the viewpoint of a sigma-space observer, there seems to be a relatively short visible cycle within a galaxy from entry at a sigma-source to passage into dark matter. Second, from the point of view of a sigma-space wave function there is a possible cycle, including dark matter, between nodes in the oscillation. The third cycle covers the logarithmic loops around $t_o$ and includes the early universe, the passage through the opacity point, the black forest (the unseen part after the opacity point), and the current visible lookback segment. The short cycle of an observer (us) will be covered last and about all that can be said about the early universe up to the opacity point has been covered. What remains is to look back again through what we see or infer has happened since the Pi points that followed emergence from the opacity point.

The logarithmic lookback shell allows us to view all timelines every cycle of pi radians in lookback angle to show us how our now zone evolved. In seminar 6, as the QTC lookback line was defined (6.3.9), present observations were shown to extend only to $z_{LT} \approx 3.5$. That is about three fourths of the way back to the opacity point beyond the second Pi

point with $z_{LT}$ beyond 1000. As the time sphere expands and dipoles decay energy density must decrease and generate progressively weaker dipole structures. This is consistent with quasar sources preceding ordinary galaxies. Their fission products are what will evolve into galaxies. Concerning what may have preceded quasars, temporal sigma-sources cannot be seen. I will provide an example of this later. Only structures that sigma-sources evolve into, which fall within our lookback zone, can be seen. Fissioning or shattering of sources, a tau phenomenon, is apparently how successive generations of sources appear to be generated. Figure 8.5 therefore has a question mark preceding quasars. Underlying properties of quantized redshifts and evolutionary aspects of QTC appear to be clear enough as timelines bearing sigma-spaces emerged from the CBR era. By using observations from the quasar and high redshift galaxy era it should be possible to infer important concepts of what might have come before quasars.

### 8.3.1 The Evolution of Sigma Sources

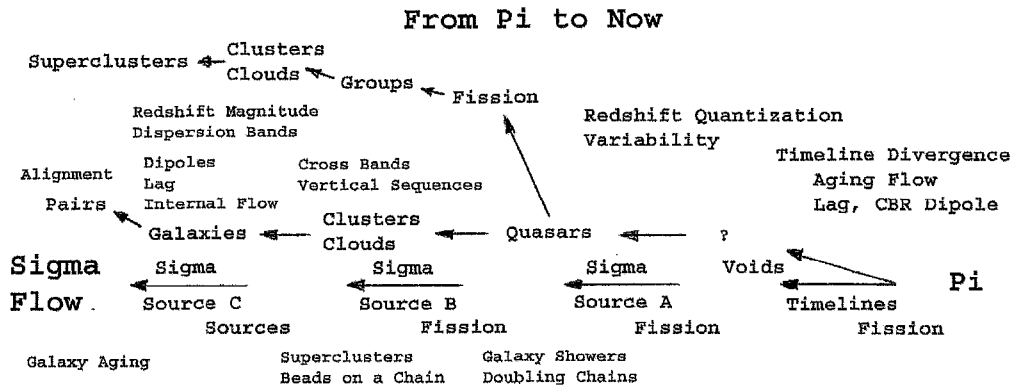


Figure 8.5: From Pi to Now.

There is no apparent reason to expect that early sigma-sources would be narrowly restricted in scale. Basic matter formation quite likely proceeded in early sigma-spaces which never emerged into conventional visibility. Although we know that enrichment of matter does occur in stars within galaxies it is quite possible in QTC that initial formation and enrichment could be established in early sources we can never see. By the time we see stars generating heavy elements there may already be enriched material. The oldest systems we see now are already well along in evolution of matter. In QTC pure hydrogen or very low metallicity stars may never be detectable. Recycling and fission events at early stages is presumably violent but at some stage the lighter elements could probably survive between generations of cycles. By the current stage of harmonic cycling remnants of galaxies themselves may survive, perhaps providing fragments which could form dwarf or irregular galaxies. If the QTC cycle pattern from sigma-source to dark matter is correct, key questions include what exactly can survive such recycle stages, what has to reform, and how long are cycles. Basic p-space matter should survive recycling earlier than stars and certainly galaxies or parts thereof. QTC presumably requires a period of early sigma-sources, shown as the question

mark at the right side of figure 8.5. Assuming dipole mass decreases with each doubling, masses were greater in earlier stages of evolution. There are many unanswered questions at this point, but the early universe was not a simple ball of hot expanding plasma if QTC is correct. I will offer a suggestion at this point of what might have proceeded quasars within what I call the 'black forest' phase of sigma-source evolution.

On June 29, 2013 after writing an early draft of the above paragraphs I paused to think about some of the questions raised. How do quasars differ from galaxies and why can we not see earlier generations of sigma-sources or many objects at much higher redshift? The answer could be remarkably simple if QTC is correct. Galaxies appear to form as outflow from massive nuclear black holes in QTC. The outflow appears to be driven by the fading of gravity, possibly as matter compresses beyond the small scale limit defining gravity (4.9.0), (7.5.0) or, perhaps more likely, by exceeding the range of temporal commonality. Dipole decay then generates the observed two stream outflow. Stepping back further to earlier sigma-sources they will be more massive, perhaps reaching a point where no outflow into visible matter from the black hole can occur within the sigma phase before recycling. Sources may be present but invisible or extremely faint. This could explain why quasars may show minimal external active interaction near the black hole horizon. As mass increases quasars should drop rapidly in number with redshift, as observed. Still more massive sources may never produce outflow or perhaps what might be seen as only a sudden flare. Infall is possible if any matter is available. Accepting the fact that we exist along with quasars, and since QTC works well back at least to quasars, we can proceed forward in time from that point. Dipole outflow and the number of galaxies should increase rapidly once quasar sources fission to lower mass dipoles. The character of outflow will be discussed further with respect to galaxy evolution. QTC can explain the galaxy-quasar link and provide plausible connections further back in time toward $t_o$ - if there ever was one.

### 8.3.2 T Families, D Doubling and Harmonic Decay Within D

It is important to pause at this point and discuss the notation and meaning of the decay process involved in QTC. Whatever galaxies are physically from the sigma viewpoint, from the energy/temporal standpoint it is increasingly clear they are quantum 'particles' which occupy specific energy levels. Their photons carry that signature plus, due to their extended sigma nature, some of their internal sigma-space properties, and geometrical distortions (cosmological corrections) due to the geometry of tau. Aging, defined geometrically as the 'flow' of sigma through tau, is quantized energy level decay in tau. For part of the remainder of seminar 8 I need to live in quantum tau to try to show what is stated above may provide a real picture of our universe.

The QTC quantum numbers T and D are defined in the opening pages of seminar 3. The T states represent ninth root powers of two which define nine T states designated 0 to 8. They appear to represent different combinations of up to 3 doublings steps about a common cosmic time (commonality) state. T defines the possible timeline forms (8.2.4). When the nine roots are scaled by the speed of light, c, and expanded by successive factors of two (indexed by the doubling number D) they generates nine sets of redshift levels (or intervals between levels within the same series). Observed from the cosmic rest frame and corrected for 3-d tau-space curvature (the cosmological correction) redshifts fit the predicted values precisely. Observationally T states associate with galaxy morphology represented primarily

by 21 cm profile width (see (3.3.3) figure 3.9). Width should define what size and type of dipole structure a galaxy contains. Transitions between T forms may occur although dipole evolution is probably determined very early in evolutionary history (8.2.4). Basic factor of two doubling decay (D levels) apply within all forms, but T values do not occur equally. T=0, pure doubling is dominant. T=6, the 2/3 form, is also common and associated with the classical picture of Keplerian dynamics (a 2-d divergence of force in 3-d space). In QTC particle physics, which is limited to three dimensions (it operates only within 3-d sigma-space), the F=2 3-d state is the equivalent of T=6 in 9-d and provides a simple 2/3 power Keplerian orbital relationship.

T=1, 5, and 7 appear to represent less common patterns based upon dipole combinations of 1, 2, 4 triad sets of doublings. They represent odd number T values adjacent to 0 and 6 formed from the 1, 2, 4 set of doublings. The 0 and 6 values of T appear to represent quad combinations of the basic 1, 2 doubling set. 1, 5, and 7 might be called 'isotopic' forms of the two dominant states. T=3 is absent or rare but can occur and its distinction is unclear. Transition connections between different T states do not appear to happen readily but can perhaps occur. States T=2, 4 and 8 are rare or nonexistent in isolated sources. However, the states appear to be present in double galaxy studies. See (3.3.10) figures 3.51-52 where T offsets of 2, 4, and 8 appear in non-isolated pairings, and 1, 3, 5, and 7 offsets appear in isolated pairs, all with respect to pure T=0 states. Note if the 1, 3, 5, 7 set is doubled you get the filled shell S, P, D, F vector model population numbers. There are also differences between even and odd D levels. Can you believe that gravitational dynamics is the basis of cosmology with such data? There is a great deal to be learned to understand T and D states. The 2, 4, 8 dipole structure is also exactly a doubled form of the basic fundamental triad, the 1 2 4 chronon, which forms the basis of force and matter substructure.

D values distinguish doubling levels and fractions within T states. Doubling is sequential in time hence D is presumably a 'distance' index within each T state. Redshift, z, distributes widely over energy levels within D states and must be used with care when defining distance and physical association. The first issue to resolve is how to get from one D fraction to another within a given T state. Rather than taking large quantum jumps it appears transitions between D levels may occur in still higher harmonics of the D level involved. Studies of redshift variability demonstrated decay 'cascades' between such levels (see(3.9.0-2) and [36]). The quasar to galaxy transition provides excellent examples.

### 8.3.3 Quasar Decay into High Redshift Galaxies

The connection between quasars and high redshift galaxies is discussed in detail in seminar 5 (5.4.0-1) and related more specifically to QTC in seminar 7 (7.6.1). Figure 8.6 (the upper left table in figure 7.14 of (7.6.1)) shows how characteristic peaks in the quasar redshift pattern, for quasars active as radio sources, transform to simple doubling fractions of c when transformed to Lehto-Tifft redshifts within QTC. This is consistent with active sources which have previously been associated with band heads and vertical sequences as key stages in redshift evolution. The first column of the table in figure 8.6 lists z(LT) redshifts corresponding to simple fractions of c. When converted to observed values, z(obs), they match the series of observed active quasar peaks z(peak) perfectly, and define the fundamental T = 0 redshift sequence. Extended studies of active quasars and active galaxies shown in seminars 5 (5.3.0) and 7 (7.6.1) confirm the presence of other related T states at

these locations. Less active objects may scatter more widely and based upon galaxy studies could represent objects in intermediate cascade states between primary levels. A detailed study of this premise should be carried out, but requires precise data properly transformed to the cosmic rest frame with full QTC cosmological corrections.

Quasar redshift peaks

| z(LT) | D=2 | z(obs) | z(peak) |
|---|---|---|---|
| c/16 | | 0.064 | 0.061 |
| c/8 | | 0.131 | |
| c/4 | 1/4 c | 0.274 | 0.30 |
| c/2 | 2/4 c | 0.601 | 0.60 |
| | 3/4 c | 0.989 | 0.96 |
| c | 4/4 c | 1.441 | 1.41 |
| | 5/4 c | 1.968 | 1.95 |

Figure 8.6: The quasar redshift pattern.

The relationship of galaxy redshift states to the basic quasar doubling states is shown in figure 8.7. The diagram shows the redshift distribution of galaxies in a study of the Hubble Deep Field (HDF) by Cohen et al [AW] (see (7,6,1) for details). The curved line is galaxy density as a function of redshift, and vertical lines at the upper boundary identify the location of the quasar c/2 and 3c/4 states. Galaxy density should and does peak below those states as lower decay states are generated from which galaxies form.

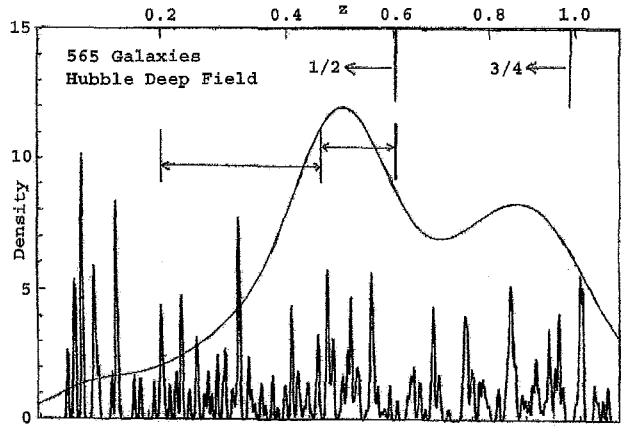


Figure 8.7: Hi z galaxy generation from quasars.

The left frame of figure 8.8 shows the galaxy pattern which appears directly below the T=0 D=1 c/2 (T-state, D-level, D-fraction) quasar state in the HDF study. The right frame shows a slightly wider redshift pattern for a different field (0053+12), again just below the T=0 D=1 c/2 quasar state. Periodic peaks appear exactly as predicted. Horizontal lines

connect related T states and identify doubling (D levels) within the T state. (A D level is the power of two of the denominator of the D level fraction which describes the degree of periodic (harmonic) decay within a D level). Three prominent peaks appear in the left frame, states associated with T=0, D=5, c/32, and D=4, c/16. If galaxies exist in the foreground they should appear below the redshift of parent quasar D fractions involved as harmonic sets at the D level (or levels) appropriate for the foreground group distance. A D level sequence begins with D *fractions* at or just below *each* quasar D level fraction (15/32 and 7/16 below the quasar D=1 1/2 fraction in the left frame. The foreground D fractions then distribute throughout *each entire* T state sequence. D values indicate the *level of decay* within each T state series involved and are a primary distance indicator. D *fractions* give the location within the D level energy pattern *but not independent distances.* The D fraction is equivalent to the redshift, however, in QTC is a measure of the degree of decay within a D level. It is *not directly a 'distance' indicator.* D fractions are *energy levels* within T, D states - 'decay multiplets'. An average over D fractions (redshifts) within a concentration may provide a distance estimate, but beware! D and D fraction values are related to the formation of redshift-magnitude bands for galaxy aggregates as will be discussed subsequently.

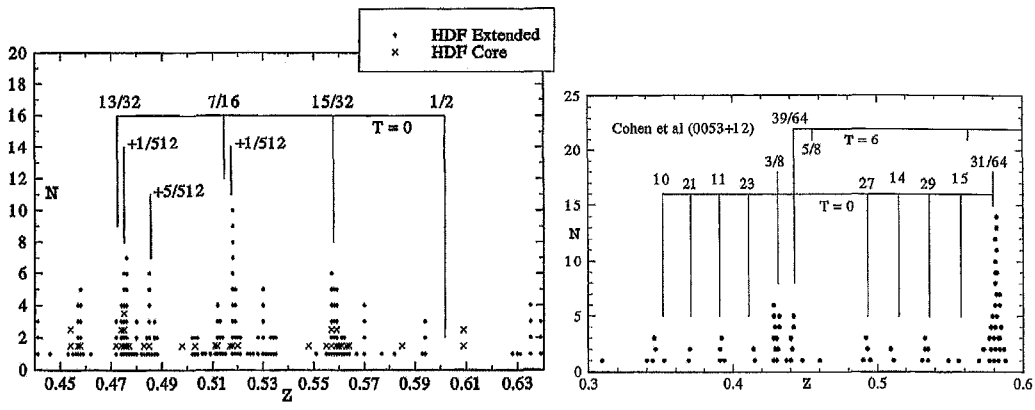


Figure 8.8: Hi z galaxy redshift cycles.

The right frame contains the beginning of four populated D fraction patterns, 31/64, 15/32, 7/16, and 3/8. Strengths of even fractions alternate with odd fractions since the even fractions fit the same levels in lower fractional series, 3/8 = 6/16 = 12/32 = 24/64 for example. The lower order fractions represent fundamental decay levels that began at earlier times, and may have completely decayed (fissioned to lower level sigma-sources in QTC). Those fractions should be empty if not masked (as 1/8 is by superimposed higher D level decay states). The T=0 c/2 state, 1/2 in figure 8.8, is indeed empty, and the 1/4 state is also empty or nearly so as I will shortly demonstrate. Decay fraction cycles in figure 8.8 *extend and overlap* through at least three D fractions before a gap appears in the pattern. Decay 'chains' are only a few D fractions long. I will return to this observation subsequently. Other T states have also begun to appear, T=6 appears in the right frame of figure 8.8. T=6 must begin at Lehto-Tifft redshift 3/4. The T=6, D=3, 5/8 fraction appears to be empty but the sample is small. 5/8 is the first D=3 level below 3/4 in the T=6 D=2 3c/4

series. The high level is empty but as seen for T=0 states the T=6, D=6 39/64 fraction is populated directly below 5/8. Objects in the 0053+12 field foreground have apparently decayed to the D=6 level.

The left frame of figure 8.8 contains information concerning the decay mode of D fractions. The D fraction 15/32 is precisely fit. Both the 7/16 and 13/32 peaks are offset by one 1/512 step, and the final 13/32 fraction shows a proceeding peak offset by 5/512. This may indicate harmonic decay through D=9 c/512 level fractions with progressively incomplete decay down through the pattern. It is interesting to again note that steps of 1 and 5 are seen while 2,4 and 8 are avoided as in missing T states. The sample is small but consistent with other decay patterns seen. The 3-level decay gap from D=6 to D=9 is also consistent with three D fractions overlap within the foreground aggregate of galaxies. Specific aggregates or gaps between them seem to contain structure of at least three fractions and several overlapping internal levels. We will see this pattern again.

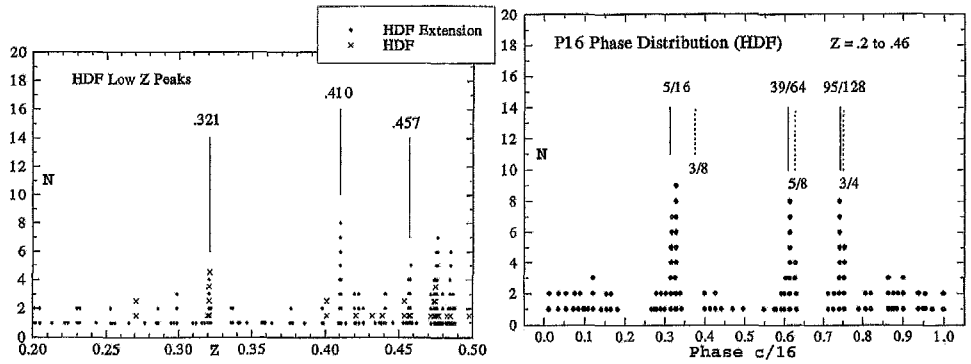


Figure 8.9: The c/16 cycle.

Figure 8.9 examines the distribution of galaxies in the HDF study by Cohen et al [AW,AX] with redshifts between 0.2 and 0.46 below the figure 8.8 HDF analysis. There are three significant peaks and numerous scattered points. As noted above redshift is not directly a distance indicator in QTC. Any peak present in standard redshifts will be present in transformed Lehto-Tifft redshifts. By dividing transformed redshifts by any expected period the resultant phase distribution will identify harmonic periods present however the points scatter. The right frame of figure 8.9 shows the phase distribution for the c/16 period, the shortest 'local' period in the quasar peak series in figure 8.6. The three peaks are immediately identified as levels of D=4 c/16, 6 c/64, and 7 c/128, one step below T level fractions 3/8, 5/8, and 3/4. The D=5 c/32 set is what appeared in the higher redshift range in figure 8.8 just below the empty D=2 c/2 quasar state. Each peak is now enhanced by isolated points or small peaks (see seminar 5 (5.6.0) figure 5.19). The D=4 c/16 point at phase 0.310, redshift 0.457 is enhanced by 11 points from isolated 3, 4, and 5/16 D=4 fractions. The c/16 period is clearly present. Note also that phases corresponding to 1/4, 1/2, and 3/8 are empty (but 1/8 may be present). As noted above the early states in the T= 0 series may be fully decayed.

One important point concerns earlier statements that D values rather than redshifts relate to distance. Figures 5.11 through 5.14 in seminar 5 (5.4.2) and figure 7.16 in seminar 7

(7.6.1) test for physical association of galaxies in pairs and groups within the three widely spaced c/32 amd c/16 peaks in the left frame of figure 8.8. The test in figure 5.12 of seminar 5 (5.4.4) compares the two widely separated peaks (25200 km/s but both in D=5, c/32 levels). The study shows strong pairing and grouping indicative of close association (0.005 of being random). Comparing the mid 7c/16 peak with the higher redshift 15c/32 peak in figure 5.13 returns an even stronger correlation, while comparing the mid 7c/16 with the lowest redshift 13c/32 peak in figure 5.14 shows the least correlation. The mid c/16 peak must actually be the earliest data, preceding both c/32 peaks in time as the smaller D value indicates. Nevertheless, the correlations show that all three peaks are actually closely associated. Consecutive D values apparently overlap in sets of three, and the redshift differences have nothing to do directly with association or relative distance. There is no significant association with galaxies not within the peaks. D clearly is an indicator of objects being associated. In QTC many if not most 'discordant redshifts' are physically associated within D families. It is unclear at this stage how to convert T, D values into distances, especially for individual galaxies. QTC interprets the aggregate in the left frame of figure 8.8 as a single cloud of galaxies in the D=4 to 5 range within the T=0, D=1 quasar family. The higher redshift pattern in the right frame is a D=5 to 6 group within the same family. The lower group is apparently a D=5 to 6 group below a 3/8 D=3 family within T=0. In QTC they are associated groups, not complex spatial structures defined by redshifts. In view of the correlations in spacing no reliable estimate of the cloud thickness is possible using redshifts, however angular grouping appears to be consistent with local aggregates.

The correlation of the redshift peaks in figure 8.8 implies that the general large scale distribution of galaxies appears to be far from random. The HDF and secondary field in figure 8.8 places all but a very few galaxies in only three or four aggregates. Furthermore, they are are not arbitrary clumps of D fractions, they all fall directly below primary doubling fractions and it is not clear that they are especially thick clouds spatially or wide time intervals in lookback. In QTC we are looking back in time at the energy decay structure of the universe. Is the D fraction pattern telling us that galaxies are only generated 'periodically'? What exactly does the pattern have to say about the actual distribution, structure and nature of galaxies? I will return to this issue in section 4. Unless one is a physicist the quantum notation may be a bit confusing. I will end section 3 with a discussion of redshift-magnitude bands, which is where I started, but I will first briefly summarize what was learned from important early studies of local galaxies. It took me 40 years to understand what redshift-magnitude bands are, including the entire journey through the universe to find the apparent answer.

### 8.3.4 Superclusters, Pairs and Clusters of Galaxies

Returning briefly to figure 8.5, the quasar pattern has now transitioned into systems of galaxies. There appear to be chains of doubling and doubling fractions that lead to pairs, groups, clusters, clouds and superclusters of galaxies as timeline structure develops. Turning first to superclusters, seminar 7 demonstrates how double galaxy studies indicate clouds of galaxies are strung together like beads on a chain to produce superclusters [79] (7.6.3). We shall now step down to the D=12 domain where we reside. There is an important gap where much *accurate* redshift work is needed in the D=6 to D=12 range. We also need more

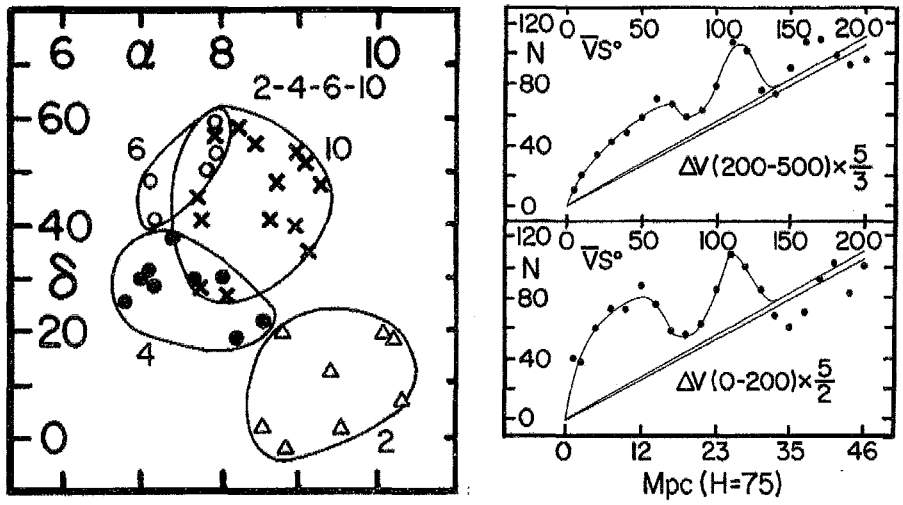


Figure 8.10: Supercluster structure and scale.

detail relating to the astrophysics of supercluster structure extending out to z=1. There is interesting substructure within the HDF D groups for example. In my view astrophysics has jumped far too fast to what was thought to be the fringe of the universe, but is not if QTC is correct. Dynamics as the basis of cosmology does not appear to apply. The left frame of figure 8.10 shows one of the supercluster chains of clouds of double galaxies projected on the sky as discussed in seminar 7 (7.6.3). This understanding is one of the remarkable results of double galaxy investigations. The distribution of mean redshift $\bar{V}$ of pairs times their separation S in degrees (proportional to their minimum separation) shown in the right frame of figure 8.10 establishes the scale and separation of distinct clouds that characterize supercluster chains. Superclusters are not continuous structures. Much more precision data will be required before local structures can be directly linked to higher redshift material.

Double galaxy studies provided much of the critical early information which opened the door to QTC. Figure 8.11 reproduces figures 2.13 and 2.21 from seminar 2 to summarize much of the outcome in one figure. Four independent double galaxy samples in the left frame verified redshift quantization first found in the Coma cluster and demonstrated the exclusion of identical redshifts in pairs. Both findings are inconsistent with classical dynamics. The right frame demonstrated alignment of independent pairs within and between supercluster clouds. The orientation pattern provides a completely independent test of the non-dynamical character of the redshift and established the sequential timeline flow relating supercluster clouds. Further evidence for exclusion and degeneracy effects involving pairs was also introduced in seminar 3 (3.10.0), and discussed above in (8.3.2), relating to rules which determine D level populations. These correlations seem to rule out galaxy formation by any means but fission or harmonic relationships. There is no evidence of dynamics to form clouds, and orientation associates the clouds as related structures.

The early global studies discussed in seminar 2 provided major steps within the development of QTC. The introduction of 21 cm radio redshifts provided the means to clearly establish

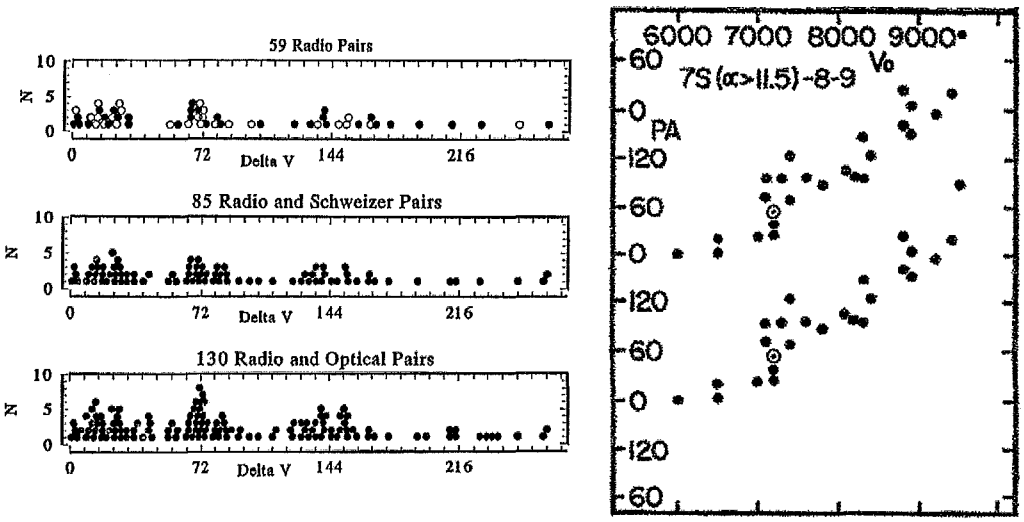


Figure 8.11: Double galaxy quantization and orientation correlations.

the global nature of redshift quantization and the precision to detect redshift variability. The detection of short periods led to recognizing the existence of harmonic cascades between more fundamental redshift intervals [Ap2], and detecting and formulating cosmological corrections (seminar 2 (2.2.7) figures 2.38-40 and (6.3.3)) to remove temporal curvature effects from redshifts. This included direct tests verifying $q_o = 1/2$ ([102] and tests shown in figure 3.21 of seminar 3 (3.5.1)). The expanding tau domain is indeed spherical. Understanding of the correction (7.7.3) then played a major role in defining photon structure and internal forces governing matter. The 21 cm profile provides a basis for distinguishing families of galaxies, understanding the dipole incorporated in nuclei and the dual streams of outflow which generates the structure of galaxies. Since the 21 cm profile defines a pattern representative of an individual galaxy, it is effectively a 'wave function' of the energy distribution. This presumably explains or contributes to the precise periods found using 21 cm data. The asymmetry and width properties provide basic keys for understanding galaxy evolution.

Global studies matured with the transfer to the cosmic background rest frame in seminar 3 (3.3.3),(3.4.0-7). In combination with the adoption and expansion of Ari Lehto's concept of how to generate quantized redshifts, and understand fundamental particles and forces, the tools were available to explore the universe. The cosmic frame removed local limitations by demonstrating that quantization was indeed a cosmic phenomenon and allowed detailed investigations of large samples for quantization and redshift variability studies. The CBR association defined the concept of timeline flow which, with relativistic time lag within matter, could readily explain the CBR dipole without recourse to dynamics. The groundwork was laid to apply quantum concepts to a variety of studies such as indicated in the latter part of seminar 3. The association of two types of dwarf galaxies with different T states (3.8.0) provides a good example (see seminar 3 at figure 3.28). Before turning to the evolutionary story of individual galaxies I will review the findings of the earliest years in seminar

1. This includes redshift-magnitude bands, which can now be understood.

### 8.3.5 Redshift-Magnitude Bands and Early Correlations

Except for my early work on nuclear photometry and radial color studies in galaxies, which ultimately ushered me into the redshift controversy and provided an interesting study in itself [9,18,20,22], redshift-magnitude bands mark the starting point of my life as a controversial scientist. Initial work defined the bands and the related correlation of morphology with redshift [28] (1.3.0). This was quickly followed by demonstrating that the bands converged toward zero redshift [34] hence were scaled versions of each other. It was immediately recognized that bands were separated vertically by 3/4 of a magnitude, a factor of two in luminosity, hence they could be generated by fissioning providing there was no dynamics to mix them up. The reduction in possible velocity dispersion to preserve banding immediately removed any evidence for dark matter (if due to dynamics). Such a model also required the morphological spread to represent structural evolution and fading, distributed over redshift evolving with time, to preserve the bands and, at that time, perhaps even some gravitational dynamics. It was hardly surprising that virtually no one was willing to believe the Coma bands were real despite the lack of any apparent errors. My announcement of the bands in August 1971 at the Amherst AAS meeting [28a] was an interesting experience.

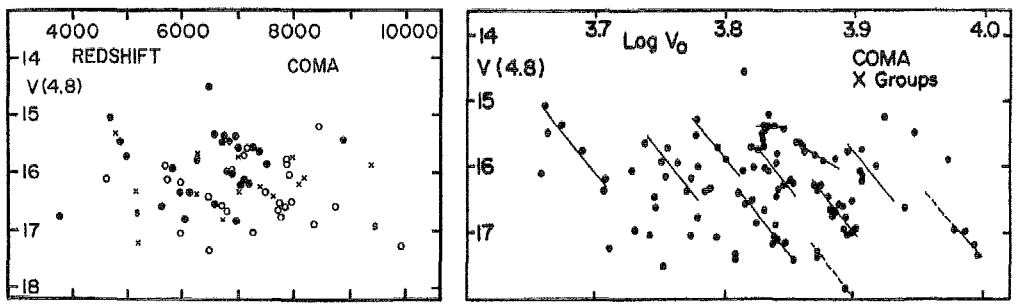


Figure 8.12: The Coma cluster Redshift-Magnitude Bands and their Cross Band structure.

The discovery and development of redshift-magnitude bands is a story in itself. Certain aspects of the story are important. The original definition of bands and cross bands through 1974 along with important morphological associations are well documented in references [34, 43 and 44] and seminar 1 and 2 proceeding double galaxy studies. Especially important findings related to vertical sequences and morphological evolution will be discussed in the following section. Figure 8.12 illustrates the band and cross band diagrams for the Coma cluster. Confirmation studies using A2199, A1367 and the Perseus cluster began as early as 1972 and are formally presented in references [34] and [57]. The first interpretation of banding (1.8.0) and relationships to active galaxies are summarized in reference [57]. Quantization of the redshift itself was suspected as early as 1973 [44] and demonstrated by 1975 [58] when a 72.5 km/s periodicity was shown to be present in the Coma cluster. The basic concepts of redshift quantization within and between galaxies were presented in three major papers in the Astrophysical Journal [55, 58, 59] submitted in June of 1975 and published

between mid 1976 and early 1977 after many reviews. Figure 2.3 in seminar 2 (2.3.1) shows the abstract of reference [58] including an editorial note reflecting disbelief but lack of any evidence of error in the content. However, with the virtually certain recognition that the redshift was a quantized entity intrinsic to galaxies, redshift-magnitude work moved mostly to the background. Working with ill defined quantities such as magnitude and morphology of fuzzy objects was difficult and tedious. The redshift is a much more precisely measurable quantity and increasingly clearly was the real 'key to cosmology'. Having followed the redshift path, however, the issue of what redshift-magnitude bands are can now be answered.

Foreground structure present in the Hubble Deep Field and related studies connected with superclusters appear to indicate that clusters or clouds of galaxies contain several overlapping D fractions involving two consecutive D levels. The three clear Coma bands spaced by doubling factors of two in luminosity appear to clearly associate primary redshift-magnitude bands with D levels in redshift decay. The Coma bands are equivalent to the three HDF redshift peaks in figure 8.8. The center band is the equivalent of the 7c/16 D=4 peak and the upper and lower Coma bands are associated with the 13c/32 and 15c/32 D=5 peaks. There is an important confirmation of this assignment. The correlation studies of the association of the three HDF peaks, (5.4.3), figures 5.11-14, demonstrated that the D=4 7c/16 mid redshift peak was in fact the oldest set of galaxies, despite the inconsistent redshift order and the fact that QTC finds all three peaks presumably form one physical aggregate (as the Coma cluster does). Emission line galaxy associations in the Coma cluster (1.6.2) figure 1.30 show precisely the same situation for the middle Coma band. The flanking bands show young active objects associated with the Coma core while the mid band harbors older low activity in outlying galaxies which in QTC correspond to earlier outflow from the sigma-source in the Coma core. The same effect produces blue redshift extensions of cluster cores.

The decay structure between the HDF D fraction peaks is barely present, but in Coma is well advanced as the extended cross band pattern which appears as harmonic uniformly spaced D fraction levels which in themselves now divide into still higher level harmonics to represent individual galaxies as indicated in figure 8.8. Band structure is progressing in decay toward lower redshift as shown in (1.7.1) figure 1.34. The lower bands with more advance harmonic decay (lower D fractions) lead at lower redshifts producing the low redshift excess seen in cluster cores as noted above. See for example figure 1.20 in seminar 1 (1.5.1). Band heads relate to the most recently generated, most advanced (toward low redshift) and most active objects. At locations further down (toward higher redshift), more evolution has occurred since formation. Structure is advanced morphologically producing the redshift-morphology correlation. Redshift is the result of decay since formation, energy decreases (redshifts) to buy time in quantum steps. A further discussion of evolution is provided in the following section. In effect, a banded redshift-magnitude structure is a set of g-space particles decaying through an energy level diagram. As an aging sigma-source evolves in the cluster core dipole driven products diverge outward to generate a cloud of galaxies as they advance in time. This generates the higher redshifted tail and radially sorted morphology seen in clusters along with a blueshifted cluster core. This is especially well illustrated in A262 (figure 1.24 in seminar 1 (1.5.0)) and the discussion of the Perseus cluster at the end of section 3 (1.3.0) of seminar 1. Eventually galaxies pass radially out of communication into dark matter. This will be discussed in the following section.

It is not entirely clear what D states are involved locally at an even later stage than the

Coma cluster. Individual galaxies locally appear to be in D fraction decay or perhaps a second level D fraction fraction decay. A dipole level of 73 km/s associates with D=12 c/4096 levels. If these are three levels in advance of the Coma cluster D fractions involved the D fractions may be D=9 c/512 levels as suggested in the HDF study. D=9 corresponds to redshift intervals less than 600 km/s which is about right for the Coma cross band spacing. Again, if intervals of about 3 levels are involved we could be associated with a D=6 c/64 band. This may be roughly right, but much more research with precision redshifts is needed to properly connect the Coma cluster with the Hubble Deep Field information. In any case welcome to a niche somewhere in our redshift-magnitude energy level if QTC is correct.

## 8.4 The Life Cycles of Galaxies

Much of this book has been devoted to individual aspects of the structure and redshift patterns within and between galaxies and larger scale aggregates of galaxies. In the ordinary day to day view from within a galaxy the impression is that although things evolve there is an overall continuity through time. This is effectively the path of classical cosmology, which ascribes our local forces and environment to all of space, but struggles to understand and connect to the small scale that has its own strange rules. As QTC has evolved it has become increasingly clear that this is not correct. QTC indicates that we are another class of 'particles' extending the hierarchy of the small scale. Why should there be a paradigm change? We recognize the small scale range limits, but not that our scale is also limited. Hence the quantum gravity problem. The evolution of the universe appears to be a decay through a series of evolutionary cycles. On the temporal (tau) scale the process appears to be the decay of an energy field which we can represent as a decay through an energy level pattern. On the spatial (sigma) scale cycles appear as a flow through time from birth to death or recycle, not just for individuals, but for the entire structure within the cycle. There are two forms of cyclical behavior, 'flowing' through a pattern in a 'harmonic' recycle process, or undergoing a discrete transition, a 'fission' between modes. To close this seminar I will identify and look at some cycles, nodes and transitions involved.

We may not know quite where quasars come from, early sources that produced them may be optically invisible (8.3.1). We do know quasars define a master set of T states (5.3.0). In Lehto-Tifft redshift format, quasars, at least active ones, occupy precise ninth root doubling fractions of c for T=0 ((8.3.3) figure 8.6) and related intervals T=1,5,6,and 7 (5.3.0). They may avoid T=2,4 and 8, although these states do appear in the recent double galaxy studies relating to degeneracy (3.10.0)(8.3.2). We do not know if there are distinguishing properties of different T state quasar families or how those states decay (as quasars) within the L-T format since those questions have never been addressed, although I have indicated that quasars contain a band pattern [36] (1.4.3). Established astrophysicists who work with quasars do not accept the concepts of QTC, but I suspect such studies would yield fascinating results. It would be especially interesting to know if quasar redshifts decay into less active levels which fit harmonic D fraction levels where galaxies are found. 'Active' galaxies presumably link to lower level D fractions of evolved quasars. Figure 5.5 in seminar 5 (5.3.0) combines quasars and active galaxies to show quasar doubling states extend to low redshifts. A precision study of the relationship of quasar D fractions to active galaxy redshifts (precision values properly transformed to L-T cosmic frame form) should be interesting.

### 8.4.1 Vertical Sequences

Quasars almost certainly generate galaxies. QTC has shown that at least the highest energy quasar D fractions of c are not occupied by galaxies (8.3.3). Those basic direct doubling energy levels appear to be reserved for pure D quasar fissioning states, at least at higher redshifts. Galaxy D fraction patterns all begin at harmonic fractions immediately below basic quasar doubling states. Decay into such sub-doubling harmonic level is inferred, but does not seem to be a simple harmonic step. The few redshifts between quasar states and the populated highest harmonic D fraction just below them in figure 8.8 contain no obvious pattern, nor perhaps should they. The first fractional level is not a simple harmonic of the upper state, it involves a substantial jump to a lower D. Nodes of all lower harmonic states come together at a quasar D doubling fraction point, but the step to higher harmonics presumably must occur later in time to populate 'foreground' energy decay levels (spatially separated clouds of galaxies) indicated by the greater D values. Such harmonic transitions must emerge later in cosmic time after a sigma-source (to put it in spatial terms) has progressed along its timeline (or aged enough to decay in quantum terms). This produces a later D fraction series with the initializing D source absent as seen. This must be a quantum transition (a long range 'energy fission' or major step in a quantum multiplet) which we apparently see as the appearance of a vertical sequence. Figure 8.13 repeats figure 7.28 from seminar 7 (7.7.1-2) discussing sigma-sources. Section (7.1.2) shows vertical sequences appear at junctions between cross bands. They apparently produce gaps between series of related doubling fractions where harmonic 'beads on a string' can be produced. Alignment then follows the timeline track. Harmonic decay presumably connects beads within strings.

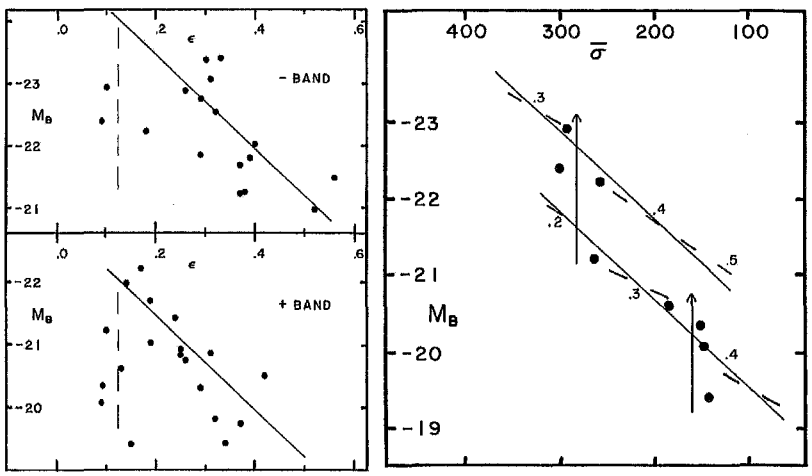


Figure 8.13: Vertical Sequences and their relationship with Cross bands .

Vertical sequences consist of near spherical E galaxies aligned in eccentricity with band heads. Their actual association is seen to be with gaps between cross bands when absolute magnitude is plotted against the luminosity related mean velocity dispersion. The newly arriving recycled galaxies mark active input locations to cross bands where galaxies begin their decay. They apparently emerge as 'recycled' E galaxies which rapidly expand. This is

in dramatic contrast to the classical dynamical understanding of ellipticals. The following is quoted from an abstract announcement of a November 2012 colloquium entitled "Obesity in the Universe: Why Did Early-Type Galaxies Grow in Size" given at Steward Observatory by a notable authority on the early universe.

> Once considered the simplest class of galaxy to model and explain, the assembly history of early type galaxies still presents many puzzles. Spectroscopic observations show that the most massive examples completed their star formation earlier than that in their less massive counterparts, in apparent contradiction to popularly-held hierarchical models. Hubble observations have also revealed that many of the most massive early types seen at high redshift are much more compact than their their present-day equivalents. This suggests they somehow expanded in size without growing significantly in mass. Clearly early type galaxies still have a lot to tell us about galaxy formation and assembly.

This behavior is in accord with QTC expectations as elliptical forms emerge from sigma-sources, rapidly expand through vertical sequences and join cross bands to begin their morphological evolution. Dynamics is not the key to understanding galaxy formation and evolution in QTC.

The actual sigma-source which generates a vertical sequence is presumed to lie in the nuclear region of a cluster or galaxy aggregate it is generating. Its products appear as faint near spherical compact E galaxies with rapid outflow as they expand. A good example of such a configuration may be the set of compact ellipticals around the giant 'D' (diffuse extended E) galaxy in the core of the A2199 cluster. Their D (doubling) value determines redshift-magnitude band association and the D fraction associates them with specific cross bands which they join to begin a decay cycle. In general terms in QTC galaxy evolution appears to proceed as follows. Initially the nuclear dipole which drives a galaxy's evolution is apparently deeply buried in a spherical cloud. The two stream expansion generates an expanding compact elliptical galaxy. As the early cloud expands and begins to cycle into dark matter the dipole property becomes progressively more structurally apparent and morphology evolves through So into the spiral categories. Galaxies eventually pass cyclically into late spirals as they decay within their cross band. Figure 8.14 in the following section illustrates this process.

Before discussing aspects of evolutionary life cycles of a galaxy within cross bands as they may undergo harmonic decay, it may be useful to comment on what a quantum transition seems to be in QTC. In its simplest form as an electron transitions between energy levels within an atom or a galaxy transitions between T,D levels or D,fractions, QTC can provide a sigma mode explanation. In an energy-wave model one can imagine slipping from one state into another if there is sufficient wave function overlap. In a time-energy (tau) mode this is a way to visualize the process. Using the asymmetry parameter for galaxy 21 cm profiles as 'wave functions', such a process was demonstrated (7.5.7) for QTC. In a sigma physical 3-d mass form that is harder to visualize. In space there can be a real change of state and even location for a physical mass without passage between locations. In QTC as an energy state is changed, an object can blink out in one point and appear in another or appear to progressively change. Objects such as Centaurus A or NGC 1275 in the Perseus cluster may be dual morphology examples. There is no distinction between points, just a change in energy state, a dramatic bit of QTC aging. Spatial location is a unique property

of sigma. Tau makes no distinction between spatial locations. Sigma space within a certain range of time is a singular point in tau where evolution can occur utilizing continuous physics. A photon may emerge to conserve energy in an energy level transition of p states, or in the case of diverging timelines an energy density imbalance may be restored with a structural modification while operating within space-time uncertainty. Temporally common spatial events are automatically entangled in QTC. Events originating within a common temporal 'uncertainty' range are in direct contact in tau despite their locations in sigma. This includes instantaneous communication of information within an uncertainty range and sets large scale range limits for forces in QTC.

I, like every other physicist, has always wondered what a quantum transition is. If QTC is correct, we may now know. We need to keep track of the energy state in both 3-d space *and* time, and recognize what the function of each space actually is.

### 8.4.2 Where Do We Fit Into QTC? Cross Band Evolution.

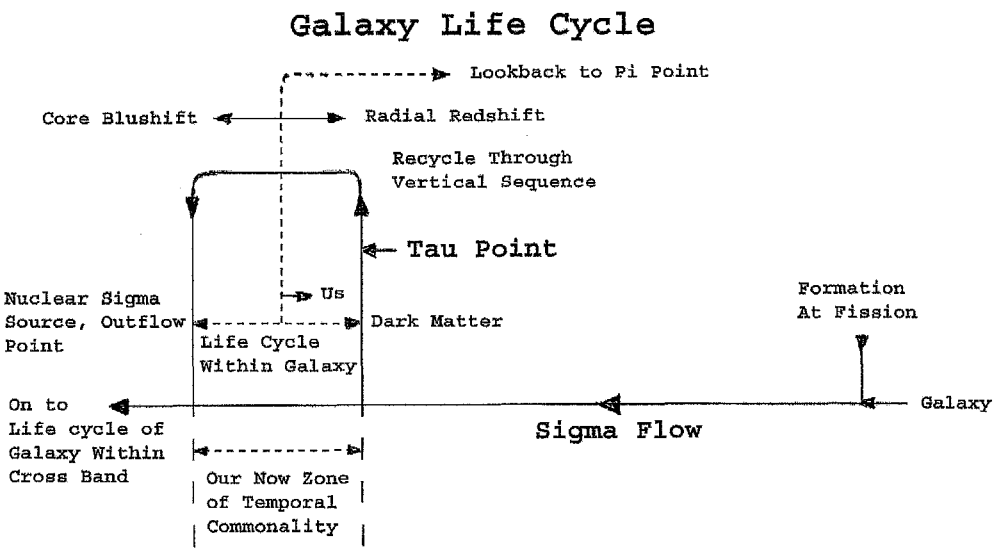


Figure 8.14: Galaxy Life Cycles.

If QTC is correct we appear to occupy a specific energy level within a cross band D fraction which falls somewhere along a redshift-magnitude band doubling level. Figure 8.14 illustrates the type of evolutionary cycle we seem to inhabit. Our galaxy may have begun as an E galaxy injected or recycled into a doubling fraction cross band. Since we reside in a moderately advanced spiral galaxy we are probably not now in a leading cross band within our D level. Thus the empty line to the right on our timeline flow in figure 8.14, which provides for earlier evolution that preceded us. The cycle toward the left shows us at a point between outflow emergence from a nuclear dipole sigma-source and entry into dark matter. Relativistically lagging matter drifts progressively behind new or recycled matter

at the leading edge of a cycle. When the aging matter enters dark matter it has fallen behind the new entry point in time. This is confirmed by noting that outlying photons begin redshifting to stay within our now zone before passing out of temporal communication with progressively younger blueshifted inflow. Radial redshifting was discussed in seminar 7 (7.5.4). The input point and output dark zone (both points in tau) may mark sequential points in time, perhaps defining the range of temporal commonality. However, matter apparently should recycle in some way within galaxies to account for observed progressive increase in metallicity over time. Both metallicity evolution and progressive morphological change between cross bands as redshift increases along redshift magnitude bands should be explained in any evolutionary theory. Recycling between cross bands may involve reentry by vertical sequences if the interpretation of section 4.1 is correct. This could shift progressively back along the redshift pattern. One other means of recycling could involve the nuclear black hole. Matter deeper in a supermassive black hole is retarded in time gravitationally, and could perhaps connect with retarded dark matter. If delay rates can be properly coordinated a recycling process through tau may be possible within the 'dark link'. This is exercise for the theoretical physicists!

Evolution within a cross band appears to be some form of harmonic passage. The cycle we occupy in figure 8.14 must be only part of the total life cycle of our galaxy. How long it takes to pass from entry to exit in this sub cycle is unclear, but it must take at least a few billion years. Because of photon redshifting we look back much further radially in time through our now corridor towards the most recent Pi point, but that interval must contain many individual inflow to exit cycles in 'lateral evolution' (7.5.3). Thus the cycles within cycles concept of QTC. Inflow to dark exit cycles are designated as lateral cycles in time.

The association of quasar D fractions in high redshift HDF foreground galaxies with cross banding in local galaxy clusters provides direct evidence for the QTC model of galaxy evolution. The HDF material in figure 8.8 shows the lead structure in cross band development at the 13c/32 D fraction point (8.3.3), and suggests that decay between the D fractions occurs in a regular manner. D fractions appear to be harmonically related. If evolutionary decay is represented as harmonic oscillation in time, galaxies exist visually only at the nodes of the oscillations. The nodal points define allowed energy levels within the decay process.

### 8.4.3 Period Tripling

Figure 1.41 in seminar 1 (1.9.0) shows cross band structure in detail as found in the Coma cluster at the birth of the quantization concept. The uppermost cross band shows a strong leading state, which could be related to a short or residual vertical sequence pattern. The cross band then extends toward higher redshift in steps close to 222 km/s. Figure 3.40 of seminar 3 (3.9.2) demonstrates that 21 cm redshift decay of galaxies in profile width range $150 < W < 300$ km/s seems to occur in periodic steps related to the 73 km/s period by a regular period doubling power of two, in this case $1/32 = 2^{-5}$ of 73.19 in the T=0 pattern for D=17. The 222 km/s seen in the Coma cluster is periodic but not a member of this series. The early periods, defined in the less precise galactocentric frame clearly demonstrated quantization but may require more precise study to properly relate them to the cosmocentric work. The 222 km/s periodicity is compatible with a series of powers of three, period tripling, connecting with the original 72.45 km/s period derived for the complete Coma cluster in the early work described in the opening pages of seminar 2 (2.2.0)

figure 2.1. Subsequent evidence from global galactocentric 21 cm studies found a 24.15 km/s period associated with dwarf galaxies which is 1/3 of 72.45 (seminar 2 figures 2.25-26 (2.5.1)). That period was subsequently shown to contain a further1/3 subdivision to 8.05 km/s [94] (seminar 2, figure 2.33 (2.6.3)), which was again shown to divide by three into the 2.67 km/s period that was used to solve the cosmological correction problem [111] (seminar 2 figure 2.35 (2.66.3)). The 2.67 km/s period is in fact a powers of two member of the T=7 series of periods. The pattern of thirds appears to represent semi-stable tripling patterns within short periodic cascades between normal doubling levels. Since period tripling is also a known process, it is possible that tripling can play a part in generating certain patterns, especially during primary transitions. Although far from established the pattern of successive thirds is observed and could be related to decay within the underlying 1 2 4 triaxial structures of matter. Along with doubling, particularly for the short periods, that decay mode may be found in some harmonic patterns within cross band evolution. It is at this short period structural level that redshift variation in quantized steps has been demonstrated [111]. Longer ninth root periodicities appear to be limited to period doubling and powers of two D fractions. There is little doubt, however, that cross band evolution involves quantized categories. This is as far as QTC has been able to probe quantized small steps involved with galaxy evolution. The work requires precise observations optically and at 21 cm, but is a key area for research on details of lateral evolution.

### 8.4.4 Morphological Evolution

Fundamental 21 cm standards were established in 1988 [105], (Ap2, Ap3) when redshift variation was detected. 21 cm observations were continued until 1995 at Green Bank. One key analysis of variation carried out in 1992 [114], (Ap2) was denied publication but contains observations and analysis made in 1991 critical for future tests. That paper shows how asymmetry relates to timing of transitions. The paper also illustrates the difficulty of publishing new concepts, or even basic data associated with such studies. I was denied an opportunity to test the concept of redshift variation further using the new GBT telescope in the later 1990s using the 1988 standards. This fundamental study remains as one of the important studies which can verify or falsify parts of QTC. It should be done by coordinating the GBT with Arecibo and a smaller telescope equivalent to the Green Bank 140 foot instrument. Such a study would test for quantization, variability and radial redshifting in one experiment. The time base to 2014 now exceeds 25 years, greater than the Tifft-Cocke to Fisher-Tully baseline that established both redshift variation and global quantization.

Figure 8.15 contains two redshift-magnitude diagrams which show direct evidence for redshift evolution within cross bands as a function of morphology. Evolution can be seen as lateral drift across cross bands. There are clear changes, but work is required to relate the process to specific quantum states. The diagrams in figure 8.15 are copies of figures 1.21 and 1.22 from seminar 1 (1.5.1). The Coma diagram on the left contains galaxies sorted morphologically which lie just outside the cluster core. They associate with the leading cross bands in the upper and middle band and show some of the core ellipticals, which fall between the cross bands, related to leading vertical sequences at band heads (8.4.1). A compact core E galaxy concentration is more readily seen in seminar 1 figure 1.20 (1,5,1) where it may represent the top of a vertical sequence feeding the CM63 cross band. In QTC the low redshift So concentration in the second Coma frame is seen as an evolved product,

shown by arrows, of the core ellipticals which arrived earlier. This is what QTC predicts as outflow in the elliptical stage drives an expanding E halo into dark matter to reveal lower redshift outflow where rotating nuclear dipole structure becomes apparent and generate So galaxies. This evolving group could also be responsible for the lower band CL54 group if it was generated by the earliest arrivals which have evolved into late spirals prior to moving into dark matter. The late type CL54 group is tightly confined to the cluster core. Being earliest to emerge in current outflow it should be lowest in redshift but still late in morphology. The most important aspect of the luminous low redshift So group is its demonstration that a strong low redshift cluster core feature, dominated by So and early spirals, should be and is seen in all clusters studied. Figures 1.24 through 1.26 in seminar1 (1.5.1) provide illustrations, a table and discussion of this low redshift feature predictable within QTC.

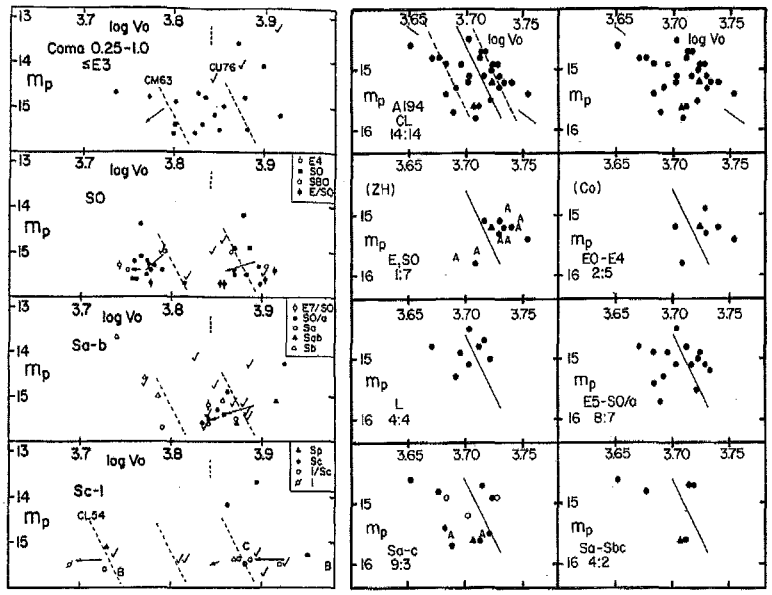


Figure 8.15: Evolution within Cross Bands.

The second, higher, redshift group in the Coma diagram associates directly with the leading upper Coma band CU76 cross band. This group associates directly with the vertical pattern of active radio and emission objects shown in figures 1.27, 1.29 and 1.30 of seminar 1 (1.6.1-2). The vertical pattern neatly splits the group between the second and third frame. This higher redshift group emerged earlier than the lower redshift feature, hence has developed further into spiral classes of morphology shown further shifted toward lower redshift in the third Coma frame of figure 8.15. This cross band group provides the higher redshift split spiral structure seen consistently in clusters, for example the 1258 +62 higher redshift aggregate shown in figure 1.25 of seminar1 (1.5.1). Still earlier emerging systems at higher redshift have had time to evolve still further and fainter providing the late morphological structure at high redshift in band diagrams as shown in the fourth Coma frame. The high redshift structure should be and is strongest in the outer portions of clusters where temporal flow has diverged furthest from the core source function. This is especially apparent in the

1258 +62 cluster diagram in figure 1.14 of seminar 1 (1.4.2). Figures 1.36 and 1.37 in seminar 1 (1.7.2) place the core and outer portion of the 1258 +62 cluster together to illustrate the QTC predicted effects contrasting young newer galaxy emergence with old advanced evolution. While checking section (1.7.2) take another look at the patterns in A262 (1.6.1) and discussion in (1.7.2). How many consistent examples does it take to believe that you at least suspect that you are witnessing the evolution of galaxies?

The right hand frame of figure 8.15 focuses on what appear to be well developed leading cross band features in the lower redshift A1367 and A194 clusters. A solid line divides two possible cross band features to show how the ratio of early to late morphological types shift between the groups. The population ratio changes steadily with morphology. The lower redshift feature has few early types and many later morphological types. *It looks exactly like an extension of the lower Coma CM pattern advanced in time one cross band lower in redshift.* To see this follow the left figure Coma CM63 pattern from E to So then switch to the right A194 frame and continue the low redshift pattern ESo to L to Sac. Now note that the higher A194 group is dominated by early morphology. This group is much less advanced in morphological evolution. As with the lower group the ESo to L to Sac pattern is an equivalent or slightly advanced match to the Coma CL76 So to Sab pattern, again shifted toward lower redshift to account for more advanced evolution in the nearer clusters.

In summary, in QTC galaxy evolution appears to proceed within cross band groups within redshift-magnitude band systems. Cross bands appear to be generated by vertical sequences where early type compact E galaxies are injected, potentially from decaying quasar states or recycled earlier galaxy cycles, into doubling fraction energy levels. Each galaxy then evolves by outflow in dual redshift streams originating from a redshift dipole sigma-source in its nucleus which appears in the form of a supermassive black hole. The spherical shroud of the source flows forward in time, expands, passes out of temporal communication with its source and progressively passes into dark matter. The source is progressively replaced by more advanced lower redshift later morphological forms. As the dipole structure becomes more apparent beginning E forms are replaced by So. The outflow cycle (lateral evolution) continues toward later spiral types, presumably passing through harmonic quantum states toward lower redshift. Cross bands apparently involve progression through quantized lower redshift energy level 'cycles' as D fractions decay. A cross band may best be described as a cross band zone. Matter may accumulate within a dark matter shroud invisible and mostly gravitationally decoupled from its original D fraction state. The oscillatory mode QTC proposes for the flow of energy through time suggests the dark stage may represent a temporal Bose mode of an oscillation away from a Fermi related node. As time proceeds to the next compact node (the next D decay fraction) where matter may recycle through vertical sequences and enter a new cross band level, a galaxy enters a new cycle. Sets of two D levels appear to form three band systems, with the center band the earliest D level and the flanking bands fitting the next D doubling level. Adjacent D fractions appear to define most cohesive individual galaxy clusters or clouds.

So emerges version 1 of Quantum Temporal Cosmology, a quantum model of the universe consistent with very many observed phenomena. many of which are inconsistent with conventional dynamics which seems to operate only within g-spaces. Galaxies seem to live their lives at nodes of a cosmic quantum oscillation. We do indeed live in an incredible universe. Thank you Mother Nature for a fantastic journey. An epilogue follows for you to ponder.

# Epilogue

I included little philosophical discussion within the main text, and prefer to refer such aspects to my colleague Stewart Barr who is well qualified to examine these issues. However, when recently reading Jim Holt's book "Why Does the World Exist?" [DI], which revolves around the cosmological issue *Why is there something rather than nothing?*, I encountered proposed answers to the question which in certain ways resembles QTC. Since QTC addresses Holt's question, and I believe answers it, some comments are warranted.

In the Interlude of chapter 7 Holt refers to an answer proposed by Robert Nozick, a Harvard philosopher, which leaves nothing unexplained at the end, referred to as a self-subsumption explanation that explains itself. I will not attempt to discuss Nozick's proposal itself, but his answer to *Why is there something rather than nothing?* was 'There isn't, "There's both".' The subsequent discussion was not very favorable to Nozick's proposition, but it was my first sight of the same answer QTC provides, "There's both". The QTC self-subsumption is

*Everything is nothing.*

Note it is not 'Every Thing is nothing'. Everything refers to the totality of the universe taken together. The QTC origin is a split in time at $t_o$. The split generates a time anti-time dipole consisting of opposed instants of time (somethings) which sum to zero (nothing) within temporal (tau) space. As my book discusses, an evolved form of that dipole structure exists as a verifiable fact in the core of galaxies today. The dipole decays within sigma-space and generates a real matter anti-matter structure. That is a real 'something' which in its dipole combination is a form of nothing. In QTC the universe as a whole is indeed a form of nothing. 'Everything together is nothing', but nothing may assume 'something' forms.

There are issues within this solution to Holt's something/nothing query. It raises the issue of what 'anti' means. In QTC the anti term distinguishes *existence in a specific fundamental form.* In QTC the split at $t_o$ is a transformation between what we conceive of as 'nothing" and the origin of time as a time anti-time dipole with a transformation into tau space, This can be interpreted as defining the quantum vacuum with a quantum fluctuation which generates a permitted quantum state of time. Only the existence state of time is involved in QTC. It does not involve a complete transformation from nothing to classical space with 1-d time which Holt discusses with John Updike in chapter 13 of his book. An intermediate stage is required. Since the inverse of time is energy (frequency of something), the split does indeed involve energy anti-energy, a property of time. The QTC event at $t_o$ is both the origin of time and a form of 'active' energy, photons or pre-photons which are constructed from the time anti-time dipole. It is through subsequent 'energy' interaction in pair formation that the next 'split', a transformation of form, occurs. Matter anti-matter *as sigma-spaces (space particles) come into existence!* Matter cannot automatically exist before the anti transition in pair formation (where the form of energy is transformed and both energy and time must be conserved since they are reciprocally connected). It is also worthy of note that the beginning point $t_o$'origin' is a theoretically unreachable limit. Although matter anti-matter transformation points are known (within uncertainty limits). What does 'origin' mean? Was there actually ever an initial origin for the universe? I may expand upon some of these concepts in a blog with Stewart Barr.

# Supplements

**Appendix 1:** Quantized Redshift Structure Within Galaxies 327

**Appendix 2:** The Case for a Time Dependent Quantized Redshift 347
An Introduction 347
Part 1: Original form 348
Part 2: Letter to Editor 365
Part 3: Revised text 373
Redshift Data tables 389

**Appendix 3:** Unpublished Redshift Data 395
**3a** 140-Foot 21-cm General data 395
**3b** Unpublished 140-foot 21-cm Redshift Standards Data 411
February, 1989 412
August, 1992 414
June, 1995, Including Wide Profile Additions 418
October, 1996, Including Wide Profile Additions 422

**Appendix 4:** References 427
**4a** W. G. Tifft Biographical Publications and Related References 427
**4b** External References and Citations 439

# Appendix 1

## Quantized Redshift Structure Within Galaxies
## Steward Observatory Preprint 513

**Abstract**

The hypothesis that a 72 km/s redshift discontinuity occurs in the nuclei of galaxies is tested against observed rotation and internal velocity dispersion (sigma) data for elliptical galaxies. The discontinuity will add to or subtract from any bulk motions present, rotation and/or expansion, to generate two specific families of rotation and dispersion behavior. Ellipticity ($\epsilon$) and maximum rotation values, $V_C$, correlate to form a two branched relationship. Both branches begin at $V_C = 36$ km/s at eccentricity = 0. One branch (reinforcing) rises smoothly with eccentricity while the other (opposed) drops to $V_C = 0$ near eccentricity = 0.2 and then rises, remaining 72 km/s below the first branch. Observations are consistent with expectations.

Radial dispersion gradients are likewise expected to divide into steep (reinforcing) and flat (opposed) families as is also observed. Combining rotation and dispersion data a critical test is developed. The steep dispersion gradient family for faint ellipticals is shown to populate the upper eccentricity-$V_C$ branch, and the flat dispersion objects to follow the lower eccentricity-$V_C$ track precisely as expected. Both rotation and radial flow are important for lower luminosity ellipticals. Rotation becomes less important in luminous objects. The $M_B$-mean dispersion relationship is found to contain an apparent banded structure. Slope, spacing, and morphological properties of dispersion bands are directly related to corresponding properties of redshift-magnitude bands.

The dual redshift model for individual galaxies is further tested by examination of newer 21-cm radio date for M31. Apparent warping and other disc disturbances arise as a natural consequence of forcing a conventional dynamical model onto the two redshift pattern. A detail analysis of the nucleus of M31 further shows 72 km/s quantization of planetary nebula velocities.

## 1.1 Introduction

There is now strong evidence that redshift intervals between galaxies within physical systems are quantized with a dominant interval near simple multiples of 72 km/s. Recently three independent test samples have confirmed the quantization originally indicated by Tifft 1976 [55]. Double galaxy differentials by both radio (Tifft 1982a [81]) and optical (Tifft 1982b [83]) techniques show the periodicity clearly as do radio redshifts within compact groups (Cocke and Tifft 1983 [84]). Figure 1 shows an analysis for characteristic redshift intervals in the combined radio data for pairs and groups. The 72 km s-1 periodicity stands out

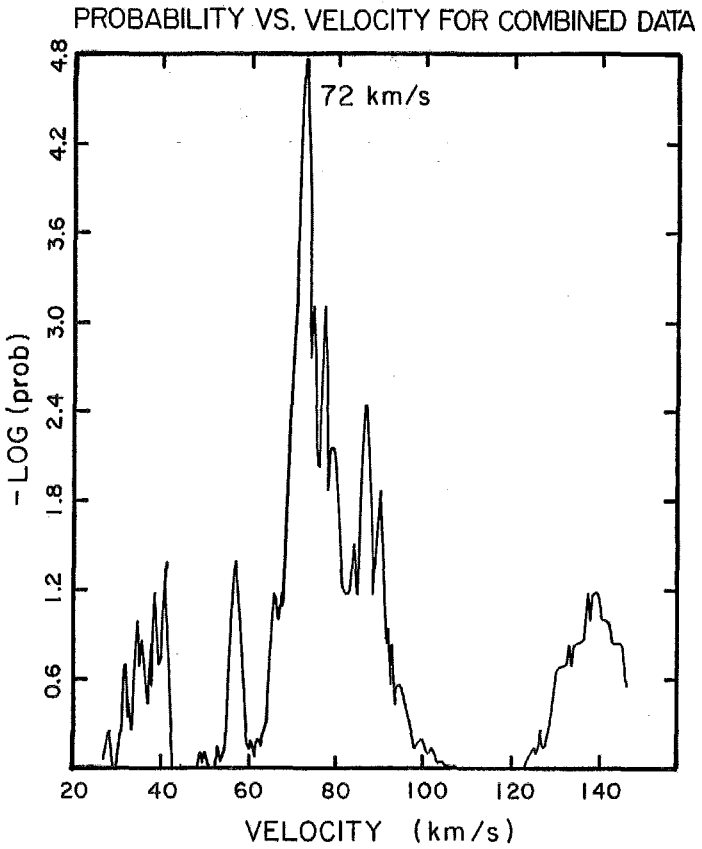


Figure 1.1: The logarithm of the probability of finding the observed periodic clumping in redshift intervals for radio data on differentials in pairs and groups, as a function of period. Procedures for grouping data and calculating probabilities are given by Cocke and Tifft (1983 [84]). Pairs and groups used are from Tifft (1982b [83]) and Cocke and Tifft (1983 [84]).

with a probability of random occurrence of only $10^{-5}$. With the optical test included the likelihood is at or below$10^{-6}$. Recent studies by Tifft and Cocke (1984 [87]) show that the periodicity is present globally, again at very high confidence levels.

Less well known is a second hypothesis made in 1976 to the effect that galaxies consist of a dominant pair of redshift states characterized by the 72 km/s interval. In this hypothesis galaxies are redshift 'dipoles' consisting of two opposed streams of material with an intrinsic redshift difference of 72 km/s. The concept was originally developed in a series of papers (Tifft 1976 [55], 1977a, b [58,59]) including modeling of rotation curves of several major spiral galaxies, our own and M31 among them. Since these papers appeared there has been a considerable increase in quality and quantity of rotation and velocity dispersion data available for dynamical analysis. Especially notable has been the great progress on E and So systems where previously only nuclear regions could be measured. Ellipticals are especially important since they rotate slowly. With spirals the redshift dipole is mixed with a much larger rotation. For ellipticals the effects are comparable hence some pronounced consequences should be present. This paper examines for such effects and also reviews some current modeling for spirals.

## 1.2 Properties of Ellipticals

Since 1977 rotation and velocity dispersion data of high quality has been published for ellipticals, So galaxies, and spiral bulges. Most of the available material on ellipticals and spiral bulges has been summarized by Davies et al (1983 [BN], henceforth DEA). Data on ellipticals and spiral bulges is therefore adopted from DEA. Values are updated from Davies and Illingworth (1983 [BR]) for four eccentric galaxies. So data is adopted from Dressler and Sandage (1983 [BP]). Table 1 summarizes basic data and derived parameters for ellipticals used in this paper. Current reviews of elliptical dynamics have been given by Illingworth (1981 [BQ], 1983 [BR]).

Peak rotational measurements in ellipticals, included in Table 1, rarely exceed 100 km/s; DEA list only two in excess of 127 km/s. Rotation curves fall into two families, slow rising and rapid rising. There is also a bimodal pattern in velocity dispersion. For many the dispersion drops with radius, however, there is a subset where dispersion remains constant and a few cases where it rises radially. Dispersion depends upon system luminosity and, according to Terlevich et al (1981 [BU]) may also depend upon flattening. Examples and illustrations of rotation and dispersion curves are given by Illingworth (1983 [BR]). There is no satisfactory explanation for the bimodal behavior of rotation and dispersion.

Rotational velocities appear to be generally sufficient to account for the shapes of spiral and So bulges as oblate rotators. The same may be true for lower luminosity ellipticals, however Vrot/dispersion is too small in giant ellipticals for rotation to be the controlling factor. Rotational velocities do not differ much between dwarf and giant ellipticals, however, dispersion drops with luminosity so for dwarfs rotation increases in relative importance. A completely satisfactory description of the shapes and controlling factors in the dynamics of giant ellipticals is still lacking.

## 1.3 The Discrete Redshift and Rotation

The discrete redshift concept introduces an intrinsic redshift discontinuity, normally 72 km/s, at the nucleus of a galaxy. This discontinuity may reinforce or cancel bulk motions,

# Table 1

## Basic Data for Ellipticals

| ID | ε | $V_{max} = V_c$ | σ | $\sigma_o - \sigma$ | σ band | $-M_B$ | Class | $V_T$ |
|---|---|---|---|---|---|---|---|---|
| N4878 | .07 | 50 ± 10 | 244 ± 28 | − 1 | ++ | 20.30 | O | 20 |
| N5638 | .09 | 62 ± 13 | 152 ± 3 | 2 | + | 20.36 | O | 32 |
| N5831 | .09 | 27 ± 9 | 148 ± 5 | 4 | + | 20.09 | O | − 3 |
| N7619 | .09 | 65 ± 14 | 298 ± 18 | 56 | +,− | 22.39 | R | 29 |
| N4374 | .10 | ≤ 38 | 261 ± 22 | 37 | + | 21.24 | R | ≤ 2 |
| I4296 | .10 | 64 ± 12 | 291 ± 11 | 9 | − | 22.94 | O | 34 |
| N3379 | .13 | 43 ± 11 | 184 ± 9 | 47 | + | 20.62 | R | 7 |
| N4486 | .14 | ≤ 20 | 303 ± 10 | 33 | + | 21.99 | : | |
| N4478 | .15 | 62 ± 4 | 142 ± 4 | 3 | ++,+ | 19.42 | O | 32 |
| N7626 | .17 | ≤ 30 | 324 ± 24 | − 54 | + | 22.23 | : | |
| N4472 | .18 | 44 ± 10 | 256 ± 18 | 54 | − | 22.23 | R | 8 |
| N4551 | .19 | 38 ± 5 | 114 ± 3 | − 4 | ++ | 18.70 | O | 8 |
| N4636 | .19 | 79 ± 30 | 189 ± 28 | 38 | +,− | 21.04 | R | 43 |
| N4649 | .19 | 60 ± 9 | 305 ± 21 | 56 | + | 21.72 | R | 24 |
| N4406 | .24 | 31 ± 16 | 244 ± 6 | 9 | + | 21.44 | O | 67 |
| N4365 | .25 | 15 ± 15 | 247 ± 16 | 17 | + | 20.94 | O | 51 |
| N5813 | .25 | 8 ± 2 | 219 ± 3 | 6 | + | 20.85 | O | 44 |
| N1600 | .26 | ≤ 30 | 304 ± 17 | 28 | − | 22.90 | : | |
| N3904 | .26 | 63 ± 3 | 203 ± 5 | − 6 | + | 20.77 | O | 99 |
| N1700 | .29 | 74 ± 30: | 256 ± 10 | − 5 | − | 22.77 | : | |
| N2778 | .29 | 99 ± 7 | 141 ± 10 | 37 | + | 20.33 | R | 63 |
| N7562 | .29 | ≤ 40 | 241 ± 12 | 33 | − | 21.87 | : | |
| N4889 | .30 | 14 ± 7 | 342 ± 20 | 12 | − | 23.39 | : | |
| N 315 | .31 | ≤ 30 | 311 ± 11 | 3 | − | 23.08 | : | |
| N1052 | .31 | 96 ± 5 | 207 ± 13 | 38 | + | 20.87 | R | 60 |
| N3557 | .32 | 178 ± 20 | (253 ± 20) | (− 31) | − | 22.56 | : | |
| N3818 | .32 | 114 ± 7 | 151 ± 10 | 45 | + | 19.83 | R | 78 |
| I2082 | .33 | < 31 | 230 ± 16 | 38 | −− | 23.25 | : | |
| A2029 | .33 | < 20 | 369 ± 5 | 6 | − | 23.42 | : | |
| N4742 | .34 | 83 ± 2 | 67 ± 6 | 43 | + | 19.44 | R | 47 |
| N5845 | .35 | 127 ± 5 | 194 ± 20 | 69 | ++ | 19.43 | R | 91 |
| N 596 | .37 | 73 ± 16 | 143 ± 14 | 22 | − | 21.24 | : | |
| N 720 | .37 | 76 ± 12 | 214 ± 11 | 25 | − | 21.70 | : | |
| N3377 | .37 | 80 ± 6 | 131 ± 8 | 21 | + | 19.76 | : | |
| N4387 | .38 | 57 ± 5 | 102 ± 3 | 9 | ++ | 18.60 | O | 93 |
| N4697 | .38 | 103 ± 3 | 161 ± 11 | 20 | − | 21.34 | : | |
| N 584 | .39 | 159 ± 5 | 183 ± 4 | 47 | −,−− | 21.81 | : | |
| N7785 | .40 | 100 ± 17: | 233 ± 9 | 7 | − | 22.03 | : | |
| N3605 | .41 | 52 ± 5 | 90 ± 3 | 1 | ++ | 18.16 | O | 88 |
| N4472 | .42 | 60 ± 3 | 183 ± 3 | − 3 | + | 20.52 | O | 96 |
| N4839 | .51 | 23 ± 10 | 255 ± 9 | 14 | −− | 23.17 | : | |
| N6909 | .52 | 23 ± 4 | 115 ± 6 | − 3 | − | 20.99 | : | |
| N2768 | .56 | 102 ± 8 | 187 ± 8 | 31 | − | 21.50 | : | |

rotation or expansion, depending upon the observers location. Figure 2 schematically illustrates the two situations, which are equally probable, for varying amounts of rotation.

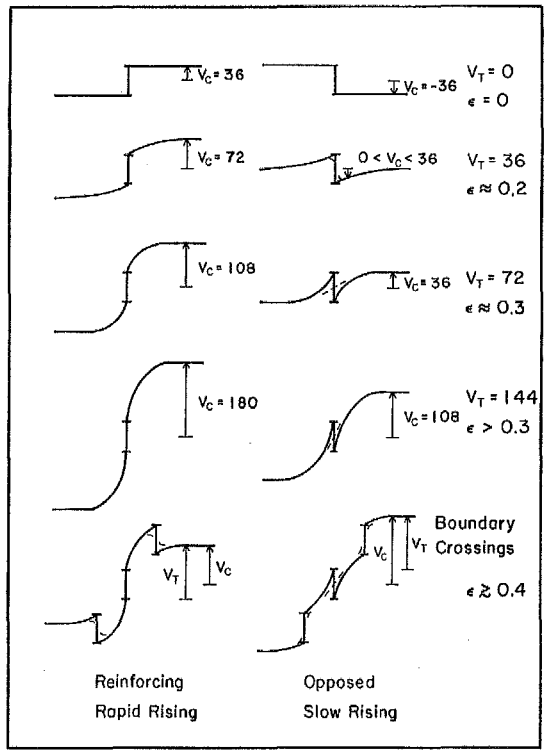


Figure 1.2: Schematic rotation curves including redshift offsets due to an intrinsic 72 km/s discontinuity at the nucleus and other boundaries between two intrinsically different opposed streams. The offset may reinforce or oppose rotation. $V_T$ is the true rotational velocity while $V_C$ is the apparent rotation ignoring the offset. Epsilon is the observed eccentricity which increases with rotation.

In the two-stream concept true rotation, $V_T$, must be measured from the ends of the discontinuity. This differs from the conventional rotation measure, $V_C$, which refers to the mean systemic redshift and is usually simply half the total differential between opposite sides. In general the sharp nuclear discontinuity itself will be considerably blurred by resolution and integration through an optically thin system where the line of sight encounters both streams. Away from the nucleus relatively pure sections of each stream should be encountered. The blurring itself is discussed in the following section. Because of the blurring the principle effects on rotation will be seen in the overall properties of $V_C$ or $V_C$ vs ellipticity rather than by detailed evaluation of specific curves.

The first obvious effect is that two families of curves can be produced, steep (reinforcing) and flat (opposed) types as observed. Since rotation velocities rarely exceed 100 km/s it is obvious that a systematic shift of 72 km/s will produce a distinctly bimodal pattern. A

second effect relates $V_C$ to eccentricity, at least to the extent that shape is influenced or determined by rotation.

For a round, non-rotating ($V_T = 0$) system the redshift dipole model has a discontinuity and two flat arms as shown at the top of figure 2. The conventional rotation measure for such systems is $V_C = 36$ km/s, however, independent of orientation. This is true even for pole-on flattened systems so long as the redshift profile does not cross multiple windings of streams. As real rotation is added to the reinforcing dipole $V_C$ rises smoothly with $V_T$ but is sytematically 36 km/s high. For this case a smooth correlation of eccentricity with $V_C$ is expected converging to 36 km/s at zero eccentricity.

For the opposed dipole the situation differs. As rotation increases from zero, $V_C$, defined by the extended side-to-side differential, drops until at $V_T = 36$ km/s it reaches zero. $V_C$ then rises smoothly with rotation but lags $V_T$ by 36 km/s. Thus a conventional rotation measure of zero is possible, but not for round systems. Zero $V_C$ will occur at some non-zero eccentricity.

From the above we see that the general rotation - eccentricity relationship should converge to $V_C = 36$ km/s at zero eccentricity. There should then be an ascending and a descending branch for small eccentricities. The descending branch will reach zero at some small eccentricity (except see below) and for higher values two parallel branches, spaced by 72 km/s will rise together. Figure 3 shows that this is what the available observations show.The zero minimum occurs close to eccentricity 0.2.

Several factors complicate the ideal form of the relationship. Inclination makes systems appear too round, although this is partially offset by projection of the rotation component. This tends to populate the region above and left of the curves in figure 3. It is easily seen for So systems where inclination can be estimated. The more inclined galaxies have accordingly been omitted from the Dressier and Sandage (1983 [BP]) list. Note that the usual procedure for correction of rotational amplitude for projection is incorrect when it includes an intrinsic component.

For the more rapidly rotating systems, larger eccentricities, another complication may enter. Multiple windings of the streams are possible and the large scale differential redshifts between sides may significantly deviate from a simple two-branched pattern. Multiple windings can further produce apparent rotational peaks at relatively small radii as illustrated at the bottom of figure 2. Such peaks are observed in ellipticals but in conventional dynamics are not expected as close to the core as observed.

A special case of peaking very near the nucleus occurs for the opposed dipole at small eccentricities, less than the zero minimum at eccentricity 0.2. For small rotations the reverse slope is so flat that nearly a constant rotation of roughly 30 km/s should be measured and interpreted to peak quite close to the nucleus. At higher rotation values the central break is largely lost and only the large scale difference between sides is seen. Above eccentricity 0.2 the reinforcing and opposed dipoles will yield $V_C$ systematically high or low, respectively, by 36 km/s. Below eccentricity 0.2 both can be measured too high, reinforcing by 36 km/s and opposed by roughly 30 km/s. Once multiple windings occur no simple correction to convert $V_C$ to $V_T$ for all cases is possible. Multiple windings at large eccentricities could cause appreciable underestimates of rotation. The first peak seen, caused by a winding, may be interpreted as the peak rotation. In fact the curve might continue to rise outside

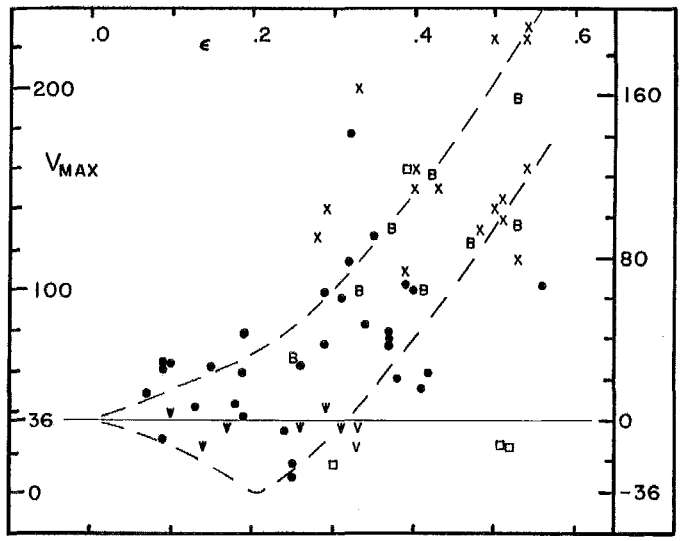


Figure 1.3: Maximum observed rotational velocities as a function of eccentricity. Filled circles refer to ellipticals from Davies et al. (1983 [BN]), open squares to ellipticals from Davies and Illingworth (1983 [BO]). Crosses designate So galaxies, with inclination $< 12^{o}$, from Dressier and Sandage (1983 [BP]) while spiral bulges from Davies et al. are designated B. Down arrows designate upper limits. The scale at the right is rotation corrected for the average nuclear 72 km/s discontinuity. The dashed lines represent rotation for reinforcement or opposition of rotation by the nuclear offset.

the observed region. In the following section we will specifically identify and correct for the dipole class when possible to convert $V_C$ to $V_T$. In general, the presence of rotation curve families, and the relationship of rotation to eccentricity are closely in accord with expectations of the two-stream intrinsic redshift model.

## 1.4 The Discrete Redshift and Velocity Dispersion

The line of sight near the nucleus of an optically thin galaxy built according to the two-stream model will generally encounter both streams. In outer regions the line of sight can be increasingly dominated by one stream. The material in an individual stream has an inherent real 'true velocity dispersion', $\sigma_T$. This dispersion, observationally, is rarely much less than 100 km/s and apparently increases with luminosity. Since this true velocity dispersion equals or exceeds the 72 km/s redshift dipole spacing, a blending of streams must yield a single broadened line. The transition from central blended streams to individual stream dominance away from the nucleus implies a typical radial drop in observed dispersion, $\sigma_C$, independent of other causes. This variation will be compounded by radial variation in $\sigma_T$ and any contributions from bulk motions, rotation or expansion. In the absence of bulk motions, the line profile produced by convolving $\sigma_T$ over the dipole is independent of the

dipole orientation.

In conventional dynamics, bulk motions can only increase observed dispersion over true dispersion. In the two-stream model observed dispersion is enhanced over true dispersion by the intrinsic dipole, and as with $V_C$, may be increased or decreased by bulk motion depending upon whether it reinforces or opposes the dipole. The motion effectively increases or decreases the dipole spacing. Small effects in line shape and symmetry would also be expected. As with rotation we have a mechanism which can alter dispersion and generate families of dispersion curves. The duality property of the two-stream model provides both a powerful test for the concept and a tool for distinguishing bulk motion from true dispersion.

Two forms of bulk motion, rotation and expansion, must be considered. Rotation will contribute to observed dispersion via gradients along the line of sight. We may investigate this through the relationship of $\sigma_C$ to $V_C$ and eccentricity. Radial flow at some level is an inherent part of the two-stream model. Galaxies are constructed from material flowing from the nuclear discontinuity in two opposed streams. Expansion effects will be a maximum if the dipole is end-on and a minimum when crosswise. Rotation is independent of orientation within the equatorial plane, and when dominant will generate an oblate figure. Two-stream expansion can generate a prolate figure or enhance flattening in a rotating oblate system. The dependence of observed dispersion on eccentricity should distinguish rotation from radial flow. Rotation, clearly present at large eccentricities, will enhance observed dispersions for large eccentricities while expansion is effective at small eccentricities.

To determine what, if any, role bulk motion plays in fixing observed dispersion we require an index sensitive to bulk motion. The line of sight through the nucleus incorporates the maximum rotational gradient (assuming a reasonable sized aperture is used) and any radial streaming effects as well as essentially equal portions of both streams. The central dispersion, $\sigma_o$, therefore maximizes the desired information. $\sigma_o$ is also highly luminosity dependent hence cannot be used directly. Instead we will use a differential index $\sigma_o - \bar{\sigma}$ where bar implies is the mean over the central region as defined and tabulated in DEA. We will assume that for such an internal differential a good degree of cancellation occurs for luminosity dependence. We are left with an index dominated by bulk motion, radial variation in true dispersion and dipole mixture gradients.

As a second consideration to reduce luminosity dependence we will work with somewhat restricted subsamples based upon the relationship of $\bar{\sigma}$ to absolute magnitude. We use $\bar{\sigma}$ since it is less sensitive to bulk motion than $\sigma_o$. We adopt $M_B$ as given by DEA for a standard cz/H distance scale. The value of H is of no consequence and we will comment later on the question of Virgocentric deviations. Figure 4 gives the relationship of $\bar{\sigma}$ to $M_B$. The diagram contains 'bands' directly analogous to redshift-magnitude bands.

The banded character of figure 4 is discussed separately in the next section since most of the following is not significantly dependent upon that interpretation. Whether due to band-related properties or simply to luminosity, it is obvious that a subsample with less luminosity range should contain less luminosity dependent effects. The subsample we initially define is the two faintest bands. The part above $M_B = -21.5$ will be included but distinguished, otherwise there is very little overlap with the brighter group. From band theory this is a rational sample since the most active or advanced evolutionary processes, which include bulk motion, are to be found in the brightest band(s) and at the luminous ends of bands.

As a second subsample we take all objects not in the first set. Table 1 identifies the band assignments according to the notation in the figure.

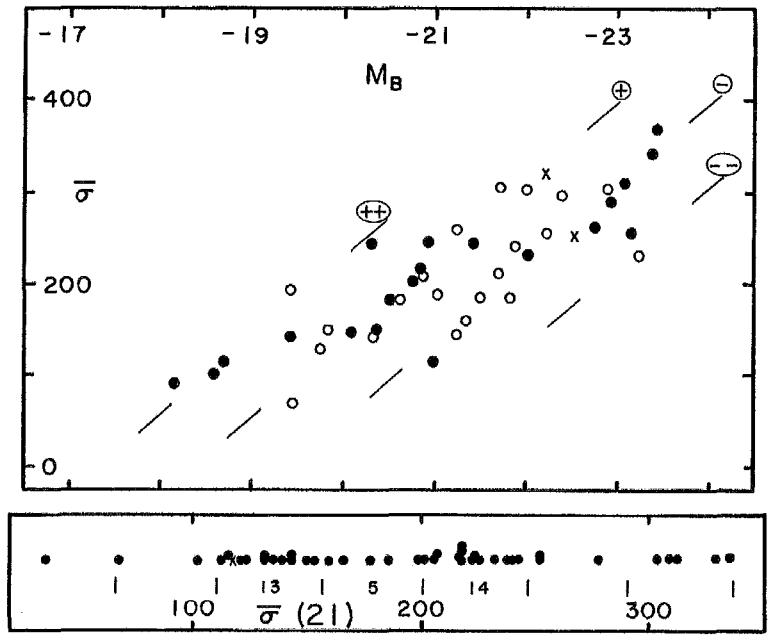


Figure 1.4: Absolute magnitude as a function of mean central region dispersion for ellipticals. Filled circles refer to galaxies with small dispersion gradients, open circles to steep gradient objects. Two galaxies with dispersion rising outward are marked x. The galaxies distribute in a banded pattern as indicated and designated by the circled symbols. At the bottom the distribution of $\bar{\sigma}$ is shown projected to $M_B = -21$, along the band direction, to demonstrate the nearly 3:1 deficiency of points through the center of the distribution.

The upper part of figure 5 demonstrates that the faint subsample shows two distinct $\sigma_o - \bar{\sigma}$ families, one near zero, the other near 40. The families are equally populated and show no dependence of either $\sigma_o - \bar{\sigma}$ or population on $M_B$ above $-19.0$. The sample below $M_B = -19.0$ is too limited at present to judge. The lower part of figure 5 shows that there is a full range of ellipticity in both families and the differential dispersion is not obviously dependent on ellipticity.

These figures show the bimodal property of dispersion characteristics of ellipticals very well. There is no way that radial variation in $\sigma_T$ can generate two families without invoking two distinct dynamical models. The families do arise naturally from bulk motion in the two-stream model. The family at 40 corresponds to motion reinforcing the dipole, the family near zero to canceling motion. The division further satisfies the requirements of random viewing geometry where the two families cannot distribute differently in parameters not influenced by dipole orientation, such as $M_B$. We designate the families R = reinforcing, O = opposed.

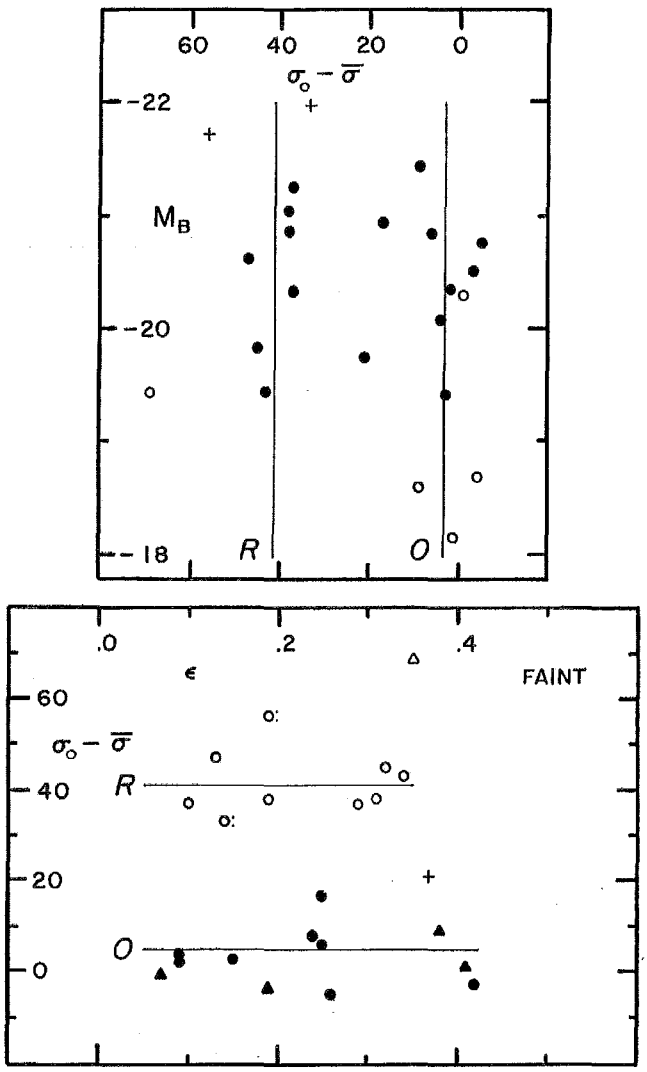


Figure 1.5: The division into two dispersion gradient families for galaxies on the two faintest dispersion bands. In the upper panel the index $\sigma_o - \bar{\sigma}$ (central - averaged dispersion) is related to absolute magnitude. Filled circles are + band objects, open circles ++ band galaxies. Above $M_B = -21.5$ galaxies are plotted with crosses. In the lower panel the $\sigma_o - \bar{\sigma}$ index is plotted against eccentricity. Circles refer to + band and triangles to ++ band galaxies. Colons denote the two objects brighter than $M_B = -21.5$. Open and filled symbols indicate the two families, R and 0, corresponding to reinforcement or opposition of motions by the nuclear redshift discontinuity. The cross is uncertain as to assignment. There is no detectable dependence of either absolute magnitude or eccentricity on dispersion gradient family assignment.

To provide a relatively constant spacing with eccentricity both expansion and rotation are involved, expansion at small eccentricity, rotation at large eccentricity. Rapid nuclear rotation decoupled from the main body, acceptable in normal dynamics, is not consistent with the two-stream concept since the streams are connected to the nucleus. A very powerful test is available to check the association of family assignment with rotation. If we correlate $\sigma_o - \bar{\sigma}$ with $V_G$ each family must behave in a characteristic way when grouped by eccentricity. For eccentricity less than 0.19 both groups should have similar $V_G$ values but for larger eccentricities the families must separate so the O-group has $V_G$ characteristically less than the R-group. The two upper panels in figure 6 illustrate this test.

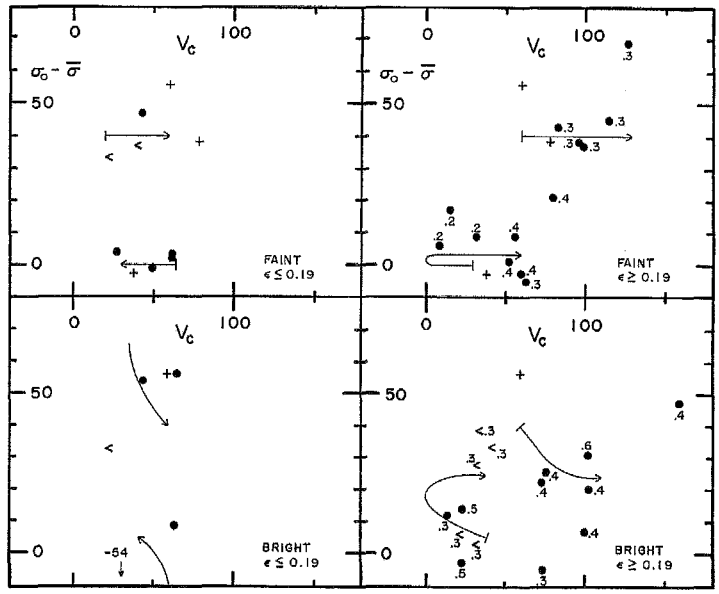


Figure 1.6: The relationship of dispersion gradient, indicated by $\sigma_o - \bar{\sigma}$ (central-averaged dispersion) to apparent maximum rotational velocity, $V_G$. The upper panels refer to the faint sample, the + and ++ band objects, while the lower panels refer to the luminous objects which populate the – and –– bands. The left panels contain objects with eccentricity = 0.19, the right panels show galaxies with eccentricity = 0.19. Objects with eccentricity = 0.19 are denoted by crosses in both sections and eccentricity is indicated beside each symbol for eccentricity > 0.19. The two dispersion gradient families follow different tracks in $V_G$ as eccentricity increases.

Both groups begin near $V_G = 36$ km/s at small eccentricity as required. The arrows indicate the direction of increasing eccentricity with the cross symbols for eccentricity 0.19. When we pass to larger eccentricities the R-group continues to shift smoothly to higher $V_G$ while the O-group drops to $V_G = 0$ and reflects. The groups have exactly the $V_G$ properties predicted by the two-stream theory. There is a precise correlation between the dispersion groups and the two branches of the $V_G$-eccentricity relationship. Figure 7 illustrates this directly by plotting the two groups separately in $V_G$-eccentricity diagrams

There is a near perfect correspondence with the two 72 km/s spaced branches. There is no reason why the position within the $V_G$ scatter at any fixed eccentricity should correlate perfectly with groupings based upon dispersion gradients unless the dipole model is basically correct and bulk motion an important contributor to observed dispersion. We therefore take this test to be a very powerful confirmation of the theory. A formal rank-sum test for the faint eccentricity greater than or equal to 0.19 sample confirms that the $V_G$ distribution in the R-group has only a 0.0001 chance of being equivalent to the O-group distribution.

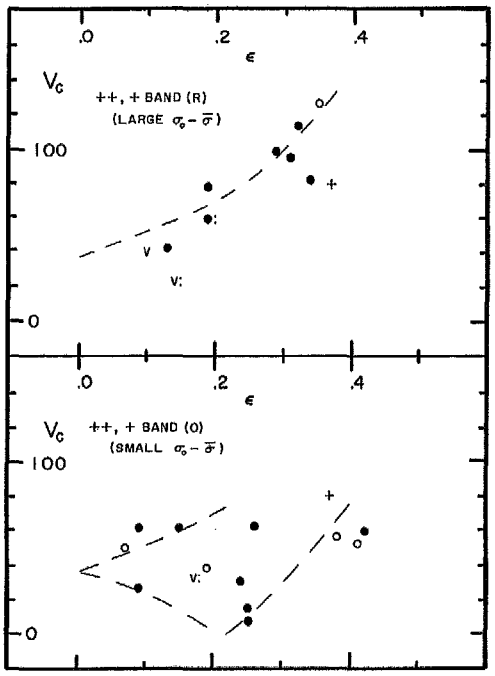


Figure 1.7: The relationship of eccentricity and apparent maximum rotational velocity for the faint sample, + (filled circles) and ++ (open circles) galaxies. The upper panel includes galaxies with steep dispersion gradients; the lower panel refers to flat gradient objects. The cross is an object which could be in either class. The two dispersion gradient families populate different branches of the $V_G$-eccentricity diagram. Large $\sigma_o - \bar{\sigma}$ objects occupy the R (reinforcing) branch while small differential dispersion objects associate with the O (opposed) branch.

The lower part of figure 6 displays the luminous galaxies. The points of low eccentricity fall at intermediate $V_G$ values as previously demonstrated. Note that the brightest points from the faint sample are repeated. If anything the brighter low eccentricity galaxies show a wider $\sigma_o - \bar{\sigma}$ separation, particularly if some weight is given to the anomalous $\sigma_o - \bar{\sigma}$ value of $-54$ for NGC 7626 which has eccentricity 0.17, $V_G$ less than or equal to 30. Further low eccentricity giants will be required to refine this impression since nearly round objects are rare in the available sample. The paucity of low eccentricity points may be due in part to selection for rotation studies.

The more eccentric giants divide into two groups as did fainter galaxies, one dropping in $V_C$, the other rising. Now, however, there is also a definite change in the differential dispersion. The luminous eccentric galaxies tend toward intermediate values. The differential dispersion index no longer provides a clear basis for family assignment although on average most O-class points (low $V_C$) fall below most R-class objects (large $V_C$). The points divide equally as geometry requires but in individual cases specific type assignment is doubtful. Comparison of the faint and bright samples in figure 6 reveals one further difference. In any given $V_C$ range the giants are consistently more flattened. This is the well recognized problem that for bright ellipticals there is insufficient rotation to provide observed flattening.

Figure 8 gives the relationship of true rotational velocity to eccentricity for the faint galaxy sample where conversion from $V_C$ to $V_T$ appears to be straight forward using family assignment from differential dispersion values.

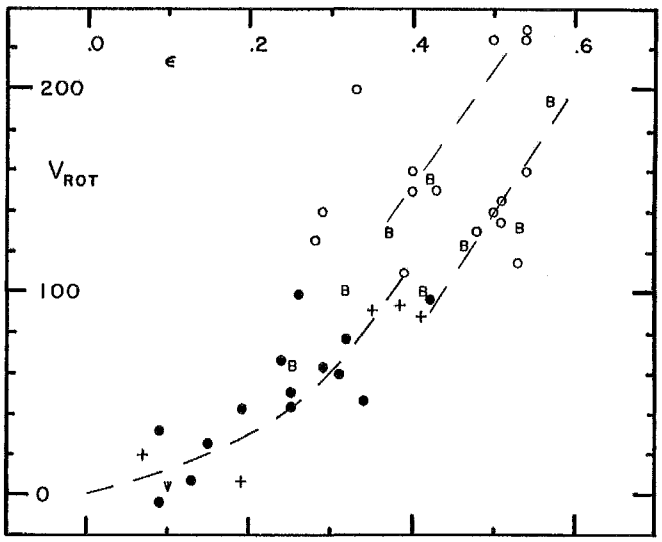


Figure 1.8: The relationship of true rotation, after correction for nuclear redshift discontinuity, to eccentricity for ellipticals on the + band (filled circles) and ++ band (crosses). So galaxies (open circle) and spiral bulges (B) are copied from figure 3 and include no discontinuity corrections. A single eccentricity growth curve now represents the ellipticals and merges smoothly with So and bulge data which still includes the dipole splitting.

$V_T$ rises smoothly from zero and merges directly with the So and spiral bulge data. The So and spiral bulge rotations are not corrected since we have no objective criterion to do so, but the dual pattern spaced by 72 km/s is easily seen. The giant ellipticals must follow a much flatter curve. $V_C$ still divides into the two dipole orientation families but rotation plays little role in $\sigma_o - \bar{\sigma}$ since both orientations converge to similar values at large eccentricities. Thus neither shape nor central dispersion of giants can be controlled by rotation. For dwarfs a general consistency of shape and dipole families with rotation is present. Central dispersion is distinctly related to rotation.

The one pattern which emerges consistently for all luminosities is the separation of dipole families at low eccentricities. This is consistent with shape if we invoke expansion to interact with the dipole shift. The implication is that expanding motion of order 50 km/s is the rule in elliptical nuclei. Similar expanding models were constructed for dipole based spirals previously (Tifft 1976 [55]). Such expansion, persistent for long times, can readily explain the giant ellipticals. Radial expansion in the rotational plane will flatten the rotation curve and enhance ellipticity as observed.

## 1.5 Dispersion Bands

The significance of the apparent banded pattern in figure 4 relating dispersion to $M_B$ can be estimated very simply. When the bands are projected to yield the distribution function shown below the main diagram the density contrast between the main bands and an equal interval midway between is close to 3:1. This contrast can occur (Tifft 1982b [83], Fig 1) only if the scatter, s, within the bands is in the range of 1/4 to 1/5 of the band spacing. The implied uncertainty in $\bar{\sigma}$ from the contrast ratio is about 20 km/s, in adequate agreement with DEA estimates which range from 3 to 30 km/s. The projected band spacing is 4 to 5 s, hence the chance of accidentally producing the central deficiency must be less than a few parts in a thousand.

Direct evaluation of significance for dispersion bands is not the only basis for believing that they could be real. Dispersion bands possess properties identical to redshift magnitude bands. Within a given physical subsystem, cluster or group, there appears to be a one-to-one correspondence. Total magnitude redshift-magnitude bands in the Coma cluster, for example, have a slope of 2.5 to 3 magnitudes across the cluster redshift width, and a one magnitude spacing. The dispersion bands have the same slope and spacing. The slope assumed above to project the pattern is not an arbitrary parameter.

A more powerful consistency check relates morphology and internal structure within bands. Redshift-magnitude bands show a morphological trend along each band. Even when E and So types dominate there is a distinct trend in ellipticity (Tifft 1973 [34], Table 4, Fig 6). Overall the DEA ellipticals under discussion show no net correlation of eccentricity with $M_B$. There is no reason to expect one. The differential effects discussed previously which relate to rotation and flattening are much smaller than the overall variation in $\bar{\sigma}$. There is therefore no dynamical reason to expect $\bar{\sigma}$ variation along a band to relate to flattening. Figure 9 shows, however, that for eccentricities greater than 0.19 there is a pronounced correlation.

Ellipticity ranges over the same interval found on the Coma cluster redshift-magnitude bands. A rank sum test for eccentricities above 0.19 on the two well populated bands indicates only a few parts in 1000 chance that the fainter galaxies in either band have the same eccentricity distribution as the brighter galaxies. Dispersion and redshift-magnitude bands are related in slope, spacing and morphological properties.

Galaxies with eccentricities less than 0.19 appear to be an exception to the morphological pattern, and, for that matter, the band pattern as well. The three most deviant points from the $\bar{\sigma} - M_B$ bands all have small eccentricities. The eight most deviant points from the

two main bands in figure 9 have another characteristic in common, they clump at particular values of $\bar{\sigma}$ as shown in figure 10.

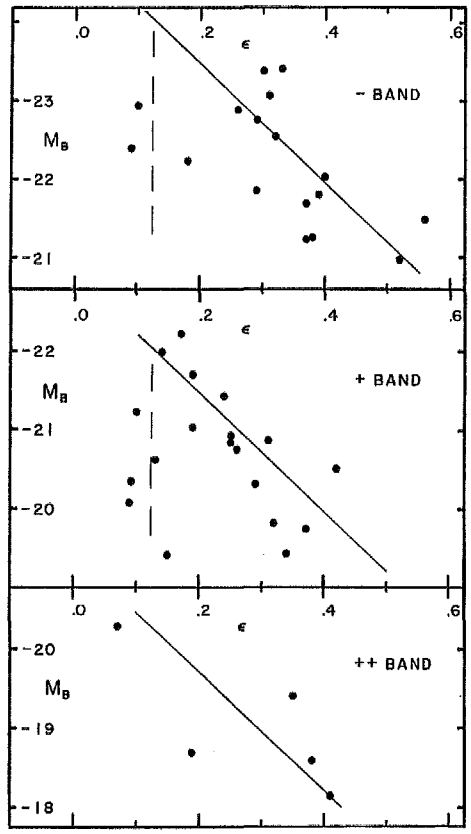


Figure 1.9: The relationship of absolute magnitudes to eccentricity for individual dispersion bands. For eccentricities $> 0.19$ each band shows a progression of eccentricity with fainter absolute magnitude.

Inspection of the general $\bar{\sigma}$ - $M_B$ band diagram suggests a wavy pattern indicated by dashed lines in figure 10. The deviant points clump at breaks in the pattern. An equivalent situation again appears in redshift-magnitude bands (Tifft 1973, 1979 [34,75]). Subgroups along bands, characterized by a slope change and morphological grouping, are separated by gaps. Associated with the gaps are scattered deviant ellipticals. The morphological evolutionary scenario associated with the groups and gaps (Tifft 1979 [75]) is directly consistent with the radial motion associated with the low eccentricity ellipticals in this paper.

Dispersion bands differ in one important respect from redshift-magnitude bands. Redshift-magnitude bands are defined in individual clusters and do not directly superimpose, Dispersion bands represent a superimposition from different redshift ranges and spatial locations. Redshift enters into dispersion bands through the determination of $M_B$ since mean group

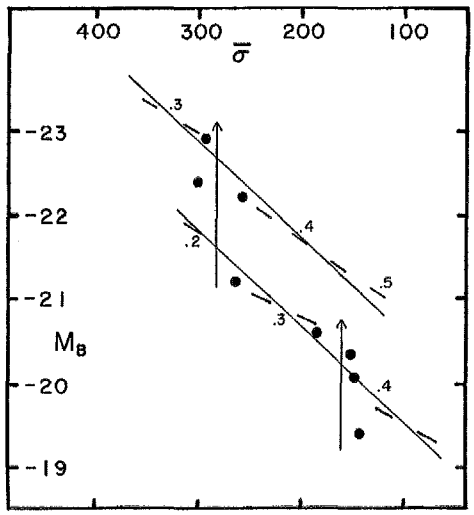


Figure 1.10: The location of deviant + and − band ellipticals with eccentricity $< 0.19$ (filled circles) within the $M_B - \bar{\sigma}$ pattern for more eccentric galaxies. The progressive eccentricity values from figure 9 are written along the bands. The low eccentricity objects appear to concentrate in specific regions where breaks in the smooth distribution of eccentric objects are suggested.

redshift is the basis for the distance estimate. Two conventions for formulating group redshifts are in use. In one case only galactocentric corrections are applied. In the second, allowance is also made for motion of our galaxy within the local supercluster. The latter correction is large enough to noticeably change distance estimates and will affect the superimposition for dispersion bands. Empirically the bands are clear if we omit the Virgocentric correction. This is consistent with the quantized redshift picture which negates relative motion of galaxies in excess of a few km/s. In the intrinsic redshift concept an apparent asymmetry in H can arise since groups at differing distances will be in slightly different evolutionary stages but will be considered to be equivalent in conventional theory.

## 1.6 Spiral Galaxies

In spiral galaxies rotation is generally large compared to any dual redshift effect. We can no longer utilize eccentricity relationships or even correct exactly for tilt which is rarely precisely known. The two-stream model is directly identified with the dual spiral arm pattern, however, and depending upon spatial and spectral resolution, several distinct effects should be present.

When the two-stream dual redshift model was introduced (Tifft, 1976 [55]) a detailed discussion of M31 was included. The study indicated that a model with the two arms differing systematically by 72 km/s was consistent with the data. Since that time a new 21-cm survey has been completed by Cram et al (1980 BM]). Results of the survey have been discussed

by Roberts et al (1978, [BS] henceforth RWC) and Whitehurst et al (1978, [BV] henceforth WRC). They demonstrate the presence of major deviations from motion expected in a simple rotating thin disc. RWC cites the behavior along a line displaced 18 arc minutes from the major axis. The pattern of velocity vs position is X shaped and interpreted in terms of a warped disc which is intersected twice in the line of sight. WRC similarly discuss data along a line displaced 49.5 arc minutes from the minor axis. They see complex multiple profiles and infer a thick disc again favoring multiple cloud intersections. Figure 11 is a representation of M31 with the spiral pattern drawn in accord with the dual redshift model.

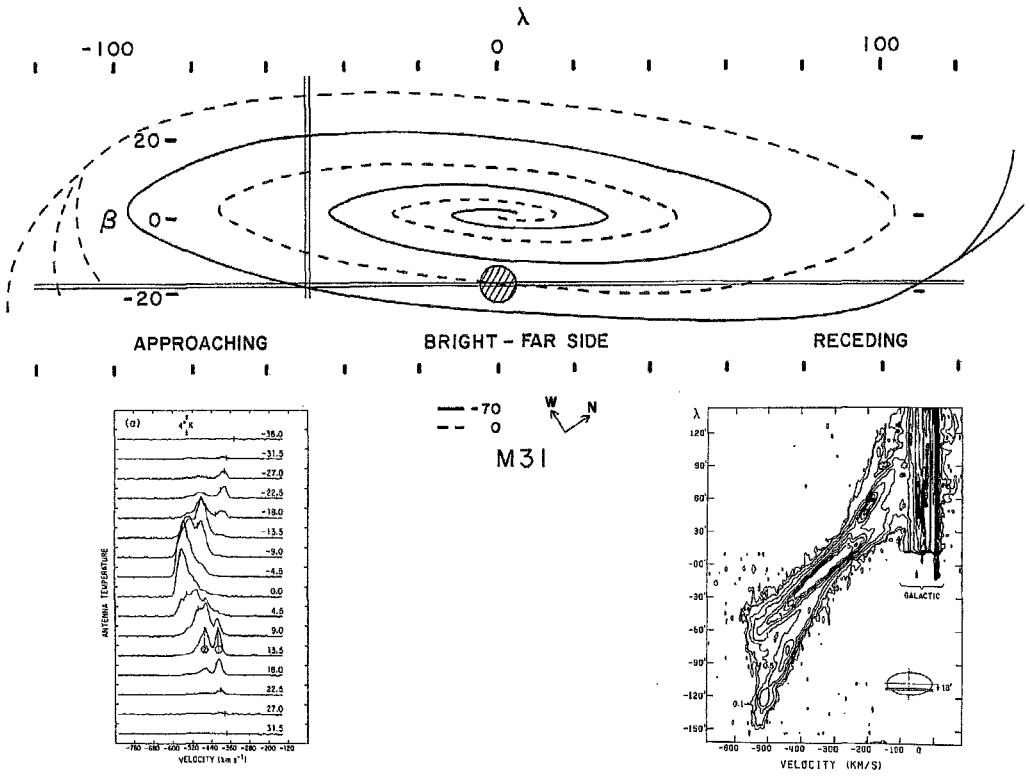


Figure 1.11: Schematic diagram of the M31 spiral pattern for the dual redshift model. The solid arm is intrinsically 72 km/s negative with respect to the dashed arm. $\lambda$ and $\beta$ are coordinates, in arc minutes, along the major and minor axis directions respectively. The insets at the bottom are reproduced from Whitehurst et al (1978 [BV]) and Roberts et al (1978 [BS]) to show 21-cm profiles and velocity patterns along lines of constant $\lambda$ or $\beta$ as indicated. The hatched circle represents the half power radio beam size. Transition between arms relate directly to velocity shifts and profile splitting.

The ends from $\lambda$ 50 to 80 are taken from Tifft (1976 [55]) and smoothly connected. The solid line refers to the arm intrinsically 72 km/s negative with respect to the dashed arm. Arm crossings on the major axis conform to Baade's locations (Baade 1948 [BL]). Insets

give the $\lambda = -49.5$ and $\beta = -18$ diagrams from WRC and RWC which we now examine from the viewpoint of the dual redshift model. Starting on the minor axis and moving NE along the $\beta = -18$ line one moves smoothly along the dashed arm to $\lambda = +70$ or $+80$ where the arm curves into the foreground. The track then crosses rapidly to the $-72$ km/s arm at $\lambda = +110$ which is where the radio map shows negatively displaced material. The displacement is close to the requisite 72 km/s with respect to the main branch of the X pattern. Moving SW from the minor axis we switch smoothly from the dashed to the solid arm. The large beam will blur the transition for even small z-heights hence the radio map should, and does, show a smooth transition toward negative values, forming one branch of the X. By $\lambda = -70$ we move beyond the $-72$ km/s material and the negative branch ends. Again the net displacement is close to 72 km/s. Further out we encounter the zero material and the other branch of the X becomes prominent again.

Analysis of the $\lambda = -49.5$ scan is similar. On the major axis the dominant material at $\lambda = -49.5$ is $-72$ km/s type and the profiles are negatively displaced. At $\beta = -10$ we cross the zero arm. The profiles shift to higher redshift and double with a separation consistent with 72 km/s. With even a modest z-height the large beam will almost always intersect material from two adjacent streams in such a scan. The double profiles persist beyond $\beta = -20$.

The two effects, profile displacement and sometimes doubling, along with an apparent warping, are natural consequences of forcing a two-stream intrinsic pattern into a conventional dynamical framework. An extreme example of warp is provided by M33 where Rogstad et al (1976 [BT]) propose a very large one in the outer regions. Studies of edge-on systems show no warps on the scale required. Further, M33 has no objects nearby that could induce such large effects nor could they persist for long times. In an open spiral such as M33 a conventional model matching the inner 'average' disc will necessarily show large deviations where one crosses the individual outer arm windings. Two anomalous quadrants are virtually certain to occur. Rogstad et al (1976 [BT]) also map a ghost component consisting of high velocity tails and secondary peaks directly compatible with a 72 km/s interval. We take the persistent occurrence of such patterns as direct evidence for the two stream intrinsic redshift model. As with ellipticals discussed earlier anomalies in conventional dynamics are natural consequences of the dual redshift model.

One further example brings together the direct multiple stream mapping for spirals and nuclear dispersion effects in spherical systems. Lawrie (1983 [BK], henceforth DGL) has made a study of planetary nebulae in the M31 nuclear bulge. The rotational gradient across the region is small as discussed by DGL. From the conventional viewpoint the observed velocity scatter provides a direct determination of the velocity dispersion in the nuclear bulge. Within the quantized multiple stream model part of the spread arises from the multiplicity of states present. If the true velocity dispersion is actually small the observed velocities should show the 72 km/s quantization.

Velocities from DGL have individual error estimates ranging from 15 to 80 km/s. The ability to detect a periodicity depends upon data uncertainty (Tifft 1982b [83]). The accurate velocities should show any periodicity clearly and it should fade out completely for the poorest data. Table 2 and figure 12 show that this is what is found.

For formal testing we employ the IN:OUT ratio test for clumping of redshift 'phase' which is the decimal part of V/72.45. Periodic data will clump at a preferred phase. Tifft and

Cocke (1984 [87]) tabulate probabilities of finding particular I/O ratio for various sample sizes. For example, the probability that 12 points selected at random will all fall within a half phase interval is 0.005. Table 2 shows that the 12 DGL planetaries with uncertainty less than 30 km/s clump within such an interval. More accurate values clump more tightly and lower quality velocities show more scatter. Figure 12 shows phase information vs position along the major axis in arc seconds. A linear phase gradient fits well with rotation of 0.25 km/s/arcsec consistent with values from DGL. Upper figure 12 distinguishes phase cycles. Observed velocities span six multiples of 72.45 km/s with the main break occurring across the nucleus. The surge of negative velocities SW of the nucleus corresponds with negative HII velocities mapped by Rubin and Ford (1971 BH]). These velocities were also shown to fit the quantified model (Tifft 1976 [55]). Nuclear and active regions appear to show a wide range of multiplicities. The multiplicity and general discontinuity at the nucleus consistently produce effects which can be discerned in both statistical properties of dynamics for oblate systems and detailed properties of objects within spirals.

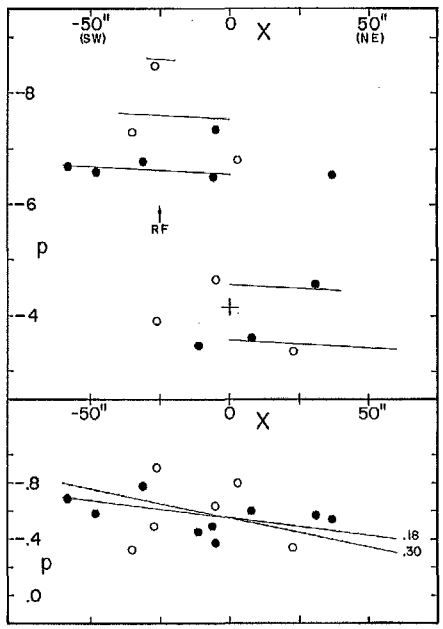


Figure 1.12: Velocity pattern of planetary nebulae in the nuclear bulge of M31. X gives locations, in arc seconds, along the major axis, p is velocity phase V/72.45. The upper panel shows individual cycles; the lower panel superimposes the cycles and shows only decimal phase. Filled circles refer to velocities with accuracies of 20 km/s or better. Open circles extend the data to uncertainties of 35 km/s. A rotational gradient is present near 0.25 km/s/arcsec. Typical values are shown in the lower panel. A cross in the upper panel is the approximate standard nuclear velocity for M31. A strong negative velocity surge SW of center corresponds to similar deviations found by Rubin and Ford (1971 [BH]) in HII (arrow denoted RF). The accurate planetary nebula velocities are periodic, Mod 72, and a nuclear redshift discontinuity is clearly seen.

The author gratefully acknowledges permission from M. S. Roberts, R. N. Whitehurst, and the D. Reidel Publishing Company to reproduce the insets in figure 11. This research has been partially supported through NSF Grant AST-83-10033.

# Appendix 2, Part 1

## The Case for a Time Dependent Quantized Redshift

Steward Observatory Preprint 1027, (Submitted 1992)

### An Introduction to this Appendix

This section of the supplements concerns the paper "The Case for a Time Dependent Quantized Redshift" [114]. The paper was prepared and submitted to the *Astrophysical Journal* in 1992, but was never published. I withdrew it after the second refereeing since it was apparent the referees would simply not pass it for publication. It is a basic paper which develops the case for redshift variability, and includes important 21 cm data from the 140-foot telescope which has never been published. The data and discussions are basic to future studies of variability.

The supplement is presented in three parts, the original paper, my response letter to the editor after the initial refereeing and the first part of the revised manuscript which contains significant revisions. My response gives a good picture of the problems involved in trying to present new fundamental concepts. The only stated objection to publication related to uncertainty in the redshift data. I found the lack of understanding of precision possible with 21 cm measures was incredible. Measures are based upon frequency measurements tied to atomic clocks. There is essentially no possibility of significant errors in comparison of redshifts obtained under nearly identical conditions as discussed in my extensive comparative studies. These studies were completely ignored by the referees, as were the many internal comparisons carried out within the paper. There is little doubt in my mind that the real reason for rejection concerned the incredible implications if the study was correct, and uncertainty was the only apparent escape. The data had to be in error and much of the data was not even mine.

I do not disagree with the importance of refereeing, but I do strongly disagree with the difficulty of presenting serious studies of new fundamental discoveries which are counter to established thought. In this case my response to the second initial referee did result in important improvement in my presentation of a model for redshift variation. The correlation analysis added to the original paper fully supported the quality of the data and brought out the clear importance of asymmetry in relation to variability timing.

I cannot include responses from the referees directly, but my response makes it quite clear what the problems were. The ApJ had reached a point where they were basically unable to find unbiased referees to even review my work. Some later papers were published in *Astrophysics and Space Science* which has a more liberal policy, but such work should not be denied publication in the principal journals. I suggest the reader form his or her own opinion after reviewing the evidence for the demonstrated precision possible with 21 cm measures.

# The Case for a Time Dependent Quantized Redshift

## Original form

**Abstract**

Second epoch 21 cm observations on standard galaxies obtained with the 140-foot telescope confirm that redshift changes appear to have occurred; a pattern of differences which correlate with global redshift phase is present. The period at which the correlations appear was previously predicted as were essentially all other parameters in the analysis. An investigation of 300-foot telescope 21 cm data extending over 10 years has been used to develop and further test a model for the way the variation occurs. Redshifts appear to be relatively stable for intervals of several years and then shift relatively rapidly by multiples of a basic period near 2.7 km/s. The trend of change is generally down in redshift so that over time a negatively displaced wing appears in the redshift residuals. The most recent 140-foot telescope observations indicate that such a shift is apparently developing in the new data. Both 21 cm profile width and shape are parameters in the proposed model for redshift variation. Longer term monitoring promises to provide a very fundamental test on the nature of the redshift.

## 2.1 Introduction

Several basic investigations of 21 cm redshifts have recently been carried out (Tifft and Cocke (1998 [96] henceforth TC), Tifft and Huchtmeier (1990 [104] henceforth TH) and Tifft (1990 [105], 1991a,b [109,111], 1992 [113] henceforth papers I–IV). The earlier papers contain modern data with an emphasis on high precision; comparisons at the level of a fraction of a km/s are readily achieved. The later series of papers establishes a system of 21 cm standard objects and examines for intersystem and time dependent effects using the new data and various older studies. Paper III, in particular, develops the concept that the redshift exhibits rapid variability. The phenomenon is intimately related to global redshift quantization. Time dependent deviations are periodic and proportional to the time intervals involved, which appears to rule out most ordinary explanation. The objective of this paper is to develop the evidence for, and the character of, the time dependent changes in the redshift. We draw upon new 21 cm data obtained in 1991 at the National Radio Astronomy Observatory 140-foot (43m) telescope, and we make specific comparisons with data from the Fisher–Tully (1981 [V] henceforth FT) redshift catalog.

The background which led to the time-dependent redshift concept was presented in Paper III and will not be repeated here. Paper III also specifies a number of critical parameters and properties which we shall briefly review. Little or no further flexibility exists with respect to these conditions; they were specified prior to obtaining the 1991 21 cm data presented in this paper. Paper III also preceded the greater part of the investigations of the FT data contained in this paper. The study of the FT data at profile widths greater than 100 km/s, contained in this paper, was precipitated as a result of the May 1991 observational findings.

Paper III specifies the solar motion and relativistic correction required for calculating the global quantization phase. The solar motion components assumed are $\theta = 232.2, \pi =$

$-36.5$, $Z = 1.2$. The new relativistic correction formalization with $q_o = 0.5$ is assumed; the actual value of $q_o$ is of little importance.

It has been clear since the earliest global studies that quantization properties depend upon 21 cm profile width, $W$. Paper III defines several important profile width intervals. Two ranges, 50 to 75 km/s, and 100 to 200 km/s are recognized as 'critical' windows where properties appear to be stable and especially clear. The narrowest profile galaxies, and objects with profiles between 75 and 100 km/s wide, are considered to be 'transition' objects. The principal transition region, $W = 75 - 100$ km/s, is readily associated with the transition from dwarf irregular galaxies to spirals with a rotating disk. For galaxies with profile widths greater than 200 km/s, the available data are more limited and the accuracy is lower. Beyond some general comparisons we will not discuss wide profile galaxies in this paper. As was the case for solar motion and relativistic corrections, the profile width windows utilized are defined by prior discussion.

Paper III also provides the basic period(s) for the current analysis. Periodicities in a time dependent situation differ somewhat from the static situation originally considered when global quantization was discovered. In the original form the period was determined to maximize clustering of redshift phase. As discussed in Paper III, if redshift is drifting differentially, maximum phase clumping will not in general yield the true period. A two dimensional analysis is required where redshift phase is plotted against the redshift difference at two epochs. The period is found to optimize 'drift-line' structure in such two dimensional diagrams. The periodic structure seen will depend upon the epochs chosen and the nature of the time drift process. An attempt to define the drift process is one objective of this paper.

As was the case for the original global quantization work, the key objects used to define the period are the narrow profile dwarf galaxies, especially those in the critical width window around $W = 60$ km/s. The critical sub-period found in Paper III is 2.6657 km/s, as shown in figure 11 of Paper III. This period appears to define a basic interval, but all cycles of this period are not equivalent in their time drift properties. This interval appears to be modulated such that specific higher multiples produce strong periodic patterns. This is, we believe, the origin of the longer periods which have been discussed in past studies. The non-equivalence of different cycles of the 2.6657 km/s period is well illustrated in figure 10 of Paper III where the period 5.3313 km/s, twice 2.6657 km/s, is utilized. These are the two periods we will use in this paper, which contains, in section 4, a further analysis of the $W = 60$ km/s FT sample. The four to five significant figure accuracy of the periods arises from the fact that they are fine tuned over more than 1000 cycles of the 2.6657 km/s period.

Since Paper III utilized the narrow critical window data to fine tune the period and solar motion, the narrow window data cannot be used to directly evaluate the significance of the periodicity in the data set. In paper III evaluations of significance were largely confined to working with higher multiples of the 2.6657 km/s-1interval. In section 5 of this paper we will demonstrate the significance of this interval in the second critical window centered around $W = 150$ km/s.

The final parameter, which we will use to distinguish subsamples, is the 21 cm profile shape or asymmetry index $A$. The precedent has been set in previous papers and is illustrated in Paper III. We will generally broadly distinguish up to three classes, distinctly negative

$A$, near symmetrical, and distinctly positive $A$. The index $A$, formally defined in TC, is a measure of the deviation of the profile midpoint by area from the midpoint defined by profile level-crossings. Profiles with negative $A$ are dominant on the high redshift side, those with positive $A$ show a low redshift dominant profile.

Section 2 presents the new 1991 NRAO 140-foot telescope data. Section 3 compares the May 1991 data with the 1988 definition observations of the 21 cm standard objects. The time dependent pattern found in this internal comparison provides the point of departure to examine a longer baseline interval, back to the 1970's using FT data, done in sections 4 and 5. Section 6 illustrates continued trends seen in October 1991 140-foot data. Discussion in section 7 includes specific predictions for future work.

## 2.2 1991 Observations

The objective of the TC and TH 21 cm investigations was to determine the precision obtainable through a study of internal and external comparisons. The first indications of a possible redshift time dependence became apparent during these studies. The work culminated with the establishment of a set of 100 standard objects defined in Paper I. Investigations of radial and temporal effects in Papers II and III indicated a need to continue observations of the standards. The first major reobservations took place between May 3–14 and October 19–24, 1991. The observations were made at the NRAO 140-foot telescope using the L-band receiver. Procedures used duplicated the original observations in nearly all respects. Total power mode was employed using the original set of positions and center velocities. Bandwidths were set at 10, 5, or 2.5 MHz, as done in 1988, according to the profile width. A few objects were observed at two bandwidths. The only change in procedure was to replace 1.25 MHz observations, used for the narrowest profiles in 1988, with 2.5 MHz observations. The reason for this change is discussed in Paper I, and concerns possible slight systematic effects in flux determinations. Regular pointing and flux calibration observations were made using standard continuum sources. Pointing deviations rarely exceed 10 arc seconds. Flux data are not presented here; no significant improvement over the 1988 data is possible at this time. A second set of galaxies emphasizing objects with wider profiles, where the standard set is deficient, was also observed. Discussion of this sample will be deferred to a later date.

Table 1 contains the May 1991 observations. TC, FT, and UGC numbers are serial identification numbers from the original TC analysis, the Fisher-Tully (1981 [V]) catalog, and the Uppsala General Catalog (Nilson 1973 [BW]). FT numbers beginning with zero, or greater than 1171, are NGC numbers. A complete description of the notation is given in TC or Paper I. The fourth column lists the bandwidth used; 2.5 MHz is abbreviated as 2. Columns Vh, W, A, and S/N list the heliocentric redshifts, profile widths at 20% of the average height of the central 80% of the profile area, the asymmetry index, and the signal-to-noise figure. Definitions of these quantities are given in TC and Paper I. The column Q contains comment codes defined in notes appended to the table. The final columns, DV and DW, give the difference in Vh and W, from the 1988 data, in the sense (new-old) = (1991-1988). Table 2 contains the October 1991 observations in a format identical to Table 1 except that all comments are appended to Table 1.

Note: The data tables for the 1991 data have been moved to the end of the article to minimize the flow of the text. The tables of data are important since this paper was rejected by the

*Astrophysical Journal* and this data has not been published. Since some minor corrections may have been made in the revised paper discussed following this version, the data tables included with this version are the tables included in the revised edition.

## 2.3 The Standards in May 1991

Three years elapsed between the establishment of the 21 cm standards in 1988 and the observations obtained in May 1991. Since FT comparisons, discussed in Paper I, suggest that deviations up to 10 km/s can occur over 10-12 years, we would expect visible changes in 3 years. Comparison of the 1988 and 1991 observations appear to confirm this expectation. Figure 1 displays the redshift difference (May 1991 - 1988), for the critical $W = 100 - 200$ km/s window, as a function of global phase at the 5.3313 km/s period.

A double cycle of phase is plotted to facilitate viewing periodic patterns. The points distribute in a sloping pattern, undisplaced from zero near phase 0.25-0.5, and maximally displaced near phase 0.75-0.0. All parameters in this diagram were fixed prior to the 1991 observations. The diagram appears to be consistent with a real phase dependent drift in redshift since normal random error would not be expected to correlate with phase.

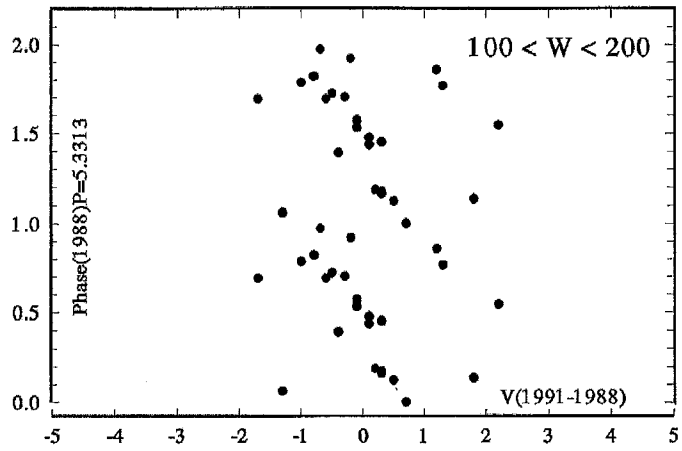


Figure 2.1: Phase-deviation diagram for the May 1991 140-foot telescope data on galaxies with profiles 100 to 200 km/s wide and S/N > 10. Phase is calculated for the 5.3313 km/s period at the epoch of the standard observations, 1988.25, and repeated in a double cycle to facilitate viewing the periodic pattern. Points distribute along sloping lines with a phase offset at zero deviation. The deviation scale is in km/s.

To examine the properties of the data in figure 1 further it is useful to perform a simple transformation. If points are moving in time, the pattern seen will depend upon the epoch at which the phase is calculated. Figure 1 is plotted at epoch 1988.25, the epoch when the standards were defined. If we assume that each point drifts at a uniform rate determined by its present displacement from zero, a point discussed further below, we can reconstruct

the diagram at any epoch. In particular we can choose an epoch where linear sloping features become horizontal. This occurs for figure 1 near 1994.0. Figure 2 shows this transformation for periods of 5.3313 and 2.6657 km/s; only the phase was advanced in this example; deviations will also change by a corresponding scale factor.

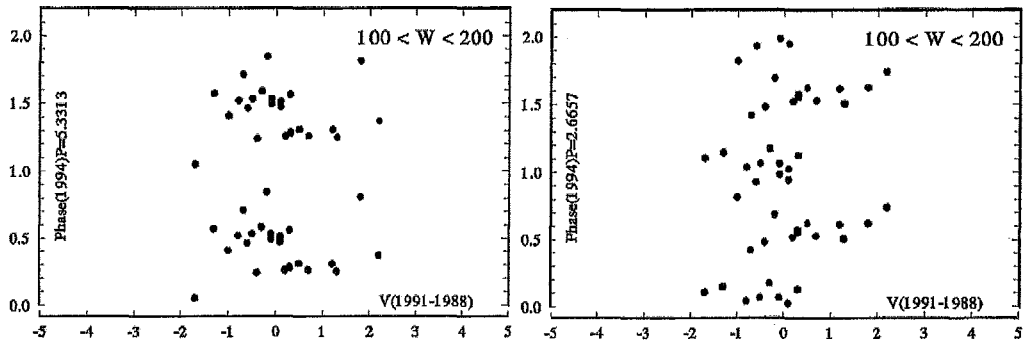


Figure 2.2: Phase-deviation diagrams for the May 1991 140-foot telescope data on galaxies with profiles 100 to 200 km/s wide and S/N > 10. The left diagram is the same as figure 1 with the epoch advanced to 1991 by assuming that phase drift is directly proportional to time. The phase offset at zero deviation is readily seen. The right panel repeats the same data at the 2.6657 km/1 period.

Several properties of the diagram are now readily apparent. There seems little doubt that the points are periodically distributed. There is, however, a distinct phase displacement at zero; positively and negatively displaced points are not continuously related. The phase shift appears to be very close to one half of the 2.6657 km/s period. Actual mean phases are close to 0.05 and 0.55. No special significance can be attached to a precise value since small solar motion uncertainties, especially in Z, could shift the mean phase slightly. Figure 2 also demonstrates the multiplicity of periods which can fit the data. Periods of 10.6626 and 21.3252 km/s also show unique patterns. Drift rates appear to vary in a regular pattern over at least four successive 5.3313 km/s levels. Although we will refer to the 2.6657 km/s interval as a basic sub-period it should be kept in mind that successive cycles are not equivalent in drift rates or timing, and only some are populated.

Although the continuous simple smooth drift rate model used to generate figure 2 is useful to illustrate some properties of the data sets, the model is not consistent with observation of discreet levels. Even if we begin with discreet levels, phase wrapping at a wide range of rates should rapidly destroy any semblance of levels. A more likely model is one where specific levels are populated for some significant period of time. Objects then cascade between levels and are seen changing levels only briefly. Such a model will change the character of figure 2 slightly. If we imagine looking at such a diagram after a time interval involving several transitions, we might still see horizontal bands, but the bands will not be continuous, there should be individual clumps separated by the transition intervals. Objects observed in transition should connect the clumps. This is the model we propose. As a first test we will examine the 10-12 year baseline data between TC and FT observations, looking at each of the two critical profile width windows in turn.

## 2.4 Properties of Narrow Profiles

300-foot (91m) telescope data for FT galaxies in the $W = 50 - 75$ km/s window were used in Paper III to determine the 2.6657 sub-periodicity and to fine tune the solar motion. We now examine that data from the viewpoint of the interlevel transition model proposed in Section 3. Figure 3 shows the $P = 5.3313$ km/s phase-deviation diagram for all TC galaxies with FT data and S/N > 10. Phase is referred to the FT epoch which is characterized as 1975 but can range from 1973 to 1977 for individual points. This diagram differs slightly from the corresponding figure in Paper III where 1988 redshifts were combined with the TC values and a slightly narrower window was used. We opt here to have the maximum possible sample in the minimum time interval. Two arrows in the figure represent transitional paths between phase states which appear as incipient clumps within the levels. The phase 0.5-0.6 level appears to have two states while the phase 0.0 level has only one.

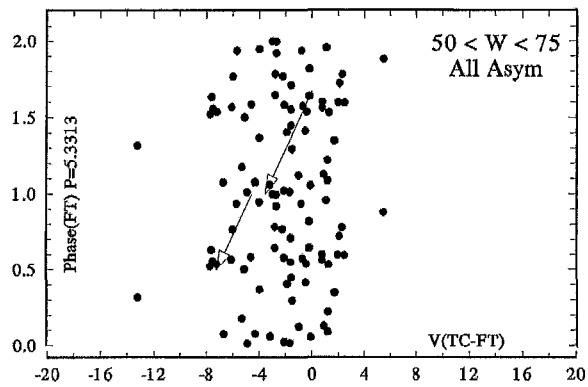


Figure 2.3: Phase-deviation diagram for TC-FT 300-foot telescope data on galaxies with profiles 50 to 75 km/s wide and S/N > 10. Phase is calculated for the 5.3313 km/s period at the FT epoch. The deviation scale is in km/s. Two vectors illustrate the tracks points would follow if undergoing a transition between levels.

In the integrated form in figure 3 there is little obvious information. To test the level and transition concept we need to divide the sample into homogeneous subsamples which we can associate with different stages. We have only one parameter to use, profile asymmetry; however, Paper III and earlier studies indicate asymmetry and phase are often correlated. In this case the correlation is quite informative. Figure 4 replots figure 3 to include only objects within 5% of symmetrical. Two of the three clumps noted above, one at each level, now stand out clearly. No points appear along a transition connection between the regions although they bear the expected relationship to each other as indicated by the upper vector in figure 3. From the perspective of the model, the symmetric profile objects can be presumed to be in stable states at the time of each observation; objects in the zero phase group must have changed states *between* the observations.

Figure 5 contains the galaxies with profiles negatively asymmetric beyond the 5% level. The right hand panel contains two circles, which mark the locations of the symmetrical profile objects, and repeats the hypothesized transition vectors from figure 3.

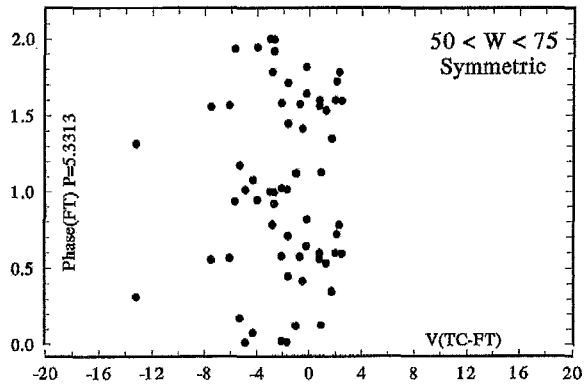


Figure 2.4: Phase-deviation diagram for TC-FT 300-foot telescope data on galaxies with symmetric profiles 50 to 75 km/s wide and S/N > 10. The figure is the same as figure 3 except it omits the galaxies with $|A| > 1.04$. Two clumps or 'states' are present.

The negative asymmetry points distribute along the transition line and extend past the phase zero clump to end at a second suggested clump near phase 0.6. A dashed region defining this clump is drawn shifted one 5.3313 km/s cycle from the clump with zero redshift displacement. The negative $A$ objects lie along tracks which begin at stationary states; from the perspective of the model they are consistent with being leading objects in a transition. The 'new' state being formed contains no objects with distinctly positive asymmetry.

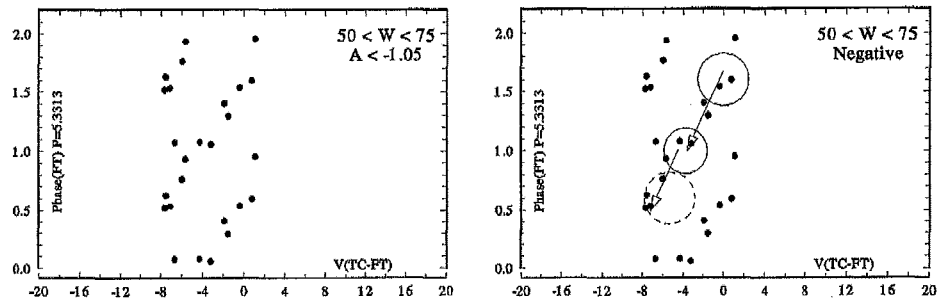


Figure 2.5: Phase-deviation diagram for TC-FT 300-foot telescope data on galaxies with negatively asymmetric profiles 50 to 75 km/s wide and S/N > 10. The figure is the same as figure 3 except it omits the galaxies with $A > -1.05$. The right panel repeats the transition vectors from figure 3 and shows the location of the symmetric profile objects with circles. The negatively asymmetric galaxies distribute along transition lines beginning at symmetric regions and end at a dashed region which may just be forming.

Figure 6 contains the galaxies with profiles positively asymmetric beyond the 5% level. These points also lie along a sloped line at the expected transition slope, but the line is

anticorrelated in location with the negative asymmetry feature associated with the transition vectors shown. The positive asymmetry feature ends at the location of the symmetrical zero phase clump, shown with a circle. The feature extends precisely one periodic cycle and begins in the fuzz to the right of the symmetrical zero phase group. This new region, shown by a dashed circle displaced by one period, contains only positively asymmetric profile objects. From the perspective of the model this region can be interpreted as the last vestige of a previous state; the positively asymmetric profile objects are consistent with being the last objects to leave a state.

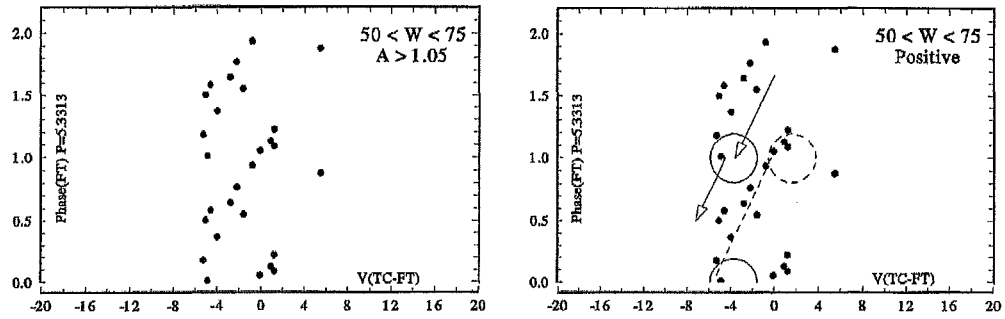


Figure 2.6: Phase-deviation diagram for TC-FT 300-foot telescope data on galaxies with positively asymmetric profiles 50 to 75 km/s wide and S/N > 10. The figure is the same as figure 3 except it omits the galaxies with $A < 1.05$. The right panel repeats the transition vectors from figure 3 and shows the location of one of the symmetric profile regions with a circle. The positively asymmetric galaxies distribute along a transition line beginning in a dashed region, which may be a remnant of a former state, and ending at the symmetric region.

It is essentially impossible to derive meaningful confidence levels for the non-random character of the narrow profile data since they have been used to tune parameters and recognize properties. The data are clearly quite consistent with a level and transition model. The ultimate test of the model in this profile width interval will come soon enough through continued precision monitoring. The principal immediate conclusion we can draw is that asymmetry distinctions provide an important means of defining subsamples.

## 2.5 Intermediate Width Profiles

Intermediate and wide profile galaxies were recognized, in Paper III, to show time dependent phase and shape correlations. The focus at that time was on the 8 km/s interval central to the discovery of time dependent changes. The 5.3313 and 2.6657 km/s periodicities were developed almost entirely in the narrow profile domain. When the May 1991 observations made it clear that the 5.3313 km/s interval was equally fundamental in the $W = 100 - 200$ km/s window, the intermediate width profile objects became an obvious testing grounds for the level and transition model. The test is a powerful one since virtually all parameters are fixed and a sizeable sample is available using the 300-foot telescope TC to FT database. As with the narrow profile analysis we omit the more fragmentary 1988 300-foot telescope

data to maximize the sample size in as short a recent time interval as possible. The TC observations extended from 1984 to 1986.

The only free parameter is the epoch at which we view the data. Variation of the epoch does not change phase relationships at a fixed redshift deviation, but it does scale deviations and shifts phases. There are two natural choices, the two epochs of observation. From the viewpoint of uncertainties, phase scatter should be minimized by choosing the epoch which has the most accurate redshifts. From the viewpoint of the level and transition model the choice of epoch can affect the appearance of a phase-deviation diagram more significantly. If, at one or both observing epochs, objects are in transition, a transition 'front' may appear as a phase gradient; this is one interpretation of figure 1. We can scale and rotate this phase line by varying the epoch and assuming a form for the drift as done in figure 2. In the discussion of the intermediate width TC-FT diagrams which follow we have opted to use an epoch of 1987. The choice of epoch is discussed further in section 6. We assume linear changes with time and epochs of 1975 and 1985 for FT and TC observations. Both deviations and phases are adjusted to the adopted epoch. Under such a transformation the time drift direction is invariant; any displacement in the deviation coordinate produces a corresponding phase shift. Points shift along lines at a fixed slope as epoch is varied.

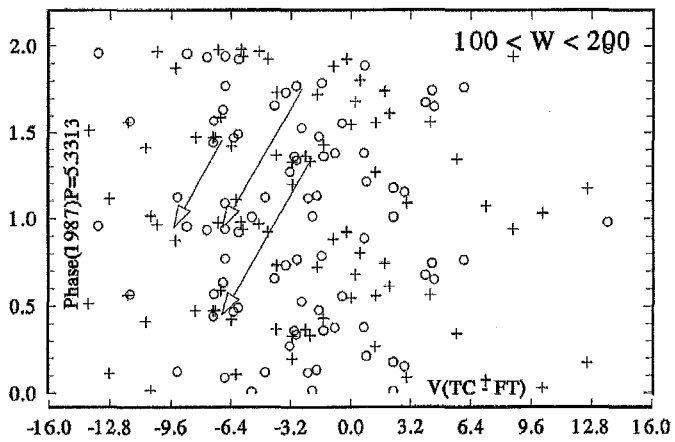


Figure 2.7: Phase-deviation diagram for TC-FT 300-foot telescope data on galaxies with profiles 100 to 200 km/s wide and S/N > 10. Open circles refer to symmetric profile objects and crosses refer to positively asymmetric objects. Phase is calculated for the 5.3313 km/s period epoch 1987 and plotted as a double cycle. The deviation scale is in km/s. The vectors illustrate tracks points would follow if undergoing a transition between levels. Each vector begins and ends at a concentration of points.

Figure 7 is the $W = 100-200$ km/s, $P = 5.3313$ km/s, phase-deviation diagram, epoch 1987, for the TC-FT data with S/N > 10 and $A > -1.05$. These data are known to show large negative deviations as demonstrated in Paper III. The negative deviations show a distinct periodic structure. The 1987 epoch was chosen because it renders the individual populated levels essentially horizontal, consistent with expected uncertainties. The older FT redshift uncertainty enters the deviation coordinate with nearly full weight while only the newer

redshift uncertainty contributes significantly to phase scatter. Figure 7 omits galaxies with significantly negatively asymmetric profiles; these objects are discussed separately below. In the $W = 100 - 200$ km/s window the galaxies with symmetric and positively asymmetric profiles appear to be indistinguishable.

Three drift line vectors are shown in figure 7. The vectors connect clumps and account for all the significant concentrations as either the starting or ending point of a vector; epoch change affects only the length of a vector, not its orientation or its association with the data points. As with the narrow profile data we find that the phase clumps are not randomly located; they associate as expected in the level and transition model. The intervals along the deviation axis were set at 2.6657 km/s before scaling for the epoch change. The vertical phase scale is set by the predetermined 5.3313 km/s periodicity and is independent of epoch. The phase changes which occur for the transitions shown in figure 7 are not obviously simply related to the period. The size of the phase change depends upon the choice of epoch, however. We will reconsider this point in section 6.

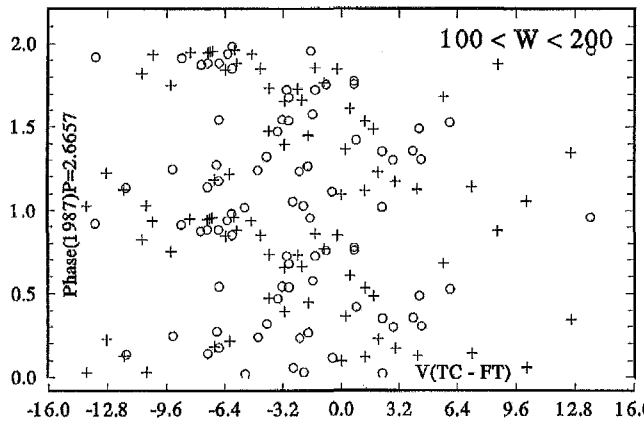


Figure 2.8: Phase-deviation diagram for TC-FT 300-foot telescope data on galaxies with profiles 100 to 200 km/s wide and S/N > 10. Symbols are the same as in figure 7. Phase is calculated for the 2.6657 km/s period epoch 1987 and plotted as a double cycle. The deviation scale is in km/s. A strong periodicity for objects with large negative deviations is present.

To demonstrate the periodicity more explicitly the data in figure 7 are replotted in figure 8 at the 2.6657 km/s period. Since we have no a priori means of predicting the phase at which maximum clumping occurs, we will discuss the clumping using the free-phase In/Out ratio technique from Tifft and Cocke (1984). Only two of the 32 points negative of deviations $-4.8$ km/s, which contains the principal clumps at $-6.4$ km/s and more deviant points, fall outside a half phase interval. Such a 16:1 concentration ratio for 32 points has a likelihood of random occurrence of less than 0.0001. There can be little doubt that the galaxies in the large negative deviation wing of the FT data are periodically distributed in redshift at the predetermined 2.6657 km/s period. We will reconsider the periodicity over a broader range of deviations in section 6.

As discussed and demonstrated in section 4, we have reason to expect asymmetry to dis-

tinguish between subsamples within a profile width interval. Restricting the asymmetry range for the narrow profile objects appeared to separate subgroups in a manner consistent with the level and transition model. We find the same situation applies to the intermediate width profile sample. Figure 9 shows the P = 5.3313 km/s phase deviation diagram for the $A < -1.04$ galaxies omitted in the previous discussion. The extreme positive, $A > 1.04$, galaxies are also shown, as are two of the transition vectors. The symmetric profile objects, which match the positive asymmetry objects very closely, are omitted for clarity. The transition vector omitted is defined almost entirely by symmetric profile objects. The negative $A$ galaxies are seen to fall systematically below the positive $A$ objects for all the significant clumps. They lie along transition vectors in advance of positive points as found for the narrow profiles. A phase shift of about 0.15 will superimpose the negative points quite precisely on the positive ones. The intermediate width profile data appear to be completely consistent with the narrow profile findings and the level and transition model.

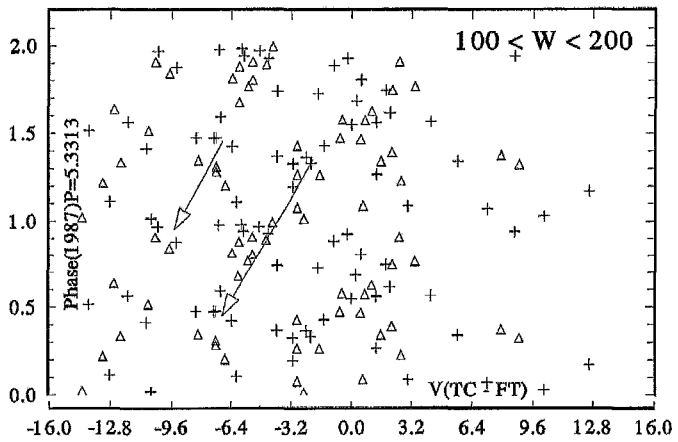


Figure 2.9: Phase-deviation diagram for TC-FT 300-foot telescope data on galaxies with profiles 100 to 200 km/s wide and S/N > 10. Crosses refer to positively asymmetric profile objects and triangles to negative ones. Phase is calculated for the 5.3313 km/s period at epoch 1987 and plotted as a double cycle. The deviation scale is in km/s. Two transition vectors are copied from figure 7. The negatively asymmetric objects are systematically shifted from positive objects in the transition direction.

The positive-negative offset in figure 9 may provide some additional information. We presume that some underlying mechanism is producing the periodicities and apparent changes we see. The phenomenon is manifest through the redshift which is estimated by means of a specific measurement algorithm. The asymmetry offset in figure 9 will include any failure of the measurement to accurately represent the underlying mechanism. The agreement of the symmetric and positive profile objects, and the small size of the negative offset, suggest that any systematic representation errors must be small. The fact that the negative, but not the positive, profiles are shifted with respect to symmetric ones suggests that it is not the asymmetry itself which produces the offset. Regardless of the interpretation, asymmetry does appear to distinguish subsamples in a consistent manner.

## 2.6 The Standards in October 1991

Solar interference disturbs baselines, especially at the wider bandwidths. The October 1991 140-foot telescope observations permitted observations of wide profile galaxies located near the sun in May and afforded an opportunity to reobserve nearly all the standards. As discussed in sections 4 and 5, the model which appears to fit the TC and FT redshift data best is one where relatively stable discreet levels are occupied for some time, followed by a brief period of transition to a different, generally lower, level. The May 1991 observations, discussed in section 3, show the appropriate periodicity but a phase gradient rather than simple displaced levels. As noted in section 5, such a gradient might occur if some objects were in the process of changing levels in May. The October observations provide an opportunity to test this idea. On the basis of the discussion in the previous sections we would expect to see a negatively displaced wing begin to develop. Concentrations of points near at least the first multiple of 2.6657 km/s should probably develop. Three or more such states seem to have appeared during the 10-12 years between the FT and TC observations; a typical time scale of about three or four years is suggested. The 1991 observations occurred three years after the establishment of the standards; consistency would suggest that deviations should begin to develop.

In figure 10 we display the distribution of redshift deviations between the two 1991 data sets and the 1988 standard values. The galaxies are separated by profile width, which also separates them fairly closely by the bandwidth used in the observations. A few points with S/N of 8 or 9 are shown as open circles, otherwise S/N is 10 or greater. Table 3 summarizes the results of the comparisons. The table contains the mean deviation, with its mean error, and the dispersion for each range of profile width and S/N indicated in figure 10. The number of objects in each sample is given; a few cases with discordant points are noted.

Random error analysis in TH and Paper I indicated typical redshift uncertainties, for S/N $>$ 10, of 0.6 km/s at a bandwidth 2.5 MHz; the uncertainty varies as the square root of the bandwidth. A horizontal line under each distribution in figure 10 gives the predicted 1 sigma scatter for redshift differences if these rules apply. These are respectively 0.85, 1.2 and 1.7 km/s. The May 1991 comparisons indicate that the actual scatter is about a factor 1.4 less. Furthermore, some of the spread arises through the non-random phase dependent correlations. The TH and Paper I estimates of uncertainty include intersystem and resolution dependent effects which may partially explain the difference. The differential internal consistency of the 140-foot data is clearly underestimated if we use the TH and Paper I values. For the purpose of discussion we will assume rms uncertainties in the 1991 data are 0.6, 0.85, and 1.2 km/s for the three deviation distributions. The data in Table 3 also show that systematic deviations in May 1991 were zero. There can be very little doubt that precise sub km/s comparisons are possible using such data.

The lower panel of figure 10 contains the October 1991 deviation distribution. The intermediate and wide profile data are noticeably shifted toward negative deviations. A marker is shown at -2.6657 km/s where we have reason to expect points to concentrate if our initial assessments of redshift time dependence are correct; the data are consistent with this expectation. Table 3 shows the scatter in the October data is greater than it appeared to be in May. This would also be expected if a real shift occurred. Since we have reason to expect deviations we have reason to question the validity of the October error estimates.

The quality of the data from both runs is excellent; the average signal-to-noise level is, if anything, slightly higher for the October data. Whereas the May deviation distributions are adequately fit with normal error distributions this is not the case in October. A normal error distribution has only one point in 20 beyond 2 sigma. If the rms uncertainties discussed for the May data apply, then the intermediate width group in October has 6 or 7, and the wide profile group has 5 or 6. In both cases the excess is on the negative side as we would expect. The mean deviation of the intermediate profile galaxies is at or beyond the 2 sigma point if the mean error of the mean from May is a proper measure of the mean uncertainty. A possible positive deviation for the narrow profiles will be briefly discussed in section 7.

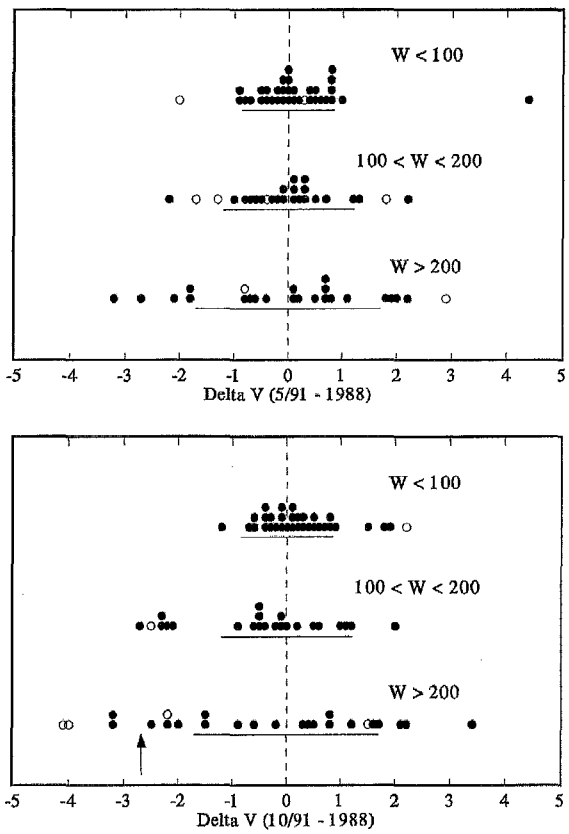


Figure 2.10: Residuals for 1991 redshift observations of the 21 cm standards established in 1988. The upper panel contains data from May, the lower from October. Open circles refer to data with S/N greater than 10. The data are separated by profile width and approximately by band width. The line beneath each distribution illustrates the typical uncertainty previously determined for intersystem comparisons. The line extends $\pm 1$ sigma. The actual scatter in May was less by a factor 1.4. The October data show a negative deviation for the wider profile data; the mark on the deviation scale at $-2.6657$ km/s indicates where the first displaced state is predicted to concentrate.

If the negative displacement in the intermediate width profile galaxy redshifts is real, the level and transition model requires the objects to be in phase or related along a transition line. Figure 11 shows that this is the case, four of the five points with $S/N > 10$ are closely grouped in phase. The October 1991 phase-deviation pattern is shown superimposed on the TC-FT diagram from figure 9 advanced to epoch 1988.25. We see that not only are the displaced points in 1991 grouped in phase, they are generally in phase with the transformation of the older data. Although the variation of epoch by a year or two will not change the phase agreement much, the transformation of the older data to an epoch in 1988 produces a pattern of levels with rather special properties. Whereas the transition intervals in figures 7 or 9 are not simple fractions of the period, they are at the 1988 epoch. The pattern of levels is a simple staggered pattern of 2.6657 km/s clumps; the 1991 phase agreement places the new data within the same pattern.

Whereas the transformation of the TC-FT data to epoch 1987 aligns the scatter generally horizontally in the main groups, the 1988 epoch aligns the groups themselves. In the 1988 alignment the 2.6657 km/s periodicity is easily demonstrated across the entire range of deviations. The half-phase In/Out concentration ratio is 3.7 for 42 positively asymmetric objects and 2.4 for 84 objects if we include the symmetric profile galaxies. The free-phase likelihoods of such concentrations occurring by accident are 0.005 and 0.003. Although we have some orientation flexibility and asymmetry restrictions the level and transition model provides guidelines which limit the choices considerably. A very high level of consistency exists throughout the TC, FT and new 140-foot telescope data.

**Table 3**

Redshift Comparisons, 1991 − 1988

| N | Run | W km s$^{-1}$ | S/N | $\Delta$V$\pm$mem km s$^{-1}$ | $\sigma$ km s$^{-1}$ | Reject |
|---|---|---|---|---|---|---|
| 32 | May | <100 | $\geq$10 | 0.05$\pm$0.10 | 0.53 | 1>3$\sigma$ |
| 34 | May | <100 | $\geq$9 | −0.00$\pm$0.11 | 0.63 | 1>3$\sigma$ |
| 22 | May | 100-200 | $\geq$10 | 0.04$\pm$0.20 | 0.89 | |
| 26 | May | 100-200 | $\geq$8 | −0.03$\pm$0.20 | 0.99 | |
| 22 | May | >200 | $\geq$10 | −0.06$\pm$0.34 | 1.53 | 1>3$\sigma$ |
| 24 | May | >200 | $\geq$8 | 0.03$\pm$0.34 | 1.59 | 1>3$\sigma$ |
| 33 | Oct | <100 | $\geq$10 | 0.18$\pm$0.12 | 0.70 | 1>3$\sigma$ |
| 34 | Oct | <100 | $\geq$9 | 0.24$\pm$0.14 | 0.77 | 1>3$\sigma$ |
| 22 | Oct | 100-200 | $\geq$10 | −0.40$\pm$0.28 | 1.27 | |
| 23 | Oct | 100-200 | $\geq$9 | −0.49$\pm$0.29 | 1.32 | |
| 21 | Oct | >200 | $\geq$10 | −0.13$\pm$0.43 | 1.88 | 1>3$\sigma$ |
| 25 | Oct | >200 | $\geq$9 | −0.46$\pm$0.44 | 2.09 | 1>3$\sigma$ |

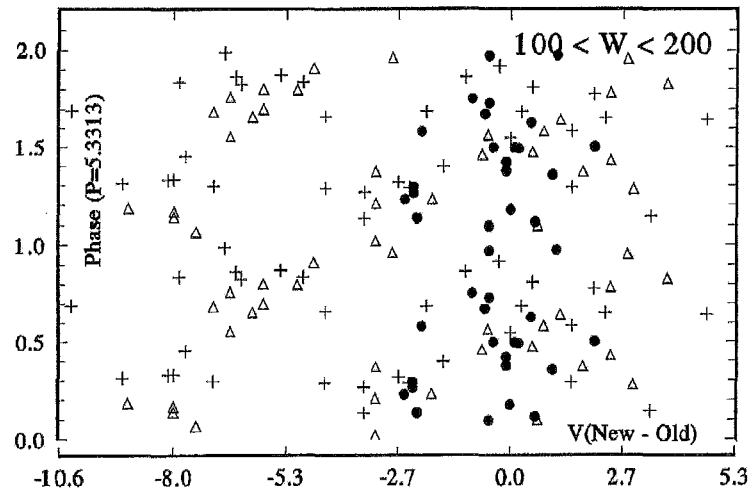


Figure 2.11: Phase-deviation diagram for the October 1991 140-foot observations (filled circles), superimposed on TC-FT 300-foot telescope data for galaxies with profiles 100 to 200 km/s wide and S/N > 10. The 300-foot data and symbols are identical to figure 9 except the epoch has been advanced to 1988.25. At his epoch the TC-FT deviations form a simple staggered pattern of displaced clumps spaced at multiples of 2.6657 km/s. The deviant points from the new October 1991 data are grouped in phase and suggest a new group, consistent with the older ones, is in the process of forming. The 140-foot data is plotted at epoch 1991.

## 2.7 Summary and Discussion

The TC study in the mid 1980s marked the beginning of a series of 21 cm observations which now extends over 7 years. The original objective of determining uncertainties and providing a set of precision redshifts was largely accomplished by the TC study and the TH and Paper I work which followed in 1987-88. The program might have ended then except for unexpected discrepancies in global phase patterns found when comparing TC and FT global periodicity studies. Deviations appeared to correlate with global redshift phase in a manner which ordinary random or systematic error could not explain. The possibility that the redshift might be varying significantly over periods of only a few years was presented in 1987 (Tifft 1988 [94]); confirmation testing using an entirely internal time baseline from 300-foot telescope data followed in 1989 (Tifft & Cocke 1990 [106]). The basis for redshift time variability was subsequently examined in detail in Paper III where the phase-deviation diagram was developed as a tool for tracking redshift changes and fine tuning global redshift parameters and the short global periodicities involved. The loss of the 300-foot telescope in 1988 prevented extending the time baseline of the large TC sample and its 1988 extensions; however, the establishment of the standards in 1988, including the 140-foot telescope, assures that basic monitoring can continue into the 90s until the Green Bank Telescope (GBT) is available. The GBT can provide a link back to TC equivalent in time baseline to TC back

to FT, but with much enhanced precision. The time dependent redshift model set forth in this paper is a first attempt to provide a model suitable to guide the future course of work.

The 140-foot second epoch observations of the standards in 1991 provided a three year time baseline, sufficient to confirm that redshift phase appears to correlate with the differences in redshift between 1988 and 1991. The periods at which the correlations appear are multiples of the 2.6657 km/s period recognized in Paper III. Subsequent reanalysis of the narrow profile 300-foot data, comparing TC and FT redshifts and distinguishing samples by profile asymmetry, has permitted refining the time drift concepts of Paper III into a level and transition model with predictive power. This model has provided the basis for a detailed analysis of intermediate width profile galaxies where we have found consistent results. A second test, using the latest 140-foot observations appears to indicate that the same patterns seen in the TC to FT comparisons are now developing in the new data.

The level and transition model views the redshift as occurring in specific relatively stable levels spaced at intervals of 2.6657 km/s. During relatively brief periods, spaced several years apart, transitions bridging one, or perhaps several, levels occur. The population within the levels appears to be modulated over a range of levels giving rise to various longer periodicities. The frequency and/or times of transition appear to differ between levels and generate larger scale patterns. Profile shape is a factor relating to the timing of transitions; negatively asymmetric profile objects tend to precede. Galaxies showing positive deviations, redshifts increasing in time, appear to be fewer in number, the dominant direction of change being down in redshift. Over time a negative deviation wing develops in the redshift residuals. The deviation seems to develop faster for wider profiles; the negative wing is less prominent for narrow profile data. Narrow and intermediate width profiles are separated by a transition region, $W = 75 - 100$ km/s, where properties appear to change.

In addition to the width dependence the character of phase-deviation diagrams changes in passing from negative to positive deviations. A phase shift typically occurs at zero deviation. There is some indication that brief positive deviations may precede a negative shift. Such a positive deviation may be present in the narrow profile data from October 1991. The current analysis is limited to galaxies with profiles less than 200 kms wide. The amount and precision of data on wider profiles is insufficient for a detailed investigation although similar trends are present.

On the basis of the model as now formulated, we can predict that continued monitoring will show the progressive development of a negative deviation wing. For narrow and intermediate width profile galaxies the wing will presumably contain displaced levels periodic in multiples of 2.6657 kms. A related but slightly different period is suspected to apply to wide profile objects. A series of regular observations will be required to determine if levels are actually stable. By the mid 1990s we would expect several displaced levels to exist. The small size and large beam of the 140-foot telescope limits the choice and number of objects being monitored to a few hundred. The 100 standards are the primary objects being observed; however, a similar list emphasizing wider profile objects has been added. When the GBT becomes available in the mid 1990s the 300-foot telescope data can be closely duplicated; overlap with more than 1000 galaxies will be possible linking FT, TC, and the GBT in a time sequence spanning 20 years. A definitive test of redshift time variability should be possible within a few years. There is some evidence that profile shape and total flux also vary. Future monitoring will address these questions as well.

The importance of resolving the question of time dependence in the redshift requires little debate. Aside from obvious implications relating to mass calculations and dark matter, an entirely new class of explanations may apply to various large scale phenomena. Several examples are illustrative. If different morphologies change at different rates or times we will observe morphological separations in redshift within individual aggregates of galaxies; such separations have been reported in clusters and among general field galaxies. One interesting example concerns the excess redshift of dwarf galaxies in small groups reported originally by Arp (see Arp & Sulentic 1985 [L]). We have seen in Paper III and this paper that the narrow profile dwarf galaxies appear to drift more slowly toward lower redshifts than the wider profile luminous galaxies; over time a net higher redshift for the dwarf galaxies in a group would be a natural consequence of this process. Although the rates of drift appear to be extraordinarily large there is good reason for believing that over long periods the differential deviations that develop must be limited. If this were not the case clusters and groups would be unrecognizable. The range of redshift in clusters and groups may provide a means of estimating the amplitude of redshift oscillations.

One of the principal difficulties in interpreting redshift-magnitude bands and morphological correlations in clusters was the apparent requirement for rapid evolution. Rapid redshift variability, along with luminosity and morphological evolution, was proposed (Tifft 1979 [75]). If the redshift variation proposed in this paper is confirmed then such models may have to be reexamined. The use of apparent large scale motion as a probe of the large scale matter distribution may be questionable as may be the interpretation of some of the large scale structure itself. If certain classes of objects evolve in redshift very slowly, number counts as a function of redshift may not reflect number or density evolution in the normal manner. It is obvious that numerous conclusions and discrepancies on the large scale relate very intimately to our understanding of the redshift phenomenon. A very critical fundamental test of the nature of the redshift is now available to us.

# Appendix 2, Part2

## The case for a Time Dependent Quantized Redshift

Letter to Editor with Response to Referees

## 2.8 Letter to Editor

Enclosed is my response to the second set of referee's reports on my paper "The Case for a Time Dependent Quantized Redshift" along with a revised text and two copies. A copy of the text with marked changes is also enclosed. The figures and tables are also enclosed as there were a few changes and corrections, so the entire manuscript is complete as enclosed. This is not, however, a new submission, the paper is actually changed only to the extent of adding statistical analysis as requested. I did rewrite section 4 because of a technical error in the original, but the result is unchanged. It took some time to find the time to do this recheck, but the paper should continue with its original submission date, there is no substantial change of intent.

I have no great difficulty with the second referee. The request for statistical discussion is easily accomplished by means of a correlation analysis. I have first demonstrated that a systematic effect is present (random errors will not explain the deviation pattern), then that the deviations correlate with phase, and phase only. I mildly disagree with the second referee about the degree of rigor or proof required. The final correlation with phase is significant at the $10^{-8}$ level. At this level it is really quite obvious. One sees statements all the time about effects being 'clearly' present without rigorous proof, I was reading one last night. The difference is what you want to see perhaps. In any case the statistics are now there when possible.

The other major intent of this paper is to introduce a model. This cannot be done with rigorous proof, but it can be and is reasonably justified. I recall that the guidelines to referees from the Journal says (or used to) that criteria for acceptance includes the presentation of new ideas or concepts. This is rarely possible in ultimate form, but if we are not allowed to do it we are in trouble. We better be able to question established viewpoints. The criteria to reject a new idea has to be actual demonstration of error, not simply hand waving about uncertainty. For all their concern, the referees have not provided a single piece of actual evidence of errors. The second referee actually says that in the middle of the second page of their report. The first referee has still not read the paper to see what was actually done. When what he thinks he is saying is done correctly there is no problem. On the question of uncertainty I do have a few things to say. In your own letter of 5 June you refer to "if one were starting out from scratch ... one would establish velocity standards". Do you or the referees realize that that was exactly what I did? The critical data in this paper is a re-observation of the standards carefully set up and inter-compared in 1987-88! Both from the presentation of the standards in ApJ Suppl **73**, and from their analysis in A& A Suppl **84** and ApJ **368** and **382** a highly consistent set of uncertainties emerges. The best prior

standards were also compared. I do not make statements or publish papers without careful checking. Have people become so used to low standards and quick and dirty work that they automatically assume anything which does not conform must be wrong? I do not find that acceptable.

The last point I need to address concerns the arguments by the first referee. The problem with this referee goes well beyond simple lack of clarity in the paper. This referee appears to be so obviously totally biased against quantization concepts that he makes the statement "'I have not been able to follow the logic ... of global quantization ...". He dismisses such discussion as "irrelevant". He has not bothered to note that the discussion in the paper revolves about a tightly defined subsample with very homogeneous properties, and has elected to use data unrelated to the sample to hand wave about 'uncertainty'. He has rediscovered bandwidth error dependence, discussed by me in A& A Suppl., **84**, and thinks he is seriously addressing the findings in this paper. When his approach is applied to the real sample it actually supports the findings. I have incorporated the analysis into the paper in Table 4. The referee has performed a very superficial analysis. In my opinion the bias of the referee is so strong that a proper review of this paper is not possible; I again request that you take that into account in proceeding with the review. I have no problem with the second referee.

I think it somewhat ironic that Scientific American (December 1992) lists my quantization work as one of their 12 challenges for 1993, but as its originator I have great difficulty pursuing the subject. I value and support the refereeing system, but it is readily abused, particularly in controversial areas.

## 2.9 Response to Second Referee

The first part of this response addresses the comments from the second referee. The referee makes two points, first, how reliable and precise are comparisons, and, second, a more formal statistical demonstration is required. The first point, as stated by the referee, is more a comment or warning than a correctable deficiency, but I will comment on it. The second point has now been, I trust, addressed by the addition of some quite specific analysis.

Before going into details I would like to correct one possible misunderstanding in the first paragraph of the report. This paper is not reporting the "discovery"' of time dependence in redshifts, that hypothesis goes back to the Venice Symposium in 1987 with even earlier roots. This paper has two objectives, specifically spelled out in the second paragraph of the introduction. 1) Develop new additional evidence. 2) Propose a model to define the phenomenon more precisely. While it is certainly appropriate to request formal demonstrations relating to the evidence, it is not reasonable to demand "proof through rigorous analysis" (what exactly is proof?), every time one enters additional evidence. This is a developmental paper, not a definitive proof of anything.

### 2.9.1 Uncertainties

Concerning uncertainties in data, the referee has gone to some length to state what I am already quite aware of. In fact the referee indirectly makes it clear that he or she knows I am aware of potential errors. The referee consistently ignores the fact, however, that I am

discussing deviations which correlate (now formally shown) with redshift phase, a property no ordinary random or systematic error can have. I would not make the suggestion that redshift is time dependent if it were based only on general systematic shifts. None of the very general discussion of uncertainties given by either referee addresses the critical point that the deviations are phase dependent and/or periodic! Ordinary errors do not produce cross correlations, they only destroy them. I will welcome any suggestions of how some error might relate to redshift phase! Beyond that the referee is guilty of exactly the same thing directed at me — hand waving. State a formal case if you have one.

I believe that I have done more than nearly anyone else to investigate and understand 21 cm redshift uncertainty. The 1987-88 multiple telescope investigations along with the original 1984-86 series of observation provided rather clear results. A set of standards was defined and extensive inter-comparisons made. If the referees are not familiar with all of this work the references are: A) ApJSuppl., **67**, 1 ,1988 (original Green Bank data with general error discussion, see also Liege Colloquium 1987, pg 83) B) A& A Suppl., **84**, 47, 1990 (Fundamental inter-comparison between Effelsberg and Greenbank, in great detail. It seems likely, based upon the content of the referee reports, that neither referee is familiar with this paper.) C) ApJSuppl., **73**, 603, 1990 (Multi-telescope standards with basic comparisons, called Paper I in present paper.) D) ApJ **368**, 105, 1991 (Effects of resolution on redshifts, called Paper II in present paper.) E) ApJ **382**, 396, 1991 (Time dependent comparisons with older redshift data and formal introduction (ApJ) of the time dependent concept including basic modifications of quantization to take time dependence into account, called Paper III in present analysis.) F) ApJSuppl., **79**, 183, 1992 (Corrections to older Green Bank redshifts for POPS software approximations, called Paper IV.)

These papers discuss the following concepts among others: 1) Contemporary redshifts with $S/N > 10$ follow the expected square-root of bandwidth dependence with a well determined scatter of 0.8 km/s for 5 MHz data (See ref B). 2) Differences in contemporary observations made with different telescopes vanish in the limit of unresolved systems. The effects of resolution on redshift accuracy has been examined. (See ref D). 3) The effect of pointing uncertainty on redshifts has been investigated (See ref B). 4) Multiple bandwidth inter-comparisons have been made (See ref C, Table 16 in particular). 5) Several system and software errors were found and corrected at Bonn and Greenbank (See ref B) 6) Direct comparisons of results using Toolbox and POPS software show no differences (See ref B), and the frequency-velocity error in such software has been specifically discussed (See refs B, C, F). 7) Comparisons against the Baiesi–Pallastrini and Palumbo standards verify their quoted uncertainties and demonstrate that the newer redshift uncertainty is undetectable in comparison (See ref E). 8) Comparison against near contemporary Arecibo precision redshifts by Lewis shows no detectable deviations in the no resolution limit, and again confirm the newer redshift uncertainties (See ref E). 9) Older redshift comparisons (FT, Roberts, Shostak, Dickel–Rood) show non-random scatter and systematic deviations; the deviations correlate with redshift phase, completely consistent with the time variation concept. (See ref E). 10) The most critical part of the present paper involves comparisons of new precision data obtained entirely with the 140-foot telescope. The internal scatter is very small, leaving little room for significant error. The 140-foot is used in the VLBA system, it is highly reliable and consistent. Finally, only the highest quality recent data is used, 10MHz data is not used to reach the major conclusions. Data is obtained in a consistent framework of high $s/n$, careful pointing checks, and extensive overlaps. I suggest that the referees examine

the picture very carefully before claiming that there is any evidence for casual treatment of uncertainty.

One final comment refers to the second referee report in the section discussing uncertainty. I find the reference to "little or no flexibility exists" with respect to previously determined parameters. I do not understand this comment. The parameters referred to are the solar motion components, relativistic corrections, and quantum periodicities. These were derived in Paper III using exclusively 300-foot data. By finding that the same parameters generate the same results using the completely independent 140-foot data seems to me to be a rather strong confirmation of quantization effects. I fail to see how this relates to the data uncertainty question. All I think I am saying is that no additional tuning of any parameters was done, the 140-foot data shows the predicted effects with no fudging.

### 2.9.2 Statistical Treatments

I will now go step by step through the formal development in the paper to clarify questions relating to statistical treatment.

The Introduction contains nothing requiring special demonstration. It mainly summarizes relevant material from prior papers. There are three changes of note. The objective of the paper is now specifically stated, a statement noting that 10 MHz data is included but that the results are based almost entirely on the more accurate narrower band data is included, and the specific correlations to be demonstrated are summarized.

Section 2, Observations, corrects a few small errors found in the main tables and adds a reminder about the minimal dependence on 10 MHz data.

Section 3 has been revised by combining discussion of May and October observations, and formally analyzing the correlations. This revision is one part of the response for a more rigorous statistical analysis. I have used a fairly obvious and straightforward correlation analysis of the data falling in the critical $100 < W < 200$ km/s window. In order to clarify several points I have summarized the relevant data in a new Table, 3. Table 4 now summarizes the general properties of the sample to explicitly demonstrate that there is *no* dependence of scatter on width within data taken at a single bandwidth, or on signal-to-noise within this particular critical sample. This addition is discussed in more detail in the section of this report responding to the first referee who insists on using unrelated 10 MHz data to argue data quality. Questions about the data must be demonstrated with this sample, not material unrelated to the conclusions.

Figure 2 is new and contains the requisite correlation diagrams. As a first step we show that the deviations between 1988 and May 1991 are significantly correlated with the deviations between 1988 and October 1991. The Spearman rank correlation significance is near $10^{-5}$ of being random. The conclusion is simply that the deviations must contain a systematic effect. Simple random error will not produce such a correlation; the result is a property of all the data, not a few large errors. As a second step the May deviations are demonstrated to correlate with redshift phase with a random likelihood of about $10^{-8}$ of being accidental. At this point I believe it should be clear why the prior specification of all quantization parameters is relevant. Absolutely no parameters were adjusted to produce this correlation. Deviation *is* correlated with redshift phase. The final step demonstrates that the deviations

increased, at a marginally significant level, by October. The entire analysis is consistent with the theme of the earlier Paper III predictions, and establishes the first point of the paper. I trust the paper now contains a sufficiently formal treatment.

The remainder of Section 3 is a slight modification of the original text which is used to introduce the topic of model development. Although the correlation analysis obviously demonstrates the significance of the periodicity, we include a direct in-out ratio evaluation in this part to support any statement that might be interpreted as unsubstantiated.

Section 4 utilizes older Fisher-Tully data compared to Tifft-Cocke redshifts to formalize the development of the transition model. The question here is *not* the basic periodicity, all such parameters and analysis fall in the domain of Paper III. This was the study that generated the predictions constraining the 140-foot data test and Section 5 periodicity testing.

This section has been almost completely rewritten, not because of any refereeing comments since there were none, but because of an error on my part in representing the model. The intent of the section, however, is what it always was, to assist in model synthesis. The 'lines' drawn on the diagrams are specific to the model and justified by it. The explanation of the pattern is given in detail. Unlike the original version a formal test is now developed to evaluate the model. This should provide some assurance that the model is not entirely speculation. It should be quite clear, however, that this paper is *not* going to do anything like providing 'rigorous' proof for the model. The model lays the groundwork for future testing. I know no other way to proceed.

The test developed utilizes a correlation of 21 cm profile shape with the timing of hypothesized redshift changes, reflected by where data points appear in a phase-deviation diagram. A correlation of this type is shown to be significant, whereas there is no direct correlation between shape and overall deviation. The latter correlation might be expected if shape differences resulted in simple systematic measurement errors. I have not included a diagram in the paper since it seems unnecessary. I have included a figure at the end of this section of the report, however. The filled circles refer to the 29 points most tightly associated with predicted locations; open circles refer to less likely associations. Model development at this stage always involves some guesswork; I trust that this specific test provides adequate formal supporting evidence.

Section 5 is relatively unchanged. A few clarifying sentences were added or revised. As in the previous section the placement of lines is governed primarily by the model and is not arbitrary. The primary test carried out here is a demonstration of the predicted redshift periodicity. This is done with a formal free-phase in-out ratio analysis applied to the points with appreciable negative deviations. This is the sample for which the model requires periodicity; the test provides an important confirmation of model predictions. In the final paragraph, however, we claim only consistency, and make it clear that we are primarily laying groundwork for longer term testing with newer precision data.

It is perhaps important to point out here that the periodicity testing in this section is largely independent of any unknown uncertainty in FT redshifts; phase is determined almost entirely by the new data at the epoch used. The FT data provide only a fairly broad distinction in deviation; any question of uncertainty in the FT data is of little import. The Effelsberg-Greenbank comparisons from 1987-88 show quite clearly that the 1984-86 300 foot telescope

redshifts used have the requisite accuracy to make this test. One might also note that the new redshifts used contain no 10 MHz observations.

Section 6 has only minor changes, primarily a reference to the discussion in section 3, and restatement of the minimal dependence on 10 MHz data. This section has two objectives, first to provide a rather straightforward internal error analysis which again fully confirms the high repeatability of the data on the standards, and second to show that May to October 1991 differences are consistent with model predictions. This completes the circle of consistency arguments, and includes one further formal periodicity test. I make no claim that the model is proven, but it is certainly well enough formally supported to guide future work, which accomplishes the second goal of this paper. This section is, incidentally, the only place in the paper where any use of 10 MHz data is made, and that is limited to a simple consistency statement.

Section 7, the summary discussion, contains only trivial changes. Aside from a straightforward summary, the objective in this section is to provide formal predictions for future testing. Just as my 1976 original quantization predictions were basic to evaluating the results obtained in the 1980s, this model is basic to evaluating projected 1990s data. If it proves wrong so be it, I stand by my predictions. The model is based upon an extensive series of consistent observations. I do not believe any ordinary errors could conceivably produce the observed effects. The observations entering into this work form one of the most consistently precise data sets ever generated at 21 cm.

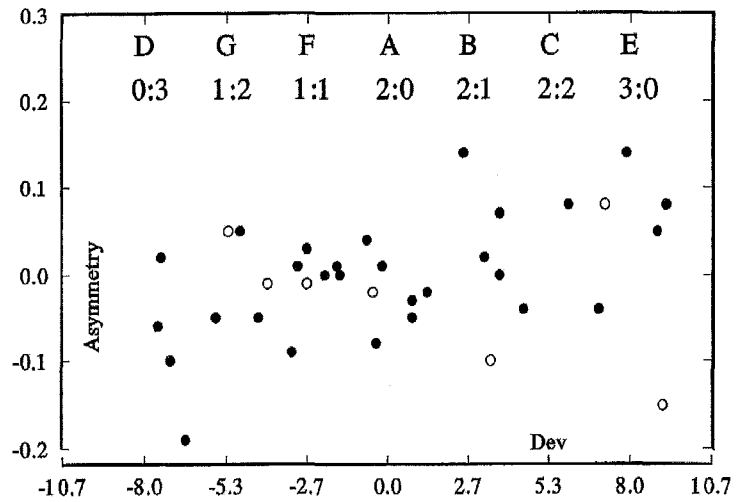


Figure 2.12: Asymmetry as a function of position in the transition timing sequence

## 2.10 Response to first referee

It is unfortunate to have to respond for a second time to a referee who does not appear to understand the paper or be familiar with the background material which has preceded it.

This paper contains general data on nearly 100 standard galaxies because it made no sense to split them up. The critical discussion in the paper, however, depends upon a specific subset, galaxies with profile widths between 100 and 200 km/s wide which have very homogeneous error properties. The referee appears to be unaware of this although it is stated many times in the paper. The referee has attempted a simple analysis of the *total* data sample, most of which does not enter into my analysis for very good reasons. Most of the statements and tests by the referee are correct but irrelevant. I will spell this out step by step. I am not a novice in the subject of redshift precision as the referee seems to presume.

I will begin by discussing a sentence in the second paragraph of the report, which excerpted states "... very wide profiles ... it is necessary to derive a systemic velocity using a tight and reproducible definition to represent the whole complex profile ...". 1) The results of this paper depend upon a specific subset of not especially wide profiles. Example: no 10 MHz data are used to reach the conclusions, but they dominate the referees analysis. The results of this paper depend upon 5 MHz bandwidth data supplemented by some 2.5 MHz bandwidth data on profiles 100 to 200 km/s wide. 2) I do not derive a systemic velocity, I derive a redshift index. Redshift stability depends on how reproducible the index is, not on its interpretation since the purpose of this work is to test the velocity interpretation.

The redshift index is very specifically defined to be as stable as possible. The procedure requires the measurement of the frequency where each wing of the profile crosses the 20% level of the height of the central 80% of the profile. The accuracy of each frequency measurement depends on the width of a channel (bandwidth/N, N = number of spectral channels), and the signal-to-noise. It in no significant way depends on the profile width since each frequency measure is obviously unaffected by the location of any other measure. 21 cm profiles are not measured like optical lines by setting a crosswire in the middle! Accuracy is a function of bandwidth used and is essentially independent of profile width unless bandwidth is changed to accommodate width. Within a given bandwidth and signal-to-noise subset the accuracy is essentially fixed as I will illustrate. This result is central to the testing in this paper. The referee for some reason has ignored (or more accurately has rediscovered) bandwidth dependence.

In the last sentence of the second paragraph the referee disclaims that accuracy can exceed 1% of profile width. Accuracy depends upon the ability to make frequency measures; when signal-to- noise is reasonably large it is a function only of the width of the individual channels in the detector system. One can interpolate a level crossing point within a fraction of a channel; at 10 MHz a channel is only 10 km/s or so wide. It should be intuitively obvious, especially at 5 MHz and below, that sub km/s repeatability can be readily achieved. In the final analysis the proof is directly visible in the observations, including section 6 of this paper. Attached are two figures and three tables. The first figure, from Tifft and Huchtmeier 1990, shows the observed scatter in V and W, as a function of bandwidth, for 300-foot (G) vs 100-meter (E) data. These are completely independent telescope and detector systems. One associated table gives the statistical comparisons; a second table, from Tifft 1990, gives internal Greenbank data on the same standards. The second figure and table is from this paper comparing 140-foot data from 1988 and 1991. These three independent comparisons show quite consistently that redshift index uncertainty is very well represented (as basic theory predicts) by a square root of bandwidth rule with an empirical sigma of 0.85 (or better) at 5MHz. This corresponds to 1.2 km/s at 10 MHz, which is only 1/2 of 1% of the

narrowest profile width (250 km/s) for which a 10 MHz bandwidth is used. Measurement error is a fraction of channel width in the autocorrelator, not the profile width. If the referee wishes to dispute this fact, or the observed level of consistency actually obtained then he will have to explain these demonstrated results.

Given the above actual data, we can now readily explain the referees findings relating to widths and S/N. By selecting objects with deviation greater than 2 km/s one selects primarily 10 MHz data. By looking at the smallest deviations one selects primarily 2.5 and 5 MHz data. It is hardly surprising that one sees a width correlation since 10 MHz is used for $W > 250km/s$, 5 MHz for $125 < W < 250km/s$, and 2.5 MHz for $W < 125km/s$. The referee has rediscovered the bandwidth dependence. The same is true for S/N which I will leave for the referee to demonstrate if he wishes. Signal and noise scale differently with bandwidth.

In contrast we will now look at what is actually done in the paper and how the results depend on W or S/N differences. That is the question the referee should have examined. First, I am quite aware of the more limited precision of the 10 MHz data. For this reason, and the fact that I have no prior specific expectations for the time dependent behavior of the redshifts of galaxies with profiles wider than about 200 km/s, the 10 MHz data is tabulated but not discussed in any detail. When a sufficient time baseline has accumulated this data will have its turn. In contrast, the previous paper (Paper III, ApJ **382**, 396, 1991), specifically identified a critical profile width window between 100 and 200 km/s, and defined the periodicity and quantization parameters that go with it. Furthermore, the measurements in this window have the necessary precision to test the concepts. Figure 1 presents the basic correlation found; The figure is now accompanied by an analysis of significance.

The specific data which enters into this study has now been put into a separate table (3). Bandwidths, widths, deviations, and S/N data are brought together for examination. If the referee is correct in his assertion that deviation is related to profile width or S/N, then here is the critical homogeneous sample for the test. Table 4 in the paper now makes that test. There is no dependence of deviation on either parameter. There is a very strong dependence upon redshift phase, however, as the subsequent correlation analysis makes quite clear.

The final paragraph of the report indicates that the referee feels that the redshift phase correlation is irrelevant in view of his demonstration of error dependence on W and S/N. In fact the referee's analysis is an artifact of the already well known bandwidth dependence. The *only* correlation in the critical sample data is the phase correlation. By the referees own statement in the final sentence he disclaims any working familiarity with global redshift quantization concepts. This is a paper dealing with that subject, and should be reviewed properly in that context.

As a final comment, the supplementary addendum by the referee adds nothing; it is an even more extreme artifact of bandwidth dependence. The referee's numbers for the width dependence can be read directly from Figure 11 in the paper, he could have saved himself the trouble of calculating them. These observations, while perfectly true, have nothing to do with the effects discussed in the paper. Random error correlates very well with bandwidth, it *should not* correlate with global redshift phase.

# Appendix 2, Part3

## The Case for a Time Dependent Quantized Redshift

Revision through Section 4

**Abstract**

Second epoch 21 cm observations on standard galaxies obtained with the 140-foot telescope contain a systematic time-dependent pattern of redshift deviations. The differences correlate strongly with global redshift phase. The period at which the correlations appear was previously predicted as were essentially all other parameters in the analysis. An investigation of 300-foot telescope 21 cm data extending over 10 years has been used to develop and further test a model for a time-dependent redshift. Redshifts seem to be relatively stable for intervals of several years and then appear to shift relatively rapidly by multiples of a basic period near 2.7 km/s. The trend of change is generally down in redshift so that over time a negatively displaced wing appears in redshift residuals. The recent 140-foot telescope observations are consistent with the development of such a shift. Both 21 cm profile width and shape are parameters in the proposed model for redshift variation. Longer term monitoring should provide a very fundamental test on the nature of the redshift.

## 2.11 Introduction

Several basic investigations of 21 cm redshifts have recently been carried out (Tifft & Cocke (1988 [96] henceforth TC), Tifft & Huchtmeier (1990 [104] henceforth TH) and Tifft (1990 [104], 1991a,b [109,111], 1992 [113] henceforth Papers I–IV). The earlier papers contain modern data with an emphasis on high precision; comparisons at the level of a fraction of a km/s are readily achieved. The later series of papers establish a system of 21 cm standard objects and examines for inter-system and time dependent effects using the new data and various older studies. Paper III, in particular, develops the concept that the redshift exhibits rapid variability. The phenomenon is intimately related to global redshift quantization. Time dependent deviations are periodic and proportional to the time intervals involved, which appears to rule out most ordinary explanations.

The objective of this paper is twofold, first to develop new evidence for time dependent changes in the redshift, and second to propose a specific model of the variation to guide future definitive testing. We draw upon new 21 cm data obtained in 1991 at the National Radio Astronomy Observatory 140-foot (43m) telescope for comparison with 1988 140-foot telescope data, and specific comparisons of TC 300-foot (91m) telescope data with data from the Fisher–Tully (1981 [V] henceforth FT) redshift catalog.

The background which led to the time-dependent redshift concept was presented in Paper III and will not be repeated here. Paper III specifies various critical parameters and properties which warrant a brief review. Little or no further flexibility exists with respect to these conditions; they were specified prior to obtaining the 1991 21 cm data presented in this

paper. Paper III also preceded the greater part of the investigations of the FT data contained in this paper. The study of the FT data at profile widths greater than 100 km/s, contained in this paper, was precipitated as a result of the May 1991 observational findings.

Paper III specifies the solar motion and relativistic correction required for calculating the global quantization phase. The solar motion components assumed are $\theta = 232.2, \pi = -36.5, Z = 1.2$. The new relativistic correction formalization with $q_o = 0.5$ is assumed; the actual value of $q_o$ is of little importance.

It has been clear since the earliest global studies that quantization properties depend upon 21 cm profile width. Paper III defines several important profile width, $W$, intervals. Two ranges, 50 to 75 km/s, and 100 to 200 km/s are recognized as 'critical' windows where properties appear to be stable and especially clear. The narrowest profile galaxies, and objects with profiles between 75 and 100 km/s wide, are considered to be 'transition' objects. The principal transition region, $W = 75 - 100$ km/s, is readily associated with the transition from dwarf irregular galaxies to spirals with a rotating disk. As was the case for solar motion and relativistic corrections, the profile width windows utilized in this paper are defined by prior discussion.

For convenience of presentation, new data on galaxies with profile widths greater than 200 km/s are listed in this paper along with the narrower profile objects. These data are more limited and the accuracy is lower since a 10 MHz bandwidth is required for such observations. Beyond some general comparisons we will not discuss wide profile galaxies in this paper. The conclusions reached in this paper rest almost entirely on high precision observations made in 2.5 and 5 MHz bands. It is commonly held that 21 cm redshift accuracy depends upon profile width. In fact accuracy is a function of bandwidth, and varies with width only to the extent that wide profiles are observed with larger bandwidths. Within a given band accuracy is essentially constant, all other factors being equal.

Paper III also provides the basic period(s) for the current analysis. Periodicities in a time dependent situation differ somewhat from the static situation originally considered when global quantization was discovered. In the original form the period was determined to maximize clustering of redshift phase. As discussed in Paper III, if redshift is drifting differentially, maximum phase clumping will not in general yield the true period. A two dimensional analysis is required where redshift phase is plotted against the redshift difference at two epochs. The period is found to optimize 'drift-line' structure in such two dimensional 'phase-deviation' diagrams. The periodic structure seen will depend upon the epochs chosen and the nature of the time drift process. An attempt to define the drift process is one objective of this paper.

As was the case for the original global quantization work, the key objects used to define the period are the narrow profile dwarf galaxies, especially those in the critical width window around $W = 60$ km/s. The critical 'sub'-period found in Paper III is 2.6657 km/s, as shown in figure 11 of Paper III. This period appears to define a basic interval, but all cycles of this period are not equivalent in their time drift properties. This interval appears to be modulated such that specific higher multiples produce strong periodic patterns. This is, we believe, the origin of the longer periods which have been discussed in past studies. The non-equivalence of different cycles of the 2.6657 km/s period is well illustrated in figure 10 of Paper III where the period 5.3313 km/s, twice 2.6657 km/s, is utilized. These are the

two periods we will utilize in this paper, which contains, in section 14, a further analysis of the $W = 60$ km/s FT sample. The four to five significant figure accuracy of the periods arises from the fact that they are fine tuned over more than 1000 cycles of the 2.6657 km/s period.

Since Paper III utilized the narrow critical window data to fine tune the period and solar motion, the narrow window data cannot be used to directly evaluate the significance of the periodicity in the data set. In paper III evaluations of significance were largely confined to working with higher multiples of the 2.6657 km/s interval. In sections 13 and 15 of this paper we will demonstrate the significance of the basic periods in the second critical window centered around $W = 150$ km/s.

The final parameter, which we will use to distinguish subsamples, is the 21 cm profile shape or asymmetry index $A$. The precedent has been set in previous papers and is illustrated in Paper III. We will generally broadly distinguish up to three classes, distinctly negative $A$, near symmetrical, and distinctly positive $A$. The index $A$, formally defined in TC, is a measure of the deviation of the profile midpoint by area from the midpoint defined by profile level-crossings. Profiles with negative $A$ are dominant on the high redshift side, those with positive $A$ show a low redshift dominant profile.

Section 12 presents the new 1991 NRAO 140-foot telescope data. Section 13 compares the 1991 140-foot telescope data with the 1988 definition observations of the 21 cm standard objects done with the 140-foot telescope. We establish three major points: 1) The deviations between data sets cannot be explained by random errors, a significant systematic effect is present; 2) The systematic effect is directly and strongly correlated with global redshift phase; 3) The deviations increased during 1991. The time dependent pattern found in the 140-foot telescope data comparison provides the point of departure to examine a longer baseline interval, back to the 1970's using TC and FT 300-foot telescope data, done in sections 4 and 5. Section 6 examines changes which occurred during 1991. Section 7 summarizes the general model proposed for redshift variation which provides specific predictions for future work.

## 2.12 1991 Observations

The objective of the TC and TH 21 cm investigations was to determine the precision obtainable through a study of internal and external comparisons. The first indications of a possible redshift time dependence became apparent during these studies. The work culminated with the establishment of a set of 100 standard objects, defined in Paper I, where the data on the standards is tabulated for each telescope independently. Radial (contemporary comparisons between different telescopes) and temporal (comparisons of data from the same telescope at different times) effects in Papers II and III indicated that further observations of the standards could provide insight into possible variations. The first major re-observations took place between May 3-14 and October 19-24, 1991. The observations were made at the NRAO 140-foot telescope using the L-band receiver. Procedures used duplicated the 1988 140-foot telescope observations in nearly all respects. Total power mode was employed using the original set of positions and center velocities. Each on-scan was combined with an off-scan observed at equivalent pointing angles. When there is any question of contamination both east and west offsets were employed and compared. North of about 15 degrees

declination zenith angles rarely exceeded 45 degrees. Galaxies further south, down to −20 degrees declination, require lower altitudes, but were almost never observed below 30 degrees altitude. A few extreme southern objects were observed close to meridian passage; none of these are used in the current analysis. Ground reflection effects are negligible and no significant interference signals were present during the 1991 observations.

Bandwidths were set at 10, 5, or 2.5 MHz, as done in 1988, according to the profile width. This is done to assure that baselines are well defined on both sides of the profile. A few objects were observed at two bandwidths to confirm the absence of any bandwidth dependent differences. The only change in procedure was to replace 1.25 MHz observations, used for the narrowest profiles in 1988, with 2.5 MHz observations. The reason for this change is discussed in Paper I, and concerns possible slight systematic effects on flux determinations. To minimize baseline distortion due to the sun, 10 MHz observations are rarely done during daylight hours. Daylight observations at 5 MHz and below rarely show major distortions and are very well fit with cubic baselines. Baselines at night are virtually flat at all bandwidths. All reductions were done using the 'RADFILES' software as discussed in Paper I. Regular pointing and flux calibration observations were made using standard continuum sources. Pointing deviations rarely exceed 10 arc seconds. Flux data are not presented here; no significant improvement over the 1988 data is possible at this time. A second set of galaxies emphasizing objects with wider profiles, where the standard set is deficient, was also observed. Discussion of this sample will be deferred to a later date. We again wish to emphasize, that while we tabulate the wide profile galaxy observations, made with 10 MHz bands, the analysis and conclusions within this paper are based almost exclusively on the more precise 2.5 and 5 MHz data alone.

Table 1 contains the May 1991 observations. TC, FT, and UGC numbers are serial identification numbers from the original TC analysis, the Fisher-Tully (1981) [V] catalog, and the Uppsala General Catalog (Nilson 1973 [BW]). FT numbers beginning with zero, or greater than 1171, are NGC numbers. A complete description of the notation is given in TC or Paper I. The fourth column lists the bandwidth used; 2.5 MHz is abbreviated as 2. Columns Vft, W, A, and S/N list the heliocentric redshifts, profile widths at 20% of the average height of the central 80% of the profile area, the asymmetry index, and the signal to-noise figure. Definitions of these quantities are given in TC and Paper I. The column Q contains comment codes defined in notes appended to the table. The final columns, DV and DW, give the difference in Vh and W, from the 1988 140-foot telescope data, in the sense (new - old) = (1991 - 1988). Table 2 contains the October 1991 observations in a format identical to Table 1 excepting that all comments are appended to Table 1.

## 2.13 The Standards in 1991

Three years elapsed between the establishment of 21 cm standards in 1988 and the observations obtained in May 1991. Since FT comparisons, discussed in Paper I, suggest deviations of up to 10 km/s can occur over 10-12 years, we would expect visible changes in 3 years. Comparison of the 1988 and 1991 140-foot telescope observations appear to confirm this expectation. Figure 13 displays the redshift difference (May 1991 - 1988), for the critical $W = 100 - 200$ km/s window, as a function of global phase at the 5.3313 km/s period.

A double cycle of phase is plotted to facilitate viewing periodic patterns. The points distribute in a sloping pattern, undisplaced from zero near phase 0.25-0.5, and maximally displaced near phase 0.75-0.0. All parameters in this diagram were fixed prior to the 1991 observations. The data appear to be consistent with a real phase dependent drift in redshift; random error would not be expected to correlate with phase. The telescope and receiver were identical at both epochs; systematic errors should be minimal and, again, should not correlate with phase.

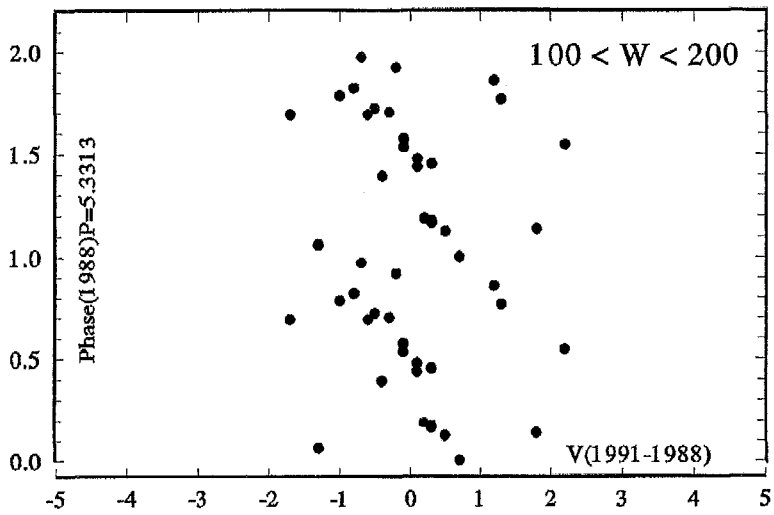


Figure 2.13: Phase-deviation diagram for the May 1991 140-foot telescope data on galaxies with profiles 100 to 200 km/s wide and S/N $\geq$ 9 at both epochs of observation. Phase is calculated for the 5.3313 km/s period at the epoch of the standard observations. Points distribute along sloping lines with a phase offset at zero dviation. The deviation scale is in km/s.

The significance and implications of the deviations between 1988 and 1991 are easily demonstrated by means of a correlation analysis. Table 3 lists the information available for galaxies with profiles 100 to 200 km/s wide. The table gives the TC identification, the bandwidth used, the profile width (1988 value), the signal-to-noise (SN) figure in 1988, May 1991 (m), and October 1991 (o), the deviation (DV) and rank order (OR) of the 1991-1988 deviations for May 1991 and October 1991, and finally the deviation (Oct 1991 - May 1991), (DVmo), and the global redshift phase, (PH88), for the 5.3313 km/s period at the 1988 standards epoch. Rank order is assigned only to objects where data are available in both May and October 1991; tie values are assigned the mean rank for the tied intervals. Deviations involving data with signal-to-noise less than 9 are not used.

The general properties of the sample as a function of bandwidth, profile width, and signal-to-noise are addressed in Table 4. The upper part lists the sample size (N), the mean deviation with the mean error of the mean, and the dispersion in the deviations, for the three time intervals subdivided by bandwidth (BW) and profile width (W). This section demonstrates

that, as expected, there is no dependence of scatter on profile width within the 5 MHz band; there may be a slight reduction, as expected, in passing to the 2.5 MHz data. The actual value of real observational scatter cannot be determined directly from the tabulated values since systematic effects, shown below, are present. The values represent upper limits to the random observational scatter; since the values refer to redshift differences the individual redshifts are clearly repeatable at sub km/s precision.

**Table 3**

Properties of 100<W<200 km $s^{-1}$ Galaxies

| TC | BW | W88 km $s^{-1}$ | SN88 | SNm | SNo | DVm km $s^{-1}$ | ORm | DVo km $s^{-1}$ | ORo | DVmo km $s^{-1}$ | PH88 |
|---|---|---|---|---|---|---|---|---|---|---|---|
| 499 | 2 | 102 | 25 | 26 | 22 | −0.1 | 10.5 | 0.5 | 5.0 | 0.6 | 0.535 |
| 432 | 2 | 103 | 46 | 33 | 48 | 0.3 | 5.0 | 0.2 | 6.0 | −0.1 | 0.454 |
| 295 | 2 | 108 | 10 | 9 | 13 | −1.3 | 19.0 | −0.5 | 13.0 | 0.8 | 0.063 |
| 345 | 2 | 110 | 11 | 9 | 14 | −0.4 | 13.0 | −0.1 | 8.5 | 0.3 | 0.394 |
| 87 | 2 | 116 | 92 | 62 | 69 | 0.7 | 2.0 | 0.6 | 4.0 | −0.1 | 0.003 |
| 23 | 2 | 123 | 18 | 19 | 20 | 1.3 | 1.0 | 1.1 | 2.0 | −0.2 | 0.767 |
| 56 | 5 | 126 | 12 | 14 | 11 | −0.5 | 14.0 | −2.3 | 18.5 | −1.8 | 0.724 |
| 413 | 5 | 128 | 46 | 19 | 17 | 0.3 | 5.0 | 1.0 | 3.0 | 0.7 | 0.167 |
| 164 | 5 | 132 | 19 | 18 | 28 | −0.8 | 17.0 | −0.5 | 13.0 | 0.3 | 0.824 |
| 259 | 5 | 132 | 36 | 23 | ... | −0.3 | ... | ... | ... | ... | 0.703 |
| 338 | 5 | 132 | 13 | 13 | ... | 1.2 | ... | ... | ... | ... | 0.860 |
| 414 | 5 | 139 | 45 | 38 | 31 | 0.1 | 8.5 | −0.1 | 8.5 | −0.2 | 0.439 |
| 358 | 5 | 139 | 18 | 11 | 17 | 2.2 | ... | −2.2 | ... | ... | 0.547 |
| 459 | 5 | 144 | 68 | ... | 44 | ... | ... | 1.2 | ... | ... | ... |
| 136 | 5 | 148 | 54 | 26 | 36 | −0.7 | 16.0 | −2.1 | 17.0 | −1.4 | 0.976 |
| 393 | 5 | 156 | 63 | 21 | 23 | −1.0 | 18.0 | −0.6 | 15.0 | 0.4 | 0.787 |
| 353 | 5 | 159 | 11 | 11 | 12 | −0.1 | 10.5 | −0.4 | 11.0 | −0.3 | 0.573 |
| 482 | 5 | 160 | 9 | 18 | 12 | 0.1 | 8.5 | −0.2 | 10.0 | −0.3 | 0.388 |
| 74 | 5 | 164 | 19 | 17 | 18 | 0.5 | 3.0 | 2.0 | 1.0 | 1.5 | 0.127 |
| 906 | 5 | 172 | 261 | 195 | 173 | −0.2 | 12.0 | −0.9 | 16.0 | −0.7 | 0.922 |
| 487 | 5 | 173 | 12 | 13 | 17 | 0.3 | 5.0 | 0.0 | 7.0 | −0.3 | 0.176 |
| 347 | 5 | 174 | 7 | 12 | 17 | ... | ... | ... | ... | −0.5 | ... |
| 81 | 5 | 176 | 36 | 27 | 24 | −0.6 | 15.0 | −2.3 | 18.5 | −1.7 | 0.692 |
| 70 | 5 | 186 | 22 | 20 | 5 | 0.1 | ... | ... | ... | ... | 0.478 |
| 322 | 5 | 188 | 10 | 9 | ... | 1.8 | ... | ... | ... | ... | 0.140 |
| 239 | 5 | 197 | 112 | 61 | 102 | 0.2 | 7.0 | −0.5 | 13.0 | −0.7 | 0.188 |

The lower section of Table 4 lists the mean and median signal-to-noise values for various deviation ranges in the two 1991 140-foot telescope observing runs. It also gives the mean signal-to-noise value for the corresponding set of standard redshifts as observed in 1988. This table demonstrates that deviation size does not correlate with signal-to-noise. Larger deviations are not associated with lower quality data. Since the few very high signal-to-noise points in the table would distort the results they are omitted in the means, but included in the median determination. Including or excluding the galaxies observed with a 2.5 MHz bandwidth also has no significant affect. The two largest deviations in the May data may be less reliable, but this could easily be due to sampling since the larger October deviations are completely consistent. Overall the data set in Table 3 appears to be very homogeneous.

**Table 4**

Comparisons Within the Critical Sample

| Combination | BW | W km s$^{-1}$ | N | ΔV±mem km s$^{-1}$ | $\sigma$ km s$^{-1}$ |
|---|---|---|---|---|---|
| 5/91−1988 | 2 | <125 | 6 | 0.08±0.45 | 0.90 |
| | 5 | <150 | 8 | 0.19±0.42 | 1.04 |
| | 5 | >150 | 10 | 0.11±0.26 | 0.74 |
| | All | All | 24 | 0.13±0.18 | 0.85 |
| 10/91−1988 | 2 | <125 | 6 | 0.30±0.28 | 0.56 |
| | 5 | <150 | 7 | −0.71±0.68 | 1.51 |
| | 5 | >150 | 8 | −0.36±0.48 | 1.19 |
| | All | All | 21 | −0.29±0.27 | 1.19 |
| 10/91−5/91 | 2 | <125 | 6 | 0.22±0.21 | 0.42 |
| | 5 | <150 | 5 | −0.48±0.62 | 1.08 |
| | 5 | >150 | 9 | −0.29±0.33 | 0.87 |
| | All | All | 20 | −0.18±0.20 | 0.83 |

| Run | Dev km s$^{-1}$ | BW | S/N | N | $\overline{S/N}$ | Med | $\overline{S/N}$ (88) |
|---|---|---|---|---|---|---|---|
| 5/91 | 0.0-0.4 | 5 | <60 | 7 | 20.3 | 19.0 | 25.9 |
| | | All | <60 | 10 | 21.0 | 23.5 | 26.3 |
| | | 5 | All | 9 | ... | 20.0 | ... |
| | | All | All | 12 | ... | 21.5 | ... |
| | 0.5-1.3 | 5 | <60 | 7 | 19.4 | 18.0 | 30.9 |
| | | All | <60 | 9 | 18.2 | 18.0 | 27.1 |
| | | All | All | 10 | ... | 18.5 | ... |
| | 1.8-2.2 | 5 | <60 | 2 | (10) | ... | (14) |
| 10/91 | 0.0-1.2 | 5 | <60 | 7 | 22.3 | 17.0 | 36.3 |
| | | All | <60 | 12 | 22.8 | 18.5 | 30.3 |
| | | 5 | All | 8 | ... | 20.0 | ... |
| | | All | All | 14 | ... | 21.0 | ... |
| | 2.0-2.3 | 5 | <60 | 5 | 21.2 | 18.0 | 27.8 |

Figure 14 contains six correlation diagrams which display relationships between deviations at different epochs, rank ordering of deviations, and redshift phase. If the deviations were simply due to random observational scatter about stationary values there should be no correlation between sets of deviations. Figure 14A, however, shows that the deviations between May 1991 and 1988 are distinctly correlated with the deviations between October 1991 and 1988. The correlation coefficient in this case is $r = 0.67$ when we omit one highly discordant point which falls far outside the correlated pattern. Following Press et al (1989 [DB]), in the simplest interpretation of correlation, the likelihood of such a value is .02 or less. A more rigorous evaluation assuming a binormal distribution in the deviations, appropriate if the deviations are actual random errors, implies a value for Student's t of 3.7. For 19 points this has a probability of occurrence of only 0.001. The most powerful test of the deviation correlation, however, employs a nonparametric Spearman rank correlation analysis. Figure

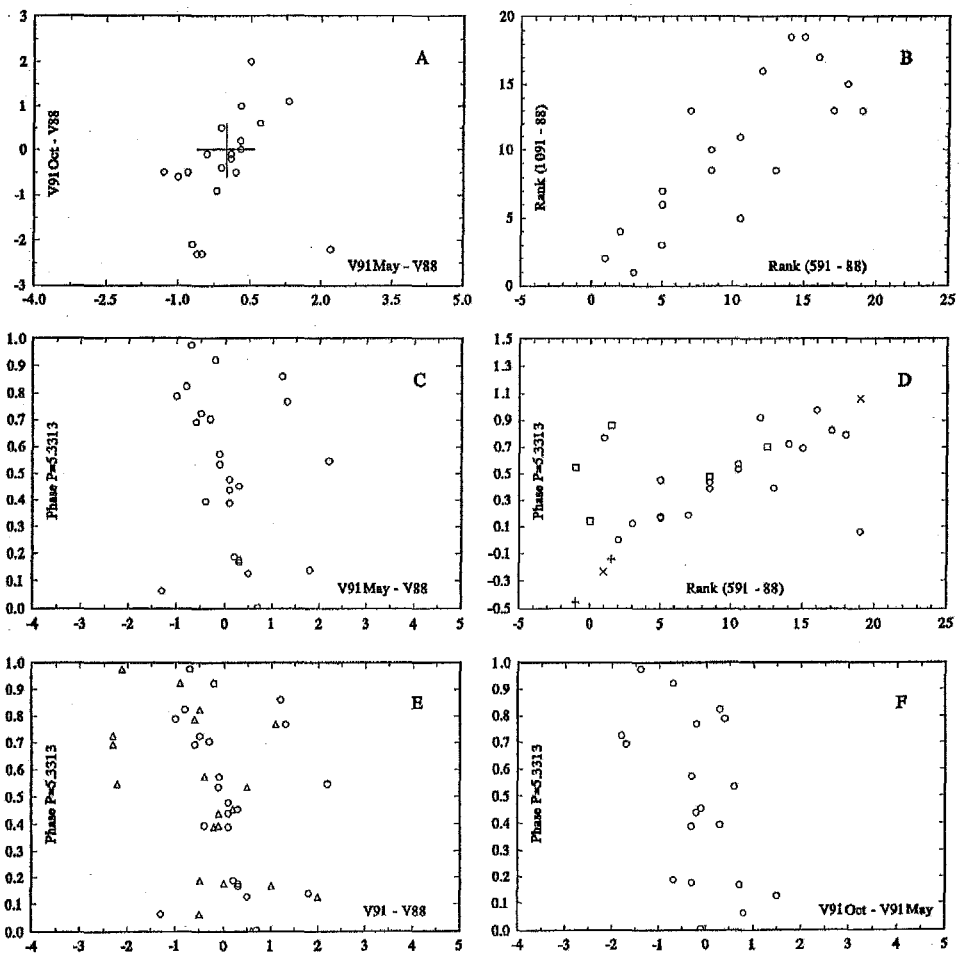


Figure 2.14: Correlation diagrams for the May 1991 140-foot telescope data in the $100 < W < 200$ km/s critical window. Frame A shows the deviations in the redshifts of the standards as observed in May and October 1991 are correlated. In frame B the data are replotted using rank order of the derivations. Frame C shows the May 1991 redshift deviations correlate with global redshift phase at the 1988 standards epoch. Frame D replots the data from frame C replacing deviation with deviation rank for the points observed at both 1991 epochs (open circles) and in 1991 May only (open squares). Observations which overlap into a second phase cycle are plotted with x or + symbols to show the correlation continuity through phase zero. Frame E replots frame C and adds the October 1991 deviations as open triangles for comparison. Frame F shows the May to October 1991 deviations as a function of global redshift phase to illustrate the apparent increase of the deviations during 1991.

14B shows the rank correlation. The correlation coefficient is 0.81, corresponding to $t = 5.7$ or a probability of $1.3 \times 10^{-5}$ of random occurrence. Even the weakest form of evaluation of correlations (Press et al 1989 [DB]) gives this a likelihood of only 0.006. In each case we have evaluated the likelihood using a one-tailed test since the prior hypothesis of variation specifies the sense of the expected correlation; deviations grow with time.

In view of the deviation correlation we can state with a high degree of confidence that the deviations contain a systematic component, they cannot be accounted for by simple random scatter. This result is general, and not affected by profile width, signal-to-noise, or any other obvious characteristics of the data points. The effect is a property of the complete set of points including both large and small deviations; it is not produced by one or two anomalous points. The residual scatter about the correlation is well below 1 km/s. The cross at the origin in figure 14A has an amplitude of 0.6 km/s. There is no reason to believe that any of the data sets are significantly different. The 1988 data set was shown in Paper II, for example, to be quite consistent between three telescopes.

Figure 14C is a phase-deviation diagram for the May 1991 deviations. It is the same as figure 1 but limited to one phase cycle. Figure 14D is the same data with deviation replaced by deviation rank. Rank is the rank within the 19 points common to both 1991 observing runs. Points observed in May 1991 only are shown with a different symbol and interpolated into the rank scale for illustration. Phase is a circular function and it is easily seen that the large apparent deviations are consistent with wrapping the tilted correlation through zero phase. This is why diagrams such as figure 1 are plotted on a double cycle. Allowing for the phase-wrap of two points, the phase-rank correlation coefficient for the 19 points common to both 1991 observing runs in Table 3 is 0.92. The additional points from May alone are consistent; it makes little difference if any particular subset of points is included or excluded. Since phase is quite uniformly distributed in this case, the evaluation of the correlation significance will be similar to a Spearman rank correlation evaluation. The chance of the phase-deviation correlation being accidental is on the order of $10^{-8}$. We conclude with a very high degree of confidence that the systematic component of the deviation correlation is directly related to global redshift phase. All the parameters entering into phase calculations were fixed independently prior to this investigation.

Figure 14E reproduces figure 14C and adds the October 1991 data using a separate symbol. The one-to-one correspondence of the points is easily seen. Along the main spine of the correlation the deviations are generally small, consistent with the discussion of small random errors given earlier. Further examination shows that the points with high phase values tend to shift to the left and include large deviations. Points at low phase values tend the other way. Panel 14F shows the pattern of October to May deviations directly. The deviant pattern has increased between May and October. The correlation coefficient is $-0.5$ which in the weak evaluation corresponds to about an 0.06 likelihood of random occurrence. A direct comparison of the mean of the 10 points with phase less than 0.5 (mean deviation $+0.16$ km/s, dispersion 0.66 km/s) with the 9 points above phase 0.5 (mean deviation $-0.53$ km/s, dispersion 0.92 km/s) gives $t = 1.7$, or a likelihood of 0.04 of coming from the same parent population. We conclude that a marginally significant increase in the deviation pattern occurred between May and October 1991. Further discussion of the increase is contained in section 2.6 which appears in Part 1.

To summarize the evaluation of the 1991 140-foot telescope data we find that a significant

non-random pattern of deviations from the 1988 standard values is present. The pattern is directly related to global redshift phase and appears to be increasing with time. The correlations are consistent with the predictions in Paper III for a time-dependent quantized redshift. In subsequent sections of this paper we examine older data from the perspective of this analysis to generate a more specific model of redshift variation.

Before examining older data samples it is useful to bring out some additional properties of the 140-foot telescope correlation shown in figure 12. We also need to address the question of how points actually shift with time within phase-deviation diagrams. Obviously, if redshifts change, the pattern in a phase-deviation diagram will change with time and depend upon the epoch at which phase is determined. By assuming a form for time dependence we can vary the epoch at which we display a diagram. Figure 13 is plotted at epoch 1988.25, the epoch when the standards were defined. If we assume that each point drifts at a uniform rate determined by its present displacement from zero, a point discussed further below, we can reconstruct the diagram at any epoch. In particular we can choose an epoch where linear sloping features become horizontal; this gives a much simpler presentation of inherent periodicities. This occurs for figure 13 near 1994.0. Figure 15 shows this transformation for periods of 5.3313 and 2.6657 km /s; only the phase was advanced in this example; deviations will also change by a corresponding scale factor.

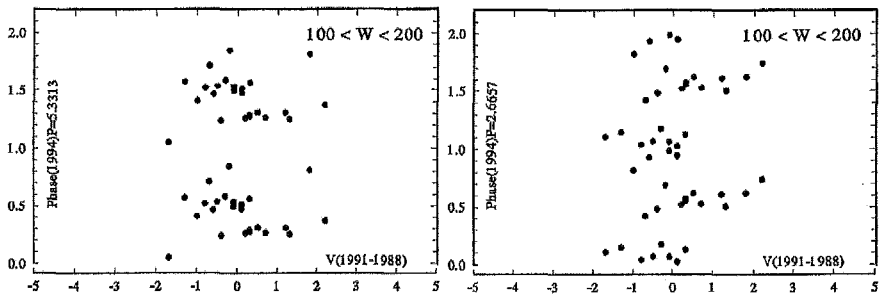


Figure 2.15: Phase-deviation diagrams for the May 1991 140-foot telescope data on galaxies with profiles 100 to 200 km/s wide and $S/N \geq 9$. The left diagram is the same as figure 13 with the epoch advanced to 1994 by assuming that phase drift is directly proportional to time. The phase offset at zero deviation is suggested. The right panel repeats the same data at the 2.6657 km/s period.

Several properties of the diagram are now apparent. There seems little doubt that the points are periodically distributed. The 11 : 1 ratio of points falling within one half phase interval is unlikely at below the 1% level, even allowing for some choice of orientation. In fact all but three points fall within 0.4 in phase. There is an apparent phase displacement at zero; positively and negatively displaced points may not be continuously related. The phase shift appears to be close to one half of the 2.6657 km/s period. Actual mean phases are close to 0.05 and 0.55. No special significance can be attached to a precise value since small solar motion uncertainties, especially in Z, could shift the mean phase slightly. Figure 15 also demonstrates the multiplicity of periods which can fit the data. Periods of 10.6626 and 21.3252 km/s also show unique patterns. Drift rates appear to vary in a regular pattern over at least four successive 5.3313 km/s levels. Although we will refer to the 2.6657 km/s

interval as a basic 'sub'-period it should be kept in mind that successive cycles are not equivalent in drift rates, and only some are populated.

Although the continuous simple smooth drift rate model used to generate Figure 15 is useful to illustrate some properties of the data sets, the model is not consistent with observation of discrete levels. Even if we begin with discrete levels, phase wrapping at a wide range of rates should rapidly destroy any semblance of levels. A more likely model is one where specific levels are populated for some significant period of time. Objects then cascade between levels and are seen changing levels only briefly. Such a model will change the character of Figure 15 slightly. If we imagine looking at such a diagram after a time interval involving several transitions, we might still see horizontal bands, but the bands will not be continuous, there should be individual clumps separated by the transition intervals. Objects observed in transition might connect the clumps. This is the type of model we propose. As a first test we will examine 10-12 year baseline data between the 300-foot telescope TC and FT observations, looking at each of the two critical profile width windows in turn.

## 2.14 Properties of Narrow Profiles

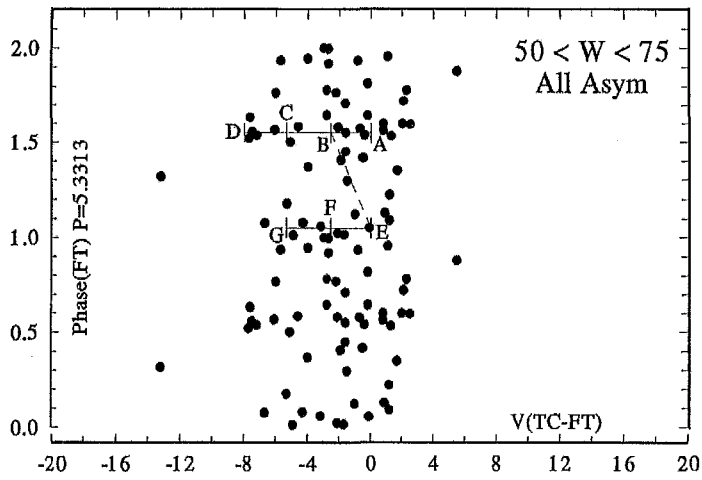


Figure 2.16: Phase-deviation diagram for TC-FT 300-foot telescope data on galaxies with profiles 50 to 75 km/s wide and $S/N > 10$. Phase is calculated for the 5.3313 km/s period at the FT epoch. The deviation scale is in km/s. The solid and dashed lines illustrate tracks galaxies would follow if undergoing transitions between levels. Letters, keyed to discussion in the text, refer to locations where objects might be expected to concentrate.

300-foot telescope data for FT galaxies in the $W = 50 - 75$ km/s window were used in Paper III to determine the 2.6657 sub-periodicity and to fine tune the solar motion. We now examine that data from the viewpoint of the interlevel transition model proposed in Section 13. Figure 16 shows the $P = 5.3313$ km/s phase-deviation diagram for all TC

galaxies with FT data and $S/N > 10$. Phase is referred to the FT epoch characterized as 1975; individual observations distribute between 1973 and 1977.

Time dependent changes will displace points horizontally in such an 'initial epoch' diagram. The diagram differs slightly from the corresponding figure in Paper III where 1988 redshifts, obtained at the 300-foot telescope, were combined with the older 300-foot telescope TC values and a slightly narrower window was used. We opt here to have the maximum possible sample in the minimum time interval. The transitional model is represented by lines connecting displaced phase states. The two horizontal lines are spaced 0.5 in phase and located at phase 0.05 and 0.55 to generally match the observed periodic data point concentrations. Seven positions along the lines, beginning at zero and spaced by 2.6657 km/s, are indicated and designated A through G. The model implies that galaxies should concentrate at these locations if they spend most of their time stationary and move quickly between states in 2.6657 km/s steps.

In accord with the model the location of a galaxy in the diagram depends upon the number and timing of transitions with respect to the FT epoch. Assuming all galaxies pass through point A, we can readily see what is required to populate other locations.

1. Objects at A show no net change between epochs.
2. Objects at phase A at the FT epoch which subsequently shift down by 1, 2, or 3 steps will be found at B, C, and D respectively.
3. Objects at E must have shifted down one step before the FT epoch and show no subsequent net change.
4. Objects at F and G will have shifted down to E before the FT epoch and have subsequently shifted again by 1 or 2 steps respectively.

Objects in transition from A to E at the FT epoch will fall along the dashed line between B and E. The exact location will depend upon how the shift divides at the FT epoch. A similar transition line will connect F downward to A in the next phase cycle. Additional subsequent shifts would displace the transition lines to the left. There is little actual evidence for such objects-in-transit; any significant numbers would rapidly destroy the phase periodicity. The simple presence of a significant periodicity requires the existence of stationary states.

Objects in transition at the time of the second observation will fall between states on the horizontal lines. This is the direction of maximum uncertainty since random errors from both epochs combine; it is unlikely that such situations could be detected using the FT data.

The transition model is certainly consistent with the data in Figure 16, but this adds little not already known since the period was previously determined. To actually test the transition model a more detailed consistency argument is required. Such an argument appears possible by making use of a 'timing sequence' for galaxies within the pattern of transitions. State A in figure 16 is simply a phase state. If galaxies, at the FT epoch, distribute over adjacent states in some 'timing pattern' of 2.6657 km/s steps, every other point in the pattern will be superimposed at point A. The alternate points will fall at phase E. If the timing of transitions can be related to some observable property of the galaxies

we might expect the property to correlate with position in the phase-deviation diagram. For example, if certain classes of galaxies were leading or lagging in transition timing a separation between successive steps along or between the horizontal sequences at phase A and E could be expected.

To test the level and transition concept using timing we must subdivide the sample into categories which might be associated with different stages. The profile asymmetry appears to be a suitable property to accomplish this; paper III and earlier studies have already indicated that asymmetry and position in a phase-deviation diagram show some form of correlation. Two correlations tests involving asymmetry are revealing. The first is a simple correlation between deviation and asymmetry. No direct correlation of this type is detected. If profile shape introduced systematic measurement shifts between data sets such a correlation should be present. Its absence implies that systematic error due to asymmetry is too small to detect. The second correlation examines asymmetry as a function of position in a timing sequence. The ordering of points now involves both phase and deviation. Transitions in a given sequence, which originates from a common phase point, may occur before or after the first epoch of observation. The number of pre first epoch transitions determines the phase a given point will have. The number of post first epoch transitions determines the deviation.

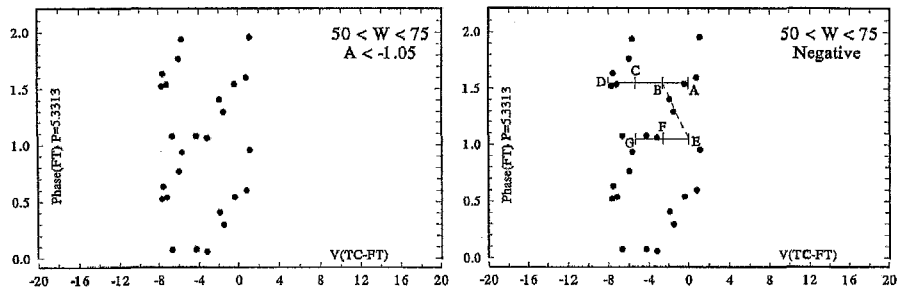


Figure 2.17: Phase-deviation diagram for TC-FT 300-foot telescope data on galaxies with negatively asymmetric profiles 50 to 75 km/s wide and $S/N > 10$. The figure is the same as figure 16 except it omits the galaxies with $A > -1.05$. The right panel repeats the transition lines and letters from figure 16. The negatively asymmetric galaxies appear to concentrate near A, D and G rather than being randomly selected from the total sample.

To introduce the timing test it is convenient to replot the data from figure 16 in separate ranges of asymmetry. Figure 17 replots figure 16 to include only those objects with negative asymmetry greater than 5%. Whereas the points in figure 16 distribute quite generally, the negative asymmetry states appear to be more restricted. The number of points is not large, but they appear to favor locations A, D and G while avoiding B, C and E. This is what one would expect to see if all these galaxies had recently undergone three steps. Those for which all three steps occurred after the FT epoch would move to D; those where the first step preceded the FT observation would be found at G. This class of galaxies can therefore be accounted for as populating recent steps in a timing sequence.

The real test of the timing concept comes when we contrast the locations of galaxies with positive asymmetry. Figure 18 replots figure 17 using only those objects with positive

asymmetry greater than 5%. The pattern is quite different; points avoid locations A, D and F and favor B, C and E, virtually the opposite of the negative asymmetry objects. This can also be accounted for if all these galaxies had recently undergone three steps. Points where all three steps preceded the FT epoch would be found at E while those with two steps preceding the FT observations would be found at B. New recent shifts could begin moving points to C and G. We again find that related points in a timing sequence are populated; these points precede the negative profile objects in transition timing.

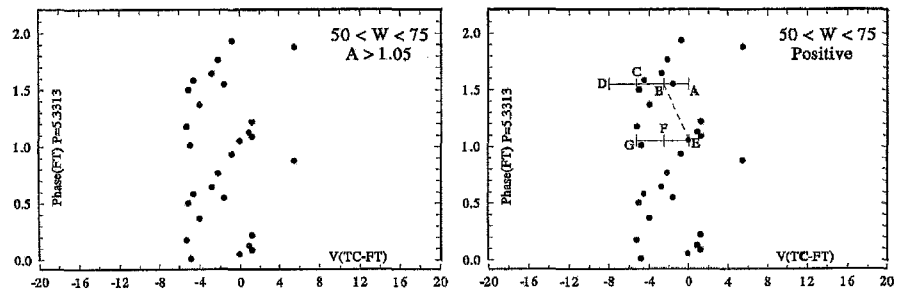


Figure 2.18: Phase-deviation diagram for TC-FT 300-foot telescope data on galaxies with positively asymmetric profiles 50 to 75 km/s wide and $S/N > 10$. The figure is the same as figure 16 except it omits the galaxies with $A < 1.05$. The right panel repeats the transition lines and letters from figure 16. The positively asymmetric galaxies appear to anti-correlate in location with the negatively asymmetric objects shown in figure 17.

Figure 19 shows both the positive (upper panel) and negative (lower panel) asymmetry galaxies and adds the symmetric profile objects (open circles). The symmetric profile galaxies concentrate distinctly at A and F. The timing sequence concept is now especially well illustrated in the E to G sequence. Positive asymmetry dominates at E, symmetric at F and negative at G. This corresponds to zero, one and two steps, since the FT epoch, for objects at phase E at the time of the FT observations.

Explanation of the displacements in figures 16-19 requires that at least three transitions have occurred to produce some of the points. For a formal correlation evaluation we will therefore examine a sequence of possible situations involving $3 \pm 1$ transitions with respect to point A. We adopt a notation $(m : n)$ for the (pre:post) transition number ratio. Point E $(3 : 0)$ is the leading point in such a transition sequence. We can account for the positions in figures 16-19 with a timing sequence E,C,B,A,F,G,D corresponding to $(3 : 0), (2 : 2), (2 : 1), (2 : 0), (1 : 1), (1 : 2), (0 : 3)$. When asymmetry is compared with position within this sequence there is a significant correlation. Using 37 objects which can be fairly unambiguously associated with the seven points, a Spearman rank correlation coefficient of 0.34 is observed. For 37 points this implies correlation at the 98 percent confidence level. The correlation coefficient rises to 0.56 for the 29 least deviant points, significant at the 99.9 percent confidence level.

The data are clearly consistent with a level and transition model. The ultimate test of such a model in this profile width interval will come through continued precision monitoring. The principal conclusion we can draw already is that asymmetry distinctions provide an important means of defining subsamples. The ordering of asymmetry subgroups in a timing

sequence of successive transitions does appear to provide a basis for observed asymmetry correlations, and provides a test of the transition model. There are certainly many variants of the introductory model presented here, involving, for example, transitions in other multiples of the 2.6657 km/s period. We have presented what appears to be one of the simplest models to introduce the concept.

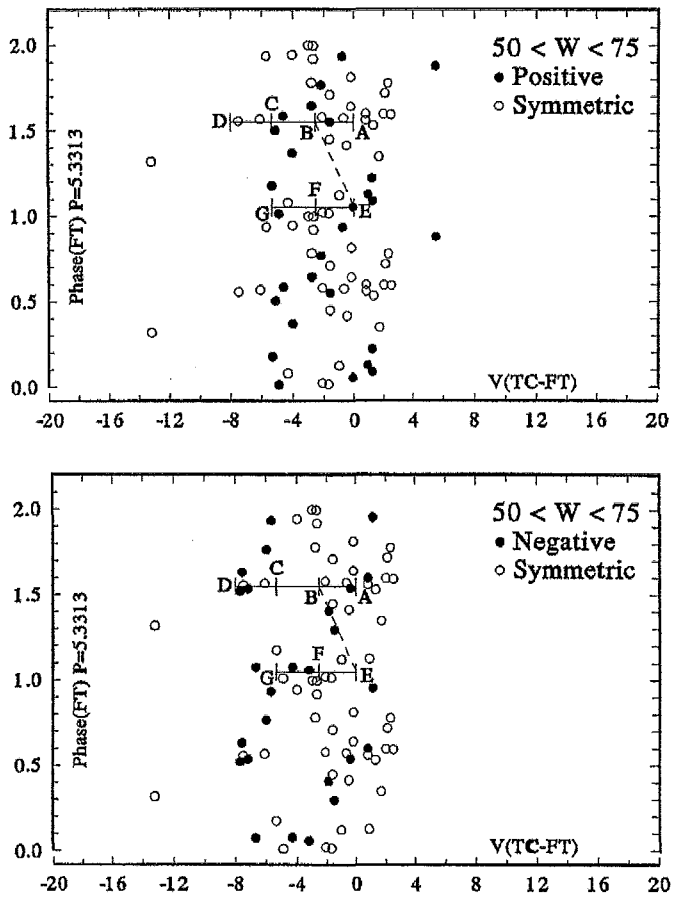


Figure 2.19: Phase-deviation diagram for TC-FT 300-foot telescope data on galaxies with symmetric profiles 50 to 75 km/s wide and $S/N > 10$ (open circles), compared with positively and negatively asymmetric profile objects (filled circles) replotted from figures 17 and 18. Progressive changes in asymmetry appear to occur along the horizontal sequences which are repeated from figure 16.

## 2.15 Sections 2.5 through 2.7 (in Part 1)

Sections 2.5, 2.6, and 2.7 in the original were not significantly changed, and may be appended directly to this revised version. Section and figure numbers are correct within each part but are shifted out of sequence because of the Latex numbering system used to combine three parts.

The final correlation discussed was not included in part 3 originally, but was included in my referee's response in part 2 as figure 12. It is reproduced here to show the actual correlation with asymmetry. Based upon the later work discussed in the book there is no doubt in my mind that this study is a direct proof that asymmetry evolution is indeed the process which leads to quantum transitions in QTC and probably in general.

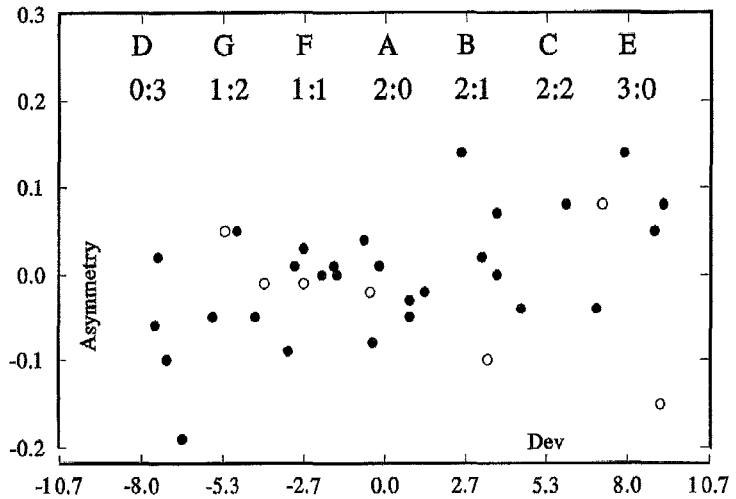


Figure 2.20: Asymmetry as a function of position in the transition timing sequence

**Table 1**

May 1991 Data

| TC | FT | UGC | BW MHz | $V_h$ km s$^{-1}$ | W km s$^{-1}$ | A | S/N | Q | DV km s$^{-1}$ | DW km s$^{-1}$ |
|---|---|---|---|---|---|---|---|---|---|---|
| 6 | 0 | 192 | 5 | −347.3 | 88.3 | −1.10 | 99.4 | | 0.9 | 1.3 |
| 6 | 0 | 192 | 2 | −347.4 | 87.2 | −1.11 | 145.3 | | 0.8 | 0.2 |
| 7 | 62 | 300 | 2 | ... | ... | ... | ... | XF | ... | ... |
| 432 | 80 | 0 | 2 | 1073.5 | 103.0 | −1.03 | 32.8 | | 0.3 | −0.2 |
| 11 | 0 | 668 | 2 | −232.4 | 38.2 | −1.01 | 250.7 | | 0.1 | 0.2 |
| 906 | 0598 | 1117 | 5 | −181.1 | 171.9 | −1.17 | 195.4 | M33 | −0.2 | −0.2 |
| 18 | 96 | 1149 | 2 | 657.6 | 75.1 | 1.07 | 121.4 | | −0.1 | −0.5 |
| 443 | 100 | 1201 | 2 | ... | ... | ... | ... | XS | ... | ... |
| 23 | 118 | 1501 | 2 | 198.5 | 124.6 | 1.23 | 19.4 | S | 1.3 | 2.1 |
| 454 | 127 | 1831 | 2 | ... | ... | ... | ... | XS | ... | ... |
| 36 | 145 | 2034 | 2 | 576.7 | 65.7 | −1.13 | 26.0 | S | −0.5 | −1.2 |
| 459 | 150 | 2080 | 2 | ... | ... | ... | ... | XS | ... | ... |
| 460 | 151 | 2082 | 2 | ... | ... | ... | ... | XS | ... | ... |
| 41 | 162 | 2193 | 2 | 517.6 | 43.1 | −1.02 | 63.2 | S | 0.4 | 0.7 |
| 43 | 168 | 2302 | 2 | 1103.5 | 70.8 | −1.10 | 26.2 | S | 0.5 | 0.9 |
| 46 | 183 | 0 | 2 | ... | ... | ... | ... | XF | ... | ... |
| 468 | 190 | 0 | 2 | ... | ... | ... | ... | XS | ... | ... |
| 473 | 206 | 2729 | 10 | 1937.7 | 264.5 | 1.14 | 11.0 | S! | −2.7 | −7.1 |
| 48 | 231 | 2855 | 10 | 1216.4 | 466.6 | 1.23 | 18.9 | S! | 1.9 | −6.9 |
| 51 | 238 | 2953 | 10 | 893.7 | 496.5 | 1.11 | 10.3 | RS | −1.8 | 3.5 |
| 477 | 242 | 3013 | 10 | 2459.1 | 349.8 | 1.03 | 10.8 | S! | −2.1 | −3.3 |
| 481 | 248 | 3137 | 5 | 995.3 | 253.3 | 1.14 | 13.5 | S | 2.2 | 3.2 |
| 482 | 251 | 3144 | 5 | 1636.9 | 162.4 | −1.13 | 18.0 | S | 0.1 | 2.0 |
| 56 | 252 | 3174 | 5 | 670.2 | 122.1 | 1.17 | 13.7 | S | −0.5 | −3.8 |
| 486 | 271 | 3273 | 5 | 617.7 | 207.6 | −1.02 | 15.6 | S | 1.8 | 2.5 |
| 487 | 277 | 3303 | 5 | 519.3 | 178.4 | −1.03 | 12.6 | S! | 0.3 | 5.1 |
| 61 | 0 | 3334 | 10 | 3930.7 | 695.0 | −1.45 | 9.5 | S | 0.7 | −38.1 |
| 64 | 0 | 3384 | 2 | 1089.8 | 92.7 | −1.08 | 19.9 | S | 0.6 | 1.0 |
| 492 | 302 | 0 | 10 | 731.8 | 328.8 | −1.11 | 23.1 | S | 0.5 | 1.6 |
| 70 | 306 | 3475 | 5 | 486.2 | 180.2 | 1.02 | 19.7 | S | 0.1 | −6.0 |
| 71 | 307 | 3496 | 2 | 1593.9 | 118.4 | 1.08 | 2.9 | FS! | 6.4 | 29.8 |
| 74 | 314 | 3574 | 5 | 1441.4 | 170.3 | −1.07 | 17.3 | S | 0.5 | 6.1 |
| 499 | 320 | 3685 | 2 | 1796.2 | 100.1 | −1.10 | 26.5 | | −0.1 | −1.7 |
| 81 | 322 | 3711 | 5 | 433.3 | 173.2 | 1.08 | 27.1 | RS | −0.6 | −3.3 |
| 83 | 325 | 3809 | 10 | 2200.7 | 476.7 | 1.06 | 12.6 | | −3.2 | −5.5 |
| 87 | 331 | 3851 | 2 | 100.6 | 115.1 | 1.00 | 61.5 | | 0.7 | −0.9 |
| 93 | 338 | 3974 | 2 | 273.4 | 89.5 | −1.05 | 34.5 | | 0.8 | 0.7 |
| 100 | 351 | 4305 | 5 | 156.7 | 73.6 | 1.03 | 156.6 | +C | 0.0 | 0.2 |
| 100 | Comp | 0 | 5 | −145.8 | 38.3 | −1.12 | 47.7 | cmp | ... | ... |
| 100 | 351 | 4305 | 2 | 156.7 | 73.5 | 1.03 | 112.1 | | 0.0 | 0.1 |

**Table 1**—*Continued*

| TC | FT | UGC | BW MHz | $V_h$ km s$^{-1}$ | W km s$^{-1}$ | A | S/N | Q | DV km s$^{-1}$ | DW km s$^{-1}$ |
|---|---|---|---|---|---|---|---|---|---|---|
| 106 | 0 | 4483 | 2 | 156.8 | 53.7 | 1.10 | 19.4 | | 0.0 | −0.8 |
| 117 | 406 | 5139 | 2 | 139.8 | 46.8 | 1.01 | 27.5 | | −0.7 | −0.8 |
| 122 | 0 | 5251 | 10 | 1480.8 | 302.2 | −1.27 | 18.6 | | 0.7 | −6.1 |
| 124 | 0 | 5280 | 10 | 1538.5 | 300.1 | −1.15 | 6.7 | FS! | 10.9 | 10.2 |
| 128 | 431 | 5373 | 2 | 301.2 | 64.8 | 1.06 | 35.8 | | 0.0 | 1.0 |
| 134 | 450 | 0 | 2 | 324.1 | 65.3 | 1.02 | 96.8 | +C | −0.2 | −0.3 |
| 134 | Comp | 0 | 2 | 133.4 | 47.3 | −1.13 | 16.2 | cmp | ... | ... |
| 136 | 456 | 5557 | 5 | 592.7 | 150.2 | 1.13 | 26.4 | | −0.7 | 2.5 |
| 143 | 485 | 5829 | 2 | 629.8 | 96.9 | 1.06 | 21.8 | | 0.1 | −1.0 |
| 150 | 507 | 6079 | 5 | 683.5 | 249.2 | −1.05 | 20.9 | | 0.7 | 1.0 |
| 917 | 3556 | 6225 | 10 | 698.1 | 337.1 | 1.01 | 25.7 | | −0.4 | 3.9 |
| 917 | 3556 | 6225 | 5 | 699.1 | 334.3 | 1.01 | 17.9 | | 0.6 | 1.1 |
| 164 | 536 | 6360 | 5 | 1153.9 | 129.8 | −1.17 | 17.6 | | −0.8 | −1.8 |
| 175 | 565 | 6628 | 2 | 848.8 | 56.0 | −1.07 | 17.4 | | −0.8 | −0.8 |
| 182 | 589 | 6817 | 2 | 241.1 | 72.1 | −1.12 | 25.3 | | −0.4 | 1.7 |
| 188 | 628 | 7047 | 2 | 206.4 | 87.0 | −1.26 | 16.7 | | 0.8 | 2.8 |
| 201 | 675 | 7278 | 2 | 292.4 | 90.7 | 1.07 | 84.1 | | −0.1 | −1.4 |
| 210 | 706 | 7534 | 2 | 723.7 | 77.7 | 1.08 | 18.9 | | 0.4 | 4.7 |
| 217 | 715 | 7577 | 2 | 199.9 | 59.7 | 1.26 | 18.1 | +C | 4.4 | 7.0 |
| 217 | Comp | 0 | 2 | 274.8 | 68.7 | −1.03 | 6.4 | cmp | ... | ... |
| 239 | 770 | 7907 | 5 | 640.0 | 192.7 | −1.14 | 60.6 | C | 0.2 | −4.4 |
| 259 | 826 | 0 | 5 | 740.6 | 133.0 | −1.22 | 23.0 | | −0.3 | 1.3 |
| 260 | 834 | 8188 | 2 | 321.9 | 59.1 | 1.11 | 26.5 | | 0.7 | 2.7 |
| 273 | 863 | 8320 | 2 | 192.1 | 87.5 | 1.05 | 24.7 | | 1.0 | −0.1 |
| 295 | 933 | 8837 | 2 | 139.7 | 109.0 | 1.21 | 9.1 | | −1.3 | 1.1 |
| 302 | 944 | 8981 | 5 | 231.4 | 200.6 | −1.31 | 205.8 | M101 | 1.1 | −0.3 |
| 304 | 947 | 9013 | 5 | 274.3 | 56.3 | 1.01 | 70.4 | C | −0.5 | −0.1 |
| 304 | 947 | 9013 | 2 | 274.3 | 56.1 | 1.00 | 76.6 | +C | −0.5 | −0.3 |
| 304 | Comp | 0 | 2 | 168.3 | 96.0 | ... | 2.8 | Gau | ... | ... |
| 308 | 966 | 9240 | 2 | 149.9 | 66.2 | −1.17 | 12.4 | | −0.3 | −5.8 |
| 322 | 999 | 0 | 5 | 1841.5 | 172.5 | 1.00 | 9.2 | | 1.8 | −15.5 |
| 328 | 0 | 9797 | 10 | 3398.8 | 387.1 | −1.13 | 11.5 | | 8.5 | 16.5 |
| 555 | 1019 | 9801 | 10 | 667.9 | 501.6 | −1.28 | 20.6 | | −0.8 | 2.1 |
| 559 | 1027 | 9906 | 10 | 655.1 | 214.2 | 1.08 | 17.4 | | −0.7 | −0.4 |
| 333 | 1028 | 9912 | 2 | 1031.0 | 57.3 | −1.07 | 11.3 | | −0.4 | −6.7 |
| 338 | 1035 | 10014 | 5 | 1121.7 | 132.8 | 1.04 | 12.8 | | 1.2 | 0.4 |
| 562 | 1042 | 10075 | 10 | 834.4 | 321.9 | 1.24 | 22.4 | | 2.0 | 1.0 |
| 345 | 1046 | 10310 | 2 | 716.6 | 103.9 | 1.04 | 8.5 | | −0.4 | −5.7 |
| 565 | 1048 | 10359 | 5 | 907.7 | 234.3 | 1.00 | 24.9 | | −0.6 | 1.8 |
| 347 | 0 | 10445 | 5 | 962.2 | 169.8 | −1.04 | 11.7 | | −2.2 | −4.5 |

Table 1—*Continued*

| TC | FT | UGC | BW MHz | $V_h$ km s$^{-1}$ | W km s$^{-1}$ | A | S/N | Q | DV km s$^{-1}$ | DW km s$^{-1}$ |
|---|---|---|---|---|---|---|---|---|---|---|
| 353 | 1056 | 10736 | 5 | 491.1 | 160.7 | −1.14 | 11.1 | | −0.1 | 1.3 |
| 354 | 1058 | 10792 | 2 | 1234.1 | 75.0 | 1.08 | 6.5 | | 1.2 | −0.2 |
| 358 | 0 | 10897 | 5 | 1322.6 | 143.7 | 1.09 | 10.9 | S | 2.2 | 5.2 |
| 364 | 1074 | 11193 | 5 | 1511.4 | 120.4 | −1.19 | 4.0 | FS | −1.7 | −3.4 |
| 932 | 6643 | 11218 | 10 | 1485.7 | 381.2 | −1.07 | 10.6 | | 0.1 | 21.9 |
| 365 | 1075 | 11220 | 2 | 1448.0 | 97.0 | 1.03 | 9.3 | | 0.3 | 7.3 |
| 583 | 1078 | 11300 | 5 | 490.8 | 228.1 | −1.06 | 13.3 | | 0.8 | 0.4 |
| 372 | −11 | 0 | 2 | −78.9 | 42.2 | 1.03 | 22.5 | | 0.0 | 4.9 |
| 373 | −15 | 0 | 2 | 1561.9 | 98.5 | 1.06 | 19.2 | | −0.9 | 5.5 |
| 374 | −12 | 0 | 2 | −56.9 | 85.9 | ... | 256.2 | Gau | −0.1 | 0.7 |
| 377 | 1082 | 0 | 2 | 1423.5 | 92.1 | 1.22 | 9.8 | | −0.9 | −3.7 |
| 379 | 0 | 11604 | 10 | 1424.6 | 343.6 | −1.10 | 8.2 | | 2.9 | 5.5 |
| 380 | 1085 | 0 | 2 | −141.4 | 34.8 | −1.09 | 12.1 | | 0.5 | −3.2 |
| 605 | 1088 | 11707 | 5 | 904.9 | 206.5 | 1.20 | 19.3 | S | ... | ... |
| 387 | 0 | 11759 | 5 | 3258.1 | 151.8 | −1.58 | 7.6 | S | −1.7 | −9.5 |
| 609 | 1093 | 11861 | 10 | 1481.2 | 273.5 | 1.05 | 12.3 | | −0.4 | 10.5 |
| 393 | 1098 | 11891 | 5 | 460.8 | 154.3 | 1.29 | 20.6 | r | −1.0 | −1.9 |
| 396 | 1107 | 0 | 2 | ... | ... | ... | ... | XF | ... | ... |
| 399 | 1113 | 12082 | 2 | 803.5 | 86.9 | −1.13 | 18.0 | | 0.8 | 0.8 |
| 402 | 1117 | 12113 | 10 | 816.9 | 535.6 | −1.11 | 8.4 | S | −0.8 | −0.8 |
| 620 | 1139 | 12392 | 2 | ... | ... | ... | ... | S | ... | ... |
| 936 | 7640 | 12554 | 10 | 371.6 | 268.8 | −1.13 | 30.2 | r | 0.2 | −0.2 |
| 412 | 1147 | 12613 | 2 | −186.6 | 42.0 | −1.34 | 18.0 | R | −0.2 | 0.0 |
| 413 | 1149 | 12632 | 5 | 422.1 | 127.7 | −1.08 | 19.3 | rS | 0.3 | −0.3 |
| 414 | 1159 | 12732 | 5 | 748.3 | 137.0 | 1.14 | 37.7 | S | 0.1 | −1.9 |
| 415 | 1160 | 12754 | 5 | 748.7 | 214.3 | 1.03 | 14.0 | S | −1.8 | −0.2 |
| 417 | 0 | 12894 | 2 | 320.7 | 79.1 | −1.59 | 8.9 | S | −2.0 | 10.4 |
| 418 | 1171 | 0 | 2 | −122.9 | 79.7 | −1.13 | 86.1 | | 0.2 | −0.6 |
| 418 | 1171 | 0 | 2 | ... | ... | ... | ... | CB | ... | ... |
| 418 | Bcmp | 0 | 2 | −185.3 | 87.1 | −1.09 | 18.2 | Bcm | ... | ... |

C = Galaxy has companion, +C = in main beam, <,> indicate below or above
cmp = Second object in main beam, Bcm = Object in West off field
CB = Object in West (CC = East) off field disturbes baseline or profile
Gau = Gauss fit to profile
F = Object too weak for effective measurements
H = Hanning smoothing employed
I = Interference, <,> indicate below or above
R = Ringing, r = minor ringing effects, <,> indicate below or above
S = Baseline disturbed by Sun, S! if effect is large
X = Not measured, XF = Too weak, XS = Solar interference
0VH = Galactic HI disturbes profile

**Table 2**

October 1991 Data

| TC | FT | UGC | BW MHz | $V_h$ km s$^{-1}$ | W km s$^{-1}$ | A | S/N | Q | DV km s$^{-1}$ | DW km s$^{-1}$ |
|---|---|---|---|---|---|---|---|---|---|---|
| 6 | 0 | 192 | 5 | −347.6 | 87.7 | −1.13 | 78.1 | | 0.6 | 0.7 |
| 6 | 0 | 192 | 2 | −347.8 | 87.5 | −1.14 | 141.5 | | 0.4 | 0.5 |
| 7 | 62 | 300 | 2 | ... | ... | ... | ... | XF | ... | ... |
| 432 | 80 | 0 | 2 | 1073.4 | 102.8 | −1.06 | 47.6 | | 0.2 | −0.4 |
| 11 | 0 | 668 | 2 | −232.4 | 38.0 | −1.02 | 247.8 | | 0.1 | 0.0 |
| 906 | 0598 | 1117 | 5 | −181.8 | 172.2 | −1.14 | 172.8 | M33 | −0.9 | 0.1 |
| 18 | 96 | 1149 | 2 | 658.0 | 75.4 | 1.07 | 115.9 | | 0.3 | −0.2 |
| 443 | 100 | 1201 | 2 | 852.7 | 335.5 | −1.12 | 27.5 | | 0.8 | 3.0 |
| 23 | 118 | 1501 | 2 | 198.3 | 123.8 | 1.21 | 20.5 | | 1.1 | 1.3 |
| 454 | 127 | 1831 | 2 | 529.8 | 481.0 | −1.16 | 16.2 | | −2.2 | −3.0 |
| 36 | 145 | 2034 | 2 | 579.1 | 62.7 | 1.02 | 32.4 | | 1.9 | −4.2 |
| 459 | 150 | 2080 | 2 | 904.9 | 145.1 | −1.04 | 44.1 | Su? | 1.2 | 1.5 |
| 460 | 151 | 2082 | 2 | 708.0 | 216.9 | −1.04 | 15.7 | | 1.6 | 0.7 |
| 41 | 162 | 2193 | 2 | 518.0 | 43.5 | −1.00 | 63.8 | | 0.8 | 1.1 |
| 43 | 168 | 2302 | 2 | 1103.5 | 71.2 | −1.12 | 39.4 | C<? | 0.5 | 1.3 |
| 46 | 183 | 0 | 2 | ... | ... | ... | ... | XF | ... | ... |
| 468 | 190 | 0 | 2 | 1710.4 | 326.7 | −1.14 | 20.2 | C>? | 2.2 | −0.5 |
| 473 | 206 | 2729 | 10 | 1943.8 | 278.0 | 1.11 | 11.3 | | 3.4 | 6.4 |
| 48 | 231 | 2855 | 10 | 1215.7 | 481.5 | 1.16 | 19.4 | | 1.2 | 8.0 |
| 51 | 238 | 2953 | 10 | 897.0 | 494.5 | 1.10 | 9.0 | R< | 1.5 | 1.5 |
| 477 | 242 | 3013 | 10 | 2458.0 | 344.2 | −1.04 | 15.4 | | −3.2 | −8.9 |
| 481 | 248 | 3137 | 5 | 990.9 | 251.1 | 1.10 | 9.4 | | −2.2 | 1.0 |
| 482 | 251 | 3144 | 5 | 1636.6 | 160.6 | −1.09 | 12.3 | | −0.2 | 0.2 |
| 56 | 252 | 3174 | 5 | 668.4 | 119.6 | 1.13 | 11.4 | | −2.3 | −6.3 |
| 486 | 271 | 3273 | 5 | 618.0 | 204.9 | 1.02 | 16.6 | | 2.1 | −0.2 |
| 487 | 277 | 3303 | 5 | 519.0 | 177.8 | −1.03 | 17.4 | | 0.0 | 4.5 |
| 61 | 0 | 3334 | 10 | 3925.9 | 697.9 | −1.36 | 9.1 | I> | −4.1 | −35.2 |
| 64 | 0 | 3384 | 2 | 1094.5 | 105.5 | 1.09 | 17.2 | | 5.3 | 13.8 |
| 492 | 302 | 0 | 10 | 733.0 | 324.7 | −1.11 | 32.0 | | 1.7 | −2.5 |
| 70 | 306 | 3475 | 5 | 486.2 | 182.2 | 1.03 | 4.8 | R | 0.1 | −4.0 |
| 71 | 307 | 3496 | 2 | ... | ... | ... | ... | XF | ... | ... |
| 74 | 314 | 3574 | 5 | 1442.9 | 161.3 | −1.02 | 17.9 | | 2.0 | −2.9 |
| 499 | 320 | 3685 | 2 | 1796.8 | 102.3 | −1.10 | 22.4 | | 0.5 | 0.5 |
| 81 | 322 | 3711 | 5 | 431.6 | 178.3 | 1.07 | 24.2 | RH | −2.3 | 1.8 |
| 83 | 325 | 3809 | 10 | 2200.7 | 471.3 | 1.05 | 13.0 | | −3.2 | −10.9 |
| 87 | 331 | 3851 | 2 | 100.5 | 115.7 | −1.02 | 69.0 | | 0.6 | −0.3 |
| 93 | 338 | 3974 | 2 | 272.8 | 89.2 | −1.09 | 36.7 | | 0.2 | 0.4 |
| 100 | 351 | 4305 | 5 | 156.7 | 73.4 | 1.03 | 164.9 | +C | 0.0 | 0.0 |
| 100 | Comp | 0 | 5 | −145.5 | 38.6 | −1.07 | 45.0 | cmp | ... | ... |
| 100 | 351 | 4305 | 2 | 156.5 | 73.3 | 1.03 | 120.8 | | −0.2 | −0.1 |

Table 2—*Continued*

| TC | FT | UGC | BW MHz | $V_h$ km s$^{-1}$ | W km s$^{-1}$ | A | S/N | Q | DV km s$^{-1}$ | DW km s$^{-1}$ |
|---|---|---|---|---|---|---|---|---|---|---|
| 106 | 0 | 4483 | 2 | 156.1 | 56.0 | 1.06 | 14.2 | | −0.7 | 1.5 |
| 117 | 406 | 5139 | 2 | 141.2 | 47.1 | 1.09 | 26.4 | | 0.7 | −0.5 |
| 122 | 0 | 5251 | 10 | 1478.1 | 304.2 | −1.35 | 19.2 | | −2.0 | −4.1 |
| 124 | 0 | 5280 | 10 | 1545.0 | 307.9 | −1.15 | 5.1 | F | 17.4 | 18.0 |
| 128 | 431 | 5373 | 2 | 301.5 | 64.4 | 1.05 | 53.7 | | 0.3 | 0.6 |
| 134 | 450 | 0 | 2 | 324.5 | 65.9 | 1.04 | 94.3 | +C | 0.2 | 0.3 |
| 134 | Comp | 0 | 2 | 132.4 | 46.4 | −1.07 | 13.5 | cmp | ... | ... |
| 136 | 456 | 5557 | 5 | 591.3 | 148.7 | 1.10 | 36.3 | | −2.1 | 1.0 |
| 143 | 485 | 5829 | 2 | 629.6 | 101.8 | 1.07 | 30.3 | | −0.1 | 3.9 |
| 150 | 507 | 6079 | 5 | 681.3 | 249.3 | −1.07 | 32.4 | | −1.5 | 1.1 |
| 917 | 3356 | 6225 | 10 | ... | ... | ... | ... | XS | ... | ... |
| 917 | 3556 | 6225 | 5 | 697.9 | 334.2 | −1.00 | 24.4 | S | −0.6 | 1.0 |
| 164 | 536 | 6360 | 5 | 1154.2 | 129.4 | −1.19 | 28.4 | S | −0.5 | −2.2 |
| 175 | 565 | 6628 | 2 | 849.2 | 56.1 | −1.05 | 32.9 | | −0.4 | −0.7 |
| 182 | 589 | 6817 | 2 | 241.6 | 70.8 | −1.09 | 39.5 | | 0.1 | 0.4 |
| 188 | 628 | 7047 | 2 | 205.3 | 90.2 | −1.23 | 26.7 | | −0.3 | 6.0 |
| 201 | 675 | 7278 | 2 | 292.5 | 92.3 | 1.06 | 74.7 | | 0.0 | 0.2 |
| 210 | 706 | 7534 | 2 | 722.1 | 74.9 | 1.04 | 19.9 | | −1.2 | 1.9 |
| 217 | 715 | 7577 | 2 | 197.0 | 55.4 | 1.08 | 28.5 | S+C | 1.5 | 2.7 |
| 217 | Comp | 0 | 2 | 271.0 | 68.2 | −1.24 | 9.5 | cmp | ... | ... |
| 239 | 770 | 7907 | 5 | 639.3 | 198.1 | −1.12 | 101.8 | C | −0.5 | 1.0 |
| 259 | 826 | 0 | 5 | ... | ... | ... | ... | XS | ... | ... |
| 260 | 834 | 8188 | 2 | 321.8 | 57.0 | 1.14 | 36.3 | | 0.6 | 0.6 |
| 273 | 863 | 8320 | 2 | 190.9 | 88.6 | 1.02 | 38.0 | S | −0.2 | 1.0 |
| 295 | 933 | 8837 | 2 | 140.5 | 113.1 | 1.20 | 13.0 | S | −0.5 | 5.2 |
| 302 | 944 | 8981 | 5 | 230.7 | 201.7 | −1.23 | 171.3 | M101 | 0.4 | 0.8 |
| 304 | 947 | 9013 | 5 | 274.5 | 57.0 | −1.01 | 70.4 | C | −0.3 | 0.6 |
| 304 | 947 | 9013 | 2 | 274.2 | 56.5 | −1.02 | 84.6 | S+C | −0.6 | 0.1 |
| 304 | Comp | 0 | 2 | 167.1 | 88.5 | ... | 2.7 | Gau | ... | ... |
| 308 | 966 | 9240 | 2 | 149.9 | 67.2 | −1.13 | 25.9 | | −0.3 | −4.8 |
| 322 | 999 | 0 | 5 | ... | ... | ... | ... | XS | ... | ... |
| 328 | 0 | 9797 | 10 | ... | ... | ... | ... | XS | ... | ... |
| 555 | 1019 | 9801 | 10 | ... | ... | ... | ... | XS | ... | ... |
| 559 | 1027 | 9906 | 10 | ... | ... | ... | ... | XS | ... | ... |
| 333 | 1028 | 9912 | 2 | 1033.2 | 60.2 | 1.03 | 14.0 | | 1.8 | −3.8 |
| 338 | 1035 | 10014 | 5 | ... | ... | ... | ... | XS | ... | ... |
| 562 | 1042 | 10075 | 10 | ... | ... | ... | ... | XS | ... | ... |
| 345 | 1046 | 10310 | 2 | 716.9 | 107.9 | 1.03 | 14.3 | | −0.1 | −1.7 |
| 565 | 1048 | 10359 | 5 | 908.1 | 235.0 | 1.05 | 22.2 | S! | −0.2 | 2.5 |
| 347 | 0 | 10445 | 5 | 961.7 | 174.1 | −1.12 | 17.2 | S! | −2.7 | −0.2 |

**Table 2**—*Continued*

| TC | FT | UGC | BW MHz | $V_h$ km s$^{-1}$ | W km s$^{-1}$ | A | S/N | Q | DV km s$^{-1}$ | DW km s$^{-1}$ |
|---|---|---|---|---|---|---|---|---|---|---|
| 353 | 1056 | 10736 | 5 | 490.8 | 160.7 | −1.07 | 12.3 | S | −0.4 | 1.3 |
| 354 | 1058 | 10792 | 2 | 1232.5 | 72.8 | −1.09 | 9.9 | | −0.4 | −2.4 |
| 358 | 0 | 10897 | 5 | 1318.2 | 138.2 | −1.01 | 16.8 | S! | −2.2 | −0.3 |
| 364 | 1074 | 11193 | 5 | ... | ... | ... | ... | XF | ... | ... |
| 932 | 6643 | 11218 | 10 | 1481.6 | 364.1 | −1.07 | 9.2 | S! | −4.0 | 4.8 |
| 365 | 1075 | 11220 | 2 | 1449.9 | 96.6 | 1.05 | 9.1 | S | 2.2 | 6.9 |
| 583 | 1078 | 11300 | 5 | 489.1 | 230.8 | −1.04 | 20.1 | | −0.9 | 3.1 |
| 372 | −11 | 0 | 2 | −79.3 | 36.1 | 1.02 | 22.0 | | −0.4 | −1.2 |
| 373 | −15 | 0 | 2 | 1563.6 | 102.8 | 1.13 | 18.7 | | 0.8 | 9.8 |
| 374 | −12 | 0 | 2 | −56.7 | 79.5 | 1.03 | 256.0 | 0VH | 0.1 | −5.7 |
| 377 | 1082 | 0 | 2 | 1423.8 | 93.3 | 1.22 | 16.2 | | −0.6 | −2.5 |
| 379 | 0 | 11604 | 10 | 1429.2 | 348.8 | −1.12 | 14.1 | | 7.5 | 10.7 |
| 380 | 1085 | 0 | 2 | −141.0 | 37.3 | −1.02 | 20.7 | | 0.9 | −0.7 |
| 605 | 1088 | 11707 | 5 | 905.6 | 207.0 | 1.23 | 18.0 | | ... | ... |
| 387 | 0 | 11759 | 5 | 3257.3 | 157.1 | −1.71 | 9.0 | | −2.5 | −4.2 |
| 609 | 1093 | 11861 | 10 | 1479.1 | 270.1 | 1.05 | 19.0 | CC? | −2.5 | 7.1 |
| 393 | 1098 | 11891 | 5 | 461.2 | 155.3 | 1.29 | 22.6 | r | −0.6 | −0.9 |
| 396 | 1107 | 0 | 2 | ... | ... | ... | ... | XF | ... | ... |
| 399 | 1113 | 12082 | 2 | 802.1 | 87.1 | −1.16 | 25.1 | | −0.6 | 1.0 |
| 402 | 1117 | 12113 | 10 | 816.2 | 533.8 | −1.16 | 17.9 | R< | −1.5 | −2.6 |
| 620 | 1139 | 12392 | 2 | 1705.9 | 305.7 | 1.45 | 19.8 | | 0.5 | −2.1 |
| 936 | 7640 | 12554 | 10 | 372.2 | 267.9 | −1.15 | 21.3 | rR | 0.8 | −1.1 |
| 412 | 1147 | 12613 | 2 | −186.5 | 41.3 | −1.32 | 19.7 | CBr | −0.1 | −0.7 |
| 413 | 1149 | 12632 | 5 | 422.8 | 125.1 | −1.03 | 17.3 | R< | 1.0 | −2.9 |
| 414 | 1159 | 12732 | 5 | 748.1 | 138.5 | 1.11 | 30.6 | | −0.1 | −0.4 |
| 415 | 1160 | 12754 | 5 | 750.8 | 213.1 | 1.03 | 16.7 | | 0.3 | −1.4 |
| 417 | 0 | 12894 | 2 | 322.8 | 76.5 | −1.51 | 7.3 | | 0.1 | 7.8 |
| 418 | 1171 | 0 | 2 | −122.7 | 78.7 | −1.12 | 79.2 | | 0.4 | −1.6 |
| 418 | 1171 | 0 | 2 | −120.5 | 75.4 | −1.14 | 80.9 | CB! | 2.6 | −4.9 |
| 418 | Bcmp | 0 | 2 | −185.4 | 89.0 | −1.12 | 17.4 | Bcm | ... | ... |

# Appendix 3a

## 140-Foot 21 cm General Data
## NRAO Greenbank, 1997 [140], Unpublished ApJ submission

**Abstract**

21 cm observations for approximately 150 galaxies observed with the NRAO 140-foot (43-m) telescope between 1988 and 1991 are reported and discussed. The galaxies include objects associated with groups or companions, and galaxies in common with other sources used to evaluate random errors and possible systematic differences. Both Effelsberg and Arecibo observations miss substantial amounts of outlying hydrogen. For disk galaxies (spirals) there is some indication that the outlying hydrogen contains a small 'excess' redshift.

## 3.1 Introduction

In 1988 a series of 21 cm observations was initiated at the NRAO 140-foot (43-m) radio telescope in Green Bank, West Virginia. Similar observations were obtained about the same time using the NRAO 300-foot (91-m) radio telescope, and the Max Planck 100-m telescope at Effelsberg, Germany. The objective was to establish a set of 21 cm standards and intercompare telescopes and operating systems to evaluate random uncertainties and possible systematic effects in 21 cm observations. The primary analysis of the 1988 standards was carried out by Tifft and Huchtmeier (1990 [104]) and Tifft (1990 [105]). Since the collapse of the 300-foot telescope late in 1988 observations of an extended set of standards and some additional comparative work has been continued using the 140-foot telescope. Now that the 140-foot instrument is being phased out as the new 100-m Green Bank Telescope nears completion, the accumulated 140-foot observations have been compiled for analysis. This paper includes data from several programs involving comparisons with Effelsberg, Arecibo and older programs where 300-foot observations existed, as well as some southern extensions of 300-foot data, and certain studies of galaxies with companions or residing in groups. A detailed discussion of primary and secondary standards is in preparation for separate publication.

## 3.2 Procedures

The procedure for making 140-foot L-band observations has been described elsewhere in detail (Tifft 1990 [105]). Briefly, the observations are made in total power mode using subtractive comparisons between the object field and equivalent blank fields on one or both sides of the object in Right Ascension. When possible the observations are made sequentially so that the hour angle track is equivalent for the on and off fields. During night observations, or day observations at bandwidths of 5 MHz or less this usually gives very flat

stable baselines. Observations with a 10 MHz bandwidth are typically done only at night. The bandwidth employed for a given object is determined by the 21 cm profile width of the galaxy to provide an adequate baseline interval around the line profile. Each observation is centered at a predetermined center frequency appropriate for the redshift of each object. The 1024 channel autocorrolator was used in conjunction with the L-Band receiver. The correlator was operated in 4 256 channel segments all centered at the same center frequency, giving two redundant bands for each of two orthogonal linear polarizations. Except in rare cases where one band was defective the four bands were always combined, using the laboratory calibrations provided by NRAO, to maximize the signal-to-noise. Bandwidths of 10, 5 and 2.5 MHz were used, corresponding roughly to 2000, 1000, and 500 km/s in redshift. The 10 MHz band was used for galaxies with profiles wider than about 250 km/s; the 2.5 MHz band was used for galaxies with profiles narrower than about 125 km/s . The channel spacing for the three bandwidths amounts to about 8.3, 4.1 or 2.1 km/s.

Each galaxy was observed consistently at coordinates which place the object close to the center of the 21 arc minute beam of the telescope. Multiple observations were normally summed and averaged unless a specific problem warranted listing the measures separately. Regular pointing and flux calibration observations on continuum sources were made. Pointing is normally maintained within about 10 arc seconds; except for one short interval, noted in the data, pointing errors are negligible. Most of the observations reported here were obtained in January, April or May of 1988. A detailed discussion of the flux calibration procedure for those periods is contained in Tifft (1990 [105]). Observations in February 1989 and May 1991 are also involved. Aperture efficiencies for those runs were measured as:

$$\eta_A = 0.579 \quad \eta_B = 0.567 \quad \eta_{AB} = 0.573 \quad \text{for } 2/89$$

$$\eta_A = 0.556 \quad \eta_B = 0.549 \quad \eta_{AB} = 0.552 \quad \text{for } 5/91$$

where A and B refer to the two polarizations. The rms uncertainty in the final mean values used is about $\pm 0.005$. Supplementary calibration data for 1989 was kindly provided by R. Giovanelli. A more detailed review of flux calibrations may be incorporated in a future discussion of the 21 cm standards.

Table 1 contains identifications, 1950 coordinates, off fields used, and center velocities assumed for the approximately 150 galaxies in this paper. The objects are divided into six 'program' classes which point to six tables where the observations are tabulated. Three of the programs involve mostly new observations which are tabulated in §3 with little discussion. These are flagged as W (for companion galaxies observed in conjunction with S. White and D. Zaritski) or G for galaxies in groups. The G objects fall into two groups, southern objects related to an Effelsberg program, and northern objects connected to work at the 300-foot NRAO telescope. The other three programs involve comparisons between Effelsberg (E), Arecibo (A) or older 300-foot data from Shostak or Dickel and Rood (O). These measures are tabulated and discussed in Section 4.

The first three columns of Table 1 identify the galaxies. Column 1 is the Tifft-Cocke (TC) number. This is a serial number, in RA order, in five overlapping series, 1-418 and 419-620 for cross reference to the extended 300-foot study by Tifft and Cocke (1988 [96]), 630-899 for the O and northern G programs at the 300-foot for cross reference to data and comparisons in Tifft (1990 [105]) and Tifft (1992 [113]), 900-936 for cross reference to Effelsberg (E)

## TABLE 1

### PARAMETERS OF PROGRAM GALAXIES

| TC | FT | UGC | Prog | RA hhmmss.s | Dec ddmmss | Off | $V_{cv}$ km $s^{-1}$ |
|---|---|---|---|---|---|---|---|
| 901 | 68 | E1 | EG | 004035.0 | −223114 | B | 361 |
| 903 | 73 | E3 | EG | 004720.0 | −211729 | B | 300 |
| 938 | 95 | G02 | G | 013255.0 | −414118 | BC | 404 |
| 940 | 102 | G03 | G | 014254.0 | −435000 | BC | 394 |
| 941 | 128 | G04 | G | 021936.0 | −210200 | BC | 1563 |
| 942 | 130 | G05 | G | 022043.1 | −205624 | BC | 1723 |
| 943 | 131 | G06 | G | 022046.3 | −212742 | BC | 1508 |
| 944 | 189 | G07 | G | 031122.5 | −255440 | BC | 1699 |
| 945 | 191 | G08 | G | 031129.0 | −252229 | BC | 1735 |
| 909 | 194 | E9 | E | 031400.0 | −242300 | B | 2077 |
| 910 | 0 | E10 | E | 032234.7 | −213048 | B | 1333 |
| 946 | 218 | Ex1 | EG | 033252.0 | −250553 | BC | 1464 |
| 947 | 220 | G09 | G | 033519.9 | −243951 | BC | 1503 |
| 674 | 0 | 3190 | O | 044943.2 | +780641 | BC | 1565 |
| 677 | 0 | 3253 | O | 050637.8 | +835948 | BC | 4138 |
| 690 | 2268 | 3653 | O | 070048.6 | +842748 | BC | 2221 |
| 694 | 323 | 3740 | O | 071022.0 | +855058 | C | 2415 |
| 0 | 0 | 3835 | A | 072159.7 | +235256 | BC | 5500 |
| 0 | 2410 | 3917 | A | 073148.8 | +325603 | BC | 4678 |
| 948 | 2424 | 3959 | W | 073716.4 | +392048 | BC | 3223 |
| 0 | 0 | 4005 | A | 074229.1 | +080317 | BC | 5044 |
| 0 | 0 | 4040 | A | 074636.0 | +340513 | BC | 4806 |
| 0 | 2596 | 4419 | A | 082436.1 | +172658 | BC | 5940 |
| 0 | 0 | 4558 | A | 084100.8 | +334150 | BC | 7673 |
| 509 | 370 | 0 | WTC | 085336.6 | −031003 | BC | 2007 |
| 949 | 390 | 4888 | W | 091327.0 | +735807 | BC | 2261 |
| 950 | 392 | G10 | G | 091536.6 | −220845 | BC | 890 |
| 951 | 399 | G11 | G | 091911.0 | −221727 | BC | 849 |
| 952 | 2870 | 5034 | W | 092415.4 | +573543 | BC | 3210 |
| 953 | 2906 | 5081 | W | 092926.6 | +083951 | BC | 2137 |
| 954 | 2939 | 5134 | W | 093524.0 | +094500 | BC | 3344 |
| 955 | 409 | G12 | G | 094155.0 | −315606 | BC | 1209 |
| 956 | 410 | G13 | G | 094237.0 | −313542 | BC | 1256 |
| 957 | 413 | G14 | G | 094318.0 | −300642 | BC | 1004 |
| 958 | 414 | G15 | G | 094327.4 | −305735 | BC | 1083 |
| 959 | 2990 | 5229 | W | 094340.0 | +055623 | BC | 3110 |
| 0 | 0 | 5248 | A | 094506.5 | +160507 | BC | 5852 |
| 714 | 3031 | 5318 | OT | 095127.6 | +691813 | BC | −40 |
| 715 | 3034 | 5322 | O | 095143.5 | +695504 | BC | 240 |
| 960 | 3043 | 5327 | W | 095241.3 | +593240 | BC | 2994 |
| 0 | 0 | 5341 | A | 095349.7 | +205310 | BC | 7568 |
| 913 | 438 | E13 | E | 100058.0 | −211118 | BC | 3069 |
| 914 | 449 | E14 | E | 100816.0 | −253440 | BC | 2515 |
| 0 | 0 | 5499 | A | 100928.0 | +280633 | BC | 4752 |
| 0 | 3270 | 5711 | A | 102842.0 | +250800 | BC | 6259 |
| 961 | T639 | Ex2 | E | 103133.0 | −273416 | BC | 2696 |
| 916 | 0 | E16 | E | 105153.0 | −175554 | B | 4134 |
| 962 | 511 | G16 | G | 110058.8 | −224829 | BC | 1104 |
| 963 | 513 | G17 | G | 110119.2 | −225828 | BC | 1195 |
| 0 | 3509 | 6134 | A | 110148.5 | +050601 | BC | 7699 |
| 964 | 522 | 6215 | W | 110803.1 | +533933 | BC | 2866 |
| 965 | 529 | 6318 | W | 111535.2 | +460116 | BC | 2339 |
| 966 | 559 | 6567 | W | 113304.8 | +704842 | BC | 2696 |
| 740 | 561 | 6579 | G | 113404.7 | +543422 | BC | 1294 |
| 967 | 3876 | 6730 | W | 114248.0 | +092600 | BC | 2871 |
| 918 | 0 | E18 | E | 115050.0 | −175318 | B | 1737 |
| 750 | 597 | 6869 | G | 115105.2 | +480816 | BC | 804 |
| 751 | 598 | 6870 | G | 115112.9 | +523620 | BC | 1054 |
| 752 | 601 | 6904 | G | 115310.0 | +553548 | BC | 848 |
| 968 | 603 | 6906 | W | 115323.0 | +070140 | BC | 2500 |
| 753 | 607 | 6918 | G | 115352.3 | +552410 | BC | 1110 |
| 754 | 606 | 6917 | G | 115354.4 | +504223 | BC | 919 |
| 756 | 615 | 6963 | G | 115557.1 | +441330 | BC | 835 |
| 758 | 619 | 6983 | G | 115634.0 | +525908 | BC | 1078 |
| 920 | 0 | E20 | E | 115758.0 | −242636 | B | 1707 |
| 969 | 631 | G18 | G | 120207.0 | −275026 | BC | 1787 |
| 970 | Ex3 | 7065 | E | 120212.0 | −022600 | BC | 5887 |
| 971 | 633 | G19 | G | 120312.5 | −273942 | BC | 1851 |
| 765 | 639 | 7096 | G | 120351.6 | +525923 | BC | 862 |
| 766 | 644 | 7125 | G | 120612.0 | +370500 | BC | 1078 |
| 767 | 653 | 7175 | G | 120824.0 | +400200 | BC | 1168 |
| 768 | 655 | 7183 | G | 120836.4 | +504551 | BC | 771 |
| 972 | 4162 | 7193 | W | 120919.4 | +242405 | BC | 2571 |
| 769 | 657 | 7207 | G | 120948.0 | +371724 | BC | 1055 |
| 770 | 662 | 7218 | G | 121024.0 | +523300 | BC | 791 |
| 774 | 679 | 0 | G | 121354.0 | −111506 | BC | 1165 |
| 775 | 682 | 7306 | G | 121421.8 | +694436 | BC | 0 |
| 776 | 683 | 0 | G | 121437.0 | −112406 | BC | 1278 |

TABLE 1—*Continued*

| TC | FT | UGC | Prog | RA hhmmss.s | Dec ddmmss | Off | $V_{cu}$ km $s^{-1}$ |
|---|---|---|---|---|---|---|---|
| 778 | 685 | 7323 | G | 121501.3 | +455400 | BC | 516 |
| 0 | 0 | 7330 | A | 121512.0 | +110700 | BC | 7289 |
| 779 | 690 | 7353 | G | 121629.7 | +473455 | BC | 450 |
| 782 | 4369 | 7489 | O | 122208.4 | +393941 | BC | 1052 |
| 787 | 727 | 7675 | OW | 122928.1 | +144150 | BC | 2272 |
| 789 | 731 | 7690 | G | 123001.4 | +425848 | BC | 540 |
| 790 | 734 | 7699 | G | 123021.2 | +375341 | BC | 503 |
| 791 | 737 | 7713 | G | 123117.1 | +152625 | BC | 262 |
| 792 | 741 | 7727 | O | 123147.9 | +082825 | BC | 1953 |
| 973 | 744 | 7747 | W | 123220.3 | +634810 | BC | 2728 |
| 793 | 745 | 0 | G | 123300.0 | −073700 | BC | 993 |
| 795 | 747 | 7772 | O | 123351.8 | +261550 | BC | 1227 |
| 796 | 748 | 7774 | G | 123354.3 | +401700 | BC | 526 |
| 797 | 751 | 7788 | G | 123425.5 | +142933 | BC | 348 |
| 0 | 0 | 7808 | A | 123606.0 | +104500 | BC | 7273 |
| 974 | 757 | 0 | W | 123801.8 | −045127 | BC | 2559 |
| 799 | 766 | 7901 | O | 124112.5 | +164005 | BC | 820 |
| 975 | 4682 | 0 | W | 124439.8 | −094726 | BC | 2307 |
| 805 | 789 | 7996 | O | 124732.4 | +412328 | BC | 307 |
| 807 | 4775 | 0 | O | 125110.4 | −062111 | BC | 1565 |
| 809 | 799 | 0 | G | 125215.5 | −095837 | BC | 1354 |
| 976 | 4793 | 8033 | W | 125216.0 | +291230 | AB | 2460 |
| 812 | 808 | 8062 | O | 125416.9 | +215718 | BC | 398 |
| 814 | 816 | 8098 | G | 125638.5 | +350656 | BC | 847 |
| 816 | 828 | 0 | OW | 130137.6 | −100422 | BC | 3110 |
| 818 | 4961 | 8185 | O | 130323.9 | +280010 | BC | 2535 |
| 977 | 836 | G20 | G | 130409.0 | −281724 | BC | 2217 |
| 978 | 837 | G21 | G | 130425.6 | −275742 | BC | 2265 |
| 819 | 0 | 8263 | O | 130848.0 | +034100 | BC | 3042 |
| 0 | 0 | 8298 | A | 131048.9 | +102727 | BC | 1156 |
| 0 | 0 | 8310 | A | 131122.8 | +172013 | BC | 6769 |
| 924 | 0 | E24 | E | 131232.0 | −174212 | B | 2784 |
| 979 | 5073 | 0 | W | 131642.0 | −143600 | BC | 2738 |
| 980 | 5116 | 8410 | W | 132036.0 | +271500 | BC | 2583 |
| 825 | 5147 | 8443 | O | 132346.8 | +022143 | BC | 1093 |
| 981 | 5172 | 8477 | W | 132653.3 | +171835 | BC | 4030 |
| 829 | 5230 | 8573 | OA | 133304.9 | +135548 | BC | 6838 |
| 829 | 5230 | 8573 | AO | 133304.9 | +135548 | BC | 6855 |
| 925 | 0 | E25 | E | 133342.2 | −285851 | B | 572 |
| 926 | 0 | E26 | E | 133431.8 | −274739 | B | 590 |
| 982 | 910 | 0 | W | 133658.5 | −111429 | BC | 2315 |
| 983 | 912 | G22 | G | 133705.2 | −312321 | BC | 417 |
| 897 | 915 | Ex4 | EG | 133846.8 | −293942 | C | 479 |
| 984 | 5351 | 8809 | W | 135118.9 | +380936 | BC | 3615 |
| 927 | 937 | E27 | E | 135501.9 | −290417 | B | 2660 |
| 0 | 0 | 8999 | A | 140222.6 | +292624 | BC | 5708 |
| 834 | 948 | 0 | O | 140357.4 | −051249 | BC | 2845 |
| 985 | 5492 | 9065 | W | 140812.0 | +195100 | BC | 2273 |
| 837 | 957 | 9127 | O | 141327.5 | +362730 | BC | 2882 |
| 928 | 961 | E28 | E | 141738.9 | −290047 | B | 1380 |
| 986 | 5633 | 9271 | W | 142536.7 | +462213 | BC | 2330 |
| 0 | 0 | 9296 | A | 142700.7 | +205233 | BC | 8868 |
| 0 | 0 | 9317 | A | 142759.1 | +274500 | BC | 4425 |
| 987 | 5665 | 9352 | W | 142957.5 | +081805 | BC | 2205 |
| 988 | 5678 | 9358 | W | 143037.1 | +580835 | BC | 1929 |
| 841 | 5668 | 9363 | O | 143054.4 | +044011 | BC | 1583 |
| 842 | 5676 | 9366 | OW | 143101.4 | +494037 | BC | 2122 |
| 844 | 989 | 9436 | O | 143641.5 | +053450 | BC | 1505 |
| 0 | 0 | 9594 | A | 145231.5 | +241744 | BC | 5194 |
| 989 | 5875 | 9745 | W | 150743.0 | +524308 | BC | 3527 |
| 0 | 0 | 9803 | A | 151513.0 | +293500 | BC | 5259 |
| 329 | 5908 | 9805 | W | 151523.0 | +553537 | BC | 3310 |
| 0 | 0 | 9910 | A | 153244.1 | +311303 | BC | 1866 |
| 990 | 32 | 9914 | W | 153250.1 | +565108 | BC | 3416 |
| 850 | 5970 | 9943 | O | 153608.1 | +122053 | BC | 1964 |
| 991 | 33 | 9971 | W | 153852.3 | +581433 | BC | 3012 |
| 0 | 0 | 10043 | A | 154630.0 | +220113 | BC | 2160 |
| 0 | 6627 | 11212 | A | 182023.5 | +154023 | BC | 5267 |
| 992 | 6796 | 11432 | W | 192048.0 | +610300 | BC | 2090 |
| 873 | 6821 | 0 | O | 194143.1 | −065718 | BC | 1523 |
| 933 | 0 | E33 | E | 194154.0 | −281700 | BC | 1987 |
| 993 | 1104 | G23 | G | 221342.0 | −214100 | BC | 2616 |
| 994 | 1105 | G24 | G | 221406.0 | −213000 | BC | 2571 |
| 886 | 7541 | 12447 | O | 231210.3 | +041543 | BC | 2676 |
| 998 | 1161 | G25 | G | 234109.0 | −321412 | BC | 267 |
| 999 | 1168 | G26 | G | 235515.5 | −325203 | BC | 231 |

data (900 + Effelsberg number) in Tifft and Huchtmeier (1990 [104]) and 937-999 for the W and southern G objects. The Arecibo objects were not assigned TC numbers. The second column is the Fisher-Tully (1981 [V]) number, which is a sequential number in the FT catalog. Numbers preceded by a zero, or greater than 1171 are NGC numbers of non-FT objects. The third column gives UGC numbers from Nilson (1973 [BW]). This column also contains cross reference E numbers and southern group G numbers. A zero in any space means the galaxy is not present in the relevant catalogs, or no TC number has been assigned.

Following the program and 1950 coordinate entries is a column noting which off field was used. The off field west of the object is designated B, and the field to the east C. A dual notation means both sides were used to identify possible contamination. The amount of the offset is a function of declination, 5 minutes below 57.7 degrees, 8 minutes up to 70.5 degrees, 12 minutes up to 77.2 degrees and larger amounts at higher declination. Refer to Tifft (1990 [105]) for details. Integration times were equal to the offset up to 77.2 degrees, then remained at 12 minutes. All integrations are sums of 1 minute subscans. During certain periods of interference some of the subscans were 'winnowed' out and this is noted in the data tables remarks. The last column is the center velocity used. The bandwidth employed is given in the data tables since some objects were observed using more than one value.

All the observations were reduced using the author's Radfiles program on either the NRAO Masscomp computer or the author's personal 486 or 586 PC systems. In this program redshifts and profile widths are defined by interactive polynomial fitting to the points where profiles cross over 20% of the average height of the central 80% of the profile area. Procedures are discussed in detail in Tifft and Cocke (1988 [96]). The signal-to-noise index is the ratio of the average height, noted above, to the rms baseline noise. Hanning smoothing is used only when there is excessive ringing in the signal due to local hydrogen or interference. The asymmetry index, $A$, is a measure of the difference in the redshift as measured by mid area and the average of the 20% crossing points of the profile. See Tifft and Cocke (1988 [96]) for a formal definition. The observed flux, F in Jy km/s is the profile area scaled by the usual areal factor ($2k/A = 1.9312$ for the 140-foot) and divided by the aperture efficiency $\eta$ noted previously.

## 3.3 Non-Comparative Work

Table 2 contains the observations of the galaxies in the Zaritsky-White (Zaritski et al 1993 [CH]) sample (Class W in Table 1). These galaxies fall in a specific redshift range, between about 2000 and 4000 km/s, and have wide 21 cm profiles. Except for three additional objects in Table 8 and two objects in the original Tifft-Cocke (1988 [96]) survey, there is little additional data for these systems. All the observations were obtained in February 1989 using a 10 MHz bandwidth. As with all the 140-foot data in this paper, the observations were directly tied to the set of 21 cm standards (Tifft 1990 [96]). Integration times typically ranged between 20 and 40 minutes to achieve a signal-to-noise level near 5.

Table 2 lists the identifications in the same form as Table 1, followed by the bandwidth used, the flux, the heliocentric redshift, the profile width, the profile asymmetry index and the signal-to-noise value. The final column gives comments in codes defined in Table 3. During the February run there was some serious interference. Observations where this was a particular problem are listed separately and flagged with an asterisk. We note that despite

TABLE 2
DATA FOR ZARITSKY-WHITE GALAXIES

| TC | FT | UGC | BW MHz | Flux a | $V_h$ b | W b | A | S/N | Comments |
|---|---|---|---|---|---|---|---|---|---|
| 948 | 2424 | 3959 | 10 | 18.5 | 3348.4 | 472.8 | 1.34 | 5.4 | n |
| 509 | 370 | 0 | 10 | 16.4 | 1992.4 | 448.6 | 1.13 | 4.2 | Ui> |
| 949 | 390 | 4888 | 10 | 25.1 | 2257.2 | 330.2 | −1.16 | 9.2 | |
| 952 | 2870 | 5034 | 10 | 15.7 | 3215.9 | 371.5 | 1.12 | 2.7 | i< |
| 953 | 2906 | 5081 | 10 | 4.4 | 2133.5 | 387.5 | −1.00 | 1.5 | u?< |
| 954 | 2939 | 5134 | 10 | 21.4 | 3339.2 | 364.8 | 1.08 | 6.4 | i<cC |
| | Comp | To E | 10 | 30.2 | 3208.9 | 189.2 | −1.13 | 7.8 | zU! |
| 959 | 2990 | 5229 | 10 | 14.8 | 3085.9 | 325.1 | −1.20 | 5.1 | il<r |
| 960 | 3043 | 5327 | 10 | 4.8 | 2997.0 | 327.1 | 1.07 | 2.9 | j<?> |
| 964 | 522 | 6215 | 10 | 26.9 | 2855.1 | 441.9 | 1.03 | 5.7 | n |
| 965 | 529 | 6318 | 10 | 34.7 | 2331.3 | 327.6 | −1.07 | 7.6 | j> |
| 966 | 559 | 6567 | 10 | 32.6 | 2692.6 | 527.8 | 1.03 | 5.9 | |
| 967 | 3876 | 6730 | 10 | 7.1 | 2902.3 | 179.4 | 1.24 | 6.1 | uI< |
| 968 | 603 | 6906 | 10 | 55.2 | 2501.7 | 472.1 | 1.00 | 10.5 | |
| 972 | 4162 | 7193 | 10 | 12.7 | 2574.9 | 339.3 | −1.05 | 4.9 | |
| | | | | 14.0 | 2577.7 | 360.2 | 1.10 | 5.4 | *IxIHK |
| 973 | 744 | 7747 | 10 | 16.0 | 2731.8 | 302.6 | −1.01 | 4.3 | U |
| | | | | 14.9 | 2733.9 | 310.2 | −1.09 | 8.1 | *II<RIH |
| | | | | 12.9 | 2734.3 | 288.5 | −1.13 | 5.9 | *IIRIH |
| 974 | 757 | 0 | 10 | 33.9 | 2539.0 | 442.9 | −1.03 | 5.1 | |
| | | | | 32.1 | 2544.0 | 452.2 | 1.16 | 8.1 | *IxIRIHK |
| 975 | 4682 | 0 | 10 | 9.7 | 2337.3 | 314.4 | 1.33 | 1.9 | uj> |
| 976 | 4793 | 8033 | 10 | 31.6 | 2493.9 | 367.3 | −1.07 | 6.6 | n |
| | | | | 34.8 | 2501.7 | 380.5 | 1.00 | 7.1 | *IxK |
| 979 | 5073 | 0 | 10 | 19.7 | 2748.3 | 411.9 | −1.36 | 3.0 | u |
| 980 | 5116 | 8410 | 10 | 5.1 | 2868.1 | 394.1 | 1.46 | 1.0 | u |
| 981 | 5172 | 8477 | 10 | 21.5 | 4032.2 | 457.0 | −1.12 | 4.8 | |
| 982 | 910 | 0 | 10 | 25.8 | 2322.2 | 375.0 | 1.23 | 5.6 | |
| 984 | 5351 | 8809 | 10 | 25.1 | 3609.8 | 459.0 | 1.00 | 8.0 | |
| 985 | 5492 | 9065 | 10 | 13.2 | 2270.0 | 403.4 | −1.15 | 3.0 | u??< |
| 986 | 5633 | 9271 | 10 | 10.4 | 2326.9 | 307.0 | 1.16 | 3.2 | u |
| 987 | 5665 | 9352 | 10 | 6.9 | 2210.8 | 277.0 | −1.18 | 3.1 | j> |
| 988 | 5678 | 9358 | 10 | 20.2 | 1918.8 | 417.8 | 1.29 | 7.1 | Ui>r |
| 989 | 5875 | 9745 | 10 | 27.0 | 3527.8 | 417.2 | 1.01 | 9.1 | ?> |
| 329 | 5908 | 9805 | 10 | 35.2 | 3304.4 | 662.1 | −1.68 | 5.6 | i<r |
| 990 | 32 | 9914 | 10 | 39.9 | 3411.8 | 630.0 | 1.06 | 8.7 | ui< |
| 991 | 33 | 9971 | 10 | 17.1 | 3014.5 | 594.6 | 1.23 | 4.2 | I<r |
| 992 | 6796 | 11432 | 10 | 12.6 | 2173.7 | 440.2 | 1.11 | 6.5 | *uHIl> |
| | | | | 12.6 | 2193.0 | 420.4 | 1.52 | 2.9 | *UHIl> |

[a] Jy km $s^{-1}$
[b] km $s^{-1}$

the serious perturbations only relatively small deviations occur in the measured parameters. Except for the measures with signal-to-noise levels less than 2 or 2.5 it is not likely that redshift uncertainty exceeds about 5 km/s.

Table 4 contains the measurements for the galaxies associated with northern groups; Table 5 contains the southern extensions. The tables differ from Table 2 only with the inclusion of a 'Run' column which indicates the month and year when the observations were made. Measures in 1988 using a composite profile are designated 'S88'. A number of interesting redshift studies of groups or companion galaxies have been made. They include findings related to redshift quantization among the closest pairs (Tifft & Cocke 1989 [100]) , more general larger scale quantization (Guthrie &; Napier 1996 [CC]), and an 'excess' redshift effect among companion galaxies (see Zaritsky 1992 [CG] for a recent discussion). Such work at 21 cm requires a small enough beam to achieve adequate resolution. A program utilizing

TABLE 3
COMMENT CODES

| Code | Comment | Code | Comment |
|---|---|---|---|
| | Problems, their locations and significance | | |
| ?, ?? | Profile edge is uncertain | < , > | Lower (edge), Upper (edge) |
| 0, 0! | Zero velocity hydrogen | < , x , > | Below, In, Above (profile) |
| r, R, R! | Ringing | ! | Emphasis |
| j, i, I, I! | Interference | : | Uncertain |
| | | * | Disturbed, Values may be biased |
| | Baselines and pointing | | |
| u, U, U! | Sloped or wavy baseline | p | Pointing error |
| n, N, N! | Noisey uneven baseline | o | Offset from normal position |
| q | Uneven region in baseline | | |
| | Operations and companions | | |
| G | Gauss fit | c, cX | Companion in on or X=off field |
| H | Hanning smoothed | d | Subtractive effect from companion |
| Av# | Average of # measures | z | Refers to companion data |
| K | Interference deglitched | Xol | Overlapping signals |
| A(B)ch | A or B channel only | W, W! | Extended wing on profile |
| w# | # subscans winnowed out | | |

the 300-foot telescope for such measures was in progress when that instrument collapsed. A few measures with the 140-foot telescope are included here, however the large beam size does not permit measures in the most interesting range where the product of the redshift and angular separation is less than about 300 km/s/degree (Tifft & Cocke 1989 [100]). The higher resolution and greater sensitivity of the new Green Bank Telescope will be required to pursue such a study effectively. Several of the measurements given here are flagged as contaminated by beam overlap. Since very precise measures of the individual objects are required for quantization work we will make no attempt to analyze the measures given here.

## 3.4 Comparative Work

The three remaining program groups (E, A, and O) permit some interesting comparisons between independent studies and instruments. Before looking at the data it is useful to summarize some earlier findings. By using flux measures for galaxies observed with telescopes which have different beam sizes one can compare the properties of the inner and outer parts of galaxies. Excess flux present in a large beam must come from the outlying hydrogen missed by a smaller beam. Tifft (1991a [109]) illustrated the effect in intercomparisons of the 140-foot, 300-foot and 100-m Effelsberg telescopes. The analysis showed some growth in profile width, perhaps not too surprising, and an excess redshift effect in the outer parts of spirals. This latter effect may be directly connected to the excess redshift

# TABLE 4

## Data For Galaxies In Groups

| TC | FT | UGC | Run | BW MHz | Flux a | $V_h$ b | W b | A | S/N | Comments |
|---|---|---|---|---|---|---|---|---|---|---|
| 740 | 561 | 6579 | 289 | 10 | 24.6 | 1290.1 | 303.9 | 1.19 | 5.9 | |
| 750 | 597 | 6869 | 588 | 5 | 40.5 | 802.8 | 283.1 | −1.07 | 6.6 | ?< |
| | | | 289 | | 43.7 | 803.2 | 290.5 | −1.05 | 7.3 | ?> |
| 751 | 598 | 6870 | 488 | 10 | 40.4 | 1050.2 | 436.2 | 1.19 | 6.0 | |
| 752 | 601 | 6904 | 488 | 5 | 13.1 | 840.2 | 294.9 | 1.45 | 1.6 | UcB |
| | Comp | To W | 488 | 5 | 11.7 | 953.3 | 60.3 | −1.04 | 7.8 | u |
| 753 | 607 | 6918 | 488 | 5 | 24.3 | 1113.1 | 253.4 | −1.07 | 4.2 | u |
| | Comp | To W | 488 | 5 | 2.0 | 957.0 | 38.0 | 1.00 | 2.1 | Gu?>dB |
| 754 | 606 | 6917 | 488 | 5 | 24.0 | 911.6 | 203.0 | −1.12 | 5.6 | u |
| | | | 289 | | 25.2 | 908.1 | 213.2 | −1.08 | 5.6 | u?< |
| 756 | 615 | 6963 | 488 | 10 | 33.7 | 835.9 | 420.3 | 1.07 | 4.1 | |
| | | | 289 | | 33.5 | 832.2 | 425.6 | 1.05 | 4.7 | 0r<ucB |
| | | | *289 | | 37.9 | 828.2 | 429.9 | 1.16 | 3.4 | AchcB?< |
| | Comp | To W | 488 | 10 | 28.6 | 810.6 | 113.7 | −1.16 | 12.6 | cB |
| | | | 289 | | 26.7 | 810.1 | 120.1 | −1.22 | 11.9 | 0r<Uz |
| | | | *289 | | 26.4 | 806.2 | 117.7 | −1.12 | 8.3 | Achz |
| 758 | 619 | 6983 | 488 | 5 | 32.3 | 1083.6 | 194.5 | −1.13 | 9.8 | |
| 765 | 639 | 7096 | 488 | 5 | 13.3 | 827.5 | 365.1 | 1.26 | 2.0 | u |
| | | | 289 | | 13.3 | 840.9 | 356.4 | −1.04 | 2.9 | ud |
| | | | 289 | | 12.3 | 849.0 | 366.6 | 1.07 | 1.9 | u |
| 766 | 644 | 7125 | 289 | 2 | 45.4 | 1069.3 | 170.6 | 1.18 | 9.6 | |
| 767 | 653 | 7175 | 488 | 2 | 10.1 | 1150.1 | 146.7 | 1.04 | 2.4 | UIw |
| 768 | 655 | 7183 | *488 | 10 | 81.9 | 461.3 | 438.1 | −1.22 | 9.5 | UI? |
| | Comp | To W | *488 | 10 | 94.8 | 770.0 | 392.1 | 1.17 | 14.1 | UI?> |
| 769 | 657 | 7207 | 488 | 2 | 5.2 | 1058.6 | 85.6 | 1.32 | 2.4 | u?>w |
| | | | 289 | | 8.3 | 1049.6 | 108.1 | 1.03 | 2.5 | u?< |
| | Comp | To W | *289 | 2 | 1.7 | 1009.6 | 43.1 | 1.00 | 1.2 | uz: |
| 770 | 662 | 7218 | 488 | 2 | 4.6 | 776.0 | 107.4 | −1.07 | 1.8 | |
| | | | 289 | | 3.9 | 778.8 | 106.5 | 1.15 | 1.4 | |
| 774 | 679 | 0 | 488 | 2 | 6.0 | 1158.1 | 127.2 | −1.17 | 1.8 | u?< |
| 775 | 682 | 7306 | 588 | 5 | 417.7 | −0.9 | 190.2 | −1.10 | 87.0 | 0<X: |
| | | | *588 | | 382.6 | −0.8 | 190.9 | −1.32 | 85.8 | *0X! |
| 776 | 683 | 0 | 488 | 2 | 5.5 | 1291.9 | 110.0 | 1.18 | 1.8 | u |
| 778 | 685 | 7323 | S88 | 2 | 42.8 | 517.2 | 140.3 | 1.17 | 18.6 | |
| | | | 488 | | 41.5 | 517.4 | 138.3 | 1.15 | 12.1 | u |
| | | | 588 | | 42.6 | 517.2 | 140.7 | 1.19 | 13.3 | ?> |
| 779 | 690 | 7353 | 488 | 10 | 367.7 | 452.4 | 444.8 | −1.01 | 53.7 | u |
| 789 | 731 | 7690 | S88 | 2 | 20.6 | 535.2 | 100.7 | −1.05 | 11.6 | u |
| | | | 488 | | 21.6 | 535.1 | 101.3 | −1.03 | 9.0 | |
| | | | 588 | | 20.3 | 535.1 | 100.7 | −1.09 | 8.2 | u |
| 790 | 734 | 7699 | 488 | 5 | 35.0 | 506.0 | 236.1 | −1.02 | 4.1 | Uiw |
| | | | *488 | | 44.1 | 493.7 | 214.5 | −1.60 | 3.6 | *UIlx |
| | | | 289 | | 29.0 | 499.7 | 213.6 | 1.18 | 7.1 | |
| 791 | 737 | 7713 | S88 | 2 | 24.8 | 261.5 | 142.5 | 1.18 | 7.6 | n |
| | | | 488 | | 22.9 | 261.5 | 137.1 | 1.22 | 5.5 | u?<?> |
| | | | 588 | | 23.1 | 259.3 | 146.0 | 1.11 | 5.5 | u?> |
| 793 | 745 | 0 | 488 | 5 | 24.6 | 986.6 | 177.9 | 1.27 | 4.7 | |
| | Comp | To W | 488 | 5 | 16.8 | 1034.8 | 223.7 | 1.01 | 2.5 | cB?< |
| 796 | 748 | 7774 | 289 | 5 | 25.1 | 527.0 | 207.4 | 1.06 | 4.9 | c:B |
| | Comp | To W | 289 | 5 | 3.4 | 677.0 | 74.8 | 1.00 | 2.0 | |
| 797 | 751 | 7788 | S88 | 5 | 9.2 | 341.2 | 167.7 | 1.02 | 5.8 | ui<H?> |
| | | | 488 | | 8.7 | 340.2 | 166.9 | −1.01 | 4.8 | uRH |
| | | | 588 | | 10.2 | 339.1 | 172.7 | 1.12 | 4.1 | 0<RH?> |
| 809 | 799 | 0 | 488 | 5 | 22.0 | 1360.6 | 221.7 | 1.43 | 3.4 | u?> |
| | Comp | To W | 488 | 5 | 20.4 | 1319.7 | 165.8 | 1.07 | 3.9 | ucB?> |
| 814 | 816 | 8098 | 488 | 2 | 38.9 | 836.9 | 117.6 | −1.16 | 12.8 | u?> |

[a] Jy km $s^{-1}$
[b] km $s^{-1}$

TABLE 5

DATA FOR GALAXIES IN SOUTHERN GROUPS

| TC | FT | UGC | Run | BW MHz | Flux a | $V_h$ b | W b | A | S/N | Comments |
|---|---|---|---|---|---|---|---|---|---|---|
| 938 | 95 | G02 | S88 | 2 | 33.7 | 393.1 | 111.0 | −1.12 | 10.3 | u |
| | | | 188 | | 30.9 | 393.7 | 110.5 | −1.12 | 6.4 | w1 |
| | | | 488 | | 35.2 | 392.5 | 109.0 | −1.10 | 7.7 | u |
| 940 | 102 | G03 | S88 | 2 | 78.1 | 392.0 | 87.5 | 1.17 | 32.8 | u |
| | | | 188 | | 80.1 | 392.1 | 87.4 | 1.13 | 20.7 | ?>w1 |
| | | | 488 | | 80.5 | 391.4 | 87.8 | 1.16 | 20.7 | u |
| 941 | 128 | G04 | *S88 | 2 | 62.1 | 1567.4 | 159.8 | 1.06 | 22.5 | *Xol |
| | | | *188 | | 60.7 | 1568.8 | 157.8 | 1.09 | 13.8 | Av2w3 |
| | | | *488 | | 68.6 | 1565.0 | 168.8 | 1.01 | 12.9 | u |
| 942 | 130 | G05 | *S88 | 5 | 22.1 | 1643.5 | 321.2 | 1.36 | 4.7 | Uc*Xol |
| | | | *188 | | 25.2 | 1645.3 | 315.1 | 1.42 | 3.9 | |
| | | | *488 | | 19.3 | 1655.3 | 317.1 | 1.25 | 2.7 | U!?< |
| 943 | 131 | G06 | *S88 | 10 | 45.0 | 1502.7 | 417.2 | 1.26 | 9.2 | Ui<*Xol |
| | | | *188 | | 46.3 | 1505.3 | 417.8 | 1.32 | 5.3 | Av2Ui<rw4 |
| | | | *488 | | 42.4 | 1502.7 | 422.1 | 1.15 | 5.4 | U! |
| 944 | 189 | G07 | S88 | 5 | 36.7 | 1688.1 | 262.1 | 1.03 | 8.0 | U |
| | | | 188 | | 37.7 | 1687.9 | 264.0 | 1.01 | 6.6 | U |
| | | | 488 | | 35.0 | 1686.5 | 259.4 | 1.03 | 5.8 | U |
| 945 | 191 | G08 | S88 | 5 | 36.6 | 1730.3 | 189.1 | 1.06 | 11.2 | U |
| | | | 188 | | 36.9 | 1730.3 | 187.8 | 1.11 | 7.9 | U |
| | | | 488 | | 37.6 | 1731.7 | 191.8 | 1.04 | 7.8 | U |
| 947 | 220 | G09 | S88 | 5 | 31.5 | 1498.4 | 216.5 | 1.01 | 7.9 | u |
| | | | 188 | | 32.3 | 1495.8 | 232.5 | 1.02 | 5.4 | w2 |
| | | | 488 | | 30.6 | 1500.6 | 214.2 | −1.01 | 6.4 | u |
| 950 | 392 | G10 | *188 | 5 | 129.6 | 886.5 | 218.7 | 1.22 | 22.4 | uw1*p |
| | | | 188 | | 137.4 | 886.0 | 215.2 | 1.04 | 31.2 | w1 |
| 951 | 399 | G11 | *188 | 2 | 31.0 | 845.2 | 132.4 | −1.07 | 6.2 | w2*p |
| | | | 188 | | 35.7 | 847.7 | 144.2 | 1.05 | 6.9 | |
| 955 | 409 | G12 | *188 | 2 | 7.9 | 1221.1 | 139.4 | 1.24 | 1.7 | w1*p |
| | | | 188 | | 8.5 | 1214.3 | 140.3 | 1.00 | 1.7 | j< |
| 956 | 410 | G13 | *188 | 2 | 44.4 | 1246.7 | 166.2 | 1.09 | 6.8 | *p |
| | | | 188 | | 52.6 | 1247.0 | 176.9 | 1.10 | 9.5 | u |
| 957 | 413 | G14 | 188 | 2 | 23.9 | 997.7 | 152.7 | 1.13 | 4.0 | |
| | | | 289 | | 23.9 | 999.3 | 155.4 | 1.16 | 4.3 | |
| 958 | 414 | G15 | *188 | 5 | 182.6 | 1089.4 | 276.7 | 1.06 | 23.5 | U*p |
| | | | 188 | | 203.6 | 1088.5 | 280.1 | 1.13 | 21.5 | w2 |
| 962 | 511 | G16 | *188 | 5 | 90.1 | 1104.8 | 318.4 | −1.63 | 11.8 | U*p*Xol |
| | | | *188 | | 86.5 | 1102.1 | 312.4 | −1.46 | 10.2 | *Xol |
| 963 | 513 | G17 | *188 | 2 | 29.9 | 1197.0 | 119.5 | −1.07 | 8.3 | U*Xol |
| | | | *188 | | 30.2 | 1198.8 | 109.9 | 1.00 | 8.5 | U*Xol |
| 969 | 631 | G18 | *S88 | 5 | 6.5 | 1750.2 | 125.1 | 1.29 | 3.7 | c*Xol |
| | | | *188 | | 10.9 | 1796.2 | 235.6 | 1.78 | 1.8 | Av2w2*Xol |
| | | | *588 | | 12.1 | 1776.4 | 206.9 | 1.56 | 2.7 | ?>*Xol |
| 971 | 633 | G19 | *S88 | 5 | 18.4 | 1844.7 | 274.7 | 1.46 | 4.8 | c*Xol |
| | | | *188 | | 19.0 | 1845.0 | 270.1 | 1.54 | 3.0 | Av2w3*Xol |
| | | | *588 | | 20.2 | 1854.7 | 294.8 | 1.43 | 3.0 | ?>*Xol |
| 977 | 836 | G20 | S88 | 2 | 17.0 | 2220.6 | 101.2 | −1.03 | 8.6 | uc:> |
| | | | 188 | | 17.0 | 2224.3 | 102.2 | 1.06 | 6.3 | u |
| | | | 588 | | 16.0 | 2216.6 | 97.0 | −1.13 | 5.1 | ?> |
| 978 | 837 | G21 | S88 | 5 | 21.7 | 2268.6 | 210.6 | −1.05 | 5.6 | uc: |
| | | | 188 | | 21.8 | 2268.2 | 218.1 | −1.07 | 4.3 | w2 |
| | | | 588 | | 23.1 | 2269.7 | 211.9 | −1.03 | 4.6 | u |
| 983 | 912 | G22 | S88 | 2 | 42.7 | 410.3 | 109.9 | 1.17 | 17.1 | |
| | | | 188 | | 44.4 | 410.4 | 121.0 | 1.14 | 11.6 | |
| | | | 588 | | 45.5 | 408.9 | 109.3 | 1.13 | 13.9 | u |
| 993 | 1104 | G23 | 588 | 5 | 18.7 | 2608.7 | 191.4 | 1.03 | 6.0 | Uc: |
| 994 | 1105 | G24 | 588 | 5 | 21.3 | 2590.4 | 232.8 | 1.07 | 6.9 | Uc: |
| 998 | 1161 | G25 | S88 | 2 | 51.7 | 267.8 | 110.2 | −1.07 | 20.3 | u |
| | | | 188 | | 53.3 | 267.5 | 110.1 | −1.07 | 14.6 | |
| | | | 588 | | 51.1 | 267.6 | 110.8 | −1.07 | 13.4 | |
| 999 | 1168 | G26 | 188 | 5 | 249.3 | 227.4 | 193.5 | −1.04 | 49.2 | U0< |

[a] Jy km $s^{-1}$
[b] km $s^{-1}$

effect in companions. Unlike the excess redshift for companions there are no significant differential volume or interloper effects, although some self absorption effects could enter. The change is not present in minimally-rotating dwarf irregulars where no notable disk is present. Recent cosmological models consistent with redshift quantization (Tifft et al 1996 [127], Tifft 1997a [129]) predict that such a radial increase in redshift may be expected in the rotating systems; observations of radial redshift gradients may provide a critical test to distinguish cosmological models and explain certain aspects of the structure of disk galaxies.

TABLE 6

DATA FOR EFFELSBERG COMPARISONS

| TC | FT | UGC | Run | BW MHz | Flux a | $V_h$ b | W b | A | S/N | $F/F_e$ | $\Delta V$ b | $\Delta W$ b | Comments |
|---|---|---|---|---|---|---|---|---|---|---|---|---|---|
| 901 | 68 | E1 | S88 | 2 | 6.3 | 362.0 | 59.0 | −1.08 | 6.4 | 1.02 | 0.0 | −7.9 | |
| | | | 188 | | 5.9 | 363.7 | 61.0 | 1.01 | 3.2 | | | | Av2w3 |
| | | | 588 | | 6.7 | 360.9 | 58.9 | −1.14 | 4.3 | | | | u |
| 903 | 73 | E3 | S88 | 2 | 4.6 | 299.9 | 49.6 | 1.62 | 4.2 | 1.37 | 3.1 | 8.3 | u?>?< |
| | | | 188 | | 4.0 | 294.2 | 44.2 | −1.05 | 2.5 | | | | Av2uw1 |
| | | | 588 | | 4.0 | 303.0 | 46.4 | 1.71 | 2.7 | | | | |
| 909 | 194 | E9 | 488 | 2 | 9.8 | 2079.9 | 155.6 | 1.06 | 2.0 | 2.13 | −2.0 | 76.4 | u |
| 910 | 0 | E10 | 488 | 2 | 2.1 | 1443.0 | 50.8 | 1.00 | 1.5 | 0.51 | 10.5 | −6.3 | Guc: |
| 946 | 218 | Ex1 | S88 | 10 | 67.5 | 1461.6 | 414.8 | 1.16 | 14.7 | | | | ui< |
| | | | 188 | | 66.7 | 1461.0 | 414.4 | 1.14 | 8.8 | | | | Av2i<r<w1 |
| | | | 488 | | 71.6 | 1463.6 | 420.7 | 1.18 | 9.4 | | | | U |
| 913 | 438 | E13 | 188 | 2 | 5.0 | 3064.2 | 80.9 | 1.07 | 2.3 | 1.39 | 2.8 | 26.2 | w1 |
| 914 | 449 | E14 | 188 | 2 | 6.6 | 2513.5 | 83.1 | 1.07 | 2.6 | 0.78 | −0.8 | 0.4 | w1 |
| 961 | T639 | Ex2 | 188 | 5 | 1.4 | 2660.9 | 139.7 | 1.00 | 0.5 | | | | Gw1 |
| 916 | 0 | E16 | 188 | 2 | 11.8 | 4129.3 | 105.6 | −1.14 | 3.9 | 1.55 | −5.1 | 25.4 | u |
| 918 | 0 | E18 | S88 | 2 | 7.3 | 1742.9 | 56.8 | −1.06 | 6.4 | 1.04 | 0.6 | −0.2 | z< |
| | | | 188 | | 8.3 | 1743.1 | 65.2 | 1.01 | 4.3 | | | | uw1 |
| | | | 588 | | 6.9 | 1744.3 | 53.1 | −1.03 | 5.2 | | | | u |
| | Comp | E18 | S88 | 2 | 0.7 | 1630.1 | 26.1 | 1.00 | 1.4 | | | | G |
| 920 | 0 | E20 | 188 | 2 | 11.4 | 1724.0 | 97.9 | 1.14 | 4.2 | 1.36 | 2.1 | 11.3 | u?>w1 |
| 970 | Ex3 | 7065 | 188 | 2 | 8.7 | 5886.8 | 66.3 | 1.03 | 4.2 | | | | u |
| 924 | 0 | E24 | 188 | 2 | 5.0 | 2784.8 | 73.4 | 1.44 | 2.4 | 1.22 | 11.0 | 6.3 | |
| 925 | 0 | E25 | 188 | 2 | 3.7 | 573.8 | 47.7 | 1.00 | 2.1 | 0.97 | 1.7 | −9.6 | Gw2 |
| 926 | 0 | E26 | 188 | 2 | 20.5 | 586.6 | 86.8 | 1.03 | 8.1 | 0.98 | −3.0 | 5.1 | |
| 897 | 915 | Ex4 | S88 | 2 | 12.2 | 479.2 | 52.9 | 1.03 | 9.5 | | | | u |
| | | | 488 | | 11.3 | 481.9 | 43.9 | 1.12 | 6.7 | | | | u?> |
| | | | 588 | | 13.6 | 475.7 | 59.6 | −1.08 | 7.5 | | | | u |
| 927 | 937 | E27 | 188 | 10 | 66.4 | 2672.9 | 530.2 | 1.11 | 5.8 | 0.90 | −5.6 | −27.8 | |
| 928 | 961 | E28 | S88 | 5 | 45.3 | 1382.7 | 178.7 | −1.09 | 12.4 | 1.25 | 0.5 | −0.7 | ui< |
| | | | 188 | | 47.6 | 1383.6 | 183.7 | −1.08 | 10.0 | | | | j<?< |
| | | | 488 | | 43.4 | 1383.1 | 177.2 | −1.08 | 8.4 | | | | |
| | | | 588 | | 42.5 | 1382.5 | 178.2 | −1.12 | 7.9 | | | | II<r |
| 933 | 0 | E33 | 588 | 2 | 9.4 | 1984.4 | 51.1 | −1.13 | 5.4 | 1.15 | −2.6 | −5.9 | u |

[a] Jy km $s^{-1}$
[b] km $s^{-1}$

Table 6 summarizes the data for observations of objects in common with Effelsberg observations by Tifft and Huchtmeier (1990 [104]). The format of the table is the same as Tables 4 and 5 with the addition of three columns giving the 140-foot to 100-m flux ratio, and the redshift and profile width differences (140-foot minus 100-m). The Effelsberg work, other than on standards, involved dwarf galaxies with narrow 21 cm profiles. Table 6 and the left panel of Figure 1 show quite clearly that a substantial amount of hydrogen in the systems falls outside of the 9 arc minute Effelsberg beam but within the 21 arc minute beam of the 140-foot instrument. The right hand panel of Figure 1 shows that there is no detectable change in the redshift, consistent with the findings for dwarf irregulars in Tifft (1991a [109]). For the six galaxies with $S/N > 3$ and $W < 100$ km/s the mean difference in redshift is $0.0 \pm 1.0$ km/s with a dispersion of $\pm 2.4$ km/s. Lower quality data is consistent as are a

few slightly wider profiles, although there are too few wider profile galaxies for a significant comparison. The scatter increases for width measurements, but again there is no significant change. For the six best narrow profile objects the mean difference is $+1.7 \pm 3.2$ km/s with a dispersion of $\pm 7.8$ km/s.

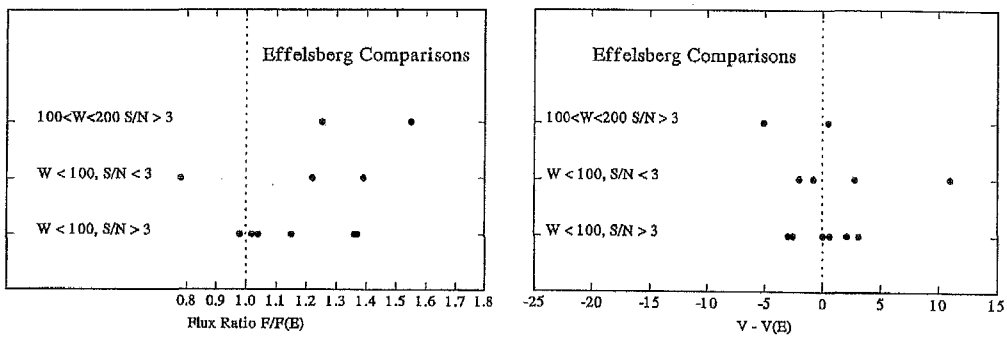


Figure 3.1: Flux and redshift comparisons for Effelsberg observations. The flux ratio 140-foot relative to Effelsberg is on the left; the difference V(140-foot) − V(Effelsberg) is on the right. Galaxies are separated according to profile widths, $W$, and signal-to-noise level, $S/N$. The large beam of the 140-foot telescope detects increased flux, but yields the same redshift for the dwarf galaxies that dominate this sample.

It appears that quite reliable redshifts, repeatable with uncertainties near 3 km/s can readily be derived above $S/N$ levels of 3 or 4 for the narrow line dwarfs observed at the 2 km/s resolution used here. Below $S/N = 3$ appreciable errors can occur in defining the edges of a profile. Significant flux underestimates occur with the smaller beam, but the redshift and profile width seem to be stable.

Table 7 includes data for galaxies in common with certain Arecibo studies by Bicay & Giovanelli (1986a,b [BX,BY], 1987 [BZ]), Haynes & Giovanelli (1984, 1986 [CD,CE]) or Freudling Haynes & Giovanelli (1988 [CB]). This work was done for two reasons, to test the consistency of the major redshift sources used in quantization studies (Tifft 1996 [125]), and to compare data for disk galaxies observed with the very different beam sizes. The table is in the same format as Table 6. Integrations of up to one hour were involved to obtain $S/N$ near 3 for the wide profile galaxies. Two objects listed in Table 1 were not detected, UGC 8310, and 8999, but only short integrations were obtained on these galaxies.

Figure 2 compares the flux and profile width measures for the Arecibo objects. There is a marked increase in flux; the filled symbols refer to the observed Arecibo values. Open symbols use the 'corrected' Arecibo values which allow for pointing errors and beam size effects. The corrections appear to remove the beam bias for the wider profiles, but do not reduce the scatter. Typically 1/3 of the outlying hydrogen in the disk systems is being missed. The corrections appear to be underestimated for the narrower profile galaxies, especially in the Freudling Haynes & Giovanelli (1988 [CB]) data.

The width comparison cannot be readily interpreted since the Arecibo widths generally refer to 50% of the average signal compared with 20% of the central flux average for the 140-foot

TABLE 7
DATA FOR ARECIBO COMPARISONS

| UGC | BW MHz | Flux a | $V_h$ b | W b | A | S/N | $F/F_a$ | $\Delta V$ b | $\Delta W$ b | Comments |
|---|---|---|---|---|---|---|---|---|---|---|
| 3835 | 10 | 12.5 | 5487.6 | 480.9 | 1.04 | 3.4 | 1.27 | −12.4 | 20.9 | |
| 3917 | 10 | 8.3 | 4674.6 | 517.7 | 1.32 | 1.9 | 1.18 | −3.4 | 14.7 | |
| 4005 | 10 | 22.6 | 5049.5 | 525.7 | −1.35 | 5.7 | 1.67 | 5.5 | 38.7 | |
| 4040 | 10 | 10.8 | 4797.0 | 487.7 | 1.06 | 3.0 | 1.59 | −9.0 | 26.7 | c:> |
| 4419 | 10 | 8.7 | 5991.6 | 555.5 | −1.37 | 2.1 | 1.21 | c | c | c:>??> |
| 4558 | 10 | 7.7 | 7678.9 | 514.8 | 1.07 | 1.9 | 1.23 | 5.9 | 24.8 | |
| 5010 | 10 | 14.5 | 4094.7 | 610.6 | −1.07 | 3.2 | 1.30 | −4.3 | 1.6 | |
| 5248 | 10 | 12.4 | 5842.9 | 544.3 | −1.21 | 3.1 | 1.10 | −9.1: | 8.3: | ??< |
| 5341 | 10 | 15.6 | 7568.5 | 640.4 | 1.01 | 2.9 | 1.42 | 0.5 | 17.4 | |
| 5499 | 10 | 15.2 | 4754.8 | 447.5 | 1.10 | 4.3 | 1.26 | 2.8 | 4.5 | u |
| 5711 | 10 | 23.8 | 6260.1 | 581.9 | −1.06 | 5.4 | 1.64 | 1.1 | 40.9 | |
| 6134 | 10 | 11.4 | 7706.9 | 478.3 | 1.26 | 3.0 | 1.31 | 7.9 | 18.3 | |
| 7330 | 10 | 9.6 | 7305.5 | 496.9 | 1.06 | 2.8 | 1.43 | c | c | ??> |
| 7808 | 10 | 15.2 | 7275.0 | 541.1 | −1.28 | 3.7 | 1.84 | 2.0 | 1.1 | u |
| 8298 | 2 | 15.6 | 1167.2 | 95.4 | 1.03 | 10.5 | 1.50 | 11.2 | 6.4 | |
| 8573 | 2 | 15.3 | 6858.3 | 169.6 | 1.07 | 3.2 | 1.73 | 3.3 | 5.6 | |
| | 5 | 18.3 | 6846.0 | 194.2 | −1.18 | 7.0 | c | c | c | W!< |
| 9296 | 2 | 1.9 | 8858.3 | 88.2 | 1.00 | 1.3 | c | c | c | G |
| 9317 | 2 | 7.0 | 4426.5 | 66.1 | −1.03 | 6.5 | 1.27 | 1.5 | −5.9 | |
| 9594 | 2 | 7.8 | 5193.4 | 70.3 | −1.08 | 6.1 | 1.76 | −0.6 | 2.3 | |
| 9803 | 2 | 1.4 | 5259.5 | 83.9 | 1.00 | 1.0 | c | c | c | G |
| 9910 | 5 | 18.5 | 1837.1 | 231.3 | −1.28 | 7.8 | 1.73 | c | c | W!< |
| 10043 | 10 | 34.8 | 2159.3 | 370.4 | −1.18 | 6.1 | 1.99 | −0.7 | 35.4 | |
| 11212 | 5 | 6.8 | 5272.8 | 135.9 | 1.03 | 3.5 | 1.38 | 5.8 | 25.9 | |

[a]Jy km $s^{-1}$
[b]km $s^{-1}$
[c]Profile distortions prevent a valid comparison

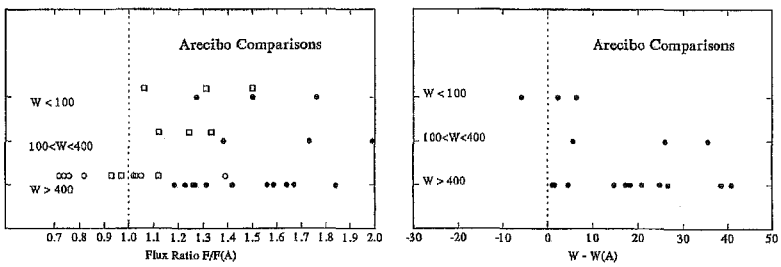


Figure 3.2: Flux and profile width comparisons for Arecibo observations. The flux ratio (140-foot)/(Arecibo) is on the left; the difference W(140-foot)−W(Arecibo) is on the right. Galaxies are separated according to profile widths, $W$, and only galaxies with well defined profiles are shown. Filled symbols refer to observed fluxes; open symbols include corrections for the small Arecibo beam. Open squares distinguish corrected data from sources other than Bicay and Giovanelli. The large beam of the 140-foot telescope detects a markedly increased flux. Most of the width difference is due to the use of different flux levels to define widths.

data. Most of the typically 5% change in width is no doubt due to this difference, although the true width of the outlying hydrogen profile may contribute. Tifft (1991a [109]) found that widths continue to slowly increase outward; the effect is generally less than 5 km/s at flux ratios of 1.3. One possible source of contamination in the 140-foot data is the inclusion of some dwarf companions in the signal. Galaxies with seriously distorted or uncertain profile edges were omitted in the comparisons, and no other peculiarities in the profiles are apparent, hence companions are not likely to be an important factor.

Figure 3 displays the redshift differences between the Arecibo and 140-foot observations.

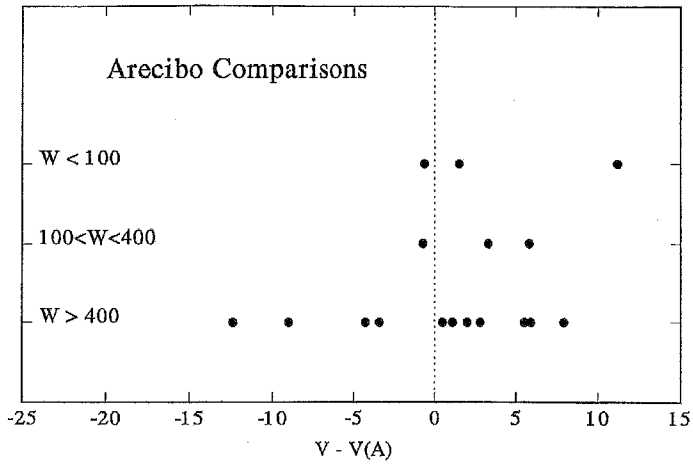


Figure 3.3: Redshift comparisons for Arecibo observations in the sense V(140-foot) − V(Arecibo). Galaxies are separated according to profile widths, $W$, and only galaxies with well defined profiles are shown. The distribution for the spirals ($W$ > 100 km/s) is consistent with a negative tail and a slight excess redshift associated with outlying hydrogen seen only by the 140-foot telescope.

As with the Effelsberg comparisons it is quite clear that there are no systematic effects in excess of two or three km/s and even at the level of $S/N \approx 3$ involved there are few random deviations in excess of about 3 km/s. Modern 21 cm parameters, carefully derived, are much more precise than commonly assumed. The precision is consistent with short periodicities seen in quantization work where data of much higher quality is generally employed.

At a more subtle level Figure 3 is consistent with a radial redshift gradient and possible variability. Except for two negative residuals near −10 km/s the bulk of the disk systems show a slight positive redshift excess. The 1991 (Tifft 1991a [109]) comparisons indicate that about a 2 km/s excess would be expected for a 30% flux deficiency. A larger sample should easily be able to detect such an effect. The negative deviation tail in the residuals is remarkably similar to the deviant tails seen in comparisons with many of the best surveys of older redshifts, notably Fisher-Tully (1981 [V]), Dickel-Rood (1978 [W]), Shostak (1975, 1978 [X,Y]), Roberts (1968 [Z]), and even the Baiesi-Pallastrini and Palumbo standards (1986 [CA]) all as discussed by Tifft (1991b [111]). These deviations are consistent with real changes (Tifft 1997b [138]), within a quantized pattern, although other explanations may yet be found. It remains a remarkable fact that few equivalent positive shifts are seen.

Table 8 contains the measurements on galaxies in common with several older studies,

TABLE 8
DATA FOR SECONDARY COMPARISONS

| TC | FT | UGC | Run | BW MHz | Flux a | $V_h$ b | W b | A | S/N | Code | ΔV b | ΔW b | Comments |
|---|---|---|---|---|---|---|---|---|---|---|---|---|---|
| 674 | 0 | 3190 | 488 | 2 | 11.9 | 1566.4 | 172.8 | −1.08 | 3.9 | S | 1.4 | −0.2 | u?> |
| 677 | 0 | 3253 | 588 | 10 | 13.5 | 4108.4 | 400.6 | 1.09 | 1.9 | | | | U! |
| 690 | 2268 | 3653 | 488 | 10 | 22.4 | 2234.6 | 405.5 | −1.03 | 5.6 | S | 3.6 | 11.5 | U |
| | | | | | | | | | | DR | 13.6 | −8.5 | |
| 694 | 323 | 3740 | 488 | 5 | 18.7 | 2414.9 | 173.1 | 1.54 | 6.0 | BP | −0.1 | | u?< |
| 714 | 3031 | 5318 | 588 | 10 | 760.9 | −30.6 | 453.0 | −1.55 | 38.9 | BP,DR | c | c | 0XrKc: |
| 715 | 3034 | 5322 | 588 | 10 | 334.6 | 182.6 | 229.7 | 1.04 | 51.8 | BP | c | | 0X<KR>c: |
| 782 | 4369 | 7489 | 488 | 5 | 8.6 | 1024.9 | 215.2 | 1.23 | 2.5 | DR | d | d | u??> |
| 787 | 727 | 7675 | 488 | 10 | 28.5 | 2277.1 | 559.8 | 1.52 | 2.8 | BP[e] | 9.1 | | u |
| | | | 289 | | 29.1 | 2285.1 | 555.2 | 1.41 | 3.4 | | | | ui>r:?> |
| 792 | 741 | 7727 | 488 | 10 | 78.0 | 1962.9 | 301.0 | 1.06 | 14.5 | BP | 9.9 | | ui< |
| 795 | 747 | 7772 | 488 | 10 | 235.6 | 1227.8 | 533.6 | −1.27 | 29.9 | BP | 0.8 | | |
| 799 | 766 | 7901 | 488 | 10 | 55.1 | 801.9 | 393.7 | −1.15 | 9.9 | BP | −18.1 | | u |
| 805 | 789 | 7996 | S88 | 5 | 38.0 | 310.8 | 242.1 | −1.69 | 10.1 | BP | 3.8 | | 0< |
| | | | 488 | | 38.2 | 315.2 | 239.4 | −1.67 | 7.4 | | | | u |
| | | | 588 | | 34.6 | 307.8 | 240.7 | −1.79 | 7.4 | | | | u0< |
| 807 | 4775 | 0 | S88 | 2 | 36.1 | 1565.3 | 143.0 | −1.12 | 12.8 | S | 0.3 | −11.0 | |
| | | | 488 | | 34.6 | 1570.3 | 135.6 | −1.01 | 9.0 | | | | u?< |
| | | | 588 | | 36.6 | 1563.0 | 141.3 | −1.18 | 9.3 | | | | ?> |
| 812 | 808 | 8062 | 488 | 10 | 45.7 | 405.7 | 336.7 | −1.37 | 8.3 | BP | 7.7 | | uR |
| | Comp | To W | | 10 | 6.8 | 768.6 | 160.2 | 1.00 | 3.9 | | | | GuRHcB |
| 816 | 828 | 0 | 588 | 10 | 52.1 | 3108.0 | 484.1 | −1.05 | 6.8 | S[c] | 2.8 | 13.3 | |
| | | | 289 | | 50.5 | 3109.6 | 486.5 | 1.04 | 8.0 | DR | −1.2 | 17.3 | J< |
| 818 | 4961 | 8185 | S88 | 5 | 15.7 | 2527.8 | 247.2 | −1.18 | 4.8 | S | −7.2 | 19.2 | u |
| | | | 488 | | 16.5 | 2532.8 | 249.6 | −1.10 | 3.5 | | | | u |
| | | | 588 | | 14.5 | 2527.0 | 241.1 | −1.23 | 3.2 | | | | u |
| 819 | 0 | 8263 | 588 | 5 | 9.5 | 3060.7 | 200.9 | 1.45 | 2.3 | S | 18.7 | −8.1 | |
| 825 | 5147 | 8443 | 488 | 2 | 15.9 | 1086.7 | 170.1 | 1.04 | 2.7 | S | −20.3 | 3.1 | |
| | | | | | | | | | | DR | −6.3 | 14.1 | |
| 829 | 5230 | 8573 | 588 | 2 | 15.3 | 6858.5 | 169.6 | 1.07 | 3.2 | S | 20.5 | 12.6 | |
| | | | 591 | 5 | 18.3 | 6846.0 | 194.2 | −1.18 | 7.0 | S | 8.0 | d | W!< |
| 834 | 948 | 0 | 588 | 2 | 29.2 | 2841.2 | 162.3 | 1.03 | 6.8 | S | −3.8 | 5.3 | |
| 837 | 957 | 9127 | 588 | 10 | 47.1 | 2876.2 | 615.9 | 1.02 | 4.4 | S | −5.8 | 5.9 | u |
| 841 | 5668 | 9363 | S88 | 2 | 42.7 | 1584.6 | 116.1 | 1.14 | 19.5 | BP | 1.6 | | |
| | | | 488 | | 42.0 | 1583.1 | 113.8 | 1.09 | 13.0 | S | 1.6 | −1.9 | u |
| | | | 588 | | 42.9 | 1585.6 | 117.5 | 1.14 | 13.5 | | | | |
| 842 | 5676 | 9366 | S88 | 10 | 31.1 | 2116.1 | 472.0 | −1.34 | 4.9 | S | −0.9 | 7.0 | uR<?> |
| | | | 488 | | 34.9 | 2117.5 | 470.3 | −1.38 | 5.0 | DR[e] | −5.9 | −20.0 | ?> |
| | | | 588 | | 28.2 | 2111.5 | 488.2 | −1.38 | 3.2 | | | | I<r |
| 844 | 989 | 9436 | 588 | 2 | 58.4 | 1508.8 | 141.8 | −1.08 | 14.8 | DR | 3.8 | −2.2 | i<r |
| 850 | 5970 | 9943 | 588 | 10 | 20.7 | 1963.9 | 365.2 | −1.01 | 7.6 | DR | −0.1 | d | I!<RIH |
| 873 | 6821 | 0 | 588 | 2 | 19.9 | 1527.9 | 150.6 | −1.15 | 6.3 | S | 4.9 | −10.4 | uI!<RHw3 |
| 886 | 7541 | 12447 | 588 | 10 | 53.4 | 2684.0 | 462.6 | −1.11 | 8.5 | BP | 6.0 | | u |
| | | | | | | | | | | S | 19.0 | −9.4 | |

[a] Jy km $s^{-1}$
[b] km $s^{-1}$
[c] Zero velocity hydrogen prevents a valid comparison
[d] Profile distortions prevent a valid comparison
[e] Object on the Zaritsky-White list

notably the work by DR = Dickel-Rood (1978 [W]) and S = Shostak (1975, 1978 [X,Y]) using the 300-foot telescope, and BP = the Baiesi-Pallastrini and Palumbo (1986 [CA]) standards which were formed as a composite of many older sources. The comparison involved is indicated in the 'Code' column of Table 8. Most of the table headings are the same as earlier tables except that no consistent flux data is available, and the BP standards have no profile width data.

Figure 4 gives the profile width and redshift comparisons possible using the older data. Since the quality of the older data is lower than the newer data discussed above, the scatter is increased. Compare, for example, the scatter in the newer data in Figure 1 or 3. Small radial or variational effects which may be present are largely masked by the scatter. There is no inconsistency in the profile widths; redshifts are also consistent on average. Any further

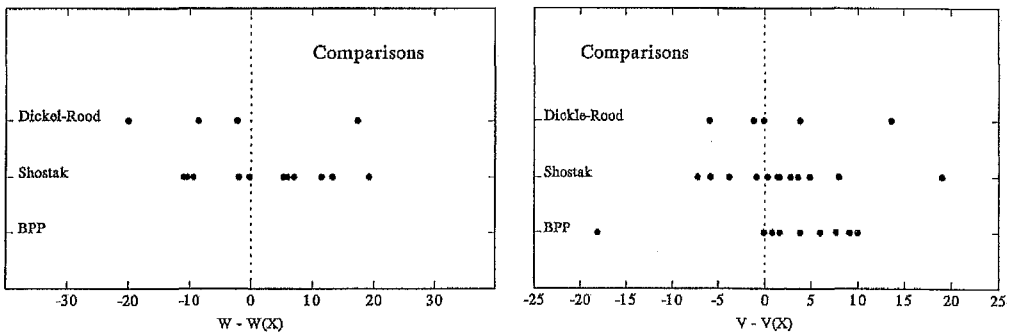


Figure 3.4: Profile width and redshift comparisons for older observations as indicated. BPP refers to the Baiesi-Pallastrini & Palumbo compilations. The differences are in the sense (140-foot) − (Other).

comparisons using these data will be deferred to a discussion of the set of 200 primary and secondary standards where an effective comparison of the 300-foot and 140-foot telescopes is possible using consistent recent observations.

# Appendix 3b

## Unpublished 140-foot 21-cm Data for Redshift Standards

### Introduction

Appendix 3b provides unpublished 140-foot 21-cm observations for the redshift standards, and additional wide profile galaxies added beginning in 1995. The table format is as described for the initial 1988 data [96], the 1991 data contained in Appendix 2 and observations of galaxies obtained for other purposes in Appendix 3a and will not be repeated here. The overall set of data is of key import as a fundamental consistent baseline for longer term investigations of redshift properties, especially variability. It has now been more than 25 years since the standards were established. Observations obtained in 1993 are omitted since there was some pointing uncertainty at that time, and in 1997 because of severe interference problems which question the use of the data within the optimal set of standards. Flux information is not included since the 1988 data [96] is available using multiple telescopes to examine radial dependence, consistency between instruments and the precision possible when comparing different data sets. Flux information is provided for the set of general data in appendix 3a.

140-Foot 1989 Unpublished Data for 21-cm Standards

| TC | FT | UGC | BW MHz | $V_h$ km/s | W km/s | A | S/N |
|---|---|---|---|---|---|---|---|
| 74 | 314 | 3574 | 5.0 | 1441.1 | 165.0 | −1.03 | 11.8 |
| 499 | 320 | 3685 | 2.5 | 1796.6 | 100.0 | −1.12 | 14.6 |
| 81 | 322 | 3711 | 5.0 | 434.6 | 176.9 | 1.16 | 15.1 |
| 87 | 331 | 3851 | 2.5 | 100.2 | 116.4 | 1.01 | 57.9 |
| 93 | 338 | 3974 | 2.5 | 272.0 | 87.6 | −1.14 | 23.9 |
| 100 | 351 | 4305 | 5.0 | 156.8 | 73.7 | 1.04 | 106.1 |
| 100 | Comp | 0 | 5.0 | −145.4 | 39.0 | −1.07 | 28.5 |
| 100 | 351 | 4305 | 2.5 | 156.6 | 72.9 | 1.03 | 85.8 |
| 100 | 351 | 4305 | 1.2 | 156.6 | 73.5 | 1.04 | 50.7 |
| 117 | 406 | 5139 | 1.2 | 140.6 | 45.6 | 1.08 | 26.4 |
| 128 | 431 | 5373 | 2.5 | 301.6 | 62.3 | 1.06 | 39.2 |
| 134 | 450 | 0 | 2.5 | 324.2 | 65.3 | 1.02 | 79.7 |
| 134 | Comp | 0 | 2.5 | 136.4 | 49.4 | 1.16 | 10.9 |
| 136 | 456 | 5557 | 5.0 | 591.7 | 148.8 | 1.09 | 20.3 |
| 143 | 485 | 5829 | 2.5 | 629.6 | 106.2 | 1.05 | 11.9 |
| 143 | 485 | 5829 | 2.5 | 628.1 | 99.6 | −1.03 | 15.7 |
| 143 | 485 | 5829 | 2.5 | 629.1 | 102.0 | 1.02 | 19.4 |
| 150 | 507 | 6079 | 10.0 | 682.8 | 247.3 | −1.06 | 23.8 |
| 150 | 507 | 6079 | 5.0 | 683.1 | 247.1 | −1.08 | 22.8 |
| 917 | 3556 | 6225 | 10.0 | 697.3 | 336.3 | 1.04 | 25.6 |
| 917 | 3556 | 6225 | 5.0 | 698.4 | 333.3 | 1.01 | 20.8 |
| 164 | 536 | 6360 | 5.0 | 1155.7 | 130.6 | −1.09 | 16.0 |
| 175 | 565 | 6628 | 1.2 | 848.1 | 55.0 | −1.10 | 13.7 |
| 182 | 589 | 6817 | 2.5 | 242.1 | 68.3 | −1.09 | 29.5 |
| 188 | 628 | 7074 | 2.5 | 205.7 | 86.2 | −1.23 | 18.7 |
| 201 | 675 | 7278 | 5.0 | 292.8 | 91.8 | 1.08 | 122.3 |
| 201 | 675 | 7278 | 2.5 | 292.2 | 91.6 | 1.06 | 82.7 |
| 201 | 675 | 7278 | 1.2 | 292.1 | 91.6 | 1.06 | 55.8 |
| 210 | 706 | 7534 | 2.5 | 723.6 | 75.1 | 1.12 | 20.2 |
| 239 | 770 | 7907 | 10.0 | 638.8 | 197.4 | −1.15 | 61.2 |
| 239 | 770 | 7907 | 5.0 | 639.1 | 195.7 | −1.12 | 49.5 |
| 259 | 826 | 0 | 5.0 | 740.5 | 133.2 | −1.27 | 26.0 |
| 260 | 834 | 8188 | 2.5 | 321.6 | 57.7 | 1.14 | 27.4 |
| 273 | 863 | 8320 | 2.5 | 191.7 | 86.3 | 1.04 | 17.1 |
| 302 | 944 | 8981 | 5.0 | 230.8 | 199.6 | −1.25 | 120.4 |

140-Foot 1989 Unpublished Data (continued)

| TC | FT | UGC | BW MHz | $V_h$ km/s | W km/s | A | S/N |
|---|---|---|---|---|---|---|---|
| 304 | 947 | 9013 | 5.0 | 274.6 | 56.7 | −1.01 | 82.1 |
| 304 | 947 | 9013 | 2.5 | 274.8 | 56.3 | −1.01 | 58.9 |
| 304 | 947 | 9013 | 1.2 | 274.8 | 55.9 | −1.02 | 47.8 |
| 308 | 966 | 9240 | 2.5 | 148.5 | 67.9 | −1.21 | 17.7 |
| 555 | 1019 | 9801 | 10.0 | 668.1 | 502.1 | −1.19 | 27.7 |
| 562 | 1042 | 10075 | 10.0 | 823.5 | 327.7 | 1.11 | 11.5 |

140-Foot 1992 Unpublished Data for 21-cm Standards

| TC | FT | UGC | BW MHz | $V_h$ km/s | W km/s | A | S/N |
|---|---|---|---|---|---|---|---|
| 6 | 0 | 192 | 5.0 | −347.6 | 87.5 | −1.12 | 82.9 |
| 6 | 0 | 192 | 2.5 | −347.3 | 87.4 | −1.11 | 117.5 |
| 432 | 80 | 0 | 2.5 | 1073.2 | 101.2 | −1.06 | 50.7 |
| 11 | 0 | 668 | 2.5 | −232.3 | 38.1 | −1.02 | 291.3 |
| 11 | 0 | 668 | 2.5 | −232.2 | 37.9 | −1.02 | 272.1 |
| 906 | 0598 | 1117 | 5.0 | −181.6 | 172.2 | −1.13 | 180.6 |
| 18 | 96 | 1149 | 2.5 | 657.8 | 75.6 | 1.08 | 111.0 |
| 18 | 96 | 1149 | 2.5 | 658.0 | 75.0 | 1.09 | 128.5 |
| 443 | 100 | 1201 | 10.0 | 849.0 | 329.0 | −1.17 | 26.3 |
| 443 | 100 | 1201 | 10.0 | 852.4 | 329.4 | −1.12 | 26.9 |
| 23 | 118 | 1501 | 2.5 | 196.4 | 124.2 | 1.13 | 13.4 |
| 23 | 118 | 1501 | 2.5 | 197.2 | 123.6 | 1.17 | 17.9 |
| 454 | 127 | 1831 | 10.0 | 530.3 | 485.4 | −1.10 | 18.2 |
| 454 | 127 | 1831 | 10.0 | 531.3 | 484.6 | −1.12 | 15.9 |
| 36 | 145 | 2034 | 2.5 | 576.8 | 63.3 | −1.06 | 19.7 |
| 36 | 145 | 2034 | 2.5 | 579.2 | 64.0 | 1.02 | 20.3 |
| 459 | 150 | 2080 | 5.0 | 904.9 | 145.8 | −1.07 | 29.0 |
| 459 | 150 | 2080 | 5.0 | 903.4 | 146.8 | −1.10 | 28.1 |
| 461 | 151 | 2082 | 5.0 | 706.5 | 212.8 | −1.07 | 10.2 |
| 461 | 151 | 2082 | 5.0 | 706.6 | 211.3 | −1.07 | 12.8 |
| 41 | 162 | 2193 | 2.5 | 517.6 | 42.2 | −1.01 | 83.5 |
| 43 | 168 | 2302 | 2.5 | 1103.5 | 69.6 | −1.12 | 41.4 |
| 468 | 190 | 0 | 10.0 | 1705.7 | 331.7 | −1.15 | 16.3 |
| 468 | 190 | 0 | 10.0 | 1706.9 | 330.3 | −1.13 | 18.6 |
| 473 | 206 | 2729 | 10.0 | 1943.2 | 272.0 | 1.16 | 16.3 |
| 48 | 231 | 2855 | 10.0 | 1212.5 | 468.9 | 1.12 | 17.2 |
| 48 | 231 | 2855 | 10.0 | 1216.3 | 475.3 | 1.11 | 19.2 |
| 51 | 238 | 2953 | 10.0 | 895.7 | 492.6 | 1.11 | 9.3 |
| 481 | 248 | 3137 | 5.0 | 993.4 | 249.2 | 1.29 | 14.1 |
| 482 | 251 | 3144 | 5.0 | 1636.0 | 165.7 | −1.10 | 18.4 |
| 56 | 252 | 3174 | 5.0 | 671.6 | 127.5 | 1.19 | 7.8 |
| 56 | 252 | 3174 | 5.0 | 670.5 | 120.3 | 1.18 | 15.2 |
| 486 | 271 | 3273 | 5.0 | 615.8 | 207.3 | −1.01 | 16.5 |
| 487 | 277 | 3303 | 5.0 | 518.3 | 178.3 | 1.03 | 10.6 |
| 487 | 277 | 3303 | 5.0 | 519.1 | 181.4 | 1.05 | 10.1 |

140-Foot 1992 Unpublished Data (continued)

| TC | FT | UGC | BW MHz | $V_h$ km/s | W km/s | A | S/N |
|---|---|---|---|---|---|---|---|
| 64 | 0 | 3384 | 2.5 | 1091.4 | 95.3 | −1.06 | 27.2 |
| 492 | 302 | 0 | 10.0 | 730.6 | 327.4 | −1.13 | 28.3 |
| 70 | 306 | 3475 | 5.0 | 483.1 | 184.7 | 1.12 | 4.2 |
| 70 | 306 | 3475 | 5.0 | 485.8 | 186.1 | 1.02 | 5.6 |
| 74 | 314 | 3574 | 5.0 | 1442.3 | 165.7 | −1.05 | 16.7 |
| 499 | 320 | 3685 | 2.5 | 1796.9 | 100.7 | −1.08 | 23.2 |
| 81 | 322 | 3711 | 5.0 | 435.5 | 177.4 | 1.05 | 22.5 |
| 87 | 331 | 3851 | 2.5 | 100.5 | 115.1 | −1.01 | 57.9 |
| 93 | 338 | 3974 | 2.5 | 272.4 | 89.4 | −1.11 | 39.4 |
| 100 | 351 | 4305 | 2.5 | 156.7 | 73.5 | 1.03 | 114.1 |
| 100 | 351 | 4305 | 2.5 | 156.5 | 73.0 | 1.03 | 139.8 |
| 100 | 351 | 4305 | 5.0 | 156.5 | 73.6 | 1.03 | 176.6 |
| 100 | Comp | 0 | 5.0 | −145.9 | 37.8 | −1.08 | 55.4 |
| 106 | 0 | 4483 | 2.5 | 156.3 | 55.7 | 1.07 | 14.7 |
| 117 | 406 | 5139 | 2.5 | 140.3 | 46.9 | 1.04 | 25.8 |
| 128 | 431 | 5373 | 2.5 | 301.3 | 64.4 | 1.04 | 56.7 |
| 134 | 450 | 0 | 2.5 | 324.4 | 65.3 | 1.04 | 84.6 |
| 134 | 450 | Comp | 2.5 | 131.9 | 46.4 | −1.28 | 9.4 |
| 136 | 456 | 5557 | 5.0 | 591.8 | 147.8 | 1.14 | 33.2 |
| 143 | 485 | 5829 | 2.5 | 629.7 | 98.0 | 1.05 | 25.6 |
| 150 | 507 | 6079 | 5.0 | 680.5 | 247.1 | −1.07 | 32.4 |
| 917 | 3556 | 6225 | 5.0 | 698.3 | 336.2 | 1.00 | 23.8 |
| 164 | 536 | 6360 | 5.0 | 1154.3 | 129.5 | −1.20 | 33.0 |
| 175 | 565 | 6628 | 2.5 | 849.4 | 57.0 | −1.07 | 27.4 |
| 182 | 589 | 6817 | 2.5 | 241.8 | 70.6 | −1.08 | 37.0 |
| 188 | 628 | 7047 | 2.5 | 205.8 | 84.8 | −1.27 | 28.0 |
| 201 | 675 | 7278 | 2.5 | 292.2 | 91.8 | 1.05 | 82.9 |
| 210 | 706 | 7534 | 2.5 | 721.9 | 72.9 | 1.02 | 27.3 |
| 212 | 715 | 7577 | 2.5 | 196.9 | 53.7 | 1.07 | 24.2 |
| 239 | 770 | 7907 | 5.0 | 638.9 | 195.7 | −1.13 | 79.5 |
| 259 | 826 | 0 | 5.0 | 742.0 | 133.9 | −1.24 | 23.1 |
| 260 | 834 | 8188 | 2.5 | 321.7 | 56.3 | 1.11 | 41.8 |
| 273 | 863 | 8320 | 2.5 | 191.1 | 88.3 | 1.02 | 46.1 |
| 295 | 933 | 8837 | 2.5 | 139.4 | 111.3 | 1.23 | 13.0 |
| 302 | 944 | 8981 | 5.0 | 231.2 | 200.1 | −1.26 | 159.0 |

140-Foot 1992 Unpublished Data (continued)

| TC | FT | UGC | BW MHz | $V_h$ km/s | W km/s | A | S/N |
|---|---|---|---|---|---|---|---|
| 304 | 947 | 9013 | 5.0 | 274.5 | 57.0 | −1.01 | 94.2 |
| 304 | 947 | 9013 | 2.5 | 274.6 | 56.5 | 1.02 | 46.8 |
| 308 | 966 | 9240 | 2.5 | 149.6 | 67.9 | −1.13 | 25.4 |
| 322 | 999 | 0 | 5.0 | 1839.1 | 176.2 | −1.04 | 12.0 |
| 328 | 0 | 9797 | 10.0 | 3391.7 | 362.9 | −1.09 | 6.5 |
| 555 | 1019 | 9801 | 10.0 | 668.2 | 501.5 | −1.26 | 29.4 |
| 559 | 1027 | 9906 | 10.0 | 654.4 | 216.9 | 1.08 | 21.1 |
| 333 | 1028 | 9912 | 2.5 | 1032.3 | 58.4 | 1.02 | 16.0 |
| 338 | 1035 | 10014 | 5.0 | 1122.1 | 129.1 | 1.18 | 14.8 |
| 562 | 1042 | 10075 | 10.0 | 834.6 | 323.0 | 1.22 | 23.5 |
| 345 | 1046 | 10310 | 2.5 | 716.9 | 104.2 | 1.09 | 12.8 |
| 565 | 1048 | 10359 | 5.0 | 907.9 | 232.7 | 1.05 | 30.0 |
| 347 | 0 | 10445 | 5.0 | 961.7 | 174.0 | −1.14 | 16.9 |
| 353 | 1056 | 10736 | 5.0 | 490.8 | 162.7 | −1.03 | 12.9 |
| 354 | 1058 | 10792 | 2.5 | 1233.1 | 73.3 | 1.02 | 10.9 |
| 358 | 0 | 10897 | 5.0 | 1318.6 | 139.9 | 1.00 | 16.2 |
| 932 | 6643 | 11218 | 10.0 | 1486.1 | 357.1 | −1.07 | 10.5 |
| 365 | 1075 | 11220 | 2.5 | 1449.4 | 93.8 | 1.07 | 11.7 |
| 583 | 1078 | 11300 | 5.0 | 489.2 | 226.9 | −1.04 | 20.3 |
| 372 | −11 | 0 | 2.5 | −79.8 | 37.0 | −1.02 | 22.7 |
| 373 | −15 | 0 | 2.5 | 1565.1 | 102.3 | 1.18 | 17.1 |
| 374 | −12 | 0 | 2.5 | −56.6 | 80.8 | 1.06 | 264.1 |
| 277 | 1082 | 0 | 2.5 | 1423.3 | 94.4 | 1.20 | 17.0 |
| 379 | 0 | 11604 | 10.0 | 1421.7 | 342.6 | −1.06 | 15.8 |
| 380 | 1085 | 0 | 2.5 | −141.1 | 36.1 | −1.05 | 22.9 |
| 605 | 1088 | 11707 | 5.0 | 906.3 | 204.7 | 1.24 | 17.0 |
| 387 | 0 | 11759 | 5.0 | 3257.7 | 162.8 | −1.63 | 9.7 |
| 609 | 1093 | 11861 | 10.0 | 1480.9 | 267.4 | 1.04 | 21.0 |
| 393 | 1098 | 11891 | 5.0 | 461.6 | 157.2 | 1.29 | 20.5 |
| 399 | 1113 | 12082 | 2.5 | 803.5 | 85.2 | −1.14 | 20.4 |
| 402 | 1117 | 12113 | 10.0 | 818.7 | 538.0 | −1.18 | 15.2 |
| 620 | 1139 | 12392 | 10.0 | 1707.7 | 305.6 | 1.50 | 19.6 |
| 936 | 7640 | 12554 | 10.0 | 372.2 | 268.8 | −1.14 | 32.7 |
| 412 | 1147 | 12613 | 2.5 | −186.0 | 42.1 | −1.28 | 16.9 |
| 413 | 1149 | 12632 | 5.0 | 423.5 | 126.4 | −1.08 | 19.3 |

140-Foot 1992 Unpublished Data (continued)

| TC | FT | UGC | BW MHz | $V_h$ km/s | W km/s | A | S/N |
|---|---|---|---|---|---|---|---|
| 414 | 1159 | 12732 | 5.0 | 748.3 | 139.6 | 1.12 | 18.6 |
| 414 | 1159 | 12732 | 5.0 | 748.5 | 137.7 | 1.12 | 35.6 |
| 415 | 1160 | 12754 | 5.0 | 749.3 | 214.4 | 1.03 | 18.4 |
| 417 | 0 | 12894 | 2.5 | 322.7 | 74.8 | −1.51 | 10.9 |
| 418 | 1171 | 0 | 2.5 | −120.9 | 75.7 | −1.12 | 83.6 |
| 418 | 1171 | 0 | 2.5 | −123.2 | 80.5 | −1.09 | 75.0 |
| 418 | Comp | 0 | 2.5 | −185.0 | 89.8 | −1.09 | 19.2 |

140-Foot 1995 Unpublished Data for 21-cm Standards

| TC | FT | UGC | BW MHz | $V_h$ km/s | W km/s | A | S/N |
|---|---|---|---|---|---|---|---|
| 6 | 0 | 192 | 5.0 | −347.4 | 87.3 | −1.11 | 69.2 |
| 6 | 0 | 192 | 2.5 | −347.5 | 86.8 | −1.12 | 141.0 |
| 432 | 80 | 0 | 2.5 | 1073.5 | 103.1 | −1.04 | 62.4 |
| 11 | 0 | 668 | 2.5 | −232.3 | 38.0 | −1.01 | 265.4 |
| 906 | 0598 | 1117 | 5.0 | −181.3 | 172.2 | −1.15 | 185.6 |
| 18 | 96 | 1149 | 2.5 | 657.5 | 75.2 | 1.06 | 123.4 |
| 23 | 118 | 1501 | 2.5 | 197.5 | 121.7 | 1.20 | 20.3 |
| 36 | 145 | 2034 | 2.5 | 578.6 | 64.3 | −1.01 | 30.4 |
| 459 | 150 | 2080 | 5.0 | 903.8 | 146.0 | −1.06 | 60.4 |
| 460 | 151 | 2082 | 5.0 | 707.0 | 213.3 | −1.08 | 16.7 |
| 41 | 162 | 2193 | 2.5 | 518.1 | 42.9 | 1.01 | 57.8 |
| 43 | 168 | 2302 | 2.5 | 1103.3 | 70.7 | −1.12 | 43.1 |
| 481 | 248 | 3137 | 5.0 | 993.0 | 249.6 | 1.25 | 15.5 |
| 486 | 271 | 3273 | 5.0 | 617.8 | 206.5 | 1.02 | 14.2 |
| 64 | 0 | 3384 | 2.5 | 1090.7 | 96.0 | −1.06 | 19.7 |
| 70 | 314 | 3574 | 5.0 | 1441.4 | 164.6 | −1.04 | 24.6 |
| 499 | 320 | 3685 | 2.5 | 1796.1 | 102.1 | −1.13 | 30.9 |
| 81 | 322 | 3711 | 5.0 | 434.0 | 180.2 | 1.12 | 28.3 |
| 87 | 331 | 3851 | 2.5 | 100.0 | 117.1 | −1.02 | 59.9 |
| 93 | 338 | 3974 | 2.5 | 272.9 | 89.8 | −1.07 | 40.1 |
| 100 | 351 | 4305 | 5.0 | 156.6 | 73.9 | 1.03 | 164.3 |
| 100 | 351 | 4305 | 2.5 | 156.4 | 73.7 | 1.03 | 135.7 |
| 117 | 406 | 5139 | 2.5 | 140.7 | 48.6 | 1.06 | 21.9 |
| 122 | 3003 | 5251 | 10.0 | 1480.2 | 301.4 | −1.27 | 28.5 |
| 128 | 431 | 5373 | 2.5 | 301.2 | 63.7 | 1.03 | 50.8 |
| 134 | 450 | 0 | 2.5 | 324.5 | 64.8 | 1.03 | 89.6 |
| 134 | Comp | 0 | 2.5 | 135.2 | 48.6 | 1.01 | 12.1 |
| 136 | 456 | 5557 | 5.0 | 592.6 | 148.5 | 1.14 | 44.3 |
| 143 | 485 | 5829 | 2.5 | 630.4 | 101.5 | 1.05 | 22.4 |
| 150 | 507 | 6079 | 5.0 | 681.7 | 248.2 | −1.08 | 38.6 |
| 917 | 3556 | 6225 | 5.0 | 698.8 | 332.8 | −1.01 | 19.5 |
| 917 | 3556 | 6225 | 10.0 | 697.3 | 336.0 | 1.02 | 24.3 |
| 182 | 589 | 6817 | 2.5 | 241.6 | 70.6 | −1.10 | 38.4 |
| 201 | 675 | 7278 | 2.5 | 292.4 | 91.2 | 1.07 | 72.8 |
| 210 | 706 | 7534 | 2.5 | 722.9 | 74.8 | 1.06 | 33.7 |

## 140-Foot 1995 Unpublished Data (continued)

| TC | FT | UGC | BW MHz | $V_h$ km/s | W km/s | A | S/N |
|---|---|---|---|---|---|---|---|
| 217 | 715 | 7577 | 2.5 | 197.4 | 54.3 | 1.10 | 29.9 |
| 239 | 770 | 7907 | 5.0 | 639.0 | 198.3 | −1.13 | 93.8 |
| 259 | 826 | 0 | 5.0 | 740.7 | 132.5 | −1.23 | 24.2 |
| 260 | 834 | 8188 | 2.5 | 321.3 | 55.8 | 1.10 | 40.9 |
| 273 | 863 | 8320 | 2.5 | 190.4 | 89.5 | −1.02 | 36.4 |
| 302 | 944 | 8981 | 5.0 | 230.8 | 200.7 | −1.22 | 160.8 |
| 304 | 947 | 9013 | 5.0 | 274.6 | 57.3 | −1.01 | 75.9 |
| 304 | 947 | 9013 | 2.5 | 274.6 | 57.0 | 1.01 | 53.2 |
| 328 | 5905 | 9797 | 10.0 | 3391.2 | 375.2 | −1.20 | 10.8 |
| 555 | 1019 | 9801 | 10.0 | 668.7 | 503.8 | −1.27 | 34.0 |
| 559 | 1027 | 9906 | 10.0 | 655.4 | 218.6 | 1.08 | 19.8 |
| 338 | 1035 | 10014 | 5.0 | 1122.1 | 132.2 | 1.13 | 17.3 |
| 562 | 1035 | 10075 | 10.0 | 832.1 | 318.5 | 1.21 | 22.5 |
| 565 | 1048 | 10359 | 5.0 | 907.3 | 233.3 | 1.04 | 38.5 |
| 358 | 6412 | 10897 | 5.0 | 1320.1 | 140.0 | 1.03 | 21.9 |
| 932 | 6643 | 11218 | 10.0 | 1485.1 | 359.8 | −1.05 | 11.8 |
| 372 | −11 | 0 | 2.5 | −79.3 | 37.0 | 1.04 | 18.5 |
| 373 | −15 | 0 | 2.5 | 1564.2 | 103.5 | 1.14 | 14.8 |
| 374 | −12 | 0 | 2.5 | −54.6 | 83.7 | 1.14 | 272.9 |
| 377 | 1082 | 0 | 2.5 | 1423.6 | 96.3 | 1.18 | 13.8 |
| 379 | 6951 | 11604 | 10.0 | 1424.0 | 353.1 | −1.09 | 14.3 |
| 380 | 1085 | 0 | 2.5 | −141.8 | 35.0 | −1.09 | 22.4 |
| 605 | 1088 | 11707 | 5.0 | 903.3 | 204.8 | 1.18 | 13.9 |
| 609 | 1093 | 11861 | 10.0 | 1481.1 | 273.3 | 1.00 | 20.0 |
| 393 | 1098 | 11891 | 5.0 | 461.0 | 153.1 | 1.34 | 21.2 |
| 399 | 1113 | 12082 | 2.5 | 802.8 | 87.5 | −1.18 | 23.6 |
| 402 | 1117 | 12113 | 10.0 | 816.2 | 532.0 | −1.13 | 16.0 |
| 620 | 1139 | 12392 | 10.0 | 1705.7 | 307.2 | 1.45 | 19.8 |
| 936 | 7640 | 12554 | 10.0 | 371.5 | 270.7 | −1.10 | 29.5 |
| 412 | 1147 | 12613 | 2.5 | −187.0 | 43.2 | −1.35 | 16.2 |
| 413 | 1149 | 12632 | 5.0 | 422.5 | 126.1 | −1.05 | 20.4 |
| 414 | 1159 | 12732 | 5.0 | 747.8 | 137.7 | 1.08 | 38.8 |
| 415 | 1160 | 12754 | 5.0 | 748.8 | 209.9 | −1.00 | 19.6 |
| 417 | 0 | 12894 | 2.5 | 321.6 | 72.2 | −1.67 | 10.0 |
| 418 | 1171 | 0 | 2.5 | −120.8 | 75.7 | −1.12 | 119.6 |

140-Foot 1995 Unpublished Data (continued)

| TC | FT | UGC | BW MHz | $V_h$ km/s | W km/s | A | S/N |
|---|---|---|---|---|---|---|---|
| 418 | 1171 | 0 | 2.5 | −123.4 | 81.0 | −1.15 | 143.8 |
| 418 | Comp | 0 | 2.5 | −184.8 | 86.6 | −1.08 | 28.5 |

140-Foot 1995 Supplementary Wide Data

| TC | FT | UGC | BW MHz | $V_h$ km/s | W km/s | A | S/N |
|---|---|---|---|---|---|---|---|
| A1 | 0045 | 0 | 5.0 | 467.7 | 188.1 | −1.00 | 36.0 |
| A2 | 0055 | 0 | 5.0 | 125.3 | 189.2 | −1.01 | 225.4 |
| A4 | 0247 | 0 | 5.0 | 155.0 | 221.3 | 1.07 | 82.0 |
| 633 | 0278 | 528 | 5.0 | 644.1 | 145.9 | 1.08 | 25.6 |
| A6 | 0300 | 0 | 5.0 | 144.3 | 161.0 | −1.10 | 136.0 |
| 635 | 81 | 0 | 5.0 | 1096.3 | 189.9 | −1.06 | 22.7 |
| 636 | 0428 | 763 | 5.0 | 1148.8 | 186.2 | −1.01 | 29.5 |
| 640 | 103 | 1249 | 5.0 | 399.3 | 277.1 | 1.62 | 16.6 |
| 648 | 0864 | 1736 | 5.0 | 1559.1 | 245.5 | 1.24 | 27.2 |
| 650 | 137G | 1913 | 5.0 | 552.5 | 224.8 | 1.08 | 62.7 |
| 652 | 153G | 2137 | 5.0 | 623.2 | 233.5 | −1.04 | 38.3 |
| 659 | 1156 | 2455 | 2.5 | 370.6 | 120.1 | −1.13 | 35.1 |
| 673 | 247 | 0 | 5.0 | 718.7 | 202.2 | 1.15 | 24.8 |
| 491 | 301 | 3439 | 5.0 | 1494.6 | 242.6 | −1.02 | 15.5 |
| 699 | 343 | 4165 | 2.5 | 515.0 | 121.4 | −1.01 | 20.6 |
| 703 | 350G | 4284 | 5.0 | 558.7 | 213.8 | 1.09 | 47.0 |
| 710 | 393G | 4936 | 2.5 | 1733.6 | 120.7 | −1.05 | 39.4 |
| 515 | 401 | 5079 | 10.0 | 555.6 | 399.2 | 1.26 | 22.7 |
| 713 | 426 | 5316 | 5.0 | 1058.4 | 233.3 | 1.09 | 31.5 |
| 716 | 433 | 5387 | 10.0 | 1123.3 | 485.2 | −1.06 | 24.4 |
| 718 | 457 | 5572 | 10.0 | 657.9 | 326.2 | −1.09 | 28.6 |
| 528 | 463 | 5637 | 5.0 | 750.8 | 192.9 | −1.20 | 29.5 |
| 723 | 483 | 5789 | 5.0 | 739.3 | 222.1 | 1.06 | 29.6 |
| 724 | 3338 | 5826 | 10.0 | 1297.2 | 364.6 | −1.16 | 21.3 |
| 725 | 3344 | 5840 | 5.0 | 589.1 | 177.0 | 1.13 | 40.0 |
| 726 | 3351 | 5850 | 10.0 | 778.3 | 295.8 | −1.07 | 8.1 |
| 727 | 3359 | 5873 | 5.0 | 1014.0 | 268.8 | −1.02 | 39.6 |
| 729 | 500 | 5986 | 10.0 | 612.1 | 276.9 | 1.36 | 33.1 |
| 731 | 3448 | 6024 | 10.0 | 1379.4 | 379.3 | 1.17 | 20.8 |
| 534 | 527 | 6277 | 5.0 | 1192.0 | 135.3 | 1.01 | 17.2 |

140-Foot 1995 Supplementary Wide Data (continued)

| TC | FT | UGC | BW MHz | $V_h$ km/s | W km/s | A | S/N |
|---|---|---|---|---|---|---|---|
| 162 | 533 | 6346 | 10.0 | 722.9 | 399.4 | −1.10 | 10.2 |
| 163 | 534 | 6350 | 10.0 | 843.7 | 489.3 | 1.23 | 32.9 |
| 737 | 552 | 6524 | 10.0 | 991.8 | 495.2 | −1.10 | 16.9 |
| 738 | 555 | 6537 | 10.0 | 864.5 | 300.6 | 1.12 | 16.1 |
| 749 | 3938 | 6856 | 2.5 | 808.5 | 112.8 | 1.08 | 37.7 |
| 195 | 650 | 7166 | 5.0 | 998.6 | 145.4 | 1.10 | 27.5 |
| 777 | 687G | 7322 | 5.0 | 244.2 | 219.6 | −1.00 | 55.5 |
| 921 | 4303 | 7420 | 5.0 | 1567.7 | 180.4 | −1.16 | 25.7 |
| 921 | Comp | 0 | 5.0 | 1276.6 | 143.1 | 1.18 | 5.0 |
| A32 | 4321 | 7450 | 10.0 | 1572.7 | 274 0 | 1.17 | 17.5 |
| 225 | 732 | 7694 | 10.0 | 1124.4 | 326.7 | −1.06 | 24.7 |
| 225 | Comp | 0 | 10.0 | 1539.6 | 176.8 | −1.15 | 3.0 |
| 229 | 0 | 7732 | 10.0 | 1805.6 | 353.7 | 1.06 | 16.0 |
| 229 | 0 | 7732 | 10.0 | 1807.5 | 355.4 | 1.04 | 11.4 |
| 794 | 746 | 7766 | 5.0 | 813.5 | 258.8 | −1.01 | 51.8 |
| 922 | 4631 | 7865 | 10.0 | 612.2 | 326.9 | 1.06 | 72.2 |
| 800 | 4654 | 7902 | 10.0 | 1035.2 | 319.0 | −1.43 | 16.2 |
| 250 | 787 | 7989 | 10.0 | 1205.2 | 422.1 | 1.23 | 15.3 |
| 806 | 788G | 0 | 5.0 | 1490.3 | 252.3 | 1.15 | 26.1 |
| 271 | 859 | 8307 | 10.0 | 875.3 | 458.5 | 1.12 | 20.7 |
| 822 | 867G | 8334 | 10.0 | 500.5 | 406.5 | 1.03 | 37.2 |
| 826 | 892 | 8490 | 2.5 | 200.4 | 132.8 | 1.04 | 46.9 |
| 827 | 893G | 8493 | 5.0 | 464.7 | 208.2 | −1.34 | 49.8 |
| 830 | 907G | 8616 | 10.0 | 1151.0 | 297.4 | −1.02 | 19.4 |
| 836 | 955 | 9119 | 10.0 | 1046.8 | 288.7 | −1.01 | 15.3 |
| 838 | 962 | 9179 | 5.0 | 303.4 | 165.1 | −1.18 | 49.3 |
| 930 | 991 | 9451 | 5.0 | 1885.9 | 239.6 | 1.06 | 16.1 |
| 930 | 991 | 9451 | 5.0 | 1878.2 | 257.2 | −1.00 | 16.1 |
| 554 | 1018 | 0 | 5.0 | 2000.2 | 204.1 | 1.02 | 16.8 |
| 855 | 6106 | 10328 | 10.0 | 1450.5 | 270.0 | 1.18 | 10.4 |
| 858 | 6217 | 10470 | 5.0 | 1353.2 | 234.0 | −1.04 | 19.2 |
| 861 | 6384 | 10891 | 10.0 | 1665.3 | 390.4 | 1.32 | 15.3 |
| 877 | 1100 | 0 | 5.0 | 1652.8 | 287.3 | 1.01 | 6.4 |
| A42 | 7793 | 0 | 5.0 | 226.2 | 193.1 | 1.03 | 32.9 |

140-Foot 1996 Unpublished Data for 21 cm Standards

| TC | FT | UGC | BW MHz | $V_h$ km/s | W km/s | A | S/N |
|---|---|---|---|---|---|---|---|
| 6 | 0 | 192 | 5.0 | −347.4 | 86.9 | −1.12 | 75.8 |
| 6 | 0 | 192 | 2.5 | −347.4 | 87.8 | −1.12 | 135.7 |
| 432 | 80 | 0 | 2.5 | 1073.3 | 103.1 | −1.05 | 60.3 |
| 11 | 0 | 668 | 2.5 | −232.4 | 38.0 | −1.02 | 255.2 |
| 906 | 0 | 1117 | 5.0 | −181.5 | 172.4 | −1.14 | 167.8 |
| 18 | 96 | 1149 | 2.5 | 657.8 | 75.2 | 1.08 | 125.5 |
| 443 | 100 | 1201 | 10.0 | 850.6 | 332.5 | −1.11 | 25.6 |
| 23 | 118 | 1501 | 2.5 | 197.3 | 122.8 | 1.18 | 23.4 |
| 454 | 127 | 1831 | 10.0 | 529.8 | 483.3 | −1.12 | 12.9 |
| 36 | 145 | 2034 | 2.5 | 579.2 | 64.6 | 1.02 | 31.5 |
| 459 | 150 | 2080 | 5.0 | 903.7 | 144.2 | −1.09 | 52.2 |
| 460 | 151 | 2082 | 5.0 | 706.9 | 212.5 | −1.04 | 17.6 |
| 41 | 162 | 2193 | 2.5 | 517.8 | 42.7 | 1.00 | 62.8 |
| 43 | 168 | 2302 | 2.5 | 1103.1 | 71.1 | −1.13 | 45.9 |
| 468 | 190 | 0 | 10.0 | 1709.4 | 329.0 | −1.14 | 30.8 |
| 48 | 231 | 2855 | 10.0 | 1214.8 | 469.6 | 1.12 | 20.4 |
| 48 | 231 | 2855 | 10.0 | 1216.1 | 478.8 | 1.13 | 18.4 |
| 48 | 231 | 2855 | 10.0 | 1214.5 | 471.8 | 1.14 | 28.8 |
| 51 | 238 | 2953 | 10.0 | 894.9 | 491.2 | 1.08 | 11.2 |
| 477 | 242 | 3013 | 10.0 | 2459.8 | 346.5 | −1.07 | 14.4 |
| 481 | 248 | 3137 | 5.0 | 993.6 | 249.3 | 1.17 | 15.2 |
| 486 | 271 | 3273 | 5.0 | 616.7 | 205.7 | 1.02 | 16.4 |
| 487 | 277 | 3303 | 5.0 | 519.4 | 177.4 | −1.02 | 16.4 |
| 61 | 1961 | 3334 | 10.0 | 3935.1 | 723.8 | −1.30 | 17.2 |
| 492 | 302 | 0 | 10.0 | 733.0 | 328.9 | −1.09 | 32.8 |
| 74 | 314 | 3574 | 5.0 | 1442.1 | 164.6 | −1.08 | 17.7 |
| 499 | 320 | 3685 | 2.5 | 1796.4 | 102.0 | −1.11 | 37.2 |
| 81 | 322 | 3711 | 5.0 | 431.3 | 176.6 | 1.05 | 20.9 |
| 87 | 331 | 3851 | 2.5 | 100.1 | 116.6 | −1.02 | 91.8 |
| 93 | 338 | 3974 | 2.5 | 272.4 | 89.9 | −1.08 | 33.3 |
| 100 | 351 | 4305 | 5.0 | 156.6 | 73.9 | 1.02 | 179.9 |
| 100 | Comp | 0 | 5.0 | −145.2 | 39.4 | −1.02 | 53.0 |
| 100 | 351 | 4305 | 2.5 | 156.8 | 73.9 | 1.04 | 131.5 |
| 117 | 406 | 5139 | 2.5 | 140.8 | 46.8 | 1.07 | 32.8 |
| 122 | 3003 | 5251 | 10.0 | 1479.6 | 304.9 | −1.24 | 28.2 |

140-Foot 1996 Unpublished Data (continued)

| TC | FT | UGC | BW MHz | $V_h$ km/s | W km/s | A | S/N |
|---|---|---|---|---|---|---|---|
| 128 | 431 | 5373 | 2.5 | 301.3 | 64.5 | 1.05 | 61.6 |
| 134 | 450 | 0 | 2.5 | 324.3 | 65.4 | 1.03 | 94.1 |
| 134 | Comp | 0 | 2.5 | 132.6 | 46.0 | −1.18 | 13.2 |
| 136 | 456 | 5557 | 5.0 | 592.8 | 149.3 | 1.12 | 35.7 |
| 143 | 485 | 5829 | 2.5 | 629.8 | 99.4 | 1.08 | 32.0 |
| 150 | 507 | 6079 | 5.0 | 683.0 | 247.5 | −1.08 | 33.1 |
| 917 | 3556 | 6225 | 10.0 | 696.8 | 335.5 | −1.02 | 26.6 |
| 917 | 3556 | 6225 | 5.0 | 698.4 | 328.6 | −1.03 | 20.2 |
| 182 | 589 | 6817 | 2.5 | 242.1 | 71.9 | −1.07 | 37.4 |
| 201 | 675 | 7278 | 2.5 | 292.1 | 92.6 | 1.06 | 83.6 |
| 210 | 706 | 7534 | 2.5 | 723.1 | 75.7 | 1.05 | 36.2 |
| 217 | 715 | 7577 | 2.5 | 197.3 | 54.3 | 1.12 | 38.0 |
| 239 | 770 | 7907 | 5.0 | 638.7 | 200.6 | −1.07 | 67.4 |
| 260 | 834 | 8188 | 2.5 | 321.5 | 55.5 | 1.13 | 42.3 |
| 273 | 863 | 8320 | 2.5 | 190.8 | 89.1 | 1.01 | 46.2 |
| 302 | 944 | 8981 | 5.0 | 230.6 | 200.7 | −1.26 | 170.0 |
| 304 | 947 | 9013 | 5.0 | 274.5 | 57.1 | 1.00 | 80.2 |
| 304 | 947 | 9013 | 2.5 | 274.3 | 55.8 | −1.02 | 60.6 |
| 308 | 966 | 9240 | 2.5 | 149.3 | 67.6 | −1.19 | 23.6 |
| 565 | 1048 | 10359 | 5.0 | 907.4 | 234.2 | 1.07 | 42.1 |
| 565 | 1048 | 10359 | 5.0 | 907.2 | 233.7 | 1.06 | 46.1 |
| 353 | 1056 | 10736 | 5.0 | 488.8 | 159.5 | −1.11 | 14.1 |
| 354 | 1058 | 10792 | 2.5 | 1233.0 | 74.5 | −1.01 | 11.8 |
| 358 | 6412 | 10897 | 5.0 | 1319.3 | 140.4 | 1.01 | 21.2 |
| 932 | 6643 | 11218 | 10.0 | 1482.6 | 365.6 | −1.05 | 12.9 |
| 365 | 1075 | 11220 | 2.5 | 1447.0 | 92.0 | 1.06 | 10.2 |
| 583 | 1078 | 11300 | 5.0 | 491.1 | 229.2 | −1.05 | 19.4 |
| 372 | −11 | 0 | 2.5 | −79.8 | 37.0 | 1.00 | 26.6 |
| 373 | −15 | 0 | 2.5 | 1563.6 | 100.4 | 1.12 | 25.6 |
| 374 | −12 | 0 | 2.5 | −55.9 | 82.0 | 1.11 | 322.8 |
| 377 | 1082 | 0 | 2.5 | 1423.2 | 94.2 | 1.12 | 18.5 |
| 379 | 0 | 11604 | 10.0 | 1428.0 | 349.8 | −1.07 | 15.6 |
| 380 | 1085 | 0 | 2.5 | −141.5 | 34.8 | −1.10 | 27.2 |
| 605 | 1088 | 11707 | 5.0 | 904.3 | 206.5 | 1.17 | 18.6 |
| 387 | 7081 | 11759 | 5.0 | 3258.6 | 163.8 | −1.64 | 9.9 |

140-Foot 1996 Unpublished Data (continued)

| TC | FT | UGC | BW MHz | $V_h$ km/s | W km/s | A | S/N |
|---|---|---|---|---|---|---|---|
| 609 | 1093 | 11861 | 10.0 | 1481.7 | 268.7 | 1.05 | 20.6 |
| 393 | 1098 | 11891 | 5.0 | 461.8 | 157.0 | 1.33 | 25.0 |
| 399 | 1113 | 12082 | 2.5 | 802.4 | 87.3 | −1.16 | 25.3 |
| 402 | 1117 | 12113 | 10.0 | 816.6 | 537.3 | −1.17 | 17.2 |
| 620 | 1139 | 12392 | 10.0 | 1708.2 | 304.7 | 1.50 | 17.0 |
| 936 | 7640 | 12554 | 10.0 | 371.8 | 270.3 | −1.14 | 30.7 |
| 412 | 1147 | 12613 | 2.5 | −186.8 | 42.0 | −1.32 | 18.8 |
| 413 | 1149 | 12632 | 5.0 | 423.1 | 125.9 | −1.04 | 21.2 |
| 414 | 1159 | 12732 | 5.0 | 748.0 | 139.1 | 1.10 | 45.0 |
| 415 | 1160 | 12754 | 5.0 | 749.3 | 211.7 | 1.02 | 20.9 |
| 418 | 1171 | 0 | 2.5 | −121.0 | 75.6 | −1.11 | 77.7 |
| 418 | 1171 | 0 | 2.5 | −123.3 | 80.2 | −1.15 | 82.7 |
| 418 | CompB | 0 | 2.5 | −183.8 | 88.7 | −1.03 | 18.5 |

140-Foot 1996 Supplementary Wide Data

| TC | FT | UGC | BW MHz | $V_h$ km/s | W km/s | A | S/N |
|---|---|---|---|---|---|---|---|
| A1 | 0045 | 0 | 5.0 | 467.3 | 185.5 | −1.02 | 37.7 |
| A2 | 0055 | 0 | 5.0 | 125.8 | 189.5 | −1.04 | 186.9 |
| A4 | 0247 | 0 | 5.0 | 154.9 | 220.1 | 1.06 | 81.6 |
| A5 | 0253 | 0 | 10.0 | 238.6 | 439.8 | −1.48 | 33.9 |
| 633 | 0278 | 528 | 5.0 | 640.9 | 145.9 | 1.07 | 28.6 |
| A6 | 0300 | 0 | 5.0 | 143.1 | 161.6 | −1.05 | 139.2 |
| 635 | 81 | 0 | 5.0 | 1095.5 | 188.6 | −1.05 | 21.2 |
| 636 | 0428 | 763 | 5.0 | 1148.3 | 186.8 | −1.03 | 29.9 |
| 640 | 103 | 1249 | 5.0 | 397.9 | 273.6 | 1.62 | 23.0 |
| 646 | 116 | 1466 | 10.0 | 2464.8 | 494.9 | −1.03 | 18.0 |
| 451 | 121 | 1554 | 10.0 | 2099.6 | 278.4 | 1.09 | 12.7 |
| 648 | 0864 | 1736 | 5.0 | 1561.0 | 245.4 | 1.21 | 30.2 |
| 453 | 126 | 0 | 10.0 | 2288.9 | 296.2 | −1.12 | 14.9 |
| 650 | 137G | 1913 | 5.0 | 552.2 | 224.5 | 1.08 | 63.4 |
| 652 | 153G | 2137 | 5.0 | 623.7 | 232.7 | 1.02 | 44.2 |
| A10 | 1055 | 2173 | 10.0 | 989.2 | 421.1 | −1.03 | 23.3 |
| 659 | 1156 | 2455 | 2.5 | 370.3 | 121.7 | −1.15 | 37.4 |
| 666 | 211 | 0 | 10.0 | 1238.5 | 270.3 | 1.05 | 35.0 |
| 673 | 247 | 0 | 5.0 | 718.6 | 206.3 | 1.12 | 29.3 |
| 483 | 259 | 0 | 10.0 | 2316.2 | 352.0 | −1.25 | 20.1 |

140-Foot 1996 Supplementary Wide Data (continued)

| TC | FT | UGC | BW MHz | $V_h$ km/s | W km/s | A | S/N |
|---|---|---|---|---|---|---|---|
| 698 | 2460 | 4097 | 10.0 | 1449.7 | 373.9 | 1.20 | 17.4 |
| 703 | 350G | 4284 | 5.0 | 559.4 | 214.4 | 1.07 | 42.6 |
| 710 | 393G | 4936 | 2.5 | 1733.8 | 120.5 | −1.03 | 52.8 |
| 710 | 393G | 4936 | 2.5 | 1733.4 | 118.4 | −1.05 | 26.7 |
| 712 | 398 | 4966 | 10.0 | 633.2 | 624.8 | −1.12 | 19.4 |
| 515 | 401 | 5079 | 10.0 | 554.5 | 402.2 | 1.24 | 24.8 |
| 713 | 426 | 5316 | 5.0 | 1059.2 | 233.9 | 1.06 | 29.3 |
| 716 | 433 | 5387 | 10.0 | 1120.5 | 480.5 | −1.05 | 23.1 |
| 523 | 445 | 5459 | 10.0 | 1108.9 | 291.0 | −1.12 | 16.1 |
| 718 | 457 | 5572 | 10.0 | 659.7 | 326.1 | −1.06 | 35.0 |
| 528 | 463 | 5637 | 5.0 | 749.9 | 197.0 | −1.16 | 29.8 |
| 723 | 483 | 5789 | 5.0 | 738.5 | 222.9 | 1.05 | 27.4 |
| 724 | 3338 | 5826 | 10.0 | 1297.9 | 365.0 | −1.18 | 21.8 |
| 725 | 3344 | 5840 | 5.0 | 589.2 | 179.1 | 1.14 | 36.4 |
| 726 | 3351 | 5850 | 10.0 | 779.4 | 292.0 | −1.01 | 9.1 |
| 727 | 3359 | 5873 | 5.0 | 1013.8 | 267.6 | −1.02 | 43.1 |
| 532 | 492 | 5882 | 10.0 | 893.7 | 365.1 | 1.03 | 19.9 |
| 728 | 3430 | 5982 | 10.0 | 1568.4 | 396.0 | −1.12 | 16.8 |
| 729 | 500 | 5986 | 10.0 | 611.7 | 282.6 | 1.31 | 33.8 |
| 731 | 3448 | 6024 | 10.0 | 1381.4 | 378.9 | 1.13 | 9.4 |
| 534 | 527 | 6277 | 5.0 | 1194.5 | 133.9 | 1.06 | 19.7 |
| 749 | 3938 | 6856 | 2.5 | 808.4 | 113.0 | 1.09 | 38.7 |
| 195 | 650 | 7166 | 5.0 | 998.3 | 147.2 | 1.06 | 30.1 |
| 777 | 687G | 7322 | 5.0 | 244.2 | 218.4 | −1.02 | 61.4 |
| 921 | 4303 | 7420 | 5.0 | 1566.8 | 179.2 | −1.09 | 34.3 |
| 921 | Comp | 0 | 5.0 | 1273.4 | 149.7 | 1.20 | 7.0 |
| 794 | 746 | 7766 | 5.0 | 813.7 | 256.9 | 1.01 | 57.3 |
| 826 | 892 | 8490 | 2.5 | 200.3 | 132.6 | 1.05 | 66.4 |
| 827 | 893G | 8493 | 5.0 | 462.5 | 203.1 | −1.38 | 66.3 |
| 838 | 962 | 9197 | 5.0 | 302.5 | 165.2 | −1.18 | 48.4 |
| 858 | 6217 | 10470 | 5.0 | 1353.1 | 234.6 | 1.01 | 18.1 |
| 858 | 6217 | 10470 | 5.0 | 1353.9 | 233.3 | 1.02 | 18.2 |
| 575 | 1065 | 11012 | 5.0 | 26.8 | 252.5 | 1.02 | 26.5 |
| 877 | 1100 | 0 | 5.0 | 1655.9 | 282.2 | −1.05 | 4.9 |
| A42 | 7793 | 0 | 5.0 | 225.7 | 195.0 | 1.06 | 39.4 |

# Appendix4a

## W. G. Tifft Biographical Publications and Related References

### Abbreviations

| | |
|---|---|
| A&A | Astronomy and Astrophysics |
| A&AS | Astronomy and Astrophysics Supplement |
| AJ | Astronomical Journal |
| Ap&SS | Astrophysics and Space Science |
| ApJ | Astrophysical Journal |
| ApJS | Astrophysical Journal Supplement |
| ApLett | Astrophysical Journal Letters |
| BAAS | Bulletin of the American Astronomical Society |
| JAA | Journal of Astrophysics and Astronomy |
| MNRAS | Monthly Notices of the Royal Astronomical Society |
| PASP | Publications of the Astronomical Society of the Pacific |
| S&T | Sky and Telescope |
| Sci | Science |

### Publications

**001** "On the Superluminous Variable Stars of the Large Magellanic Cloud' (paper)
Shapley, H., Nail, V. M., Tifft, W. G., (1951), AJ **56**, 139
AAS paper, Washington, 1951 (abstract)
**001a** "Gigantic Variable Stars" (news article)
(1951), Science News Letter June 30, pg 406 [Pub 6/51]

**002** "Discussion of the Binary Star BD −12 2918" (paper)
Tifft, W. G., (1955), AJ **60**, 144 [Rec 9/54, Pub 5/55]

**003** "The Interpretation of Photoelectric Colors for Stars of Types B-F" (paper)
Bonsack, W. K., Greenstein, J. L., Mathis, J. S., Melbourne, W. G., Neugebauer, G., Newburn, R. L., Olsen, K. H., Tifft, W. G., Wahlquist, H. D., Wallerstein, G.,
(1957), ApJ **125**, 139 [Rec 9/56, Pub 1/57]
**003a** Mount Wilson and Palomar Reprint 237

**004** "MWC 603, A High Velocity Symbiotic Star" (paper)
Tifft, W. G., Greenstein, J. L., (1958), ApJ **127**, 160 [Rec 9/57, Pub 5/58]
**004a** Mount Wilson and Palomar Reprint 268
**004b** Memoires Soc. R. Liege, quatrieme serie tome XX, pg 449 (abstract)

**005** "A System of Three-Color Photometry, With Applications
To Galactic Structure in Cygnus" (paper)
Tifft, W. G., (1958), AJ **63**, 127 [Rec 9/57, Pub 4/58]
**005a** Mount Wilson and Palomar Reprint 269

**006** "T Sextantis, An RR Lyrae Star of Type 'c' " (paper)
Tifft, W. G., Smith, Harlan J., (1958), ApJ **127**, 591 [Rec 12/57, Pub 5/58]
**006a** (1958), AJ **63**, 54 AAS paper, Indianapolis 12/57 (abstract)
**006b** Mount Wilson and Palomar Reprint 280

**007** "Classical Cepheids in Galactic Clusters" (Letter)
Tifft, W. G., (1959), ApJ **129**, 241 [Pub 1/59]

**008** "Multicolor Photolectric Photometry of Bright Galaxies I" (thesis paper I)
Tifft, W. G., (1961), AJ **66**, 390 [Rec 5/61, Pub 10/61]

**009** "Multicolor Photolectric Photometry of Bright Galaxies II" (thesis paper II)
Tifft, W. G., (1963), AJ **68**, 302 [Rec 3/63, Pub 6/63]
**009a** (1958), PASP **70**, 463 ASP paper (abstract)

**010** "Magellanic Cloud Investigations, I. The Region of NGC 121" (paper)
Tifft, W. G., (1963), MNRAS **125**, 199 [Rec 4/62, Rev 6/62]
**010a** (1961), AJ **66**, 297 AAS paper, Nantucket 6/61 (abstract)
**010b** Mount Stromlo Preprint 60

**011** "Magellanic Cloud Investigations, II. 47 Tucanae" (paper)
Tifft, W. G., (1963), MNRAS **126**, 209 [Pub /63]

**012** "West Ford Dipole Belt: Photometric Observations" (paper)
Tifft, W. G., Sinton, W. M., Priser, J.B., Hoag, A. A., (1963) Sci **141**, 798 [Pub 8/63]

**013** "DH Pegasi, An RR Lyrae Star of Type c" (paper)
Tifft, W. G., (1964), ApJ **139**, 451 [Rec 10/63, Pub 2/64]

**014** "Old and Intermediate Populations in the Magellanic Clouds" (paper)
Tifft, W. G., (1964) IAU-URSI Symposium 20, 349
"The Galaxy and the Magellanic Clouds"
Australian Academy of Science, Canberra, Australia

**015** "The Overall Spectrum of Astronomical Research Possibilities Utilizing Manned Earth-Orbital Spacecraft", (paper)
Tifft, W. G., Gill, J. R., Roberts, L., (1965),
AAS Science and Technology Series, **4**, 283 [Symp Washington, 3/65, Pub /65]
"Scientific Experiments for Manned Orbital Flight", ed Badgley, P. C.

**016** "A Proposed Multispectral Photography Experiment for AES Lunar Orbital Mission"
Cronin, J. F., Adams, J. B., Colwell, R. N., Tifft, W. G., (1965) (paper)
Advances in the Astronautical Sciences **20**, Part I, 435
" Post Apollo Space Exploration" [Amer. Astronautical Soc 5/65, Chicago]

**017** "Astronomy Space and the Moon" (article)
Tifft, W. G., (1966), Astronautics and Aeronautics, December [Pub 12/66]
**017a** Space Frontiers, (1967) **6**, No.2 (abstracted version)

**018** "Photometric Anomalies in the Nuclei of Galaxies" (paper)
Tifft, W. G., (1968), AJ **73**, 879 [Pub 11/68]
Conference on Seyfert Galaxies and Related Objects, Tucson 2/68

**019** "Optical Space Astronomy" (paper)
Tifft, W. G., (1969),
Advances in the Astronautical Sciences **25**, 521
"Advanced Space Experiments" [Conf 9/68 Ann Arbor] [Pub /69]

**020** "Multicolor Photolectric Photometry of Bright Galaxies III" (paper)
Tifft, W. G., (1969), AJ **74**, 354 [Rec 12/68, Pub 4/69]

**021** "Scientific Uses of the Large Space telescope" (contributor)
Code, A. D., Frederick, L. W., Low, F. J., Munch, G., Smith, H. J., Spitzer, L., Tifft, W. G., Whipple, F. L., (1969), [Woods Hole Conf 1965, Pub 1969.]
Ad-Hoc Committee On the Large Space Telescope
Academy of Science Publication

**022** "The Correlation of Optical Anomalies and Small Radio Sources in Galaxy Nuclei"
Tifft, W. G., (1970), ApLett (1970) **7**, 7 [Rec final 8/70, Pub 11/70]
**022a** (1969), BAAS **1**, 207 AAS paper 7.02, Austin 12/68) (abstract)

**023** "Magellanic Cloud Investigations III, the LMC Bar" (paper)
Tifft, W. G., Snell, C. M., (1971), MNRAS **151**, 365 [Rec 8/70, Pub /71]
**023a** Steward Observatory Preprint 31

**024** "Star Clustering Near the NGC 68-72 Group of Galaxies" (paper)
Tifft, W. G., Gregory, S. A., (1971), PASP **83**, 810 [Rec 10/71, Acc 10/71]

**025** "Rapid Evolution of Galactic Nuclei" (paper)
Tifft, W. G., (1971), IAU Symposium 44, Pg 367 [Symp 8/70]
'External Galaxies and Quasi-Stellar Sources", Uppsala
**025a** Steward Observatory Preprint 32, August 1970

**026** "Two Dimensional Area Scanning with Image Disectors" (paper)
Tifft, W. G., (1972), PASP **84**, 137 [Rec 10/29/71]
Santa Cruz Conference, September 1971

**027** "Evolution in Galaxy Nuclei I, Comparison of the Coma and Virgo Clusters"
Tifft, W. G., (1971) (unpublished paper) [Sub ApJ 3/71]
**027a** Steward Observatory Preprint 37

**028** "The Correlation of Redshift with Magnitude and Morphology in the Coma Cluster"
Tifft, W. G., (1972), ApJ **175**, 613 (paper) [Rec 8/71, Rev 1/72, Pub 8/72]
**028a** Tifft, W. G., (1971), BAAS **3**, 391 AAS paper Amherst 8/71 (abstract)
**028b** Steward Observatory Preprint 40, August, 1971
**028c** Steward Observatory Preprint 43, March, 1972

**029** "Nonvelocity Redshifts in Galaxies" (News and Views article)
Nature (1971) **234**, 505 (good summary at the time) [Pub 12/71]

**030** "NGC 2818, An Open Cluster Containing a Planetary Nebula" (paper) [Rec 12/71]
Tifft, W. G., Connolly, L. P., Webb, D. F., (1972), MNRAS **158**, 47 [Rev 1/72]
**030a** Steward Observatory Preprint 41

**031** "Redshift, Morphology and Integrated Magnitude Relationships in the Coma Cluster"
Tifft, W. G., (1972), BAAS **4**, 238 AAS paper, Seattle 4/72 (abstract)

**032** "Evidence for a Non-Doppler Compoment in Redshifts of Normal Galaxies"
Tifft, W. G., (1972), (unpublished paper) [Sub, Nature 1972]
**032a** Steward Observatory Preprint 45, 1972

**033** Mercury (1972) 1 No.4, 15 (book review)
Tifft, W. G., Muller, S. "The Magellanic Clouds" [Pub 7-8/72]

**034** "Properties of the Redshift-Magnitude Bands in the Coma Cluster" (paper)
Tifft, W. G., (1973), ApJ **179**, 29 [Rec 7/72, Pub 1/73]
**034a** Steward Observatory Preprint 46, July, 1972

**035** "Spectroscopy of Outlying Faint Galaxies in the Region of the Coma Cluster" (paper)
Tifft, W. G., Gregory, S. A., (1973), ApJ **181**, 15 [Rec 10/72, Pub 4/73]
**035a** Steward Observatory Preprint 49, 1972

**036** "Redshift-Magnitude Bands, Quasi-Stellar Sources and Systems of Redshift" (paper)
Tifft, W. G., (1973), ApJ **181**, 305 [Rec 8/72, Pub 4/73
**036a** Tifft, W. G., (1973), BAAS **5**, 40 AAS paper, Las Cruces 1/73 (abstract)
**036b** Steward Observatory Preprint 47, August, 1972, 47R

**037** "Redshift-Magnitude Bands and Quasi-Stellar Absorption Line Multiple Redshifts"
Tifft, W. G. (1973) (unpublished paper) [Sub ApJ, 1973]
**037a** Steward Observatory Preprint 48, 1973

**038** "Revised New General Catalogue of Nonstellar Astronomical Objects" (book)
Sulentic, J. W., Tifft, W. G., (1973), University of Arizona Press [Pub /73]

**039** "Galaxy Photometry I. Techniques" (paper)
Tifft, W. G., (1973), AJ **78**, 594 [Rec 2/73, Rev 5/73, Pub 7/73]
**039a** Steward Observatory Preprint 53, January, 1973

**040** "Photoelectric Photometry of Some Galaxies in the Region of the Virgo Cluster"
Tifft, W. G., (1973), PASP **85**, 283 (paper) [Rec 2/73, Pub 6/73]
**040a** Steward Observatory Preprint 52, January, 1973

**041** "Magellanic Cloud Investigations IV, The LMC Blue Globular Cluster NGC 1850"
Tifft, W. G., Connolly, L. P., (1973), MNRAS **163**, 93 (paper) [Rec 11/72, Acc 2/73]
**041a** Steward Observatory Preprint 50, November, 1972

**042** "Investigations of the Cancer Cluster of Galaxies" (paper) [Rec 4/73, Pub 10/73]
Tifft, W. G., Jewsbury, C. P., Sargent, T. A., (1973), ApJ **185**, 115
**042a** Steward Observatory Preprint 58

**043** "The Definition, Visibility and Significance of redshift-Magnitude Bands" (paper)
Tifft, W. G., (1974), ApJ **188**, 221 [Rec 5/73, Rev 6/73, Pub 3/74]
**043a** Steward Observatory Preprint 61, June, 1973

**044** "Fine Structure Within the Redshift-Magnitude Correlation for Galaxies" (paper)
Tifft, W. G., (1974), IAU Symposium 58, 243 [Pub 1974]
"The Formation and Dynamics of Galaxies", Canberra, August, 1973
**044a** Steward Observatory Preprint 64 , August, 1973

**045** "Galaxies, the Redshift, and Gravity" (essay)
Tifft, W. G., (1974), Essay for 1974 Gravity Foundation Competition [Sub 4/74]
**045a** Steward Observatory Preprint 70, April, 1974

**046** "Digicon Photometry of an Intergalactic Bridge" (paper) [Rec 5/74, Pub 10/74]
Beaver, E. A., Harms, R. J., Tifft, W. G., Sargent, T. A., (1974), PASP **86**, 639

**047** "The Degree of Optical Variability of Quasi-Stellar Objects" (paper)
Grandi, S. A., Tifft, W. G., (1974), PASP **86**, 873 [Rec 7/74, Pub 12/74]

**048** "A Spectroscopic Survey of Some High Latitude Blue Variables" (paper)
Bond, H. E., Tifft, W. G., (1974), PASP **86**, 981 [Rec 7/22/74, Pub 12/74]

**049** "Redshift Disersion of the X-Ray Cluster of galaxies A1367" (paper)
Tifft, W. G., Tarenghi, M., (1975), ApJLett **198**, L7 [Rec 12/74, Rev 2/75]

**050** "Radio Galaxies in the Coma Cluster" (paper)
Tifft, W. G., Tarenghi, M., (1975), ApJ **199**, 10 [Rec 11/74, Rev 1/75, Pub 7/75]

**051** "The NGC 507 Cluster of Galaxies" (paper) [Rec 10/74, Pub 7/75]
Tifft, W. G., Hilsman, K. A., Corrado, L. C., (1975), ApJ **199**, 16

**052** "Direct Observation of the Large Scale Distributiom of Galaxies" (paper)
Tifft, W. G., Gregory, S. A., (1976), ApJ **205**, 6 [Rec 8/75, Pub 5/76]

**053** "Systematic Redshifts in the Outer regions of the Coma Cluster" (paper)
Gregory, S. A., Tifft, W. G., (1976), ApJ **205**, 716 [Rec 8/75, Rev 10/75, Pub 5/76]

**054** "Gross Optical Properties of the Coma Cluster" (paper)
Gregory, S. A., Tifft, W. G., (1976), ApJ **206**, 934 [Rec 8/75, Rev 12/75, Pub 6/76]

**055** "Discrete States of Redshift and Galaxy Dynamics I,
Internal motions in Single Galaxies" (paper)
Tifft, W. G., (1976), ApJ **206**, 38 [Rec 6/75, Rev 10/75, Pub 5/76]

**056** "Redshift Patterns in Coma Cluster Emission Line and Radio Galaxies" (paper)
Tifft, W. G., (1976), BAAS **8**, 310 AAS paper, Haverford 6/76) (abstract)
**056a** Science News (1976) **110**, 6 (news note) [ /76]

**057** "Redshift-Magnitude Bands in Clusters of Galaxies" (paper)
Tifft, W. G., (1976), IAU Colloquium 37 (1976) Pg 159, [Conf 9/76, Pub 9/77]
"Decalages Vers Le Rouge Et Expansion De L'Univers", Paris, September 1976

**058** "Discrete States of Redshift and Galaxy Dynamics II. Systems of Galaxies" (paper)
Tifft, W. G., (1977), ApJ **211**, 31 [Rec 6/75, Rev 12/75, 3/76, Pub 1/77]

**059** "Discrete States of Redshift and Galaxy Dynamics III. Abnormal Galaxies and Stars"
Tifft, W. G., (1977), ApJ **211**, 377 (paper) [Rec 6/75, Rev 3/76, Pub 1/77]

**060** "Magellanic Cloud Investigations V. The LMC Blue Cluster NGC 1854" (paper)
Connolly, L. P., Tifft, W. G., (1977), MNRAS **180**, 401 [Rec 8/76, Pub /77]

**061** "Radio Galaxies in the Coma Cluster II" (paper)
Tifft, W. G., Tarenghi, M., (1977), ApJ **217**, 944 [Rec 2/77, Acc 4/77, Pub 11/77]

**062** "Redshift-Magnitude Bands and the Evolution of Galaxies I. New Observations"
Tifft, W. G., (1978), ApJ **222**, 54 (paper) [Rec 5/77, Acc 9/77, Pub 5/78]
**062a** Steward Observatory Preprint 134a

**063** "Redshift-Magnitude Bands and the Evolution of Galaxies I. Data Analysis"
Tifft, W. G., (1978), ApJ **222**, 421 (paper) [Rec 5/77, Acc 11/77, Pub 6/78]
**063a** Steward Observatory Preprint 134b

**064** "Redshift Correlations Inconsistent with Gravitational Forces Between Galaxies"
Tifft, W. G., (1977), Abstracts of Contributed Papers, (1977) Pg 335 (abstract)
8th International Conference on General Relativity and Gravitation,
Waterloo, Ontario, Canada, August 1977 (GR8 paper) [Conf 8/77]

**065** "A Group of Galaxies in Cetus With A Redshift Discrepancy" (paper)
Karachentsev, I. D., Tifft, W. G., (1978), A&A **63**, 411 [Rec 9/77, Pub 2/78]
**065a** Steward Observatory Preprint 132

**066** "The Simpkin Effect" (paper)
Tifft, W. G., (1978), ApJ **220**, 418 [Rec 6/77, Acc 8/77, Pub 3/78]
**066a** Steward Observatory Preprint 140

**067** "The Absolute Solar Motion and the Discrete Redshift" (paper)
Tifft, W. G., (1978), ApJ **221**, 756 [Rec 7/77, Acc 11/77, Pub 5/78]
**067a** Steward Observatory Preprint 145b

**068** "The Discrete Redshift and Asymmetry in HI Profiles" (paper)
Tifft, W. G., (1978), ApJ **221**, 449 [Rec 7/77, Acc 11/77, Pub 4/78]
**068a** Steward Observatory Preprint 145a

**069** "A Radio Continuum Survey of Isolated Pairs of Galaxies" (paper) [Rec 10/77]
Stocke, J. T., Tifft, W. G., Kaftan-Kassim, M. A., (1978), AJ **83**, 322 [Rev 1/78]
**069a** Steward Observatory Preprint 143

**070** "The Structure of the Hercules Supercluster" (paper)
Tarenghi, M., Tifft, W. G., Chincarini, C., Rood, H. J., Thompson, L. A.,
IAU Symposium 79 (1977) Pg 263, [Symp 9/77]
"The Large Scale Structure of the Universe" Tallin, Estonia, September, 1977

**071** "Observations of the Large Scale Distribution of Galaxies" (paper)
Tifft, W. G., Gregory, S. A.,
IAU Symposium 79 (1977) Pg 267 [Symp 9/77]
"The Large Scale Structure of the Universe", Tallin, Estonia, September, 1977

**072** Sky & Telescope (1978) **50**, 520 Tifft, W. G., (book review)
Conference, Yale University, May, 1977, ed Tinsley, B. M., Larson, R. B.,
"The Evolution of Galaxies and Stellar Populations" (Yale University, July1977)

**073** "New Redshifts of Parent Galaxies of Supernovae" (paper) [Rec 6/78, Rev 8/78]
Barbon, R., Capaccioli, M., Tifft, W. G., (1979), A&AS **36**, 129 [Pub 1979]

**074** "Band Theory Applied to the Coma/A1367 Supercluster" (paper)
Tifft, W. G., Gregory, S. A., (1979), ApJ **231**, 23 [Rec 1/78, Acc 1/79, Pub 7/79]
**074a** Steward Observatory Preprint 158, January 1978

**075** "Structure Within Redshift-Magnitude Bands, Morphological Evolution" (paper)
Tifft, W. G., (1979), ApJ **233**, 799 [Rec 8/78, Acc 5/79, Pub 11/79]
**075a** Steward Observatory Preprint 179, May, 1978

**076** "The Hercules Supercluster I. Basic data" (paper)
Tarenghi, M., Tifft, W. G., Chincarini, C., Rood, H. J., Thompson, L. A.,
(1979), ApJ **234**, 793 [Rec 11/78, Acc 6/79, Pub 12/79]
**076a** ESO Scientific Preprint 65, August, 1979

**077** "Evidence For A Totally Intrinsic Redshift"
Tifft, W. G., (1979), (unpublished paper) [Submitted, Nature, June, 1979]
**077a** Steward Observatory Preprint 234a

**078** "Periodicity in the Redshift Intervals for Double Galaxies" (paper)
Tifft, W. G., (1980), ApJ **236**, 70 [Rec 8/79, Acc 8/79, Pub 2/80]
**078a** Steward Observatory Preprint 234b

**079** "Double Galaxies As Indicators of large Scale Structure" (paper)
Tifft, W. G., (1980), ApJ **239**, 445 [Rec 12/79, Acc 1/80, Pub 7/80]
**079a** Steward Observatory Preprint 247, 1972

**080** "The Perseus Supercluster" (paper) [Rec 2/80, Acc 7/80, Pub 1/81]
Gregory, S. A., Thompson, L. A., Tifft, W. G., (1981), ApJ **243**, 411
**080a** Gregory, S. A., Thompson, L. A., Tifft, W. G., (1978), BAAS **10**, 622, (paper)
AAS meeting Mexico City, January, 1979 (abstract)

**081** "Quantum Effects in the Redshift Intervals for Double Galaxies" (paper)
Tifft, W. G., (1982), ApJ **257**, 442 [Rec 6/81, Acc 1/82, Pub 6/82]
**081a** Steward Observatory Preprint 325

**082** "Double Galaxy Investigations I, Observations" (paper)
Tifft, W. G., (1982), ApJS **50**, 319
**082a** Steward Observatory Preprint 344

**083** "Double Galaxy Investigations II,
The Redshift Periodicity in Optically Observed Pairs" (paper)
Tifft, W. G., (1982), ApJ **262**, 44 (paper) [Rec 10/81, Acc 5/82, Pub 11/82]
**083a** Steward Observatory Preprint 348

**084** "Redshift Quantization in Compact Groups of Galaxies" (paper)
Cocke, W. J., Tifft, W. G., (1983), ApJ **268**, 56 [Rec 5/82, Acc 10/82, Pub 5/83]
**084a** Steward Observatory Preprint 391

**085** "Quantized Redshift Structure Within Galaxies" (paper)
Tifft, W. G., (1984), (unpublished paper) [submitted ApJ, 1984]
**085a** Steward Observatory Preprint 513
**085b** W. G. Tifft "Redshift Key to Cosmology", Appendix 1 (book in preparation, 2014)

**086** "Double Galaxy Investigations III, The Differential Redshift Distribution
and Emission Line Correlations" (paper)
Tifft, W. G., (1985), ApJ **288**, 65 [Rec 3/84, Acc, 7/84, Pub, 1/85]
**086a** Steward Observatory Preprint 389

**087** "Global Redshift Quantization" (paper)
Tifft, W. G., Cocke, W. J., (1985), ApJ **287**, 492 [Rec 4/84, Acc 6/84, Pub 12/84]
**087a** Steward Observatory Preprint 517

**088** "Status of Quantized Extragalactic Redshifts" (abstract)
Tifft, W. G.,Cocke, W. J., (1985), BAAS **16**, 950 (poster paper)
AAS poster, 30.16 Tucson, January, 1985 [AAS 1/85]
**088a** AAS Poster Paper 30.16

**089** "Redshifts of Emission Line Galaxies Near the Bootes Void" (abstract)
Gregory, S. A., Tifft, W. G., Kirshner, R. P., Moody, J. W.,
(1985), BAAS **16**, 961 (paper)
AAS poster, 34.03 Tucson, January, 1985 [AAS 1/85]
**089a** AAS Poster Paper 34.03

**090** "A Spectroscopic Survey of Case Emission Line Galaxies in the Direction of
the Bootes Void" (paper) [Rec 11/85, Acc 4/86, Pub 11/86]
Tifft, W. G., Kirshner, R. P., Gregory, S. A., Moody, J. W., (1986), ApJ **310**, 75
**090a** Steward Observatory Preprint 608

**091** "Photometry and Redshifts for Galaxies in the Direction of the Coma Void"
Gregory, S. A., Moody, J. W., Laubscher, B., Tifft, W. G.,
(1986), BAAS **18**, 692 (abstract) [AAS x/86]
**091a** AAS Paper xx.xx , 1986

**092** "Quantized Galaxy Redshifts" (article)
Tifft, W. G., Cocke, W. J., (1987), Sky & Telescope **73**, 19 [Pub 1/87]
**092a** See also Letter (1987) Sky & Telescope **73**, 454

**093** "Results From High Precision 21-cm Redshift Measurements" (paper)
Tifft, W. G., (1987), 27th Liege International Astrophysical Colloquium (1987) Pg 83
"Observational Astrophysics with High Precision Data" Univ. Liege [Conf 6/87]

**094** "Quantization and Time Dependence in the Redshift" (paper)
Tifft, W. G., (1987), Venice Symposium, Pg 173, Venice, May, 1987 [Symp 5/87]
"New Ideas in Astronomy", Cambridge University Press

**095** "Observations of Quantization in Galaxy Redshifts" (paper)
International Union Radio Science
Tifft, W. G., (1988), Program and Abstracts Pg 235, (abstract)
National Radio Science Meeting, Univ. Colorado, January, 1988 [Conf 1/88]

**096** "Uncertainties in 21-cm Redshifts I. Data" (paper)
Tifft, W. G., Cocke, W. J., (1988), ApJS **67**, 1 [Rec 4/87, Acc 9/87, Pub 5/88]
**096a** Steward Observatory Preprint 730, 1987

**097** "Redshift Studies of Large Scale Structure I: The South Coma Void Region" (paper)
Tifft, W. G., Gregory, S. A., (1988), AJ **95**, 651 [Rec 7/87, Rev 11/87, Pub 3/88]

**098** "Redshift Studies of Large Scale Structure II: A Faint Sample in the Direction of
the Coma/A1367 Supercluster" (paper) [Rec 7/87, Rev 11/87, Pub 3/88]
Gregory, S. A., Tifft, W. G., Moody, J. W., (1988), AJ **95**, 662

**099** "Redshift Quantization - Many Lines of Evidence" (paper)
Tifft, W. G., Cocke, W. J., (1988), BAAS **20**, 719
AAS poster paper, Kansas City, June, 1988 [AAS 6/88]
**099a** AAS Poster paper, 1988

**100** "Quantization of Redshift Differences in Isolated Galaxy Pairs" (paper)
Tifft, W. G., Cocke, W. J., (1989), ApJ **336**, 128 [Rec 12/87, Acc 6/88, Pub 1/89]
**100a** Steward Observatory Preprint 779, 1987

**101** "How Can Astronomical Redshifts be Quantized" (article) [Pub 1-2/89]
D. Cherry., 21st Century Science and Technology (1989) **2** Jan-Feb, Pg57

**102** "Redshift Quantization in the Lyman-Alpha Forest and Measurement of qo" (paper)
Cocke, W. J., Tifft, W. G., (1989), ApJ **346**, 613 [Rec 11/88, Acc 5/89, Pub 11/89]
**102a** Steward Observatory Preprint 846, 1988

**103** American Scientist (1989) May Pg xx Tifft, W. G., (Book Review)
S. Narlikar., "The Primeval Universe" [Pub 5/89]

**104** "Comparison Between 21-cm Data from Effelsberg and Greenbank" (paper)
Tifft, W. G., Huchtmeier, W. K.,
(1990), A&AS **84**, 47 [Rec 7/89, Acc 12/89, Pub 7/90]
**104a** Steward Observatory Preprint 871, 1988

**105** "Propereties of the Redshift I, Data and Calibrations" (paper)
Tifft, W. G., (1990), ApJS **73**, 603 [Rec 10/89, Acc 12/89, Pub 8/90]
**105a** Steward Observatory Preprint 901, 1989

**106** "Properties of the Redshift" (paper)
Tifft, W. G., Cocke, W. J., (1989), NASA Conf Publ 3098, Pg 479
IAU Colloqium 124, Tuscaloosa, December, 1989 [Conf 12.89]
' 'Paired and Interacting Galaxies"

**107** "Panel Discussion on Redshift Problems" (edited papers)
Panel discussion: Tifft, W. G., Schneider, S., Burbidge, G., Sharp, N., Roberts, M.
Tifft, W. G, ed., (1989) NASA Conf Publ 3098 Pg 459
IAU Colloquium 124, Tuscaloosa, December, 1989 [Conf 12/89]
"Paired and Interacting Galaxies"

**108** "A Fundamental Test for Time Variation in Redshifts of Galaxies" (abstract)
Tifft, W. G., (1990), BAAS **22**, 841 (poster paper)
AAS poster 30.02, Albuquerque, June, 1990 [AAS 6/90]
**108a** AAS Poster Paper 30.02

**109** "Properties of the Redshift II, Radial Variation" (paper)
Tifft, W. G., (1991), ApJ **368**, 105 [Rec 3/90, Acc 8/90, Pub 2/91]
**109a** Steward Observatory Preprint 937, 1990

**110** "Statistical Procedure and the Significance of Periodicities
in Double Galaxy Redshifts" (paper)
Cocke, W. J., Tifft, W. G., (1991), ApJ **368**, 383 [Rec 9/89, Acc 8/90, Pub 2/91]
**110a** Steward Observatory Preprint 899, 1989

**111** "Properties of the Redshift III, Temporal Variation" (paper)
Tifft, W. G., (1991), ApJ **382**, 396 [Rec 1/91, Acc 6/91, Pub 12/91]
**111a** Steward Observatory Preprint 988, 1990

**112** "Variability in the Broad Line Spectrum of Markarian 372" (paper) [Rec 4/91]
Gregory, S. A., Tifft, W. G., Cocke, W. J., (1991), AJ **102**, 1977 [Rev 8/91]

**113** "Properties of the Redshift IV, "Reference Data" (paper)
Tifft, W. G., (1992), ApJS **79**, 183 [Rec 8/91, Pub 4/92]
**113a** Steward Observatory Preprint 1010, 1992

**114** "The Case for a Time Dependent Quantized Redshift" (paper)
Tifft, W. G., (1992), (unpublished paper) [Submitted ApJ, 1992]
**114a** Steward Observatory Preprint 1027, 1992
**114b** W. G. Tifft "Redshift Key to Cosmology", Appendix 2 (book in preparation, 2014)

**115** "Quantized Redshifts: What's Going On Here" (news note) [Pub 8/92]
Sky & Telescope (1992) **84**, 128 [corresp 2/11/92]

**116** "Jumps in Star Speeds Perplex Astronomers" (news item) [Pub 9/92]
Browne, M. W., (1992), New York Times (Science Times) 9/15/92, Pg B5

**117** "The New Challenges, Quantum Dissidents" (article) [Pub 12/92]
Beardsley, J., (1992), Scientific American, Dec., Pg 39

**118** "Man Stops Universe, Maybe" (article) [Pub 4/93]
Sobel, D., (1993), Discover Magazine, April, Pg 20

**119** "A Time Dependent Quantized Redshift" abstract
Tifft, W. G., (1993), BAAS **24**, 1223 (poster paper)
AAS Poster Paper 65.14, Phoenix, January, 1993 [AAS 1/93]
**119a** AAS Poster Paper 65.14

**120** "Redshift Quantization - A Review" (invited review paper)
Tifft, W. G., (1993) "Plasma Astrophysics and Cosmology", pg 25
IEEE International Workshop, Princeton, May, 1993 [Conf 5/93, Pub 5/95]
Peratt, A. L. ed "Plasma Astrophysics and Cosmology",
(Kluwer Academic Publishers), 1995
**120a** Tifft, W. G., (1995), Ap&SS **227**, 25
**120b** Steward Observatory Preprint 1143, 1993

**121** "Redshift Quantization in the Cosmic Background Rest Frame" (abstract)
Tifft, W. G., Cocke, W. J., (1993), BAAS **25**, 796 (poster paper)
AAS Poster Paper, 5.14, Berkeley, June, 1993 [AAS 6/93]
**121a** AAS Poster Paper 5.14

**122** "A Periodicity Rule for Redshift Quantization" ( abstract)
Tifft, W. G., (1994), BAAS **26**, 1407 (poster paper)
AAS Poster Paper 56.05, Tucson, January, 1995 [AAS 1/95]
**122a** AAS Poster Paper 56.05

**123** "Redshift Quantization in the Cosmic Background Rest Frame" (abstract)
Cocke, W. J., Tifft, W. G., (1994), BAAS **26**, 1409 (poster paper)
AAS Poster Paper 57.05, Tucson, January, 1995 [AAS 1/95]
**123a** AAS Poster Paper 57.05

**124** "Global Redshift Periodicities: Association with the Cosmic Background Radiation"
Cocke, W. J., Tifft, W. G., (1996), Ap&SS **239**, 35 (paper) [Rec 2/96, Acc 2/96]
**124a** Steward Observatory Preprint 1114, 1993

**125** "Global Redshift Periodicities, The Periodicity Structure" (paper)
Tifft, W. G., (1996), ApJ **468**, 491 [Rec 9/96]
**125a** Steward Observatory Preprint 1142, 1993, revised, 1995

**126** "A Brief History of Quantized Time" (article)
Tifft, W. G., (1995), Mercury Magazine **24**, 12

**127** "Quantum Cosmology" (paper) [Rec 11/95, Acc 3/96, Pub 4/96]
Tifft, W. G., Cocke, W. J., DeVito, C. D., (1996), Ap&SS **238**, 247
**127a** Steward Observatory Preprint 1266, 1995

**128** "Connections Between Fundamental Particles, Redshifts and Cosmology" (abstract)
Tifft, W. G., (1996), BAAS **28**, 841 (poster paper)
AAS Poster Poster 12.06, Madison, June, 1996 [AAS 6/96]
**128a** AAS Poster Paper 12.06

**129** "Evidence for Quantized and Variable Redshifts in the CBR Rest Frame" (paper)
Tifft, W. G., (1996)"Conference on Time in Physics and Cosmology", Pg 29
Conference on Time in Physics in Cosmology, Tucson, April, 1996 [Pub 1997]
"Modern Mathematical. Models of Time in Physics and Cosmology",
(Kluwer Academic Publishers), 1997
**129a** Tifft, W. G., (1997), Ap&SS **244**, 29

**130** "Three-Dimensional Quantized Time in Cosmology" (paper)
Tifft, W. G., (1996)" Conference on Time in Physics and Cosmology", Pg 187
Conference on Time in Physics in Cosmology, Tucson, April, 1996 [Pub 1997]
"Modern Mathematical Models of Time in Physics and Cosmology",
(Kluwer Academic Publishers), 1997
**130a** Tifft, W. G., (1997), Ap&SS **244**, 187

**131** "Modern Mathematical Models of Time in Physics and Cosmology" (Conf Ed)
Proceedings of Conference on Time in Physics and Cosmology, Tucson 4/96
ed. Tifft, W. G., Cocke, W. J., (Kluwer Academic Publishers) 1997 [Conf 4/96]

**132** "Scientists Hit Galactic G-Spot" (news article) [Pub 10/96]
Hawkes, N., (1996), London Times, 'Mind and Matter', Oct. 24, Pg18

**133** "Galaxies Cosmology and the Redshift" (local review)
Tifft, W. G., (1997) (unpublished NRAO review, begin Seminar concept)

**134** "Cosmological Redshifts and Fundamental Particle Theory" (unpublished)
Tifft, W. G., (1996-97 at NRAO), (considered for Physics Essays submission)
Basis for development of Seminar series in 2000,
First part published as basis of Bangladore review, see ref 135
Balance includes particle physics beginning for 2000 seminar summary

**135** "Redshift Quantization in the Cosmic Background Rest Frame" (review)
Tifft, W. G., (1997), JAA (India) **18**, 415 (invited review)
Bangalore India Cosmology Workshop, January, 1997 [Conf 1/97]
**135b** http://www.cv.nrao.ed/library/nrao-preprints.html (1997)

**136** "True To His Observations" (W.G.Tifft, bio and science) [Pub 3/97]
Yule, L., (1997) World and I Magazine, **12** No.3 (March), Pg 170

**137** "Is Time Quantized?" (Internet comments, request from Scientific American)
Tifft, W. G., http://www.sciam.com (1997) April

**138** "Global Redshift Periodicities, Variability" (paper)
Tifft, W. G., (1997), ApJ **485**, 465 [Rec 9/96, Acc 3/97, Pub 8/97]
**138a** http://www.cv.nrao.ed/library/nrao-preprints.html (1997)

**139** "Redshift Quantization in Virgo Cluster Dwarfs" (paper)
Tifft, W. G., (1997) (unpublished paper, in archive) [Sub ApJ March, 1997]
**139b** http://www.cv.nrao.ed/library/nrao-preprints.html (1997)

**140** "140-Foot 21 cm Data, General Data" (paper)
Tifft, W. G., (1997) (unpublished paper) [Sub ApJ April, 1997]
**140a** http://www.cv.nrao.ed/library/nrao-preprints.html (1997)
**140b** W. G. Tifft "Redshift Key to Cosmology", Appendix 3 (book in preparation, 2014)

**141** "The redshift As A Factor in Galaxy Evolution" (local draft paper)
Tifft, W. G., (1997-8) (early galaxy evelution concepts, in archive)

**142** "Resistance To New Results in Astronomy" (invited paper)
Tifft, W. G., (1999) (unpublished format)
Presented at Society for Scientific Exploration meeting, Albuquerque, 1999 [for archive]

**143** "The Arizona/New Mexico Spectroscopic Survey of Galaxies I - Data For the Western End of the Perseus Supercluster" (paper) Gregory, S. A., Tifft, W. G., Moody, J. W., Newberry, M. V., Hall, S. M., (2000), AJ **119 Pt2**, 545 [Rec 4/99, Acc 11/99, Pub 2/2000]

**143a** Steward Observatory Preprint 1507, 2000

**144** "The Arizona/New Mexico Spectroscopic Survey of Galaxies II - Structures In The Perseus Supercluster' ' (paper) Gregory, S. A., Tifft, W. G., Moody, J. W., Newberry, M. V., Hall, S. M., (2000), AJ **119 Pt2**, 567 [Rec 4/99, Acc 11/99, Pub 2/2000]

**144a** Steward Observatory Preprint 1508, 2000

**145** "The Arizona/New Mexico Spectroscopic Survey of Galaxies III - On Galaxy Populations" (paper) Gregory, S. A., Tifft, W. G., Moody, J. W., Newbury, M. V., Hall, S. M., (2000), AJ **119 Pt2**, 573 [Rec 4/99 Acc, 11/99, Pub 2/2000

**145a** Steward Observatory Preprint 1509, 2000

**146** "What Is The Cosmic Redshift? Correlations and Implications, 1970-1978" Tifft, W. G., (2000), Special Seminar Series on the Redshift as a Factor in Cosmology Included on SASTPC.org web site (Version 10/27/2000) Tifft, W. G., (seminar)

**146a** Basis for revised version in"Redshift, Key to Cosmology", Chapter 1

**147** "Is The Redshift Quantized, Variable?, The Empirical Period 1973-1992" Tifft, W. G., (2000), Special Seminar Series on the Redshift as a Factor in Cosmology Included on SASTPC.org web site (Version 11/27/2000) Tifft, W. G., (seminar)

**147a** Basis for revised version in"Redshift, Key to Cosmology", Chapter 2

**148** "Redshifts and the Dimensions of Time, Defining the Properties of a New Cosmology, 1993 t0 Date" (seminar) Tifft, W. G., (2000), Special Seminar Series on the Redshift as a Factor in Cosmology Included on SASTPC.org web site (Version 11/10/2000) Tifft, W. G., (seminar)

**148a** Basis for revised version in"Redshift, Key to Cosmology", Chapter 3

**149** "Particle Physics and the Dimensions of Time, New Viewpoints on Matter And Energy" (seminar) (delayed release) Tifft, W. G., (2000), Special Seminar Series on the Redshift as a Factor in Cosmology

**149a** "Masses of the Stable Particles" (1999) Tifft, W. G., (special internal)

**149b** Basis for revised version in"Redshift, Key to Cosmology", Chapter 4

**150** "Radial Redshifting in Disk Galaxies" (paper) Tifft, W. G., (2001), Steward Observatory Internal Symposium (2001)

**151** "Redshift Periodicities, The Galaxy-Quasar Connection" (invited paper) Hoyle Memorial Conference, Cardiff U.K. (2002) Tifft, W. G., (2003), Ap&SS **285**, 429

**152** "New Percival Lowell Society Members Janet and Bill Tifft" (article) Tweed, R. (2008), Lowell Observer **80**, 4

Many of the references can be read and downloaded on the SASTPC.org web site.

# Appendix 4b

## External References and Citations

**Abbreviations**

| | |
|---|---|
| A&A | Astronomy and Astrophysics |
| A&AS | Astronomy and Astrophysics Supplement |
| AJ | Astronomical Journal |
| Ap&SS | Astrophysics and Space Science |
| ApJ | Astrophysical Journal |
| ApJS | Astrophysical Journal Supplement |
| ApLett | Astrophysical Journal Letters |
| JRAS Canada | Journal of the Royal Astronomical Society of Canada |
| MNRAS | Monthly Notices of the Royal Astronomical Society |
| PASP | Publications of the Astronomical Society of the Pacific |
| S&T | Sky and Telescope |
| Ann. Rev. Astron. Astroph. | Annual Review of Astronomy and Astrophysics |
| Chinese J. Phys | Chinese Journal of Physics |
| Comm. Special Ap. Obs. USSR | [Full title?] |
| Phys. Rev. D | Physics Review D |
| Texas Symp. Proc. Ann. New York Acad. of Sci. | [Full Title?] |

## Seminar 1

**A:** Hoyle, P., Burbidge, G., Narliker, J. V., "A Different Approach to Cosmology", pg 188 (Cambridge, Cambridge Univ. Press).

**B:** Rood, H.J., Baum, W.A., (1967), AJ **72**, 398.

**C:** Weedman, D.W., (1975), ApJ **195**, 587.

**D:** Simkin, S.M., (1977), A&A **55**, 369.

**E:** Fisher, D., et.al., (1998), ApJ **498**, 195.

**F:** van Dokkum, P.G., et.al., (1998), ApJ **500**, 714.

**G:** Sulentic, J.W., (1984), ApJ **286**, 442.

## Seminar 2

**H:** Peterson, D. D., (1979), ApJS **40**, 527.

**I :** Sharp, N. A., (1984), ApJ **286**, 437.

**J :** Sharp, N. A., (1990), ApJ **534**, 418.

**K:** Arp, H., (1986), A&A **156**, 207.

**L:** Arp, H., Sulentic, J. W., (1985), ApJ **291**, 88.

**M:** Personal Communication, preprint, early version of N.

**N:** Schneider, S. E., Salpeter, E. E., (1992), ApJ **385**, 32.

**O:** Schweizer, L. Y., (1987), ApJS **64**, 427.

**P:** White, S., et.al., (1983), MNRAS **303**, 701.

**Q:** Newman, W. I., et.al., (1989), ApJ **344**, 111.

**R:** Karachentsev, I. D., (1972), Comm Special Ap. Obs. USSR, **7**, 1.

**S:** Karachentsev, I. D., (1980), ApJS **44**, 137.

**T:** Sulentic, J. W., (1982), ApJ **252**, 439.

**U:** Fisher, J. R., Tully, R.B., (1975), A&A **44**, 151.

**V:** Fisher, J. R., Tully, R.B., (1981), ApJS **47**, 139.

**W:** Dickel, J. R., Rood, H.J., (1978), ApJ **223**, 391.

**X:** Shostak, G. S., (1975), ApJ **198**, 527.

**Y:** Shostak, G. S., (1978), A&A **68**, 321.

**Z:** Roberts, M. S., (1968), AJ **73**, 945.

**AA:** Cocke, W. J., (1983), ApLett **23**, 239.

**AB:** Giovanelli, R., Haynes, M., (1985), AJ **90**, 2445.

**AC:** Giovanelli, R., Haynes, M., (1989), AJ **97**, 633.

**AD:** Napier, W. M., Guthrie, B. N. G., Napier, B., (1988), "New Ideas in Astronomy", pg 291, (Cambridge, Cambridge Univ. Press). [Venice Symposium]

**AE:** Croasdale, M., (1989), ApJ **345**, 72.

**AF:** Guthrie, B. N. G., Napier, W. N., (1991), MNRAS **253**, 533.

**AG:** Lehto, A., (1990), Chinese J. Phys. **28**, 215.

**AH:** Lewis, B. M., (1983), AJ **88**, 962.

## Seminar 3

**AI :** Mateo, M. L., (1998), Ann. Rev. Astron. Astroph. **36**, 435.

## Seminar 4

**AJ :** Lehto, A., (1996), Ap&SS **244**, 321.

**AK:** Rohlf, J. W., (1994), "Modern Physics from $\alpha$ to $Z_o$", (J. Wiley & Sons, New York).

**AL:** Phys. Rev. D, Particles and Fields 1 July (2002), Vol 66, Part 1 Third Series No 1-I.

## Seminar 5

**AM:** Burbidge, G., Napier, W.M., (2001), AJ **121**, 21.

**AN:** Burbidge, E. M., Sargent, W., (1970), in D. J. K. O'Connell (ed), "Nuclei of Galaxies", pg 351, (North Holland).

**AO:** Napier, W.M., (2003), Ap&SS **285**, 513, Hoyle Memorial Conference, Cardiff, (2002).

**AP:** Karlsson, K. G., (1977), A&A **58**, 237.

**AQ:** Burbidge, G., (1980), Texas Symp. Proc. Ann. New York Acad. of Sci.

**AR:** Hawkins, E., Maddox, S.J., Merrifield, M.R., (2002), MNRAS **336**, L13.

**AS:** Arp, H., Bi, H. G., Chu, Y., Zhu, X., (1990), A&A **239**, 33.

**AT:** Veron-Cetty, M. P., Veron, P., (1996), "A Catalog of Quasars and Active Galaxies", ESO Scientific Report, electronic form.

**AU:** Schmidt, M., Green, R.F., (1983), ApJ **269**, 352.

**AV:** Cohen, J. G., et.al., (1996), ApJ **471**, L5.

**AW:** Cohen, J. G., et.al., (1999), ApJS **120**, 171.

**AX:** Cohen, J. G., et.al., (2000), ApJ **538**, 29.

**AY:** Burbidge, G., (1968), ApJ **154**, L41.

## Seminar 6

**AZ:** Gurvits, L. I., (1994), ApJ **425**, 442.

**BA:** [Type 1a supernovae dark energy article].

**BB:** Carroll, B. W., Ostlie, D. A., (1996), "An Introduction to Modern Astrophysics", (Addison-Wesley Publishing Co, Inc.).

## Seminar 7

**BC:** Miller, J. L., (2012), *Physics Today* **65**, 9, 12.

**BD:** Zimmerman, R., (2012), S&T Oct 2012, 52.

## Seminar 8

**BE:** Chodos, A., (2014), *Physics Today* **67**, 5, 11.

**BF:** MacRobert, A., (2014), S&T July 2014, 20.

**BG:** Blau, S. K., (2013), *Physics Today* **66**, 6, 12.

**BH:** Rubin, V. C., Ford, W.K.Jr., (1971), ApJ **170**, 25.

**BI :** Walker, M. F., (1974), PASP **86**, 861.

**BJ :** Morton, D. C., Thuan, T.X., (1973), ApJ **180**, 705.

**BK:** Lawrie, D. G., (1983), ApJ **273**, 563.

## Appendix 1

**BL:** Baade, W., (1948), "Stellar Populations", ed D. J. K. O'Connell, (New York, Interscience), 1.

**BM:** Cram, T. R., Roberts, M.S., Whitehurst, R.N., (1980), A&AS **40**, 215.

**BN:** Davies, R. L., Efstathiou, G., Fall, S. M., Illingworth, G., Schecter, P. L., (1983), ApJ **266**, 41. [DEA].

**BO:** Davies, R. L., Illingworth, G., (1983), ApJ **266**, 516.

**BP:** Dressler, A., Sandage, A.R., (1983), ApJ **265**, 664.

**BQ:** Illingworth, G., (1981), "Structure and Evolution of Normal Galaxies", ed. Fall, Lyndon-Bell, (Cambridge, Cambridge Univ. Press).

**BR:** Illingworth, G., (1983), IAU Symp. **100** (Preprint).

**BS:** Roberts, M. S., Whitehouse, R.N., Cram, T.R., (1978), "Structure and Properties of Nearby Galaxies"; Proceedings of the Symposium, Bad Muenstereifel, West Germany, August 22-26, (1977), (Dordrecht, D. Reidel Publishing Co.), 169.

**BT:** Rogstad, D., Wright, M., Lockhart, I., (1976), ApJ **204**, 703.

**BU:** Terlevich, R., Davies, R. L., Faber, S., Burstein, D., (1981), MNRAS **196**, 381.

**BV:** Roberts, M. S., Whitehouse, R. N., Cram, T. R., (1978), "Structure and Properties of Nearby Galaxies"; Proceedings of the Symposium, Bad Muenstereifel, West Germany, August 22-26, (1977), (Dordrecht, D. Reidel Publishing Co.), 175.

## Appendix 2

**BW:** Nilson, P., (1973), "Uppsala General Catalog of Galaxies", Nova Acta Reg. Soc. Upsaliensis Ser V:A., Vol 1.

## Appendix 3a

**BX:** Bicay, M. D., Giovanelli, R., (1986), AJ **91**, 705.

**BY:** Bicay, M. D., Giovanelli, R., (1986), AJ **91**, 732.

**BZ:** Bicay, M. D., Giovanelli, R., (1987), AJ **93**, 1326.

**CA:** Baiesi-Pillastrini, G.C., Palumbo, G.G.C., (1986), A&A **163**, 1.

**CB:** Freudling, W., Haynes, M. P., Giovanelli, R., (1988), AJ **96**, 1791.

**CC:** Guthrie, B. N. G., Napier, W. N., (1996), A&A **310**, 353.

**CD:** Haynes, M. P., Giovanelli, R., (1984), AJ **86**, 758.

**CE:** Haynes, M. P., Giovanelli, R., (1986), ApJ **306**, 466.

**CF:** Roberts, M. S., (1984), AJ **73**, 945.

**CG:** Zaritzky, D., (1992), ApJ **400**, 74.

**CH:** Zaritzky, D., Smith, R., Frenk, C., White S. D. M., (1993), ApJ **405**, 464.

## Later Additions

**DA:** King, Stephen, (1990), "Four Past Midnight", 'The Langoliers', Penguin Books, Ltd., 1.

**DB:** Press, W. H., Flannery, B. P.,Teukolsky, S. A., & Vetterling, W. T. (1989), "Numerical Recipes (Fortran)", (Cambridge : Cambridge).

**DC:** Cocke, W. J., DeVito, C. D., Pitucco, A., (1997), Ap&SS **244**, 143, [(1996) Time Conf. Proc.] (CDP).

**DD:** Hoffman, G. L., Helou, G., Salpeter, E. E., Glosson, J., Sandage, A., (1997), ApJS **63**, 247.

**DE:** Lake, R. G., Roeder, R. C., (1972), JRAS Canada **66**, 11.

**DF:** Napier, W. N., Guthrie, B. N. G., (1997), Ap&SS **244**, 57, [(1996) Time Conf. Proc.].

**DG:** Newman, W., Terzian, Y., (1997), Ap&SS **244**, 127, [(1996) Time Conf. Proc.].

**DH:** Yu, J. T., Peebles, P. J. E., (1969), ApJ **158**, 103.

**DI:** Holt, J. (2012),"Why Does the World Exist?", pg 135 (Profile Books Ltd).